Molecular beam epitaxy growth and optical characterization of GaN/AlGaN nanowire heterostructures emitting in the ultraviolet

Matthias Belloeil

To cite this version:

Matthias Belloeil. Molecular beam epitaxy growth and optical characterization of GaN/AlGaN nanowire heterostructures emitting in the ultraviolet. Materials Science [cond-mat.mtrl-sci]. Université Grenoble Alpes, 2017. English. NNT : 2017GREAY021 . tel-01661587

HAL Id: tel-01661587
https://theses.hal.science/tel-01661587

Submitted on 12 Dec 2017

Communauté
UNIVERSITÉ Grenoble Alpes

THÈSE

Pour obtenir le grade de

DOCTEUR DE LA
COMMUNAUTÉ UNIVERSITÉ GRENOBLE ALPES

Spécialité : PHYSIQUE DES MATERIAUX
Arrêté ministériel : 25 mai 2016

Présentée par

Matthias BELLOEIL

Thèse dirigée par **Bruno DAUDIN**, CEA
et co-dirigée par **Bruno GAYRAL**, CEA

préparée au sein du **Laboratoire PHotonique, ELectronique et Ingéniérie QuantiqueS**
dans **l'École Doctorale Physique**

Croissance par épitaxie par jets moléculaires et caractérisation optique d'hétérostructures de nanofils GaN/AlGaN émettant dans l'ultraviolet

Molecular beam epitaxy growth and optical characterization of GaN/AlGaN nanowire heterostructures emitting in the ultraviolet

Thèse soutenue publiquement le **12 mai 2017**,
devant le jury composé de :

Monsieur ENRIQUE CALLEJA PARDO
PROFESSEUR, UNIV. POLYTECHNIQUE DE MADRID - ESPAGNE, Rapporteur
Monsieur RAPHAËL BUTTE
MAITRE D'ENSEIGNEMENT ET DE RECHERCHE, ECOLE POLYTECH. FEDERALE LAUSANNE SUISSE, Rapporteur
Monsieur PIERRE LEFEBVRE
DIRECTEUR DE RECHERCHE, CNRS DELEGATION LANGUEDOC-ROUSSILLON, Examinateur
Monsieur JOËL LEYMARIE
PROFESSEUR, UNIV. BLAISE PASCAL, CLERMONT-FERRAND, Examinateur
Monsieur HUBERT RENEVIER
PROFESSEUR, GRENOBLE INP, Président

Contents

Acknowledgements

On the 25th of November 2013, I started my PhD at CEA Grenoble. After many samples grown and analyzed with varying degrees of success, it comes to an end. Therefore, now is the time to thank all the people whom I have interacted with and who supported me during these 3 years. I apologize in advance to those I may have inadvertently forgotten in the following.

First of all, I would like to express my gratitude to my supervisors, Bruno GAYRAL and Bruno DAUDIN, for their guidance and advices as well as for giving me the opportunity to be a part of their nitride materials research team within the INAC/NPSC laboratory.

I then warmly thank all the members of the jury for having accepted to assess my work: Enrique CALLEJA and Raphaël BUTTÉ for the reports, Joël LEYMARIE, Hubert RENEVIER and Pierre LEFEBVRE for the reviews.

I also sincerely thank all our collaborators external to INAC: Hubert RENEVIER for supervising the resonant X-ray diffraction experiments at Synchrotron and for helping me process the data, Ana CROS for Raman and Kelvin probe force microscopy characterizations, Mathieu KOCIAK and Luis TIZEI for cathodoluminescence experiments, as well as Pierre LEFEBVRE, Thierry GUILLET, Pierre VALVIN, and Christelle BRIMONT for their warm welcome at Montpellier and for the time-resolved photoluminescence experiments.

As for internal collaborators, special thanks to Yoann CURE, Yann GENUIST and Didier BOILOT for technical support on the molecular beam epitaxy machine, especially during the second half of my PhD which was particularly challenging given the number of required interventions. I also thank Nicolas MOLLARD and Eric ROBIN for their training and advices on electron microscopy techniques, Fabrice DONATINI for his training on the cathodoluminescence setup at Neel Institute, Edith BELLET-AMALRIC for her training and discussions regarding X-ray diffraction, Lynda AMICHI and Catherine BOUGEROL for the electron microscopy and atom probe tomography experiments, Joël BLEUSE for his help on the time-resolved photoluminescence setup of the laboratory, Joël EYMERY and Christophe DURAND for their kindness and fruitful discussion, and Jean DUSSAUD for his general support.

Thanks to all PhD and post-doctoral students who are or were in the same boat. First, the team members: Thomas AUZELLE for having trained me on the molecular beam epitaxy setup and for helpful discussions, Xin ZHANG for his support, Zhihua FANG who shared my office and has tolerated me for three years, which is not always easy, as well as the two last PhD students whom I wish good luck, Madalina SILADIE, who will pursue the work on AlGaN nanowires, and Marion GRUART. Next, the other students at NPSC: Anna, Caroline, Agnès, Thibault, Damien, Samuel, Emanuel, Tobias, Jonas, Mark, Sirona, Mathieu, Akhil, Amine, Maria, David, Daria, Siew li and others for livening things up at and out of the lab. Last, I do not forget all the other students met at CEA, or during GANEX meetings and other events: special thanks to Fabien, Louis, Maxime, Aurélien, Damien, and Gautier for their sense of humor and kindness.

Finally, I would like to thank my family, especially my parents and my brothers, as well as my close friends who have supported me for all these years, whatever the challenges in life.

Main acronyms

III-N: III-Nitride

A°X: Acceptor-bound eXciton

AFM: Atomic Force Microscopy

AlGaN: Aluminum Gallium Nitride

AlInN: Aluminum Indium Nitride

AlN: Aluminum Nitride

BL: Blue Luminescence (band)

BF: Bright Field

CCD: Charge-Coupled Device

CF: Crystal-Field

CL: Cathodoluminescence

CPD: Contact Potential Difference

CVD: Chemical Vapor Deposition

CW: Continuous-Wave

D°X: Donor-bound eXciton

DAP: Donor-Acceptor Pair

DF: Dark Field

(E)DAFS: (Extended) Diffraction Anomalous Fine Structure

EDX: Energy-Dispersive X-ray

EQE: External Quantum Efficiency

ESRF: European Synchrotron Radiation Facility

(E)XAFS: (Extended) X-ray Absorption Fine Structure

FM: Frank-van der Merwe

FWHM: Full Width at Half Maximum

FX: Free eXciton

GaN: Gallium Nitride

(HA)ADF: (High-Angle) Annular Dark-Field

HBT: Hanbury Brown and Twiss

HEMT: High Electron Mobility Transistor

HF: HydroFluoric acid

HR: High-Resolution

HVPE: Hybrid Vapor-Phase Epitaxy

InGaN: Indium Gallium Nitride

InN: Indium Nitride

IQE: Internal Quantum Efficiency

IR: InfraRed

KPFM: Kelvin Probe Force Microscopy

LD: Laser Diode

LED: Light-Emitting Diode

LO: Longitudinal Optical

MAD: Multi-wavelength Anomalous Diffraction

MD: Misfit Dislocation

ML: MonoLayer

MOVPE: MetalOrganic Vapor Phase Epitaxy

NBE: Near Band Edge

NID: Non-Intentionally Doped

NW: NanoWire

(µ-)PL: (micro-)PhotoLuminescence

(PA-)MBE: (Plasma-Assisted) Molecular Beam Epitaxy

PMT: Photomultiplicator

QCSE: Quantum-Confined Stark Effect

QD: Quantum Dot

QDisk: Quantum Disk

QW: Quantum Well

QWire: Quantum Wire

RF: Radio-Frequency

RHEED: Reflection High Energy Electron Diffraction

RSM: Reciprocal Space Map

SAG: Selective Area Growth

SCCM: Standard Cubic Centimeters per Minute

SEM: Scanning Electron Microscopy

SO: Spin-Orbit

(S)TEM: (Scanning) Transmission Electron Microscopy

SF: Stacking Fault

SK: Stranski-Krastanov

TD: Threading Dislocation

TO: Transverse Optical

UHV: Ultra High Vacuum

UV: UltraViolet

VW: Volmer-Weber

WZ: Wurtzite

XRD: X-Ray Diffraction

ZB: Zinc Blende

ZnO: Zinc Oxide

0. Introduction

Over the past 25 years, semiconductors of the III-Nitride (III-N) family, namely gallium nitride (GaN), aluminum nitride (AlN), indium nitride (InN) and their associated alloys, have been arousing increasing interest at both academic and industrial levels, especially since the fabrication of the first III-N-based light-emitting diodes (LEDs) and laser diodes (LDs) in the 1990s [1-8]. In virtue of their direct bandgap and the wide range of emission wavelengths covered by the different nitride alloys, spanning from the near infrared (IR) to the deep ultraviolet (UV) over the whole visible spectrum, III-N semiconductors have been thenceforth largely used for manufacturing optoelectronic devices such as blue/green/white LEDs and violet/blue/green LDs, particularly the 405 nm LDs used in the Blu-Ray technology [9]. In addition to their interesting optoelectronic properties, III-N materials exhibit great chemical stability, high electron mobilities, significant breakdown voltages, and good thermal conductivity, making them suitable for a broad range of devices operating at high temperature, high frequency and/or high power [10-13].

0.1 Brief history of III-Nitride semiconductor research: from prehistory to the recent interest for nanowires

The first papers about III-N semiconductors date from the beginning of the 20th century and report growth of polycrystalline AlN [14], GaN [15] and InN [16] in 1907, 1932 and 1938, respectively. Yet, the epitaxial growth of III-N two-dimensional (2D) layers was achieved no earlier than in the 1960s and 1970s. Indeed, GaN grown in epitaxy on sapphire was reported for the first time in 1969, using the hybrid vapor phase epitaxy (HVPE) technique [17], while growth of nitride epilayers by other methods such as metalorganic vapor phase epitaxy (MOVPE) or molecular beam epitaxy (MBE) was notified respectively in 1971 [18] and in 1975 [19]. The three latter techniques will be briefly presented in Subpart 1.3.1. GaN grown at that time exhibited poor crystal quality and high *n*-type conductivity, although it was not intentionally doped. Efforts aiming at enhancing its crystal quality and at smoothing layers finally led to the growth of the first high-crystalline quality GaN film in 1986, deposited on an AlN buffer layer [20]. Then, the first GaN p-doped layer was achieved in 1989 using magnesium (Mg) dopants [21]. The two latter breakthroughs paved the way for the achievements in III-N-based optoelectronics mentioned above. In acknowledgements of their pioneering and tremendous work in the latter field, Akasaki, Nakamura and Amano were awarded the 2014 Nobel Prize in physics.

Interestingly, during the crusade led in the 1980s and early 1990s to optimize GaN film growth conditions, GaN was noticed to grow as coalesced columnar crystals [22]. A few years later, in 1997-1998, it was shown that GaN synthesized by MBE could nucleate as well-separated nanocolumns [23, 24], under specific growth conditions (explicated further in Subpart 2.1.3.1): the first self-induced nitride nanowires (NWs) were born, starting within the III-N community a new research field whose interest mainly lies in:

- The absence of extended crystallographic defects, such as dislocations (described in Subpart 1.3.2.2) or grain boundaries commonly observed in the 2D case, in these bottom-up nanostructures [25], even when grown on highly mismatched substrates. This feature results from the high aspect ratio (length/diameter) of NWs allowing easy strain relaxation around their periphery and will be tackled in the following of the manuscript.
- The relative versatility of the NW growth allowing one to tune, in some extent, their dimensions, density and structure, as detailed further in Subpart 2.1.3.1, and to overcome the fundamental limits of conventional top-down approaches such as lithography [26, 27].
- The more straightforward growth of heterostructures along non-polar directions, in order to cancel the quantum-confined Stark effect (QCSE) explained later in Subpart 1.2.3.2. Indeed, such growth remains challenging for 2D layers owing to the strong anisotropy of non-polar surface properties [28-30], resulting in higher density of threading dislocations and stacking faults (SFs) than 2D growth along polar direction [31] or NW radial growth on lateral facets [32, 33].

Growth of NWs by other techniques which would allow large scale production, such as chemical vapor deposition (CVD) or vapor phase epitaxy (VPE), was also investigated and turned out to be more challenging. Catalyst-assisted approaches were firstly investigated in the early 2000s [34, 35] but the spatial orientation and/or epitaxial relation of columns with the substrate appeared difficult to control. Pre-patterned substrates were then used to improve the NW orientation [36, 37], which significantly complicates the overall procedure. Concomitantly, catalyst-induced NW growth got better mastered [38, 39]. Eventually, self-assembled well-oriented GaN NWs were successfully synthesized by MOVPE on a silicon nitride (SiN_x) buffer layer pre-deposited in situ [40] or on bare sapphire [41]. Regarding the HVPE technique, growth of ultra-long GaN NWs, interesting for industrial purpose, was recently reported [42]. It must be noted that the use of catalyst in the elaboration of nanocolumns may result in the degradation of NW structural and optical properties, in view of studies performed on MBE samples [43]. Indeed, such NWs contained more basal-plane SFs and luminesced more weakly than catalyst-free NWs due to contamination from the metal seed [44].

Regarding applications, III-N wires are considered as serious challengers of conventional 2D layers in order to push further the efficiency of devices or, at least, to reduce the production costs. In optoelectronics, companies such as Aledia or Glō [45, 46] are aiming at manufacturing highly efficient and cheaper white LEDs, based on GaN wires grown on inexpensive silicon (Si) substrates. Moreover, the higher aspect ratio of NWs is expected to lead to reduction in device volumes, in other words decrease in the amount of deposited material, while preserving, or even increasing, efficiency. In this perspective, the growth of radial heterostructures on large NW lateral facets in order to suppress QCSE has been considered for devices. In particular, LEDs based on such structures have been already demonstrated, as reported for radial InGaN/GaN [47-49] quantum wells (QWs). Other types of radial devices, like high electron mobility transistors (HEMT) and photovoltaic cells, were also elaborated, respectively using GaN/AlGaN/AlN [50] and InGaN/GaN [51-53] core-shell structures.

In virtue of their unique properties, nitride NWs opened new application fields that were hardly accessible to thin films. For instance, their dimensions make them the smallest dielectric objects permitting optical waveguiding [54, 55] or electrical contacting [56-58]. As another example, such NWs present, due to their anisotropic geometry, optical and electrical properties both depending on their orientation, which emphasizes their potential for polarization-dependent detectors [59]. In addition, in view of their high surface-to-volume ratio, III-N NWs exhibit enhanced interaction with the surrounding medium, making them particularly suitable not only for chemical [60-62] or biological [63, 64] nanosensing but also for chemicals generation, resulting for instance from water splitting [65, 66]. Finally, given their interesting piezoelectric properties (see related coefficients defined in Subpart 1.1.3), nitride NWs are promising for piezoelectric nanosensors [67] and nanogenerators [68].

0.2 Context and motivations of the present research

My PhD work is focused on III-N semiconductors emitting in the UV over the 200-350 nm range, namely the AlGaN alloy. The latter material has great potential for solid-state UV-light-emitting devices, namely LEDs and lasers, intended for a broad range of applications in the UV-A (3D printing, UV curing), -B (plant growth lighting, dermatological phototherapy around 310 nm) and -C range (sterilization and water purification around 260 nm, sensing at lower wavelengths) [69], as depicted in Figure 0.2.1 (a). The development of such AlGaN-based devices as an alternative to sources currently available over the investigated emission range presents strong economic, environmental and societal interests. Indeed, most commercial UV sources are still gas-based (mercury lamps, deuterium lamps, excimer lasers, etc.), and therefore inefficient, environmentally harmful and difficult to transport [69, 70], on the whole.

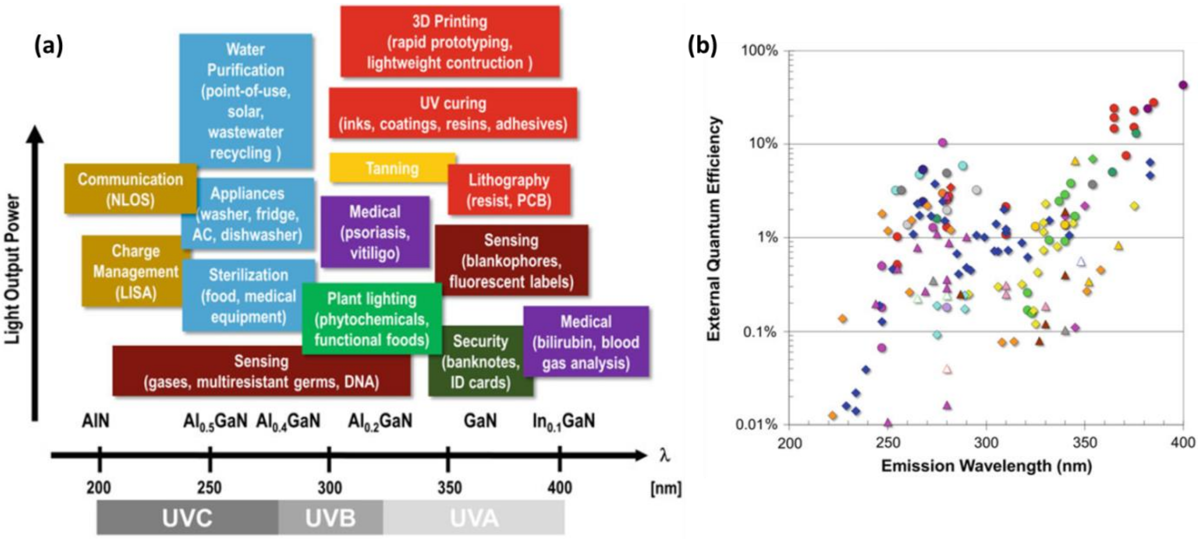

Figure 0.2.1: (a) Applications of UV-light emitting devices in the UV-A (400-320 nm), UV-B (320-280 nm) and UV-C range (280-200 nm). (b) External quantum efficiency (EQE) of 2D UV-LEDs as a function of emission wavelength (2016). Taken from [69].

During this PhD, Al(Ga)N was grown as NWs in order to attain higher material crystalline quality than for 2D layers, which results from the absence of extended defects such as dislocations or grain boundaries in these nanostructures [71, 72], as already mentioned in Subpart 0.1. Regarding applications, this enhancement should allow NW-based UV-LEDs to reach much higher efficiency than their 2D counterparts. So far, only low efficiencies have been reported for 2D structures, especially for short emission wavelengths [69, 73] as exhibited in Figure 0.2.1 (b). It must be noted that the use of NWs is expected to result in much lower efficiency improvement for LEDs emitting in the visible range, since conventional 2D LEDs made of InGaN/GaN heterostructures already exhibit very high efficiency, attributed to very marked carrier localization in the InGaN alloy [74], as well as to extremely efficient photon extraction designs. Indeed, internal quantum efficiencies (IQEs) above 90% [69, 75] and external quantum efficiencies (EQEs) around 85% [76] were reported for such devices.

High-efficiency UV-LEDs based on Al(Ga)N NWs were demonstrated recently, following two different approaches: p-i-n NW junctions [77-82] and polarization-induced doping in NW structures [83-87], both grown by MBE on top of self-induced and randomly organized GaN NW templates by MBE. Regarding the first approach, an IQE of about 80% was even reached for AlN NW-based LEDs emitting at 210 nm [78]. At higher emission wavelengths, droop-free LEDs with intrinsic active zones consisting of Ga-rich $Al_xGa_{1-x}N/Al_yGa_{1-y}N$ quantum disks (QDisks) were recently reported [88]. Organized arrays of AlGaN p-i-n junctions were also achieved by selective area growth (SAG) of GaN NW templates [89]. As for the second approach, the desired polarization-induced doping type results from both compositional grading (Al-rich to Al-poor $Al_xGa_{1-x}N$ or reverse) [90, 91] and NW polarity

[92]. It can be also complemented by the conventional and intentional introduction of dopant impurities [83, 93, 94]. For both types of structure, very thin tunnel junctions were also investigated and demonstrated to improve carrier injection within the active zone [95-97].

In addition, AlGaN NW-based lasers, operating in the UV-B and -C range at both low and room temperatures, were reported [81, 82, 98-100]. In such devices, consisting in p-i-n NW junctions similar to those in LEDs mentioned above, lasing was demonstrated to result from two main features: first, the optical confinement along the vertical direction (c-axis) due to the effective refractive index variation induced by the NW inverted tapered geometry; second, the optical micro- (μ-)/nano-cavities that are spontaneously formed by ensembles of self-organized NWs. Their formation probability can be maximized for specific fill factors, which depend on the average NW diameter and the NW density. The latter can be easily tuned through changes in growth kinetic parameters, which will be highlighted in Subpart 2.1.3.1.

At last, for both LEDs and lasers based on Al-rich AlGaN or AlN NWs, light extraction issues, due to the switch of emitted light polarization that will be detailed further in Subpart 1.2.1.1, can be partially solved by optimizing the NW geometry [101], namely the NW dimensions, the NW spacing and the thickness of various NW sections within the structure.

Although the brief overview of the III-N field, given in the previous subpart and the present one, emphasizes that a significant part of this research community is directing its efforts towards the development of devices, there is still a large interest, shared by several research groups like ours, in understanding the fundamental properties of nitride semiconductor materials. The latter approach is anyway required to completely control every step of the fabrication of devices.

In the case of AlGaN NWs, the issue of alloy inhomogeneity at the nanoscale remains obscure. In order to make it clearer, the latter and associated carrier localization will be investigated, especially through optical characterization, in chapter 3. For our experiments, AlGaN NWs will be grown in various conditions in order to potentially tune the compositional fluctuations within the alloy and therefore probe, if possible, localization centers of different sizes and Al compositions.

Concomitantly, doping in Al(Ga)N NWs, especially p-type, is far from being understood and controlled as well. In particular, the issue of dopant incorporation as well as optical and electrical activation in such NWs remains unclear. The latter will be examined in Al(Ga)N NW pn junctions in chapter 4.

0.3 Organization of the manuscript

In the first chapter of this manuscript, we will introduce the basic properties of III-N materials needed for the understanding of the manuscript. More specifically, the structural and electronic properties of nitride semiconductors will be highlighted, before briefly describing the main techniques allowing their epitaxial growth.

Then, in chapter 2, the numerous experimental methods used to grow and characterize our NW samples during this PhD will be presented more or less exhaustively. We will primarily detail the MBE growth technique, focusing on the specificities of the MBE machine and the growth of GaN and $Al_xGa_{1-x}N$ NWs. Then, the structural and optical characterization techniques used in the present work will be described in order to fully understand the following pages.

Next, in chapter 3, we will investigate fundamental properties of non-intentionally doped (NID) $Al_xGa_{1-x}N$ NW sections grown in various conditions on top of GaN NW templates. After presenting the structural peculiarities of grown samples, their optical properties will be examined. We will especially scrutinize the carrier localization observed in very small volume of $Al_xGa_{1-x}N$ material, namely single dispersed NWs.

Finally, in chapter 4, doping in $Al_xGa_{1-x}N$ NW sections, still grown on top of GaN NW templates, will be explored. In particular, $Al_xGa_{1-x}N$ pn junctions will be investigated in order to evidence peculiar structural, optical and electrical signatures resulting from n- and p-doping. Concomitantly, AlN samples will be also studied.

In addition, two annexes are appended to this manuscript: Annex 1 provides general notions about crystallography in hexagonal structures, whereas Annex 2 presents extra resonant X-ray diffraction (XRD) experiments and related results.

0.4 Collaborations

Before ending this introduction, it must be emphasized that the results presented hereafter are the fruit of several collaborations, both internal to the “Nanophysics and semiconductors” (NPSC) group within the “Institut nanoscience et cryogénie” (INAC) and external to the laboratory. The collaborators who contributed the most directly to the achievement of this manuscript are named below.

MBE growth was performed under the supervision of my PhD advisor Bruno Daudin (NPSC) and in collaboration with current and former PhD students from the group.

Photoluminescence (PL) results were mostly obtained under the supervision of my PhD co-advisor Bruno Gayral (NPSC). A few time-resolved PL (TRPL) experiments were also performed at Charles Coulomb laboratory in Montpellier, in collaboration with Pierre Valvin, Thierry Guillet, Christelle Brimont and Pierre Lefebvre.

Nano-cathodoluminescence (nanoCL) investigations were performed by Mathieu Kociak and Luiz Tizei from “Laboratoire de physique des solides” (LPS), Orsay.

Raman and Kelvin probe force microcopy (KPFM) analysis were carried out in collaboration with Ana Cros’ group, from the Institute of material science, University of Valencia, Spain.

Resonant XRD characterizations were achieved under the supervision of Hubert Renevier from the “Laboratoire des Matériaux et du Génie Physique” (LMGP) of Grenoble.

A few electron microscopy observations were carried out in collaboration with Lynda Amichi and Catherine Bougerol (NPSC).

1. Properties and growth of standard III-Nitride semiconductors

1.0 Introduction

This first chapter intends to give an overview of the basic properties of III-N semiconductors, only focusing on the GaN, AlN and InN binaries, especially GaN and AlN, as well as their associated ternary alloys. Its aim is not to be exhaustive but to give the most relevant notions for the comprehension of the manuscript. First, the structural properties of nitrides will be presented. Second, our focus will turn toward the electronic properties of nitrides. Last, we will briefly describe the main techniques allowing the epitaxial growth of III-N semiconductors.

1.1 Structural properties of III-Nitride semiconductors

The objective of the following subparts is to get acquainted with the basic structural properties of III-N materials at the center of this work. We will first describe the crystal structure of the most common crystal phases of nitrides (wurtzite and zinc-blende). Then, the notion of polarity in wurtzite crystals will be defined. Finally, the peculiarities of polarization in wurtzite nitrides will be introduced.

1.1.1 Crystal structures of nitride materials

The nitride semiconductor family (InN, GaN, AlN, as well as their ternary and quaternary alloys) can crystallize in three different arrangements: the wurtzite (WZ) (α-phase), the zinc-blende (ZB) (β-phase) and the rock salt (γ-phase). Given that the rock salt structure can only be obtained under extreme conditions incompatible with epitaxial growth, such as very high pressures [13, 102], we will no longer consider this phase in the following of the manuscript. The two other phases, WZ and ZB, are described hereafter. A few properties will be also provided for materials related to the substrates we mainly used during this PhD: Si and silicon nitride (Si_3N_4). Si_3N_4 (β-phase, hexagonal) is obtained when nitriding the Si wafers before growing III-N materials.

The WZ and ZB structures for III-N semiconductors are presented in Figure 1.1.1.1, whereas the related unit cells are given in Figure 1.1.1.2. The diamond structure for Si is also provided in Figure A.1.3.1 of Annex 1.3.

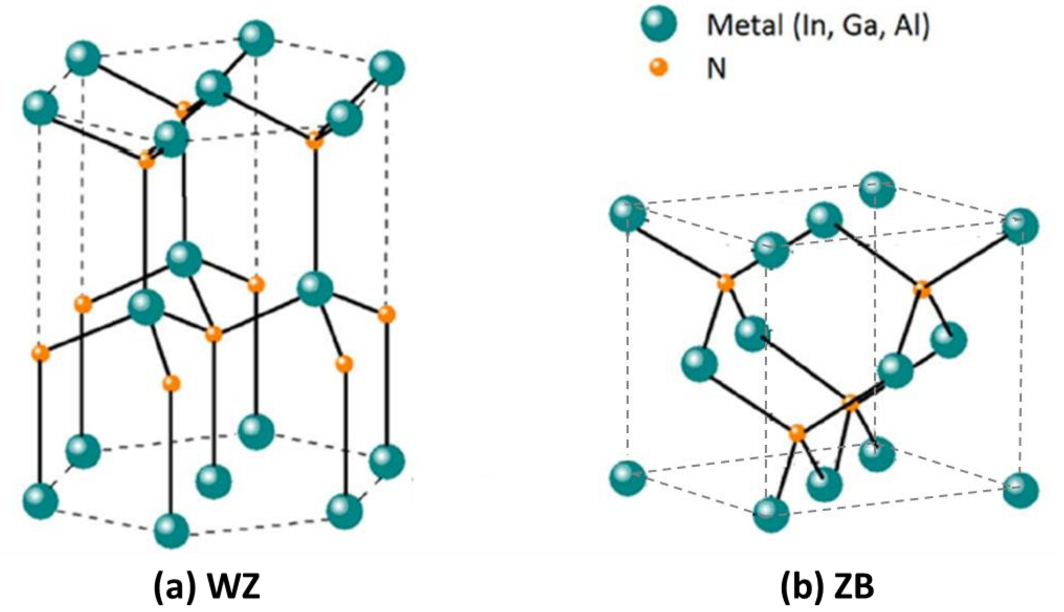

Figure 1.1.1.1: Sketch for: (a) the ideal wurtzite (WZ) and (b) the ideal zinc-blende (ZB) structures of III-N semiconductors. Adapted from [103].

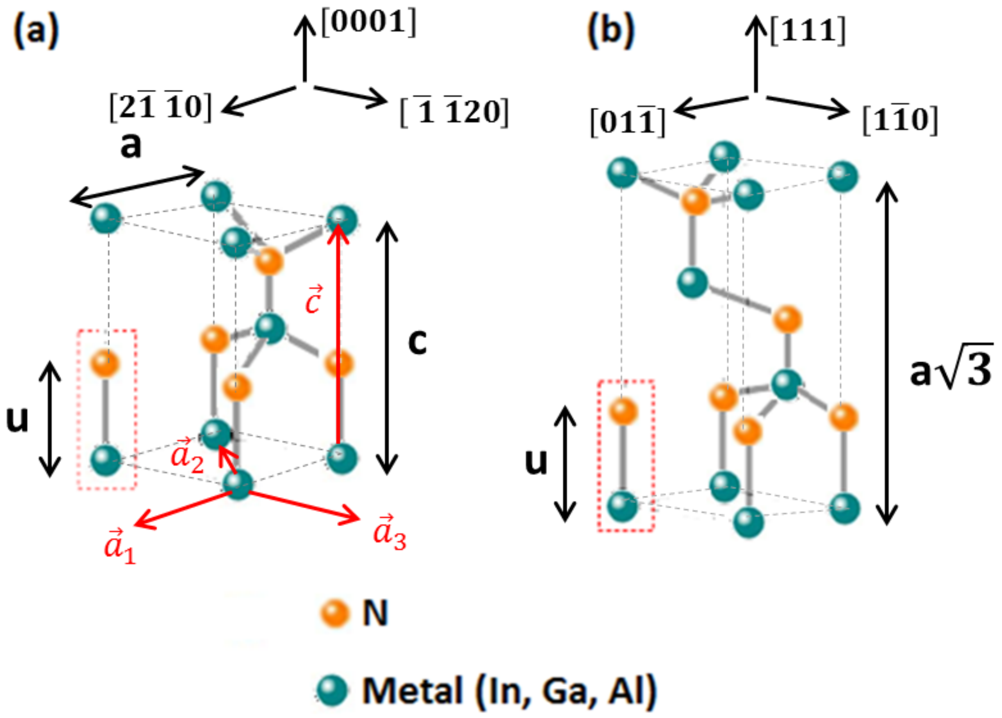

Figure 1.1.1.2: Sketch of the ideal unit cell of (a) the WZ structure and (b) the ZB structure, for nitrides. The basal vectors are also given for the WZ unit cell.

The WZ structure belongs to the space group $P6_3mc$ and is composed of two interpenetrating hexagonal close-packed sublattices, formed by the metallic and the N atoms respectively and ideally shifted by $u = \frac{3}{8}c$ in the [0001] direction (see Annex 1.1 for the four index notation description). Thus, each atom is tetrahedrically coordinated with bond lengths equal to $\frac{3}{8}c$. In other words, each group-III element (respectively N atoms) is bonded to four N atoms (respectively four group-III elements). In practice, for nitride semiconductors, the WZ cell is not perfect and the c/a ratio slightly differs from the ideal case ($c/a = 1.633$). Consequently, the tetrahedra formed by the atoms are deformed (either stretched or compressed) in the [0001] direction. Lattice parameters a and c, u as well as the effective c/a ratio of WZ nitride binaries, Si and Si_3N_4 are given in Table 1.1.1.1, listing other properties as well and described in the following.

	AlN	GaN	InN	Si	Si_3N_4
Hexagonal - a	3.112 Å	3.189 Å	3.548 Å		7.595 Å
Hexagonal - c	4.982 Å	5.185 Å	5.760 Å		~3 Å
Hexagonal - c/a	1.601	1.626	1.609		
Hexagonal (WZ) - u	1.903 Å	1.955 Å	2.171 Å		
Diamond - a				5.43088 Å	
Thermodynamic energy difference between WZ and ZB (meV.at^{-1})	18.4	9.9	11.4		

Table 1.1.1.1: Main lattice parameters and ratios (values at 300 K) for the nitride binaries, Si and Si_3N_4. Values taken from [104, 105].

The primitive unit cell (see Figure 1.1.1.2) of WZ nitrides contains 4 atoms: 2 metallic ones (gallium (Ga), aluminum (Al), or indium (In)) and 2 nitrogen (N) ones. The coordinates of these atoms are:

$$\begin{gathered} Metal_1 = 0\vec{a}_1 + 0\vec{a}_2 + 0\vec{c} \\ Metal_2 = \frac{2}{3}\vec{a}_1 + \frac{1}{3}\vec{a}_2 + \frac{1}{2}\vec{c} \\ N_1 = 0\vec{a}_1 + 0\vec{a}_2 + u\vec{c} \\ N_2 = \frac{2}{3}\vec{a}_1 + \frac{1}{3}\vec{a}_2 + (\frac{1}{2} + u)\vec{c} \end{gathered} \tag{1.1.1.1}$$

where $\vec{a}_1$, $\vec{a}_2$ and $\vec{c}$ are the basal vectors of the hexagonal cell displayed in Figure 1.1.1.2 and more detailed in Annex 1.1.

The ZB phase is constituted of two face centered cubic lattice shifted of $\frac{1}{4}\sqrt{3}a$ in the [111] direction (see Figure 1.1.1.2). In this case, each atom is tetrahedrically coordinated as well but the corresponding plane sequences along the [111] direction is ABCABC (see Figure 1.1.1.3) where the C plane is rotated by 60° compared to A. In other words, ZB [111] direction resembles WZ [0001] direction except for the 60° rotation in its tetrahedra.

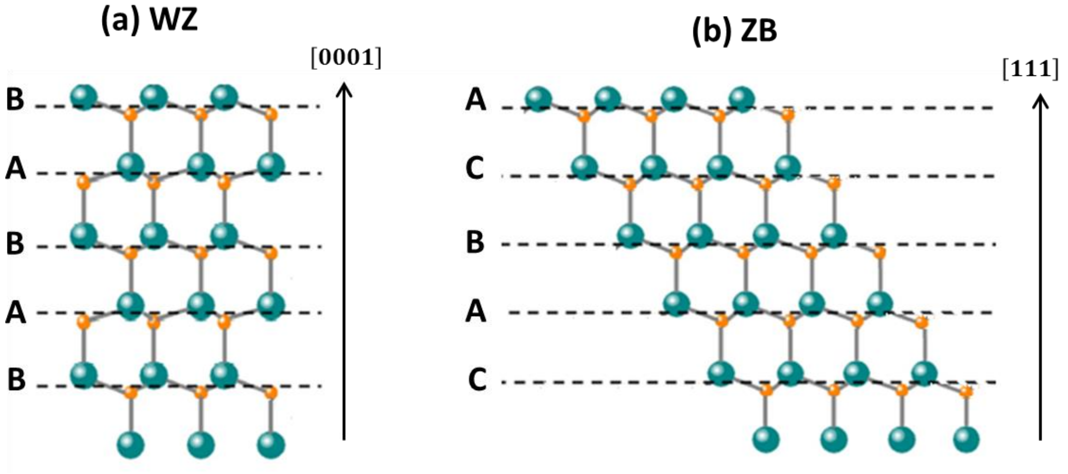

Figure 1.1.1.3: Sketch of (a) WZ and (b) ZB stacking sequences for III-N semiconductors.

The WZ phase was shown to be more thermodynamically stable than the ZB phase, although the gain in energy per atom of the WZ phase in comparison with the ZB one is not so large (see Table 1.1.1.1) [106]. Consequently, it is possible to grow ZB nitrides either by using cubic substrates [107, 108] or by introduction of SFs inside a WZ section [109]. In this work, the used substrates (mostly Si (111)) and growth conditions were such that we were not confronted to the ZB phase, but only to WZ. Therefore, we will not focus much on the ZB phase in the following of the manuscript. In the NW case, growth on two types of surface can occur: c-planes and m-planes, which respectively constitute the apex and the sidewalls of the NWs. Such planes are more described in Annex 1.1. It is worth noting that these two types of planes do not have the same atomic surface density, whatever the nitride binaries (see Table 1.1.1.2). This difference of atomic surface density leads to different growth rates: in the same growth conditions, the m-plane/c-plane growth rate ratios can be directly derived from the ratios of atomic surface densities given in Table 1.1.1.2 and are respectively about 0.924, 0.939 and 0.937 for AlN, GaN and InN.

	AlN	GaN	InN	Si	Si_3N_4
c-plane (0001) – N	5.962	5.677	4.586	-	4.004
c-plane (0001) – metal	5.962	5.677	4.586	3.915	3.003
m-plane $(1\bar{1}00)$ – N	6.450	6.048	4.893	-	-
m-plane $(1\bar{1}00)$ – metal	6.450	6.048	4.893	-	-

Table 1.1.1.2: Surface atomic densities (in a single monolayer, units: 10^{14} atoms.cm^{-2}) for the nitride binaries, Si and Si_3N_4. These densities are given for metallic and N species, as well as for c- and m- planes. Values deduced from [105].

1.1.2 Polarity in wurtzite nitrides

The absence of center of symmetry in the WZ structure (see Figure 1.1.1.1) implies that the $[0001]$ and the $[000\bar{1}]$ directions are not equivalent. In order to distinguish them, we usually consider the direction of the metal-N bond that is collinear to the c-axis of the WZ cell. The vector going from the metallic atom and pointing towards N conventionally defines [0001], the positive direction of the c-axis (Figure 1.1.2.1). A structure is said to be metal-polar when its growth direction is $[0001]$. Reciprocally, a structure is said to be N-polar when its growth direction is $[000\bar{1}]$.

The knowledge and control of the polarity of a given structure is not to be neglected, as polarity has several consequences on growth (incorporation rate of extra atoms for doping and alloying [110], incorporation of defects [111-113], adatom mobility [114]) and band engineering [92, 115, 116]. Its determination is not trivial, especially for small objects such as nitride NWs. To do so, various techniques exist, such as anomalous XRD [117, 118], KOH selective etching [117], KPFM [119], Convergent Beam Electron Diffraction (CBED) [120], Low Energy Electron Diffraction (LEED) [121], Electron Energy Loss Spectroscopy (EELS) [122] or X-ray Photo-electron Diffraction (XPD) [123]. All these techniques were reported to allow the successful determination of the polarity of single or ensembles of GaN NWs. A few of them were used in the context of this PhD work to determine either polarity or for other purposes, and will be detailed in the following of the manuscript.

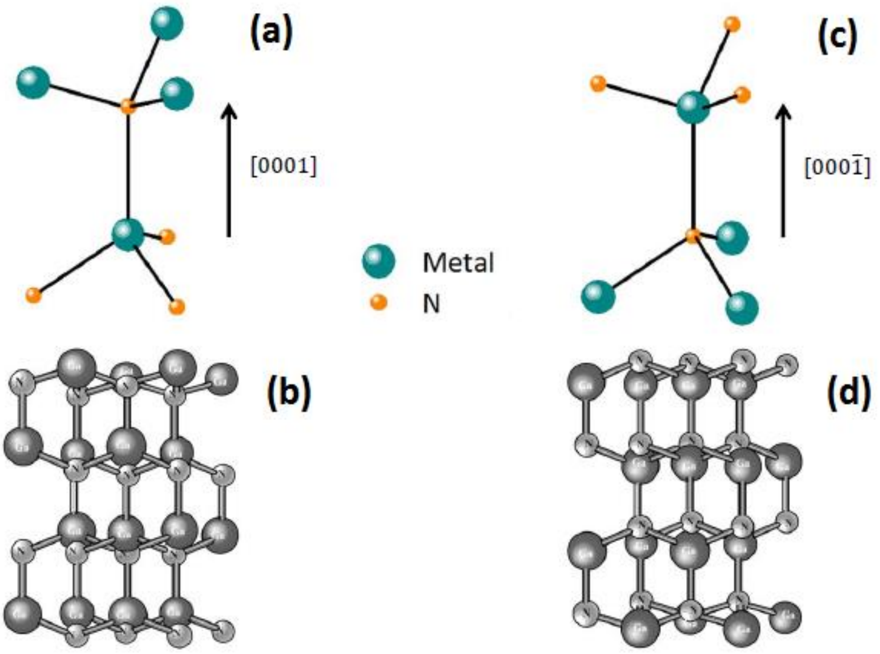

Figure 1.1.2.1: (a) Metal-polar and (c) N-polar directions in the nitride WZ cell. When the growth direction is along the $[0001]$ direction, the structure is said to be metal-polar. Reciprocally, when the growth direction is along $[000\bar{1}]$, a structure is N-polar. Taken from [103] (b) Ga-polar and (d) N-polar stick-and-ball representations of WZ GaN. Sketches taken from [102].

1.1.3 Spontaneous and piezoelectric polarization in wurtzite nitrides

In WZ nitrides, the difference of electronegativity between metallic and N atoms induces local spontaneous polarization vectors along each III-N bond. Due to the non-centrosymmetric character of the WZ cell, amplified by the c/a ratio deviation from its theoretical value, these polarization vectors do not compensate. Consequently, a residual total spontaneous polarization remains along the c-axis (also called polar direction) in the WZ cell. Values of this spontaneous polarization vector can be found in the literature [124, 125].

Moreover, strain within the structure, inducing crystal deformation (changes in lattice parameters) and generally resulting from heteroepitaxial growth further described in Subpart 1.3, produces an additional piezoelectric polarization. Thus, in a given nitride material, the overall polarization, for which the related vector will be noted $\vec{P}$, is given by both the spontaneous and the piezoelectric polarization. Depending on whether the material is stretched or compressed (tensile or compressive strain), the piezoelectric contribution to the overall polarization either adds to or subtracts from the spontaneous one. The three components P_i^{piezo} of the piezoelectric polarization vector $\vec{P}^{piezo}$, where $i = \{x, y, z\}$, can be expressed as:

$$P_i^{piezo} = \sum_{j=1}^{3}\sum_{k=1}^{3} e_{ijk}\epsilon_{jk} \qquad (1.1.3.1)$$

where e_{ijk} are the 27 piezoelectric coefficients and ϵ_{jk} is the strain tensor. Taking into account the WZ structure symmetry, Equation (1.1.3.1) can be reduced. Replacing the pairs of indices $jk = \{xx, yy, zz, yz, zx, xy\}$ by the indices $\{1, 2, 3, 4, 5, 6\}$ here in order to lighten notations, we can rewrite Equation (1.1.3.1) as [126]:

$$\begin{pmatrix} P_1^{piezo} \\ P_2^{piezo} \\ P_3^{piezo} \end{pmatrix} = \begin{pmatrix} 0 & 0 & 0 & 0 & e_{15} & 0 \\ 0 & 0 & 0 & e_{15} & 0 & 0 \\ e_{13} & e_{31} & e_{33} & 0 & 0 & 0 \end{pmatrix} \begin{pmatrix} \epsilon_1 \\ \epsilon_2 \\ \epsilon_3 \\ \epsilon_4 \\ \epsilon_5 \\ \epsilon_6 \end{pmatrix} \qquad (1.1.3.2)$$

Different values of the piezoelectric coefficient e_{ij} can be found in the literature [124, 127]. In spite of the disparities, all the reported values for nitrides are always about one order of magnitude larger than those for other families of III-V or II-VI semiconductors (except zinc oxide (ZnO)), which results from the more significant ionic character of III-N bonds discussed later in Subpart 1.2.1.1.

We will see in Subpart 1.2.3.2 that the overall polarization described in this subpart can have spectacular effects on the band structure of nitride heterostructures.

1.2 Electronic properties of III-Nitride semiconductors

The electronic properties of nitrides directly affect their optical properties. Indeed, photons emitted by such materials originate from electronic transitions, namely carrier recombinations. Moreover, many electronic properties for the AlGaN/GaN NWs investigated in this work can be derived from those for bulk materials. Thus, in order to fully understand the emission properties of our NW samples, the knowledge of the general electronic properties of WZ nitride binaries, namely their band structure, is first required. Then, we will get acquainted with the peculiarities of ternary alloys. Eventually, we will finally highlight the effect of material dimensionality, including quantum objects and NWs, on the band structure of WZ nitrides.

1.2.1 Band structure of bulk wurtzite III-Nitride binary crystals

1.2.1.1 Bandgap of bulk wurtzite nitride binary crystals

For III-N semiconductors, the band structure is formed by the interaction between the valence orbits s and p of both metal and N atoms (s^2p^1 for metals and s^2p^3 for N). For a given nitride binary, the energy value of the bandgap separating the conduction band from the valence band in the band structure depends on several parameters, including:

- The covalence of the metal-N bond. The latter is function of the atom size and the bond length u.
- The ionic character of the metal-N bond C_{ionic}, calculated using Pauling's law from the electronegativity difference $\Delta\chi$ between the metal and the N atom. Such character reflects the average energy gap between the orbitals of both atoms.
- The metallic character of each element, which is related to the energy gap between their s and p orbitals $E_p - E_s$.

Values for u, $\Delta\chi$, C_{ionic} and $E_p - E_s$ for the metal atom are given in Table 1.2.1.1. It can be directly noticed from the latter that the covalence of the metal-bond, related to u, is the main parameter governing the bandgap value.

Nitrides exhibit a direct bandgap, which means that the minimum of their conduction band is right above the maximum of their valence band at the Γ point of the Brillouin zone. In the following, we will only focus on the band structure region around this Γ point. In the WZ arrangement, strong crystal-field (CF) and spin-orbit (SO) interactions induce a splitting of the six-fold degenerate level usually associated with cubic systems. Consequently, as sketched in Figure 1.2.1.1 (a), the band structure for WZ nitrides presents three valence subbands: the heavy holes (HH) band, the light holes (LH) band and the split-off band. More specifically, HH and LH subbands are lifted by the SO splitting and the split-off band by the crystal field. Figure 1.2.1.1 (b) highlights the band structure peculiarities for the GaN and AlN binaries: the three resulting energy gaps, labeled A (namely the bandgap E_g), B and C from the lowest to the highest gap, and their associated transition polarizations are represented. In addition, the energies Δ_{SO} and Δ_{CF}, respectively related to SO and CF splitting, are indicated. Experimental values of the three energy gaps, as well as Δ_{CF} and Δ_{SO}, are provided in Table 1.2.1.1.

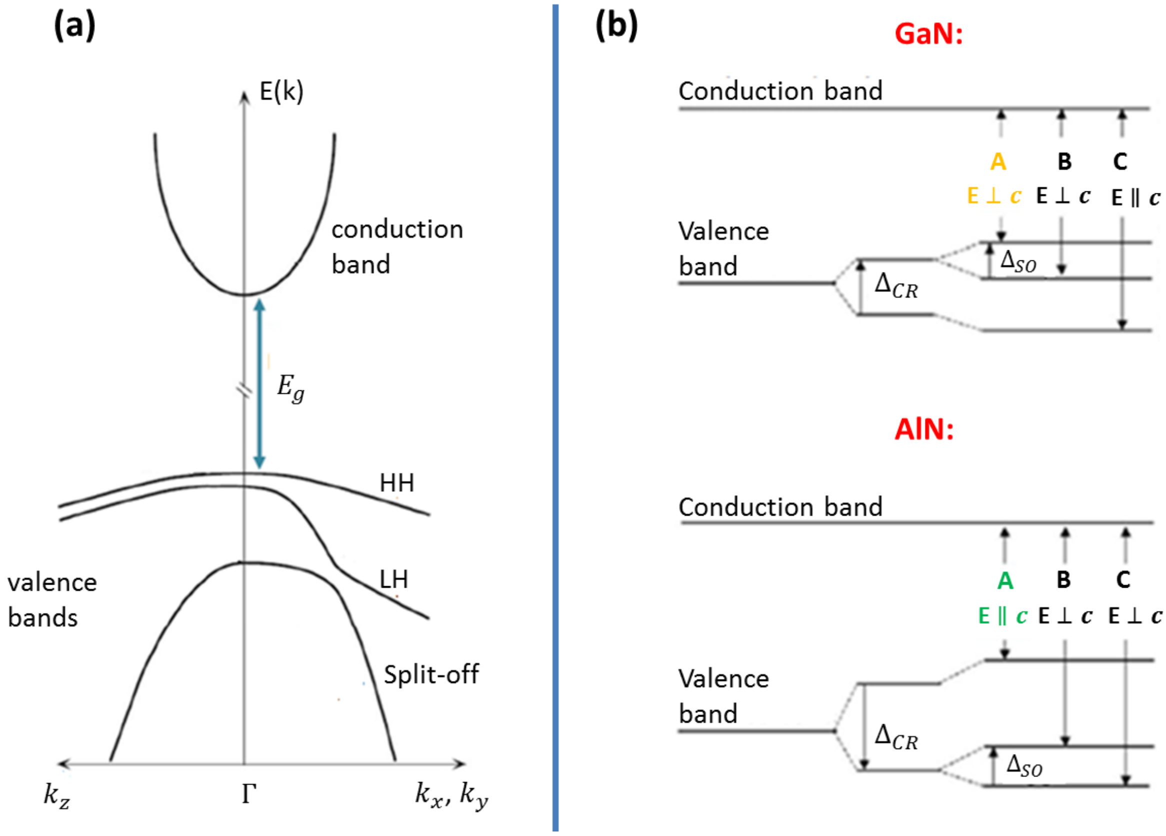

Figure 1.2.1.1: (a) General shape of the band structure for WZ nitrides around the Γ point of Brillouin zone. (b) More detailed sketch of the band structure at Γ, for GaN at the top and AlN at the bottom. Adapted from [102, 105].

	AlN	GaN	InN
u (Å)	1.903	1.955	2.171
$\Delta\chi$ (eV)	1.43	1.23	1.26
C_{ionic} (%)	72	51	54
$E_p^{III} - E_s^{III}$ (eV)	5.25	6.47	5.43
E_g (or E_g^A) (eV)	6.088	3.505	0.78
Δ_{CF} (meV)	-225	11	17
Δ_{SO} (meV)	19	22	3
E_g^B (eV)	6.304	3.511	0.782
E_g^C (eV)	6.319	3.532	0.798

Table 1.2.1.1: Experimental values at cryogenic temperature (≤5 K) of the three bandgap energies, crystal field and spin-orbit splitting energies for nitride binaries. Values taken from [13, 102] for GaN, from [102] for InN, and from [13, 128] for AlN.

Due to the very strong ionic character of the Al-N bond, the Δ_{CF} value in AlN is significant and negative, contrary to the one in GaN. Therefore, the valence bands of AlN are reversed with respect to those of GaN, as shown in Figure 1.2.1.1 (b). Furthermore, because of different valence band symmetries, the polarization of light resulting from the main transition (the A-one, of lower energy) differs: the related electric field $\vec{E}$ is perpendicular to the c-axis for GaN, whereas it is parallel to c-axis for AlN. In other words, the luminescence intensity will be maximal in parallel to the c-axis for GaN, and perpendicularly to the c-axis for AlN. The latter causes light extraction issues in optoelectronic devices (LEDs [69, 70] and lasers [69, 129]) based on AlN or AlGaN ($Al_xGa_{1-x}N$) with an Al composition (x, more rigorously called AlN molar fraction) high enough to exhibit the crossover of the valence sub-bands. The latter occurs for AlN molar fractions above x=0.09±0.05 for strain-free $Al_xGa_{1-x}N$ and above higher x values for compressively strained AlGaN layers (for instance, above 0.42 for $Al_xGa_{1-x}N/Al_{x+0.2}Ga_{0.8-x}N$ quantum wells) [130].

Finally, we can notice that E_g values span from 0.78 eV for InN to 6.095 eV for AlN. Therefore, a large electromagnetic region going from the near IR to the deep UV can be covered by tuning the composition of the nitride alloys, making them suitable for harvesting the full solar spectrum [131]. The band structure peculiarities of these alloys will be presented further in Subpart 1.2.2.

1.2.1.2 Other electronic transitions in bulk wurtzite nitride binaries

We have already seen three electronic transitions in Subpart 1.2.1.1, labeled A, B, and C. These transitions, intrinsic to nitride materials, correspond to the radiative recombination of an electron excited into the conduction band with a hole (electron vacancy) in the valence band. Such excitation is typically provided in spectroscopy experiments (see 2.3 for optical characterization techniques) by a laser or an electron beam of energy superior to the bandgap energy. Once excited into the conduction band (respectively the valence band), the electron (respectively the hole) first relaxes, non-radiatively through the emission of phonons (quasiparticles associated with the crystal vibration modes), towards lower energy levels (by convention, the energy scale is inverted for holes), before the radiative recombination of carriers occurs. Thus, the energy of the resulting emission is lower than the absorption energy, and we call Stokes shift the positive difference between the energies corresponding to the band maxima of the absorption and emission spectra of the same electronic transition. Coming back to the case of the three A, B and C transitions, the A-one, of lower energy, will be therefore the most occupied one at cryogenic material temperature.

Before recombining, electron-hole pairs can form quasiparticles called excitons (noted X) through Coulombian interactions, resulting in a decrease in the transition energy equal to the exciton binding energy, noted E_X^b. Therefore, taking the example of the main A-transition, the latter, which involves a free exciton A noted FX_A, can be observed at:

$$E_{X_A} = E_g - E_{X_A}^b \tag{1.2.1.1}$$

in spectroscopy experiments. Excitons are more or less "free" (delocalized) within the material, depending on the spatial extension of their wavefunctions. In such pairs, the average distance between electron and hole can be described by the exciton Bohr radius a_B^X. Both E_X^b and a_B^X directly depend on the bulk material properties and can be reasonably described by the Wannier-Mott model [132, 133] as follows for bulk GaN, AlN and InN:

$$E_X^b = R_y \frac{\mu}{m_0} \frac{1}{\varepsilon^2} \tag{1.2.1.2}$$

$$a_B^X = a_B^H \frac{m_0}{\mu} \varepsilon = \frac{e^2}{2\varepsilon E_X^b} \tag{1.2.1.3}$$

where R_y is the Rydberg constant, m_0 is the electron mass, μ is the reduced mass of the exciton ($1/\mu\ = 1/m_e^* + 1/m_h^*$ with m_e^* and m_h^* the effective mass of electron and holes in the material, respectively), ε is the dielectric constant of the material, a_B^H is the Bohr radius of hydrogen atom and e is the electronic charge. In view of their dependence on ε and μ, which tend to respectively decrease and increase with the bandgap, E_X^b and a_B^X are respectively higher and smaller for higher bandgaps, as highlighted in Table 1.2.1.2.

	AlN	GaN	InN
ε	8.5	9.9	13.7
E_g (or E_g^A) (eV)	6.088	3.505	0.78
$a_B^{X_A}\ u$ (Å)	14	25	
$E_{X_A}^b$ (meV)	54	27	
$E_{D^\circ X_A}^b$ (meV)	18	7	
$E_{A^\circ X_A}^b$ (meV)	35	12	

Table 1.2.1.2: Dielectric constant and main values related to the A-exciton for the three binaries. Taken from [13, 128] for AlN, from [13, 134] for GaN, and from [102] for InN.

Moving within the nitride material, a given electron-hole pair, whether unbound or bound as an exciton, can also encounter structural defects or impurities (generally non-ionized) and then be trapped by or bound to the latter, as depicted for an exciton in Figure 1.2.1.2. In their vicinity, such extrinsic objects exhibit electronic configurations different from the surrounding bulk nitride material, which induces extrinsic energy levels within the bandgap of this material. In the case of substitutional atomic impurities and point defects like vacancies, interstitial or antisite defects, their associated levels can be closer to either the conduction band or the valence band, meaning that these impurities or defects respectively behave as donors or acceptors (of electrons). These levels are said to be “shallow” if they are close to either the conduction or the valence band. In contrast to shallow levels, other ones are “deep” and can be even located around the middle of the bandgap [135].

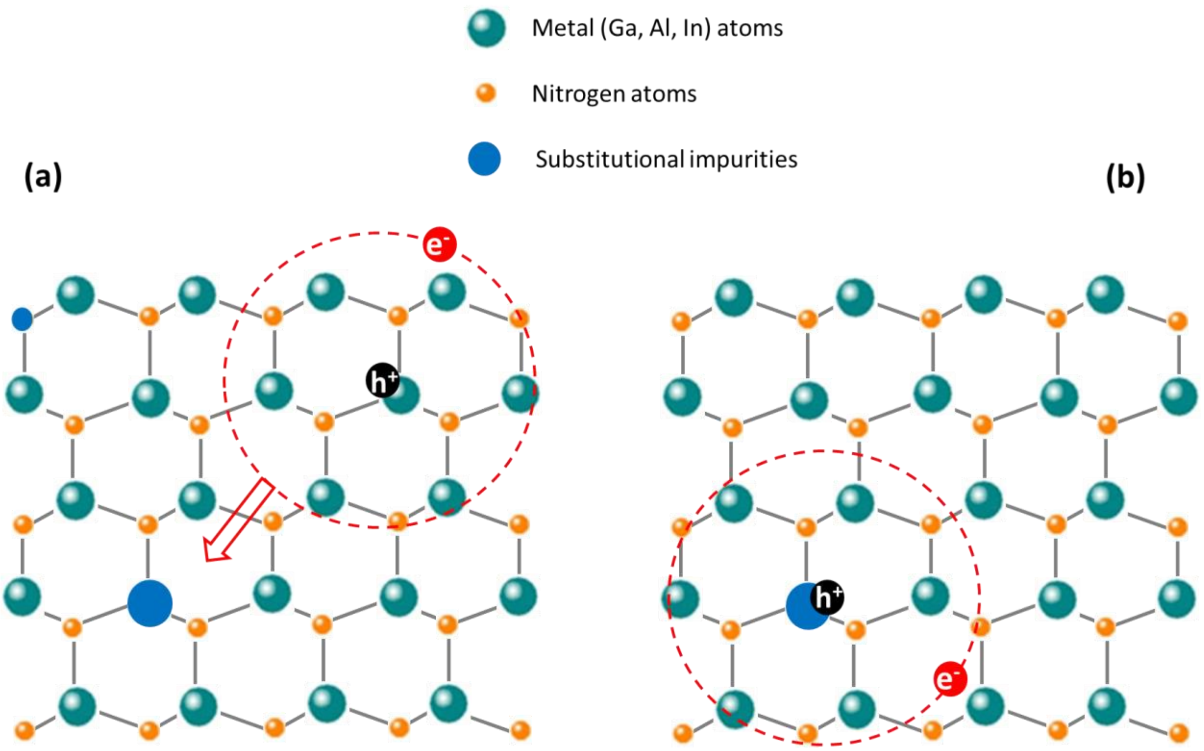

Figure 1.2.1.2: Illustration of an exciton moving within a WZ nitride material: (a) Exciton moving freely. (b) Binding to a substitutional impurity.

Regarding excitonic transitions of extrinsic nature, excitons bound to a donor and those bound to an acceptor are noted $D°X$ and $A°X$, respectively. Considering X_A excitons of the A-transition, their recombinations when bound to donor or acceptor can be expressed as follows:

$$\begin{gathered} D°X_A \rightarrow D° + E_{D°X_A} \\ A°X_A \rightarrow D° + E_{A°X_A} \end{gathered} \qquad (1.2.1.4)$$

The latter lead to emission energies $E_{D°X_A}$ and $E_{A°X_A}$ respectively equal to:

$$\begin{gathered} E_{D°X_A} = E_g - E^b_{X_A} - E^b_{D°X_A} = E_{X_A} - E^b_{D°X_A} \qquad (1.2.1.5) \\ E_{A°X_A} = E_g - E^b_{X_A} - E^b_{A°X_A} = E_{X_A} - E^b_{A°X_A} \end{gathered}$$

Such emission energies related to $D°X$ and $A°X$ complexes are lowered by the binding energy of the exciton bound respectively to a donor and to an acceptor, i.e. $E^b_{D°X_A}$ and $E^b_{A°X_A}$ in the case of X_A. Consequently, complexes involving shallow donors exhibit emission energies close to those of free exciton recombination: the related transitions are commonly called near band edge (NBE) transitions. Typical shallow donors in nitrides are non-intentionally introduced oxygen (O) impurities substituting N (noted O_N) and Si dopants substituting metal atoms, whereas residual carbon (C) impurities substituting N (noted C_N) and Mg dopants substituting metal atoms are common shallow acceptors [128, 134]. Consequently, when performing higher Si n-doping or Mg p-doping during growth, the intensity of the emission resulting from the corresponding "shallow" $D°X$ or $A°X$ excitonic transition will be more significant. Other NBE transitions can stem from excitons bound to extended defects such as SFs [136] or to inversion domain boundaries [111]. Other radiative and extrinsic transitions, "deeper" than those previously presented and of non-excitonic nature, can also be observed for nitrides in spectroscopy:

- Donor-acceptor pair transitions (DAP), corresponding to the carrier recombination between a neutral donor and an acceptor, and emitting at E_{DAP}, such as:

  $$A^\circ + D^\circ \rightarrow A^- + D^+ + E_{DAP} \qquad (1.2.1.6)$$

  with

  $$E_{DAP} = E_g - E_D^b - E_A^b + e^2/(\varepsilon\, d_{DA}) \qquad (1.2.1.7)$$

  where d_{DA} is the donor-acceptor distance and E_D^b (respectively E_A^b) is the binding energy of the electron to the donor (respectively of the hole to the acceptor). It must be noted that the donor ionization energy E_D^b is empirically related to $E_{D^\circ X}^b$ by Haynes' rule [137, 138]. Such transitions are generally quite broad and asymmetric, respectively due to variation of d_{DA} and its high average magnitude making recombination less probable than for closer centers. In the case of nitrides, DAP transitions involving typical shallow donors or shallow acceptors or both are commonly observed [128, 134, 139].

- Free-to-bound transitions (eA or hD), corresponding to a recombination of an acceptor (respectively a donor) with an electron (respectively a hole) and emitting at E_{eA} (respectively E_{hD}):

  $$A^\circ + e^- \rightarrow A^- + E_{eA} \quad \text{(respectively } D^\circ + h^+ \rightarrow D^+ + E_{hD}\text{)} \qquad (1.2.1.8)$$

  where

  $$E_{eA} = E_g - E_A^b \quad \text{(respectively } E_{hD} = E_g - E_D^b\text{)} \qquad (1.2.1.9)$$

  Due to the easier donor ionization, eA transitions are much more commonly observed than hD ones in nitrides [134].

- Transitions involving at least one deep level. For instance, the widely investigated broad "yellow band" emission commonly observed in GaN films or the "blue/violet" band emission in AlN layers stem from such transitions. In both cases, the origin of the latter is still under debate and being investigated. Indeed, for GaN, they are either assigned to complexes of defects/impurities comprising C_N and O_N [140, 141] or attributed to other complexes including

Ga vacancies (noted V_{Ga}) and O_N [142]. As for AlN, such transitions are thought to be related to complexes formed by V_{Al} and O_N [143].

Eventually, electronic transitions can be non-radiative. Indeed, carrier recombinations do not always generate photons, especially those involving deep defects trapping carriers. Thus, crystal of low structural quality will not luminesce intensively. For instance, extended defects such as dislocations were demonstrated to behave as non-radiative recombination centers [144], which can be problematic for optoelectronic devices. Indeed, if the dislocation density is significant, the carrier diffusion length is likely to be longer than the dislocation spacing and the light emission efficiency is therefore lowered. In the perspective of enhancing such devices, intense efforts are being made to improve the III-N structure crystalline quality. In this context, nitride NWs constitute an alternative to epitaxial layers, as already mentioned. Indeed, in view of their high surface-to-volume ratio (length/diameter), they naturally grow relaxed, dislocation-free unlike their 2D counterparts and almost exempt of other defects [25, 71, 72], as supported by typical PL spectra recorded for nitride binary NWs and provided in the experimental method Subpart 2.3.1.2. The latter will consist in a direct application of the notions introduced in the present section. To conclude, Figure 1.2.1.3 sums up the main types of transitions that can be encountered in nitrides. In addition, very exhaustive reviews gathering the many transitions reported for nitrides can be found in the literature for GaN [134] and AlN [128].

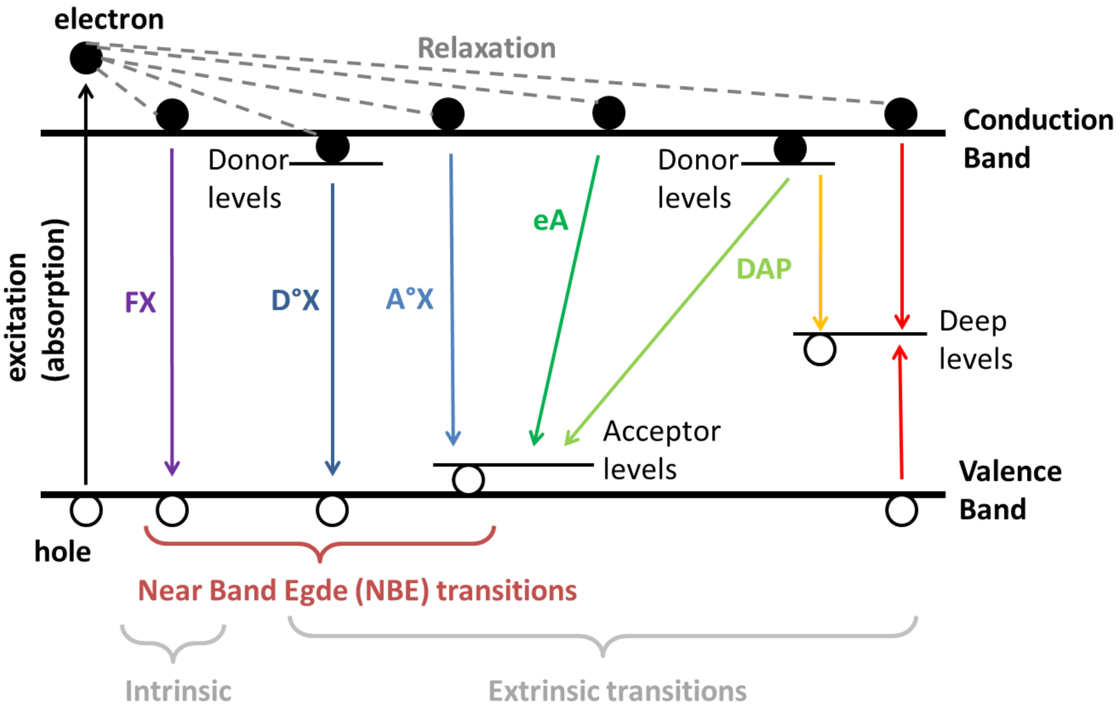

Figure 1.2.1.3: Illustration of the main types of radiative electronic transitions.

1.2.1.3 Effect of external parameters on the band structure of bulk nitride binaries

Given that heterostructures were grown and temperature- or power-dependent optical characterization experiments were performed during this PhD, we will briefly present the effect of three external parameters in the following of this section: strain, excitation power density, and material temperature. We will detail a bit more the latter parameter.

Strain, generally resulting from heteroepitaxial growth as detailed in Subpart 1.3, induces slight modifications of nitride material lattice parameters and therefore of the metal-N bond length. Consequently, the covalence of such bond will change, leading to shifts of the bandgap and other related transitions. Figure 1.2.1.4 illustrates the linear dependence of the bandgap energy on strain for GaN and AlN.

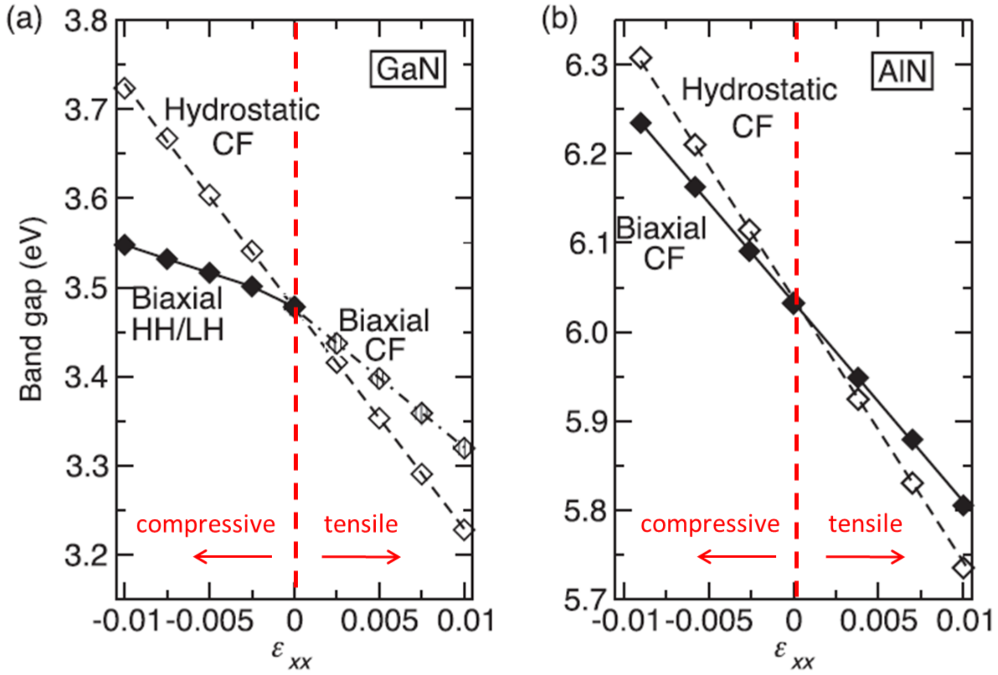

Figure 1.2.1.4: Dependence of bandgap on in-plane strain for (a) GaN and (b) AlN under hydrostatic and biaxial stresses. Adapted from [145].

The emission energy shift of a given transition may also be caused by the variation of nitride material temperature. Indeed, the corresponding thermal expansion first induces a modification of nitride lattice parameters, resulting in a slight change in emission energy for the band gap and related transitions. Second, phonon states of higher energy get more populated when increasing temperature. Consequently, recombination of carriers coupled with such phonons usually leads to emission red-shift more significant than the one induced by the mere thermal expansion [146-148]. Regarding the bandgap transition, several models have been widely used to approach its evolution with temperature, including Varshni law [149] and Bose-Einstein model [150]. The first one is the most commonly used but is purely empirical, whereas the second one has physical meaning and is furthermore adapted to wide bandgap semiconductors. A third model by Pässler [151], more complex and more accurate at low temperatures, could also be used but we will stick in the following of the manuscript to the more common Varshni and Bose-Einstein laws. The corresponding expressions are given below:

$$E_g^{V.}(T) = E_g(0K) - \frac{\alpha T^2}{\beta + T} \tag{1.2.1.10}$$

where α and β are the Varshni empirical coefficients.

$$E_g^{B.E.}(T) = E_g(0K) - \frac{2\alpha_B}{e^{\Theta_B/T} - 1} \tag{1.2.1.11}$$

where α_B is the electron-phonon coupling constant and Θ_B is the characteristic Bose-Einstein temperature (related to the average phonon frequency). Typical value ranges are provided for parameters of both models in Table 1.2.1.3. The significant shift of E_g with temperature over the 5-300K range is shown for GaN and AlN in Figure 1.2.1.5.

	α (meV/K)	β (K)	α_B (meV)	Θ_B (K)
GaN	0.8-1.3	800-1400	80-140	300-450
AlN	1.7-2.7	1500-2600	100-400	400-700

Table 1.2.1.3: Common parameter values of Varshni and Bose-Einstein models for GaN and AlN, taken from [152] for GaN and from [153] for AlN.

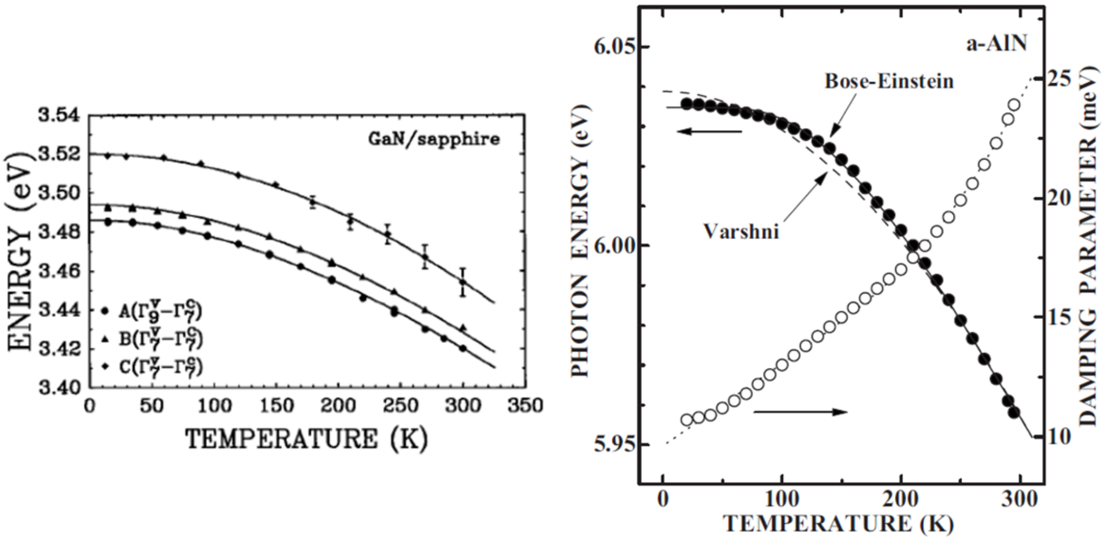

Figure 1.2.1.5: Experimental evolution of bandgap with temperature for (a) GaN and (b) AlN. Taken from [154] for (a) and from [153] for (b).

At higher material temperatures, the phonon-carrier coupling may not only lead to the decrease in the emission energy resulting from a given transition, but may also induce:

- The broadening of this emission. The linewidth can be expressed as follows:

$$\Gamma(T) = \Gamma_0 + \Gamma_A T + \frac{\Gamma_{LO}}{e^{\frac{\hbar\omega_{LO}}{k_B T}} - 1} \tag{1.2.1.12}$$

  where Γ_A and Γ_{LO} are respectively the coupling force of acoustic and longitudinal optical (LO) phonons, and ω_{LO} is the vibration frequency of LO phonons. At low temperatures, the contribution of phonons to the broadening of emission mostly stems from the acoustic phonons whereas the interaction of LO ones (also called Fröhlich coupling) gets progressively more significant when increasing temperatures [148, 152, 153].
- The appearance of phonon replicas for this transition, observable in spectroscopy. Their emission is red-shifted with respect to the main transition by multiples n of $\hbar\omega_{LO}$ (91 meV for GaN [13, 134] and 110 meV for AlN [128]) whereas their intensity decreases with n [155]. For instance, due to large phonon-carrier coupling for the DAP transition (related to its polar nature), several phonon replicas are commonly observed for the latter in spectroscopy at cryogenic temperature ([128, 134, 139]).

Moreover, increasing material temperature can favor or disadvantage certain transitions defined in Subpart 1.2.1.2 with respect to other ones. Indeed, it can result in the more significant intensity quenching of a given transition compared to other ones, due to exciton dissociation, exciton unbinding from defects/impurities, or thermal escape of carriers towards other levels. For instance, free A-excitons can be dissociated at high enough temperatures, and their related intensity follows a typical Arrhenius law with an activation energy equal to its binding energy $E_{X_A}^b$. In other words, free A-excitons exhibiting higher $E_{X_A}^b$ than 25 meV ($k_B T$ at 300 K) are stable and can be observed at room temperature (especially for AlN in view of Table 1.2.1.2) whereas those with low $E_{X_A}^b$ are only observable at low temperatures. Another typical example is provided by the DAP and eA transitions. At higher temperatures, the first ones get less observable, due to donor ionization, and red-shift, due to the decrease in the number of recombination centers (i.e. the average value of d_{DA} defined in Subpart 1.2.1.2 decreases). In contrast, eA transitions can be more easily evidenced when donor ionization is favored [134].

Eventually, excitation power density is usually set low when performing spectroscopy, in order to avoid saturating the possible energy levels related to defects, since their concentrations and associated lifetimes are finite [134]. Therefore, at higher excitation power densities, certain transitions will saturate more slowly and be favored at the expense of other ones. Coming back to the example of DAP and eA transitions, the first one will blue-shift when increasing power density (increase in the average value of d_{DA}), whereas the second one will be more easily observable owing to the resulting increase in the number of electrons excited in the conduction band [134].

1.2.2 Peculiarities of nitride ternary alloys

1.2.2.1 Bandgap of ternary alloys

By definition, a perfectly disordered alloy does not exhibit long-range chemical order and invariance by translation. Therefore, inferring a band structure from crystal periodicity is not quite accurate. However, it is experimentally observed that an alloy presents a bandgap which depends on the molar fraction of mixed nitride binaries. In the case of a nitride ternary alloy $M_xM'_{1-x}N$, the variation of the bandgap energy with the MN molar fraction x can be approached by the following relation:

$$E_g[M_xM'_{1-x}N] = xE_g[MN] + (1-x)E_g[M'N] - bx(1-x) \qquad (1.2.2.1)$$

where b is the bowing parameter, which accounts for the deviation from linearity. Theoretical and experimental values of bowing parameters for $Al_xGa_{1-x}N$ [130, 156-161], $In_xGa_{1-x}N$ [162-165] and $Al_xIn_{1-x}N$ [166-169], can be found in the literature. However, discrepancies on the reported values can be noticed. For instance, they globally vary from -0.8 eV to +2.6 eV range for $Al_xGa_{1-x}N$. More refined $Al_xGa_{1-x}N$ layers and associated techniques yield a value of +1 eV that will be used for b [13, 170] in the following, unless specified otherwise. Using the latter and emission energy values for A-exciton given in Subpart 1.2.1 for GaN and AlN, the evolution of $Al_xGa_{1-x}N$ bandgap with x is sketched in Figure 1.2.2.1.

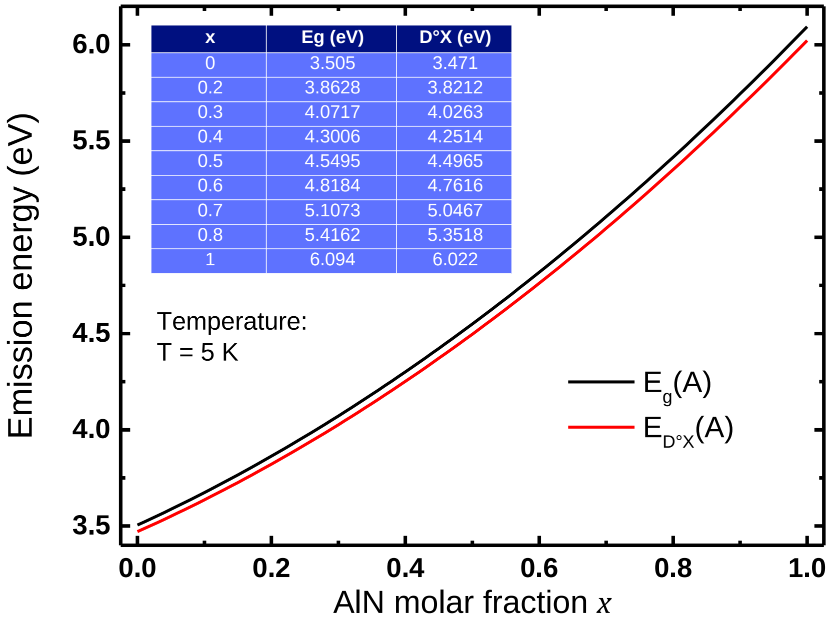

x	Eg (eV)	D°X (eV)
0	3.505	3.471
0.2	3.8628	3.8212
0.3	4.0717	4.0263
0.4	4.3006	4.2514
0.5	4.5495	4.4965
0.6	4.8184	4.7616
0.7	5.1073	5.0467
0.8	5.4162	5.3518
1	6.094	6.022

Figure 1.2.2.1: Evolution, at low temperature (5 K), of the bandgap and the donor bound exciton energy with AlN molar fraction, for A-exciton. Some values are given in the table given in inset. A bowing parameter of 1 eV was used.

1.2.2.2 Broadening of emission for nitride ternary alloys

When considering a given metallic atom M in a perfectly disordered alloy $M_xM'_{1-x}N$ of MN molar fraction x, the latter atom can be surrounded by 13 different configurations for the neighboring metallic atoms (second neighbors, the first one being N atoms). Each configuration inducing a different bandgap, the resulting emission will therefore be intrinsically broader than for nitride binaries. Models for this broadening can be found in the literature, such as Goede's model, which can also be used for II-VI [171] and other III-V alloys [172]. The latter is actually derived from a binomial law related to the probability to find a certain number of metallic atoms M among the number of cations $n_{cations}(x)$ in the volume V_{exc} probed by the exciton of the transition. Knowing that there are 2 cations in the WZ primitive unit cell of volume $V_{WZ} = \sqrt{3}/2\, a^2(x)c(x)$, that $n_{cations}(x) = 2V_{exc}(x)/V_{WZ}(x)$, we can approximate the binomial law by a Gaussian of linewidth expressed as:

$$FWHM_{E_g}(x) = \frac{dE_g(x)}{dx} 2 \left(\frac{2\ln(2)\, x(1-x)}{n_{cations}(x)} \right)^{\frac{1}{2}} \qquad (1.2.2.2)$$

Considering a spherical volume for V_{exc}, using linear interpolation (Vegard's law) between nitride binary values for the exciton Bohr radius and the WZ lattice parameters, and using Equation (1.2.2.1) for E_g, such Gaussian linewidth can be sketched as a function of x for $\text{Al}_x\text{Ga}_{1-x}\text{N}$, as shown in Figure 1.2.2.2.

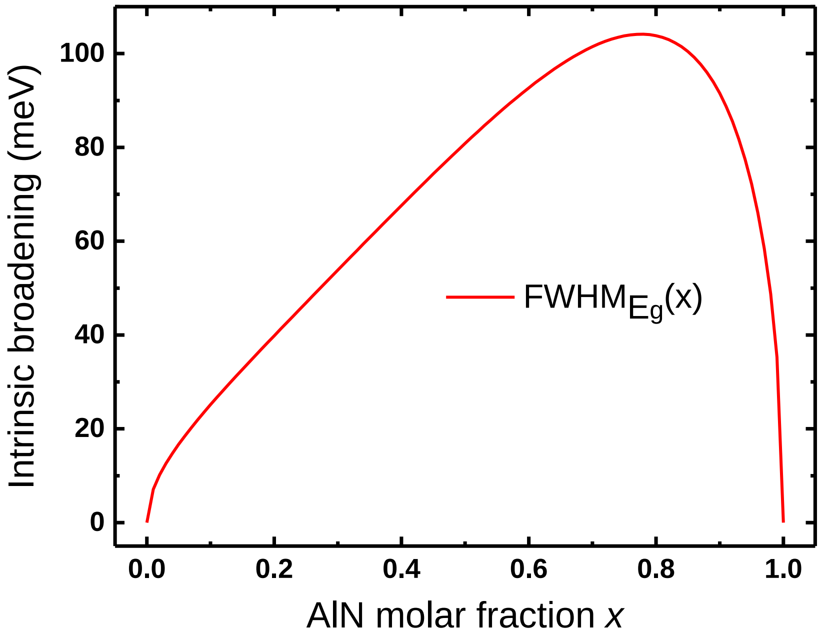

Figure 1.2.2.2: Linewidth broadening intrinsic to random atomic distribution in $Al_xGa_{1-x}N$, using Goede's model.

For $Al_xGa_{1-x}N$, a maximal broadening of 104 meV is obtained for $x = 0.78$. The related Gaussian must be then convoluted with other intrinsic contributions that must be taken into account for any nitride material: a Lorentzian homogeneous broadening related to carrier lifetime and another inhomogeneous one depending on the local environment (impurities or defects, strain, etc.). The mere broadening intrinsic to random alloy compositional fluctuation given by the model is well above the state-of-the-art experimental values reported for AlGaN alloys of similar AlN molar fractions, in the 2D (≈60 meV) [160, 173, 174] and the NW case (≈55-60 meV) [175]. Such discrepancy can be firstly explained by the imperfections of this simple model. Indeed, the latter describes well the broadening evolution with the AlN molar fraction but only considers free excitons whereas the latter are likely to be bound [176], so that the probed excitonic volume is different in reality. In addition, carriers thermalize towards lower energy levels in experiments, which narrows the emission energy range. Improvements of the Goede's model were performed to take into account such effects and better fit experimental data [176-178].

1.2.2.3 Stokes shift in nitride ternary alloys

As previously mentioned, the Stokes shift is the energy difference between the absorption energy and the lower emission energy. In nitride alloys, such shift is induced by the thermalization of carriers towards the lowest levels induced by the alloy disorder described in Subpart 1.2.2.2. Therefore, the resulting difference is typically of the order of the alloy broad emission linewidth. However, if carriers are strongly localized, they do not thermalize, resulting in small Stokes shifts. In this case, when increasing the material temperature, carriers are provided enough energy to be able to get over the potential barrier induced by their localized state. They can then thermalize towards the lowest levels, leading to lower emission energy (Figure 1.2.2.3 (a) to (b)). When further increasing the material temperature, carriers can access higher energy levels, resulting in higher emission energy (Figure 1.2.2.3 (b) to (c)). Finally, at even higher temperatures, the extended levels related to the average alloy bandgap can be occupied (Figure 1.2.2.3 (d)), and we retrieve the classical monotonous decrease in the bandgap energy with temperature (see Varshni and Bose-Einstein law in 1.2.1.2). As illustrated in Figure 1.2.2.3, the variation of emission energy with temperature typically follows an "S-shape" [179] and so does the Stokes shift, since the contribution of the various energy levels to absorption does not change. Such S-shape was widely reported for nitride ternary alloys, namely AlGaN [156, 158, 174, 180-185], InGaN [186, 187] and AlInN [188].

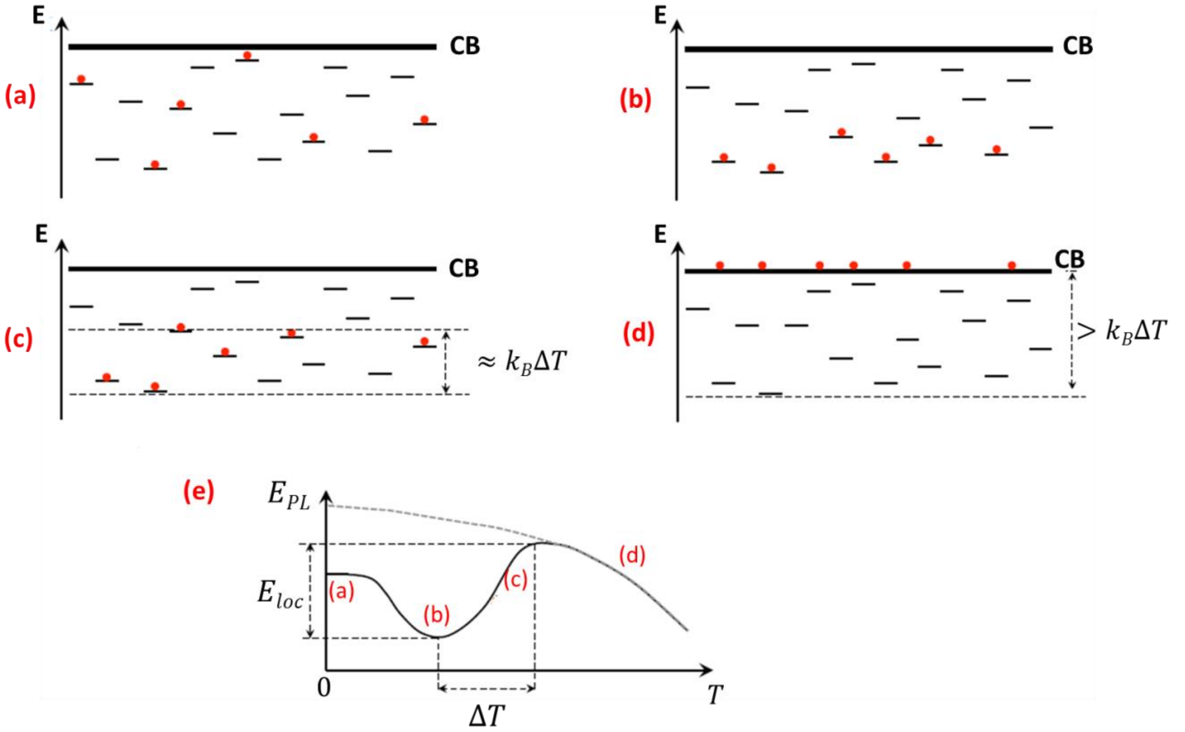

Figure 1.2.2.3: Typical evolution of the emission energy of an alloy exhibiting strong carrier localization when increasing material temperature: "S-shape" curve. Adapted from [139].

When dealing with a non-perfectly disordered $M_xM'_{1-x}N$ alloy with $E_g[MN] < E_g[M'N]$, its composition can vary locally, inducing M-richer regions surrounded by M'-richer barriers. Consequently, the energy levels are lower within these M-richer regions and carriers will preferentially recombine there. The resulting emission will be the dominant contribution to the alloy luminescence, whereas the related energy levels will weakly contribute to absorption, leading to higher Stokes shift. To conclude, the Stokes shift can be seen as a tool to assess the degree of disorder in a given nitride alloy: the more significant the shift, the more ordered the alloy.

1.2.3 Effect of the dimensionality of nitride objects

The dimensionality d of nitride objects can be seen as the number of degrees of freedom for carriers within such objects. Consequently, it is equal to 3 for bulk material (no carrier confinement), to 2 in quantum wells (QWs, 1D confinement), to 1 in quantum wires (QWires, 2D confinement) and to 0 for quantum dots (QDs, 3D confinement).

1.2.3.1 Effects intrinsic to carrier quantum confinement in nitrides

Decreasing the nitride object dimensionality d, leading to an enhancement of carrier quantum confinement, first modifies the density of states for carriers, as displayed in Figure 1.2.3.1 (a). Such density, noted *D,* can be expressed as a function of energy *E* and object dimensionality *d* as follows:

$$D(E) \propto \begin{cases} E^{\frac{d}{2}-1}, \ if\ d > 0, \\ \delta(E), \ if\ d = 0. \end{cases} \qquad (1.2.3.1)$$

In addition, the resulting enhanced quantum confinement in a given crystal direction will induce a quantization of the allowed energy levels for carriers confined in this direction [189]. Indeed, the energy of the n^{th} level is equal to (for infinite potential barriers):

$$E_n = \frac{\hbar^2 k^2(n)}{2m} \qquad (1.2.3.2)$$

with:

$$k = \sqrt{{k_x}^2 + {k_y}^2 + {k_y}^2} \qquad (1.2.3.3)$$

and, for quantum confinement in a given direction $i = \{x, y, z\}$:

$$k_i(n) = \frac{\pi n}{L_i} \qquad (1.2.3.4)$$

where $\hbar$ is the reduced Planck constant, *k* the wavevector norm, *m* the effective mass of the carrier, L_i the characteristic dimension of the quantum object in the confinement direction, and *n* the quantization index. Such quantization is represented in Figure 1.2.3.1 (b) for electrons and is similar for holes.

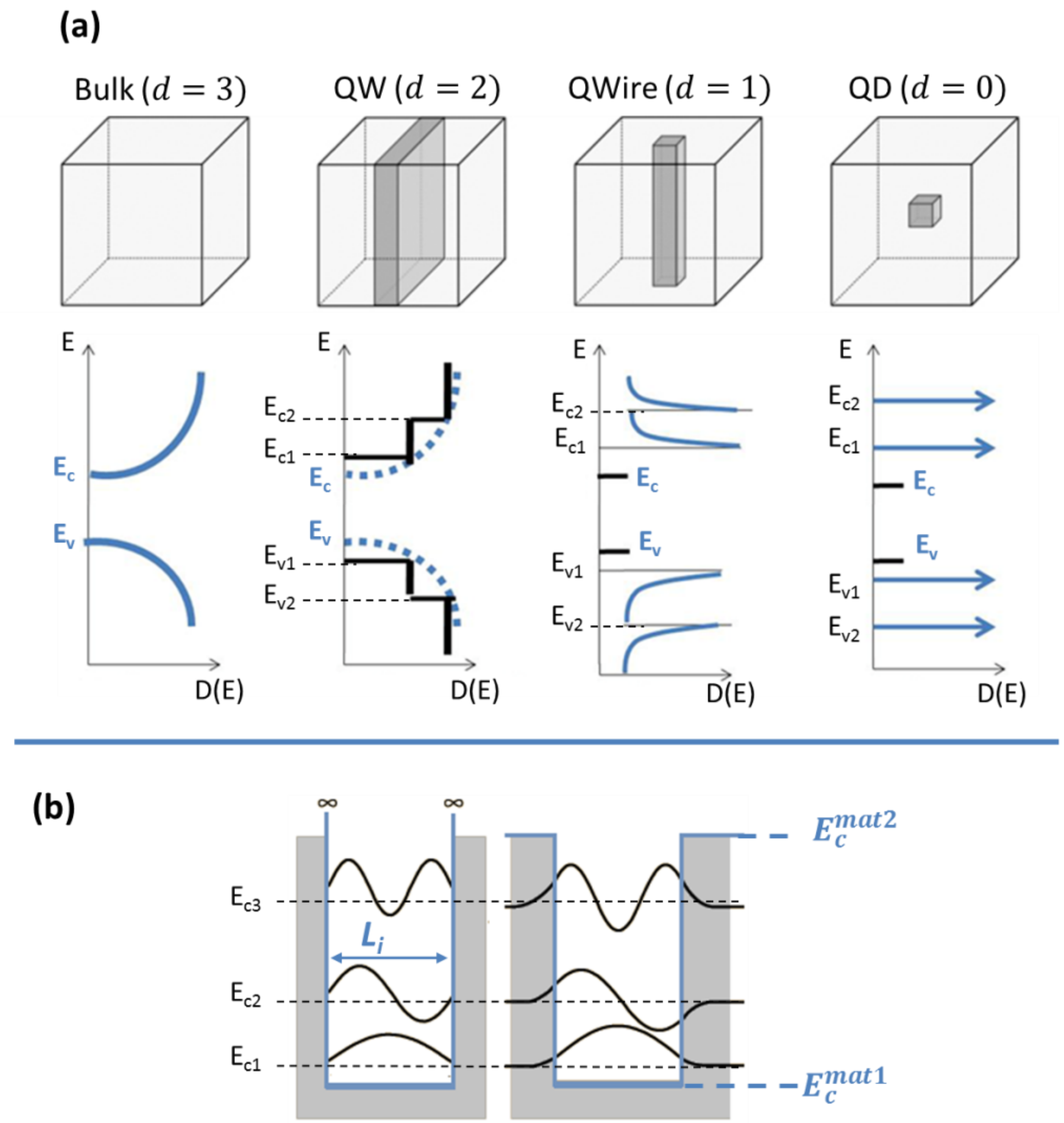

Figure 1.2.3.1: (a) Evolution of carrier state densities *D(E)* with dimensionality. The critical points E_{cn} and E_{vn} are called Van Hove singularities. (b) Quantization of allowed energy levels for electrons confined in a given direction i={x,y,z}, in the case of infinite barrier potentials (left schematic) and finite ones (right schematic, closer to reality) resulting from a nitride material 1/material 2 quantum object/barrier heterostructure. Wavefunctions are also sketched for the first three quantized levels E_{cn}. This depiction is similar for holes and not shown here.

Such quantum confinement can be effective in two distinct regimes:

- The strong quantum confinement regime. In this case, one of the nitride object dimensions is inferior to the corresponding exciton Bohr radius, and the wavefunctions of both excitons and holes are separately confined.

- The weak quantum confinement regime. All the object dimensions are superior to the exciton Bohr radius, but at least one of them remains close to the latter. In such regime, only the exciton center of mass is confined.

In both regimes, the emission will be blue-shifted. For the strong quantum confinement regime, more common and sought in nitride heterostructures, the bandgap energy will be increased as follows [190]:

$$E = E_g + E_e^c + E_h^c + E_X^b \tag{1.2.3.5}$$

where E_e^c and E_h^c are the confinement energies of respectively the electron and the hole within the potential barrier associated with the quantum object. For instance, the emission of GaN/AlN QDs and QDisks can be blue-shifted up to ≈4.4 eV for the smallest ones [115, 191]. In such quantum objects, the overlap of carrier wavefunctions is stronger and their spatial extension is smaller, so that the related oscillator strength and radiative efficiency are significantly increased [189].

A decrease in either dimensionality d of a nitride object or its characteristic dimensions along confinement directions is also expected to lead to an increase in the binding energy of involved excitons and a lowering of the corresponding Bohr radius (in other words the volume probed by the exciton) [189], as theoretically predicted and experimentally verified for Wannier-Mott excitons confined in QWs [192, 193], QWires [194, 195] and QDs [196, 197] made of direct bandgap semiconductors. Concomitantly, the related radiative lifetime is expected to decrease when increasing the oscillator strength (which depends on the quantum confinement), as demonstrated for QWs [198, 199], QWires [200, 201] and QDs [196, 202, 203]. Regarding nitride semiconductors, exciton binding energy values up to ≈45-50 meV were reported for thin GaN/$Al_xGa_{1-x}N$ QWs [204, 205], as illustrated in Figure 1.2.3.2, which represents an increase of about 25 meV with respect to the bulk value (27 meV for GaN). It must be noted that exciton binding energy values get lower than the bulk one for thick wells, which is a consequence of the large polarization in nitride heterostructures that will be explained in Subpart 1.2.3.2. As for smaller nitride object dimensionalities, significant enhancements of the binding energy were also reported with respect to the bulk, for GaN/$Al_xGa_{1-x}N$ QDs (E_X^b ≈40-60 meV for the smallest dots) [206] and InGaN/GaN QDs (E_X^b ≈60 meV for small dots) [207].

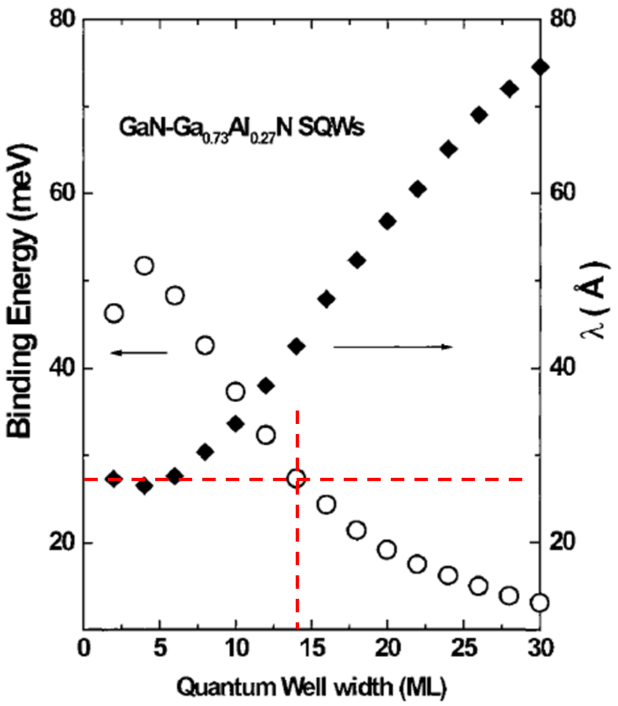

Figure 1.2.3.2: Evolution of E_X^b with QW width for GaN/AlGaN QWs. Taken from [205]. Above QW thickness of about 14 ML, the E_X^b value gets inferior to the one for bulk GaN.

1.2.3.2 A consequence of the nitride peculiar polarization: the quantum-confined Stark effect (QCSE)

In the case of nitride heterostructures grown along the polar direction (c-axis), the effect of the overall polarization $\vec{P}$ introduced in Subpart 1.1.3 will be to generate surface charge sheets $\sigma_{interface}$ at the interface between two adjacent nitride material layers, when a polarization discontinuity $\Delta\vec{P}$ appears. This discontinuity can be expressed as:

$$\sigma_{interface} = \Delta\vec{P}.\vec{n} \tag{1.2.3.6}$$

with $\vec{n}$ the normal vector to the interface. The sheet carrier concentration can be significant enough to generate a 2D electron gas, even without intentional doping, making such interfaces particularly suited for devices like HEMTs [208].

However, the large polarization discontinuity can severely impact the band structure of stacked nitride heterostructures. In order to highlight this feature, we will focus in the following on the simple example of a classical double heterostructure: a nitride QW sandwiched by barriers made of another nitride material. In this case, surface charge sheets at each interface are of opposite signs. Though the type of charges confined at each interface depends on the heterostructure polarity, in both configurations, the distribution of positive and negative charges induces the presence of an electric field within the well. This electric field causes a bending of the conduction and valence bands inside the QW, as sketched in Figure 1.2.3.3. Consequently, the first electron level in the conduction band and the first hole level in the valence band get energetically closer, leading to a red-shift of the QW emission wavelength. Moreover, the electron and the hole wavefunctions are spatially separated, which reduces their overlap and therefore the transition oscillator strength. In other words, the recombination of carriers is made harder, increasing their lifetime inside the QW. This phenomenon is called the QCSE and is schematically illustrated in Figure 1.2.3.3 for a GaN QW embedded in AlN barriers.

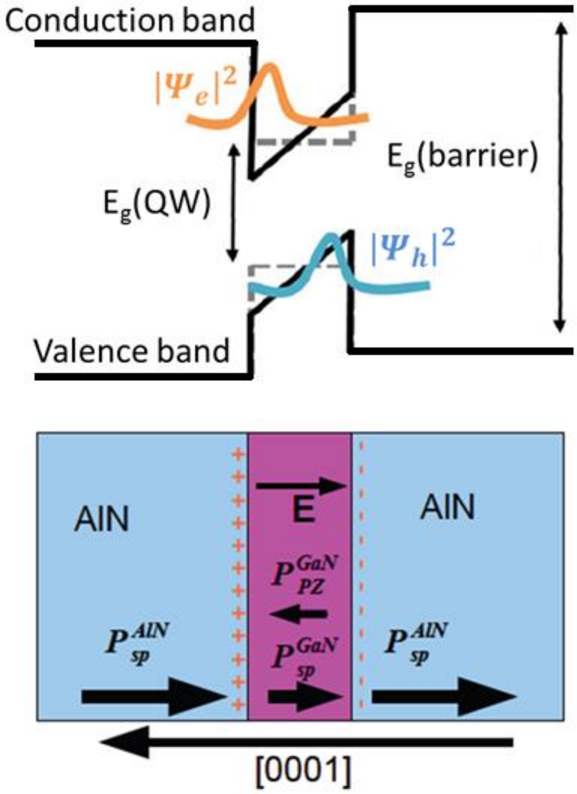

Figure 1.2.3.3: Illustration of the effect of the electric field in a polar GaN/AlN QW. The bottom part shows the structure with the different contribution to the polarization. The upper part presents the calculated band structure, with the electron (respectively hole) probability density distribution $|\Psi_e|^2$ (respectively $|\Psi_h|^2$).

Such effect was widely reported for various nitride quantum GaN objects embedded in $Al_xGa_{1-x}N$ such as GaN/AlN QWs [191], QDisks [115] or dots [209, 210]. Typical values of the electric field within such quantum structures are of the order of 5-10 $MV.cm^{-1}$ [208-210]. Consequently, for too thick quantum objects, such fields cause a red-shift of the emission energy well below the bandgap of GaN [115, 116, 210], lead to a decrease in exciton binding energy [211] and significantly lengthen the radiative lifetime [210, 212], as highlighted in Figure 1.2.3.4. Significant QCSE was also reported for

$In_xGa_{1-x}N/GaN$ QWs [213, 214], dots [207, 215] and QDisks [216, 217]. Taking QCSE into account, the bandgap energy in quantum objects can be written, completing Equation (1.2.3.5) [190]:

$$E = E_g + E_e^c + E_h^c + E_X^b - E^{QCSE} \tag{1.2.3.7}$$

where:

$$E^{QCSE} = eL\|\vec{E}\| = eL\frac{\|\Delta\vec{P}\|}{\varepsilon} \tag{1.2.3.8}$$

with E^{QCSE} the emission energy shift due to QCSE, L the dimension of the quantum object along the polar direction, $\|\vec{E}\|$ the norm of the electric field along the polar direction within the quantum object, and ε the dielectric constant of the quantum object material.

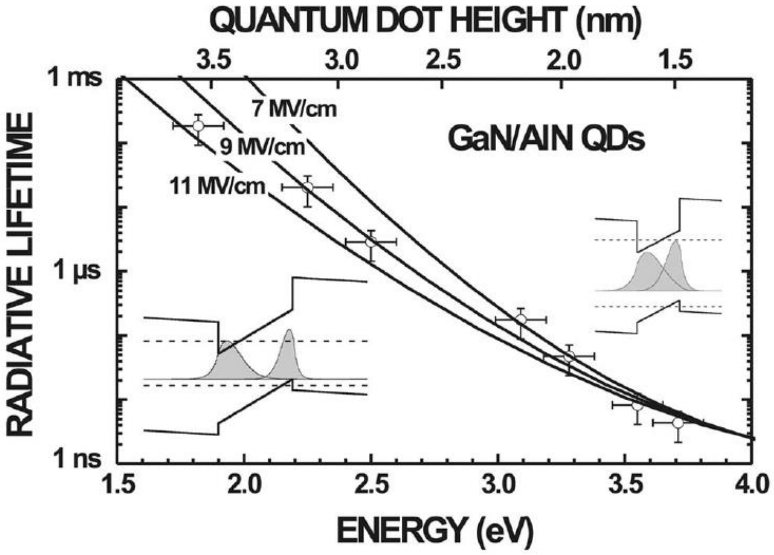

Figure 1.2.3.4: Evolution of the radiative lifetime as a function of the QD size and the corresponding emission energy. Taken from [210].

In order to reduce and even get rid of the QCSE completely, growth of heterostructures along semi-polar and non-polar directions (perpendicular to the c-axis) has been investigated in the 2D case on non-polar [218-221] or semi-polar [222, 223] planes, as well as along NW facets [32].

1.2.3.3 The case of nitride nanowires

In standard self-induced nitride NWs grown by MBE, the NW diameter is of the order of a few tens of nm. As this dimension is by far superior to the corresponding exciton Bohr radius, the strong quantum confinement regime can be excluded. Regarding the weak regime, calculations were performed for standard 40 nm wide GaN NWs grown by PA-MBE, leading to confinement energy of the order of 1 meV [224]. Given that the induced shift is inferior to typical emission linewidths, it can be safely concluded that no quantum confinement occurs for both bound and free excitons [224]. However, standard NWs can be easily thinned by thermal dissociation of GaN at the end of growth run, within the MBE chamber [225, 226]. Indeed, GaN decomposition in vacuum is a thermally activated process already operating at 750°C for the (0001) GaN facet [227]. Such thinning process was demonstrated to induce a strong dielectric confinement for GaN NWs thinned down to a few nanometers (6 nm), leading to a blue-shift of the emission and an increase in the radiative efficiency [226].

Except for thinned nitride NWs, we have just seen that the electronic properties of common nitride NWs can be interpreted in a way similar to the corresponding bulk material. However, surface effects in WZ nitride NWs must not be forgotten. Indeed, dangling bonds along the NW sidewalls can adsorb molecules or atoms, such as oxygen, which get ionized and bring negative charges onto the surface [228, 229]. Such charges lead to a bending of both valence and conduction bands, as illustrated in Figure 1.2.3.5, and set the Fermi level along the whole NW diameter. A charge transfer is then induced: electrons and holes get separated, leading to depletion zones close to the NW surface and to a decrease in the radiative efficiency [229]. Such issue can be problematic for narrow and unpassivated NWs, especially if surface states behave as non-radiative traps: NWs may not even luminesce at all, as reported for arsenide NWs less than 200 nm wide [230]. These surface states can also be related to radiative deep defects, as evidenced for several nitride NW samples emitting within the yellow or blue defect-related bands [231-233]. In contrast, the issue turns out to be much less troublesome for self-induced binary nitride NWs of small diameter (typically 20-50 nm wide) grown by MBE, in view of their strong NBE luminescence (see Subpart 2.3.1.2 for instance). Nevertheless, it must be noted that, for the latter NWs, excitons recombining near the surface may cause a slight shift and a broadening of the NBE luminescence [234].

In order to solve surface-effect issues, investigation of surface passivation has been widely carried out in the recent years for NWs of various semiconductor families, either chemically [235] or using coating [230, 236]. In the case of nitride alloy NWs, the phenomenon is not expected to be significant, given that core-shell structures spontaneously grow. For instance, in the case of AlGaN NWs, an Al-richer shell is expected to naturally passivate the AlGaN core. Indeed, such shell, which can be observed on microscopy images in the following of the manuscript, exhibits a higher bandgap than the NW core, which should lead to a better confinement of carriers within the core.

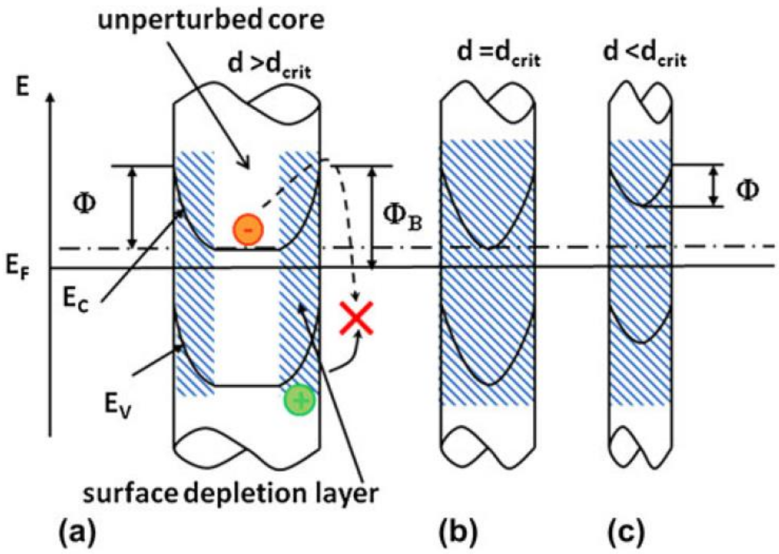

Figure 1.2.3.5: Band bending and resulting depletion zone for wide (a) to narrower (c) NWs. Taken from [229].

1.2.3.4 *Effect of excitation in nitride quantum heterostructures*

In the case of nitride quantum heterostructures of high structural quality, increasing the excitation power density has two well-known consequences that we will briefly describe in the following of this section.

First, in the case of nitride quantum objects grown along the polar direction and thick enough to exhibit a significant QCSE effect, the large electric field within the object will be screened. Therefore, at high enough power, the QCSE cancels out and the emission is blue-shifted, as evidenced for nitride QWs [213, 237] or QDs [238, 239].

Second, more than one electron-hole pair can populate an energy level within quantum objects at high enough excitation powers. Figure 1.2.3.6 depicts a simple model describing the dependence on power density of the luminescence: the two-level system [190], which includes the ground state and the first excited state. Owing to the spin degeneracy, this first state can contain up to a set of two electron-hole pairs interacting between each other and called a biexciton. Therefore, three configurations are possible: an empty dot (noted 0), a dot with one exciton (noted X), and a dot with two (biexciton noted XX). The system dynamics can be then described by the following rate equations:

$$\begin{aligned} \frac{dp_0}{dt} &= -\Gamma p_0 + \frac{p_X}{\tau_X} \\ \frac{dp_X}{dt} &= -\Gamma p_X - \frac{p_X}{\tau_X} + \frac{p_{XX}}{\tau_{XX}} + \Gamma p_{XX} \\ \frac{dp_{XX}}{dt} &= -\frac{p_{XX}}{\tau_{XX}} + \Gamma p_X \end{aligned} \tag{1.2.3.9}$$

where p_0 (respectively p_X, p_{XX}) is the probability for the dot to be in the ground (respectively excitonic, biexcitonic) state, τ_X (respectively τ_{XX}) is the radiative lifetime of the exciton (respectively the biexciton) and Γ is the pumping (excitation) rate. Some of these parameters are indicated in Figure 1.2.3.6. Consequently, in the steady state regime, we can derive from Equations (1.2.3.9):

$$\begin{aligned} I_X &\propto \frac{p_X}{\tau_X} = \frac{1}{\tau_X + \frac{1}{\Gamma} + \Gamma\, \tau_X\, \tau_{XX}} \\ I_{XX} &\propto \frac{p_{XX}}{\tau_{XX}} = \frac{1}{\tau_{XX} + \frac{1}{\Gamma} + \frac{1}{\Gamma^2\, \tau_X}} \end{aligned} \tag{1.2.3.10}$$

At low enough excitation powers ($\Gamma \ll 1$), Equations (1.2.3.10) can be rewritten:

$$\begin{aligned} I_X &\propto \frac{\Gamma}{1 + \Gamma\, \tau_X + \Gamma^2\, \tau_X\, \tau_{XX}} = \Gamma\left(1 - \Gamma\, \tau_X + o(\Gamma)\right) \approx \Gamma - \Gamma^2\, \tau_X \\ I_{XX} &\propto \frac{\Gamma^2 \tau_X}{1 + \Gamma\, \tau_X + \Gamma^2\, \tau_X\, \tau_{XX}} = \Gamma^2 \tau_X \left(1 - \Gamma\, \tau_X + o(\Gamma)\right) \approx \Gamma^2\, \tau_X \end{aligned} \tag{1.2.3.11}$$

whereas at very high excitation powers ($\Gamma \gg 1$), for which the probability of getting biexcitons is extremely significant, Equations (1.2.3.10) provide:

$$\begin{aligned} I_X &\propto \frac{\frac{1}{\Gamma\, \tau_X\, \tau_{XX}}}{1 + \frac{1}{\Gamma\, \tau_{XX}} + \frac{1}{\Gamma^2\, \tau_X\, \tau_{XX}}} = \frac{1}{\Gamma\, \tau_X\, \tau_{XX}}\left(1 - \frac{1}{\Gamma\, \tau_{XX}} + o\left(\frac{1}{\Gamma}\right)\right) \approx \frac{1}{\Gamma\, \tau_X\, \tau_{XX}} \\ I_{XX} &\propto \frac{\frac{1}{\tau_{XX}}}{1 + \frac{1}{\Gamma\, \tau_{XX}} + \frac{1}{\Gamma^2\, \tau_X\, \tau_{XX}}} = \frac{1}{\tau_{XX}}\left(1 - \frac{1}{\Gamma\, \tau_{XX}} + o\left(\frac{1}{\Gamma}\right)\right) \approx \frac{1}{\tau_{XX}} - \frac{1}{\Gamma\, \tau_{XX}^2} \end{aligned} \tag{1.2.3.12}$$

It can be directly seen from Equation (1.2.3.11) that at low pumping rates, the dependence of the luminescence intensity on excitation power will be mainly linear for excitons, while it will be quadratic for biexcitons. At very high excitation powers, the model leads to luminescence intensity converging towards 0 for exciton and saturating for biexciton (see Equation (1.2.3.12)), which is questionable: we would rather expect both intensities to saturate. In reality, other channels (related to other excited states) must be considered in this case [190]. Nevertheless, in the context of this PhD work, the low pumping rate approximation will be sufficient, in view of the investigated excitation power ranges.

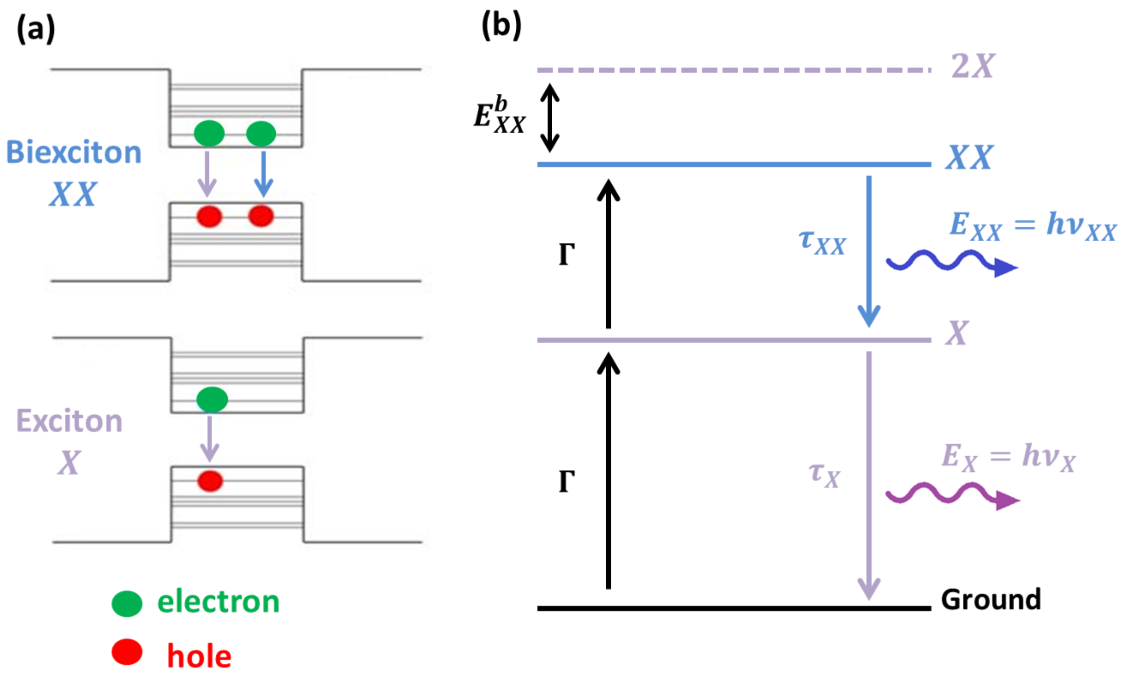

Figure 1.2.3.6: (a) Sketch of exciton X and biexciton XX confined into a quantum object. (b) Illustration of the “two-level model”: the ground state, X state, XX state and 2X state are sketched. The different parameters describing the system dynamics are indicated. The resulting XX and X emission energies E_X and E_{XX} are also represented, as well as the biexciton binding energy E^b_{XX} (positive here).

When considering a biexciton within a quantum object, additional Coulombian interactions must be taken into account, in comparison with the case of single exciton. Indeed, the two holes repel each other, and so do the two electrons, whereas extra attractive interactions due to the second electron-hole pair must be considered. Consequently, the biexciton emission energy, also represented in Figure 1.2.3.6, will be different from the exciton one, and can be simply expressed as [240]:

$$E^b_{XX} = E_X - E_{XX} = -(2J_{eh} + J_{ee} + J_{hh}) \tag{1.2.3.13}$$

where J_{eh}, J_{ee}, and J_{hh} are respectively the negative term corresponding to the Coulombian interaction between electron-hole pairs, and the positive terms related to the repulsive electron-electron and hole-hole interactions.

When increasing the carrier quantum confinement by reducing either dimensionality of a nitride object or its characteristic dimensions along confinement directions, the biexciton emission energy is expected to be enhanced, as theoretically demonstrated and experimentally verified for Wannier-Mott excitons confined in QWs [241, 242], QWires [194] or QDs [243, 244] made of direct bandgap semiconductors. In the case of nitride semiconductors, numerous biexciton binding energies were reported, especially for GaN/Al$_x$Ga$_{1-x}$N and In$_x$Ga$_{1-x}$N/GaN quantum objects. The energy values can vary from negative to positive depending on the object dimensions, as observed for GaN/Al$_x$Ga$_{1-x}$N (≈ -30 to +7 meV) [245-247] and In$_x$Ga$_{1-x}$N/GaN (≈ -16 to +16 meV) [248-250] quantum dots. Such variation is attributed to the built-in electric field within quantum dots described in Subpart 1.2.3.2. Indeed, when the dot size increases, especially in the polar direction, the QCSE term gets more significant and therefore reduces the overlap of carrier wavefunctions, leading to dominant repulsive hole-hole and electron-electron interactions at the expense of attractive electron-hole interactions. In other words, J_{ee} and J_{hh} values increase, while the $|J_{eh}|$ value decreases. Consequently, the biexciton binding energy diminishes and can be even negative. In contrast, extremely high biexciton binding energy values can be reached for optimized nitride heterostructures. A record value of +52 meV was obtained for a very small single GaN dot embedded into AlGaN on top of a NW [251], as shown in Figure 1.2.3.7, corresponding to about 9 times the value reported for bulk GaN (+5.7 meV) [252]. Other biexciton binding energy values higher than average were also reported, for thin InGaN/GaN (≈+15 meV) [253] and GaN/AlN (≈+20-40 meV) [254] QDisks in NWs.

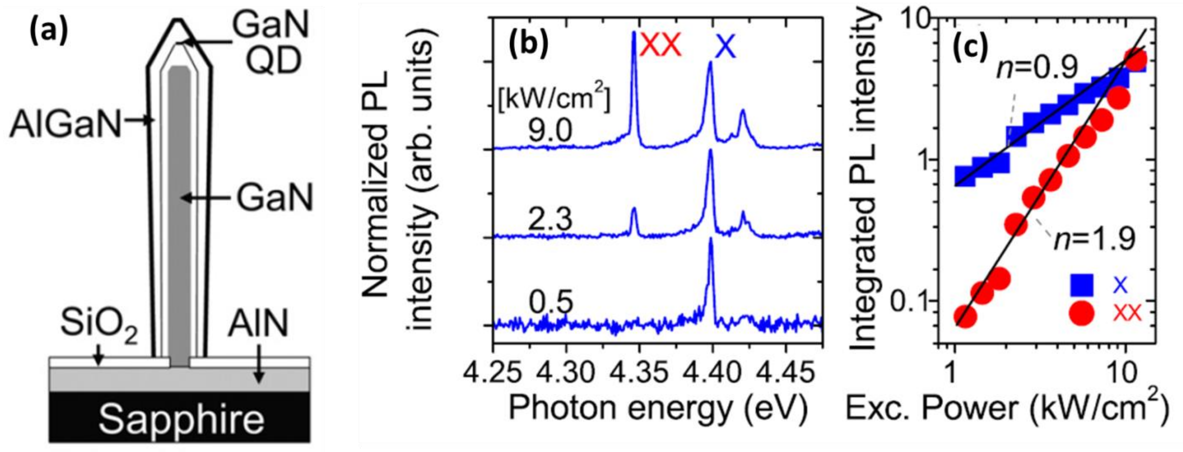

Figure 1.2.3.7: (a) Schematic of the NW heterostructure including the single GaN QD (b) Emission lines for biexciton XX and exciton separated by 52 meV. Due to extreme quantum confinement, the lines are blue-shifted up to around 4.4 eV (c) Linear and quadratic dependence of luminescence intensities on power, respectively for X and XX lines. The simple "two-level" model works well here: we are very likely within the low pumping rate range. Taken from [251].

1.3 Growth of III-Nitride semiconductors

In the following, we will first briefly present the mere epitaxial growth techniques for nitrides, which allow higher structural quality than other non-epitaxial techniques. We will more insist on the differences between techniques than on their exhaustive description. Second, we will describe the main growth mechanisms encountered in epitaxy, including the main kinetic processes, the strain relaxation mechanisms and the main growth modes of III-N semiconductors.

Before going further, let us remind that epitaxy consists in growing a given material on top of another crystalline one, generally a substrate or a template, while keeping an epitaxial relationship with the latter (lattice adaptation). We then distinguish homoepitaxy from heteroepitaxy. The latter, in contrast to homoepitaxy, means depositing a material on top of a different and lattice-mismatched one, which will lead to strain relaxation mechanisms that can deform the crystal. As for homoepitaxy, it leads to better crystalline quality, but the convenient matched substrates or templates are generally much more scarce or costly. In the case of III-N semiconductors, Si and sapphire substrates are commonly used, since they are cheap and of very high crystalline quality.

1.3.1 Main existing epitaxial growth techniques

To grow III-N semiconductors, two main epitaxial growth techniques exist:

- The VPE method, derived from the CVD technique. This technique uses precursors, generally either metalorganic (for the MOVPE technique [255]) or hydride (for HVPE [256]) compounds, containing the elements required for nitride growth. For instance, in MOVPE, used Ga- and N-precursors can be respectively trimethylgallium (TMGa) or triethylgallium (TEGa) and ammonia (NH_3). Brought by a carrier gas (generally hydrogen (H_2) or nitrogen (N_2)), these precursor compounds impinge in vapor phase on the substrate mounted on an oven inside a reactor. A chemical reaction then occurs at the heated substrate surface: the precursors first decompose in the absence of oxygen (pyrolysis), leaving the atomic elements to be incorporated on the substrate surface. Next, these species bond to the surface, creating a new crystalline layer, whereas the reaction by-products are evacuated out of the reactor by the carrier gas. Growth rates can exceed 100 µm/h in VPE.

- The MBE [257] technique, presenting the peculiarity of being operated in an ultra-high vacuum (UHV) chamber (typically around 10^{-10} mbar), which results in residual impurity concentrations inside grown samples lower than for VPE. Contrary to the latter, the deposition is physical: the precursors are the atomic elements themselves, which impinge on the substrate at low atomic fluxes to remain in UHV conditions. The latter significantly limit the growth rates, which are of the order of 1 µm/h. In addition, growth occurs far from thermodynamic equilibrium: it depends much on kinetics and surface phenomena presented in Subpart 1.3.2. It must be noted that for nitride growth in MBE, two sources are mainly used for the N atoms:

NH_3 or N-plasma. In the first case, N is obtained by thermal dissociation of NH_3 onto the substrate surface, whereas N_2 is dissociated by an electronic discharge in the second one. These two sources induce different growth conditions, so that comparing the corresponding growth mechanisms and parameters is uneasy. In the following of the manuscript, we will focus more on the plasma-assisted MBE (PA-MBE) technique used during this PhD. The specificities of our setup will be detailed in Subpart 2.1.1.

In view of the lower growth rates, lower sample homogeneity and reproducibility, but better residual impurity concentrations, MBE is much more used in fundamental research, whereas VPE, and especially MOVPE, is the most common industrial technique. For both techniques, the sources used for metallic and N species must be as pure as possible in order to avoid any contamination by undesirable elements. In the following of the manuscript, we will mainly focus on and refer to the MBE technique at the center of this work.

1.3.2 Main epitaxial growth mechanisms

1.3.2.1 Main kinetic and surface phenomena

Occurring far from thermodynamic equilibrium, MBE growth mostly depends on the kinetic processes illustrated in Figure 1.3.2.1. When reaching the surface of the sample being grown, the impinging atoms are first physisorbed: they are adsorbed via Van der Waals forces onto the surface (weak interaction with the latter). Then, the adsorbed atoms (called adatoms) which are not incorporated yet may diffuse on the surface and/or desorb. In a next stage, the adatoms which did not desorb chemisorb, meaning that they form chemical bonds with the sample surface and therefore change the chemical nature of the interface. At sufficiently high growth temperatures, the adatoms diffuse until being incorporated either by forming stable aggregates (nucleation of precursors, more detailed in Subpart 1.3.2.3) or by bonding at step edges (step-flow growth mode, more detailed in Subpart 1.3.2.3) [258]. Naturally, the occurrence and the magnitude of these surface phenomena depend both on the nature of the impinging atoms and on their local environment on the sample surface (chemical nature of this surface, types of sites: dangling bond, vacancy, step edge, etc.). In addition, they can be controlled to some extent by adjusting the main growth parameters, which are either kinetics-related (growth temperature and impinging atom fluxes) or of geometrical nature (the incidence angle of the impinging atoms). Such parameters will be exhaustively defined in Subpart 2.1.1 dedicated to our MBE setup.

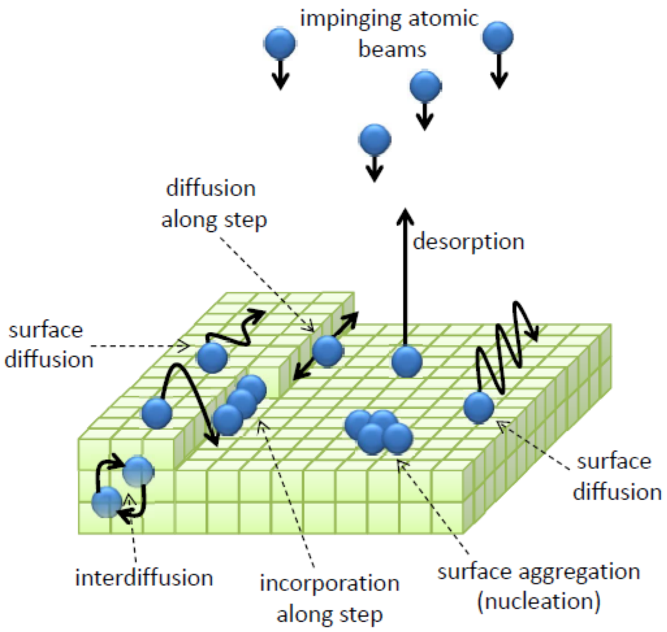

Figure 1.3.2.1: Sketch illustrating the main surface phenomena occurring during growth. Taken from [103].

We will describe the primary influence of such surface phenomena in the peculiar case of GaN and $Al_xGa_{1-x}N$ NW growth, respectively in Subparts 2.1.3 and 2.1.4.

1.3.2.2 Strain relaxation mechanisms

A given nitride material is generally grown in heteroepitaxy. In order to keep an epitaxial relationship with the material below, the deposited crystal undergoes strain, adapting its lattice parameter while storing elastic energy. Above a certain threshold depending on the lattice mismatch, this strain must be relaxed, either elastically or plastically.

Elastic relaxation consists in relieving the excess of stored energy through a shape transition which can be mathematically described. For small deformations, the stress σ_{ij} within the structure is indeed related to the strain ϵ_{kl} through Hooke's law:

$$\sigma_{ij} = \sum_k \sum_l C_{ijkl} . \epsilon_{kl} \tag{1.3.2.1}$$

with C_{ijkl} the fourth-ranked tensor of the elastic stiffnesses which can be reduced to a 6×6 matrix (second-rank tensor) due to the WZ symmetry. Consequently, we can rewrite Equation (1.3.2.1) as [126]:

$$\begin{pmatrix} \sigma_1 \\ \sigma_2 \\ \sigma_3 \\ \sigma_4 \\ \sigma_5 \\ \sigma_6 \end{pmatrix} = \begin{pmatrix} C_{11} & C_{12} & C_{13} & 0 & 0 & 0 \\ C_{12} & C_{11} & C_{13} & 0 & 0 & 0 \\ C_{13} & C_{13} & C_{33} & 0 & 0 & 0 \\ 0 & 0 & 0 & C_{44} & 0 & 0 \\ 0 & 0 & 0 & 0 & C_{44} & 0 \\ 0 & 0 & 0 & 0 & 0 & (C_{11}-C_{12})/2 \end{pmatrix} \begin{pmatrix} \epsilon_1 \\ \epsilon_2 \\ \epsilon_3 \\ \epsilon_4 \\ \epsilon_5 \\ \epsilon_6 \end{pmatrix} \tag{1.3.2.2}$$

where the pairs of indices $kl = \{xx, yy, zz, yz, zx, xy\}$ are replaced by the indices $\{1, 2, 3, 4, 5, 6\}$ to lighten notations, like in 1.1.3. Theoretical values of these coefficients can be easily found for bulk WZ nitride binaries [105, 259, 260]. Experimental values were also widely reported from characterization of either bulk or epilayer samples, for GaN [261-263], AlN [264] and InN [265, 266]. Table 1.3.2.1 gives values of several coefficients for GaN and AlN that will be needed for processing results of XRD experiments described in Subpart 2.2.2.

	AlN	GaN	InN
C_{13} (GPa)	108	106	91
C_{33} (GPa)	373	398	243

Table 1.3.2.1: Values of C_{13} and C_{13} elastic stiffnesses for AlN, GaN and InN, taken from [13, 102].

The other way of relieving the stored energy excess is to relax plastically. This consists in either introducing dislocations or cracks in the sample, which are both extended defects within the crystalline arrangement. In III-N semiconductors, the most common kinds of dislocations are misfit dislocations (MDs) and threading dislocations (TDs). MDs, illustrated in Figure 1.3.2.2 (a), are a consequence of the mismatch between the substrate and the epilayer. Remaining confined at the interface, they efficiently relieve the strain. On the other hand, TDs propagate through the whole layer and can be of three types: pure edge, pure screw or mixed. Pure edge and pure screw TDs are depicted respectively by Figure 1.3.2.2 (b) and (c). An edge dislocation can be seen as an extra atomic layer in the crystal. Their dislocation line vector $\vec{l}$ is perpendicular to the Burgers vector $\vec{b}$. As for screw dislocations, their dislocation line vector $\vec{l}$ is parallel to the Burgers vector $\vec{b}$.

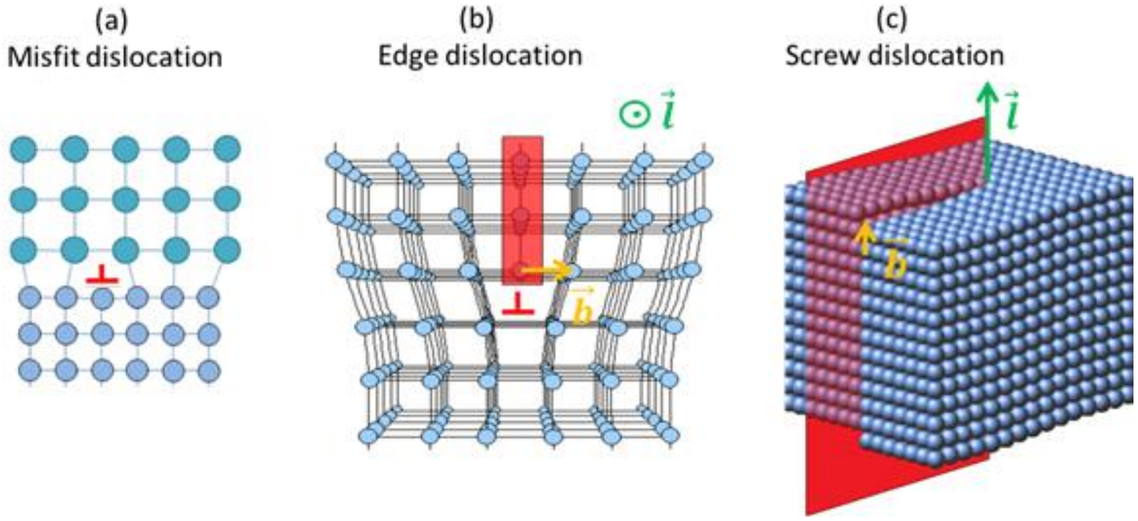

Figure 1.3.2.2: Sketch of the different types of dislocations: (a) misfit, (b) pure edge, (c) pure screw. Dislocation areas are represented in red. Burgers and dislocation line vectors are respectively labeled in orange and green.

Plastic relaxation commonly occurs in 2D nitride structures grown by heteroepitaxy, which may result in a high density of TDs [267] detrimental to light emission efficiency [144]. In nitride epilayers, typical TD densities over the 10^7 – 10^{10} cm^{-2} range are commonly observed. In contrast, given the PhD context, we mainly expected to deal with elastic relaxation processes when growing $Al_xGa_{1-x}N$/GaN NW heterostructures, due to efficient strain relief by NW sidewalls. Indeed, plastic relaxation only occurs during nitride NW nucleation through a MD which remains at the NWs/substrate interfaces [268], so that NWs are expected to be dislocation-free, unless peculiar NW growth is performed. For instance, dislocations were observed in core/shell GaN/AlN [103, 269] and In-rich InGaN/GaN [270] NWs with thick shells obtained in specific conditions.

1.3.2.3 Main epitaxial growth modes

First, we will shortly present the three main primary growth modes by which nitride films grow epitaxially on top of a crystalline substrate or a given nitride material previously deposited. Depending on the chemical potential of the first few deposited layers, one mode will be favored with respect to the others. Such potential is mostly function of the strain in these layers and of the kinetics (growth temperature and impinging fluxes), favoring either adatom-adatom (3D clustering or islanding) or adatom-surface (smoother layer) interactions. These three modes, illustrated in Figure 1.3.2.3, are the following:

- The Frank-van der Merwe (FM) mode, namely the layer-by-layer growth. Adatoms progressively incorporate on the surface until a full layer is completed. In the case of 2D nitride growth by MBE, such mode is typically observed when growing a material in homoepitaxy in N-rich (ratio of impinging metal atomic flux over N inferior to 1) or very slightly metal-rich (ratio remaining close to 1) conditions over growth temperature ranges ensuring proper adatom diffusion while limiting their desorption (typically 650-750°C). It is also obtained for growth of strained nitride material over the same growth temperature ranges, but in regimes metal-rich enough to accumulate a Ga bilayer. Consequently, the FM mode allows the growth of nitride 2D layers such as QWs [191] or thicker films [271]. It is notably used to calibrate the atomic fluxes of our MBE setup, as described in Subpart 2.1.2.3.

- The Volmer-Weber mode (VW), consisting in the direct formation of 3D islands on top of the surface, through elastic relaxation. In the case of 2D nitride growth by MBE, such mode was less sought and reported, in view of the lower structural quality of films resulting from the coalescence of 3D islands [272, 273].
- The Stranski-Krastanov mode (SK), which is a combination of the FM and VW modes: layer-plus-island. In the case of 2D nitride growth by MBE, such mode is commonly observed when growing a given nitride material in compression on top of another one, in N-rich conditions or over higher temperature ranges than FM mode to increase metal adatom desorption. It has been widely used to grow nitride QDs on 2D layers such as GaN/AlN [274] or InGaN/GaN dots [275].

In addition, two other growth modes, sketched in Figure 1.3.2.3 as well, can originate from the primary ones:

- The step-flow mode, which actually derives from the FM mode. Indeed, in the case of 2D nitride growth by MBE, we can transit from the FM mode to the step-flow one by simply increasing the impinging metal flux to be in metal-richer conditions, while remaining over the same growth temperature ranges convenient for 2D growth. Doing so improves the mobility of metal adatoms so that they can more easily incorporate at step edges. This growth mode was demonstrated to give layers of better structural quality than the FM mode, given that the metal excess limits the surface roughening resulting from N-rich growth [276, 277].
- The columnar growth mode, namely self-induced NW growth. In the case of nitride growth by MBE, such mode stems from the VW one, when growing on mismatched substrates like Si wafers. Indeed, 3D island precursors are first formed through elastic relaxation on the substrate surface, before relaxing into NW by introduction of MDs remaining at the NW/substrate interfaces [268]. As previously mentioned, we will detail the peculiarities of nitride NW growth by PA-MBE in Subparts 2.1.3 and 2.1.4.

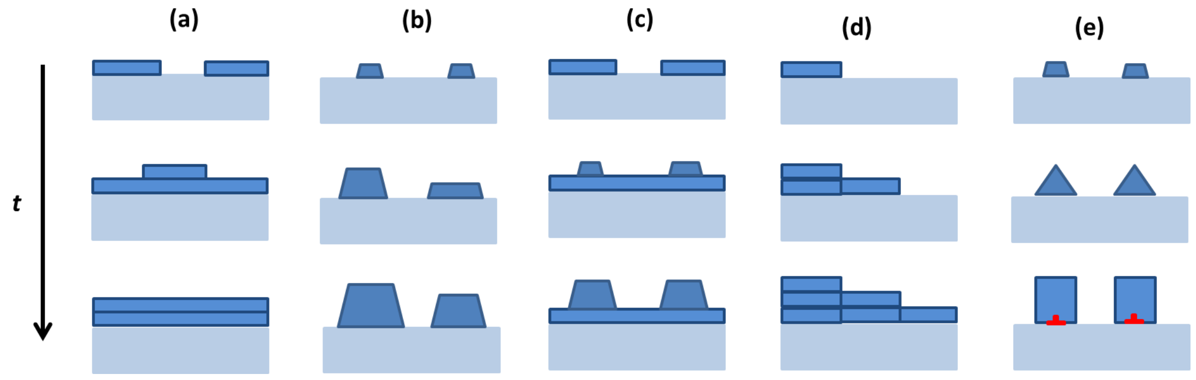

Figure 1.3.2.3: Various growth modes possible in PA-MBE. Primary modes: (a) Frank-van der Merwe mode, (b) Volmer-Weber mode, (c) Stranski-Krastanov mode. Additional mode: (d) Step-flow mode, (e) Self-induced columnar mode (misfit dislocations shown in red).

By extension, all the three primary modes can be retrieved in the case of nitride NW growth by MBE. First, as already mentioned, the VW mode is involved in the nucleation process of nitride NWs. Second, similarly to the "layer-by-layer" 2D growth (FM), the equivalent mode for nitride NWs, which could be called "section by section", occurs for typical NW growth conditions: weakly strain-affected, N-rich regime and growth temperature range convenient for NW growth. Last, the SK mode can be triggered when growing a nitride material NW section in compression on top of the previous one. However, reaching conditions favorable to the SK transition is less trivial than in the 2D case, as compressive strain is efficiently relaxed by the NW sidewalls. To hinder such relaxation, the NWs can be widened to allow the SK mode, as theoretically predicted [278] and experimentally observed [225].

2. Experimental methods

2.0 Introduction

This second chapter is aimed at presenting the numerous techniques used to grow and characterize our NW samples during this PhD. First, after a brief overview in chapter 1 of the MBE growth technique, the latter will be more detailed in the following: we will especially focus on the peculiarities of our MBE setup and its use for growing GaN NW templates and $Al_xGa_{1-x}N$ NW sections on top. In a next stage, the structural and optical characterization techniques used during this PhD work will be described. For a given technique, the related description will be more or less exhaustive, depending on its complexity, its contribution to the PhD results and the amount of time it was used. We will particularly insist on the interest and application of such techniques in the PhD context and provide the main technical details required for a full understanding of performed experiments and associated results.

2.1 Our growth technique: plasma-assisted molecular beam epitaxy (PA-MBE)

2.1.1 Presentation of the molecular beam epitaxy setup

2.1.1.1 The molecular beam epitaxy chamber

All the samples synthesized during this experimental work were grown in a PA-MBE setup designed by the company MECA2000. As sketched below in Figure 2.1.1.1 (a), the sample is placed inside our MBE chamber in which an UHV below 10^{-10} mbar can be reached (even below 5.10^{-11} mbar after a few weeks of pumping) thanks to a pumping system composed of a primary pump (scroll pump) and several secondary pumps (two turbo-molecular pumps and one ionic pump). UHV conditions ensure not only a very low rate of residual impurities in grown samples, as already mentioned in Subpart 1.3.1, but also ballistic trajectory for atoms during growth. In this case, their mean free path (about 10 m) is by far superior to the distance separating the effusion cells from the sample: we are working in what is called the Knudsen conditions. Samples can be introduced or taken out without degrading the chamber vacuum (especially with impurities such as oxygen) thanks to two airlocks: the entrance airlock is exposed at ambient air when recuperating samples and is pumped around 10^{-8} mbar otherwise, whereas the transfer airlock remains over a 10^{-10}-10^{-8} mbar range. Most impurities which were not removed by pumping within the chamber are trapped by a cryopanel cooled down by liquid nitrogen. The latter is necessary when operating effusion cells at high temperatures (above 800°C) during growth, as the panel area which surrounds the cells would expand too much and break otherwise. Several Bayard-Alpert gauges are placed in the chamber and airlocks to measure residual pressure in real time, whereas a quadrupole mass spectrometer (QMS) gives us the composition of residual gases in the chamber.

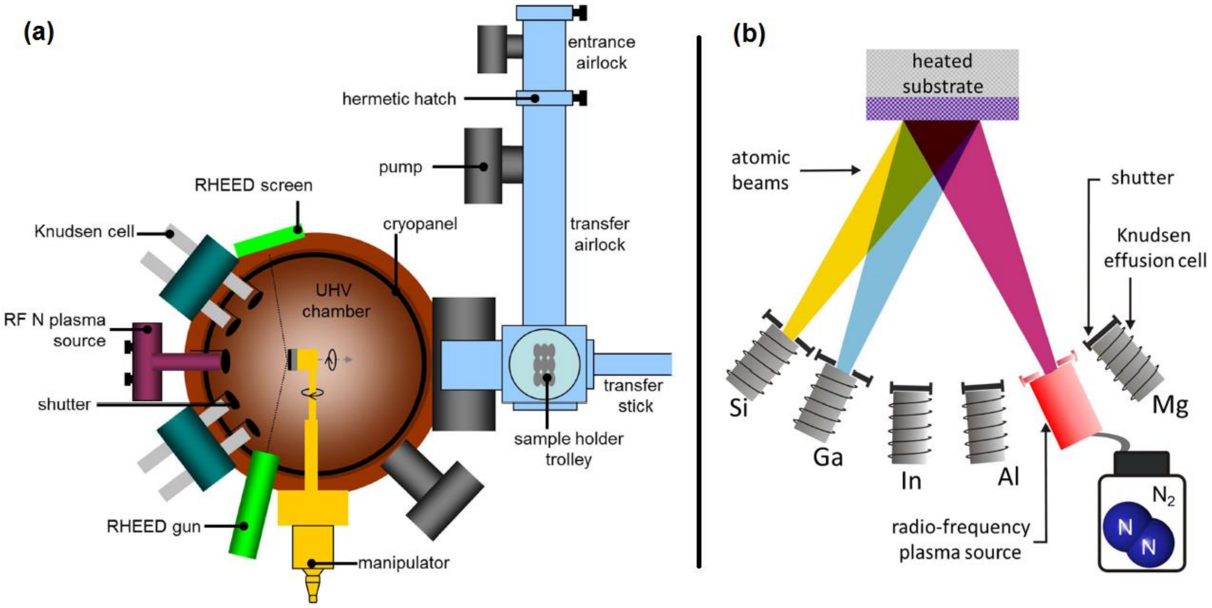

Figure 2.1.1.1: (a) Sketch of the Meca2000 PA-MBE machine used to grow samples during this PhD. (b) Schematic of the principle of growth in a PA-MBE. From [103].

2.1.1.2 The effusion and plasma cells

Regarding the effusion cells, each one contains loads of a pure metallic element (Al, Ga or In) or dopants (Si for n-doping, Mg for p-doping) placed in a pBN crucible. Load purities are typically comprised between 6N and 8N (xN means less than one atomic impurity per 10^x atoms). The temperature $T_{element}$ of each effusion cell can be varied to tailor the related atomic flux $\phi_{element}$ required for the sample growth. At high effusion cell temperatures, the partial pressure is of the order of 10^{-7}-10^{-6} mbar for the related metallic element gas-phase. As for the N plasma cell, from the company RIBER, it dissociates N_2 molecules thanks to a radio-frequency (RF) electronic discharge. In this case, both the flux of the incoming stream of N_2 molecules and the RF power injected in the plasma are parameters to tune the atomic flux. Given that only 1% of N_2 is dissociated, the N_2 flux is set at a related partial pressure of about 10^{-5} mbar, in order to have an active N flux ϕ_N of the same order of magnitude as the metallic fluxes ϕ_{metals}. Such conditions put us on the edge of the ballistic regime and are typically reached with the following parameters: a N_2 flux of 0.6 sccm (standard cubic centimeters per minute) and a RF power W_{plasma} of 300 W for the plasma cell mostly used during this PhD. Another plasma cell, also manufactured by RIBER, allowing higher growth rates, and operating at $\phi(N_2) = 1.4$ sccm, $W_{plasma} = 450$ W, was mounted and used for a few months, before being replaced by the initial one because of malfunction. The various ϕ_{metals} fluxes can be measured by a pressure gauge installed in place of the sample. However, these measurements are not very accurate and do not allow us to know ϕ_N. We will see in the following a more convenient method based on the monitoring of nitride 2D layer growth thanks to reflection high energy electron diffraction (RHEED) we describe afterwards in Subpart 2.1.2.3. All the cells have their own shutter to prevent the atomic beams from reaching the sample when required.

As for the geometrical configuration of cells, they are all disposed along an arc centered on the sample so that all the atomic beams converge towards the sample center, as displayed in Figure 2.1.1.1 (b). Consequently, assuming constant and collimated atomic beams leaving the cells, the atomic fluxes impinging on the sample surface depend on the beam incidence angle with respect to the sample surface normal (θ not equal to 0 for most cells). The sample can be also tilted away from the main axis of the MBE chamber, in order to change the incidence angle of the atomic beams. However, this tilt angle θ_{subs} was set to 0° for every growth run. The sample is initially a 2-inch bare Si (111) wafer used as a substrate for most NW growth runs and is mounted indium-free on a molybdenum holder (a molyblock) with a hole, in opposition to the method often used to stick smaller substrates with indium by capillarity. Finally, the sample can be rotated (at about 5 rpm) during growth in order to ensure the flux homogeneity on the substrate. Figure 2.1.1.2 introduces notation formalism used in the following of the manuscript.

2.1.1.3 *The regulation of sample temperature*

In order to tune the diffusion of atoms that have just impinged and adsorbed on the sample surface (adatoms), or desorption of these adatoms, the substrate temperature can be regulated by an oven comprising a tungsten filament heating the sample backside by radiation. Nonetheless, due to the UHV, the temperature of the substrate and its environment are not homogeneous, which makes the accurate temperature measurement of the surface not trivial. Three parameters can be used to estimate this temperature, as indicated in Figure 2.1.1.2:

- The temperature T_{subs} measured by a thermocouple in contact with the sample rear side. Nevertheless, this method is far from being accurate or reproducible. Indeed, the measurement depends on the environment geometry, which implies significant variations of the measured temperature as function of the used molyblock or the exact position of the thermocouple with respect to the sample.

- The electrical power in the oven filament P_{oven}. However, like the previous method, using this parameter does not ensure accurate or reproducible measurement. Indeed, the filament ages on a time scale of several months and its diameter progressively decreases, which increases the filament resistance and consequently its efficiency. In addition, the molyblock thermal inertia is not negligible.
- The characteristic desorption time of metallic adatoms t_{des} on the bare Si (111) surface, especially of Ga adatoms t_{des}^{Ga} in view of our growth temperature range, probed in situ by RHEED. This method is considered as the most reliable, when comparing several growth runs performed on various molyblocks, and will be detailed a bit further in Subpart 2.1.2.2 Hence, the calibration of substrate temperature as function of desorption time was systematically carried out prior to each growth. It must be known that temperature is inhomogeneous along the substrate radius due to the oven geometry, which can induce significant measurement errors if the calibration is not carefully performed at the Si wafer center. To a lesser extent, surface roughness can also be a source of error.

In the following chapters, desorption times must be firstly considered when checking and comparing sample growth conditions. The related substrate temperatures T_{subs} given in °C are those displayed by the thermocouple, unless specified otherwise, and will be also given if the thermocouple was operational at the time of the growth. As already mentioned, these thermocouple temperatures are far from being absolute, especially when comparing with reports published by other laboratories, and tend to be overestimated. It must also be noted that the temperature gradient along the substrate radius depends on the geometry of the mounted oven and its filament. This gradient is more significant when using an oven comprising a round filament, in comparison with the flat filament we mainly worked with. In both cases, a mainly monotonous decrease of the temperature from the center to the edge is obtained. Starting from the center, the temperature difference remains low along the first 10-15 mm of the 1-inch radius, ensuring a rather homogeneous growth over the related substrate area, but gets abrupt for the last 10 mm and reaches at least 30-35°C with respect to the center [103]. Such a difference can be advantageously used to explore different growth conditions on a single substrate.

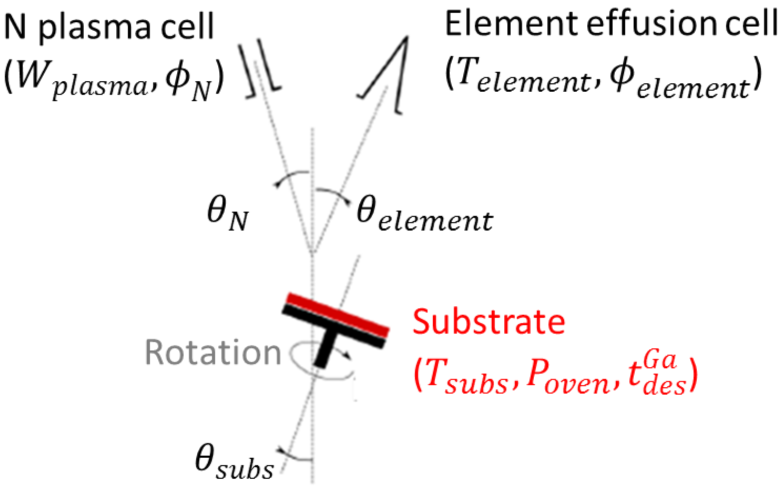

Figure 2.1.1.2: Sketch of the MBE chamber giving the main notation formalism.

2.1.1.4 In situ monitoring with reflection high energy electron diffraction (RHEED)

In order to monitor the sample surface in situ, a RHEED gun is installed in the chamber. A collimated electron beam (spot size of the order of 1 mm) is emitted from this gun towards the sample at grazing incidence (small angle, typically of the order of 2-3°) and the resulting diffracted beam pattern can be observed on a phosphorescent screen. The latter is recorded in real-time with a camera, which allows a numerical analysis. In virtue of the wave-particle duality, the impinging electrons have a de Broglie wavelength λ, associated to their momentum p by $\lambda = h/p$ with h the Planck constant. When accelerated by a high voltage, the speed of the extracted electrons is close to the speed of light c [279]. Thus, the relativistic expression of the momentum p must be considered:

$$\lambda_{e^-} = \frac{h}{\sqrt{2m_0eV\left(1+\frac{eV}{2m_0c^2}\right)}} \tag{2.1.1.1}$$

with m_0 the rest mass of the electron, e its charge and V the accelerating voltage. In our case, the accelerating voltage used is 32 kV, so that the electron wavelength is equal to about $0.00675\ nm$. The incident electron beam is scattered by the atoms of the first atomic layers of the surface for which periodicity gives rise to a diffraction pattern at specific azimuthal angles (rotation axis parallel to the sample surface normal). This diffraction pattern corresponds to the intersection of the surface electronic density Fourier transform with the Ewald sphere of radius $k_0 = \frac{2\pi}{\lambda_{e^-}}$, as shown in Figure 2.1.1.3.

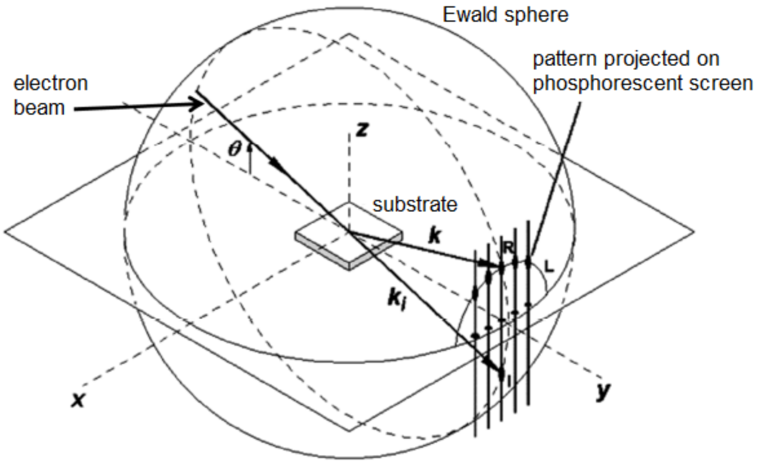

Figure 2.1.1.3: Sketch illustrating the principle of RHEED. Taken from [103].

Real-time analyses of such patterns enable to follow ongoing modifications of the surface during growth. Figure 2.1.1.4 illustrates some of the typical RHEED patterns and their associated surface morphology.

- In the ideal case of a perfect surface, the surface electronic density Fourier transform consists in rods perpendicular to this surface. The intersection of the Ewald sphere with these rods corresponds to infinitesimal spots placed on an arc. In practice, streaks are obtained instead of spots due to the non-ideal character of the experiment [280]. Indeed, rods have a finite thickness because of thermal agitation within the crystal. Moreover, the beam slightly diverges both in angle and in energy, which results in a dispersion in k_0, the radius of the Ewald sphere: the latter is not an ideal sphere but has a shell with a finite thickness Δk_0. Finally, the Ewald radius is much larger that the characteristic dimensions of the reciprocal lattice ($k_0 \cong 930$ nm^{-1} whereas $a^* = \frac{2\pi}{a}$ is over the 10-20 nm^{-1} range for probed Si and nitride materials). In other words, the Ewald sphere is almost flat in the area where it intersects the rods, so that the real intersection occurs on a certain length [281]: hence, we observe long streaks parallel to the sample surface normal.
- For a polycrystal, all sorts of in-plane periodicities can be encountered. The rods are oriented in all directions and intersect the Ewald sphere nearly everywhere. Consequently, the observed pattern has a ring-shape. In terms of epitaxy, the apparition of such a ring-like pattern generally means that grains with different orientations are growing, signs of a poor crystal quality.
- If the surface contains small surface steps or a certain degree of roughness, the diffraction pattern is seen by transmission through the asperities. In this particular case, the spots are not to be confused with the intersection of infinitesimal surface rods with the Ewald sphere. Hence, the intensity of the streaks we would obtain with a flat surface is modulated, which gives sort of uncomplete streaks on the pattern [282].

- If islands are present on the surface, diffraction on the island facets induce additional lines on the pattern. More specifically, islands high enough such as NWs introduce an out-of-plane periodicity, which is visible on the pattern by transmission of the electron beam through the other islands. RHEED spots lengthen due to the rods on the facets.

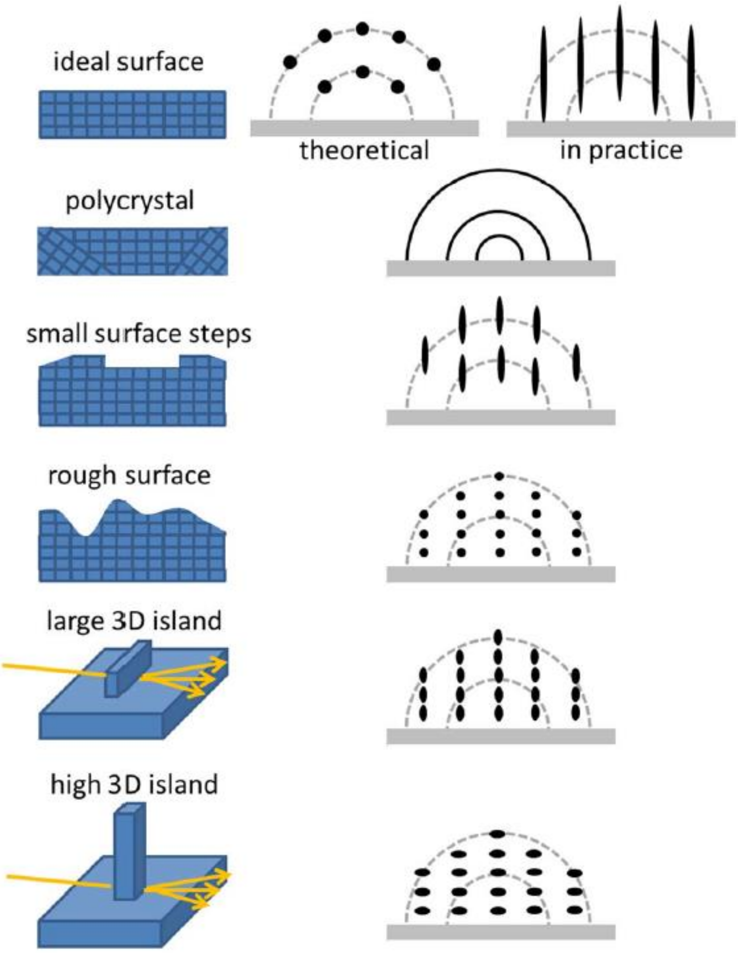

Figure 2.1.1.4: Sketches of several typical surface morphologies that can be obtained when growing and their related RHEED patterns. Taken from [103].

It must be known that most electrons do not undergo single elastic scattering but multiple ones [283]. Consequently, we usually do not draw quantitative data from the RHEED diffracted intensities. However, values can be extracted from the periodicity observed in the patterns. For small enough beam incidence angles, the horizontal distance Δx between two fringes (or two arrays of spots) on the RHEED pattern can be related to the inter-planar in-plane distances d by $\Delta x = (\lambda_e - D)/d$ where D is the distance between the surface of the probed sample and the RHEED screen, typically of the order of 1 m. As we are in reciprocal space, the distance between two fringes on the screen is inversely proportional to the *d* spacing.

As already mentioned, RHEED is necessary for calibration of temperature before growth and of atomic fluxes that we will describe in Subparts 2.1.2.2 and 2.1.2.3, respectively.

2.1.2 Preparation of substrates and calibrations

2.1.2.1 Preparation of substrates

During this PhD, we mainly used Si (111) wafers. For nitride NW growth by MBE, such substrates combine numerous advantages compared to other substrates commonly used for nitride growth such as sapphire or SiC. Indeed, they are first much cheaper. Second, their manufacturing, especially by Czochralski process, is perfectly mastered, which results in ultra-high quality wafers. Last, both their p- and n-doping are completely controlled. Contrary to 2D heteroepitaxy, their large lattice mismatch with nitrides (17% with GaN and 19% with AlN) is not an issue here, as nitride NWs plastically relieve this mismatch at the interface, allowing the crystal to subsequently grow with a perfect crystalline quality [268]. The Si (111) wafers used for our growth runs were 2-inch wide, highly n-doped (equivalent resistivity lower than $0.005\ \Omega.\mathrm{cm}$) and $275\ \mu\mathrm{m}$ thick.

Such Si wafer must be deoxidized before its introduction in the MBE chamber. To do so, it is dipped in hydrofluoric acid (HF) diluted at 10% during $45\ \mathrm{s} \pm 3\ \mathrm{s}$ to remove the native SiO_2 oxide from its surface, and rinsed with deionized water. Then, it is immediately placed onto the internal rim of a molyblock and maintained thanks to two molybdenum clamps. Once the molyblock is positioned onto the MBE chamber oven, the wafer is preheated for 30 minutes at about 300°C in order to outgas possible hydrocarbons from its surface, before rising temperature up to about 900°C for about 15 minutes in order to remove the few remaining oxide. Over a certain temperature range, a neat and typical Si (111) 7×7 reconstruction appears on RHEED screen [284-289] (absolute temperature range of the order of 600-850°C), if the wafer surface was properly cleaned. This re-arrangement of the topmost atomic monolayer (ML) is a well-known phenomenon occurring in UHV conditions to minimize the crystal energy. The atoms of this topmost layer change periodicity, which is 7 times larger than the bulk atoms underneath in the case of Si (111). Figure 2.1.2.1 shows a schematic representation of the 7×7 reconstruction and the corresponding RHEED patterns for two specific azimuths: $[11\bar{2}]$ and $[1\bar{1}0]$ when expressed with indices belonging to the Si cubic cell, which correspond to $[1\bar{1}00]$ and $[11\bar{2}0]$ in the Si reduced hexagonal cell, respectively, more convenient when working with WZ nitrides (see Annex 1.3).

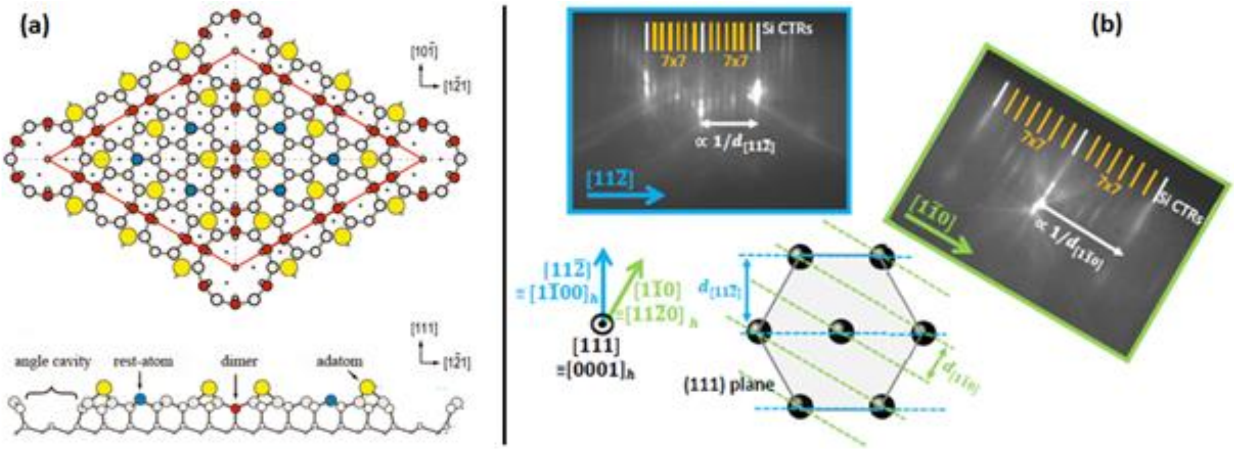

Figure 2.1.2.1: (a) 7 X 7 Si (111) surface reconstruction structure (top view at the top and side view at the bottom). (b) 7 X 7 Si (111) surface reconstruction observed on RHEED along $[11\bar{2}]$ and $[1\bar{1}0]$ azimuths, taken from [103].

We also worked sometimes with 10 mm x 10 mm pieces of GaN (or AlN) epilayers grown on c-plane sapphire, for atomic flux calibrations detailed in Subpart 2.1.2.3. Such pieces must be degreased before being stuck with In on a plain molyblock by capillarity. To do so, they are successively dipped in dichloromethane, acetone and methanol for 5 minutes each. Once the molyblock is introduced in the chamber, the temperature is raised for atomic flux calibrations over ranges typically used for growing GaN or AlN 2D layers (of the order of 650-750°C). It must be noted that the temperature cannot be raised much above 750°C without risking of unsticking the bulk piece.

2.1.2.2 RHEED calibration of growth temperature with a Si (111) wafer

As previously mentioned in Subpart 2.1.1.3, a procedure was used to calibrate the substrate surface temperature prior to each growth on Si (111) wafer. This reported procedure relies on the dependence of Ga desorption time t_{des}^{Ga} on the substrate temperature [290, 291]. In practice, we follow the 7 × 7 reconstruction transient response for the $[11\bar{2}]$ azimuth while operating the Ga shutter, as illustrated in Figure 2.1.2.2.

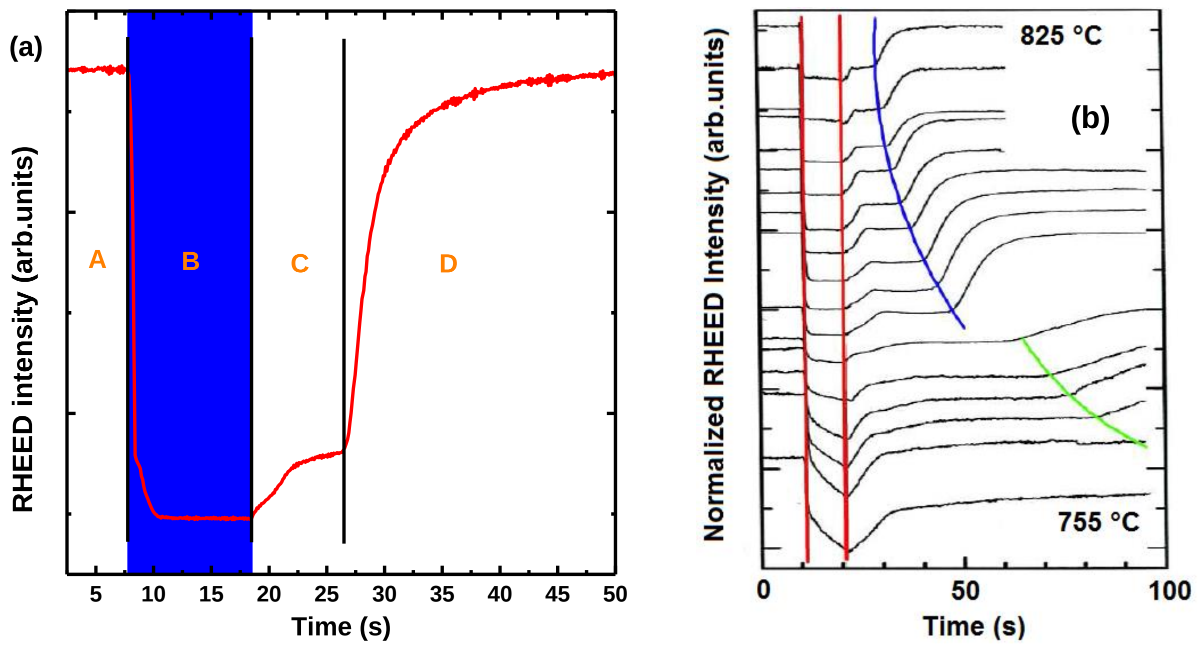

Figure 2.1.2.2: (a) 7 X 7 Si (111) surface reconstruction transient response. The Ga shutter is opened at the end of zone A. Zone B corresponds to the 10 s period during which the Si surface is covered with Ga adatoms. At the end of Zone B, the Ga shutter is closed. The delay between the Ga shutter closure and the end of Step C corresponding to the first inflexion point is defined as the Ga desorption time t_{des}^{Ga}. (b) Transient responses recorded at various substrate temperatures (highest to lowest T_{subs} from top to bottom) with 10 s of Ga deposition (similar to zone B in (a)). For low T_{subs}, the RHEED intensity does not reach a constant value in zone B but keeps decreasing, meaning that we are no longer in the Ga auto-regulated regime mentioned below. Taken from [291].

Once the temperature of the substrate is stabilized, its surface is exposed to a Ga flux ϕ_{Ga} during 10 s: as exhibited in Figure 2.1.2.2 (a), which shows a typical transient response obtained for the procedure, this Ga coverage leads to a drop of the 7 × 7 reconstruction RHEED intensity (zone B). After 10 s, the Ga shutter is closed: while Ga atoms are no longer provided, the ones already adsorbed on the Si (111) surface start to desorb, as the 7 × 7 intensity rises. Two stages can then be identified, distinguished by the inflexion point between zones C and D. Figure 2.1.2.2 (b) shows transient responses obtained at different substrate surface temperatures displayed by the thermocouple. It can be seen that the inflexion point delimiting zones C and D is sensitive to the temperature change. Hence, the time between the Ga shutter closure and the inflexion point, which defines the characteristic desorption time introduced in Subpart 2.1.1.3, directly reflects the wafer surface temperature, allowing reproducibility from sample to sample whatever the molyblock holding the Si wafer (the related measurement uncertainty is of the order of 0.2 s). In view of the decrease in temperature along the wafer radius described in Subpart 2.1.1.3, the calibration must be carefully performed at the wafer center every time in order to ensure this reproducibility. To do so, we first measure, for a given filament electrical power or a given thermocouple temperature, Ga desorption times at several electron beam positions on the wafer, the smallest measured desorption time corresponding to the substrate center area. This procedure is very reliable since the characteristic desorption time t_{des}^{Ga} is stable when changing ϕ_{Ga} and Ga deposition time over wide ranges, a consequence of the Ga auto-regulated regime [292], as shown in Figure 2.1.2.3.

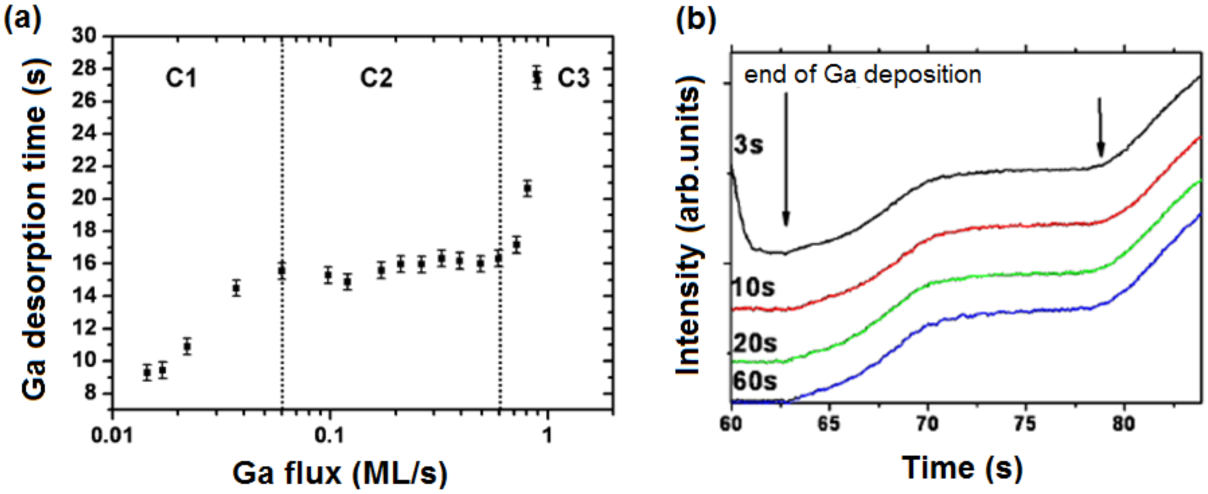

Figure 2.1.2.3: (a) Ga desorption time t_{des}^{Ga} versus Ga flux ϕ_{Ga}, for a given substrate temperature T_{subs}. Ga shutter was opened during 10 s. It can be seen that t_{des}^{Ga} remains stable (around 16 s) in zone C2, over about a ϕ_{Ga} decade. (b) Transient responses recorded for several Ga deposition durations (3, 10, 20 and 60 s), with $\phi_{Ga} = 0.25$ ML/s, value belonging to zone C2 in (a). t_{des}^{Ga} remains stable as well, around 16 s. From [292].

It can also be used to evaluate the real Si (111) surface temperatures. Indeed, we previously mentioned in Subpart 2.1.2.2 that the 7 × 7 reconstruction disappears above about 850°C according to the literature. Consequently, by comparing the temperature of the 7 × 7 reconstruction disappearance displayed by the thermocouple to the real one, we can estimate the discrepancy between displayed and real temperatures [103]. In practice, such estimation remains rough, since the values of the 7 × 7 temperature reported in literature vary over the 830-870°C range [285, 287, 289], and is valid only for temperature ranges close to the 7 × 7 disappearance temperature, such as typical NW growth temperatures. From the knowledge of this discrepancy, abacus of roughly estimated wafer surface temperature as a function of Ga desorption time can be deduced [103]. However, unless specified otherwise, temperatures given in °C in the following chapters will still be those displayed by the thermocouple, mainly for two reasons. First, the shift with respect to the real temperature can vary with both the oven, which was changed during PhD, and the used molyblocks, in addition to the uncertainty on the real 7 × 7 disappearance temperature. Second, in some cases, we will work over wide temperature ranges for which the simple shift subtraction performed above is not accurate.

2.1.2.3 RHEED calibration of atomic fluxes

After each maintenance opening of the MBE chamber, especially when metallic cells are refilled, the calibration of effective Al, Ga and N atomic fluxes must be performed. Note that an atomic flux said to be effective (written ϕ^{eff} in the following) refers to the impinging atoms that will be incorporated, excluding the atom flux losses caused by the setup geometry (beam incidence angles), adatom diffusion out of the sample surface or adatom desorption. Such calibration is done through the observation of RHEED oscillations when growing GaN or AlN 2D layers [293] over a bulk GaN 2D template. The principle is based on the monitoring of the specular RHEED spot intensity during the growth of a 2D layer in the Frank-van der Merwe mode described in Subpart 1.3.2.3 (ML by ML). This specular RHEED spot results from the simple reflection of the electron beam on the substrate surface. On the one hand, when a ML is completed, the roughness of the surface reaches a minimum, implying its larger reflectance. Hence, the specular RHEED spot intensity reaches a local maximum in this case. On the other hand, when a ML is half completed, the several islands constituting the uncompleted ML increase the surface roughness, which induces a more pronounced scattering of the impinging electrons and then results in a loss of intensity for the specular spot. Therefore, during one oscillation of the specular RHEED spot intensity, a ML was grown. Such calibration method allows us to determine a growth rate in ML/s. An example of RHEED oscillations observed during the growth of GaN is shown in Figure 2.1.2.4.

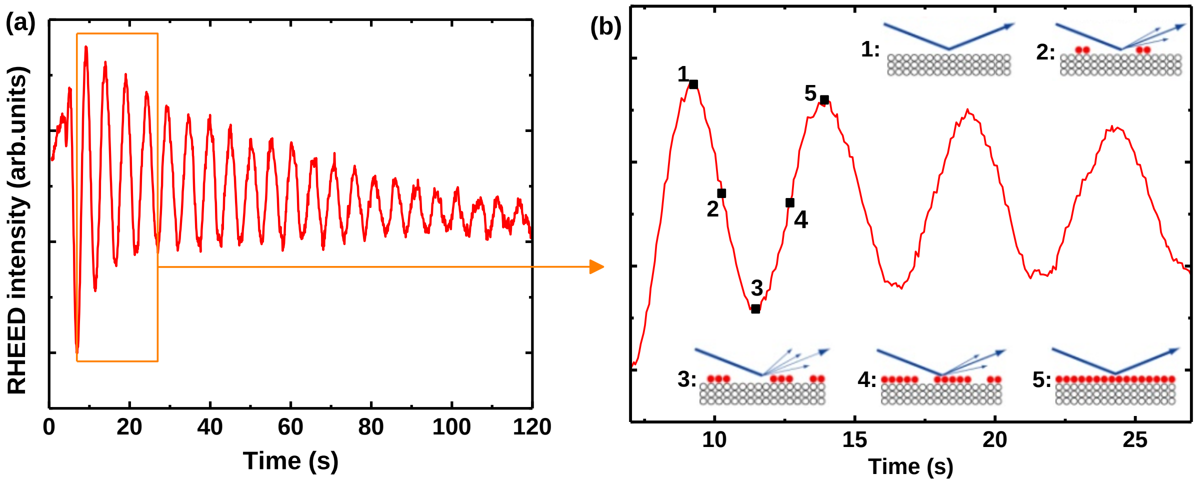

Figure 2.1.2.4: (a) Experimental RHEED oscillations recorded when growing a GaN 2D layer. (b) Principle of the RHEED oscillation technique used to calibrate the atomic fluxes is illustrated: when considering one period, the RHEED intensity is minimal when the top layer being grown is half completed (3) and maximal for fully completed top layers (1 and 5). The oscillations shown are those from the orange frame in (a).

For nitride growth, the protocol used to estimate the growth rates from RHEED oscillations is as follows. One of the atomic fluxes is kept constant, usually the N flux, whereas the other one, usually the metal flux, is tuned over a wide flux range by changing the related cell temperature. If the growth rate increases when increasing the metal flux, the metal is the limiting reactant, i.e. the N flux is larger than the metal flux and the growth is in the so-called N-rich regime. In this case, the growth rate depends on the effective metal flux ϕ_{metal}^{eff}. If the growth rate does not increase when increasing the metal flux, then N is the limiting reactant, i.e. the metal flux is larger than the N flux and the growth is in the so-called metal-rich regime. In this case, the growth rate depends on the effective N flux ϕ_{N}^{eff}. An example of calibration curves obtained for several metallic cells with this method is shown in Figure 2.1.2.5. The inflexion point for a given curve defines the cell temperature at which stoichiometry is reached for this cell. Between two MBE maintenance openings, typically separated by 3 to 6 months, fluctuations in the atomic fluxes in a range of 5-10% can be expected, so that the accuracy of the fluxes given throughout the manuscript is of this order.

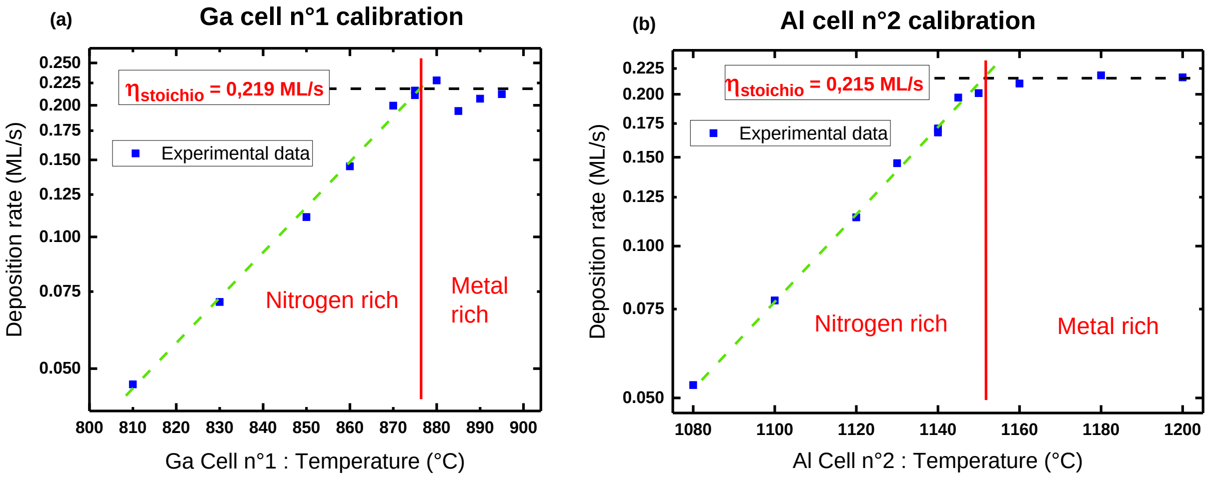

Figure 2.1.2.5: Calibration curves obtained from the RHEED oscillation technique, for: (a) a Ga cell, (b) an Al cell. The green and dark dashed lines are guides for the eyes (deposition rate axis on logarithm scale) in the N-rich region and for the limiting N flux ϕ_N in the metal-rich region, respectively.

Knowing the nitride binary growth rates, the effective atomic fluxes ϕ^{eff} can be derived by adapting the following relationship derived from previously reported models [294, 295]:

$$\eta_{binary} = \frac{\phi_{metal}\cos(\theta_{metal,hkil}) + \phi_N \cos(\theta_{N,hkil})}{\sigma_{binary,hkil}} \tag{2.1.2.1}$$

where η_{binary} is the growth rate for a given nitride binary, ϕ are the atomic fluxes leaving the cells (adatom diffusion and desorption losses neglected in the formula above), $\sigma_{binary,hkil} = \sigma_{metal,hkil} + \sigma_{N,hkil}$ is the atomic surface density (see Table 1.1.1.2 for atomic surface density values) for a given incident plane $(hkil)$ and θ is the incidence angles between the atomic beams and the normal to the incident plane $(hkil)$.

Indeed, for the N-rich regime, the effective metal flux ϕ_{metal}^{eff} being the limiting factor here, we can rewrite Equation (2.1.2.1) as:

$$\eta_{binary} = \frac{2\phi_{metal}^{eff}}{\sigma_{binary,0001}} \tag{2.1.2.2}$$

whereas, for the metal-rich regime, the effective N flux ϕ_{N}^{eff} being the limiting factor now, we obtain:

$$\eta_{binary} = \frac{2\phi_{N}^{eff}}{\sigma_{binary,0001}} \tag{2.1.2.3}$$

We directly notice that the AlN and GaN growth rate maximal values, corresponding to the growth rate $\eta_{Stoichio}$ at stoichiometry, slightly differ, due to the different atomic surface density σ for these binaries. It must be noted that the metal and N fluxes leaving the cells, ϕ_{metal} and ϕ_N, can be roughly estimated, neglecting the adatom diffusion and desorption losses, knowing the experimental geometry (namely the incidence angles), and using $\phi_{metal} = \phi_{metal}^{eff} / \cos(\theta_{metal,0001})$ as well as $\phi_N = \phi_N^{eff} / \cos(\theta_{N,0001})$.

We will see in Subpart 2.1.4 that, in practice, the effective growth rates are different when growing NWs, since surface phenomena such as Ga adatom diffusion are much more significant in the latter case compared to the present 2D layer growth-based calibration. Specific calibration can be performed in order to improve the accuracy of growth rate measurements in the NW case and will be detailed afterwards in Subpart 2.1.4.2.

2.1.3 GaN nanowire growth

2.1.3.1 GaN nanowire growth on Si (111)

Nucleation of GaN NWs grown by PA-MBE on bare Si (111), like those shown in Figure 2.1.3.1 (a), is self-induced (no catalyst required) and mostly occurs in the N-rich regime and for high substrate temperatures, where desorption and even decomposition of GaN become significant [227]. Such nucleation conditions can be summed up in a growth diagram [296], as shown in Figure 2.1.3.1 (b). For practicality, in the following of the manuscript, only the flux ratio referred to as the III/N ratio will be given, instead of the absolute values of the atomic fluxes. From the growth diagram, it can be seen that nucleation of NWs occurs more easily when using III/N ratios lower than 1 (N-rich regime) and growth temperatures higher than those typically used for 2D layer growth. However, NWs can also be grown with an III/N ratio above 1 at even higher temperature [297], due to the more significant desorption of Ga adatoms.

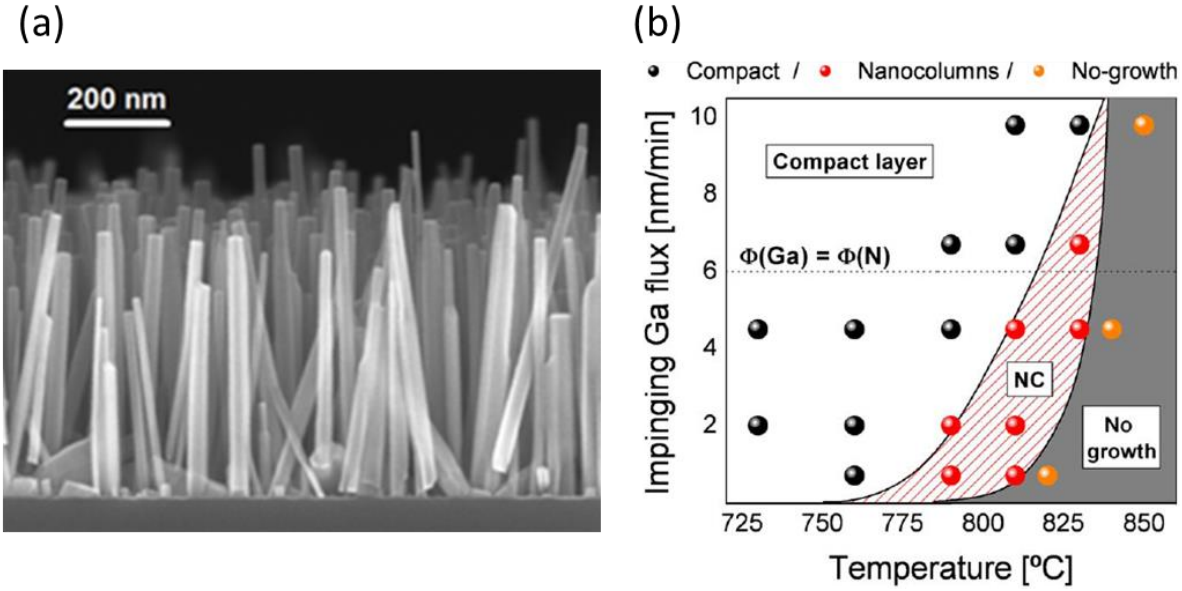

Figure 2.1.3.1: (a) GaN NWs grown by PA-MBE on bare Si (111). (b) Growth diagram for the self-organized nucleation of GaN NWs on Si (111), as function of the Ga flux ϕ_{Ga} and the substrate temperature T_{subs}. From [296].

Similarly to NW nucleation conditions, the NW density is directly related to kinetic parameters and gets lower for higher substrate temperature, as shown in Figure 2.1.3.2 (a), or for lower III/N ratio [298, 299]. This trend can be explained in terms of incubation time, which corresponds to the duration required for the 3D island precursors to reach their kinetics-independent critical size and relax into NWs [268]. As exhibited in Figure 2.1.3.2 (b), this incubation time increases when increasing substrate temperature or decreasing the III/N ratio [300]. In other words, due to higher Ga desorption/ GaN decomposition or lower supply in Ga adatoms, the size increase of precursors takes longer and their formation probability decreases, leading to a lower NW density. Consequently, knowing that the temperature progressively decreases along the Si (111) wafer radius, the NW density increases from the wafer center to its edge, hence the necessity to perform temperature calibration described in Subpart 2.1.2.2 very carefully.

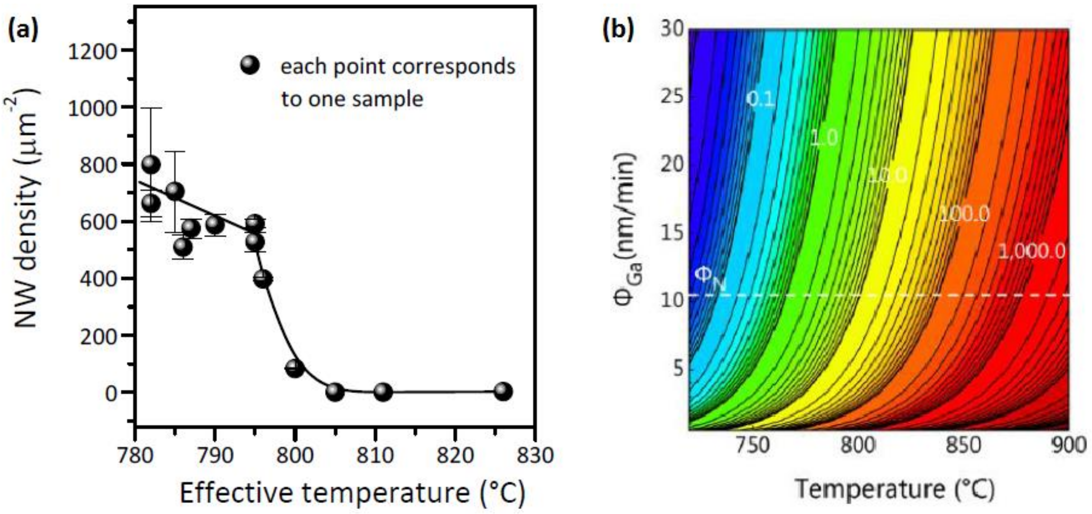

Figure 2.1.3.2: (a) GaN NW density at the Si wafer center versus the substrate temperature T_{subs}. Taken from [103, 298]. (b) Diagram giving the incubation time for GaN NWs nucleation on Si (111), as a function of ϕ_{Ga} and the substrate temperature (ϕ_N fixed). Taken from [300].

Moreover, we directly observe from Figure 2.1.3.4 (a) that typical GaN NWs can exhibit a very high aspect ratio for long enough growth time. Such a feature can be explained by the quasi-one dimensional NW growth, meaning that the NW axial growth rate is much higher than the radial one. The latter is mostly the result of the following contributions:

- The higher stability of non-polar facets with respect to polar facets, as demonstrated by surface energy calculations [301].
- The preferential adsorption and higher stability of N atoms on polar facets, in comparison with non-polar facets [29, 114].
- The geometry of the incident atomic beams: the angles of beams with respect to the substrate (c-plane) normal remain low during our growth runs, contrary to the angles of beams with respect to the m-plane normal. Consequently, the radial growth rate remains low, as theoretically predicted by geometrical models [294, 295] and experimentally observed [302].
- The diffusion of Ga adatoms along the NW sidewalls, for typical NW growth temperature ranges. These adatoms were evidenced to reach preferential incorporation sites at the NW top [303], despite the existence of rather high diffusion barriers along the c-axis on NW side facets [29]. The contribution of such diffusion to the axial growth rate was shown to be particularly significant for NW lengths inferior to the Ga adatom diffusion length [304].

Even if it remains low in comparison with the axial growth rate, the radial counterpart is non-negligible, especially at the beginning of the growth, as NWs were observed to enlarge from the 3D island critical size until reaching a wider and constant diameter [298]. This behavior was fully explained by a reported growth model emphasizing a self-regulated NW diameter [305]. At a given growth temperature, the latter can be increased with the III/N ratio. Indeed, if the NW axial growth rate saturates due to the limited N flux, an increase in the impinging Ga flux will lead to a NW enlargement until reaching a new equilibrium.

When growing longer, coalescence between neighboring NWs is more likely to occur and will reduce the NW density [299, 306, 307], as shown in Figure 2.1.3.3. Indeed, the NW first widens, as we have just seen that its diameter converges progressively until an equilibrium value. Second, NW bundling phenomena were evidenced from a certain critical NW length [307].

These results observed for GaN NWs nucleated on bare Si (111) can be extrapolated for growth on other types of materials such as AlN buffers. We will notably grow NWs on the latter and briefly present them in the next subpart.

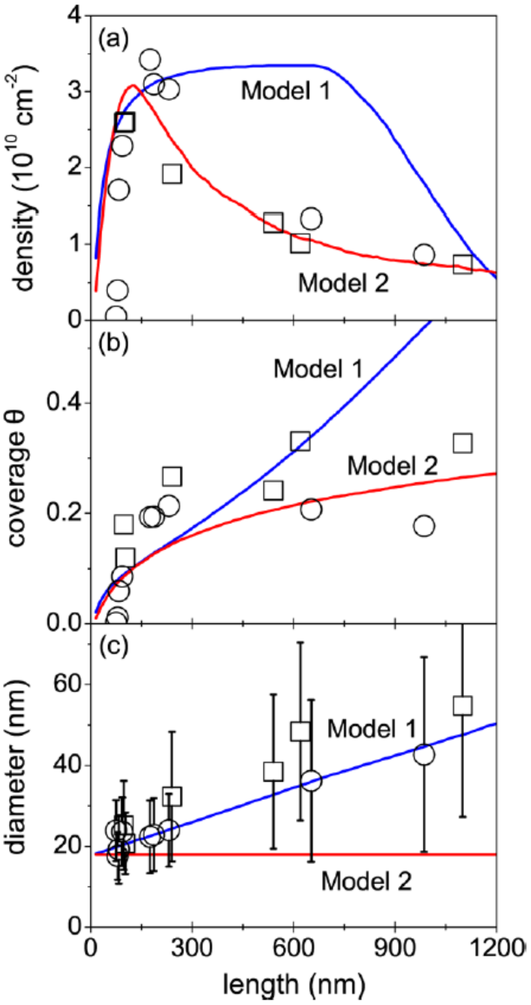

Figure 2.1.3.3: Evolution of NW density, substrate surface coverage (namely the fill factor) and NW diameter with NW length (in order words, growth duration), for GaN NWs grown on Si (111). Model 1 (blue) is based on the assumptions of a continuous radial growth of all nanowires and the preferential diffusion of Ga adatoms on the substrate toward already existing nanowires so that new nanowires do not nucleate at distances from the existing nanowires shorter than the Ga diffusion length on the substrate (taken to be 30 nm). Model 2 (red) simulates the coalescence by bundling. In this second model, radial growth is absent, and nanowire nucleation ceases because of the shadowing of the substrate from the impinging fluxes by already existing nanowires. From [307].

2.1.3.2 GaN nanowire growth on AlN buffer

An AlN buffer is in fact a thin AlN film (a few nanometer thick) that can be grown on our Si (111) wafers or on other substrate materials such as sapphire [308]. As shown in Figure 2.1.3.4, such a buffer leads to better GaN NW orientation, as well as better density homogeneity on the substrate, than for growth on bare Si (111) [309, 310]. Indeed, in the latter case, the broken-ring RHEED pattern highlights a significant twist, i.e. a spread in the in-plane orientation called in-plane mosaicity, and a higher average tilt, i.e. an out-of-plane mosaicity, can be directly observed on scanning electron microscopy (SEM) images. In addition, for given growth conditions, GaN NW nucleation is faster on AlN buffer than on bare Si (111), mainly because of the formation and amorphization of β-Si_3N_4 before NW nucleation start [312] and inducing an additional delay.

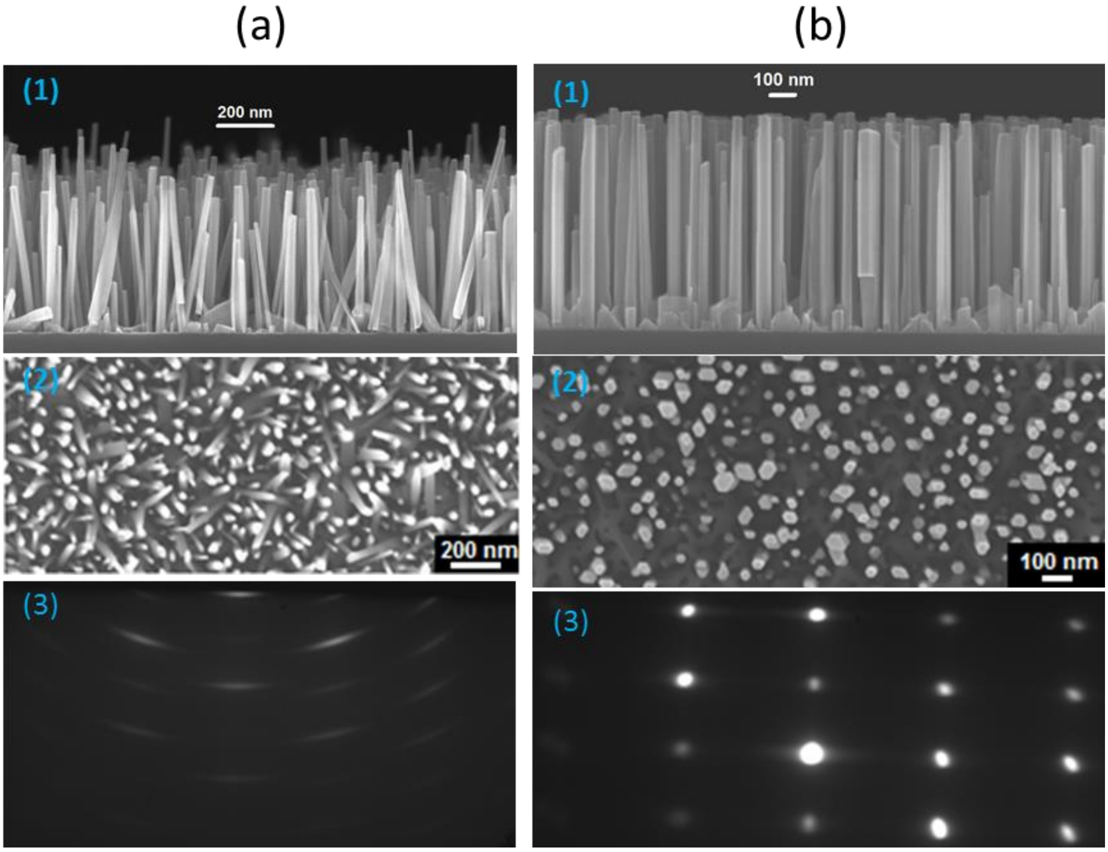

Figure 2.1.3.4: Comparison of GaN NWs grown: (a) without AlN buffer (sample N2470), (b) with a buffer (sample N2469). (1) Side-view SEM images. (2) Top-view SEM images (3) RHEED pattern image recorded along the $[11\bar{2}]$ azimuth.

Nevertheless, growing such a buffer may alter reproducibility from sample to sample, if this step is not carefully performed every time. Indeed, the AlN buffer structure was observed to influence both the GaN NW density [291, 308], higher than on bare Si (111) for given GaN NW growth conditions, and NW polarity [225, 313]. Regarding our runs, when growing an AlN buffer, Al is first deposited and subsequently nitrided. Such operation is repeated 3 times identically, so that about 4 nm of AlN is grown. A typical RHEED image of the thin AlN buffer is given in Figure 2.1.3.5. Such thickness allows the growth of well-aligned GaN NWs while keeping the nucleation time short [314].

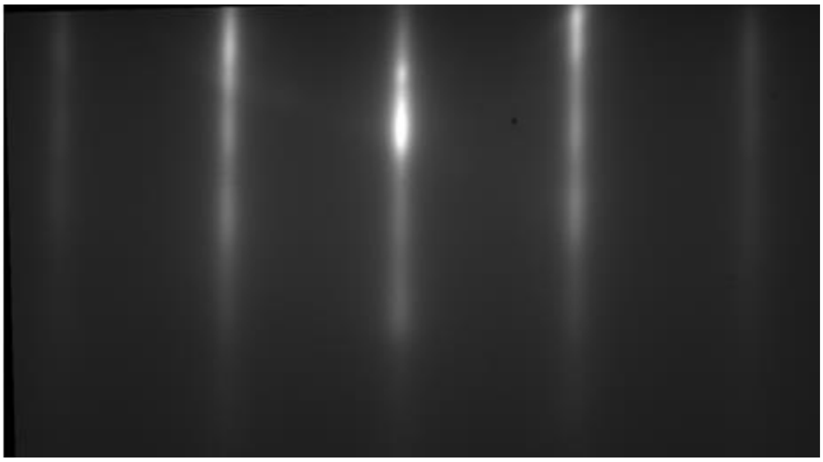

Figure 2.1.3.5: Typical RHEED of thin AlN buffer grown on Si (111) along the $[11\bar{2}]$ azimuth.

2.1.4 $Al_xGa_{1-x}N$ nanowire growth

2.1.4.1 AlGaN nanowire growth peculiarities

In this PhD work, the growth of GaN NW templates, detailed in Subpart 2.1.3, was first performed for all samples, before growing any Al(Ga)N-based NW structures. Two main reasons justify this approach:

- The non-triviality of NW nucleation for such ternary alloy, in view of the very different reactivity to growth conditions for the three involved elements.
- The limitations of the MBE oven. Indeed, in view of previous investigations of AlN NW growth [315], nucleating well-separated Al-rich Al(Ga)N NWs would require higher growth temperature ranges, not accessible with the present oven filament.

In view of the reactivity difference mentioned just before between species, especially for metallic elements, controlling both the average AlN molar fraction x of an $Al_xGa_{1-x}N$ NW section and its homogeneity are not trivial. Indeed, diffusion length and desorption rate are much more significant for Ga than for Al over the investigated substrate temperature ranges. Provided that the latter is high enough to promote NW growth, impinging Ga atoms can diffuse along the NW sidewalls to reach the preferential incorporation sites located at NW tops, as already mentioned in Subpart 2.1.3. They are then either incorporated at the NW top or desorbed (more or less quickly depending on substrate temperature) in case of too significant Ga adatom accumulation. The latter can be either due to Ga-rich growth conditions or caused by the natural Al preferential incorporation at the expense of Ga [316, 317], given that the Al-N bond is more stable: its energy is higher than the Ga-N one (2.88 eV versus 2.20 eV) [318]. All the surface phenomena previously presented and involved in the AlGaN NW growth are summed up in Figure 2.1.4.1. Knowing these growth mechanisms, we can easily understand why compositional fluctuations can be observed within AlGaN NWs [319-325], why an Al-richer shell grows on sidewalls [319, 321-329], or why an Al-richer 2D layer can grow between the GaN NW templates [71, 72, 330-334] when the density of the latter is not high enough to take advantage of the shadowing effect depicted in Figure 2.1.4.2. Depending on the experimental needs (characterization of as-grown ensembles of NWs or single dispersed NWs or both), the NW density must be carefully controlled. Indeed, the parasitic Al-richer layer must be avoided for macro-characterization of as-grown NWs, whereas NW dispersion will be easier when reducing NW density.

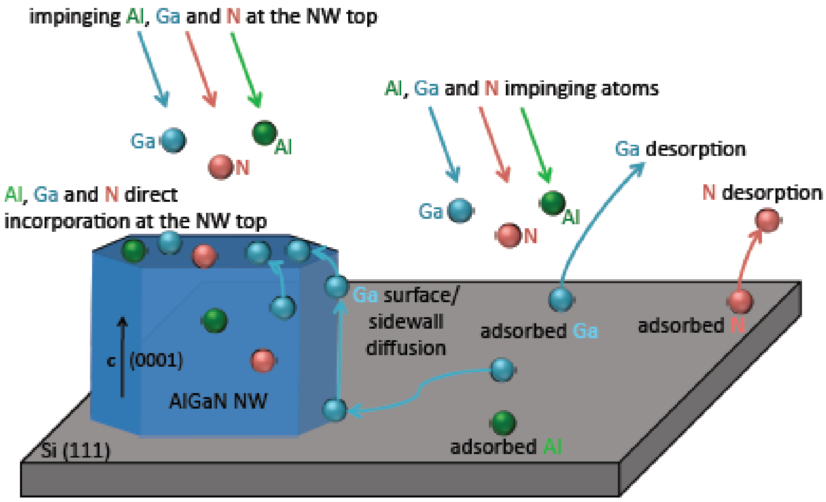

Figure 2.1.4.1: Sketch illustrating the main surface phenomena involved in the AlGaN NW growth mechanisms. Ga adatoms notably diffuse much more than Al ones. Taken from [139].

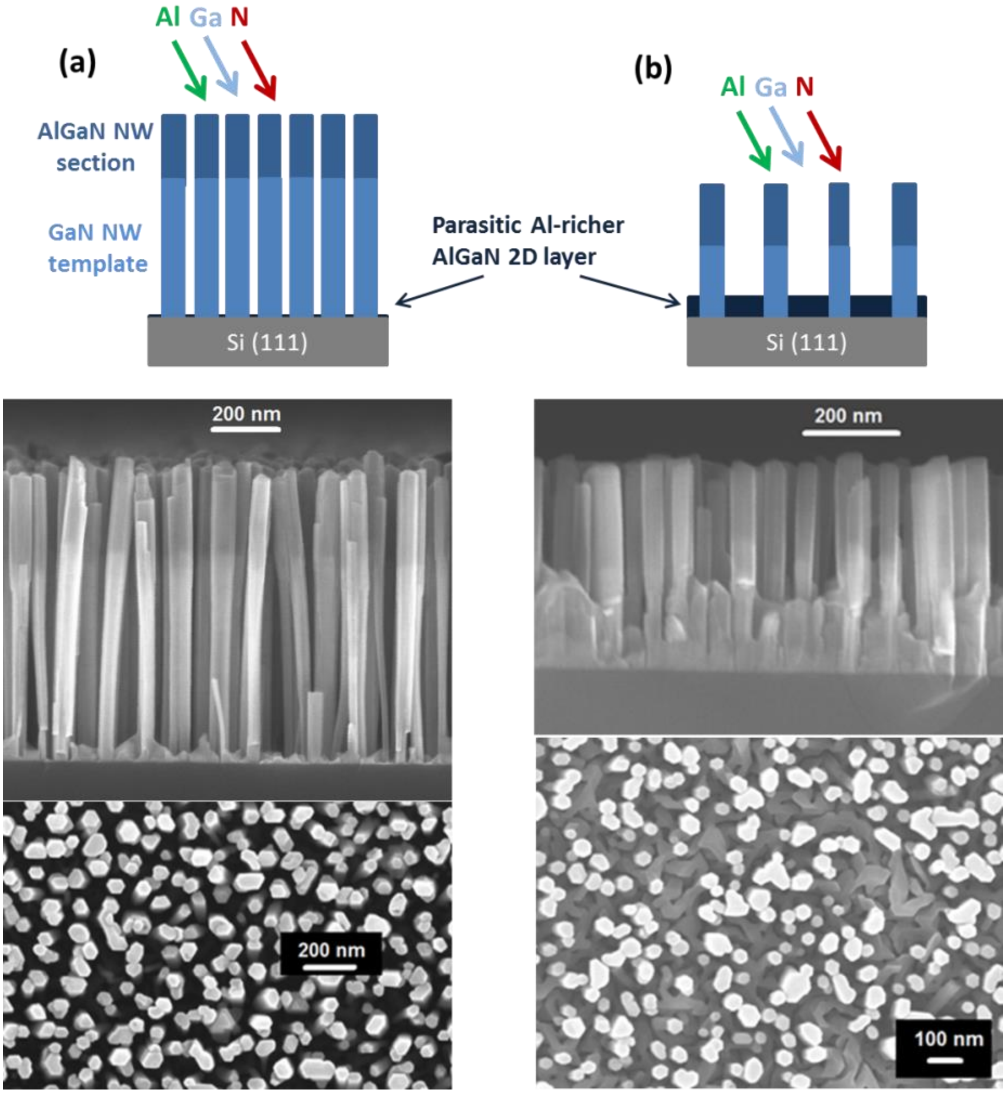

Figure 2.1.4.2: Sketch illustrating the shadowing effect. When growing AlGaN on top of dense and long enough GaN NW templates like in (a), the Al atoms impinging on the sample at a certain angle with respect to the wafer surface normal are unlikely to reach the NW bottoms due to their low diffusion length and will be mainly incorporated at the NW top. On the contrary, in (b), a significant number of adatoms reach the wafer, so that an Al-rich AlGaN 2D layer can form between the NWs. Typical side-view and top-view SEM images are given for (a) and (b) (for samples N2330 and N2501, respectively).

In addition to kinetics, the effect of strain in the NW section must also be considered, even if strain relaxation mechanisms are eased by the NW sidewalls and the lattice parameter mismatch for a given $Al_xGa_{1-x}N/Al_yGa_{1-y}N$ structure (stacked sections or core/shell structures) remains small and far from being as detrimental as for $In_xGa_{1-x}N/GaN$ [270, 335]. In the latter case, the strain relaxation was observed to be plastic for high In content. When $Al_xGa_{1-x}N$ is being grown on top of an Al-richer $Al_yGa_{1-y}N$ NW section, it undergoes compressive strain, making Ga adatom incorporation even less favorable until this strain is relieved: this is called the “strain pulling effect”, which may lead to significant composition gradients in the AlGaN alloy [336, 337].

Consequently, a trade-off on the main growth parameters, namely the AlGaN growth temperature and the atomic fluxes, must be found in order to promote the NW growth while controlling the average AlN molar fraction and the alloy homogeneity. This compromise will be harder to reach than in the 2D layer growth case, since the best growth results for such layers are obtained for conditions hardly compatible with non-coalesced NW growth [160, 338-342]: low growth temperatures to limit the Ga adatom diffusion with respect to the Al one and metal-rich regime to ensure a good adatom coverage/mobility over the whole surface. In order to help reaching the trade-off, it must be noted that In can be used as a surfactant to improve metallic adatom mobility, as already reported for 2D growth [343] or in the NW case [290].

2.1.4.2 Additional calibration for GaN and $Al_xGa_{1-x}N$ nanowire growth

The additional calibration step that will be described in the following complements the RHEED calibration of atomic fluxes presented in Subpart 2.1.2.3. Given that the latter is performed on GaN 2D templates at typical 2D growth temperature, the Ga adatom diffusion along the NW sidewalls and the possible Ga desorption occurring over higher temperature ranges required for NW growth are not taken into account. Therefore, the axial growth rate of GaN NW is not accurately measured by the RHEED calibration method. In contrast, the difference between the 2D AlN growth rate and the AlN NW axial growth rate is expected to be less significant over typical GaN NW growth temperature ranges. Indeed, in the latter case, Al diffusion length and Al desorption rate remain low compared to those of Ga [303]. Another method than RHEED-based calibration must be then used to measure the NW growth rates more properly, especially those of GaN. One way to gain accuracy on the latter is to grow, at substrate temperatures corresponding to those used for AlGaN NW section growth, several GaN (respectively AlN) NW sections at various Ga cell temperatures between thin AlN (respectively GaN) NW markers, on top of GaN NW templates dense enough to take advantage of the shadowing effect and similar to those typically grown for AlGaN NW sections. Next, we disperse the resulting NWs on specific transmission electron microscopy (TEM) grids described in Subpart 2.2.1.2 and we finally measure the length of the GaN (respectively AlN) NW sections using a scanning transmission electron microscope (STEM) presented in 2.2.1.2. Knowing the growth time of such sections, we can deduce the GaN (respectively AlN) NW axial growth rates. This method is derived from the protocol used to demonstrate significant Ga diffusion along NW side facets [303]. Typical SEM/STEM images of NW sections grown between markers used for calibration are given in Figure 2.1.4.3, for both GaN and AlN sections. The related NW axial growth rates are provided in Figure 2.1.4.4 (a) and (b), respectively, and compared to those obtained using the RHEED oscillation-based technique on 2D layers grown at lower temperatures. As expected, the GaN NW growth rates are much higher than those for the 2D case, due to adatom diffusion along NW sidewalls: they are even almost doubled for some Ga cell temperatures (820°C for instance) leading to N-rich NW growth regime. As for those of AlN NW, the difference is far from being negligible, in contrast to the previous report using this technique [303]. The latter discrepancy can be explained by the higher growth temperatures we used in comparison with this report.

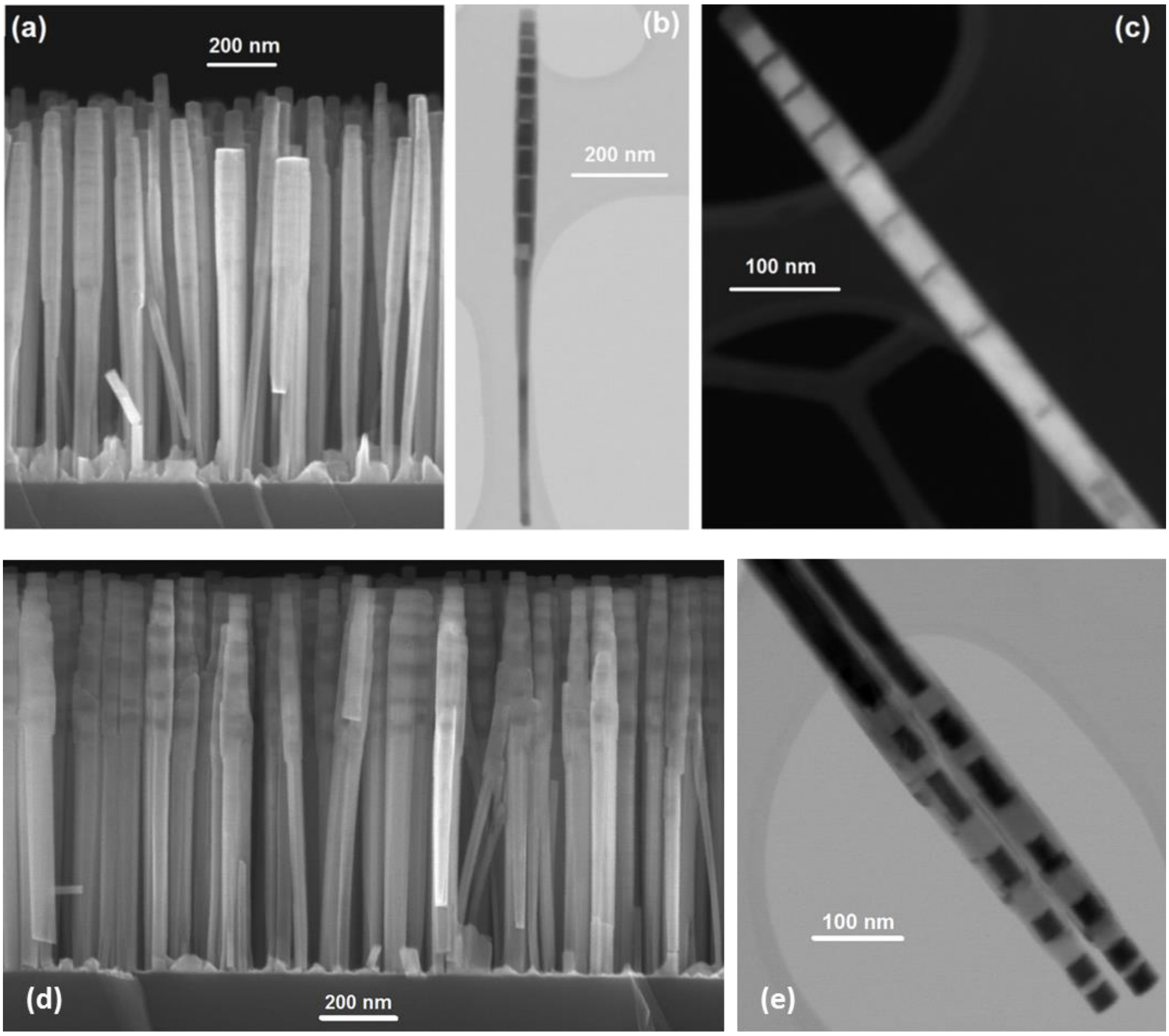

Figure 2.1.4.3: (a) Typical SEM image of NWs grown for these calibrations: GaN NW sections grown between thin AlN markers, on top of GaN NW templates (sample N2474). (b) Typical STEM-BF image of such NW dispersed on TEM grid. (c) STEM-ADF image of the upper part of such dispersed NW: GaN NW sections and AlN markers. (d) SEM image of an alternation of rather long GaN and AlN NW sections, grown on top of GaN NW templates (sample N2323). NW growth rates could be inferred for both binaries from the analysis of this sample. Those for AlN were slightly underestimated due to the longer distance for Al adatoms impinging the NW sidewalls to travel to the NW top, given the longer GaN markers. (e) STEM-BF image of the upper part of two single dispersed NWs from the latter sample.

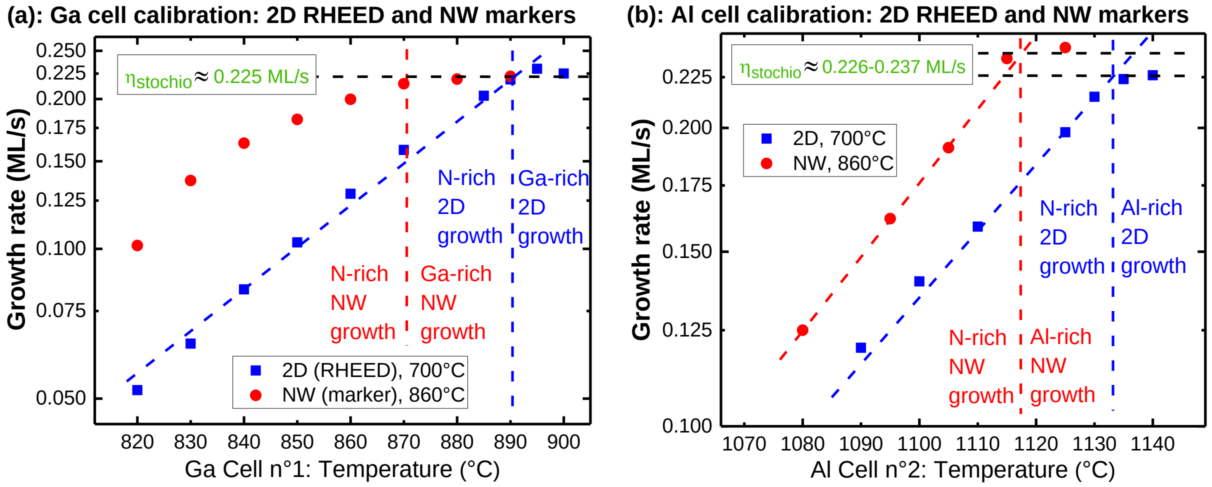

Figure 2.1.4.4: (a) Comparison of GaN growth rates derived from the NW marker calibration technique performed on a NW sample (N2474) grown at typical NW high growth temperature (T_{subs} = 860°C, t_{des}^{Ga} = 5 s) with those obtained from RHEED technique carried out on a GaN 2D template at typical 2D growth temperature (T_{subs} ≈ 700°C). The two growth runs were performed consecutively. In view of the growth rate difference in N-rich regime, Ga diffusion along NW sidewalls is significant here. (b) Comparison of AlN growth rates derived from the NW marker calibration technique performed on a NW sample (N2323) grown at typical NW high growth temperature (T_{subs} = 865°C, t_{des}^{Ga} = 5 s) with those obtained from RHEED technique carried out on an AlN 2D template at typical 2D growth temperature (T_{subs} ≈ 700°C). In view of the growth rate difference in N-rich regime, Al diffusion along NW sidewalls is far from being negligible here.

Such protocol can be used not only to provide more accurate results for nitride binary NW axial growth rates, but also to estimate, when needed, the nominal AlN molar fraction in AlGaN NW sections more precisely than with the RHEED 2D method, which implies adapting the formalism introduced in Subpart 2.1.2.3 to the AlGaN case. First, the AlN molar fraction x is defined by the following ratio:

$$x = \frac{N_{Al}}{N_{Al} + N_{Ga}} \tag{2.1.4.1}$$

where N_{Al} and N_{Ga} are the incorporated Al and Ga atom numbers, respectively. As we form a stoichiometric material, we can write, between the metallic and the N atoms:

$$N_{Al} + N_{Ga} = N_N \tag{2.1.4.2}$$

For NW growth, we mostly worked in N-rich conditions, so that we were not limited by the N flux ϕ_N. In such conditions, we can then write $\phi_{Al}^{eff} + \phi_{Ga}^{eff} < \phi_N$, $N_{Al} = \phi_{Al}^{eff}$ and $N_{Ga} = \phi_{Ga}^{eff}$, with ϕ_{Al}^{eff} and ϕ_{Ga}^{eff} respectively the effective Al and Ga fluxes. Consequently, we can write the nominal AlN molar fraction x_{nom} as:

$$x_{nom} = \frac{\phi_{Al}^{eff}}{\phi_{Al}^{eff} + \phi_{Ga}^{eff}} \qquad (2.1.4.3)$$

and, using Equations (2.1.4.3) and (2.1.2.2), we can approach $x_{nominal}$ as a function of atomic surface densities $\sigma_{binary,0001}$ and experimental binary NW growth rates η_{binary}, measured using the marker technique and therefore corresponding to the NW axial growth rate:

$$x_{nom} = \frac{\eta_{AlN}\sigma_{AlN,0001}}{\eta_{AlN}\sigma_{AlN,0001} + \eta_{GaN}\sigma_{GaN,0001}} \qquad (2.1.4.4)$$

Such approximation remains valid, as long as the NW radial growth rates remain low compared to the axial ones. In this case, the assumption seems reasonable. Indeed, the used experimental geometry first does not favor radial growth at all. Second, when observing the GaN NW cores between markers on typical STEM images such as those in Figure 2.1.4.3, their diameter remains almost constant all along the NW axis. As for AlN NW sections grown between markers, this is less true in view of AlN NW broadening. The latter is visible in Figure 2.1.4.5 (a), which shows typical SEM images of AlN NW sections grown on top of GaN NW templates at very high substrate temperatures. However, in view of Figure 2.1.4.5 (b), the AlN NW radial growth rates eventually decrease, as the increasing NW diameter seems to converge toward an equilibrium value (slightly inverted tapered geometry). Similarly to the case of GaN NWs [305], such convergence towards larger NW diameter could be explained in two phases. First, in spite of being in N-rich conditions, the amount of active N species available for axial growth may be finite. Indeed, in view of the very high substrate temperature, the Al adatoms are more mobile and can reach more easily the NW top, which may result in an excess of metallic species there with respect to N ones and lead to NW radial growth. The contribution to the latter of Al adatoms that do not reach the NW top and get incorporated along the sidewalls must not be forgotten, but it is likely to be minor in view of NW diameter convergence, especially since the shadowing effect gets more significant with NWs lengthening and broadening. Second, NW radial growth ceases when the Al adatom density at the NW top is reduced to a certain critical value, leading to mostly axial NW growth.

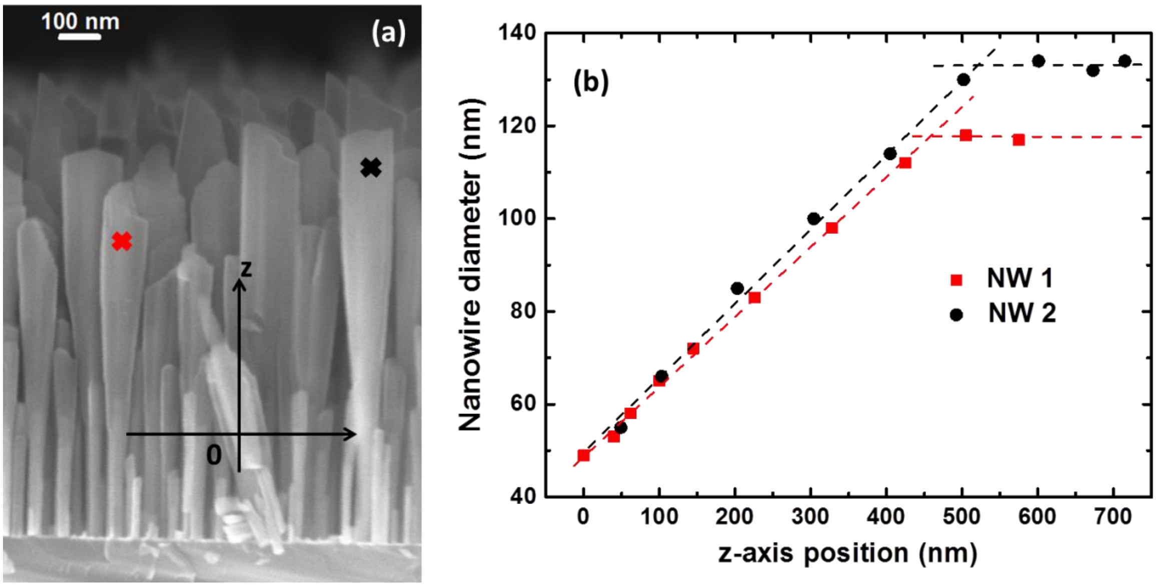

Figure 2.1.4.5: (a) Typical SEM image (sample N2535) of long AlN NW sections (darker) grown in N-rich conditions at very high substrate temperatures (T_{subs} = 930°C, t_{des}^{Ga} ≈1 s), on top of GaN NW templates (brighter). (b) Evolution of the AlN NW section diameter with position along the z-axis, given for two random typical NWs (red cross for NW 1 and black cross for NW 2).

At substrate temperatures close to the upper bound of the typical GaN NW growth temperature range (corresponding to Ga desorption times of the order of 5s), Al diffusion is already far from being negligible, in view of the difference between results of RHEED-based 2D calibration and the NW marker technique exhibited in Figure 2.1.4.4 (b). Therefore, a convergence towards an equilibrium diameter, similar to the one exhibited in Figure 2.1.4.5, is likely to be observed as well for long AlN NW sections grown at such temperatures. Regarding our calibration protocol, one way to be more accurate on the NW axial growth rate η_{AlN} values would be to grow, on top of GaN NW templates, a first AlN section long enough to reach negligible radial growth rates, before starting to grow GaN marker/AlN section structures.

In our experiments, x_{nom} approximated rather well the real x, noted x_{exp} and measured post-growth by XRD. Indeed, for AlGaN NW sample growth calibrated from this method (x_{exp} over the 0.4-0.6 range, for which the interaction and competition between metallic species are the most significant), disparities between x_{nom} calculated from the experimental η_{GaN} and η_{AlN} values and x_{exp} remained low (within± 0.05). These minor discrepancies can be mainly explained by the fact that:

- Our NW calibration method does not consider the interaction and competition between the two metallic species when growing AlGaN.
- The assumption on AlN NW radial growth rate is less true than for GaN over the typical growth range

As for metal-rich conditions, as N is the limiting species, we can write $\phi_{Al} + \phi_{Ga} > \phi_N^{eff}$ and $N_N = \phi_N^{eff}$, which gives:

$$x_{nom} = \frac{N_{Al}}{\phi_N^{eff}} \cong \frac{\phi_{Al}^{eff}}{\phi_N^{eff}} \tag{2.1.4.5}$$

The last approximation can be performed if $\phi_{Al} < \phi_N^{eff}$ and considering that Al is preferentially incorporated at the expense of Ga. Thus, using Equation (2.1.2.3), we obtain x as a function of the binary growth rates:

$$x_{nom} = \frac{\eta_{AlN}}{\eta_{Stoichio}} \tag{2.1.4.6}$$

with $\eta_{Stoichio}$ corresponding to the AlN growth rate at stoichiometry and expressed in AlN ML/s.

In this work, AlGaN NWs were mostly grown in N-rich conditions. Therefore, we will estimate x_{nom} for the latter NWs using the approximation given in Equation (2.1.4.4).

2.2 Structural characterization techniques

2.2.1 Electron microscopy

In order to image nano-objects that we grow, electron microscopy [344, 345] is required, since optical microscopy is limited by diffraction limit (of the order of visible photon wavelength). Indeed, the electrons used in such microscopes have a much shorter wavelength, which notably depends on the electron acceleration voltage. This wavelength can vary over a 0.025-0.4 Å range for an acceleration voltage between 200 kV and 1 kV. If the electron beam is coherent enough, it is even possible to image atomic columns in high resolution (HR) electron microscopy.

The electron beam is created by an electron gun, which can be either a thermionic source (a metallic filament, typically in LaB_6, heated at high temperatures, of the order of 2000°C) or a field effect gun (sharp tip, typically in tungsten, from which electrons are extracted by tunnel effect through high acceleration voltage). Compared to thermionic sources, field effect guns (FEGs) are able to produce electron beams smaller in diameter and more coherent. Moreover, they allow us to reach higher source brightness. In most cases, we used microscopes equipped with FEG sources in our experiments. Electrons are then accelerated by high voltage and collimated thanks to several electromagnetic lenses which are part of what is called the microscope column and which modify the electron trajectory through electromagnetic fields. Increasing the acceleration voltage allows electrons to go through a more significant thickness of matter. Higher voltages are notably used in transmission microscopy. However, more energetic electrons can cause more severe electron-irradiation damages through elastic scattering (electrostatic charging, atomic displacement, electron-beam sputtering) or inelastic scattering (sample heating, radiolysis, hydrocarbon contamination) [346]. As for the electromagnetic lenses, the latter actually consist in coils crossed by electronic current and their focal distance can be tuned by varying the current intensity. These lenses are far from being perfect. Indeed, they cause astigmatism and spherical aberrations that can be corrected with the proper deflectors (very common in SEM microscopes) and spherical aberration correctors (only found in state-of-the-art transmission microscopes), respectively. Such aberrations can also be reduced by decreasing the electron beam size with diaphragms.

The electrons impinging on the sample interact with matter, which modifies their trajectory (elastic interaction with atom nuclei) or their energy (inelastic interaction with atom electrons). In the latter case, other particles such as photons or secondary electrons can be emitted. As for elastic interactions, changes in electron trajectories degrade the spatial resolution. Indeed, the atoms interacting with the beam are not only comprised in a cylinder of diameter equal to the beam diameter but in a bigger volume called “the interaction volume”, depicted in Figure 2.2.1.1. This volume is bigger when investigating a material containing light atoms or when increasing the acceleration voltage and must be considered, especially for thick as-grown samples. It can be simulated with Monte-Carlo-based software such as Casino: an example is given in Figure 2.2.1.2. In the case of nitride NWs grown by MBE and dispersed on thin TEM grids, the “interaction volume” is no longer a problem as the material volume crossed by the beam is very small. Depending on the detectors and their position with respect to the electron trajectories, various signals can be recorded in order to obtain images containing different information, as indicated in Figure 2.2.1.1. We will present in the following the ones that were mainly used during this PhD.

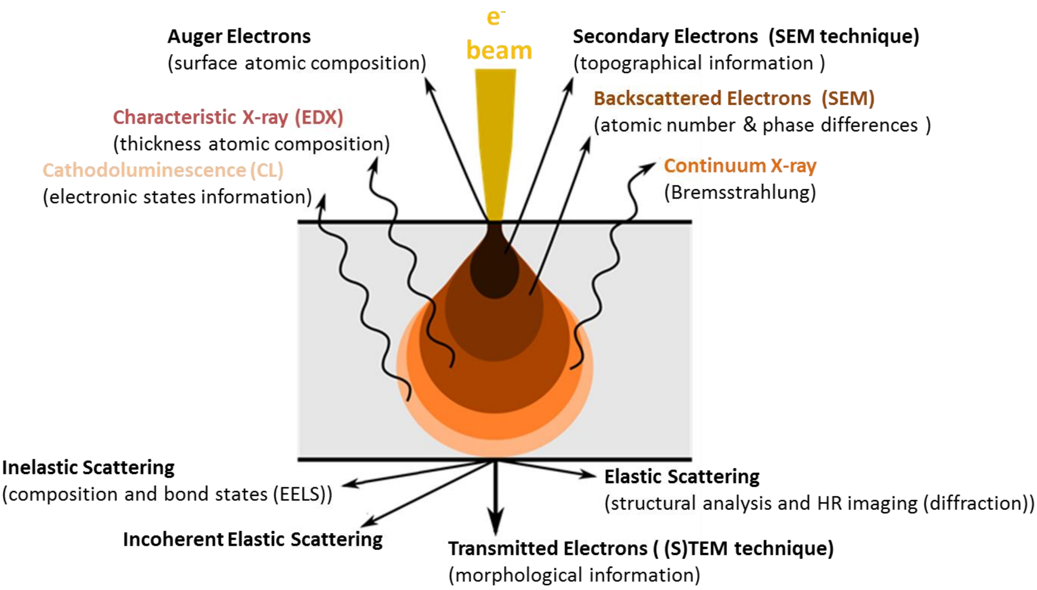

Figure 2.2.1.1: Sketch of the interaction volume, illustrating the volume of atoms interacting with the incident electron beam. The different emitted particles are exhibited as well and can be collected with the appropriate detectors when performing the related techniques.

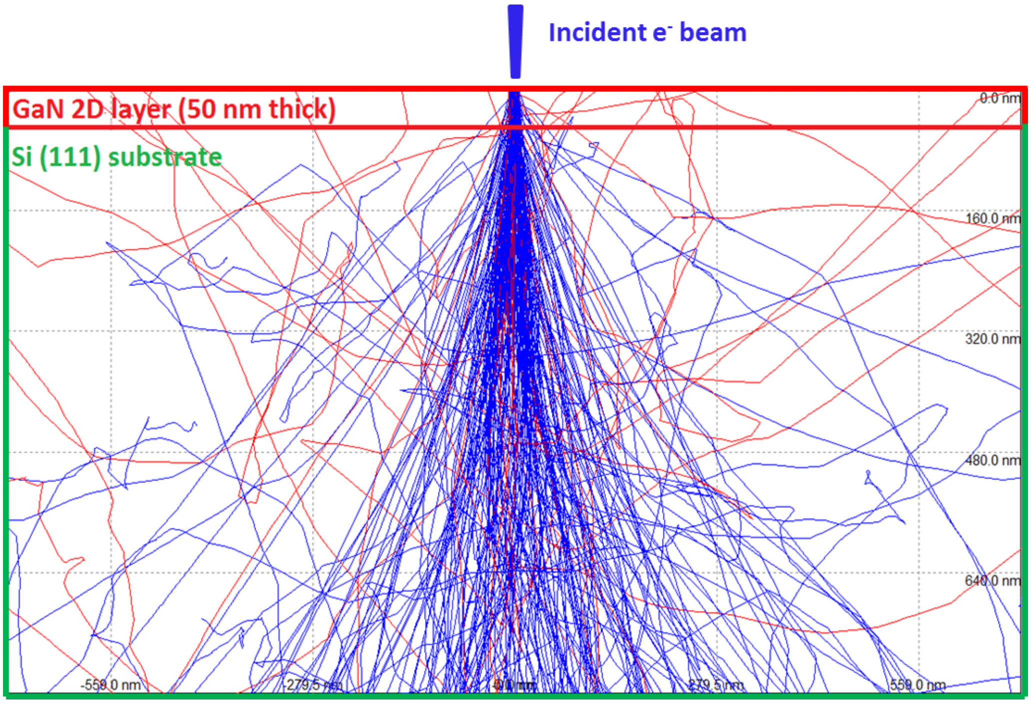

Figure 2.2.1.2: Results of a simulation run under Casino software illustrating the need of having thin samples for higher resolution electron microscopy experiments such as (S)TEM or EDX. Here, the simulated sample is composed of a 50 nm thick GaN 2D layer grown on top of a bulk Si (111) substrate and excited with a 10 nm wide electron beam accelerated at 20 keV. Such layer thickness is comparable to the typical diameter of nitride NWs grown by MBE dispersed on thin grids and probed by (S)TEM. We can see that the interaction volume remains very close to the beam cylindrical volume in the GaN 2D layer, whereas it gets significant in the substrate, degrading the experimental resolution. When exciting thin samples such as dispersed NWs mentioned just above, this interaction volume remains small. Thus, in the latter case, the resolution mainly depends on the mere electron probe size.

2.2.1.1 Scanning electron microscopy (SEM)

In this microscope mode, the electron beam scans the sample thanks to scanning coils located at the bottom part of the microscope column. The detected electrons are either secondary or retro-scattered electrons, depending on the voltage applied to the grid of the Everhart-Thornley detector. Moreover, the acceleration voltage value is low, typically over the 1-30 kV range. Consequently, information mainly comes from the sample surface. Recorded images allow us to get a 3D overview over a more or less magnified area of the sample surface. This characterization technique does not require complicated sample preparation (just to cut a sample piece with a diamond tip) and is usually the first characterization technique to be performed after growth.

We mainly used the Zeiss Ultra55 microscope of CEA-Grenoble/INAC, either to observe as-grown samples or to locate NWs dispersed on specific substrates. The acceleration voltage could be set up to 30 kV but a 10 kV voltage was typically used in order to avoid charging effect phenomena, which occur when the investigated material is not conductive enough. The electron beam current could be set up to 100 nA. The electron probe size was typically of the order of 1 nm, and so was the ultimate resolution. The detected electrons are secondary ones and could be collected by two detectors: the first one was located in the SEM chamber whereas the other one was located in the microscope column ("in-lens" detector). Figure 2.2.1.3 gives a sketch of the column.

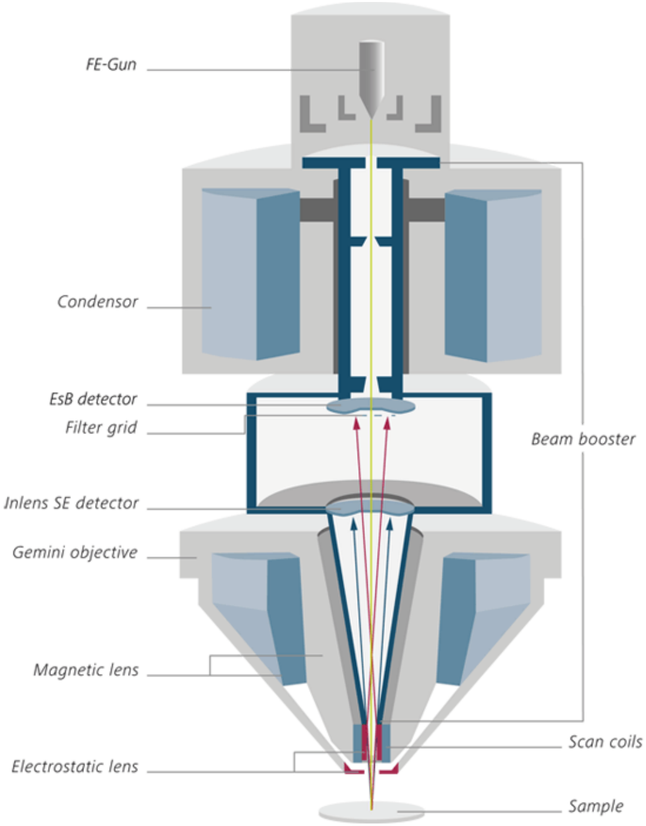

Figure 2.2.1.3: Schematic of a Zeiss Ultra55 microscope column. From [347].

A few cathodoluminescence (CL) experiments were also carried out in another SEM setup (FEI Quanta 200) at Neel Institute, Grenoble (see 2.3.2.1). The setup best resolution is of the order of 3 nm. The acceleration voltage could be tuned over the 200V- 30 kV range and the electron beam current between 5 pA and 50 nA.

2.2.1.2 Scanning transmission electron microscopy (STEM)

In this microscope mode, the electron beam is focused as much as possible, and electrons are detected after having crossed the sample. In order to detect electrons which are directly transmitted without any diffraction or scattering, a detector is placed on the microscope axis. In this case, we record images in bright field (BF) mode. An annular detector is also placed around the central detector to detect diffracted electrons. In this case, we record images in annular dark field mode (ADF). Moreover, electrons scattered at higher angle can be detected in high-angle annular dark field (HAADF) mode. In the latter case, as the number of high-angle scattered electrons is roughly proportional to the square of atomic number Z, the recorded images especially highlight the chemical contrast, more than simple ADF. The heavier the atoms, the more intense the HAADF signal and the brighter the image.

Several microscopes were used in STEM configuration during this PhD, including:

- The Zeiss Ultra55 microscope (at INAC, Grenoble), also used for standard SEM, for most sessions of low resolution (LR) STEM. The typical acceleration voltage covered the 20-30 kV range.
- A STEM Hitachi 5500 (at INAC, Grenoble), with a better spatial resolution than the one of Zeiss Ultra55 in low resolution mode and a slightly better vacuum limiting the sample contamination. The acceleration voltage was also of the order of 30 kV.
- A STEM VG HB501 (at LPS, for nanoCL experiments, see related Subpart 2.3.2.2). The used acceleration voltage was 60 kV. The high brightness of the cold FEG allowed one to obtain a typical beam current of 300 pA in an electron beam with diameter as small as 0.5 nm. As mechanical noise degrades the resolution, the effective spatial resolution was of the order of 1 nm.

In view of this work context, the HAADF mode was particularly interesting to image chemical contrast in AlGaN NWs: Ga being heavier than Al, it appears brighter on HAADF images. Regarding the sample preparation for STEM, NWs were mostly mechanically dispersed on TEM grids. The latter are made of Copper (Cu) and covered by a thin C film. Figure 2.2.1.4 gives an overview of such a grid. Some NW dispersion tries were also performed using a chemical approach: in this case, a small sample piece was placed into an ultrasonic bath in ethanol for a few minutes. Then, a drop (or a few) of the solution was deposited on the grid. Sample preparation for the TEM and EDX (Energy-dispersive X-ray) techniques (when analyzing single NWs) presented afterwards is identical.

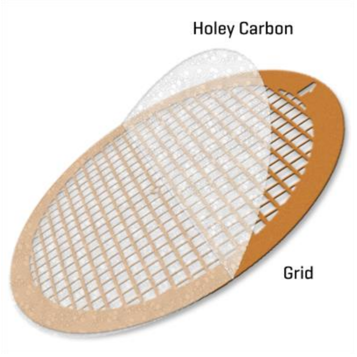

Figure 2.2.1.4: Sketch of a TEM grid, exhibiting the thin carbon film covering the copper part.

2.2.1.3 Energy-dispersive X-ray (EDX)

EDX technique is a chemical analysis allowing the quantification of elements present in a sample. The principle is briefly explained in the following sentences: at rest, an atom within the sample contains ground state (or unexcited) electrons in discrete energy levels or electron shells bound to the nucleus. The electron beam impinging on a given atom of the sample may excite an electron in an inner shell (K, L, M…), ejecting it from the shell while creating a hole where the electron was. An electron from an outer, higher-energy shell then fills the hole, and the difference in energy between the higher-energy shell and the lower energy shell may be released in the form of an X-ray photon. The number and energy of the X-ray photons emitted from the sample can be measured by an EDX spectrometer. As the energies of the X-rays are characteristic of the difference in energy between the two shells and of the atomic structure of the emitting element, EDX thus allows the elemental composition of the sample to be determined. Figure 2.2.1.5 illustrates the EDX principle and gives the main characteristic transition energy values for Al, Ga and N atoms.

We can then quantify the elements with respect to each other, by comparing the integrated intensity of rays in EDX spectra, characteristic of the elements probed by the electron beam. This intensity depends on several parameters: some only depend on the element itself whereas others depend on the used equipment or the sample. Quantification thus requires intensity calibration, which can be implemented in EDX data processing software from quantitative analysis performed on a well-known reference sample. It must be noted that light elements (such as B, C, N, O) are more difficult to quantify with EDX, as the recorded intensity is lower for these elements. In this case, electron energy loss spectroscopy (EELS) is more suited. The sample thickness and density are also criteria not to be neglected when carrying out quantitative analysis, inasmuch as X-ray photons emitted by the deepest sample regions are absorbed by neighboring atoms, particularly those closer to the sample surface. This X-ray absorption process also impacts the EDX spatial resolution, as it results in an X-ray emission volume slightly bigger than the real interaction volume. In the case of thin samples such as dispersed and thin nitride NWs, the latter issue is not significant.

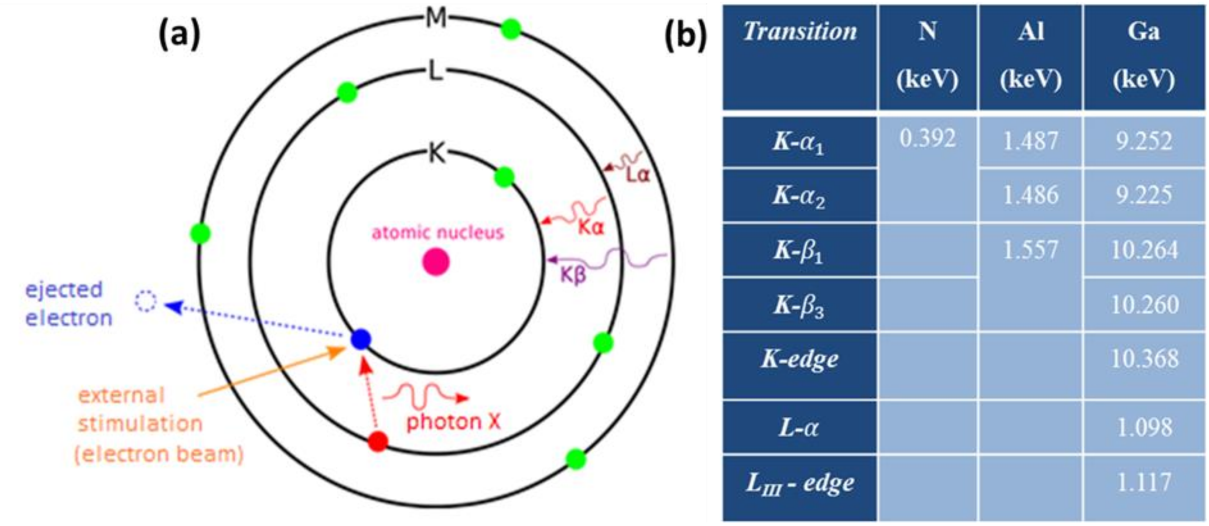

Transition	N (keV)	Al (keV)	Ga (keV)
$K\text{-}\alpha_1$	0.392	1.487	9.252
$K\text{-}\alpha_2$		1.486	9.225
$K\text{-}\beta_1$		1.557	10.264
$K\text{-}\beta_3$			10.260
K-edge			10.368
L-α			1.098
L_{III} *- edge*			1.117

Figure 2.2.1.5: (a) Sketch of the EDX principle. (b) Table providing the main shell transition energies for the Al, Ga and N species (values taken from [348]).

The microscope used for EDX was mainly the Zeiss Ultra55. In our experiments, the used sample holder was made of graphite in order to ensure that EDX signals (especially X-ray emission by Al) only originated from the investigated samples which were mostly MBE-grown AlGaN NWs dispersed on TEM grids. For the latter, the EDX spatial resolution was of the order of 10 nm so that we could quantify the Al content quite locally along the axis or the radius of NWs. Quantification was performed using a technique called IZAC which combines the common Cliff-Lorimer (k-factor) [349] method and the correction of X-ray absorption, taking into account the sample thickness and density. Such technique provides satisfactory accuracy, close to the one reached by another technique more commonly used but more complex, the ζ-factor method [350, 351]. The EDX setup was calibrated at the beginning of each session done using a very well-known reference copper grid.

2.2.2 X-ray diffraction (XRD)

For measurements on single crystal, the XRD technique [352] consists in sending a focused monochromatic beam of X-ray photons at a given incident angle ω onto the crystal sample mounted on a goniometer. As atoms can elastically scatter an X-ray wave, the crystal will then produce, by definition, a regular array of waves. Although these waves cancel one another out in most directions through destructive interference, they add constructively in a few specific directions, determined by Bragg's law:

$$2d_{(hkl)}\sin(\theta) = n\lambda_{XRD} \tag{2.2.2.1}$$

where:

- $d_{(hkl)}$ the spacing (or interplanar distance) between two consecutive diffracting atomic planes belonging to the (hkl) plane family.
- θ the scattering angle related to this plane family.
- λ_{XRD} the wavelength of the X-ray incident beam.
- n the diffraction order.

Diffraction can occur because the X-ray wavelength is of the order of the spacing between planes in the crystal.

Experimentally, we can select one of these specific directions, namely one specific (hkl) set, by positioning the beam source at the right incidence angle ω, orientating the crystal properly with the goniometer and placing the XRD detector at the right scattering angle θ. The chosen direction will then appear as a spot called the (hkl) reflection on the recorded diffraction pattern, belonging to the reciprocal space. By slightly tuning the experimental geometry (see Figure 2.2.2.1) in order to move around the (hkl) spot in the reciprocal space, a full cartography of the (hkl) reflection, called the reciprocal space map (RSM), can be recorded, providing valuable information about crystal properties (crystal quality, strain, average composition in alloys…).

XRD experiments were carried out at the NPSC laboratory for many as-grown $Al_xGa_{1-x}N$ NW section samples, mostly in order to estimate the average AlN molar fraction in AlGaN NWs from the measurements of the c and a lattice parameters of the alloy. We were then able to adjust the nominal fluxes for the next growth runs if necessary. In view of the significant number of samples, the lattice parameters were not determined, for most samples, from whole RSMs recorded for certain reflections, but following a much less time-consuming method called the extended Bond technique, with no or minor accuracy loss [353-355].

The latter consists in performing $2\theta - \omega$ scans for several symmetric reflections ($\omega = \theta$), such as (002), (004) and (006) for WZ nitrides, and ω scans for several asymmetric reflections ($\omega = \theta \pm \alpha$), such as (104), (105), and (114) for WZ nitrides. Figure 2.2.2.1 illustrates the experimental geometry in the real and reciprocal spaces, representing ω, θ and α. Roughly, when performing a $2\theta - \omega$ scan, we move in the reciprocal space following the scattering vector $\vec{Q} = \vec{k}' - \vec{k}$ direction ($\vec{k}$ and $\vec{k}'$ being the incident and outgoing wavevectors), respectively, while we move perpendicularly to $\vec{Q}$ when carrying out a ω scan.

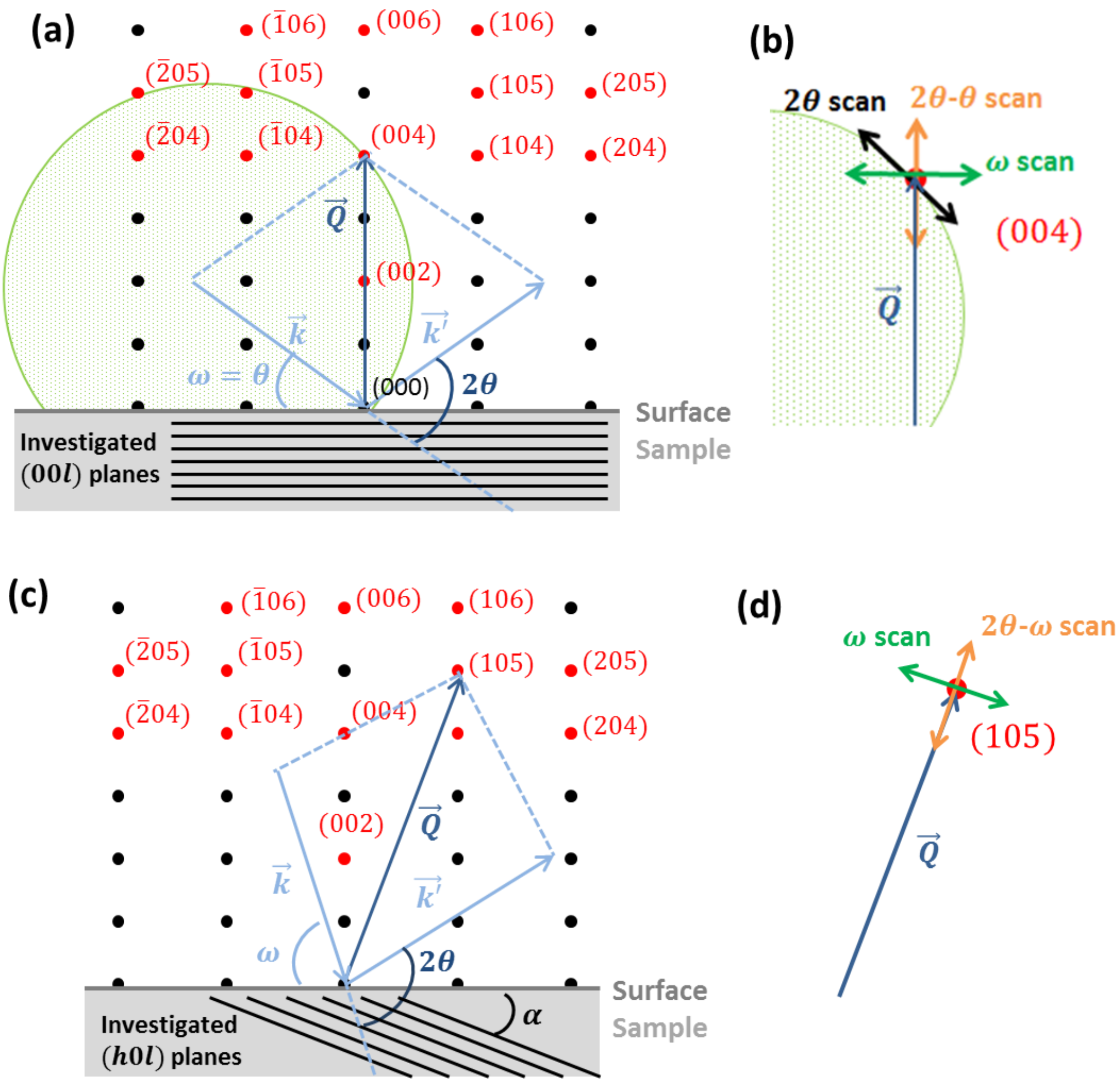

Figure 2.2.2.1: Sketch superimposing the "real space" (setup geometry: sample, investigated planes, incident and outgoing X-ray beam) and the "reciprocal space" (dots corresponding to reflections), for: (a) symmetric reflections $(00l)$, (b) asymmetric reflections $(h0l)$. As an example, the wavevectors ($\vec{k}$ and $\vec{k}'$) and the scattering vector ($\vec{Q}$) are drawn in (a) for the (004) reflection and in (b) for the (105) reflection. It must be noted that the Ewald sphere of radius $\|\vec{k}\|$ is displayed in (a) and intersects the (004) dot, meaning that we are fulfilling the diffraction conditions for this plane. In addition, the red dots indicate the diffracting planes allowed for WZ nitrides. (b) and (d) show how we move into the "reciprocal space" when performing the different types of scans, for symmetric and asymmetric reflections, respectively.

Performing $2\theta - \theta$ scans first allow us to derive the c lattice parameter value, by direct application of Bragg's law (see Equation (2.2.2.1)) for symmetric reflections. The expression of $d_{(hkl)}$ for the WZ structure is given in Annex 1.2 (Equation (A.1.2.1)). In the case of symmetric reflections $(00l)$, this expression can be simplified as $d_{(00l)} = c/l$. Then, the ω scans are performed for both grazing incidence and grazing emergence (respectively $\omega^- = \theta - \alpha$ and $\omega^+ = \theta + \alpha$). They give access to the c/a ratio value (and thus to the a lattice parameter value) from the following equations (in the WZ case for c/a):

$$\omega^+ - \omega^- = 2\alpha$$

$$\frac{c}{a} = \sqrt{\left(\frac{1}{cos^2(\alpha)} - 1\right)\left(\frac{l^2}{h^2 + k^2 + hk}\right)\frac{3}{4}} \qquad (2.2.2.2)$$

The c/a ratio expression is derived from Equation (A.1.2.2) (Annex 1.2), α corresponding to the angle between the $(hkil)$ plane related to the investigated reflection and the surface plane (0001) or $(000\bar{1})$. Typical values for such angles are provided in Annex 1.2 (see Table A.1.2.1).

In practice, ω does not correspond to a physical reality and should be defined as $\omega = \theta \pm \alpha + \omega_0$, with ω_0 the XRD setup offset angle. This offset is eliminated by subtracting ω angles for grazing incidence and emergence when estimating c/a (see Equation (2.2.2.2)).

Averaging the c and a values obtained for several reflections allows us to reduce the error bar. It must be noted that the higher the scattering angle (i.e. the higher the Miller indices), the more accurate the measurement. Once these average c and a values are known, the average AlN molar fraction x in our $\mathrm{Al}_x\mathrm{Ga}_{1-x}\mathrm{N}$ NW section sample can be derived by combining Vegard’s law with the following expression linking the strained and unstrained c parameters [355]:

$$c_{unstrained}(x) = \frac{c_{strained} + a_{strained} \times D^{0001}(x) \times T(x)}{1 + D^{0001}(x)} \qquad (2.2.2.3)$$

where:

- $c_{strained}$ and $a_{strained}$ correspond to the average c and a values just determined experimentally.
- $D^{0001}(x) = 2\frac{C_{13}}{C_{33}}(x)$ in the WZ case (C_{ij} defined in Subpart 1.3.2.2) is the elastic parameter.
- $T(x) = c_{unstrained}(x) \,/\, a_{unstrained}(x)$ is the lattice parameter ratio of relaxed lattice parameters.

Such combination therefore results in a polynomial that we must solve to derive the AlN molar fraction x.

The present method was successfully applied to pseudomorphically strained, partially relaxed, or completely relaxed $\mathrm{In}_x\mathrm{Ga}_{1-x}\mathrm{N}$ 2D layers grown on GaN templates and can be used for other structures, as long as the strain remains uniaxial [355]. In the case of $\mathrm{Al}_x\mathrm{Ga}_{1-x}\mathrm{N}$ NW sections grown on GaN NWs, a slight bias resulting from the thin Al-richer shell wrapping the AlGaN core must be considered when estimating AlN molar fraction with this procedure, but the latter still provides accurate results, especially when the AlGaN NW section length is large compared to the GaN NW template diameter and knowing that the shell thickness progressively decreases along the NW growth axis. Such long NW sections are generally quasi-relaxed, as supported by former XRD and Raman data [139, 322]. In addition, it must not be forgotten that the values of relaxed c and a lattice parameters, as well as those of the elastic parameter D^{0001}, are taken for GaN and AlN from experimental reports presenting disparities [13, 102] and that the use of Vegard's law, especially for approximating $D^{0001}(x)$ for $Al_xGa_{1-x}N$, does not allow the absolute determination of these parameters for the alloy, which increases the uncertainty on the estimation of AlN molar fraction.

Two XRD setups were easily accessible in the NPSC lab. The first setup was a PANalytical Empyrean with a 2D detector from PIXcel and a X-ray tube made of Cobalt (Co) so that the X-ray wavelength was 178.9 pm (for K- α_1 line). As for the second setup, its tube was made of Cu so that the X-ray wavelength was shorter (154.1 pm, for K- α_1 line) and allowed to reach higher scattering angles than with the first setup. Moreover, its overall angular resolution was better than that of the first setup. However, for practicality, we mainly used the first setup which was much more user-friendly / less time-consuming and sufficient in terms of angular resolution for our needs. It must be noted that there was no monochromator on the PANalytical setup so that both K- α_1 and K- α_2 (respectively 179.3 pm and 154.4 pm for Co and Cu) contributions had to be taken into account when fitting XRD scan data (using PANalytical High Score plus software) with Pseudo-Voigt functions. Such function consists in the weighted sum of a Lorentzian, which physically matches emitted X-ray lines very well, and a Gaussian, which describes the instrumental response. In reality, the XRD scans that we observe correspond to the convolution of such lines with the setup response, in other words the convolution of Lorentzian functions with Gaussian called Voigt functions. However, these functions are much more complicated to compute than Pseudo-Voigt functions while being well approximated by the latter so that we preferentially use Pseudo-Voigt.

Figure 2.2.2.2 provides examples of experimental $2\theta - \theta$ and ω scans recorded with the PANalytical setup. The detail of investigated samples and reflections is provided in the figure caption. Globally, it can be noticed that XRD peaks are quite broad for both types of scans. Regarding $2\theta - \theta$ ones, in the case of AlGaN NWs, the broad linewidths are likely to mostly result from composition gradient within the alloy along the growth c-axis, but can also be induced by strain gradient or μ-strain in the same direction [356]. As for ω scans, the related lines are broadened by mosaicity (tilt), size effects (limited lateral size, namely the NW diameter), and possible lateral μ-strain [356].

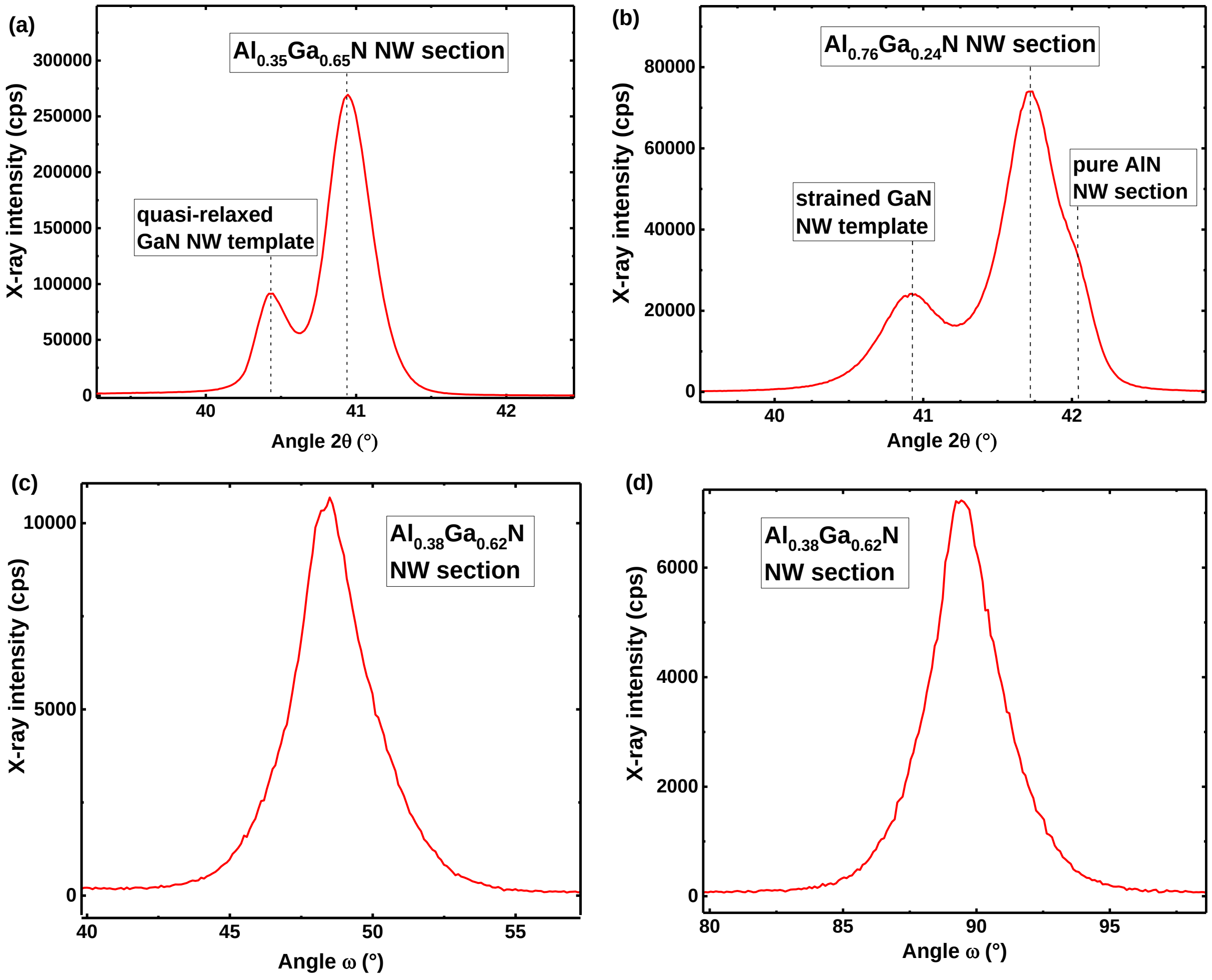

Figure 2.2.2.2: (a) (002) $2\theta - \theta$ scan for as-grown $Al_{0.35}Ga_{0.65}N$ NW sections (sample N2520) on top of GaN NW templates. (b) (002) $2\theta - \theta$ scan for as-grown $Al_{0.76}Ga_{0.24}N$ NW sections (sample N2569) on top of GaN NW templates. The GaN-related line is shifted due to strain resulting from the Al-richer and thicker shell that grew around the NW templates. A shoulder related to the presence of pure AlN section can also be observed. The latter will be discussed further in chapter 3. (c) (105) ω^- scan (grazing incidence) for as-grown $Al_{0.38}Ga_{0.62}N$ NW sections (sample N2555) on top of GaN NWs. (d) Associated (105) ω^+ scan (grazing emergence) for the same as-grown $Al_{0.38}Ga_{0.62}N$ NWs (sample N2555). It must be noted that all the provided AlN molar fractions in this figure were experimentally determined by the present technique.

2.2.3 Atomic-force microscopy (AFM)

The AFM technique [357] relies on the interaction between sample surface atoms and a sharp tip (probe) placed at the edge of a cantilever (typically made of Si or SiN). The latter can be displaced in all space directions, so that we can scan the whole sample surface. Analyzing the cantilever deflections allows us to determine the exact position of the tip and to measure the various interaction forces between the tip and the sample. By varying the distance between the tip and the investigated surface, we can measure various kinds of forces, which results in different applications when AFM is used in one of the three following modes:

- The contact mode: the tip, in firm contact with the sample so that the overall force is repulsive, is dragged across the surface and the surface contours are measured either using the deflection of the cantilever directly or, more commonly, using the feedback signal required to keep the cantilever at a constant position.
- The tapping mode, in which the cantilever is driven to oscillate up and down at or near its resonance frequency. In this case, the frequency and amplitude of the driving signal are kept constant, leading to constant amplitude for the cantilever oscillations as long as there is no drift or interaction with the surface. The interaction of the forces acting on the cantilever when the tip comes close to the surface causes this cantilever oscillation amplitude to decrease in this case. A feedback loop system then adjusts the cantilever height to maintain fixed amplitude, while the cantilever is scanned over the sample. A tapping AFM image is therefore produced by imaging the force of the intermittent contacts of the tip with the sample surface.
- The non-contact mode, in which the tip of the cantilever does not touch the sample surface. The cantilever is vibrating at either its resonant frequency (frequency modulation), or just above at fixed amplitude (amplitude modulation). Longer-range forces involved in this mode, such as Van der Waals forces, cause a change in the cantilever resonance frequency or amplitude. Depending on the chosen modulation, the feedback loop system maintains a constant frequency or oscillation amplitude by adjusting the average tip-to-sample distance. Measuring the tip-to-sample distance at each scanned point allows us to construct a topographic image of the sample surface.

Basic structural investigation of AlGaN NW samples was performed on a few NWs with a standard AFM setup at the NPSC lab. Moreover, standard AFM and KPFM experiments were performed at the Institute of material science, in Valencia, Spain. The KPFM technique is a variant of the non-contact AFM mode and allows us to measure the contact potential difference (V_{CPD}) between the sample surface and the AFM tip, as depicted in Figure 2.2.3.1. Such potential difference can notably be used to infer:

- The polarity of a crystal by taking advantage of the different surface potentials of the (0001) and $(000\overline{1})$ facets [119].
- The presence of a PN junction, as the surface potential is different between the n-doped and the p-doped regions [358] (see Figure 2.2.3.2).

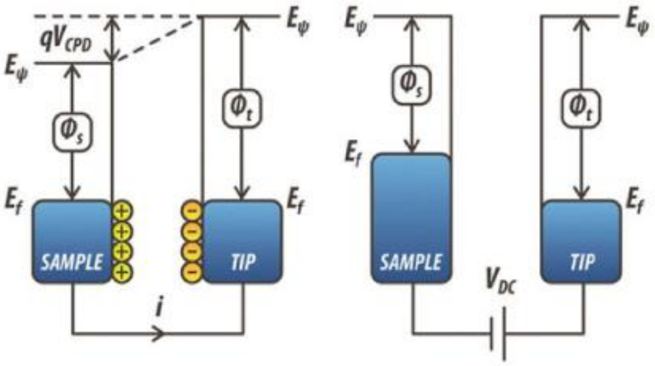

Figure 2.2.3.1: Sketch illustrating the tip-sample contact potential difference. Taken from [225].

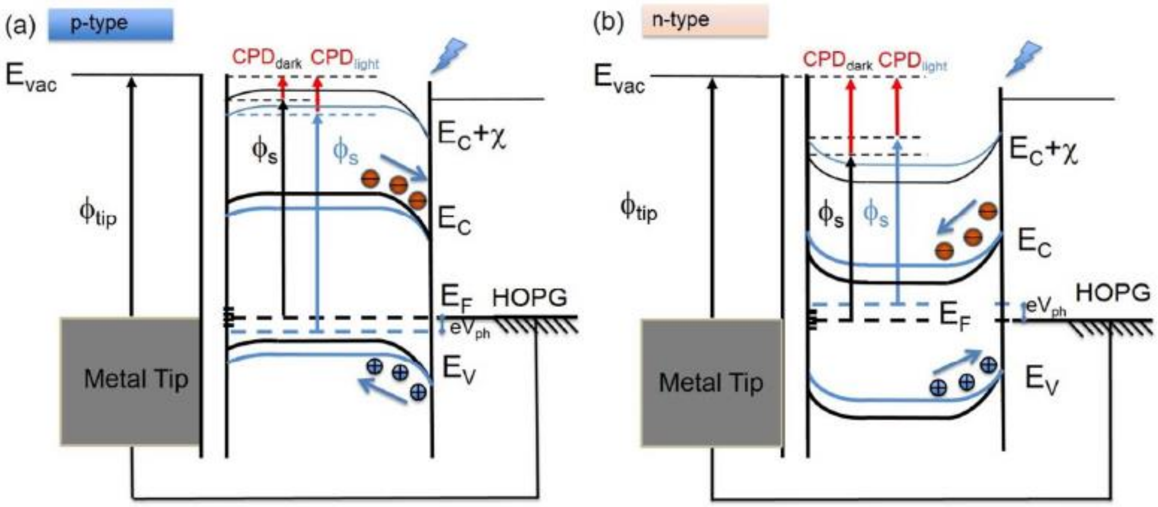

Figure 2.2.3.2: Sketch of the tip-sample contact potential difference for nitride material of different doping type: (a) p-type, (b) n-type. The potential difference varies with the doping type, so that the latter can be inferred from KPFM measurements. For both sketches, the left and right parts give the band structure respectively without and with illumination. The latter changes the surface potential, providing more investigation possibilities when performing KPFM experiments. Taken from [358].

2.3 Optical characterization techniques

Measurements of optical properties for a given material first require exciting this material. To do so, several excitation sources can be used: photon sources, such as laser beams, or electron sources like electron beam probes in electron microscopes. Then, the optical material response of the material is recorded with the proper detector. When recording the photons emitted by the sample, we perform PL in the case of photon sources whereas CL is carried out in the other case. The optical phonons can also be monitored: when the excitation source is photons, Raman spectroscopy can be performed. The three mentioned techniques will be described in the following.

2.3.1 Photoluminescence (PL)

Let us briefly remind that the PL technique [359] consists in exciting an investigated sample with a light source and then collecting the light subsequently emitted by the sample at a lower energy than the excitation light source. The photons impinging on the sample can be absorbed so as to generate electron-hole pairs. Then the carriers first thermalize non-radiatively towards lower energy levels, before they recombine, whether radiatively or non-radiatively. Therefore this technique probes the latter levels, which can be impurities levels. As detailed in Subpart 1.2.1.2, transitions that we typically observe can be related to recombinations of free excitons, to excitonic recombinations of carriers bound to different types of impurities or defects present in the sample, or to non-excitonic ones. The analysis of the collected light allows us to characterize various material properties such as its crystalline quality, its purity, the type of defects it contains, or also its chemical composition in the case of ternary alloys such as AlGaN.

2.3.1.1 Photoluminescence with a continuous-wave laser excitation (CW-PL)

Two types of PL experiments could be performed at different scales, depending on the size of the incident beam spot: macro-PL, for which the laser spot diameter is of the order of 50 µm and which is used to excite as-grown samples, and µ-PL, for which the spot size is reduced to the order of 1 µm using a microscope objective (numerical aperture (NA) equal to 0.4) and which allows us to probe single dispersed objects such as nitride NWs.

In the following of this manuscript, most macro-PL and µ-PL spectra were recorded in the INAC/NPSC laboratory on a PL setup equipped with a continuous-wave (CW) frequency-doubled solid-state laser (model MX488-1000 from Coherent). The excitation wavelength was 244 nm (5.08 eV) and allowed us to excite $Al_xGa_{1-x}N$ alloy up to an AlN molar fraction x of the order of 0.6-0.7. Al-richer samples were characterized at Charles Coulomb laboratory in Montpellier using a macro-PL setup equipped with a quadrupled Ti-Sapphire laser emitting around 200 nm. For all PL experiments, the sample was installed in a cryostat which could be cooled down to 5 K using liquid helium. For temperature-dependent measurements, the sample temperature could be set at any temperature over the 5-350 K range thanks to a resistive heater placed in the cryostat. As for power-dependent experiments, gradual densities were set on the optical path to tune the laser beam power typically between 1 μW and a few mWs.

Regarding the details of the macro-PL setup of NPSC laboratory, the focused 244 nm laser beam impinged on the sample with an angle of about 45°. Luminescence was then collected perpendicularly to the sample surface and refocused at the spectrometer (spectrometer focal length of 460 mm) entrance thanks to a pair of lens (which are UV achromatic doublets). It was then dispersed by a 600 lines/mm grating (or an 1800 lines/mm grating we almost did not use) and detected by a charge-coupled device (CCD) camera cooled down by liquid nitrogen. In addition to the two gratings, the slit width was adjustable, so that the spectral resolution and the macro-PL signal-to-noise ratio could be tuned. The ultimate spectral resolution that could be reached with this setup was of the order of 400 μeV, measured on a mercury lamp line emitting at 365 nm.

As for the μ-PL setup, the 244 nm laser beam is filtered by a pin-hole in order to suppress the beam spatial inhomogeneities and is then expanded in order to cover the whole microscope objective entrance. The spectrometer (focal length of 550 mm) is equipped with 3 gratings (600, 1200 and 3600 lines/mm) and adjustable slits in order to tailor the spectral resolution and the μ-PL signal-to-noise ratio. The ultimate resolution we can reach with the μ-PL setup was of the order of 80 μeV at 365 nm. Here, we mainly worked with the 1200 lines/mm grating, allowing a spectral resolution of about 500 μeV at 365 nm. A dichroic filter cuts all luminescence below 266 nm in μ-PL spectra. In addition to the laser beam, a LED emitting at 405 nm lightened the sample surface in order to allow us to view the sample surface on a camera and spot objects such as dispersed wires. Small controlled displacements over the sample surface were made possible thanks to the piezoelectric platform on which the microscope objective is mounted. Figure 2.3.1.1 illustrates the μ-PL setup used at NPSC.

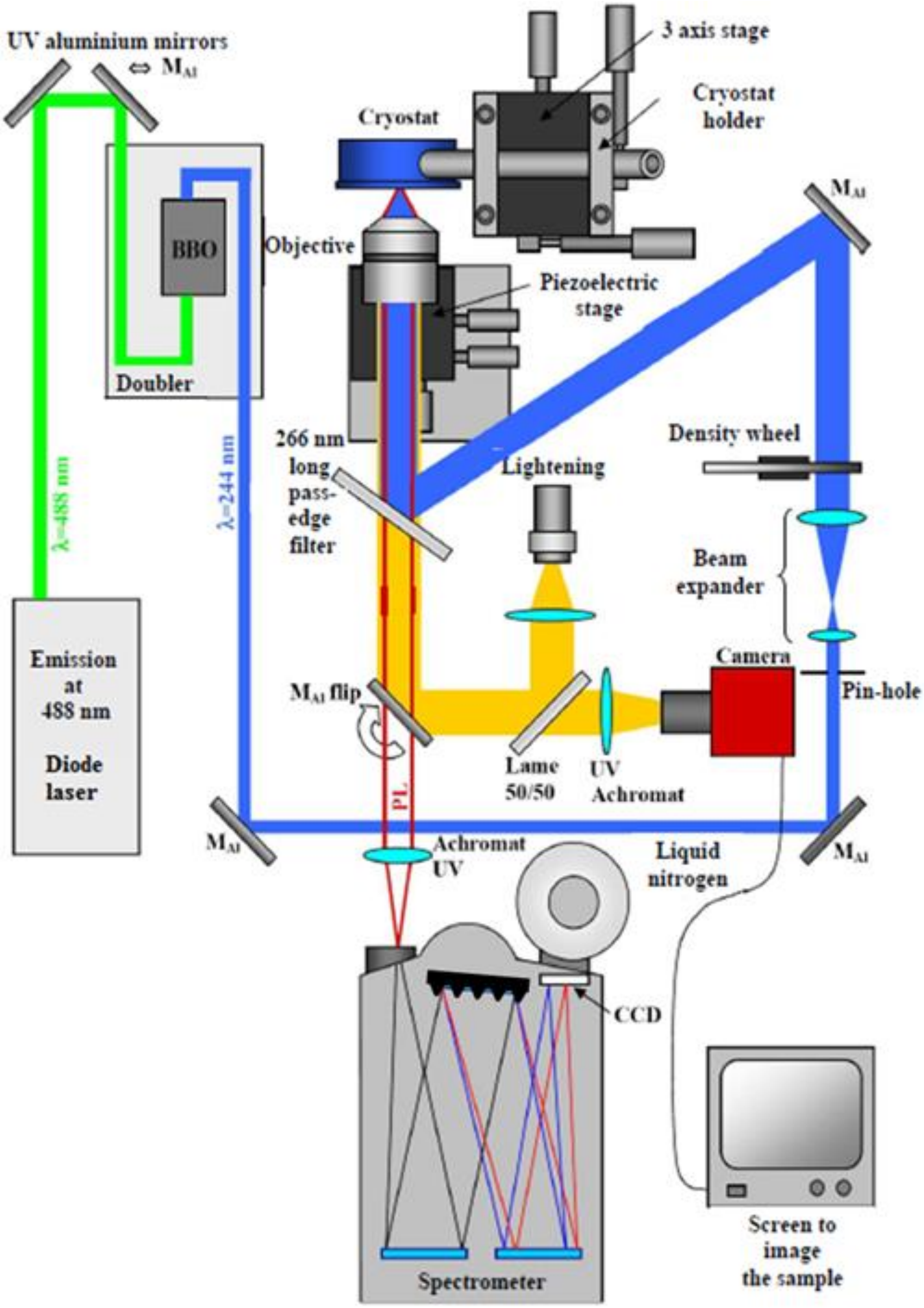

Figure 2.3.1.1: Schematic of the µ-PL setup with the CW laser. From [224].

2.3.1.2 Typical continuous-wave photoluminescence spectra of high-structural quality nitride binary nanowires grown by molecular beam epitaxy

In this section, typical PL data for self-induced and almost strain-free GaN and AlN NWs grown by MBE will be presented, as a practical case of Subpart 1.2.1.2. As previously mentioned, such NWs are expected to exhibit optical properties close to the bulk case in view of their dimensions, to be relaxed or quasi-relaxed, and to be almost defect-free. Spectra for good quality 2D epilayer samples will be also provided for both nitride binaries, as references. During experiments, excitation power densities were kept low in order to avoid saturating defects to the benefit of the NBE transitions, while used spectrometers were set to ensure a proper spectral resolution.

Self-induced GaN NWs are sporadically grown (typical diameter and length: 40 and 500 nm) and then optically characterized, in order to assess the vacuum within the MBE chamber. Indeed, optical transitions, especially those at NBE presented in Subpart 1.2.1.2 and related to excitons bound to impurities or defects, are very well known for such GaN NWs, and the vacuum quality can be directly inferred from the analysis of the resulting PL spectra (the presence and position of lines, their intensity with respect to others and their linewidth). Within the MBE chamber, the most common impurities are residual oxygen (vacuum) and Si (within metallic loads in effusion cells and in used wafers), so that the dominant transition at cryogenic temperatures is the $D^\circ X_A$ related to the O_N and/or Si_{Ga} donor [360]. The related line intensity with respect to those of other lines and its linewidth will be then scrutinized. Figure 2.3.1.2 shows typical spectra for two ensembles of self-induced GaN NWs grown on Si (111) by MBE and for one GaN 2D layer grown on sapphire by MOCVD, added as a reference (a few µm thick, manufacturer: LUMILOG), over a wide energy range (a) and around the NBE (b):

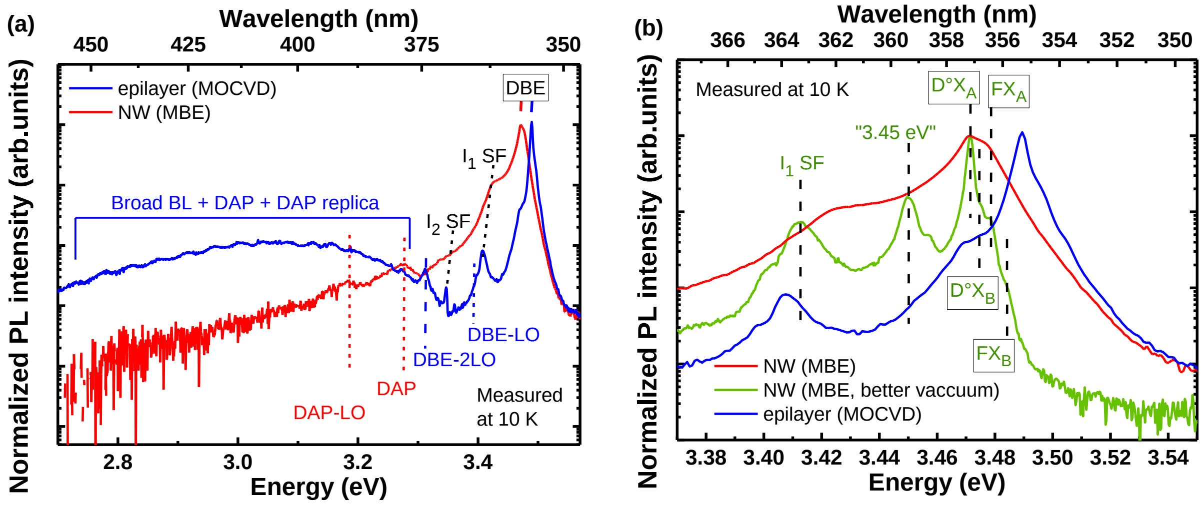

Figure 2.3.1.2: (a) PL spectra measured at low temperature (10 K) over a wide-range for an ensemble of GaN NWs grown by MBE and a GaN epilayer grown by CVD. The most visible transitions are labeled in red for the NWs, in blue for the CVD layer and in black for both. (b) PL spectra around the NBE for two ensembles of GaN NWs grown in different MBE chamber vacuum (samples N2473 and N1111) and for the CVD layer. The lines are labeled for the most resolved spectrum, namely the green one corresponding to GaN NWs grown in better vacuum (sample N1111). The red and blue curves correspond to the same spectra as in (a).

First, no deep transitions are observed in GaN NW spectra, as shown in Figure 2.3.1.2 (a): the visible lines of lowest energy correspond to the DAP transition around 3.26 eV and its phonon replica regularly spaced by 91 meV. In contrast, a broad blue luminescence (BL) band is observed for the epilayer, but its intensity remains low compared to the dominant NBE. Second, the intensity ratio between the main $D°X_A$ (also noted DBE) line around 3.471 eV and all other transitions remains large. Both features are first signs of decent structural quality, at least. It can be noticed that the lines for the 2D layer sample are globally blue-shifted compared to those of NWs, which results from the biaxial compressive strain induced by heteroepitaxial growth on sapphire [361], as explained in Subpart 1.2.1.3. Then, our focus turns towards the other NBE lines, exhibited in Figure 2.3.1.2 (b). Those around 3.41-3.42 eV and 3.35-3.36 eV are respectively attributed to prismatic (I_1) and basal (I_2) SFs [362, 363]. Regarding the line at 3.45 eV clearly resolved in one of GaN NW spectra, its origin has been debated for a long time. Indeed, some reports assigned this line with NW sub-surface point defects like V_{Ga} [234, 364] whereas others attributed it to the two-electron satellite (TES) of the donor bound exciton like in bulk GaN [365, 366]. Then, the latter attribution was refuted [224, 367], before the line got recently reassigned to inversion domain boundaries in NWs [368, 369], as already reported for GaN 2D epilayers [370]. Regarding the D°X linewidths, they are equal to about 5, 13 and 2 meV, respectively for the epilayer, and GaN NW ensembles grown short and long time after a MBE chamber opening. The latter value is good when compared to literature values [224] but remains wider than the state-of-the-art (0.5-1 meV [299]). Two reasons can be given to explain this difference. First, the MBE chamber vacuum may have been worse in our case. Second, the two main growth kinetic parameters, namely the substrate temperature and the Ga flux, were not optimal and both lower for our growth run. It must be noted that such linewidths for GaN NWs remain wider than those reached for homoepitaxial 2D layers. Indeed, linewidths of the order of 100 μeV were reported for such layers [371, 372]. Such difference with respect to the 2D case was attributed to strain inhomogeneities and surface effects in NWs [373, 374].

Up to now, the literature about fundamental optical properties of AlN NWs has remained extremely scarce. Indeed, only one report is available for self-induced AlN NWs grown by MBE [315], whereas the case of AlN NW sections grown on top of GaN NW templates (similarly to the $Al_xGa_{1-x}N$ sections presented in Subpart 2.1.4.1) has been barely more addressed [139, 375, 376]. Figure 2.3.1.3 provides PL data recorded prior to this PhD work for both types of AlN NWs (grown using our MBE setup), as well as a spectrum recorded for an AlN 2D layer grown on sapphire by MOCVD (thickness: 1μm, manufacturer: DOWA) and undergoing biaxial compressive strain [315].

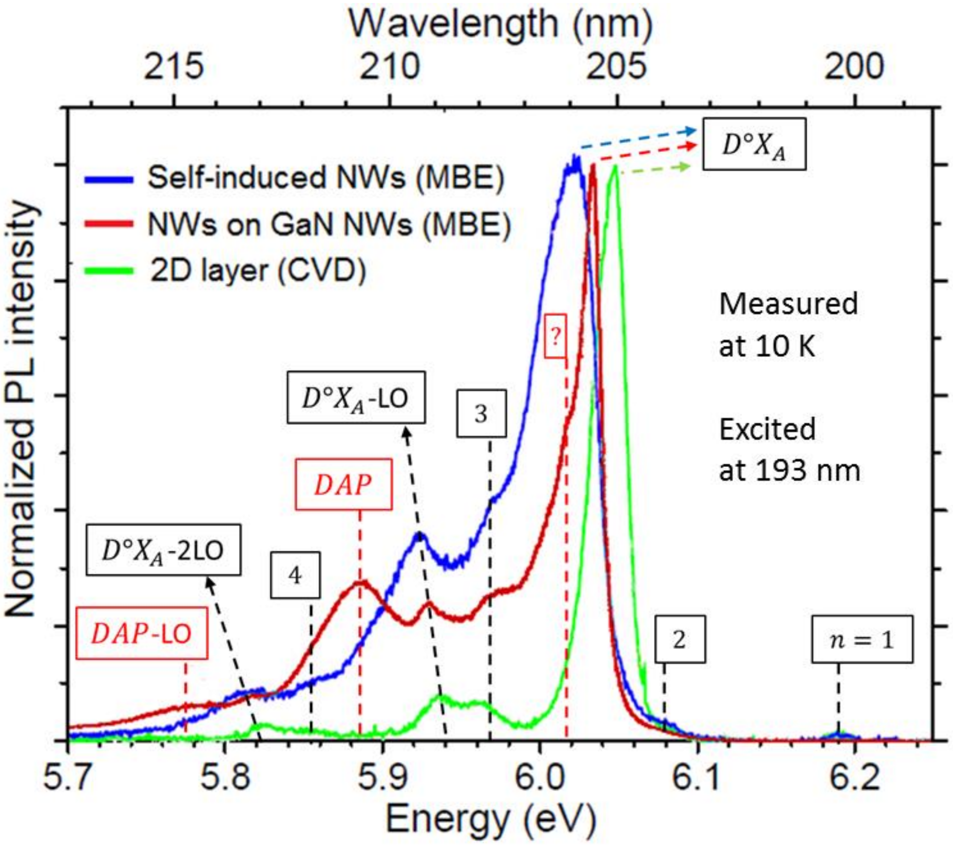

Figure 2.3.1.3: PL spectra measured at 10 K around NBE for an AlN layer grown by MOCVD [315], an ensemble of self-induced AlN NWs (sample N1145) [315] and an ensemble of AlN NW sections grown on GaN NW templates (sample N1629) [139]. Shared transitions are labeled in black, whereas those proper to AlN grown on GaN NWs are indicated in red. The transitions numbered from n=1 to 4 were convincingly attributed to Raman signals resulting from the high excitation density (line emission energy: $E = E_{laser} - (n+1) * E_{LO,AlN}$ with $E_{LO,AlN} = 110\ meV$) [139], similarly to former reports [377].

In the three cases, no intense lines or bands are clearly visible below 5.6-5.7 eV and the spectrum is dominated by NBE transitions, meaning that all samples are free of deep defects and at least of decent structural quality. Spectra for self-induced AlN NWs and the 2D layer exhibit the same transitions ($D°X_A$ and phonon replica spaced by multiples of the LO phonon energy (110 meV)), except that the related emission energies are globally blue-shifted by about a dozen of meV for the epilayer. The latter feature was expected in view of the compressive strain within the AlN 2D layer. According to the literature, the average values of FX_A and donor binding energy are respectively 6.040 eV and 18 meV for bulk AlN [128], giving a $D°X_A$ emission energy of 6.022 eV, which matches the 6.02 eV value reported for (almost) strain-free and self-induced AlN NWs [315].

Regarding AlN on GaN NWs, their $D°X_A$ energy value of 6.035 eV, intemediate between the relaxed AlN value of 6.022 eV and the 6.047 eV value for the MOCVD epilayer, seems to infer that the AlN grown on top of GaN templates are probably not fully relaxed. However, Raman measurements highlighted that they actually are: it must not be forgotten that the 6.022 eV is an average value and that disparities from the latter can be observed [128]. Similarly to the case of GaN, the $D°X_A$ linewidth of 9 meV for AlN NWs remains larger than those of state-of-the-art layers (of the order of 500 µeV [378]) but is comparable or even inferior to other values reported for AlN NWs [315, 375]. A shouldering around 6.017 eV remains unassigned for such NWs, as exhibited in Figure 2.3.1.3. In view of the 18 meV difference with $D°X_A$ energy (i.e. 36 meV with FX_A when taking into account the average $E^b_{D°X_A}$ value), the latter is very likely to be either related to other donors (Si, O) or corresponding to the $A°X_A$ transition when comparing to the literature. Indeed, the reported average transition values are 26.6, 26.9 and 35.1 meV below FX_A, respectively for $Si°X_A$, $O°X_A$, and $A°X_A$ [128]. Given the disparities on the reported values for donor bound excitonic transitions, it is difficult to conclude without performing additional experiments. DAP at about 5.867 eV and associated replicas spaced by 110 meV were also evidenced through power-dependent PL measurements, for the first time in AlN [139], as labeled in Figure 2.3.1.3. The latter transitions may be related to surface effects, since they have never been observed in the 2D case so far.

Fundamental optical properties were reported afterwards for similar AlN NWs grown on GaN NW templates by another group [375]. Interestingly, the main line was also observed around the same energy (6.03 eV) but clear replicas of the latter were evidenced to be spaced by about 100 meV instead of 110 meV in our case. Such feature was correlated to surface-optical (SO) phonons through micro-Raman scattering experiments rather than the commonly reported LO phonons. In addition, Mg-doped AlN on GaN NW templates were optically characterized [78, 376], highlighting two main contributions: the NBE assigned to be dominated by the $Mg°X_A$ transition, and a deeper one at 5.45 eV attributed to a DAP transition between a shallow donor level and the Mg-acceptor one, which is consistent with other reports for the 2D case [128, 379]. Other lines were also evidenced at room temperature around 4.57 eV and 3.9 eV. The latter were associated with deeper and defect-related DAP transitions, respectively involving deep donor/shallow acceptor and shallow donor/deep acceptor couples, as previously reported for 2D layers [128, 380].

2.3.1.3 Time-resolved photoluminescence (TRPL)

Macro- and µ-TRPL experiments were also performed at NPSC in order to study the PL dynamics (luminescence decays). The laser was in this case a Ti-Sapphire laser (Mira from Coherent) emitting either 200 fs or 2 ps wide (more stable in the ps mode) pulses over the 710-940 nm range. The standard cavity emits with a repetition rate of 76 MHz that is adjustable thanks to a cavity dumper. The pulse was then frequency tripled in order to reach UV excitation. For Al-richer samples, a few experiments were carried out at Charles Coulomb laboratory, where the frequency can be quadrupled.

The optics (lenses, mirrors, splitters, pin-holes, etc.…) used in both macro-TRPL and μ-TRPL setups were identical to those used in their CW counterparts. The spectrometer of this setup (focal length 330mm) was equipped with a 600 lines/mm grating and the used photomultiplier (PMT ,model Picoquant PMA Hybrid 6) detector allowed us to reach an overall time resolution of 40 ps. The width of the entrance slit could be varied to tailor the TRPL signal ratio and the spectral resolution. As for the lateral slit width, its width could be adjusted to increase the number of photons impinging on the PMT at the expense of the spectral resolution.

Temperature-dependent TRPL were also carried out to assess non-radiative processes. Doing so implies to make some assumptions described in the following on the experimental data, namely the collected intensity of a given TRPL line I_{exp} and the corresponding decay τ_{exp} recorded at several sample temperatures T. In this perspective, it must be first reminded that I_{exp} depends on several elemental mechanisms subsequent to the excitation impinging on the nitride sample and given in chronological order: the absorption of photons exciting carriers, the relaxation of excited carriers, their radiative recombinations and the collection of sample luminescence depending on the experimental setup. Each mechanism having a certain efficiency that may depend on T, I_{exp} can be expressed, as a function of T:

$$I_{exp}(T) = I_{exc}\, \eta_{abs}(T)\, \eta_{rel}(T)\, \eta_{rad}(T)\, \eta_{coll} \qquad (2.3.1.1)$$

Where I_{exc} the excitation intensity, and η_{abs}, η_{rel}, η_{rad}, η_{coll} are the efficiency of the absorption, the relaxation, the radiation and the collection mechanisms, respectively. First, I_{exc} and η_{coll} can be considered as constant, if the experimental settings are kept constant. Then, knowing that only two recorded parameters $I_{exp}(T)$ and $\tau_{exp}(T)$ are at our disposal, we can only describe only two independent parameters of the model, which implies to remove variables. As we aim at estimating the non-radiative contribution with respect to the radiative one, one independent parameter must account for each one: τ_{nrad} corresponding to the non-radiative recombination time and τ_{rad} for its radiative counterpart. η_{rad} can be written as a function of these two decay times:

$$\eta_{rad}(T) = \frac{\tau_{nrad}(T)}{\tau_{nrad}(T) + \tau_{rad}(T)} \qquad (2.3.1.2)$$

Therefore η_{abs} and η_{rel} variables must be removed and considered as independent of sample temperature. Depending on the investigated sample, such assumption can be questionable. For example, when exciting 2D nitride QDs grown through SK mode, the presence of a thin wetting layer below the QDs (thickness of a couple of MLs) makes this hypothesis less true, especially for η_{rel} [190]. Thus, it can be written:

$$I_{exp}(T) = I_{exc}\,\eta_{abs}\,\eta_{rel}\,\eta_{coll}\,\eta_{rad}(T) = I_0\,\frac{\tau_{nrad}(T)}{\tau_{nrad}(T) + \tau_{rad}(T)} \tag{2.3.1.3}$$

As for the experimental decay τ_{exp}, provided that the relaxation time is much shorter than the recombination time (which is a reasonable assumption in view of typical relaxation time in nitrides [381]), it can be expressed as:

$$\tau_{exp}(T) = \frac{\tau_{nrad}(T)\,\tau_{rad}(T)}{\tau_{nrad}(T) + \tau_{rad}(T)} \tag{2.3.1.4}$$

To remove the I_0 variable, it must be assumed that $\eta_{rad}(T \leq 5\,K) = 1$, meaning that $\tau_{nrad}(T) \gg \tau_{rad}(T)$ at cryogenic temperatures. Such assumption can be considered as valid if τ_{exp} remains almost constant over low temperature ranges. Finally, we can write:

$$\begin{aligned} \tau_{rad}(T) &= \tau_{exp}(T)\,\frac{I_{exp}(T \leq 5\,K)}{I_{exp}(T)} \\ \tau_{nrad}(T) &= \frac{\tau_{exp}(T)}{1 - \dfrac{I_{exp}(T)}{I_{exp}(T \leq 5\,K)}} \end{aligned} \tag{2.3.1.5}$$

This simple model was used to process the temperature-dependent TRPL data presented in the following of the manuscript.

2.3.1.4 Photon correlation experiments (HBT)

Hanbury Brown and Twiss-type (HBT) photon correlation experiments [382] were also carried out in order to classify the investigated emitters, which can be, as illustrated in Figure 2.3.1.4 (a):

- Coherent, meaning that the emitted photon stream is totally random. Laser beam sources are typical examples of such emitters.
- Chaotic. In this case, the emitted photon stream is said to be bunched. For instance, thermal light sources belong to this class.
- Non-classical. In the latter case, the photon stream is said to be antibunched and quantum effects must be considered. For example, single QD emitters, single impurities in semiconductor matrices, single molecules or single atoms can meet these criteria.

During HBT experiments, when counting photons on two distinct detectors, we actually record photon correlation histograms corresponding to the second-order correlation function $g^2(\tau)$, where τ corresponds to the time difference between a count registered on a given detector and a count recorded on the other one. $g^2(\tau)$ can be expressed as:

$$g^2(\tau) = \frac{\langle I_1(t) I_2(t+\tau)\rangle}{\langle I_1(t)\rangle\langle I_2(t+\tau)\rangle} = \frac{\langle N_1(t) N_2(t+\tau)\rangle}{\langle N_1(t)\rangle\langle N_2(t+\tau)\rangle} \tag{2.3.1.6}$$

where I_1 (respectively I_2) is the light intensity impinging on the first detector (respectively the second one) and N_1 (respectively I_2) is the number of counts on the first detector (respectively the second one), N being proportional to I from an experimental point of view.

In terms of physical meaning, $g^2(\tau)$, also called the degree of second-order coherence, quantifies the intensity fluctuations over a certain time scale equal to the coherence time τ_c and corresponds to the probability of counting a photon on the second detector at time $t+\tau$ after having detected a photon at time t on the first detector. Therefore, in view of Figure 2.3.1.4 (a), we would have, first in the case of a chaotic light, $\forall\tau, g^2(\tau) \geq 1$ and an autocorrelation $g^2(0) > 1$. Second, for a coherent light, $\forall\tau, g^2(\tau) = 1$. Last, regarding the non-classical case, $g^2(\tau) \leq 1$ and $g^2(0) < 1$. In the latter case, if $g^2(0) < 0.5$, we are sure of dealing with a single quantum emitter [383, 384]. Figure 2.3.1.4 (b) exhibit the typical shapes of $g^2(\tau)$ for each case.

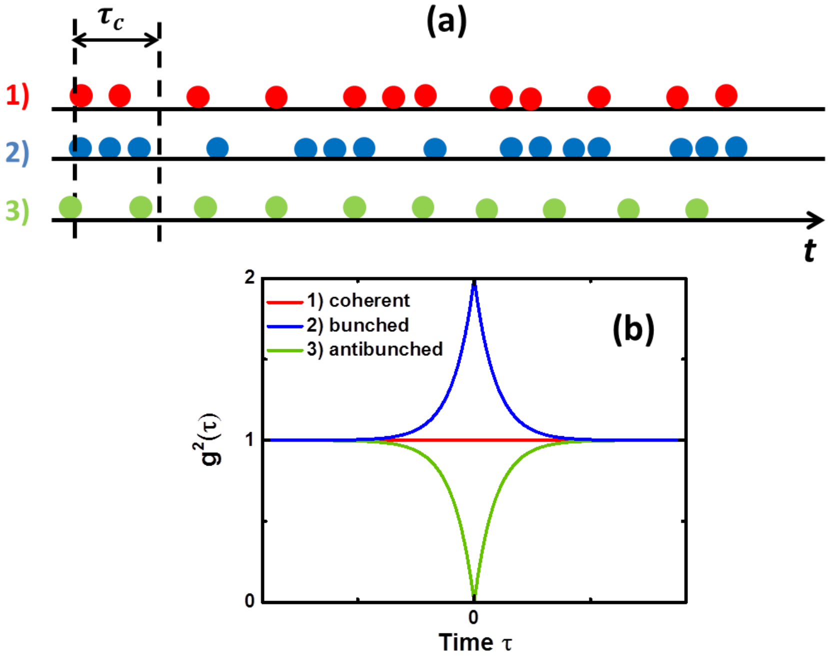

Figure 2.3.1.4: (a) Illustration of the photon streams for 1) coherent light, 2) bunched light, 3) antibunched light. (b) Shape of the second-order correlation function $g^2(\tau)$ for 1), 2) and 3).

For the needs of these experiments, a 50-50 plate beam splitter exit and two PMT detectors linked to a correlation card were added at the spectrometer lateral exit on the μ-PL CW setup. The lateral slit width could be adjusted to increase the number of counts on both detectors at the expense of the spectral resolution. A lens (designed for the UV range) was also placed between this lateral exit and the beam splitter in order to refocus the beam on the PMTs. A sketch completing the μ-PL setup shown in Figure 2.3.1.1 is given below in Figure 2.3.1.5.

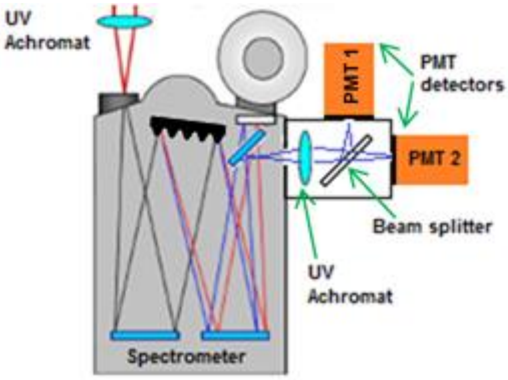

Figure 2.3.1.5: Sketch displaying the photon-correlation experiment equipment installed on the μ-PL setup spectrometer.

The two PMTs and the correlation card are designed by Picoquant, and the models are respectively the PMA 175 and the TimeHarp 260 Pico. Each PMT detector has a typical instrument response below 180 ps. As for the correlation card, the base resolution was 25 ps. A variable delay between the two detectors could be set, depending on experimental needs. In our case, a 20 ns delay was set.

2.3.2 Cathodoluminescence (CL)

The principle of CL technique [385] is close to PL, when considering the deexcitation processes (non-radiative and radiative excitonic recombinations, etc.…) occurring once the material is excited and the detection equipment used to collect the resulting luminescence. The main difference comes from the excitation source, which consists here in an electron probe, typically a microscope electron beam. First, contrary to PL, any semiconductor material will be excited whatever its bandgap. Indeed, in view of the typical acceleration voltage range (10-30 kV), each impinging electron will create many electron-hole pairs, and the luminescence resulting from their recombination can be collected if the detection chain is adapted to the material emission range. However, the detection equipment starts showing its limitations when getting below 200 nm, as air absorption gets large in this spectral range. Second, due to the numerous processes occurring when the electron probe interacts with matter, energy losses are significant (of the order of 60% prior to carrier relaxation) [386]. Third, due to the typical impinging electron current densities, it is more difficult to vary the excitation power density over several orders of magnitudes as it can be done in PL, and notably to reach low excitation regimes.

Regarding the data acquisition, three modes are typically used in CL:

a. The spectroscopic mode, which basically consisted in focusing the beam over the region of interest and recording the related spectrum with a CCD.
b. The imaging mode, which consisted in recording both the luminescence signal on a PMT detector at a given energy / wavelength and the related structural information (microscope image).
c. The spectral imaging mode or spectral cartography mode. In this mode, the beam is scanned over the region of interest with a constant step. At each scan position, structural (BF, ADF) and optical (CL) signals are acquired simultaneously. At the end of the acquisition, both the images (BF and ADF) and the spectral map are reconstructed: at each pixel of the image corresponds a given spectrum, allowing us to correlate both structural and spectroscopic information precisely.

It must be noted that the spatial resolution of recorded CL images is lower in general than for other electron microscopy techniques, as created excitons can diffuse much more in the material. In addition, the spatial extension of the excitonic wavefunction can be significant in bulk material. For instance, excitons can move over several micrometers in materials such as bulk arsenides [387, 388], making the CL technique inadequate for getting short-scale information in this case but still applicable for other purposes such as exciton diffusion length measurements [388-389]. However, regarding wider bandgap materials such as AlGaN, both phenomena are reduced so that we can obtain information on a scale of the order of 15 nm for bulk [139, 320]. The CL spatial resolution can be even improved (down to a few nanometers) when working with very small radiative objects such as nitride QDisks/QDs, for which carrier diffusion is reduced [391-393].

2.3.2.1 Cathodoluminescence in a SEM microscope

The SEM microscope is a FEI Quanta 200 from Neel Institute described in Subpart 2.2.1.1. The sample temperature could be varied over the 5-300K range thanks to a liquid helium dewar and the sample holder heater. The photons emitted by the sample were first collected by a parabolic mirror and then focused, thanks to a pair of mirrors, on the entrance slit of a 460 mm focal length monochromator. The latter has two gratings (600 lines/mm and 1800 lines/mm) and is associated with two detectors: a CCD, allowing the quick recording of simple spectra, and a PMT detector for panchromatic imaging. The first two acquisition modes, a. and b., were mainly used with this setup. Figure 2.3.2.1 (a) illustrates the principle of the CL in a SEM setup.

2.3.2.2 Cathodoluminescence in a STEM microscope

The STEM setup VG HB501 is briefly described in 2.2.1.2. Samples are cooled down to 150 K by liquid nitrogen. The CL signal was collected by a parabolic mirror and transmitted to the spectrometer entrance through an optical fiber. The best spectral resolution is of the order of 4 meV at 300 nm. Experiments were mainly performed in the third acquisition mode, the spectral cartography mode (c). Figure 2.3.2.1 (b) illustrates the principle of the CL in a STEM setup.

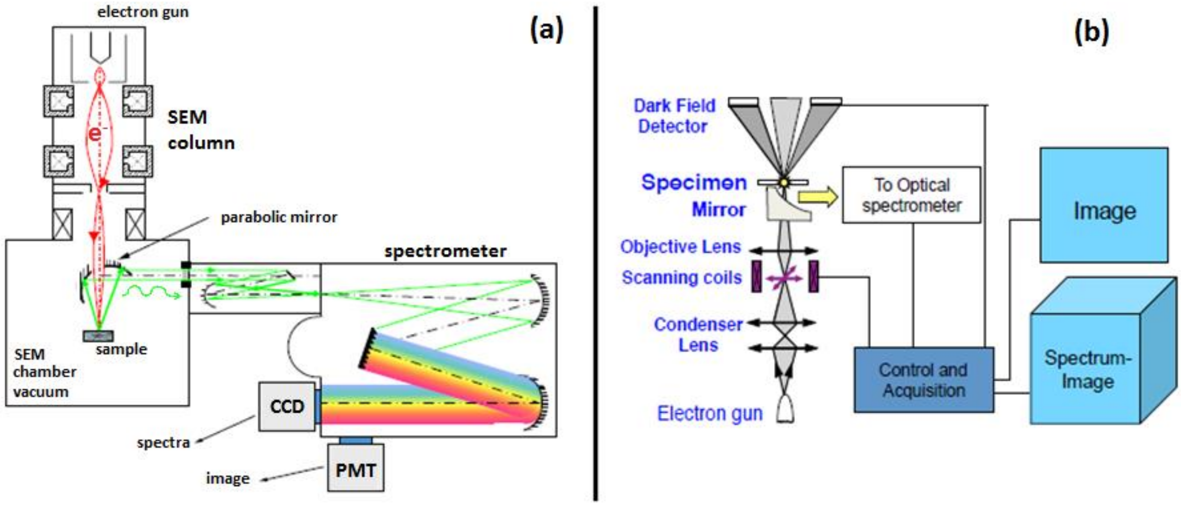

Figure 2.3.2.1: Principle of: (a) a CL setup in a MEB setup (Neel Institute FEI setup), (b) a CL setup in a STEM (LPS setup), taken from [391].

2.3.3 Raman spectroscopy

Raman spectroscopy [359, 394] experiments were also performed on AlGaN NW samples at the Institute of material science, in Valencia, Spain. They rely on inelastic scattering, or Raman scattering, of monochromatic light, usually from a laser, focused on the sample (crystal or molecule). The laser beam interacts with sample vibrations, resulting in the energy of the laser photons being shifted up or down. The retroscattered light is then analyzed: the shift in energy gives information about the vibrational modes (phonons) in the system. Depending on the scattering geometry configuration, we can collect several types of optically active phonon modes. Figure 2.3.3.1 illustrates the six optical phonon modes that can be measured for the WZ nitride structure (see previous reports for more details about modes and configurations [395]):

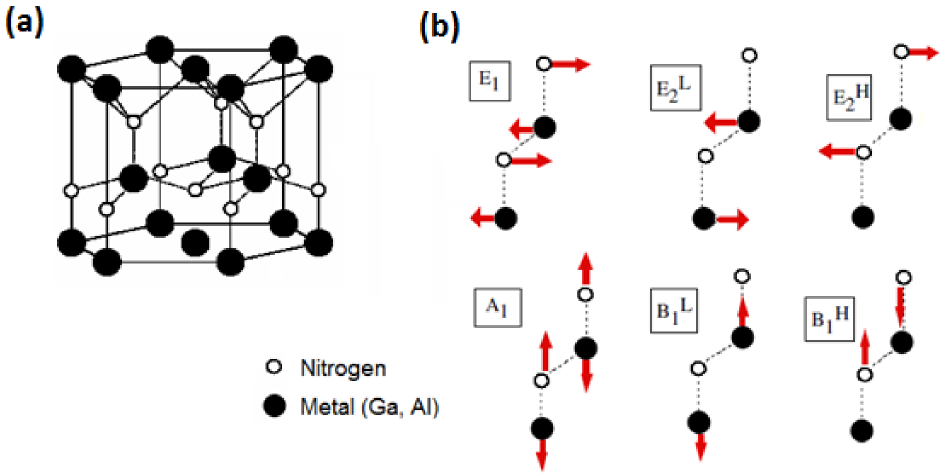

Figure 2.3.3.1: (a) Sketch of the crystal structure for WZ AlGaN. (b) Sketches illustrating the six optical phonon modes for such structure.

The optical phonon modes presented above, which can be longitudinal (noted LO) or transverse (noted TO), can notably provide information about the crystalline quality or strain within the sample. In the case of an alloy, they can also be used to estimate the average composition. Indeed, when considering the E_2^H vibration mode for instance (also noted E_{2h} in the following), two frequencies are observed in $Al_xGa_{1-x}N$: the first one is associated with the Ga-N bond (E_{2h} GaN-like) whereas the other one is related to the Al-N bond (E_{2h} AlN-like) [396, 397]. Both frequencies were demonstrated to vary with the average AlN molar fraction in fully relaxed AlGaN. Consequently, our samples must be relaxed as well, in order to compare results with previous studies used as calibration. In the case of AlGaN NWs, such a hypothesis is very reasonable. Theoretical Raman shift values at room temperature (300 K) are provided for relaxed GaN and AlN in Table 2.3.3.1, for a few modes. For practical reasons, Raman spectroscopy was not much used to estimate the average AlN molar fraction of our AlGaN samples, as XRD setups were directly at our disposal in the NPSC laboratory, but rather for other purpose that will be described further.

Phonon modes	GaN (cm^{-1})	AlN (cm^{-1})
E_2^L (low)	144	248
E_2^H (high)	567	657
A_1(TO)	532	610
E_1(TO)	559	670
A_1(LO)	734	890
E_1(LO)	741	912

Table 2.3.3.1: Theoretical Raman frequency values for relaxed GaN and AlN at 300 K, provided for several modes.

It must be noted that configurational disorder in the $Al_xGa_{1-x}N$ alloy may result in asymmetric Raman line shapes for both E_2 and A_1 phonon modes and small variations in the measured phonon frequencies related to $Al_xGa_{1-x}N$. In addition, the Raman signal analysis obtained for AlGaN samples is complicated owing to the Si (111) substrate. Indeed, the Raman signal of Si is between those of GaN and AlN and consequently overlaps the signal of $Al_xGa_{1-x}N$. Therefore, a reference spectrum for a bare Si (111) wafer must be absolutely recorded and subtracted to the AlGaN spectrum, in order to extract the Raman shift values conveniently.

In our experiments, the samples were excited at room temperature with a doubled YAG laser emitting at 532 nm and were either as-grown or dispersed AlGaN NWs. In the latter case, the diameter of the laser beam spot was of the order of 1 µm thanks to a microscope objective (100x, NA=0.9). The main scattering geometry configuration used for measurements was $Z(XX)\bar{Z}$, which allows E_2 and A_1(LO) modes.

3. Investigation of carrier localization in $Al_xGa_{1-x}N$ nanowires

3.0 Introduction

In order to fully master the manufacturing of AlGaN NW-based optoelectronic devices mentioned in section 0.2 and enhance even more their efficiency, fundamental properties of such NWs must be examined more deeply to better comprehend and control them. In particular, the issue of alloy inhomogeneity at nanoscale in III-N ternary alloy NWs has been investigated in the recent years, more widely for InGaN NWs [270, 335, 398-403] than for AlInN NWs [188, 404] or AlGaN NWs [319, 323-325, 329], but remains far from being completely understood. In this perspective, regarding the AlGaN alloy, our team previously demonstrated that the structural properties of NID AlGaN NW sections grown by PA-MBE in N-rich conditions at high substrate temperatures (T_{subs} over 810-840°C, t_{des}^{Ga} over 7-25 s) on top of GaN NW templates are governed by the presence of Al composition inhomogeneities, as exhibited from Figure 3.0.1 (a) to (d). A growth model, which mostly relies on kinetics considerations already presented in Subpart 2.1.4 and including the competition between the incorporation of the two metallic species, was proposed to explain their formation [139, 321, 322]. As for the optical properties of such sections, carrier localization was evidenced through PL experiments performed on dispersed AlGaN NWs, as shown in Figure 3.0.1 (e) and (f), and assigned to compositional fluctuations in the alloy [139, 321, 322].

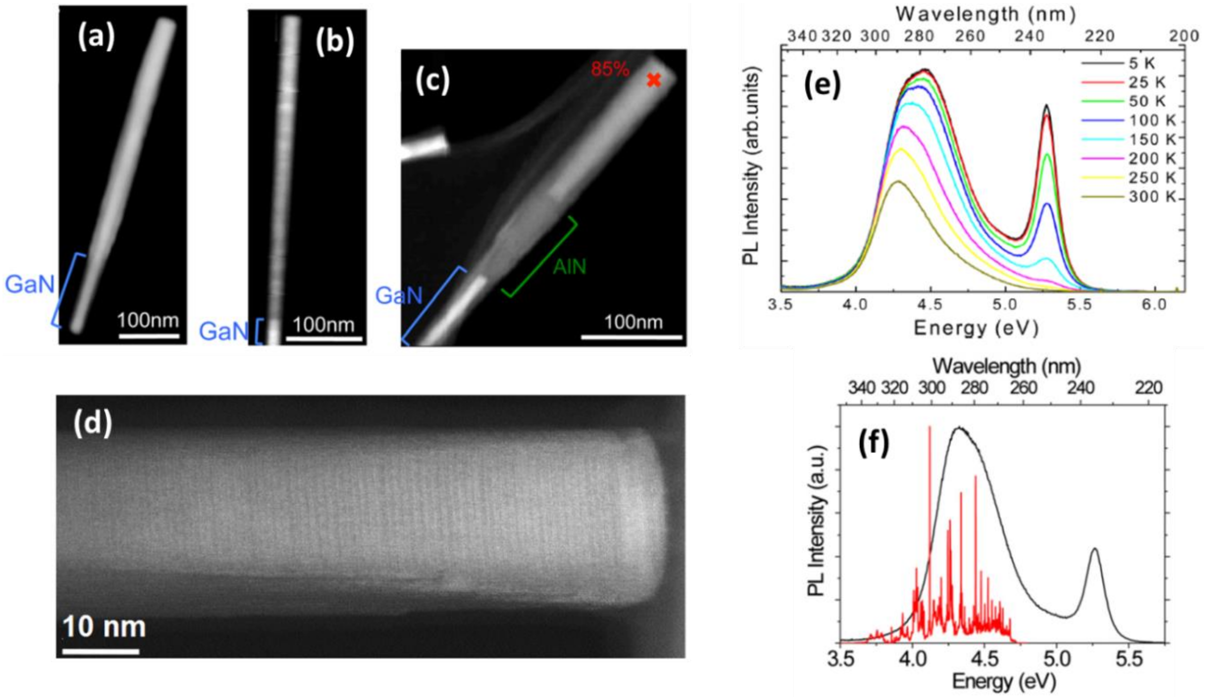

Figure 3.0.1: ADF-STEM images of $Al_xGa_{1-x}N$ NW sections grown in N-rich conditions at high substrate temperatures (T_{subs} = 825°C, t_{des}^{Ga} = 8 s) on top of GaN NW templates with average AlN molar fraction x = (a) 0.3, (b) & (d) 0.5, (c) 0.8. Depending on the AlN molar fraction, the "macro-"structural properties of AlGaN NW vary here: (a) alloy seeming rather homogeneous, (b) & (d) macro-compositional fluctuations directly visible in the alloy (chemical contrast), (c) pure AlN section nucleating before an alloy appearing rather homogeneous. The latter images are examples highlighting the sensibility of these structural properties to kinetics. (e) Temperature-dependent macro-PL spectra for an ensemble of $Al_{0.8}Ga_{0.2}N$ NW sections, revealing low quenching with temperature at lower emission energy (f) µ-PL spectrum of dispersed $Al_{0.8}Ga_{0.2}N$ NWs at cryogenic temperature (5 K), exhibiting sharp lines and superimposed with the macro-PL spectrum. (e) and (f) highlight signs of strong carrier localization. Taken from [321, 322].

Furthermore, nanoCL experiments carried out on dispersed AlGaN NW sections revealed position-dependent luminescence occurring over a wide wavelength range, as illustrated in Figure 3.0.2. This was attributed to a composition gradient along the NW growth axis, resulting from nanometric compositional fluctuations that were observed until a steady-state regime leading to a more homogeneous alloy was reached [139, 320, 321]. Similar experiments were performed more recently by another group, highlighting very marked compositional inhomogeneities in investigated Al-rich AlGaN NW sections as well, in contrast to their very Al-poor counterparts [329].

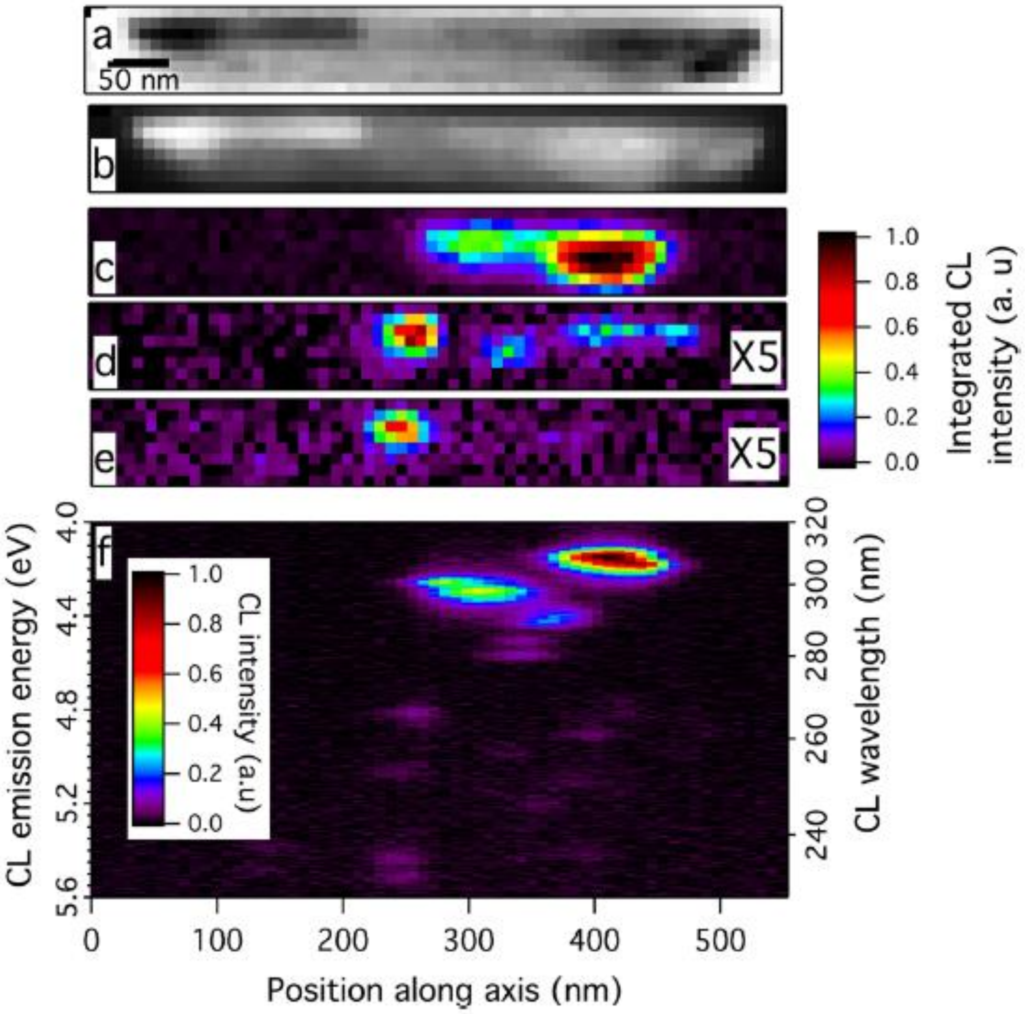

Figure 3.0.2: NanoCL spectral imaging for an $Al_{0.8}Ga_{0.2}N$ NW. (a) BF image (Al-rich regions are brighter). (b) DF image (Al-rich regions are darker). (c) to (e) CL maps extracted from a spectral image, integrated on a 200 meV range with mean energy value of 4.15 eV, 4.80 eV and 5.50 eV, respectively. The intensity scale is arbitrary, but the same for the three maps (intensity scaled by a factor of 5 for (d) and (e)). (f) Spectral profile: intensity, integrated over the width of the NW, as a function of the energy and the position along the NW axis. The combination of all images highlights the position-dependent luminescence energy, from high energy in the section bottom part to lower energy in the top part. Taken from [139, 321].

It appears from results of these previous works that carrier localization effects associated with alloy fluctuations within NWs can be partly controlled by growth parameters, opening the way to localization engineering and to enhancement of room-temperature UV-light emission with respect to the high IQE values already reported for Al(Ga)N NWs (about 80% for AlN NW [78, 79], around 50% for AlGaN of low Al composition emitting around 335 nm and 70-80% for AlGaN with higher Al content emitting around 265 nm [325]). To move forward in this direction, we will investigate more deeply such localization in the following. Its dependence on growth kinetic parameters will be notably studied.

3.1 Growth and basic structural properties of investigated AlGaN nanowire sections

To study the dependence of carrier localization in AlGaN NWs on growth kinetic parameters (namely growth temperature and atomic fluxes setting the average AlN molar fraction), several series of samples, consisting of NID $Al_xGa_{1-x}N$ NW sections on top of GaN NW templates as described in Subpart 2.1.4, were grown in N-rich conditions using the PA-MBE setup detailed in Subpart 2.1.1. For a given sample series, metallic fluxes were fixed to the same values so that the nominal AlN molar fraction was set to a value comprised over the 0.3-0.7 range, whereas AlGaN growth temperature was varied over the 650-875°C range. For all samples, the growth of GaN NW templates, presented in Subpart 2.1.3, was performed in identical conditions in order to be as reproducible as possible from one sample to another. In particular, the NW template density had to be carefully controlled to take advantage of the shadowing effect and avoid the formation of a 2D layer between NWs, while preventing them from coalescing and keeping the possibility to disperse them rather easily, as described in Subpart 2.1.4.1. A typical density of 2-2.5 10^{10} cm^{-2} allowed us to use the same samples for both macro- and µ-characterizations. As for dimensions of NW templates, the latter were typically 30 nm ± 15 nm wide and grown long enough, typically 500-600 nm long, in order to favor shadowing effect and to spot dispersed NWs more easily by SEM.

The metallic fluxes were calibrated using both the RHEED-based method and the additional NW marker technique, respectively presented in Subparts 2.1.2.3 and 2.1.4.2, whereas the N flux was kept identical all the time (same parameters for the used N plasma cell). For the growth of AlGaN NW sections, the effective NW growth rates estimated for GaN and AlN with the marker technique were fixed as a function of the desired nominal AlN molar fraction, and such that their sum was very slightly inferior (or at most equal) to stoichiometry (effective III/N ratio $\cong 1$) in order to ensure being within the N-rich regime and avoid significant NW broadening, while remaining as close as possible to metallic flux conditions typically resulting in high crystal quality and smooth surface in the 2D case (see Subparts 1.3.2.3 and 2.1.4.1). As for GaN NW templates, they were grown using a typical III/N ratio equal to 1/3 as estimated from RHEED-based calibration. It must be noted that stoichiometry corresponds to a growth rate of about 0.25 ML/s for the mostly used N plasma cell versus 0.7 ML/s for the other and “faster” one. Most AlGaN NW section samples were grown with the “slower” cell, whereas the AlGaN QDisk samples presented further in Subpart 3.2.7 were grown using the “faster” cell. During any growth run, the substrate was continuously rotated to promote growth homogeneity, since the atomic flux incidence angles were not equal to 0, as previously mentioned in Subpart 2.1.

Regarding substrate temperatures T_{subs}, they were set, depending on our experimental needs, by measuring before each growth, when possible, the corresponding Ga desorption times t_{des}^{Ga} following the exposure of the Si (111) wafer surface to Ga flux in order to ensure reproducibility, as presented in

Subpart 2.1.2.2. For this purpose, the Si substrates had to be deoxidized before their introduction in the MBE chamber and outgassed once mounted inside until the appearance of the 7x7 Si (111) surface reconstruction, as detailed in Subpart 2.1.2.1. Typically, GaN NW templates were grown at substrate temperatures corresponding to t_{des}^{Ga} = 7 s or t_{des}^{Ga} = 5 s, when growing respectively on bare Si and thin AlN buffer. The latter, which was about 4 nm thick, could be grown prior to GaN deposition on the Si substrate to improve the NW orientation and reduce the NW nucleation time, as described in Subpart 2.1.3.2.

Directly after growth, basic macro-characterization experiments, namely SEM (see Subpart 2.2.1.1), XRD (see method described in Subpart 2.2.2) and CW macro-PL (see Subpart 2.3.1.1) experiments were systematically performed, in this order, for almost all as-grown samples. STEM (see Subpart 2.2.1.2) and EDX (see Subpart 2.2.1.3) experiments were then carried out on dispersed NWs from well-chosen samples. More complex experiments were also performed on specific samples: for instance, resonant XRD experiments presented in Annex 2 allowed us to check that the NID AlGaN NWs studied during this PhD are mostly N-polar.

Figure 3.1.1 provides typical electron microscopy images of AlGaN NW sections grown with the same atomic fluxes (nominal AlN molar fraction x_{nom} = 0.6 here) at various growth temperatures. In addition, Figure 3.1.2 provides electron microscopy images of AlGaN NW sections grown this time at the same temperature but at various AlN molar fractions.

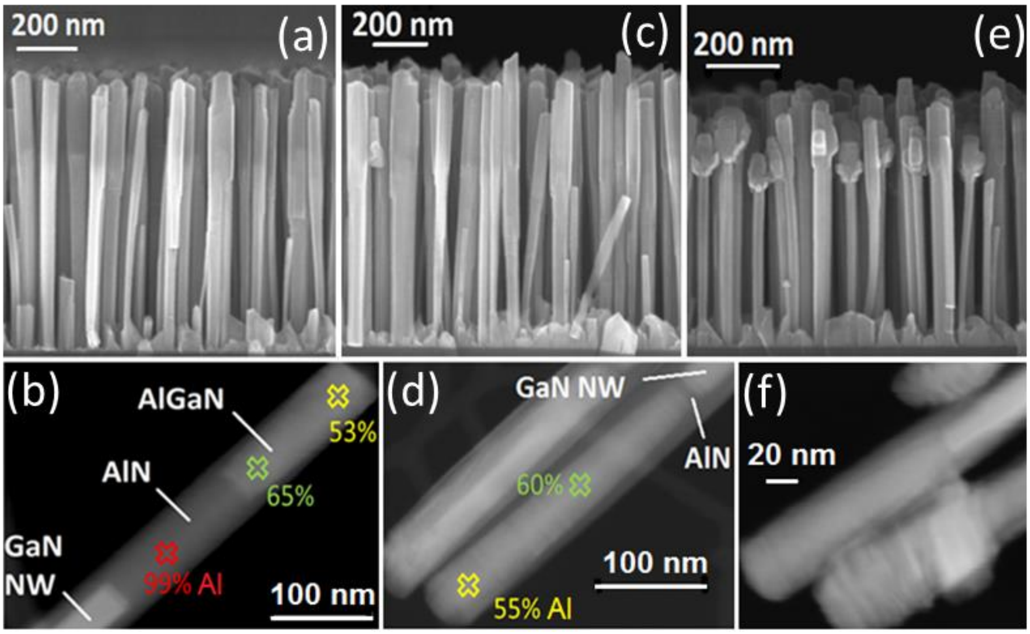

Figure 3.1.1: Typical SEM and STEM-HAADF images respectively for as-grown and dispersed $Al_{0.6}Ga_{0.4}N$ NW sections, grown at: (a) & (b) T_{subs} = 865°C (t_{des}^{Ga} = 5 s), sample N2330, (c) & (d) T_{subs} = 780°C, sample N2325, (t_{des}^{Ga} = 60 s), (e) & (f) T_{subs} = 650°C, sample N2348. The average AlN molar fractions obtained by XRD are respectively equal to 0.66, 0.59 and 0.56 for sample N2330, N2325 and N2348. Local Al composition obtained by EDX is given at several points labeled by crosses for some NWs.

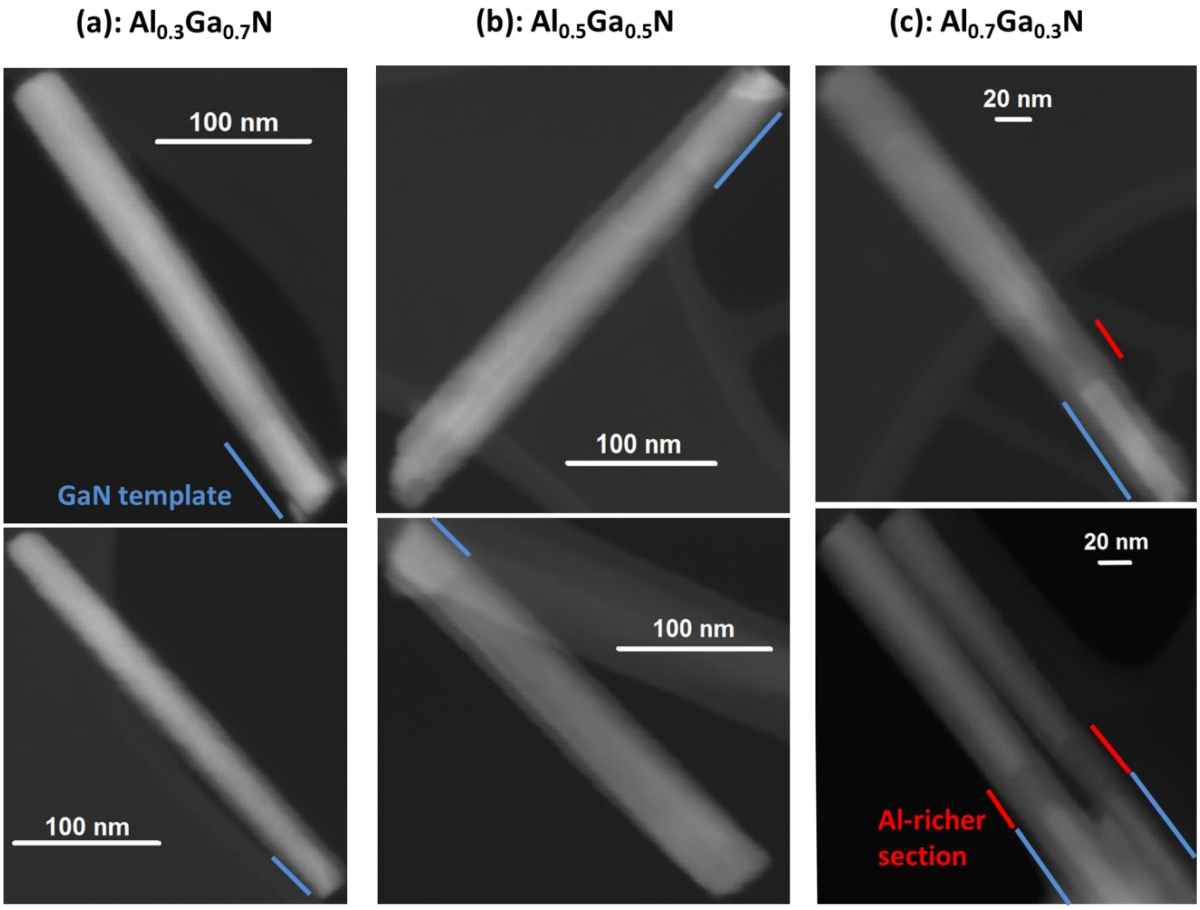

Figure 3.1.2: STEM-HAADF images of dispersed AlGaN NW sections grown at the same low substrate temperature (T_{subs} ≈ 780-790°C, t_{des}^{Ga} = 60 s), but at various nominal AlN molar fractions: (a) x = 0.3, sample N2499 (b) x = 0.5, sample N2504 (c) x = 0.7, sample N2507. The GaN NW templates are labeled with blue lines, whereas the Al-richer sections are indicated in red. The chemical contrast between the NW templates and the AlGaN section gets more significant when increasing the AlN molar fraction, from (a) to (c). Even at lower growth temperature, the Al-richer section remains present for high targeted Al content (nominal x = 0.7 in (c))

As displayed in the two latter figures through atomic contrast and EDX measurements, the formation of an Al-richer section, even pure AlN for high targeted Al content, was systematically observed prior to AlGaN when growing NWs at high nominal AlN molar fractions and high substrate temperatures, despite the unfavorable lattice mismatch between the GaN NW template and AlN. However, it was noted on the whole that this Al-richer section was dramatically shortened when decreasing growth temperature. Indeed, in the case of the sample series exhibited in Figure 3.1.1, the length of the latter section decreased from above one hundred nanometers when grown at high temperatures (T_{subs} = 865°C, corresponding to t_{des}^{Ga} = 5 s) to a few nanometers (5-10 nm) for lower growth temperatures (below T_{subs} = 780°C, corresponding to t_{des}^{Ga} = 60 s). This decrease in Al-richer section length also occurs when diminishing the Al/Ga flux ratio, that is to say the nominal AlN molar fraction, as shown in Figure 3.1.2 and similarly to previous reports [139]. Decreasing even more AlGaN growth temperature (below T_{subs} = 700°C and even down to 650°C) allowed us to reduce this undesired section more, even to suppress it completely for some NWs, but at the expense of NW macro-structural properties, as visible in Figure 3.1.1 (e) and (f). Indeed, a larger and larger part of NW population exhibits an irregular shape for lower and lower growth temperature, with parasitic growth on NW sidewalls. Such features go hand in hand with the degradation of macro-optical properties, as shown further in Subpart 3.2.1. In view of the latter observations, the preferential nucleation of this Al-richer section is clearly governed by kinetic processes introduced in Subpart 1.3.2.1 and detailed for the peculiar case of AlGaN NW growth in Subpart 2.1.4.1: preferential incorporation of Al adatoms, Ga adatom desorption, etc.…

As expected given the latter processes explained in previous subparts, when decreasing substrate temperature, the average AlN molar fraction determined by XRD got lower for fixed atomic fluxes, varying for instance from 0.66 to 0.56 for AlGaN NWs of the sample series exhibited in Figure 3.1.1, due to lower Ga desorption promoting its incorporation. More generally, Ga incorporation got progressively favored during NW growth, since a progressive decrease in AlN molar fraction along growth axis was evidenced through EDX experiments whatever the substrate temperature, as highlighted for instance for $Al_{0.6}Ga_{0.4}N$ NW sections of Figure 3.1.1 and consistent with Al composition gradients reported in previous works [139, 319-321, 323]. Such features can be assigned to reservoirs of Ga adatoms that accumulate on top of NWs more or less significantly depending on substrate temperature, making their incorporation more probable than the Al ones at one point, and to progressive strain relaxation mechanism.

It must be pointed out that the values of local AlN molar fraction obtained by EDX within the AlGaN NW core were slightly biased by the thin Al-richer shell that systematically formed due to lower Al adatom diffusion, as explained in Subpart 2.1.4.1. The contribution of the latter could not be easily decorrelated but could be approximated, knowing the shell thickness and composition as well as NW and AlGaN core diameters, by the following relationship [319]:

$$x_{core}d_{core} + x_{shell}2t_{shell} = x_{center}d_{NW} \tag{3.1.1.1}$$

where x_{core}, x_{shell}, and x_{center} are the AlN molar fractions respectively of the AlGaN core, of the Al-richer shell, and measured at the NW center by EDX, whereas d_{core}, d_{NW} and t_{shell} are respectively the core diameter, full NW diameter, and the shell thickness.

Finally, Figure 3.1.3 provides SEM images taken along the wafer radius for a given AlGaN NW sample, illustrating the variation of substrate temperature from the wafer center to the edge described in Subpart 2.1.1.3. Such variation will be also highlighted through macro-PL characterization in Subpart 3.2.1. Given the latter variation, NW macro-structural properties remain similar when considering NWs less than 10-15 mm away from the wafer center, whereas they abruptly change outside this region, when getting closer to the substrate edge. Consequently, most macro-structural characterizations such as XRD and NW dispersions for µ-structural characterizations like EDX were performed as close to the wafer center as possible, remaining within the area where substrate temperature variation was low during growth.

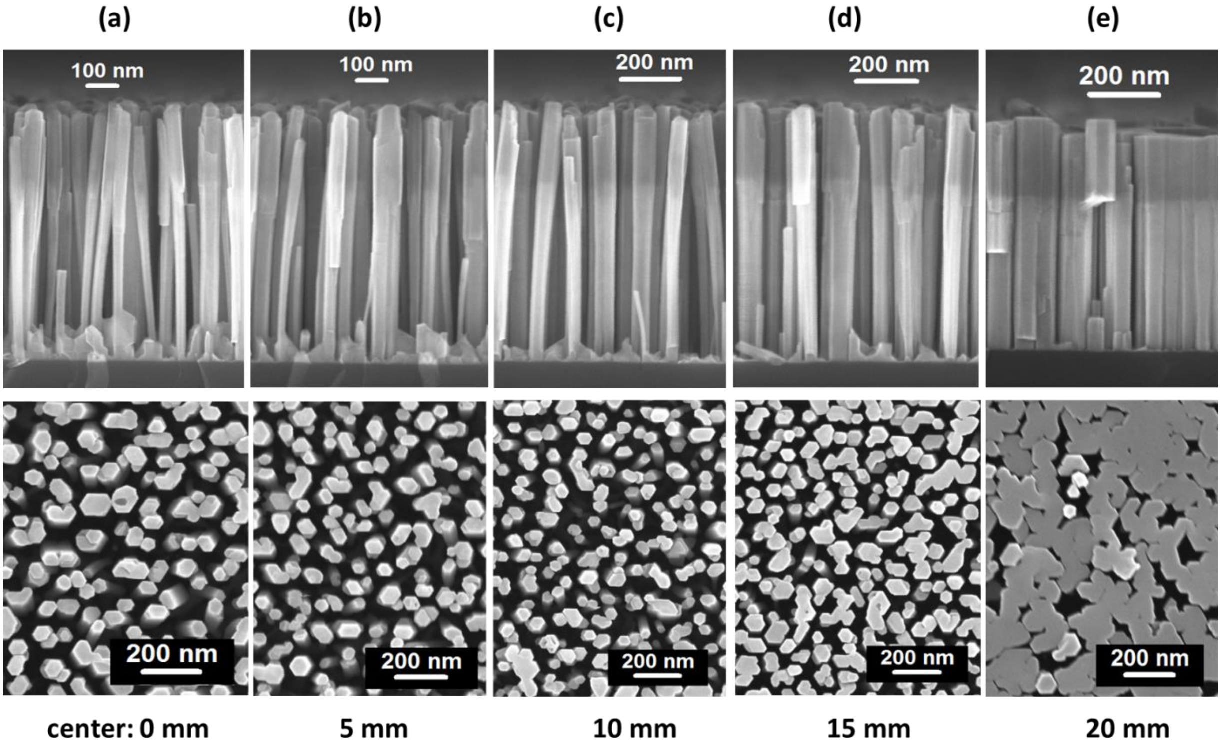

Figure 3.1.3: Side-view and top-view SEM images taken for a given wafer (sample N2330, Al$_{0.6}$Ga$_{0.4}$N NWs, T_{subs} = 865°C, i.e. t_{des}^{Ga} = 5 s) at: (a) 0 mm (center), (b) 5 mm, (c) 10 mm, (d) 15 mm, (e) 20 mm from the wafer center. NW density and dimensions remain similar over the 0-10/12 mm range, due to almost constant substrate temperature over this range, and abruptly change above, owing to the brutal decrease in temperature: when getting closer to the wafer edge, the NW density increases due to lower incubation time, whereas the NW length decreases due to lower Ga diffusion length.

3.2 Optical properties of AlGaN nanowire sections

3.2.1 Average luminescence of as-grown AlGaN nanowires grown in various conditions

Before investigating the localization properties at the scale of single NWs, we first looked at the macro-optical properties of as-grown ensembles of AlGaN NW sections, for several series of samples grown in various conditions described in Subpart 3.1. Most macro-PL experiments were carried out with the setup detailed in Subpart 2.3.1.1 and equipped with the 244 nm CW laser, limiting the acquisition range to an average AlN molar fraction less than 0.65-0.75 (depending on the Stokes shift). In this case, the spot diameter was of the order of 50 µm, meaning that we were exciting about 5 10^5 NWs for a typical NW density of 2.5 10^{10} cm^{-2}.

First, Figure 3.2.1.1 shows the normalized macro-PL spectra recorded at low temperature and low excitation power for AlGaN NW samples all grown at high temperatures ($T_{subs} > 810°C$, $t_{des}^{Ga} < 25$ s) but at various several nominal AlN molar fractions over the 0.35-0.75 range. A blue-shift is globally observed as expected when increasing the average AlN molar fraction over the investigated range. The related Stokes shifts are provided in Figure 3.2.1.2 and were estimated by subtracting the experimental emission energies corresponding to NBE (main peak of highest energy) from the theoretical NBE energies calculated using D°X emission energy values for binaries, the AlN molar fractions measured by XRD (see Subpart 2.2.2) and a bowing parameter value of +1 eV (see Figure 1.2.2.1). The Stokes shift does not vary much for low Al contents within AlGaN NW sections but abruptly increases for AlN molar fractions above 0.5 up to an estimated value around 600 meV for a molar fraction value of 0.75, evidencing a less and less disordered alloy, in other words a less homogeneous alloy, for higher Al contents. Such increase with Al composition was also reported in previous works [180, 181]. In addition, such high Stokes shift values are not surprising for Al-rich AlGaN and consistent with other works reporting shifts of hundreds of meV even up to 950 meV [182, 405, 406].

The related linewidths of the main NBE peak (of highest energy) were also derived from each PL spectrum, by fitting the part above the GaN bandgap with multiple Gaussian functions as illustrated in Figure 3.2.1.3 (a). It can be noticed on Figure 3.2.1.3 (b) that on the whole, the linewidth, corresponding to the Gaussian full width at half maximum (FWHM), slightly increases with AlN molar fraction from 130 meV up to 230 meV for $x \approx 0.75$ (sample N2501), excluding the point corresponding to one of the 60% Al samples (N2196) of lower quality than the others. In view of Subpart 1.2.2.2, the AlN molar fraction value of 0.75 roughly corresponds to the value for which the linewidth is expected to be maximal, and the related linewidth magnitude is well above the state-of-the-art value of 60 meV reached for similar Al content [160, 175]. However, in the latter case, AlGaN was grown, contrary to our samples, in metal-rich conditions which result in more homogeneous alloy, as already mentioned in Subpart 2.1.4.1, but are not compatible with the growth of NWs separated enough for single NW dispersion. Linewidth values comparable to ours are much more commonly reported for 2D layers [182] and NWs [81, 139, 327].

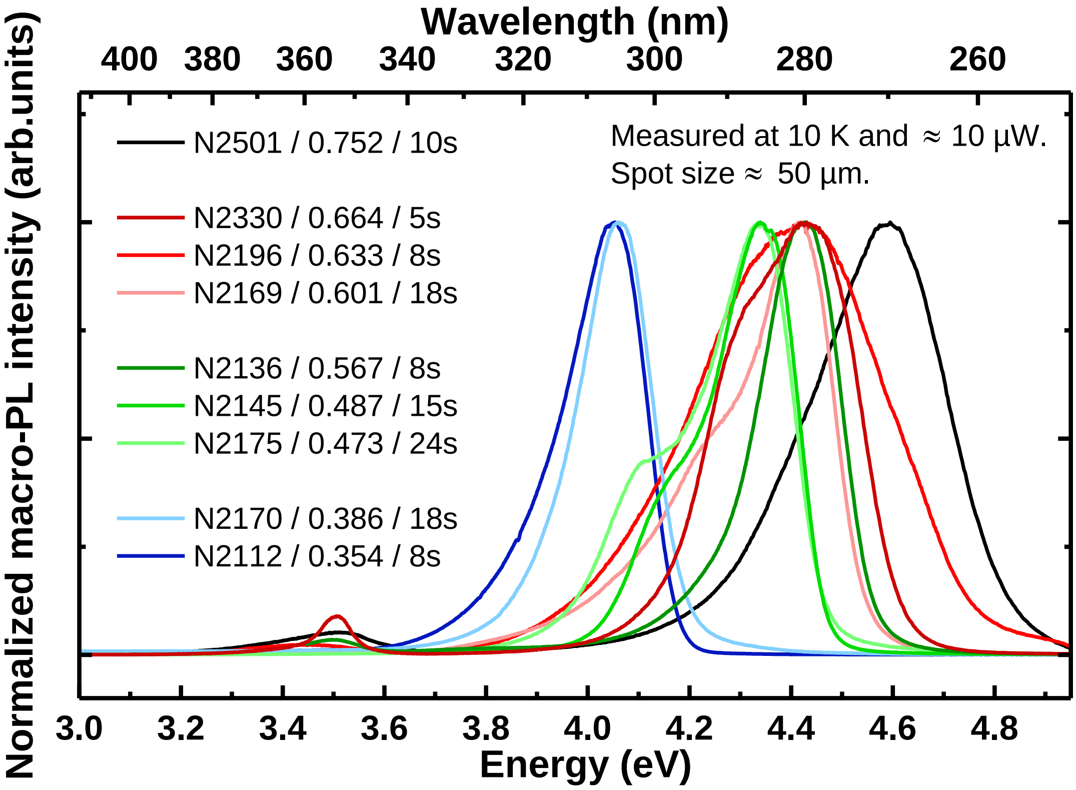

Figure 3.2.1.1: Macro-PL spectra for several AlGaN NW section samples grown at high temperatures (T_{subs} > 810°C, t_{des}^{Ga} < 25 s) and at various nominal AlN molar fractions: 0.35, 0.5, 0.6 and 0.75, gathered in 4 groups respectively labeled in blue, green, red and black. For each spectrum, the sample number, the average AlN molar fraction x determined by XRD and the Ga desorption time indicating growth temperature are provided in legend.

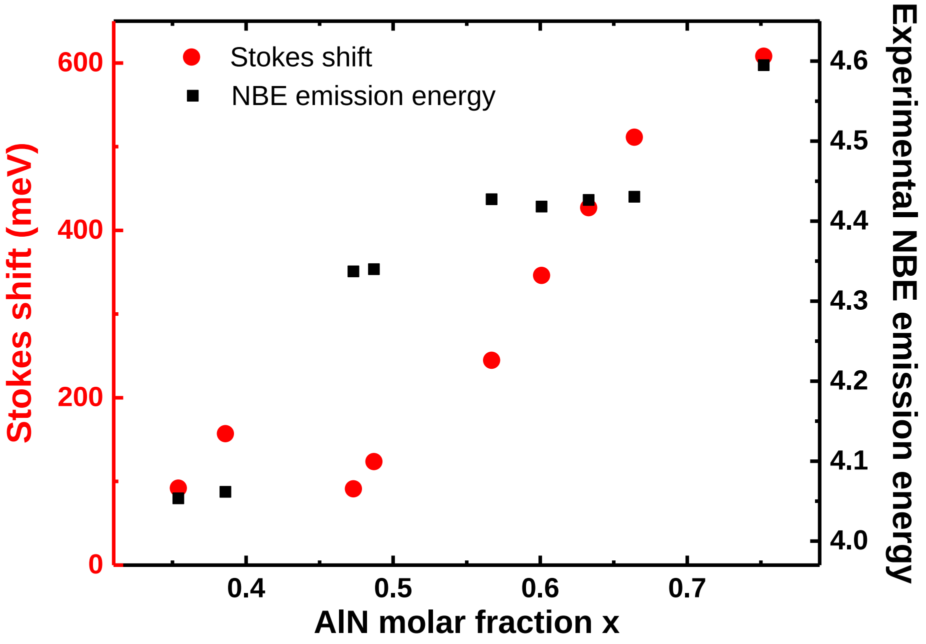

Figure 3.2.1.2: Evolution of Stokes shift with AlN molar fraction labeled in red circles, for all the samples investigated in Figure 3.2.1.1. The related evolution of the experimental NBE emission energy is also provided and labeled in black squares.

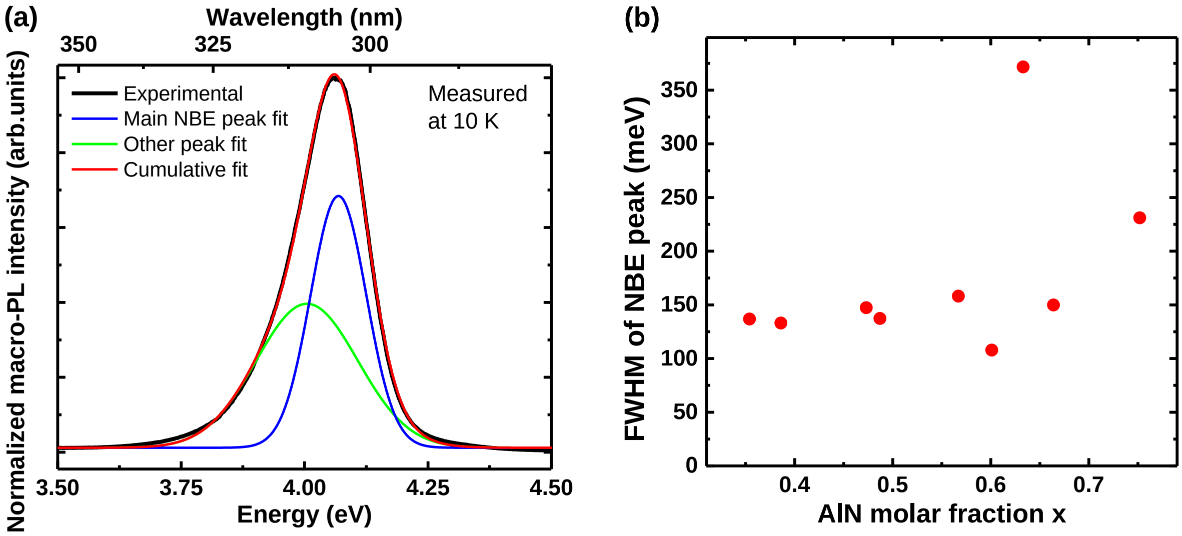

Figure 3.2.1.3: (a) Example of NBE peak fit performed with Gaussian lines (sample N2170). (b) Evolution of the linewidth of main NBE peak (blue line in (a)) with the AlN molar fraction, for the samples investigated in Figure 3.2.1.1.

Next, AlGaN NW sections grown with the same metallic fluxes but at various temperatures over a wide 650-865°C range were also macro-optically characterized. Figure 3.2.1.4 shows the macro-PL spectra recorded in the same conditions (low temperature and excitation power, normalized acquisition time) for as-grown $Al_{0.6}Ga_{0.4}N$ NWs from the same sample series. It can be seen that the macro-optical properties of NWs degrade when decreasing too much the AlGaN growth temperature. Indeed, the PL intensity significantly weakens for AlGaN NW samples grown below 750°C for this sample series, which is likely due to the increase in non-radiative recombinations occurring at structural defects for which the formation probability increases when lowering growth temperature. Moreover, the peaks tend to red-shift as well when decreasing growth temperature, which can be notably explained by a lower average AlN molar fraction in the AlGaN section. Indeed, XRD measurements (see Subpart 2.2.2) gave us an average AlN molar fraction varying from about 0.66 at 865°C to about 0.56 at 700°C (about 0.59 at 780°C). During growth, Ga desorbs less at lower temperature so that we incorporate more Ga to the expense of Al in this case and obtain a Ga-richer AlGaN alloy emitting at lower energies.

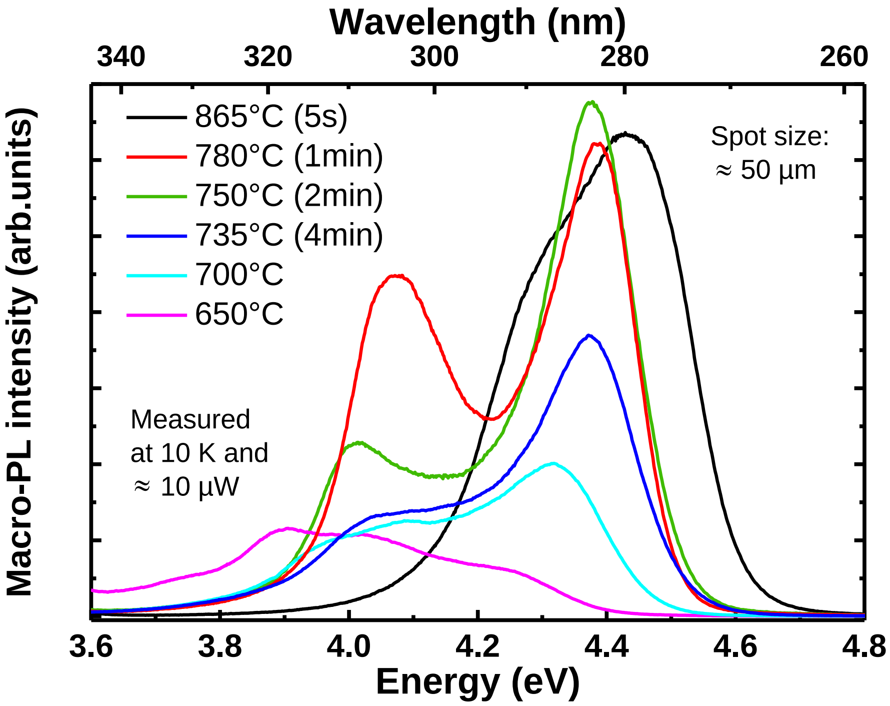

Figure 3.2.1.4: Macro-PL spectra recorded at low temperature (10 K) for several $Al_{0.6}Ga_{0.4}N$ NW section samples grown using the same recipe except that AlGaN growth temperature was varied over a 650-865°C range (T_{subs}). The corresponding t_{des}^{Ga} is given between brackets in legend. Samples from 865°C to 650°C: N2330, N2325, N2326, N2327, N2352, N2348.

In addition to the previous remarks, extra peaks or shoulderings can be clearly observed at lower emission energy in Figure 3.2.1.4, whatever the growth temperature, similarly to a few spectra displayed previously in Figure 3.2.1.1. These additional peaks likely correspond to the NBE of AlGaN alloys exhibiting different composition (lower Al one), which is very plausible in view of the inhomogeneity of samples highlighted by high Stokes shift values. Similar observations have already been made for AlGaN 2D layers [407] and NWs [139, 321, 322]. Temperature- and power-dependent macro-PL experiments were also performed to assess the behavior of these additional peaks compared to the main NBE one at higher energy and to support our assumption. Figure 3.2.1.5 provides the evolution of macro-PL spectra with temperature, recorded at low excitation power (typically 10 µW), for two samples from the series investigated in Figure 3.2.1.4. It can be seen on the whole that the PL intensity significantly quenches above 100 K. Indeed, the IQE, which can be estimated by the ratio between the PL intensity at room temperature and the one at cryogenic temperature (noted I_{300K}/I_{10K} ratio) of the main NBE peak at higher energy, is of the order of or inferior to 1% in the present case. When considering all samples probed by temperature-dependent macro-PL, the IQE at room temperature was observed to vary over the 0.1-10% range and globally to increase with Al content, reaching about 8% for the Al-richest sample of the series (x ≈ 0.75). Regarding other peaks at lower energy observed above the GaN bandgap, their PL intensity quenching with temperature was globally observed to be less significant. This is directly visible in the case of Figure 3.2.1.5 (b) and is likely to be partly due to carrier thermal escape towards lower energy levels with increasing temperature, similarly to previous reports [139, 321, 322, 407]. However, associated I_{300K}/I_{10K} ratios remained low on the whole, barely higher than IQE values related to the main NBE peaks. The temperature dependence of peak emission energies is also provided for the example of Figure 3.2.1.5 (a) in Figure 3.2.1.6 (a), revealing a strictly monotonous evolution fitted with Varshni and Bose-Einstein laws: no clear S-shape was evidenced for the present example, which was also the case for all other examined samples. The resulting fitting parameters are provided in Figure 3.2.1.6 (b), leading in this case to values (especially for characteristic temperatures) below the ranges typically reported in the literature for related GaN and AlN binaries, but highlight a similar trend between the peaks attributed to NBEs for AlGaN of different composition.

In virtue of the absence of net S-shapes, the low I_{300K}/I_{10K} ratios for any AlGaN-related peak and the low density of non-radiative centers related to crystallographic defects expected in our NWs, carrier localization is weak in these samples. The upward trend in the latter ratios with increasing AlN molar fraction is consistent with the literature, both for NWs [325] and films [156, 174, 180, 408]. In the 2D case, the localization energy, derived from S-shape curves, was clearly evidenced to rise with AlN molar fraction over the Al composition range investigated in this study. Nonetheless, given our high estimated Stokes shift values emphasizing alloy inhomogeneity, we would have expected stronger localization associated with lower PL intensity quenching when increasing temperature, in view of the 30-80% IQE value range reported for AlGaN epilayers [409] and AlGaN NWs grown in conditions close to ours [77, 325]. It must be noted that that the disparity on IQE values notified in literature is substantial. Indeed, values similar to ours can be easily found for AlN molar fractions over the 0.3-0.8 range, both in the 2D [160, 184, 407, 410] and NW [139, 322, 324] cases.

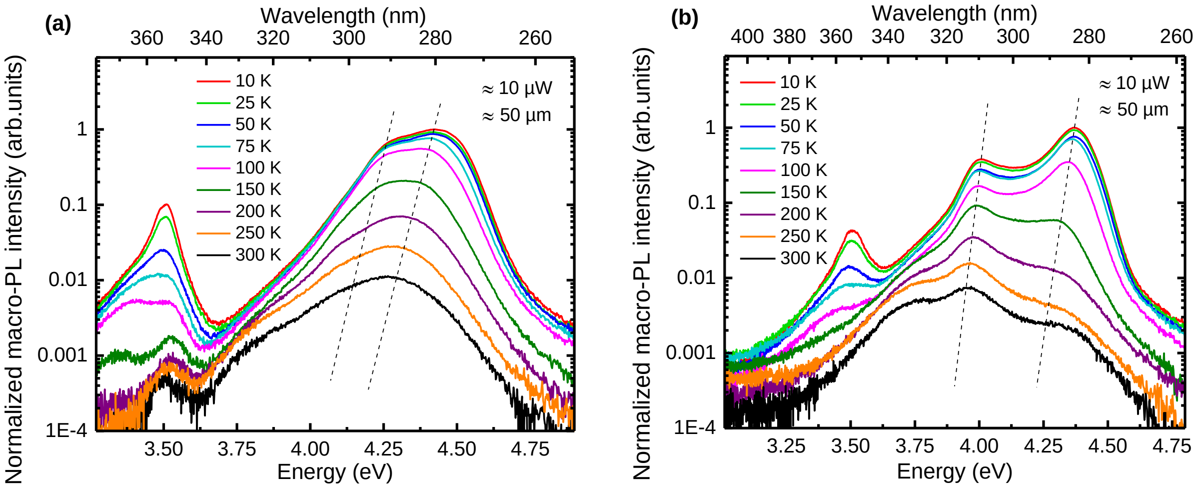

Figure 3.2.1.5: Temperature-dependent macro-PL over the 10-300 K range for as-grown Al$_{0.6}$Ga$_{0.4}$N NWs grown at (a) T_{subs} = 865°C, t_{des}^{Ga} = 5 s (sample N2330) and (b) T_{subs} = 750°C, t_{des}^{Ga} = 120 s (sample N2326). Dashed guidelines are sketched for the main peaks/shoulders.

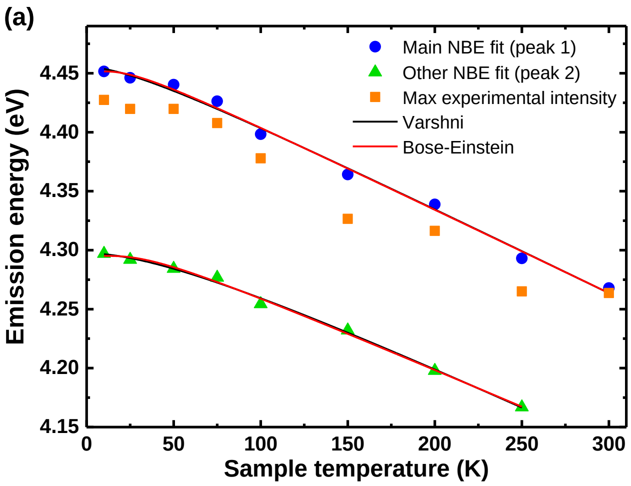

(b)

Fitting parameters	Peak 1	Peak 2
E_0 (Varshni, eV)	4.4551 ±0.0051	4.2974 ±0.0025
α (meV/K)	0.723 ±0.055	0.696 ±0.068
β (K)	39.96 ±27.26	82.52 ±32.73
E_0 (Bose–Einstein, eV)	4.4516 ±0.0047	4.2951 ±0.0025
α_B (meV)	26.32 ±11.15	32.36 ±8.65
Θ_B (K)	74.09 ±28.63	102.41 ±23.00

Figure 3.2.1.6: (a) Evolution with temperature of the emission energy, from spectra of Figure 3.2.1.5 (a), for the Gaussian line fitting the main NBE at higher energy (peak 1), the one fitting the NBE shouldering at lower energy (peak 2), and the maximum experimental intensity. Gaussian fits were performed similarly to Figure 3.2.1.3. (b) Parameter values resulting from fitting peak 1 and peak 2 with Varshni and Bose-Einstein laws.

As for power-dependent experiments, typical spectra are provided in Figure 3.2.1.7 for two samples exhibiting as well several peaks attributed to alloy inhomogeneity. Given that all spectra do not shift with power, it can be first inferred that the peaks at lower energy do not originate from power-sensitive defects such as DAPs. Second, it can be directly seen that the emission energy of the peak at lower energy for the sample of Figure 3.2.1.7 (a) differs from the other sample of Figure 3.2.1.7, in contrast to the main NBE peak at higher energy and emitted around 4.155 eV in both cases. More generally, we did not evidence, from the comparative analysis of samples belonging to a same series such as those of Figure 3.2.1.7 and Figure 3.2.1.4 or from the comparison between sample series, any specific trend about the features (not only emission energy, but also linewidth and intensity) of lower energy peaks with respect to those of main NBE emission at higher energy. If such a trend had been highlighted, it would have been a clue of the presence within samples of defects or impurities exhibiting specific optical signature as previously explained in Subparts 1.2.1.2 and 2.3.1.2.

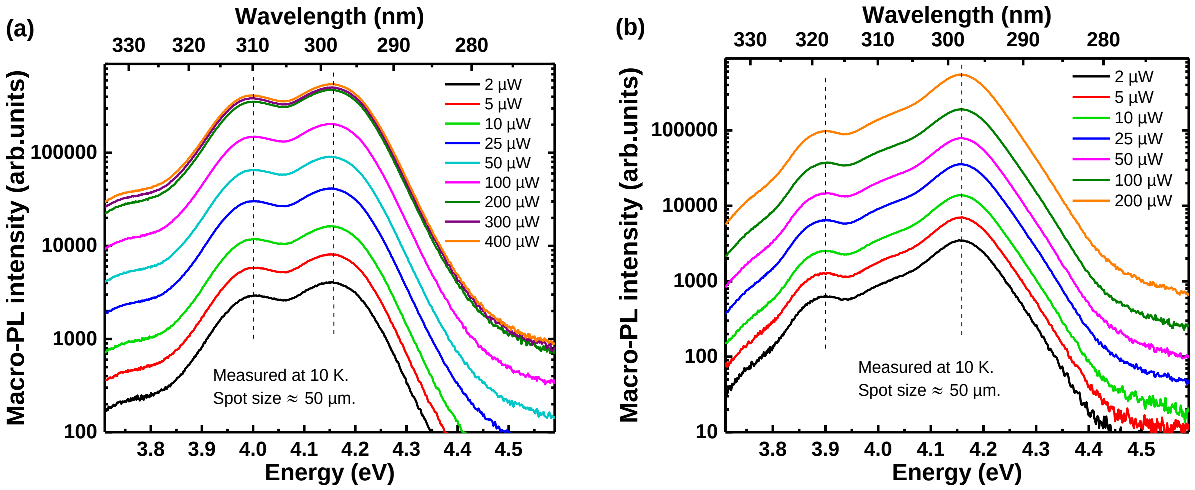

Figure 3.2.1.7: Power-dependent macro-PL spectra for Al$_{0.5}$Ga$_{0.5}$N NWs grown at (a) T_{subs} = 840°C, t_{des}^{Ga} = 10 s (sample N2502) and (b) T_{subs} = 790°C, t_{des}^{Ga} = 60 s (sample N2504). Dashed guidelines are sketched for the main peaks.

Finally, similarly to the macro-structural characterization data presented in Figure 3.1.3, macro-PL spectra were recorded along the wafer radius for the same sample, as displayed in Figure 3.2.1.8. It can be directly seen from the latter that the PL spectrum shape is similar when remaining less than 10 mm away from the wafer center, in contrast to the substrate edge, which is consistent with the evolution along the wafer radius of macro-structural properties provided in Subpart 3.1. However, it can be noticed that the emission slightly blue-shifts when getting further than 15 mm from the wafer center, which may seem contradictory in view of kinetics considerations presented in previous subparts. Indeed, we would rather expect to make Ga incorporation easier, given the decrease in temperature along the wafer radius (starting from the wafer center), and therefore observe an emission red-shift. A first plausible explanation would be that, in the present case, AlGaN NW sections are quite short on the whole (less than 320 nm) and get shorter when getting closer to the wafer edge (from the analysis of SEM images provided in Figure 3.1.3, the sections are about 290-300, 250-260, and 200-210 nm long, respectively at 10, 15 and 20 mm away from the wafer center), considering that the Al-richer sections preferentially nucleating on top of GaN NW templates (pure AlN for this Al-rich sample example, see Figure 3.1.1 (b)) are likely to be of same length along the wafer radius (despite the estimated 20-30°C decrease along wafer radius, substrate temperature remains high everywhere given that T_{subs} = 865°C here). Therefore, knowing that Ga incorporation gets progressively easier during the alloy growth (leading to alloy compositional gradient along the NW growth axis) until a steady state regime (associated with a more homogeneous alloy) is reached as previously described, higher average AlN molar fractions may be obtained for wafer areas exhibiting AlGaN NW sections shorter than for other zones and too short to reach this steady state regime. A lower Stokes shift, consistent with the growth of a more homogeneous alloy usually observed at lower temperatures, would also explain the wafer edge blue-shifted emission convincingly. For other characterized samples exhibiting longer and/or Ga-richer AlGaN NW sections, wafer edge emission was globally observed to be red-shifted compared to wafer center emission, consistently with kinetics considerations.

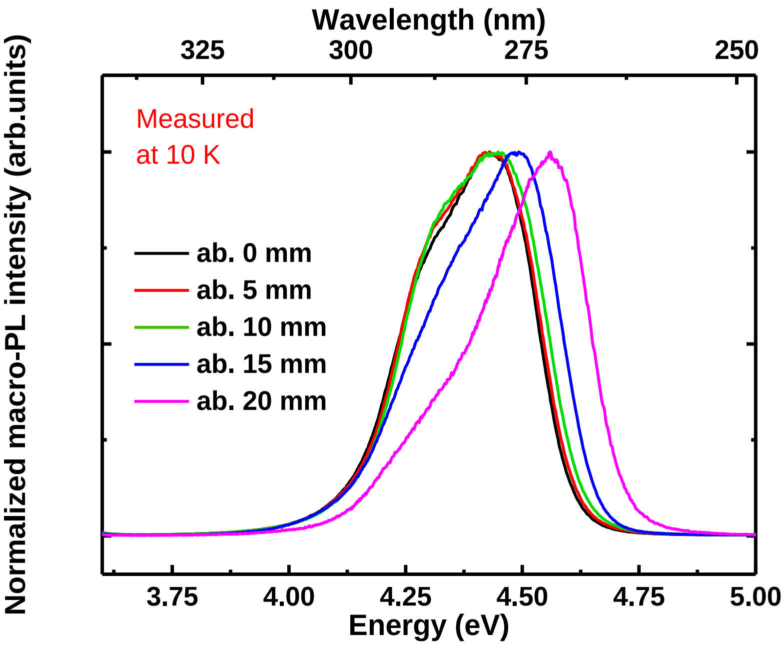

Figure 3.2.1.8: Evolution of PL spectra recorded at low temperature (10 K) with the wafer radius (for the same sample N2330 as Figure 3.1.3: $Al_{0.6}Ga_{0.4}N$ NWs, T_{subs} = 865°C, i.e. t_{des}^{Ga} = 5 s).

In view of Figure 3.2.1.8 and related comments, dispersions of NWs prior to their µ-optical characterization were carried out as close to the wafer center as possible, remaining within the area where substrate temperature variation was low during growth. The results of such µ-characterization performed to investigate localization properties will be now presented in the following subparts.

3.2.2 Luminescence of single AlGaN nanowires grown in various conditions

In order to assess the dependence of localization on growth kinetic parameters, we first performed µ-PL experiments on dispersed AlGaN NW sections grown in various conditions within the N-rich regime, as described in Subpart 3.1 (T_{subs} varied over a 650-875°C range, AlN molar fraction x varied over the 0.3-0.7 range). Such experiments were carried out with the same CW laser as macro-PL (244 nm emission, setup described in Subpart 2.3.1.1). The spot size of the order of 1 µm allowed us to excite individual or small bunches of NWs mechanically dispersed on Si substrates.

Figure 3.2.2.1 displays typical µ-PL spectra recorded at low temperature (10 K) for $Al_xGa_{1-x}N$ NWs grown at several average AlN molar fractions (x = 0.4, 0.5 and 0.7). They all reveal numerous sharp emission lines typical of localized exciton emission, whatever the average AlN molar fraction.

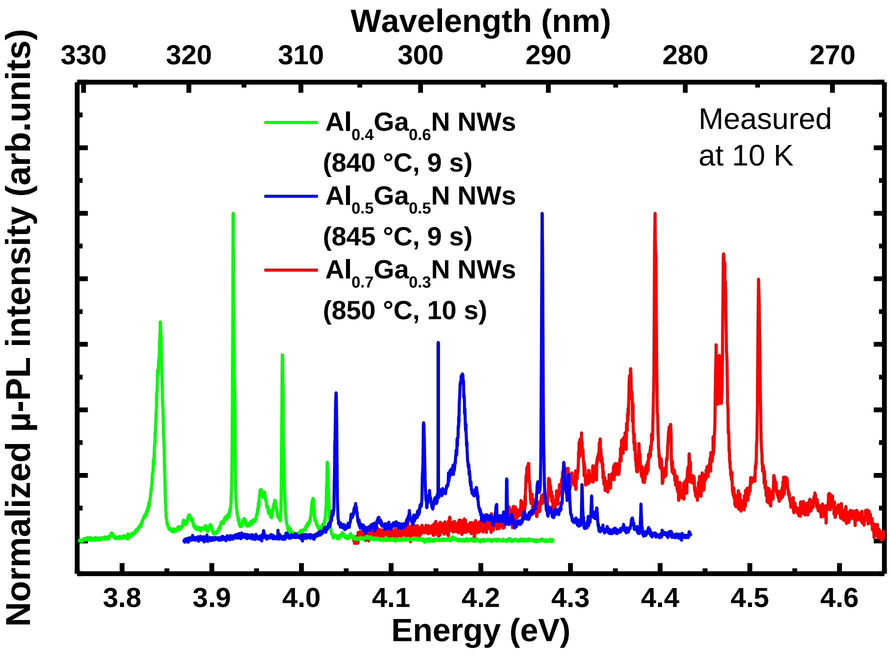

Figure 3.2.2.1: Low temperature (10 K) µ-PL spectra for $Al_xGa_{1-x}N$ NW sections of various AlN molar fractions and dispersed on Si substrates (samples N2235, N2240 and N2501 from lowest to highest AlN molar fraction x). AlGaN NW growth temperature and the corresponding Ga desorption time are indicated between brackets in legend (T_{subs}, t_{des}^{Ga}). For all samples, T_{subs} = 840-850°C, t_{des}^{Ga} = 9-10 s.

In addition, Figure 3.2.2.2 shows some of the µ-PL results, obtained at low sample temperature (10 K) for dispersed $Al_{0.6}Ga_{0.4}N$ NW sections grown at various temperatures between T_{subs} = 650°C and 865°C. Similar sharp lines can be observed as well, whatever the growth temperature.

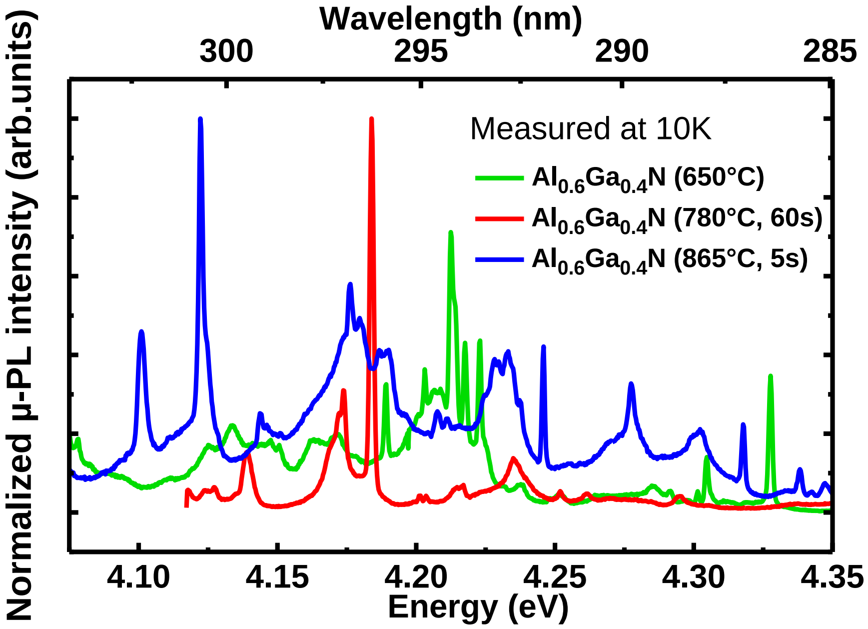

Figure 3.2.2.2: Low temperature (10 K) µ-PL spectra for $Al_{0.6}Ga_{0.4}N$ NWs dispersed on Si substrates (samples N2348, N2325, N2330 from lowest to highest temperature). AlGaN NW growth temperature and the corresponding Ga desorption time are indicated between brackets in legend (T_{subs}, t_{des}^{Ga}).

In the latter μ-PL experiments, presented in Figure 3.2.2.1 and Figure 3.2.2.2, the exact number of excited AlGaN NWs was not known. Consequently, we could not know if we were exciting a few NWs emitting numerous lines each or many NWs emitting few lines each. Therefore, AlGaN NWs were mechanically dispersed on specific Si substrates having etched markers, so that single (or very few) and isolated NWs could be located precisely by SEM before carrying out μ-PL experiments. In other words, we ensured that a small and well defined amount of alloy material was excited by the laser. Such NWs were briefly spotted at low SEM magnification in order to limit the possible degradation of their optical properties by the electron beam [346], as illustrated in Figure 3.2.2.3 (a) for a single $Al_{0.6}Ga_{0.4}N$ NW section on top of its GaN NW template.

Statistics performed from μ-PL spectra recorded for isolated NWs resulted in a typical and significant spectral line density of the order of 10^5 μm^{-3}, i.e. 10^{17} cm^{-3}. The detail is provided for a series of $Al_{0.6}Ga_{0.4}N$ NW samples in the following. For the latter, we analyzed about 20 isolated NWs grown at low enough temperatures (typically T_{subs} over 750-780°C, corresponding to t_{des}^{Ga} of the order of 1-2 min) in order to limit the length of the pure Al-richer section preferentially nucleating on the GaN NW base to a few nanometers. The excited volume of AlGaN material was thus more accurately estimated than for NWs grown at higher temperatures, since in the latter case the disparity on the parasitic Al-richer section length values would be significant compared to the one on AlN+AlGaN section length ones. The probed single AlGaN NWs present a typical volume of about 2.3 10^5 nm^3 corresponding to a reverse top-truncated cone which is 275 nm long, 25 nm wide at the bottom and 40 nm wide at the top. These three dimensional values correspond to average values extracted from statistics performed on highly magnified STEM images recorded for single AlGaN NWs of investigated samples (estimated standard deviation of 15, 3 and 4 nm respectively for the length, the bottom and top diameters). Figure 3.2.2.3 (b) exhibits the μ-PL data related to the dispersed NW of Figure 3.2.2.3 (a) and the number of spectral lines. Using the same counting protocol for all spectra led to an estimated average of 40 lines per wire (and an estimated standard deviation of 10), corresponding to a typical value of 1.8 10^5 μm^{-3} for the spectral line density, i.e. 1.8 10^{17} cm^{-3}. The latter is above or of the order of magnitude of the residual "shallow" impurity concentrations in $Al_xGa_{1-x}N$, commonly reported to be over the 10^{16}-10^{17} cm^{-3} range [411, 412]. In addition, a capture radius of the order of 10-15 nm could be directly estimated from this density value. Such density value implies that localized carrier recombination is unlikely to be related to the mere excitons bound to shallow substitutional impurities, which will be further supported by temperature-dependent μ-PL experiments in Subpart 3.2.4.

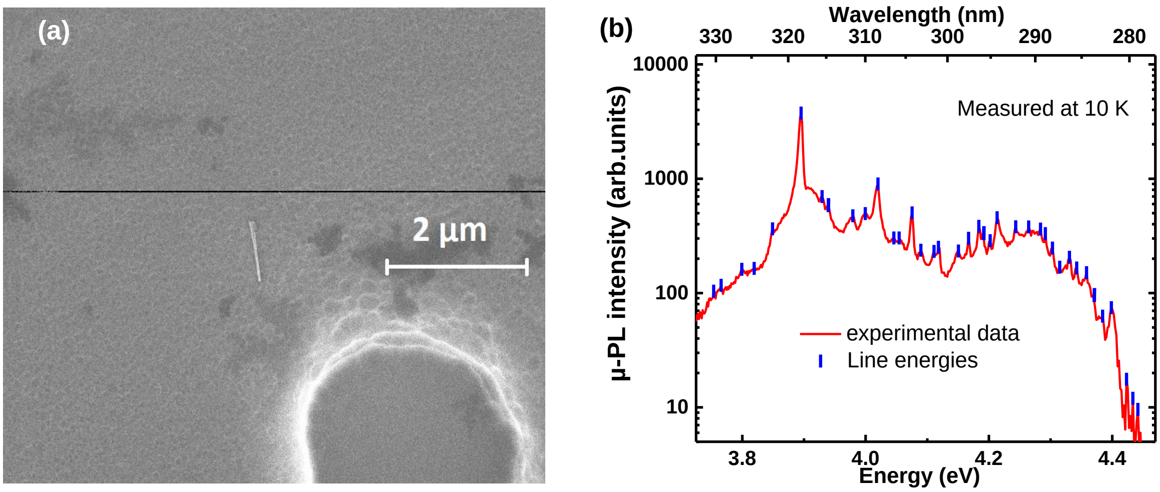

Figure 3.2.2.3: (a) SEM image of a single $Al_{0.6}Ga_{0.4}N$ NW (sample N2326) grown at T_{subs} = 750°C (t_{des}^{Ga} = 120 s) and dispersed on an etched Si substrate (hole markers). (b) µ-PL spectrum for the single NW shown in (a): 38 lines were counted over the emission range (3.7-4.5 eV).

When focusing on individual µ-PL lines, statistics performed on the latter led to typical linewidth values of a few meVs. These values actually correspond to the FWHM of Lorentzian functions fitting µ-PL lines isolated enough on µ-PL spectra recorded at cryogenic temperatures (10 K), as shown in Figure 3.2.2.4. Physically, such functions describe very well the intrinsic broadening of spectral lines [413] but do not fit perfectly our experimental data, as it can be seen in Figure 3.2.2.4. In reality, other factors (instrumental response, inhomogeneous broadening) must be also taken into account, so that the line shape rather corresponds to the convolution of a Lorentzian with a Gaussian, namely a Voigt function. However, the latter is complicated to compute but can be well approximated by Pseudo-Voigt functions, similarly to the case of XRD lines as described in Subpart 2.2.2. For practicality, we chose to keep fitting with Lorentzian functions which gave reasonable fits. The investigated lines were emitted over the 3.7-4.5 eV range by dispersed $Al_{0.4}Ga_{0.6}N$, $Al_{0.5}Ga_{0.5}N$ and $Al_{0.6}Ga_{0.4}N$ NWs from 5 different samples grown at rather high temperatures (T_{subs} > 800°C, t_{des}^{Ga} < 30 s). Figure 3.2.2.5 (a) gives the distribution of all FWHM values for the numerous investigated lines (about 100) whatever their emission energy, with respect to an estimated FWHM mean of about 2.5 meV. It can be seen that most FWHM values are comprised between 1 and 5 meV and very dispersed over this range. Figure 3.2.2.5 (b) shows the evolution of estimated FWHM means for every 0.15 eV range over the whole 3.75-4.5 eV range. It must be noted that there are at least 10 FWHM values per 0.15 eV range and that the standard deviation is similar for each range. No specific trend regarding the evolution of linewidth with emission energy emerged from this last dataset.

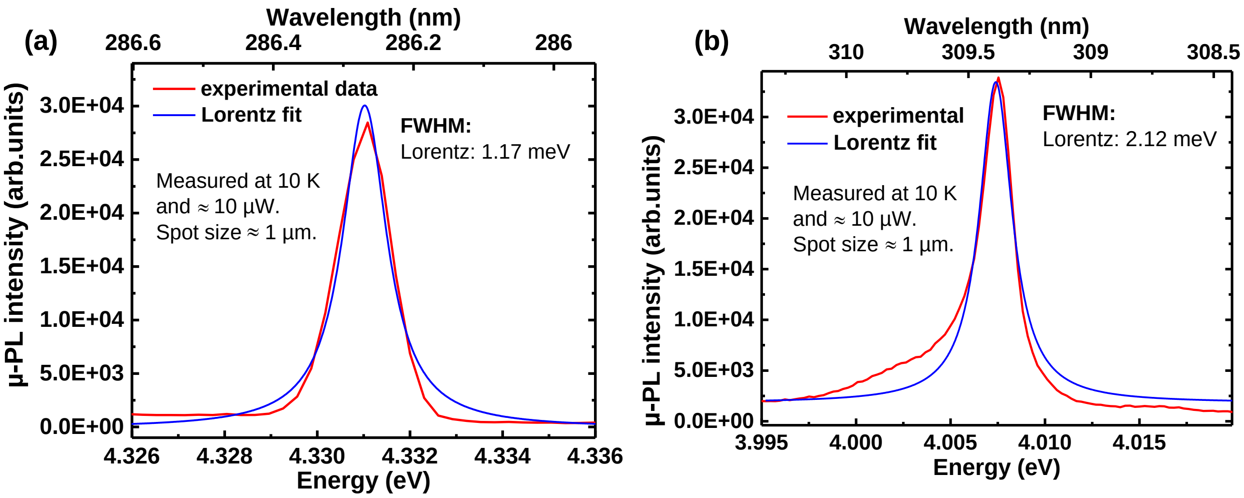

Figure 3.2.2.4: μ-PL lines emitted by (a) $Al_{0.6}Ga_{0.4}N$ NW (sample N2330) and (b) $Al_{0.4}Ga_{0.6}N$ NW (sample N2235) grown at high temperature (T_{subs} > 800°C, t_{des}^{Ga} < 30 s). These lines were recorded at cryogenic temperature (10 K) and fitted with Lorentzian function. The FWHM value is given in legend.

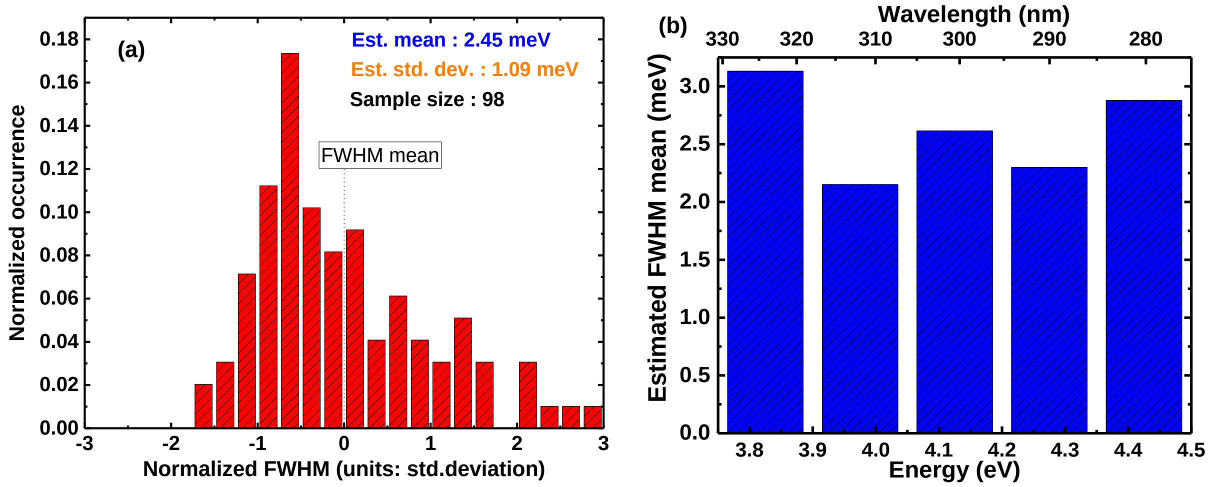

Figure 3.2.2.5: (a) Distribution of FWHM values (whatever the related line emission energy) with respect to the estimated FWHM mean value (2.45 meV). The abscissa is centered on the estimated mean and normalized with respect to the estimated standard deviation (1.09 meV). (b) Evolution of the FWHM mean value with emission energy/wavelength (for every 0.15 eV range).

These linewidths are quite small compared to the usual linewidth of ternary alloys, but rather large compared to what is usually observed for an isolated enough QD. Indeed, linewidth values can be as low as a few tens of μeV for arsenide QDs [414]. However, in the case of III-N QDs, time-dependent spectral diffusion effects related to trapped charges usually broaden the emitted lines [415, 416], resulting in linewidth values of the same order of magnitude as ours. The latter effects mostly depend on the dot and its close environment, not on its emission energy.

3.2.3 Evidence of a quantum-dot like behavior for localization centers

In order to check whether each line stems from a single localization center, HBT-type [382] photon correlation experiments were carried out on dispersed NWs. The corresponding setup is detailed in Subpart 2.3.1.4, whereas the experiment principle is briefly reminded and illustrated for a single dispersed AlGaN NW excited by the 244 nm CW laser in Figure 3.2.3.1. The typical integration time required for performing second-order correlation measurements was of the order of 1 hour, after having selected a proper µ-PL line: the latter had to be intense enough (ideally superior to 10000 counts per second) at a reasonable incident optical power (of the order of 10-25 µW).

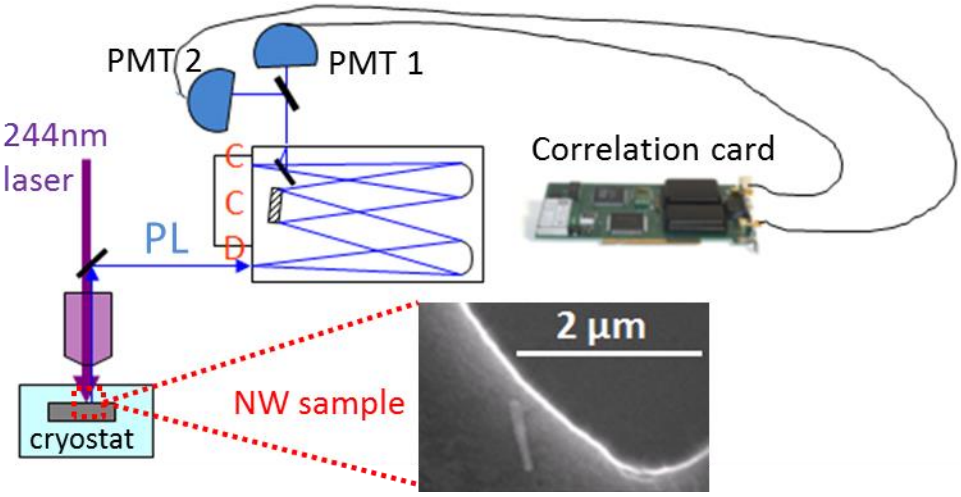

Figure 3.2.3.1: Principle of the photon correlation experiment reminded and illustrated for a single AlGaN NW dispersed on a hole-marked Si wafer, as shown on the SEM image.

These experiments performed on a few wires from samples of different series (various AlN molar fraction and growth temperature) revealed antibunching, typical of a quantum dot-like (QD-like) behavior [417], as shown in Figure 3.2.3.2 and Figure 3.2.3.3. The latter give examples of experimental second-order intensity correlation related to the µ-PL lines framed in red and emitted by dispersed $Al_{0.5}Ga_{0.5}N$ (growth at T_{subs} = 850°C, t_{des}^{Ga} = 7 s) and $Al_{0.4}Ga_{0.6}N$ NWs (growth at T_{subs} = 840°C, t_{des}^{Ga} = 9 s). The associated fit was done using a simple two-level atom model described in Subpart 1.2.3.4 and considering that the biexciton population could be discarded in view of the rather low excitation power used, which led to the following expression for the second-order intensity correlation [190]:

$$g^2(\tau) = 1 - A_0 e^{-\frac{|\tau|}{\tau_0}} \tag{3.2.3.1}$$

where A_0 is the dip depth and τ_0 is the characteristic time depending on the radiative lifetime τ_x and the pumping rate Γ, such as $1/\tau_0 = 1/\tau_x + \Gamma$. At low excitation power, Γ is low, so that τ_0 is close to τ_x.

Parameter values τ_0 = 0.31 ns and A_0 = 0.57 were obtained, the latter being in very good agreement with the experimental autocorrelation value $g^2(0)$ equal to 0.43 and below the 0.5 limit for single photon emission [383, 384]. The $g^2(0)$ value would be lower with a better detector time resolution and without the background contribution which is not subtracted here.

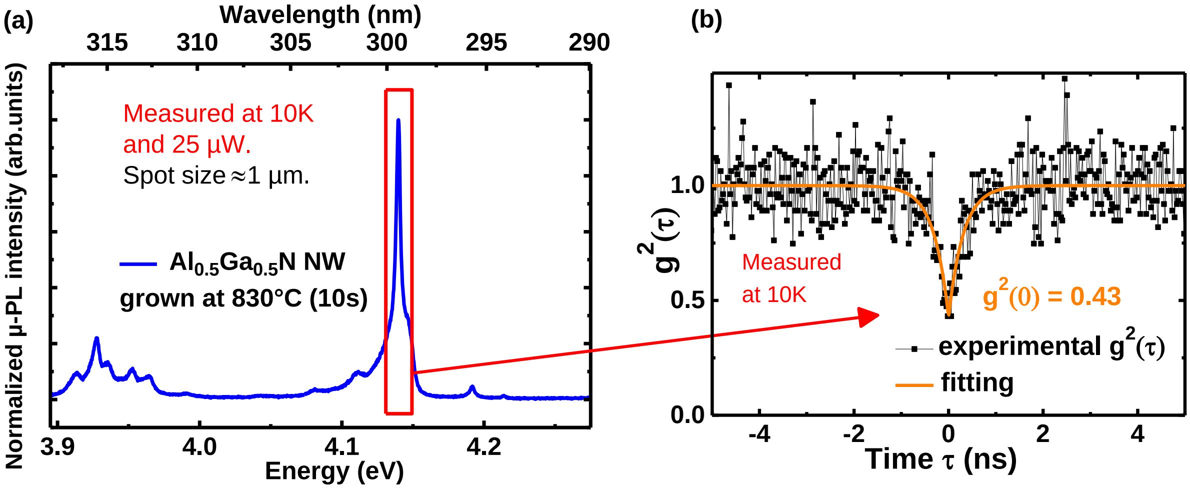

Figure 3.2.3.2: (a) Low temperature (10 K) μ-PL spectrum recorded at an excitation power of 25 μW for an $Al_{0.5}Ga_{0.5}N$ NW (sample N2136) grown at T_{subs} = 850°C, corresponding to t_{des}^{Ga} = 7 s. (b) Experimental second-order intensity correlation $g^2(\tau)$ related to the μ-PL line framed in red in (a). The orange fitting curve corresponds to a two-level atom model.

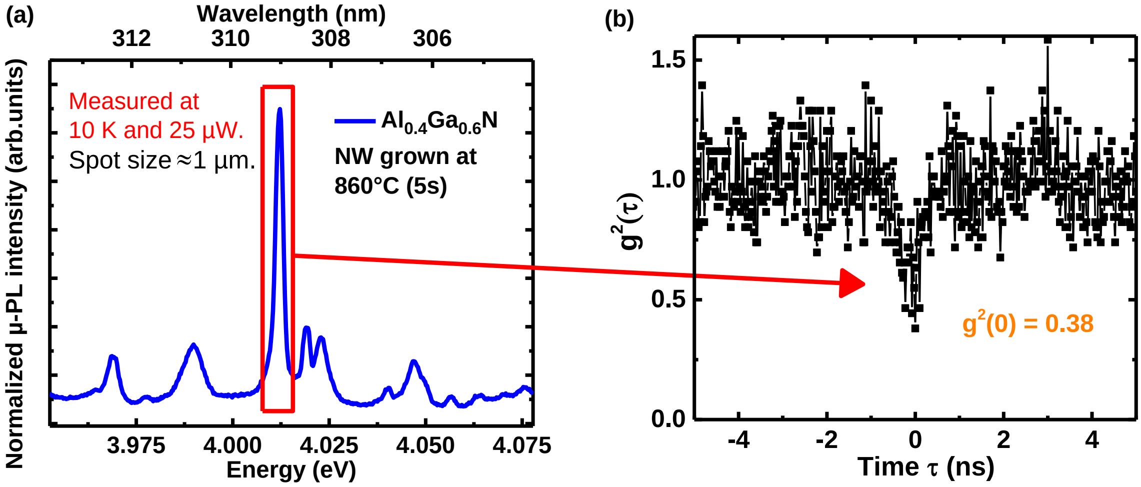

Figure 3.2.3.3: (a) Low temperature (10 K) μ-PL spectrum recorded at an excitation power of 25 μW for an $Al_{0.4}Ga_{0.6}N$ NW (sample N2235) grown at T_{subs} = 840°C, corresponding to t_{des}^{Ga} = 9 s. (b) Experimental second-order intensity correlation $g^2(\tau)$ related to the μ-PL line framed in red in (a).

We also investigated the temperature-dependence of the second-order correlation function: no crossing of the 0.5 limit was observed when increasing the sample temperature at least up to 100 K, as exhibited in Figure 3.2.3.4 for the µ-PL line of Figure 3.2.3.2. In other words, we were sure of maintaining single-photon emission up to the latter temperature.

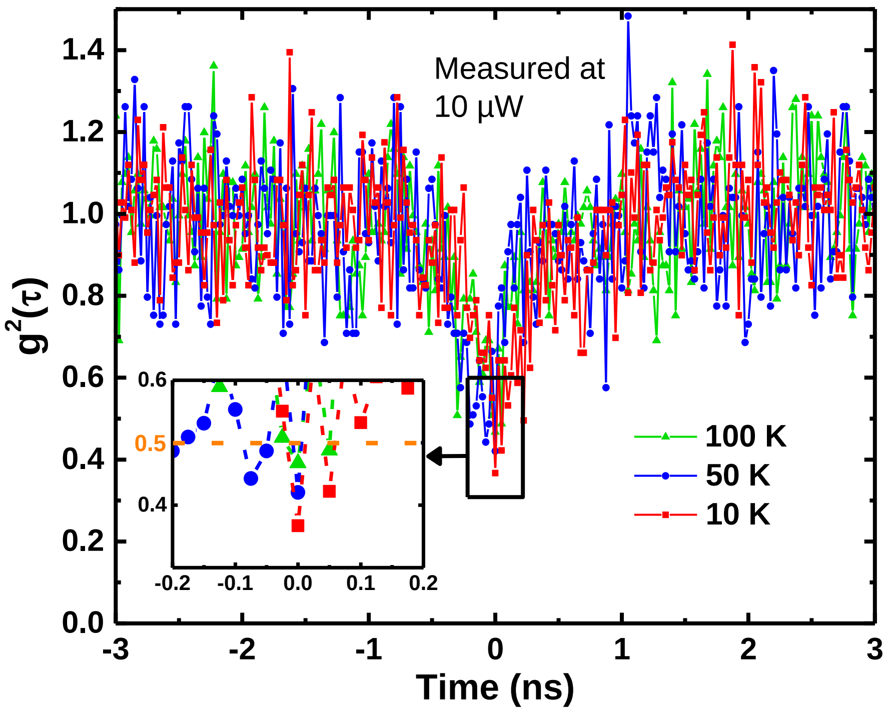

Figure 3.2.3.4: Experimental second-order correlation function $g^2(\tau)$ recorded at various sample temperatures for the µ-PL line of Figure 3.2.3.2. $g^2(0)$ = 0.38 at 10 K, $g^2(0)$ = 0.44 at 50 K and $g^2(0)$ = 0.47 at 100 K.

In view of the long typical integration time (at least 1 hour in general), especially for less intense µ-PL lines when increasing the sample temperature, and frequent cryostat drifts, it was difficult to record photon correlation histograms at higher temperatures for the same µ-PL sharp line [418]. In view of the typical evolution of µ-PL data above 50 K, the crossing of the 0.5 value is very likely to be observed before reaching 150 K. Let us remind that the measured value of $g^2(0)$ was biased (overestimated) by the time resolution of our photomultiplier detectors (180 ps for each one, leading to 255 ps when convoluting Gaussian instrumental responses for both detectors), which is comparable to the lifetime of the transitions we probed (see Subpart 3.2.6), and by the background contribution.

In addition, some power-dependent second-order correlation measurements were carried out at 10 K on the same line at 10 µW, 25 µW and 100 µW, giving $g^2(0)$ values respectively equal to 0.38, 0.43 and 0.55, as shown in Figure 3.2.3.5. Considering a low bias on the measured $g^2(0)$ value, the crossing of the real 0.5 value is likely to be observed for an excitation power of the order of 100 µW: we are then no longer sure to be in a pure single-photon emission regime, which was expected in view of the significant power density. An extra line related to biexcitonic emission is likely to be clearly visible when increasing power even more, which will be further discussed in Subpart 3.2.5.

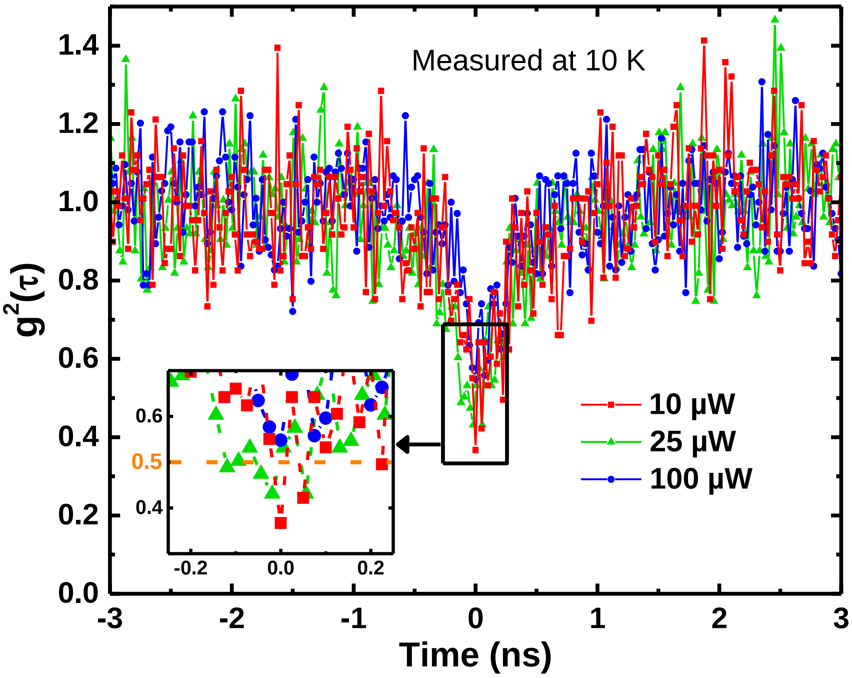

Figure 3.2.3.5: Experimental second-order correlation function $g^2(\tau)$ recorded at various excitation powers for the µ-PL line of Figure 3.2.3.2. $g^2(0)$ = 0.38 at 10 µW, $g^2(0)$ = 0.43 at 25 µW and $g^2(0)$ = 0.55 at 100 µW.

3.2.4 Attribution of the quantum dot-like behavior to compositional fluctuations in AlGaN nanowires

After having shown that each line originates from a single localization center, we then sought to identify the type of centers that we are dealing with. Actually, we wondered whether the observed µ-PL sharp lines stem from QD-like structures spontaneously induced by compositional fluctuations in the AlGaN alloy, namely Ga-richer regions surrounded by Al-richer barriers, or whether they are due to recombination of electron-hole pairs trapped by or bound to impurities or defects present in AlGaN NW sections.

First, contrary to other reported NW systems such as crystal phase quantum structures [419, 420], these lines are unlikely to be related to excitons bound to SFs. Regarding the latter, high-resolution (HR) microscopy carried out on a few NWs with AlGaN sections grown at high temperatures previously reported [139] and presenting µ-PL sharp lines as well exhibit very few or no SFs.

Second, the possibility of lines stemming from deeper QD-like impurity or defect centers, as reported for instance for arsenide epitaxial layers intentionally doped [421, 422] or unintentionally contaminated [423], can also be discarded. Indeed, no intentional doping was performed during the growth of the investigated samples, whereas the MBE chamber vacuum was very good during growth (of the order of 10^{-10} mbar before turning on N plasma cell, low partial pressures for residual gases according to QMS). In the latter report, unintentional contamination was convincingly assigned to stem from the used Si and Ge substrates. In our case, in view of the temperatures reached by the Si (111) wafer during growth, Si atoms were likely to diffuse from the substrate into the NWs [424], but mainly in their bottom part, namely the GaN NW templates, and near surface [425]. Consequently, residual Si concentration in the top part, in other words the AlGaN NW section, is likely to be very low. Moreover, Si mainly behaves as a shallow donor in nitrides, a case that will be discussed further in this section. Furthermore, macro-PL data for all investigated sample series did not exhibit any extra band/peak in addition to those attributed to the AlGaN NBE, the GaN NBE and GaN donor acceptor pairs (DAPs), and no sharp lines similar to those observed over the emission energy range corresponding to the broad macro-PL emission assigned to the AlGaN NBE were present below the latter range, as shown in Figure 3.2.4.1. On the latter, macro-PL for as-grown samples and µ-PL data recorded for bunches of dispersed NWs are superimposed. The AlGaN NBE emission range on macro-PL spectra recorded for an ensemble of NWs corresponds to the sum of sharp µ-PL lines observed when performing spatially resolved PL, as it is usual for a QD system and observed as well for previously reported AlGaN NWs grown at high temperature [139].

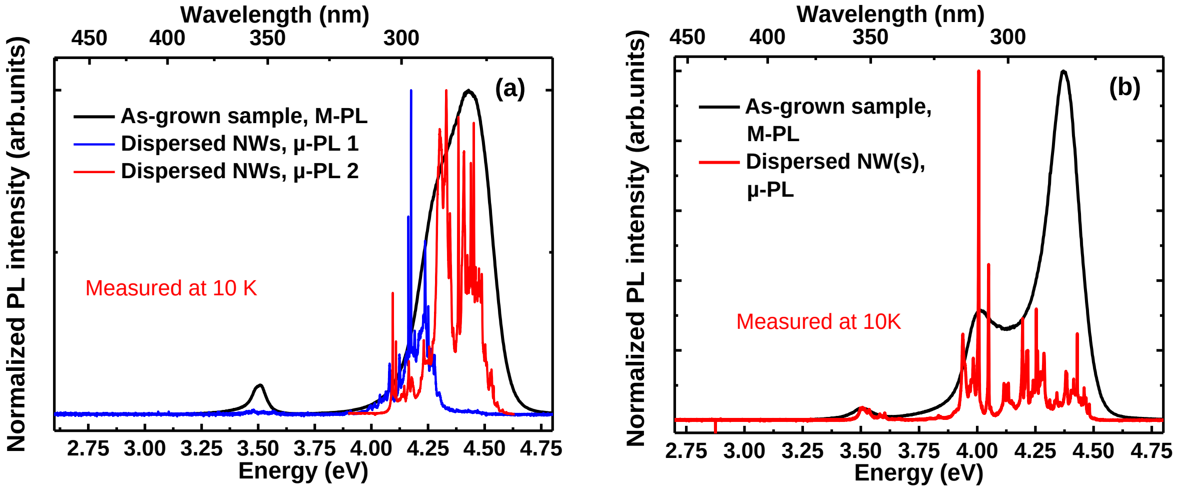

Figure 3.2.4.1: Macro-PL and µ-PL data recorded at 10 K and superimposed for $Al_{0.6}Ga_{0.4}N$ NW samples grown at (a): T_{subs} = 865°C (corresponding to t_{des}^{Ga} = 5 s, sample N2330), (b) T_{subs} = 750°C (t_{des}^{Ga} = 120s, sample N2326).

In addition to previous points, power-dependent µ-PL measurements performed using the µ-CW PL setup detailed in Subpart 2.3.1.1 did not reveal either a complete saturation or even a square root dependence of the PL intensity at moderate/high excitation power as often observed for nitrides in deeper defect-related PL studies [134, 426, 427]. We typically worked with excitation power between 1 µW and 1 mW. Knowing that the spot area was of the order of 1 µm^2 on samples, the associated excitation densities were comprised between 10^2 and 10^5 W.cm^{-2}, which is well above the 10^{-2}-1 W.cm^{-2} range from which this square root dependence can be observed [134]. Examples of such power-dependent measurements are given below in Figure 3.2.4.2 and afterwards in Subpart 3.2.5, only evidencing linear or superlinear dependences of line intensity on excitation power.

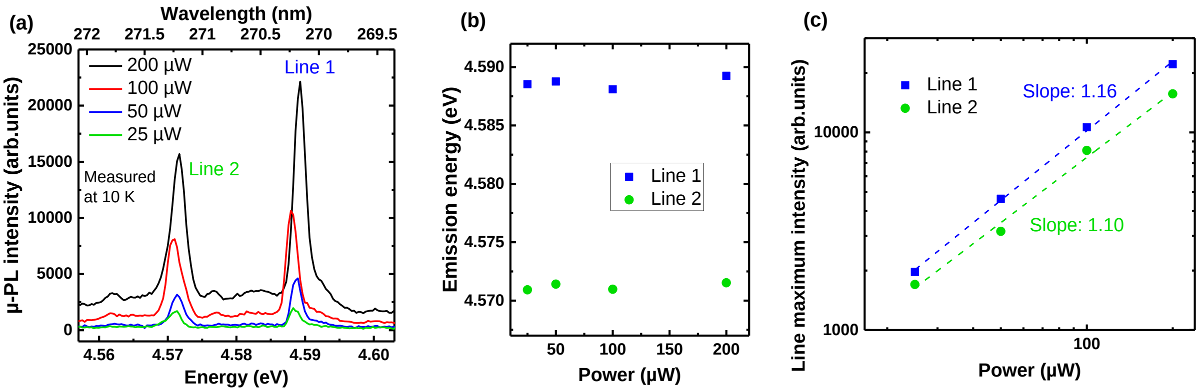

Figure 3.2.4.2: (a) Evolution with excitation power (values in legend) of two μ-PL lines emitted by $Al_{0.6}Ga_{0.4}N$ NW section (sample N2196) grown at high temperatures (T_{subs} > 830°C, t_{des}^{Ga} < 10 s). (b) Evolution of line emission energy with power. (c) Line maximum intensity versus excitation power, both on logarithm scales. Linear fits on logarithm scale result in slopes of 1.16 and 1.10, typical of linear dependence.

Last, the possibility of emission stemming from excitons bound to shallower impurities acting as donors rather than being localized in Ga-richer regions remains to be investigated. In the first case, the variation in emission wavelengths would be due to variations in AlGaN composition on a “large” spatial scale, i.e. much larger than the typical extent of a donor-bound exciton. In short, the mere observation of sharp lines does not tell us whether we observe excitons localized due to short-scale alloy inhomogeneity or whether we observe donor-bound excitons in locally homogeneous AlGaN alloy. In order to distinguish between the two situations, we performed temperature dependent μ-PL on single NWs. Typical results are presented in Figure 3.2.4.3 and Figure 3.2.4.4 for single dispersed NWs. It can be observed that the line intensity significantly quenches above 50 K, which was expected when looking at the quenching of macro-PL spectra given in Subpart 3.2.1 (see Figure 3.2.1.5). Furthermore, the line emission energy red-shifts monotonously with increasing temperature over the 10-120 K range, which is consistent with the redshift of the bandgap usually observed for a free exciton in a bulk system (see Subpart 1.2.1.3) or in a quantum structure such as a high-quality QW or a QD, as shown in Figure 3.2.4.3 (b) and Figure 3.2.4.4 (b). In the case of a neutral donor-bound exciton, we would observe a thermalization towards the free exciton in this temperature range, and hence a vanishing of the low temperature line while a new line (free exciton line) would appear at higher energy by a few meV. The related binding energy of the exciton bound to neutral shallow donor can be reasonably approximated by direct linear interpolation between the values reported for GaN and AlN (respectively about 7 meV [134] and about 18 meV [128]), which would for instance yield a value of the order of 13.5 meV for $Al_{0.6}Ga_{0.4}N$. As thermalization towards free exciton was not observed in any emission line that we probed, localization centers cannot be donors, confirming the initial assumption made in Subpart 3.2.2 from the spectral line density typically superior or equal to residual donor impurity concentrations.

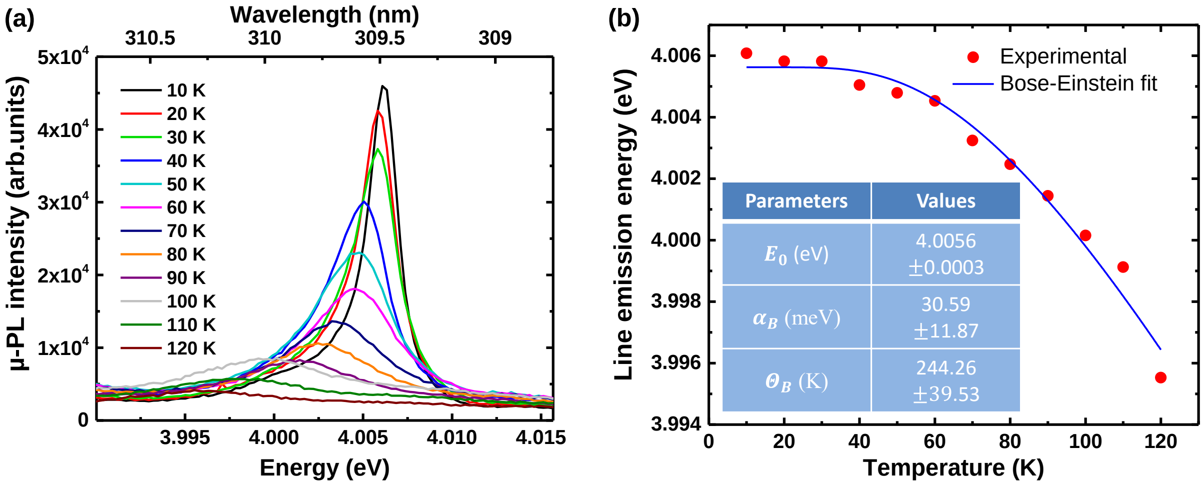

Parameters	Values
E_0 (eV)	4.0056 ±0.0003
α_B (meV)	30.59 ±11.87
Θ_B (K)	244.26 ±39.53

Figure 3.2.4.3: (a) 10-120 K range µ-PL spectra for a line emitted by a dispersed $Al_{0.6}Ga_{0.4}N$ NW section (sample N2326) grown at T_{subs} = 750°C (t_{des}^{Ga} = 120 s). (b) Line energy versus sample temperature. A monotonous energy decrease of the order of 10 meV over the 10-120 K range can be observed. A fit with Bose-Einstein laws is also provided (fitting algorithm did not converge for Varshni): the resulting values of characteristic parameters given in the table inset are slightly below the typical ranges of those obtained for AlN and GaN binaries but remain coherent.

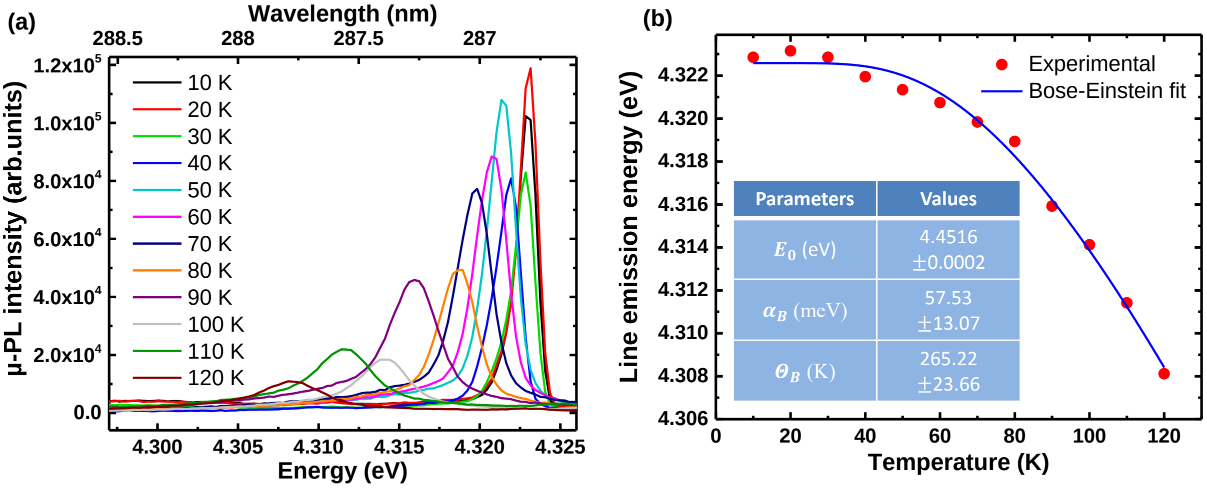

Parameters	Values
E_0 (eV)	4.4516 ±0.0002
α_B (meV)	57.53 ±13.07
Θ_B (K)	265.22 ±23.66

Figure 3.2.4.4: (a) 10-120 K range µ-PL spectra for a line emitted by a dispersed $Al_{0.6}Ga_{0.4}N$ NW section (sample N2330) grown at T_{subs} = 865°C (t_{des}^{Ga} = 5 s) on a GaN NW base. (b) Line energy versus sample temperature. A monotonous energy decrease of the order of 15 meV over the 10-120 K range can be observed. A fit with Bose-Einstein laws is also provided (fitting algorithm did not converge for Varshni): the resulting values of characteristic parameters provided in the table inset are slightly below the typical ranges of those obtained for AlN and GaN binaries but remain coherent and comparable to those of Figure 3.2.4.3.

We can thus safely conclude from these experiments that the main localization mechanism is a QD-like confinement with the exciton being localized in Ga-richer regions surrounded by Al-richer barriers. Such regions were expected to be numerous within the AlGaN NW sections given the alloy inhomogeneity emphasized by high linewidth and Stokes shift values evidenced in Subpart 3.2.1 thanks to macro-PL characterization. In view of μ-optical characterization results presented so far, these regions are likely to be of very small size, at least in the polar direction, and to present low chemical contrast with respect to the barriers. In other words, we are likely dealing with spontaneously formed QDs mostly resulting from the mere random compositional fluctuations intrinsic to alloy [172] rather than bigger objects such as clusters. Indeed, all the power-dependent experiments did not exhibit any clear QCSE usually observed for WZ III-N quantum objects thick enough along the polar direction. Moreover, the few evidenced biexciton binding energies were positive, consistent with the absence of QCSE, but low, which supports the assumption of weak carrier confinement within QD-like Ga-richer regions surrounded by barriers barely Al-richer. The chemical contrast between both was estimated to be of the order of 5-10% for AlGaN NW sections of similar Al content [325]. Last, both temperature-dependent macro- and μ-PL experiments revealed a significant quenching of PL intensity, consistent with the weak localization assumption.

3.2.5 Confirmation of the quantum-dot like behavior through power-dependent photoluminescence experiments

In order to support observations evidenced in Subparts 3.2.3 and 3.2.4, power-dependent μ-PL experiments were performed at low temperature (10 K) on single dispersed AlGaN NWs (excited by the same 244 nm CW laser) to probe for biexcitonic features. Depending on the investigated emission line, the excitation power was varied between 10-25 μW and 0.2-1 mW. Knowing that the spot area on samples was of the order of 1 μm², the corresponding excitation power density range was quite significant and comprised between 10^3 and 10^5 W.cm^{-2}.

To ease the observation of biexcitonic emission during experiments, we only investigated doublets of sharp lines clearly visible on μ-PL spectra at high excitation power, as isolated as possible, and distant from 60-70 meV at most, knowing that 52 meV is the largest value ever reported so far for the biexciton binding energy in well-defined III-V binary semiconductor QDs [251] (see Subpart 1.2.3.4) and that 48-56 meV are the largest values reported for thick AlGaN films (for very Al-rich alloy ($x \cong 0.8$) grown in heteroepitaxy [428]). The latter value range is surprisingly high, since the biexciton binding energy values for GaN and AlN 2D layers are respectively equal to 5.7 meV [252] and 19.3 meV [429] (22.6 meV when averaging all the reported values [128]). Such improvement with respect to values reported for binaries was attributed to the strong localization of biexcitons due to alloy disorder. When adding quantum confinement, biexciton binding energies for AlGaN increase even more, as reported for Al-rich AlGaN-based quantum wells ($Al_{0.6}Ga_{0.4}N/Al_{0.7}Ga_{0.3}N$) exhibiting a record value of 136 meV [430]. An enhancement with respect to the estimated biexciton binding energy value from linear interpolation between values for GaN and AlN was also noted for very Ga-rich AlGaN 2D epitaxial layers [431, 432].

Globally, it turned out that the spectral density of sharp lines was too large for our experiments: for many tries, when increasing the excitation power, we could observe new emission lines which appeared with superlinear power dependences and which could not be clearly correlated with those observed at lower excitation power. Consequently, in the latter cases, we could not clearly assign these extra lines to biexcitonic emission and extract the biexciton binding energy. Yet, several samples with shorter AlGaN sections (AlN molar fraction between 0.4 and 0.6) grown at high substrate temperatures (T_{subs} > 830°C, t_{des}^{Ga} < 10 s) had been specifically grown for these experiments in order to reduce the number of lines in μ-PL spectra. Eventually, we managed to get a few well-isolated doublets, exhibiting for some of them superlinear dependence of PL intensity on power. In the following, we will detail typical results, obtained for two doublets among the most isolated ones that we probed. The related doublet gaps were mostly comprised over a 5-20 meV range which roughly corresponds to the range delimited by the biexciton binding energy values reported for GaN and AlN.

For some investigated doublets such as the one displayed in Figure 3.2.5.1 (a) and separated by 8 meV whatever the excitation power according to Figure 3.2.5.1 (b), it was clear that the μ-PL intensity of the extra line possibly associated with a biexciton did not exhibit a quadratic dependence but more a linear one over the excitation power range, as shown in Figure 3.2.5.2. In other words, it was not possible to extract any biexciton binding energy in these cases. Indeed, linear fits on logarithmic scale performed on the evolution with power of the μ-PL line maximum intensity, read directly without fitting the lines in view of the low background and clear line separation, led to slopes of the order of 1, i.e. comprised over the 0.8-1.2 range, as exhibited in Figure 3.2.5.2 (a). The evolution of integrated intensity, in other words the surface below the line, was also checked and is provided in Figure 3.2.5.2 (b) in order to take into account the possible linewidth evolution with power. To derive the integrated intensity of each line, the latter were fitted at each excitation power with Gaussian function for practicality, rather than Lorentzian or Pseudo-Voigt functions which better match physical reality: the fitting algorithm convergence was reached more easily with Gaussian while fitting very well the data, as shown in Figure 3.2.5.3, which resulted in accurate integrated intensity values highlighting the same trend as in Figure 3.2.5.2 (a). Indeed, slopes of 0.81 and 0.80 were obtained from linear fits on logarithm scale performed on the evolution of integrated intensity, respectively for line 1 and line 2.

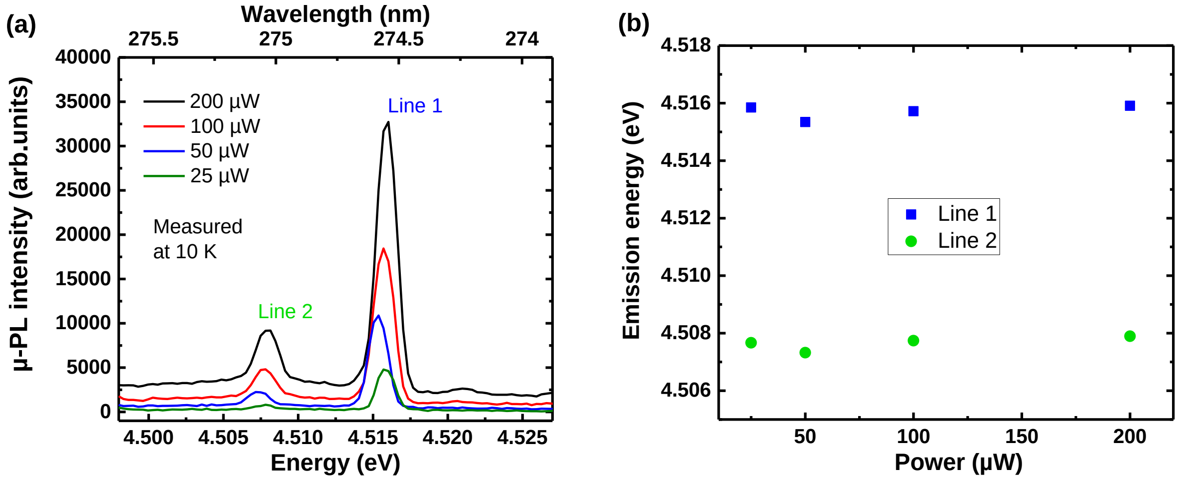

Figure 3.2.5.1: (a) Evolution with excitation power (values in legend) of a μ-PL line doublet emitted by Al$_{0.5}$Ga$_{0.5}$N NW section (sample N2136), grown at high temperatures (T_{subs} > 830°C, t_{des}^{Ga} < 10 s). (b) The dependence of doublet intensities on excitation power remains linear here.

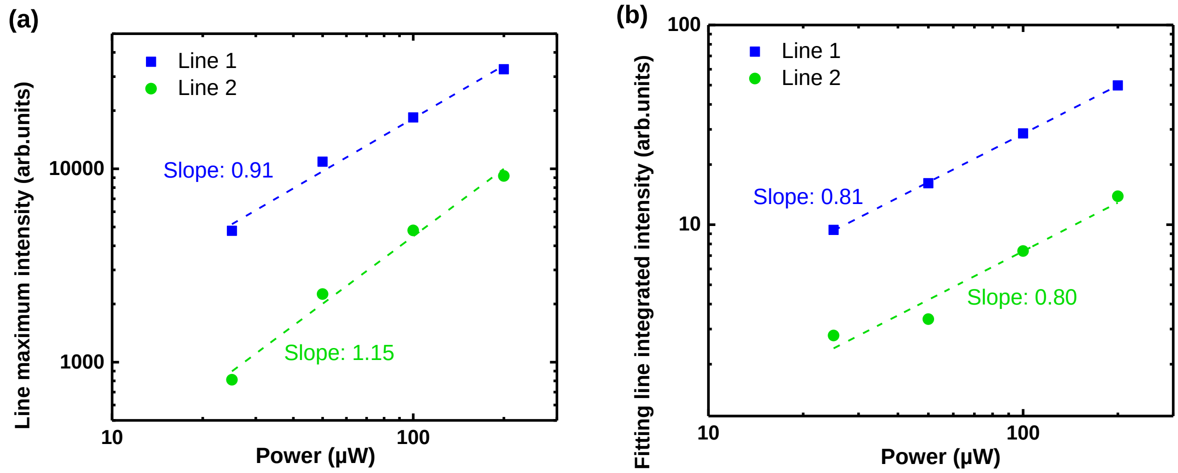

Figure 3.2.5.2: (a) μ-PL line maximum intensity of the two lines of Figure 3.2.5.1 versus excitation power, both on logarithmic scale. The dependence of line 1 and line 2 on power is linear. Indeed, linear fits on logarithm scale (solid lines displayed on graph) lead to slopes of 0.91 and 1.15. (b) Fitting line integrated intensity as a function of excitation power, leading to the same trend: similar slopes of 0.81 and 0.80, respectively for line 1 and line 2.

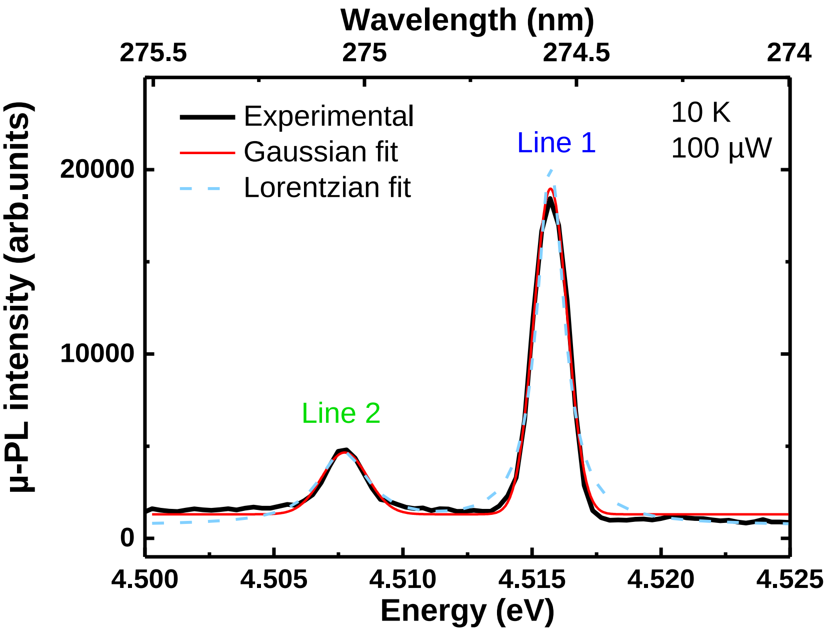

Figure 3.2.5.3: Fit performed with 2 Gaussian (solid line) and 2 Lorentzian (dashed) functions for the spectrum recorded at 10K, 100 µW. Gaussian fits better here than Lorentzian, giving more accurate results for line integrated intensities. Pseudo-Voigt could be used to better match physical reality but the fitting algorithm converges less easily in that case.

However, for a few isolated doublets such as the one displayed in Figure 3.2.5.4 (a), the dependence of line intensity on power was much more quadratic than linear for one of the two lines, as shown in Figure 3.2.5.5, but the doublet energy gaps seemed low for an exciton/biexciton couple in a rather Al-rich AlGaN alloy, mainly remaining over a 5-15 meV range for the probed doublets. In our example of Figure 3.2.5.4 (a), the related biexciton binding energy would be +5 meV whatever the investigated excitation power in view of Figure 3.2.5.4 (b). Figure 3.2.5.5 (a) provides, for both lines, the evolution of the maximum intensity with power on logarithm scale, read directly without fitting in view of the very low background and clear line separation. Linear fits performed on logarithmic scale in Figure 3.2.5.5 (a) result in slopes of 0.81 and 1.51 respectively for line 1 and line 2, that is to say a factor of the order of 2 in both cases highlighting a quadratic-like dependence attributed to biexcitonic emission. However, the discrepancy on both slope values is not negligible with respect to the expected values of 1 and 2. To support our claim, the evolution with power of the line integrated intensity was then investigated, as displayed in Figure 3.2.5.5 (b). To do so, the lines were also fitted for each power with Gaussian function for practicality, as illustrated in Figure 3.2.5.6 and similarly to Figure 3.2.5.3. Slopes of 0.83 and 1.52 were then derived from linear fits on logarithm scale performed on the evolution of integrated intensity, respectively for line 1 and line 2, evidencing the same trend as in Figure 3.2.5.5 (a).

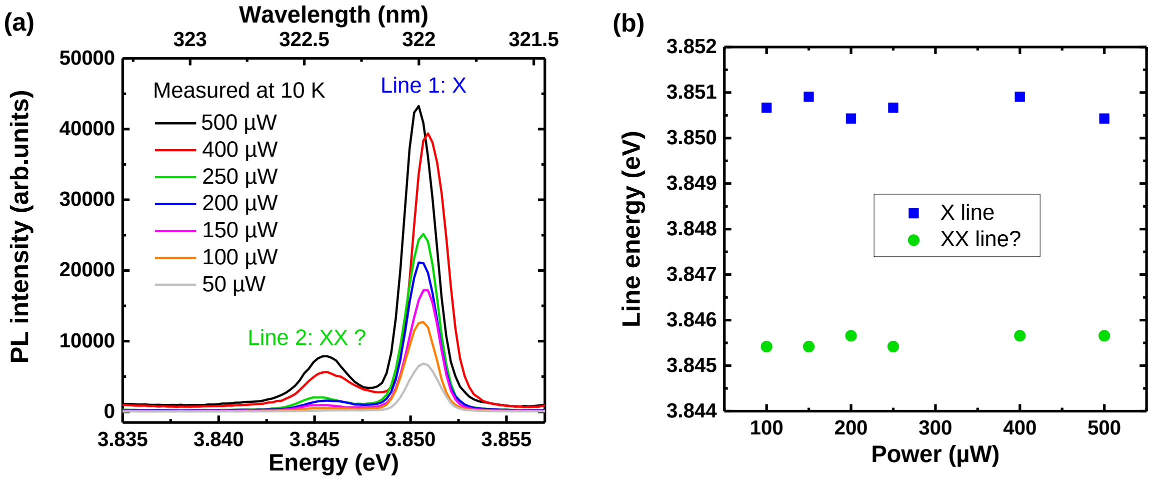

Figure 3.2.5.4: (a) Evolution with excitation power (values in legend) of a µ-PL line doublet emitted by $Al_{0.5}Ga_{0.5}N$ NW section (sample N2136) grown at high temperature (T_{subs} > 830°C, t_{des}^{Ga} < 10 s). (b) Evolution of the energy of the two lines with power. The gap between them is around 5 meV.

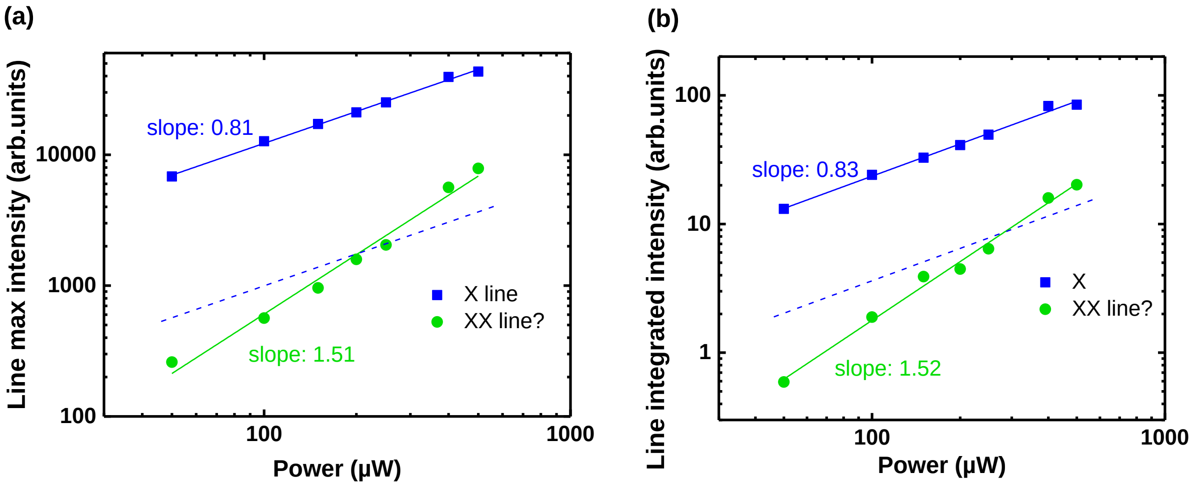

Figure 3.2.5.5: (a) µ-PL line maximum intensity of the two lines of Figure 3.2.5.4 versus excitation power, both on logarithmic scale. The dependence of line 1 and line 2 on power is quasi-linear and quasi-quadratic, respectively. Indeed, linear fits on logarithmic scale (solid lines displayed on graph) lead to slopes of 0.81 and 1.51, i.e. a factor of the order of 2 between both lines. The dashed blue line is parallel to the solid blue line. (b) Line integrated intensity as a function of excitation power, leading to the same trend: slopes of 0.83 and 1.52, respectively for line 1 and line 2.

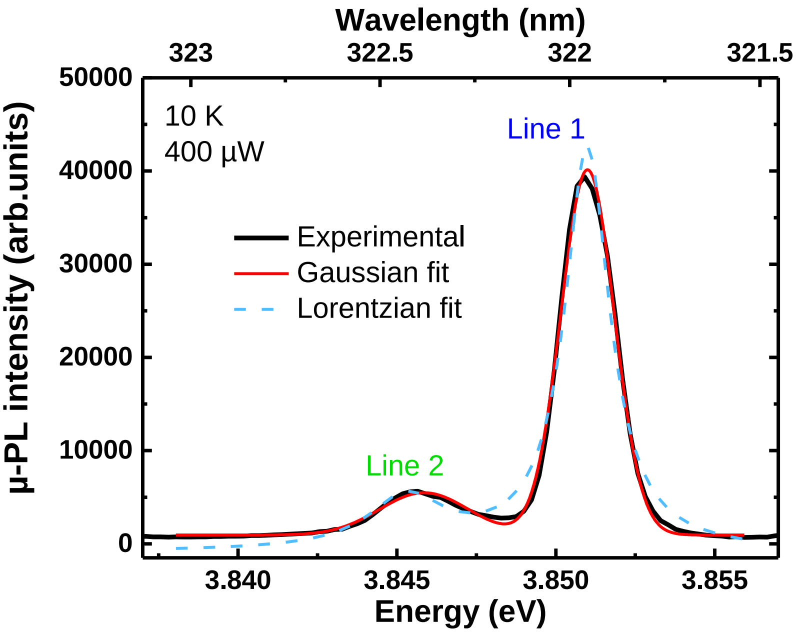

Figure 3.2.5.6: Fit performed with 2 Gaussian (solid line) and 2 Lorentzian (dashed) functions for the spectrum recorded at 10 K, 400 µW. Gaussian fits better here than Lorentzian, giving more accurate results for line integrated intensities. Pseudo-Voigt could be used to better match physical reality but the fitting algorithm converges less easily in that case.

3.2.6 Micro-photoluminescence dynamics of AlGaN nanowires

After having identified the QD-like centers as compositional fluctuations in AlGaN NWs, we investigated their homogeneity in size within such NWs grown in various conditions. One way to proceed is to probe by µ-TRPL many individual µ-PL lines emitted by dispersed AlGaN NW sections from several samples grown at various growth temperatures and AlN molar fraction (in N-rich conditions). The samples were excited at low temperature (10 K) and low excitation power (≈ 1 µW) by a tripled Ti-sapphire pulsed laser emitting around 244 nm and with a repetition rate of 76 MHz. The beam spot size was similar to the one for CW µ-PL setup (same microscope objective). More details about the TRPL setup are given in 2.3.1.3.

Figure 3.2.6.1 sums up the results for a series of $Al_{0.6}Ga_{0.4}N$ NW samples, for which short decay times versus wavelengths of µ-PL sharp emission lines are plotted. The top right corner inset gives an example of decay for an emission line from an $Al_{0.6}Ga_{0.4}N$ NW and illustrates how lifetimes were extracted: all experimental decays were fitted with a monoexponential decay function:

$$y_{monoexp.}(t) = y_0 + A_1 e^{-(t-t_0)/t_1} \qquad (3.2.6.1)$$

where y_0, t_0 , A_1 and t_1 are the TRPL intensity offset, the time offset, the TRPL intensity maximum and the short decay time, respectively. A biexponential function could have been used in order to better fit the decay tail and obtain a rough estimation of long decay time but in view of the fast drop in TRPL intensity at short times (by about two orders of magnitude as visible in Figure 3.2.6.1 (b)) and the low dynamics at the decay tail, it was chosen to focus only on the first part of decays.

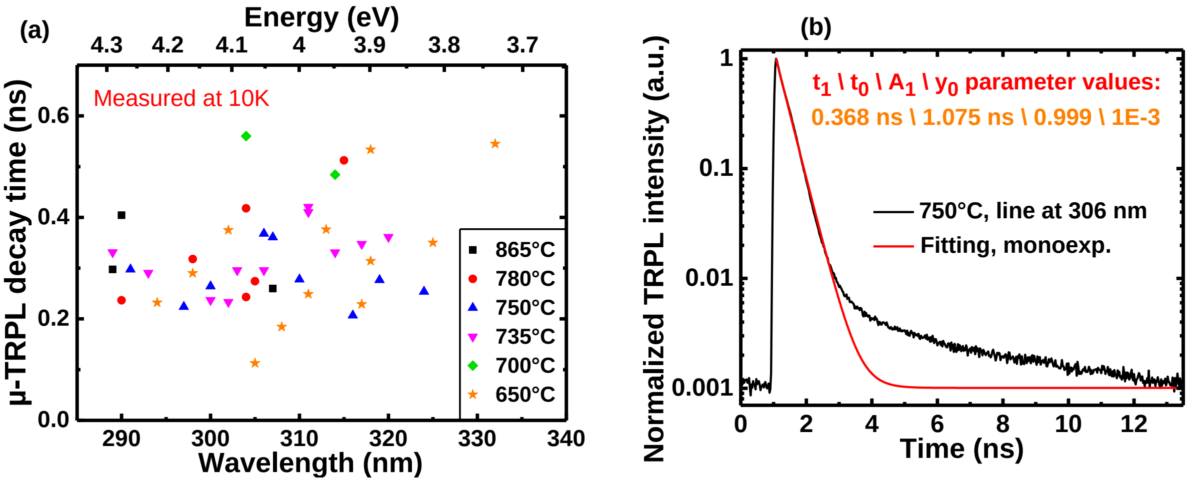

Figure 3.2.6.1: (a) Low temperature (10 K) µ-TRPL short component of decay time versus sharp line wavelength/emission energy, for several dispersed $Al_{0.6}Ga_{0.4}N$ NWs from samples grown at various thermocouple temperatures indicated in legend. (b) Decay example for a µ-PL emission line at 306 nm from a NW (sample N2326) grown at T_{subs} = 750°C (t_{des}^{Ga} = 120 s), and fitted with monoexponential decay. The fit parameter values are labeled in orange.

On the one hand, taking into account all investigated samples, performed statistics revealed that short decay times at 10 K are mostly distributed over the 200-400 ps range, around an estimated mean decay time of 320 ps, as shown in Figure 3.2.6.2. Data displayed in this Figure 3.2.6.2 gathers about 60 values of short decay times measured by µ-TRPL at 10 K and related to lines emitted by dispersed $Al_{0.3}Ga_{0.7}N$, $Al_{0.5}Ga_{0.5}N$ and $Al_{0.6}Ga_{0.4}N$ NW sections over a 280-340 nm range. The values of characteristic τ_0 times at low excitation power obtained by fitting antibunching curves (see Subpart 3.2.3) are consistent with such a range.

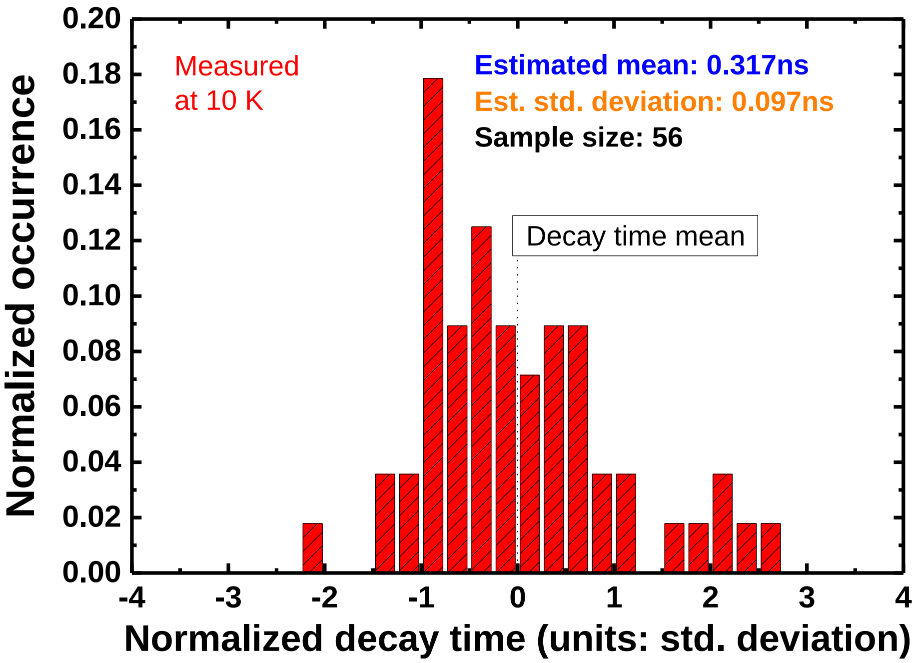

Figure 3.2.6.2: Distribution of short decay time values (whatever the related line emission energy) with respect to the estimated mean value (317 ps). The decay times are related to µ-PL lines emitted by $Al_{0.3}Ga_{0.7}N$, $Al_{0.5}Ga_{0.5}N$ and $Al_{0.6}Ga_{0.4}N$ NW sections. The abscissa is centered on the estimated mean and normalized with respect to the estimated standard deviation (97 ps).

Second, statistics underscored a slight increase in the decay time when decreasing the emission energy / increasing the wavelength over the investigated range at 10 K, as shown in Figure 3.2.6.3. Figure 3.2.6.3 (b) shows the evolution of estimated decay time means respectively for every 15 nm range over the whole 280-340 nm range. We can note that the slight increase in short decay times when decreasing the emission energy / increasing the wavelength is consistent with a λ^2 dependence which will be discussed further in this section. The decay time data used for performing statistics is shown in Figure 3.2.6.3 (a), on which λ^2 and λ laws are sketched as a guideline.

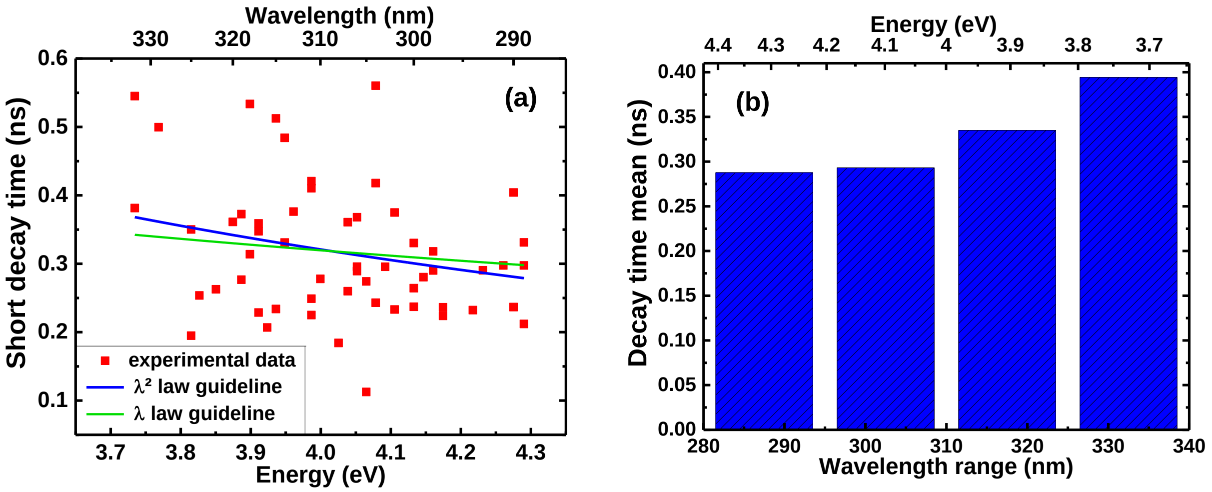

Figure 3.2.6.3: (a) Short decay time versus emission energy/wavelength, related to data exhibited in Figure 3.2.6.2. λ^2 and λ guidelines are sketched (respectively solid blue line and green line). (b) Evolution of the short decay time mean with emission wavelength/energy (for each 15 nm range), from data displayed in (a).

On the other hand, when comparing samples within the $Al_{0.6}Ga_{0.4}N$ series, no clear change correlated to AlGaN growth temperature was observed, meaning that the decay times related to µ-PL sharp lines associated with alloy fluctuations are independent of growth temperature, over the investigated ranges. The average AlN molar fraction in the section has no clear influence as well, given that the same experiments done on NWs from $Al_{0.3}Ga_{0.7}N$ and $Al_{0.5}Ga_{0.5}N$ series led to similar results, when comparing decay times linked to sharp lines emitted within similar wavelength ranges.

We then checked that the measured decay times were mainly radiative at low temperature. At 10 K, non-radiative surface recombinations are unlikely to occur in AlGaN NW sections, as the latter are surrounded by a thin Al-rich shell (see Subpart 3.1). As for recombination at point defects, this possibility has been already discussed in Subpart 3.2.4 and is unlikely as well. To give a demonstration of purely radiative recombination is a quite challenging task, as highlighted for instance by the abundant literature and debates on the IQE of InGaN/GaN QWs [433-436]. One reasonable way of probing non-radiative recombinations is to assume that they are thermally activated so that temperature-dependent PL and time-resolved PL can give a fair estimate of the importance of the radiative to non-radiative recombinations ratio [437]. We thus carried out temperature-dependent µ-TRPL experiments on dispersed AlGaN NW sections. Three datasets are exhibited in Figure 3.2.6.4, Figure 3.2.6.5 and Figure 3.2.6.6 over a 10-120 K range for three different lines, emitted at 320, 301 and 317 nm by $Al_{0.6}Ga_{0.4}N$ NW sections grown at T_{subs} = 700°C, 865°C and 750°C (corresponding to t_{des}^{Ga} = 5 s and 120 s for the two latter temperatures), respectively. In good agreement with temperature-dependent µ-PL data shown in Subpart 3.2.4, the line intensity as well as the decay time was fairly constant in the 10-60 K range, so that we estimated that non-radiative recombinations (or at least thermally activated non-radiative recombinations) could be neglected in this temperature range. Provided several assumptions detailed in Subpart 2.3.1.3, we could extract the radiative and non-radiative decay times from the µ-TRPL data (intensity and short decay times). Such times are also provided in the examples of Figure 3.2.6.4, Figure 3.2.6.5 and Figure 3.2.6.6 below. The crossing of radiative and non-radiative decay times was typically observed between 100 and 120 K. To compare, such value is inferior, as expected, to the crossing reported for well-defined GaN QDs surrounded by AlN barriers [190] (around 160 K derived for m-plane QDs [438] from the same model) but superior to the one observed for well-defined GaN QWires [190] (below 100 K for such wires grown in m-plane as well [438]).

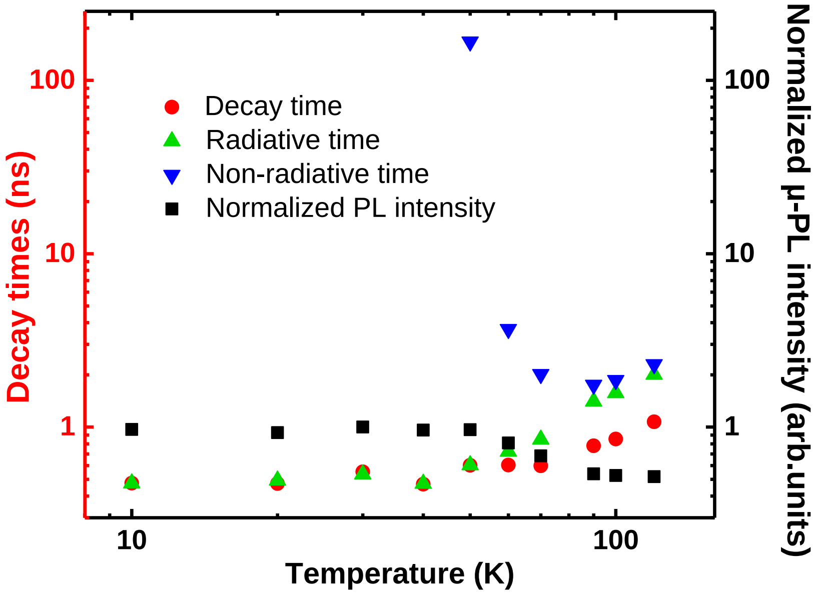

Figure 3.2.6.4: Temperature-dependent µ-TRPL data (decay times and µ-PL intensity) for a line emitted at 320 nm by an $Al_{0.6}Ga_{0.4}N$ NW grown at T_{subs} = 700°C (sample N2352). The decay times labeled with red round symbols correspond to the short component of experimental decays extracted from monoexponential fits. The radiative and non-radiative decay times are inferred from the model described in Subpart 2.3.1.3.

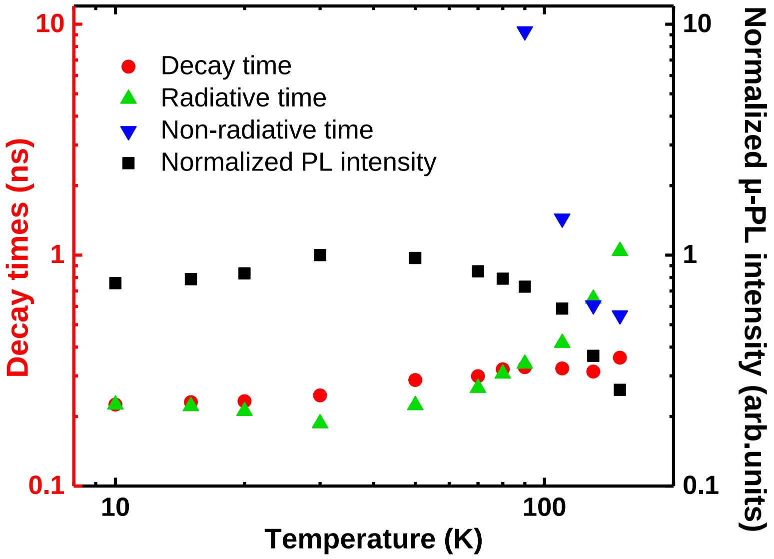

Figure 3.2.6.5: Temperature-dependent µ-TRPL data (decay times and µ-PL intensity) for a line emitted at 301 nm by an $Al_{0.6}Ga_{0.4}N$ NW (sample N2330) grown at T_{subs} = 865°C (corresponding to t_{des}^{Ga} = 5 s). The decay times labeled with red round symbols correspond to the short component of experimental decays extracted from monoexponential fits. The radiative and non-radiative times are deduced from the model described in Subpart 2.3.1.3.

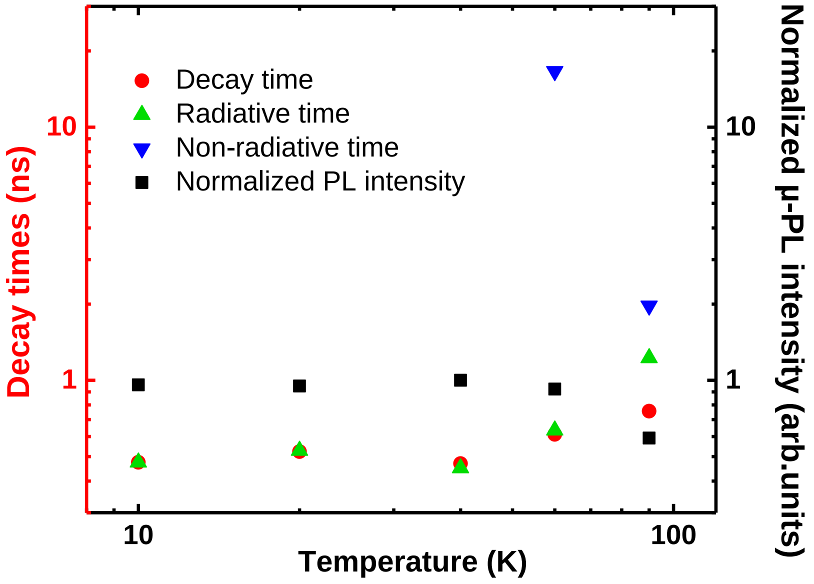

Figure 3.2.6.6: Temperature-dependent µ-TRPL data (decay times and µ-PL intensity) for a line emitted at 317 nm by an $Al_{0.6}Ga_{0.4}N$ NW (sample N2326) grown at T_{subs} = 750°C (corresponding to t_{des}^{Ga} = 120 s). The decay times labeled with red round symbols correspond to the short component of experimental decays extracted from monoexponential fits. The radiative and non-radiative times are inferred from the model described in Subpart 2.3.1.3.

As already mentioned in Subpart 1.2.3.1, it was theoretically and experimentally demonstrated that the radiative lifetime in a QD is inversely proportional to the oscillator strength [196, 202, 203], which depends on the spatial coherent extension of the exciton (leading to giant oscillator strength in the case of large spatial extension [439-441]). This lifetime also depends on the emission energy / emission wavelength (dependence of the lifetime as λ^2) [442], as follows [416, 443, 444]:

$$\tau_{rad} = \frac{3c^3\varepsilon_0 m_e h^2}{2\pi e^2}\frac{1}{nE^2 f} \tag{3.2.6.2}$$

where c is the speed of light, ε_0 is the vacuum permittivity, h the Planck constant, e the electron charge, m_e the electron mass, n the refractive index of the medium, E the exciton emission energy and f the oscillator strength. In the case of the giant oscillator strength effect mentioned above, f mostly depends on the large exciton spatial extension and gets proportional to the average coherence volume probed by excitons:

$$f \propto V_{exc} \propto (a_B^X)^3 \tag{3.2.6.3}$$

where V_{exc} is the coherence volume of the confined exciton and a_B^X is the exciton Bohr radius. In contrast, in the strong confinement regime, f no longer depends on the latter volume in view of the perfect electron-hole overlap and gets inversely proportional to the emission energy, such as:

$$f \propto \frac{E_P}{E} \tag{3.2.6.4}$$

with E_P the Kane energy, namely the interband matrix element [445]. It must be noted that, even for GaN, the value of the Kane energy is not well known and varies from 15.7 eV [446] to 7.7 eV [447]. Also, from Equation (3.2.6.2), we see that to evaluate the radiative lifetime, we also need the refractive index as an input, which for subwavelength structures like NWs is expected to be anisotropic and smaller than the AlGaN refractive index [448]. For E_P= 15.7 eV and a refractive index of 2.3 (i.e. bulk AlGaN), Equation (3.2.6.2) yields a lifetime of 500 ps. For E_P=7.7 eV and n=1.5 (effective refractive index of the NW in vacuum), we find a radiative lifetime of 1.5 ns. This seems a bit high and the latter E_P value should be taken cautiously as most references rather yield an E_P of around 15 eV (which we assume to be similar in AlGaN). What can be said at any rate is that we expect a radiative lifetime for strongly confined electron-hole pairs in such NWs to be in the 600-700 ps range. The fact that we see large enough variations of measured lifetimes for various localization centers, and with most measured lifetimes in the 200-400 ps range is a good indication that we are not strictly in the strongly confined regime.

Overall, using Equations (3.2.6.2) to (3.2.6.4), τ_{rad} is inversely proportional to V_{exc} and proportional to λ, respectively for giant oscillator strength and strong confinement regimes.

In our experiments, we did not measure strong variations of PL decay times corresponding to the radiative decay time at low temperature. Indeed, the radiative lifetime dependence on emission energy is only consistent with a λ^2 trend over the investigated energy range, showing that the spatial extension of the confined excitons was about the same for all emission energies. The confinement scheme was thus quite homogeneous for our localization centers, the deviation from homogeneity being given by the standard deviation estimated in the statistics we made over several lines and displayed in Figure 3.2.6.2 and Figure 3.2.6.3.

Figure 3.2.6.7 illustrates with reasonable values (600 ps for the radiative lifetime of strongly confined excitons) the expected evolution of radiative lifetime as a function of exciton wavefunction extension, with a light-matter coupling situation at the onset of giant oscillator strength. Indeed, when comparing theoretical lifetime values with the experimental ones in the 200-400 ps range, we can derive a wavefunction radius over a 3-4 nm value range, which belongs to an intermediate regime between strong confinement and giant oscillator strength consistent with the rather weak carrier localization evidenced in previous subparts. Note that at this stage, we have inferred a rather isotropic confinement and wavefunction extension, which might not be the case depending on possible anisotropies of local ordering.

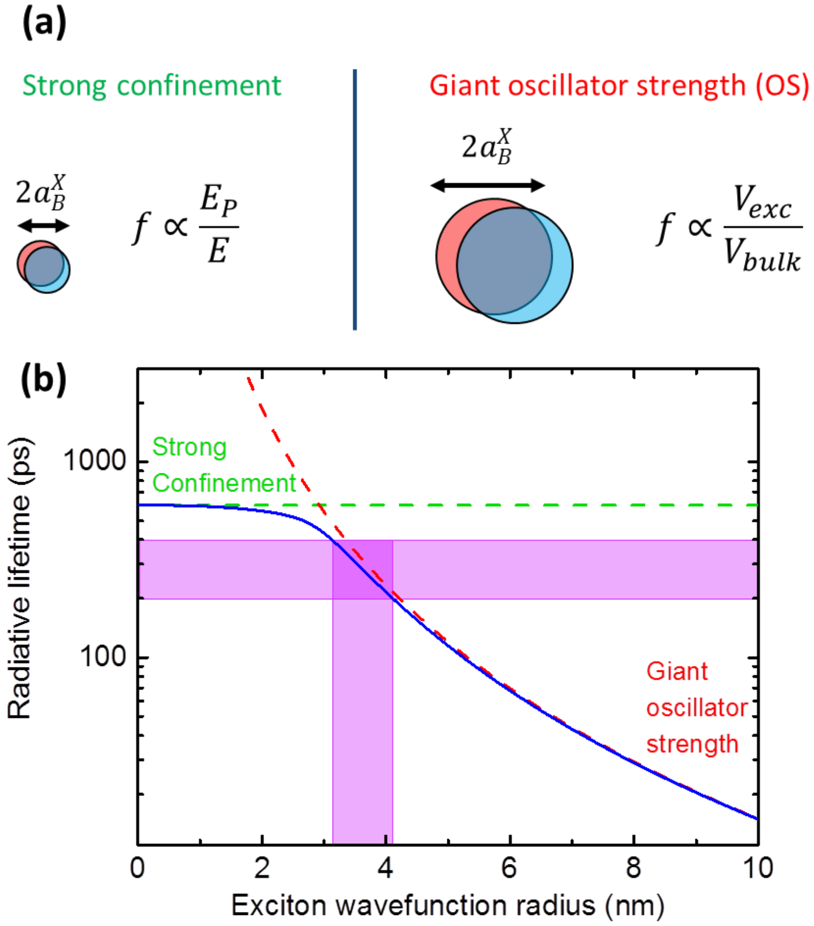

Figure 3.2.6.7: (a) Illustration of the exciton Bohr radius and the oscillator strength approximation in the strong confinement and giant oscillator strength regimes. (b) Sketch of the radiative lifetime, using Equation (3.2.6.2). The green and red dashed lines correspond respectively to the strong confinement and giant oscillator strength limits.

3.2.7 Localization attributed to compositional fluctuations at very short scale.

In a next stage, we wondered about carrier localization in even smaller quantity of AlGaN material and under additional quantum confinement. For our studies, thin AlGaN QDisks were grown between AlN NW barriers in slightly N-rich conditions on top of GaN NW bases, following the same protocol as for longer NW sections regarding the calibrations of metallic fluxes, the growth temperature determination and the NW density control. The QDisk thickness was varied over the 2-10 nm range and the nominal AlN molar fraction over the 0.3-0.5 range. Figure 3.2.7.1 provides typical SEM and STEM images for some of the grown samples. Figure 3.2.7.2 (a) shows µ-PL spectra recorded for single dispersed NWs presenting the thinnest AlGaN QDisks (thickness mostly varying over the 2-2.5 nm range) of the sample series and excited with the 244 nm CW laser on the µ-PL setup detailed in Subpart 2.3.1.1, whereas Figure 3.2.7.2 (b) displays typical STEM images zoomed on the top of NWs from the same sample. The related µ-PL experiments were carried out at low temperature (10 K) on single NWs located on Si substrates beforehand by SEM and revealed sharp lines presenting µ-optical properties (linewidths, associated short decay times over shared emission range) similar to those exhibited for longer AlGaN sections. This is in strong contrast with what was observed for similar quantum disks made of GaN for which there was a single emitted line at low temperature [254]. Despite the fact that a single “structural” AlGaN QDisk is defined in each NW, several emission lines corresponding to several localization centers within the AlGaN disk were observed. Our experiment demonstrates that for AlGaN quantum structures in NWs, the emission properties are not solely imposed by the geometric confinement, but also by localization at shorter spatial scales due to the compositional fluctuations inherent to a ternary alloy and caused by the random distribution of Al and Ga on the cation sites of the crystal [172].

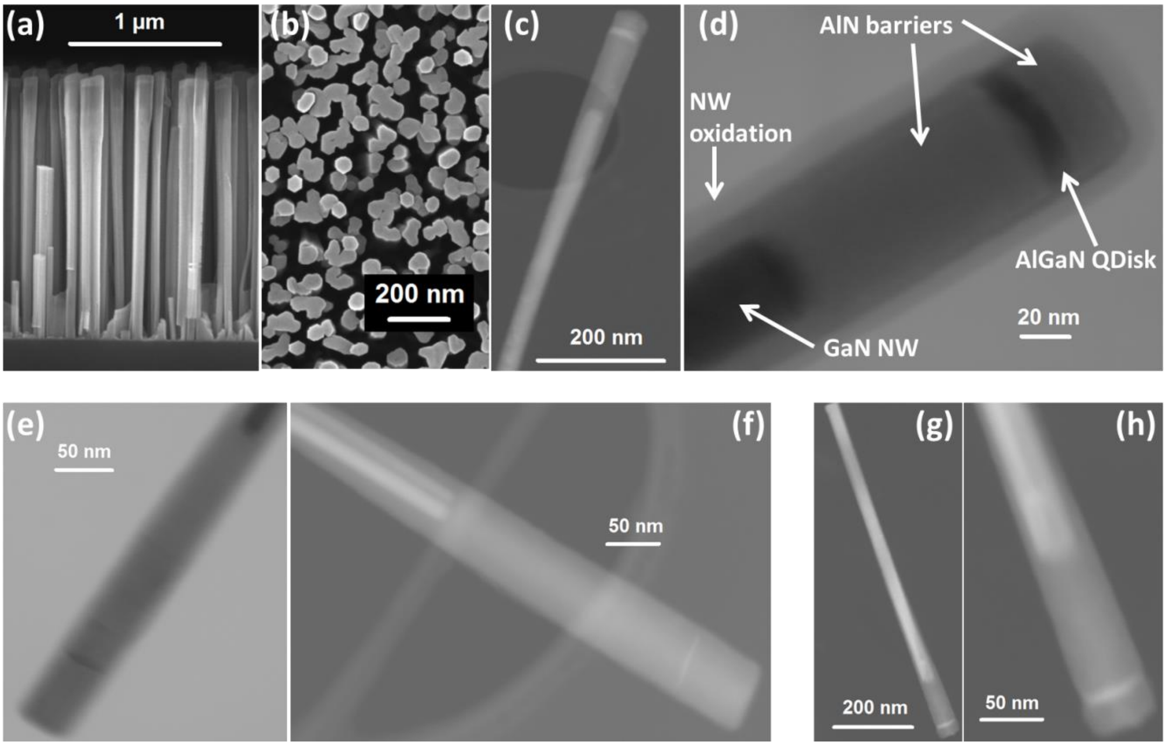

Figure 3.2.7.1: Typical side-view (a) and top-view (b) SEM images of as-grown samples consisting in AlGaN QDisks inserted in AlN barriers grown on GaN NW bases (sample N2254). More or less zoomed STEM-ADF or STEM-BF images of single dispersed AlGaN QDisks: their thickness was estimated at 9, 2 and 6 nm respectively for (c) & (d), (e) & (f), and (g) & (h) (respectively for samples N2254, N2270, and N2253). The nominal AlN molar fraction in the AlGaN disk is x = 0.4 for N2270 and x = 0.3 for the other two samples.

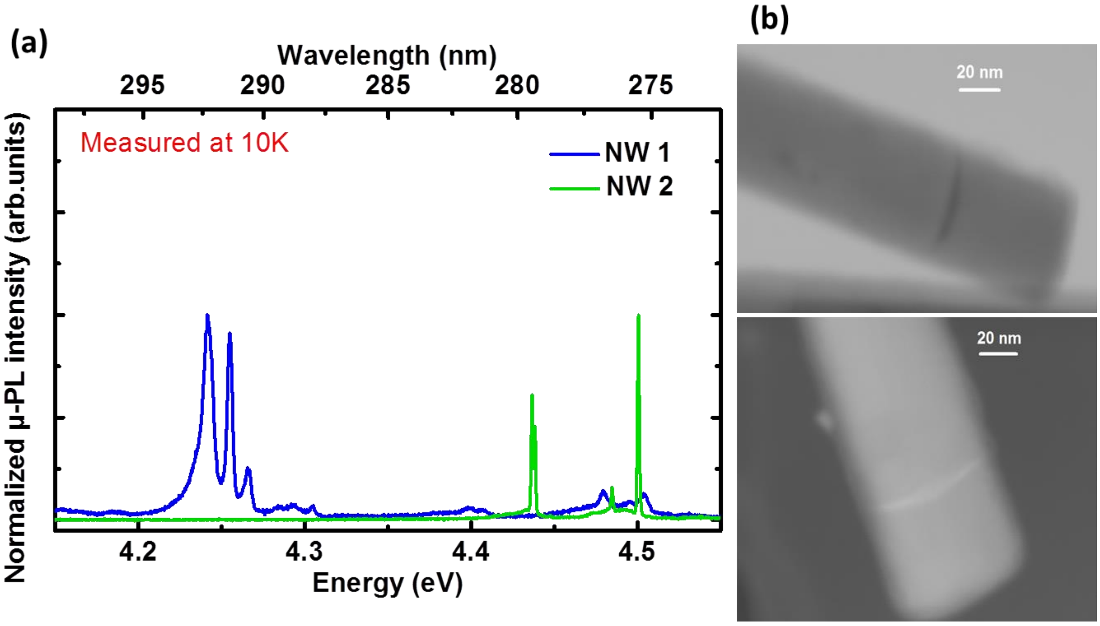

Figure 3.2.7.2: (a) Low temperature (10 K) µ-PL spectra for two single dispersed NWs with AlGaN QDisks inserted in AlN grown on a GaN NW base (sample N2270). (b) Typical STEM-BF (top) and STEM-HAADF (bottom) images zoomed on the QDisk. The nominal AlN molar fraction in the disk is x = 0.4 and the average disk thickness for the sample was estimated at 2 nm.

More details about the QDisk emission properties are given in the following. Figure 3.2.7.3 shows macro-PL spectra recorded at 10 and 300 K for a few samples excited with the 244 nm CW laser on the macro-PL setup described in Subpart 2.3.1.1: two QDisk samples (of two different thicknesses) and two reference samples (one with an AlGaN NW short section without AlN capping and the other one with a pure AlN NW section). The spectrum for the AlN reference exhibits a band around 4.6 eV attributed to deeper defects in AlN [128] and present in most spectra. A lower PL quenching with temperature was observed for PL emission peaks around 4.2 eV (respectively 3.8 eV) for the 2 nm QDisk sample (respectively the thicker one), when comparing with the AlGaN NW reference sample. Such an observation is consistent with stronger carrier localization attributed to extra quantum confinement in QDisks. The broad emission for the latter peaks is assigned to compositional fluctuations inherent to the alloy within QDisks and disparity from QDisk to QDisk on both their thickness and Al composition. When comparing emission from the AlGaN NW section reference and the one from 4 nm thick AlGaN QDisks grown with the same metallic fluxes (same nominal AlN molar fraction, $x_{Al} = 0.3$), the latter is slightly red-shifted (emission around 3.75 eV when fitting spectrum (not shown here) versus 3.93 eV for the section reference sample N2257), which is very likely due to non-negligible QCSE effect for such thickness. In the more extreme case of GaN/AlN QDisk system, such QCSE starts being non negligible for disk thickness of the order of 2 nm, the latter value depending also on the barrier dimensions [115, 116]. However, it was not possible to accurately determine the AlN molar fraction in AlGaN QDisks by EDX, as parts of AlN barriers were integrated as well during the experiments, especially for the thinnest disks, and to compare it with the one obtained for longer AlGaN NW section. Consequently, decorrelating the different contributions to the emission energy ("intrinsic" AlGaN luminescence, quantum confinement, QCSE) is far from being trivial. Some EDX data, much more qualitative than quantitative, is provided in Figure 3.2.7.4 for a sample presenting disks thicker than those investigated in Figure 3.2.7.3 and for which less AlN from barriers is integrated.

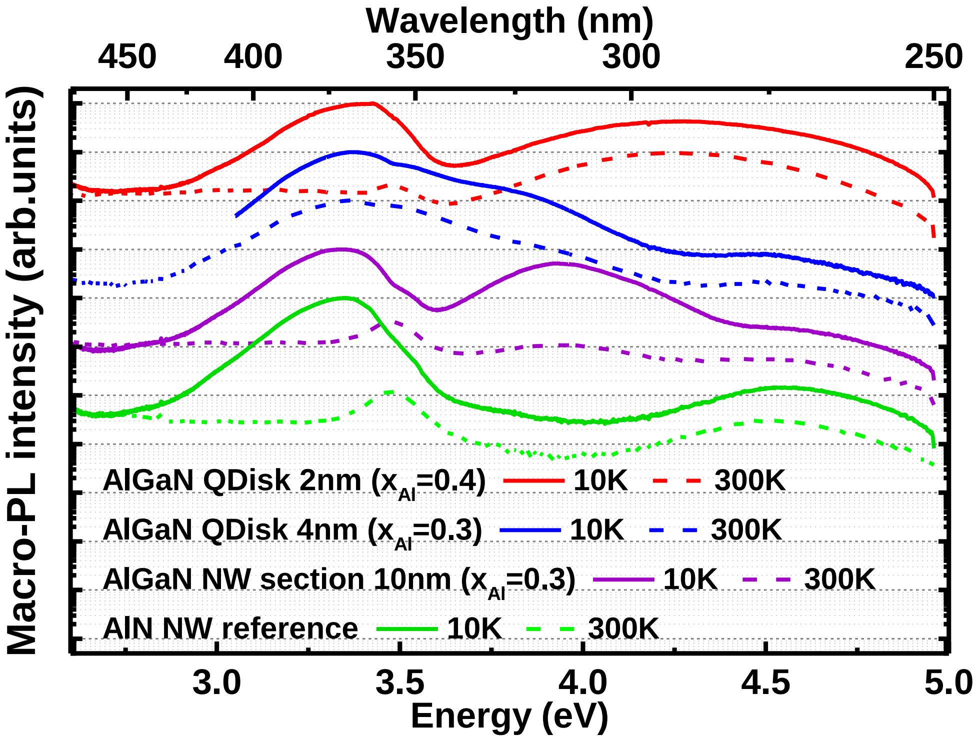

Figure 3.2.7.3: Macro-PL spectra recorded at low (10 K, solid line) and room-temperature (300 K, dashed line) for four samples: two different AlGaN QDisk samples labeled in red and blue (respectively samples N2270 and N2260, the estimated thickness and nominal AlN molar fraction are given for each) and two references labeled in purple and green (respectively sample N2257, presenting AlGaN NW sections without AlN top barriers/cappings, and sample N2265, consisting in pure AlN NW sections grown on top of GaN NW templates).

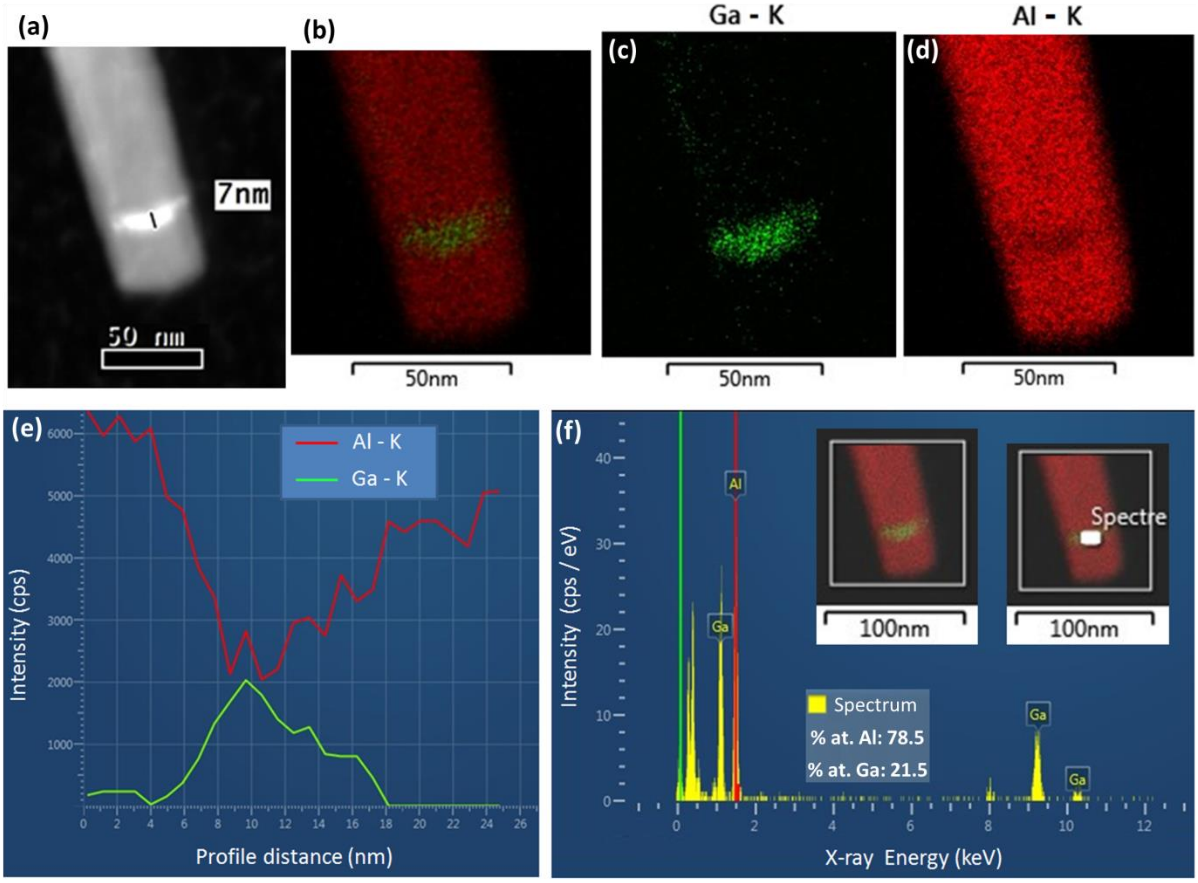

Figure 3.2.7.4: (a) STEM image of investigated QDisk (sample N2253, nominal AlN molar fraction x = 0.3). (b) EDX map with Ga-K and Al-K contribution superimposed. (c) EDX map of Ga-K contribution. (d) EDX map of Al-K contribution. (e) Line profile for Ga-K and Al-K taken along the NW c-axis and including the QDisk. (f) EDX spectrum recorded within QDisk. In view of the high Al atomic percentage in comparison with nominal $x_{Al} = 0.3$, non-negligible amount of AlN from the barriers is integrated, since the mere contribution of the shell cannot explain the discrepancy in view of its rather low thickness.

Low-resolution CL experiments (in the SEM setup, see Subpart 2.3.2.1) were performed as well on single QDisks. Typical results are given for two NWs from the 2 nm thick QDisk sample in Figure 3.2.7.5. Luminescence between 3.5 eV (GaN NBE) and 4.6 eV (AlN deep defect) seems to originate from areas corresponding to QDisks, which is consistent with observations made in temperature-dependent macro-PL. Similarly to the case of macro-PL broad emission, the difference of emission energy range between the two NWs is assigned to disparity on both disk thickness and AlN molar fraction from one NW to another one. It must be noted that CL spectra exhibit several lines much broader than those obtained in µ-PL, which is attributed to the different excitation nature and the lower CL setup resolution.

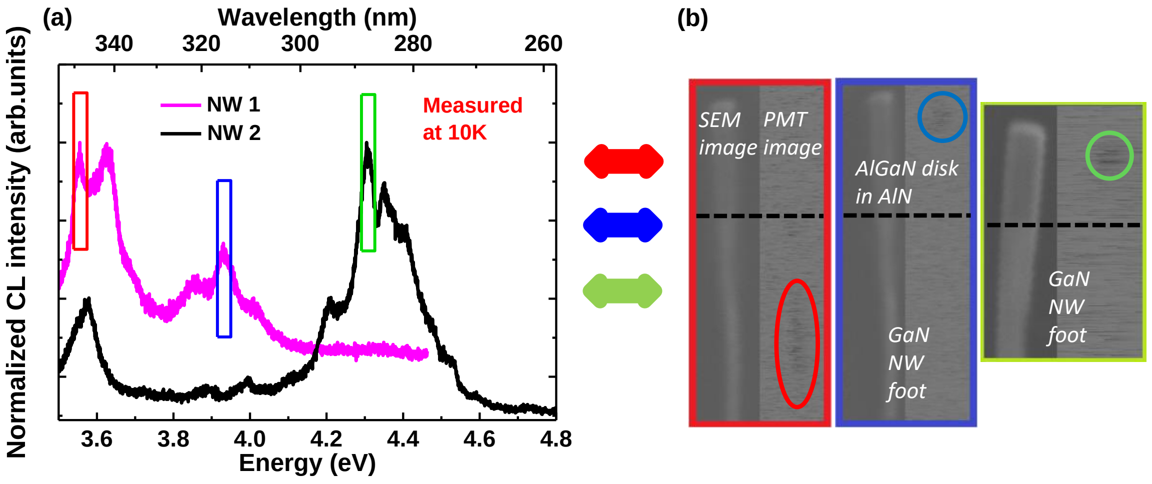

Figure 3.2.7.5: (a) CL spectra recorded at 10 K for two single NWs with an AlGaN/AlN QDisk (sample N2270). (b) SEM image on left and corresponding PMT image on right, for each rectangular frame in Figure (a). The oval/circular frames surround the luminescence visible on the PMT image and correspond to the rectangular frames of the same color in spectra of Figure (a), whereas the dashed black lines underline the separation between the GaN NW base and the AlGaN/AlN QDisk on both SEM and PMT images.

The red and blue frames are respectively related to emission close to the GaN bandgap (corresponding to the GaN NW base) and above the bandgap (around 3.9 eV and corresponding to the AlGaN QDisk area), for NW 1. Regarding NW 2, the green frame is related to emission above the bandgap (around 4.3 eV and corresponding to the AlGaN QDisk area).

Similarly to the case of longer AlGaN NW sections investigated in Subpart 3.2.5, power-dependent µ-PL measurements were also carried out on QDisk samples excited with the 244 nm CW laser, in order to probe biexciton emission more easily. Given that the number of µ-PL lines is proportional to the AlGaN volume, as explained in Subpart 3.2.2, we mainly investigated the 2 nm thick QDisk sample ($x_{Al} = 0.4$). Typical power-dependent µ-PL spectra presenting three main peaks are shown in Figure 3.2.7.6 (a). The latter spectra are fitted with four Lorentzian functions for practicality, rather than Pseudo-Voigt ones converging less easily: three for the main lines and a wider fourth one for the shouldering present at lower energies, as shown in Figure 3.2.7.6 (b). These four lines fit very well the spectra on the whole, except a slight shouldering appearing on the spectrum recorded at the highest excitation power (1 mW). When considering the maximum intensity of fitting lines, a superlinear dependence on the excitation power for line 2 (emission around 4.255 eV) and a linear trend for the three neighboring lines (line 1 emitted at 4.266 eV, line 3 at 4.242 eV and line 4 at 4.233) can be observed in Figure 3.2.7.7 (a). Indeed, linear fits carried out on log scale curves give slopes of 1.12, 1.57, 0.93 and 0.95 respectively for line 1, line 2, line 3 and the line 4. The trend is even clearer when considering the integrated line intensity, as shown in Figure 3.2.7.7 (b): the slopes resulting from linear fits give slope of 0.89, 1.79, 1.08 and 1.08, respectively from line 1 to line 4. As exhibited in Figure 3.2.7.8, no emission blue-shift is evidenced for all the lines when increasing excitation power.

Indeed, the energy gap between line 1 and line 2 remains equal to about +11 meV, whereas the other energy differences are negative and remain of the order of -13 meV and -22 meV respectively for line 3/line 2 and line 4/line 2 couples, whatever the excitation power in Figure 3.2.7.8. Consequently, the line 1/line 2 couple corresponds to the exciton/biexciton emission more likely than the other ones, since the related biexciton binding energy is expected to be positive. Indeed, the QCSE is negligible in view of power-dependent µ-PL experiments, as expected in our thin QDisks, while positive biexciton binding energies for QD-like centers in longer NW sections without extra quantum confinement were observed in Subpart 3.2.5. Two main points are subjects to debate: first, this value of +11 meV seems rather low in view of the additional quantum confinement, but not inconsistent since the latter is likely not to be very strong for a 2-2.5 nm thick disk and linear interpolation between the biexciton binding energy values for bulk binaries leads to +12 meV for bulk $Al_{0.4}Ga_{0.6}N$. Second, the maximum intensity of the biexciton line is already superior to the one of the exciton line at the lowest investigated excitation power (30 µW), which may seem strange. However, it must not be forgotten that such power already corresponds to significant power density in view of the spot size. In addition, when considering the evolution of integrated intensity, the latter is first higher for the exciton line, before observing a crossing around 60 µW.

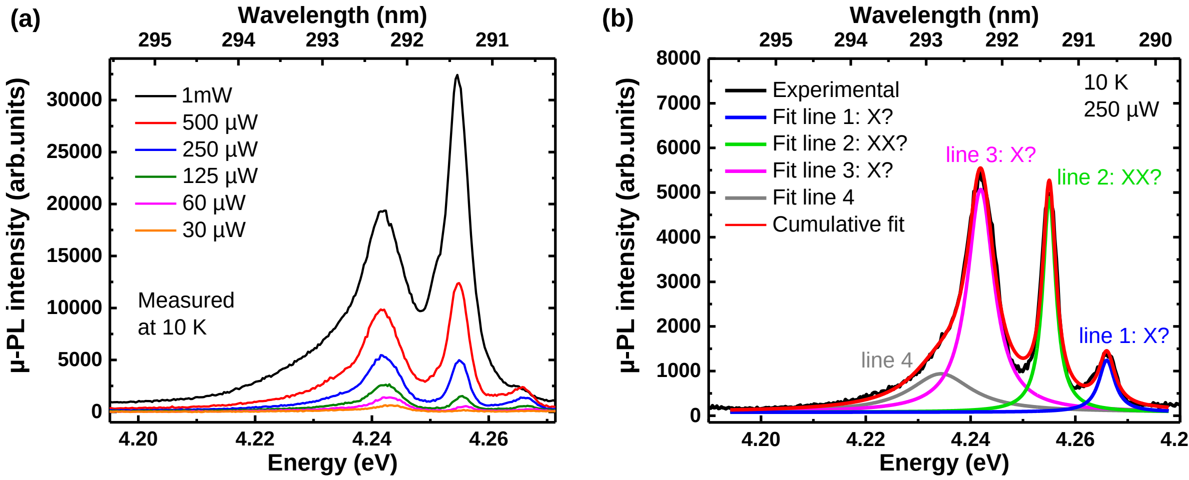

Figure 3.2.7.6: (a) Power-dependent (power given in legend) µ-PL spectra recorded at 10 K for lines emitted by a thin (2 nm thick) AlGaN disk in AlN (sample N2270). (b) Fit performed with 4 Lorentzian for the spectrum recorded at 10K, 250 µW.

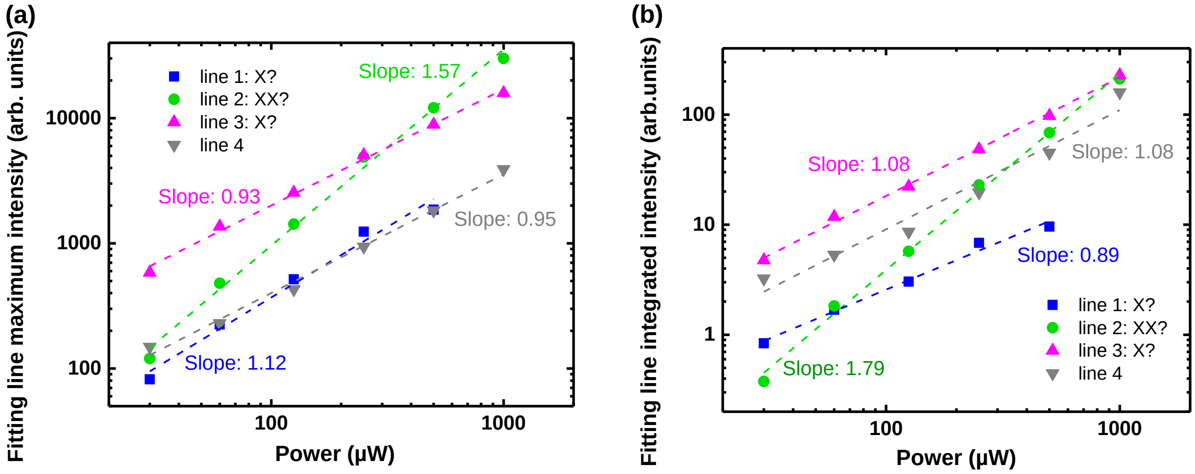

Figure 3.2.7.7: (a) Maximum intensity versus excitation power, both on logarithmic scale, for the four fitting lines of Figure 3.2.7.6. Linear fits (dashed lines) on logarithmic scale give slopes of 1.12, 1.57, 0.93 and 0.95, respectively from line 1 to line 4. (b) Integrated intensity versus excitation power for the four fitting lines of Figure 3.2.7.6. Linear fits on logarithmic scale give slopes of 0.89, 1.79, 1.08 and 1.08, respectively from line 1 to line 4, confirming the trend exhibited in (a). The evolution of line 2 (green) with power is much more quadratic than linear and thus consistent with biexcitonic emission. Both line 1 (blue) and line 3 (magenta) could correspond to the related excitonic emission, in view of slope values.

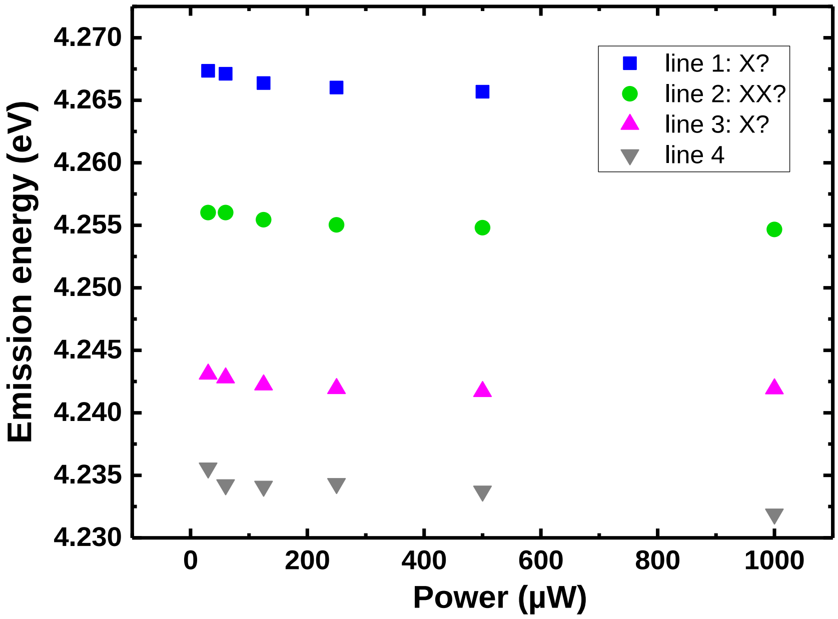

Figure 3.2.7.8: Line emission energy versus excitation power, for the four fitting lines. No significant shift, especially towards blue, is observed.

3.3 Additional discussion, conclusion and prospects of the chapter

3.3.1 Macro-structural properties of AlGaN nanowire sections.

In summary, the experimental data reported in Subpart 3.1 established that a compromise must be found on growth temperature for AlGaN NW sections grown in N-rich conditions, with the view of making emitting devices based on them. Indeed, decreasing temperature allows us to reduce the length of the unwanted Al-richer section, which preferentially nucleates on top of the GaN template and would act as detrimental carrier blocking layer in a LED, but may degrade the macro- structural and optical properties of the AlGaN NW section. In view of the unfavorable GaN/AlN lattice mismatch, these sections are unlikely the result of elastic energy minimization. The significant decrease in the length of the latter, when lowering its growth temperature, rather supports the model previously reported suggesting a growth mechanism driven by kinetic parameters [139, 321, 322].

In addition to the decrease in substrate temperature, it must be stressed that various tries were unsuccessfully performed to completely remove this parasitic Al-richer section. Ga adatoms were notably accumulated at the end of the GaN NW template growth before opening the Al and N cell shutters to grow AlGaN, in order to create a significant Ga reservoir on NW tops and favor their direct incorporation. We also widened the GaN NW base tops, by lowering the substrate temperature and increasing the Ga flux to promote radial growth as described in Subpart 2.1.3.1, before starting to grow AlGaN, in order to alter strain relaxation mechanism in NWs and probe for possible dependence of Al-richer section nucleation on such mechanism. In the case of NW broadening small enough to avoid substantial NW coalescence, no noticeable difference on the Al-richer section length with respect to the one for non-widened NWs has been observed on dispersed NWs in STEM so far. In the perspective of elaborating Al-rich AlGaN UV-LEDs, it would be interesting to attempt to grow AlGaN sections on even wider GaN templates, in spite of more significant coalescence, in order to get closer to the 2D case for which this Al-richer section has never been reported.

Interestingly, the scarce literature in the field also reports cases of AlGaN NWs grown in conditions very similar to ours and for which the Al-richer section is missing, making a full understanding of its formation still obscure at this stage [175, 325]. In order to make it clearer, atomistic simulations considering an AlGaN/GaN NW heterostructure and taking the system geometry, chemical considerations and strain relaxation mechanism into account are planned in a near future, as part of one of the next team projects.

3.3.2 Micro-optical properties of AlGaN nanowire sections.

To sum up, a significant spectral density of sharp emission lines was first evidenced through optical characterization of single dispersed AlGaN NW sections grown by MBE and further attributed to compositional inhomogeneities at small scale in such sections. Antibunching was observed at low excitation powers for these lines, showing that the AlGaN alloy in NWs behaves as a collection of Ga-rich localization centers acting as QDs [417], in absence of the well-known compositional fluctuations associated with extended defects in 2D AlGaN layers [449, 450]. Such behavior is supported by a few power-dependent µ-PL results consistent with biexcitonic emission. More statistics on related biexciton binding energy, measured over wider emission energy range, would be needed to go even further.

We note that in a simple PL experiment we can easily probe a single NW with a very low volume (typically 10^{-3} μm^3 or less) of high quality AlGaN alloy, while probing such a low volume in a thin film would require the use of either near-field optical spectroscopy or highly complex patterning techniques to isolate a film volume close to those of NWs. Then our result provides a clue that localization centers in AlGaN are of intrinsic origin, different for instance of those associated with Ga segregation in grain boundaries as observed in 2D layers [451, 452]. By probing many individual lines in µ-TRPL, we have then shown that the various localization centers in AlGaN NW sections are quite homogeneous in size.

As reported in several works [139, 175, 321, 322, 324, 327] through macro-PL experiments, tuning the growth kinetic parameters fixing the average Al composition within the alloy, namely metallic fluxes and growth temperature, of AlGaN NWs shifts their emission energy and impacts their linewidth. However, over shared emission wavelength range, the µ-optical properties of alloy fluctuations are similar, whatever the growth conditions explored in this study. Indeed, around a given emission wavelength, the lifetimes and linewidths related to probed µ-PL sharp lines were observed not to vary much, just as the evolution of these lines with sample temperature. Consequently, it can be inferred that Ga-richer regions emitting at a certain wavelength and exhibiting similar µ-optical properties can be obtained over a wide range of growth kinetic parameter values, opening the way to carrier localization engineering. The latter would require atomistic simulations to derive the electronic structure obtained for various atomic configurations within the AlGaN alloy inducing the sharp lines observed in µ-PL spectra. Such simulations are considered as well, as part of one of the next team projects. In addition, it would be interesting to explore even broader value ranges for AlGaN growth kinetic parameters, especially metallic fluxes. In the present work, we mostly used effective III/N flux ratios over the 1/2-1 range for the alloy in order to ensure fast enough growth of well-separated NWs, whatever the growth temperature. Increasing (respectively decreasing) the latter ratio above (respectively below) the latter range, for a fixed growth temperature, should favor the growth of more homogeneous (respectively inhomogeneous) alloy, as reported recently [175].

Even in very small quantity of AlGaN material such as AlGaN/AlN QDisks as thin as 2 nm, compositional fluctuations associated with carrier localization were evidenced, similar to those highlighted in longer AlGaN NW sections: comparable sharp lines, signs of biexcitonic emission, etc. More statistics on related biexciton binding energy, measured over wider emission energy range, would be required to go even further, as already mentioned for long AlGaN sections. In the case of QDisks, the issue is even more complex since two "scales" of confinement are entangled: a weaker one related to Ga-richer regions and another one intrinsic to the disk/barrier quantum structure. Decorrelating both contributions is not trivial, since the Al composition profile must be accurately known within the QDisk region in order to quantify the quantum confinement, as well as possible QCSE, induced by the QDisk properly and separately from smaller potential fluctuations induced by compositional inhomogeneities. Additional experiments, especially higher resolution electron microscopy techniques (HR(S)TEM combined with EDX), are needed to go further.

At this stage, we may question the origin of the small-scale fluctuations responsible for carrier localization in AlGaN NWs. These fluctuations could result from the presence of an Al-rich shell around AlGaN NWs, which is a consequence of the relatively small Al diffusion length along the NW m-plane with respect to the Ga one and likely contributes to strain building-up in the AlGaN core as previously observed in the extreme case of GaN/AlN core/shell NW heterostructures [103, 269]. Although experimental evidence is still missing, we tentatively suggest that such a strain induced by the formation of the AlN-rich shell around the AlGaN NW section could play a role in a local chemical ordering, similar to the case of InGaN/GaN core/shell NWs [453, 454]. Resonant XRD experiments were recently performed on AlGaN NWs to acquire short-range structural information and to support or invalidate the latter assumption. Preliminary results of these experiments are provided in Annex 2.

4. Another step towards UV-LEDs: study of $Al_xGa_{1-x}N$ nanowire pn junctions

4.0 Introduction

In addition to the fundamental properties of NID AlGaN NWs, those of their intentionally doped counterparts must be better understood in order to fully master both the emission and electrical injection of AlGaN NW-based optoelectronic devices such as UV-LEDs. As already mentioned in Subpart 0.2, $Al_xGa_{1-x}N$ NW LEDs relying on p-i-n junction structures [77-82] or polarization-induced doping supplemented with dopant incorporation [83, 93, 94] were demonstrated, operating for some of them at room temperature and even reaching IQEs up to 80% for AlN NW p-i-n devices [78]. However, the full understanding of their operation is still unclear, especially regarding the incorporation and activation of dopants in AlGaN and AlN NWs, the literature about the latter remaining scarce.

In the 2D case, works are much more numerous. The most commonly reported doping agents for n- and p-doping in $Al_xGa_{1-x}N$ are respectively Si and Mg, due to their large availability as well as their lower formation and ionization energies than those of other possible dopant species [128, 134]. It must be noted that, when only taking energetic considerations into account in the case of p-doping, Be is more suited than Mg but can incorporate as well on interstitial sites due to its too small atomic radius and then acts as a double donor [134]. In the following, we will mainly focus on the Si and Mg dopants that we used in this PhD work. Theoretical and experimental values for impurity donor and acceptor formation and ionization energies can be found in the literature for the following doped WZ nitrides: Si-GaN [134, 455], Mg-GaN [134, 456, 457], Si-AlN [128, 458-460], Mg-AlN [128, 379, 380, 456, 459], Si-AlGaN [461-465] and Mg-AlGaN [462, 465-467].

For a given AlN molar fraction x, n-doping of $Al_xGa_{1-x}N$ layers is easier to perform than p-doping, given the lower formation and ionization energy for the Si donor compared to the Mg acceptor. It must be also reminded that undoped $Al_xGa_{1-x}N$ is intrinsically of n-type, due to the incorporation during growth of V_N defects or O_N impurities acting as donors. In addition, complexes can form during growth between impurities and dopant species, especially Mg-H complexes which can make the p-dopants optically and electrically inactive [21, 468]. However, the binding energy of these Mg-H complexes remain low (0.7 eV in GaN for electrically neutral complexes [134]), so that they can be dissociated through post-growth thermal annealing in order to activate the Mg dopants [466, 469, 470]. The two latter phenomena highly depend on the used growth method: residual oxygen and hydrogen impurities are much less present within MBE chambers under UHV than for MOVPE or

HVPE growth technique using oxygen and/or hydrogen compounds. Consequently, post-growth thermal processes are much more needed in the latter case [471, 472].

When increasing x within $Al_xGa_{1-x}N$ films, doping becomes more challenging. Indeed, regarding n-doping, the Si donor ionization energy first increases with AlN molar fraction (from about 25 meV to 86 meV for x varying from 0 to 1 [463]), the Si-related energy levels being deeper in AlN than in GaN. Moreover, the density of defects compensating the free electrons also increases with Al content within the alloy, complicating n-doping even more [473-476]. As for p-doping, the issue is even more problematic, since the Mg acceptor ionization energy varies from around 225 meV for GaN [134, 457] to about 510 meV [128, 379] for AlN. In addition, similarly to electron compensation resulting from Si-doping, free hole compensation effects were also reported for Mg-doped $Al_xGa_{1-x}N$ films [380, 477]. Therefore, only a very small fraction of the Mg acceptors are ionized at room temperature in the latter layers. For both doping types, various approaches have been explored for AlGaN 2D layers in order to cope with the latter issues, including growth of $Al_xGa_{1-x}N/Al_yGa_{1-y}N$ superlattices [478], δ-doping [479], polarization-induced doping [480-482], UV-illumination during growth [483] and atomic flux ratio optimization [484].

In the case of $Al_xGa_{1-x}N$ NWs, doping is expected to be easier than for 2D layers. Indeed, a decrease of donor and acceptor formation energy is likely to occur in such NWs, as theoretically shown for InN [485, 486] and AlN [78] NWs (see Figure 4.0.1 (b) and Figure 4.0.2 (b) & (c)). Moreover, due to the large amount of free surfaces in NWs, relaxation of elastic strain induced by the presence of dopants is facilitated, making their incorporation easier while avoiding/reducing the formation of extended defects usually observed in the 2D case (dislocations [487, 488], cracks [488, 489], pyramidal defects [490, 491]) resulting from or being amplified by this incorporation. Both phenomena may lead to an increase in the Si solubility limit within $Al_xGa_{1-x}N$ NWs, as shown recently for Si-doped GaN NWs [425, 492, 493]. Indeed, in the latter case, atomic concentrations of 2.5 10^{20} atoms.cm^{-3} [425, 493] (see Figure 4.0.1 (a)) and 9 10^{20} atoms.cm^{-3} [492] were found, which is well above the theoretical limit of 5 10^{19} at.cm^{-3} [494]. Easier Mg incorporation in $Al_xGa_{1-x}N$ NWs is also expected, similarly to Mg-doped GaN NWs demonstrated to exhibit atomic concentrations by far superior to their 2D counterparts [492]. For both doping types, NW morphology and typical diameter can also change upon significant enough doping concentration [364, 425, 492, 493]. For instance, heavily Si-doped GaN NWs grown by MBE are much broader than their NID counterparts and exhibit a 12-fold symmetry top facet instead of the 6-fold one usually observed [425].

Nonetheless, dopant incorporation is far from being homogeneous along the NW radius. Indeed, Si dopants were shown to segregate in the periphery of GaN NWs [425, 492, 493], as depicted in Figure 4.0.1 (a). The same trend is also expected for Mg species, knowing that Mg was observed to segregate near surface in Mg-doped GaN films [495, 496] and in view of ab initio simulations [78, 486] performed for InN and AlN NWs, as illustrated in Figure 4.0.2. This results in variation of electrical properties along the NW radial direction, in addition to those induced by compositional fluctuations inherent to the AlGaN alloy, especially along NW growth axis, as reported in InGaN NWs [497]. Another downside is that the ionization energy of donors and acceptors can be higher in NWs than in the bulk case, leading to a decrease in doping efficiency, as shown in Figure 4.0.1 (c) [498]. However, this effect is expected to be detrimental in the case of NWs much narrower than ours exhibiting strong dielectric confinement, such as those described in Subpart 1.2.3.3.

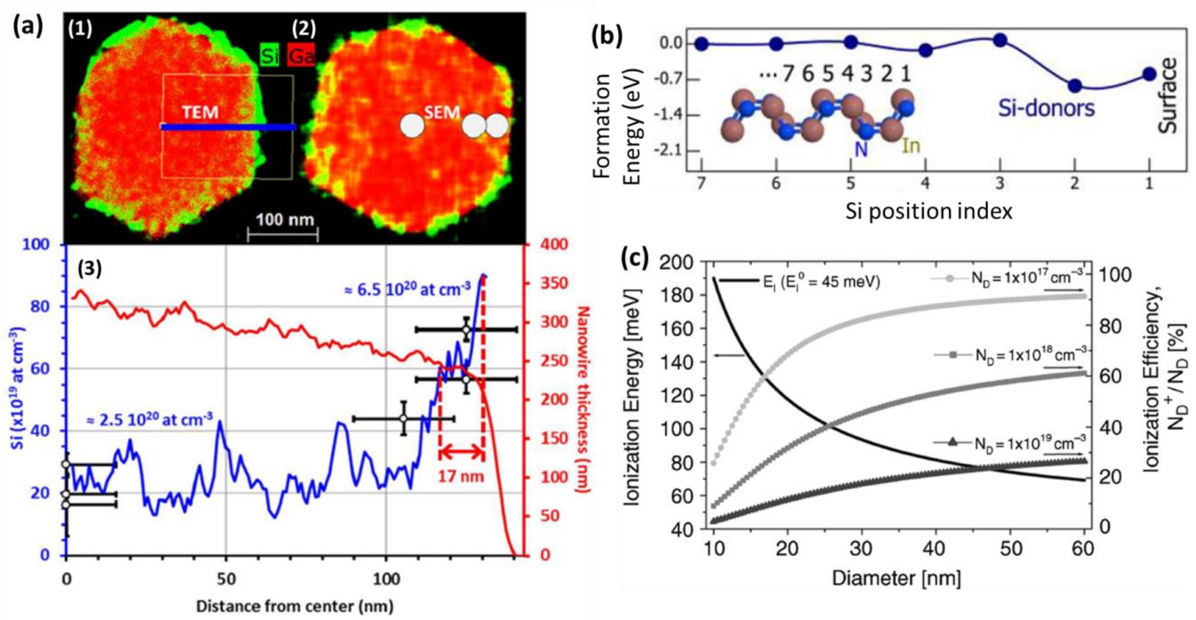

Figure 4.0.1: (a) EDX maps (1) and (2) of two highly Si-doped GaN NWs. Si and Ga elements are highlighted in green and in red, respectively. Atomic concentration data in (3) correspond to the blue line in (1) and white dots in (2). Taken from [425]. (b) Ab initio calculation showing that the formation energy for In-substitutional Si doping near the InN m-plane surface is significantly lower than that in the bulk. Taken from [485]. (c) Ionization energy and ionization efficiency for P impurities in Si NWs as a function of the NW diameter. Taken from [498]. Curves would exhibit similar shapes and would be shifted towards smaller diameters (towards left) in the case of nitride NWs (notably due to the smaller carrier Bohr radius in nitrides than in Si).

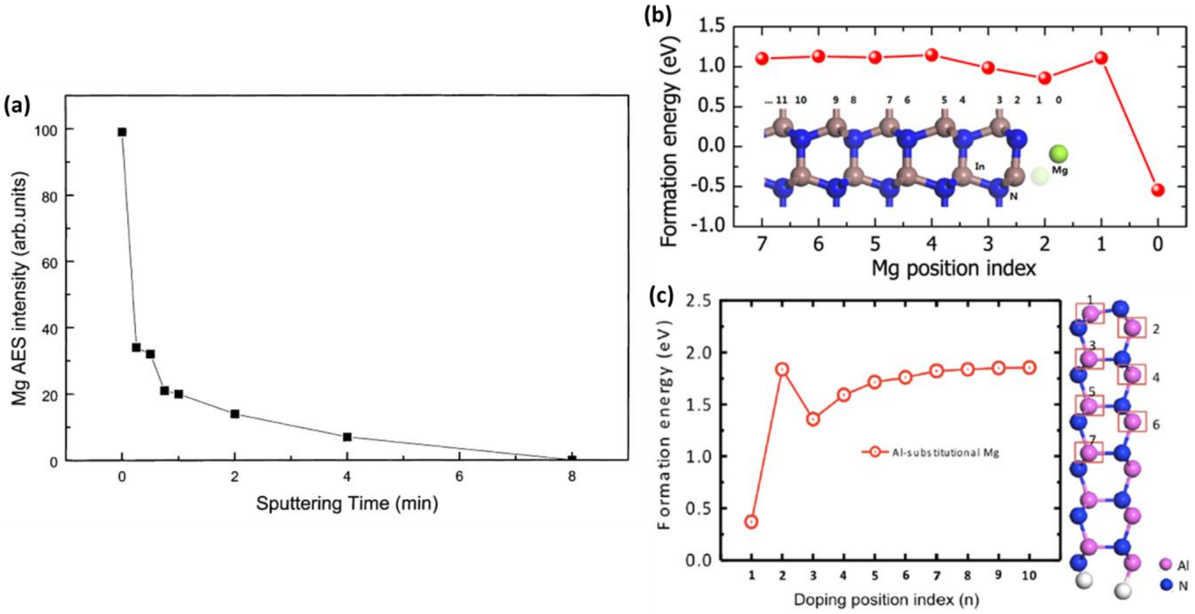

Figure 4.0.2: (a) Auger electron spectroscopy depth profile of Mg distribution in the surface region of the Mg-doped GaN. The sputtering time is related to depth by a sputtering rate of 20 nm/min. (b) In-substitutional Mg acceptor formation energy near surface along the NW radial direction. Index 0 is the closest position to NW surface. (c) Al-substitutional Mg formation energy along the nanowire radial direction. Index 1 indicates the surface. In both cases, the formation energy is lower significantly near surface, and the structure used for ab initio calculations is sketched.

In the following, doped AlGaN and AlN NWs, especially NW pn junctions, will be investigated. We will first present the studied samples, before getting to the details of the structural and optical characterization results.

4.1 Growth conditions of investigated doped $Al_xGa_{1-x}N$ and AlN nanowire samples

For our experimental needs, a few series of samples, consisting of long doped $Al_xGa_{1-x}N$ NW sections on top of n-doped GaN NW templates, were grown in N-rich conditions using the PA-MBE setup detailed in Subpart 2.1.1. Only Si and Mg dopants were used to perform respectively n-doping and p-doping. The doped sections were mostly pn junctions, the p-doped AlGaN part being grown last in this case. Each doping type section was at least 500 nm long, which was required for some of the performed experiments (μ-Raman and KPFM) in view of their instrumental resolution and/or the expected evolution of band structure along NW junction axis. Adopted growth conditions mostly resulted in pn junction length of the order of 1.5 μm. For a given NW pn junction sample series, atomic fluxes were set to the same values so that the nominal AlN molar fraction x was fixed (over the 0.35-1 range), whereas growth temperature was varied over the 780-920°C range depending on the targeted x and the doping type. At low enough substrate temperatures, the length of Al-richer sections preferentially nucleating on top of GaN templates is expected to be low, as seen in chapter 3, and Mg incorporation is expected to be significant, due to limited Mg surface desorption, as reported in other works [78, 81, 493]. In addition, a few reference samples, either only n-doped or only p-doped or NID, were grown as well for some of the investigated junction AlN molar fractions. The GaN NW templates, for which growth is presented in Subpart 2.1.3, were self-nucleated at substrate temperatures as high as possible in order to lower NW density and avoid coalescence as much as possible, which was not trivial at all in view of required NW length and NW broadening which may result from lower growth temperature and/or from dopant incorporation. After nucleation, the substrate temperature could be lowered a bit to limit Ga desorption and to reach higher GaN NW axial growth rates. These templates were typically 40 nm $\pm$ 15 nm wide and their length could abruptly vary along the substrate radius, from a few hundreds of nm in the hotter areas to more than 1.0 - 1.5 µm out of them. The latter observation was expected given the extremely high substrate temperatures used for GaN NW growth (see Figure 4.2.2.2 for instance).

The metallic fluxes were calibrated using both the RHEED-based method and the additional NW marker technique, respectively presented in Subparts 2.1.2.3 and 2.1.4.2, whereas the N flux was kept identical all the time (same parameters for the used N plasma cell). For growth of long doped AlGaN NW sections, the effective NW growth rates estimated for GaN and AlN with the marker technique were fixed in function of the desired nominal AlN molar fraction and such that their sum was inferior to stoichiometry in order to limit coalescence resulting from NW broadening, especially when growing at lower temperature, while maintaining growth rates high enough in order to keep reasonable growth duration. Knowing also that Mg was shown to incorporate more significantly when lowering metallic fluxes for AlN NWs [78], the effective III/N ratio was typically set over the 1/2-2/3 range. Regarding GaN NW templates, they were grown using a typical Ga/N ratio equal to 1/3 and estimated from RHEED-based calibration. It must be noted that we used the plasma cell allowing a maximum growth rate of about 0.25 ML/s for all the samples presented in the following: therefore, the related growth runs lasted very long (of the order of 15-20 hours for pn junction samples). As for dopant atomic fluxes, they were set based on another work reported for GaN NW grown on our setup [425, 493], : typical effusion cell temperatures of 900°C and over the 220-250°C were mostly used respectively for Si and Mg cells, leading to carrier concentrations of the order of 5.10^{18}-10^{19} cm^{-3} for Si-doped GaN NWs grown at high substrate temperatures (corresponding t_{des}^{Ga} over the 3-7 s range) [425] and over the 10^{17}-10^{18} cm^{-3} range for Mg-doped GaN NWs depending on their growth temperature (corresponding t_{des}^{Ga} over the 3-20 s range) [493]. The Si cell temperature was not set higher than 900°C in order to avoid significant broadening observed for GaN NWs when using higher Si atom flux [425], whereas the Mg cell temperature was fixed high enough to ensure significant Mg incorporation, as observed for GaN NWs [493]. During any growth run, the substrate was continuously rotated to promote growth homogeneity, since the flux incidence angles were not equal to 0, as previously mentioned in Subpart 2.1.

Regarding substrate temperatures T_{subs}, they were set, depending on our experimental needs, by measuring before each growth, when possible, the corresponding Ga desorption times t_{des}^{Ga} following the exposure of the Si (111) wafer surface to Ga flux in order to ensure reproducibility, as presented in Subpart 2.1.2.2. For this purpose, the Si substrates had to be deoxidized before their introduction in the MBE chamber and outgassed once mounted inside until the appearance of the 7x7 Si (111) surface reconstruction, as detailed in Subpart 2.1.2.1. GaN NW templates were grown on a thin AlN buffer (about 3 nm thick) in order to improve the NW orientation and reduce the NW nucleation time compared to growth on bare Si. In view of the very high substrate temperatures used to grow GaN NWs (of the order of 890-900°C, in others words $t_{des}^{Ga} < 3$ s), nucleation of the latter was typically of the order of 1h-1h30 when grown on AlN buffer. As for the 780-920°C range used to grown AlGaN, it corresponds to t_{des}^{Ga} over the 2-60 s range. It must be noted that the MBE oven round filament was replaced by a flat one (inducing a more abrupt temperature gradient along wafer radius), between growth of samples N2531 and N2535.

Table 4.1.1 provides the list of samples from the series investigated in the following, recapitulating for each one the main growth parameters and dimensional features.

Sample		n- $Al_xGa_{1-x}N$		p- $Al_xGa_{1-x}N$		Structural parameters	
Reference number	Nominal x_{Al} (%)	t_{des}^{Ga} (s)	T_{Si} (°C)	t_{des}^{Ga} (s)	T_{Mg} (°C)	Average top radius (nm)	Hollow NW population (%)
N2495*	0	3.5	900	14	220	-	-
N2518	35	10	900	60	220	110	-
N2520	35	10	900	20	220	90	-
N2540	35	10	NID	-	-	62	-
N2547	35	10	900	10	220	70	-
N2555	35	10	900	-	-	49	-
N2561	35	-	-	10	220	55	-
N2549	60	10	NID	-	-	70	-
N2551	60	10	900	10	220	49	-
N2569	75	20	900	10	220	117	-
N2577	75	20	NID	-	-	coalescence	-

Table 4.1.1: part 1 (AlGaN samples).

N2577	75	20	NID	-	-	coalescence	-
Reference number	Nominal x_{Al} (%)	t_{des}^{Ga} (s)	T_{Si} (°C)	t_{des}^{Ga} (s)	T_{Mg} (°C)	Average top radius (nm)	Hollow NW population (%)
N2524	100	3	900	10	220	150	96
N2527	100	3	900	3	220	100	63
N2531	100	2	900	2	220	105	53
N2535	100	2	NID	-	-	87	17
N2538	100	2	900	2	250	87	5
N2541	100	2	900	10	250	90	33

Table 4.1.1: part 2 (AlN samples). For both table parts, the main growth parameters of interest are provided for the various investigated samples of the series: nominal AlN molar fraction x_{Al}, n- and p- $Al_xGa_{1-x}N$ growth temperatures (t_{des}^{Ga}), as well as dopant cell temperatures. The pn junction samples are labeled in red the first column, the NID reference samples in green and other doped references in blue. Some structural parameters such as average top diameter (p-part) for all samples and hollow NW population (defined in the next subpart) for AlN NWs are also provided. *: sample N2495 details and characterization can be found in another work [493].

Directly after growth, basic macro-characterization experiments, namely SEM (see Subpart 2.2.1.1), XRD (see Subpart 2.2.2) and CW macro-PL (see Subpart 2.3.1.1) experiments were systematically performed, in this order for almost all as-grown samples. Common µ-characterization experiments on dispersed NWs such as STEM (see Subpart 2.2.1.2) or EDX (see Subpart 2.2.1.3) experiments were also carried out for well-chosen samples.

4.2 Structural properties of $Al_xGa_{1-x}N$ nanowire pn junctions

4.2.1 Highlighting AlGaN nanowire pn junctions through structural characterization

First, electron microscopy was used to evidence specific features peculiar to AlGaN NW junctions. Figure 4.2.1.1 provides typical side-view and top-view SEM images of several AlGaN NW pn junction samples grown with the same atomic fluxes (nominal AlN molar fraction x_{nom} = 0.35 in the present case) but at various growth temperatures for the p-part. When setting low enough substrate temperatures for p-part growth, the different NW parts are well delimited, as visible in Figure 4.2.1.1 (a), (b) and in the inset framed in yellow zooming on a typical NW: a clear NW broadening can be observed from one given NW section to another. The NW top enlargement is assigned to significant incorporation of Mg atoms which are thought to preferentially segregate near NW sidewalls, as already mentioned in the introduction. In the following, the p-part growth temperature was not lowered below 800°C (corresponding t_{des}^{Ga} < 30 s) in order to avoid parasitic lateral growth such as the one highlighted by the dashed green frame. When increasing growth temperature, Mg incorporation is likely to be less significant in view of the absence of net NW top widening, as observable in Figure 4.2.1.1 (c) and supported by the values of average NW top radii provided in Table 4.1.1. Indeed, the latter values decrease from 110 to 70 nm when reducing the Ga desorption time from 60 s to 10 s. For the smallest desorption time, the enlargement with respect to NID NWs shown in Figure 4.2.1.1 (d) is even almost negligible: the average top radius for the latter NWs was estimated at 62 nm (see Table 4.1.1).

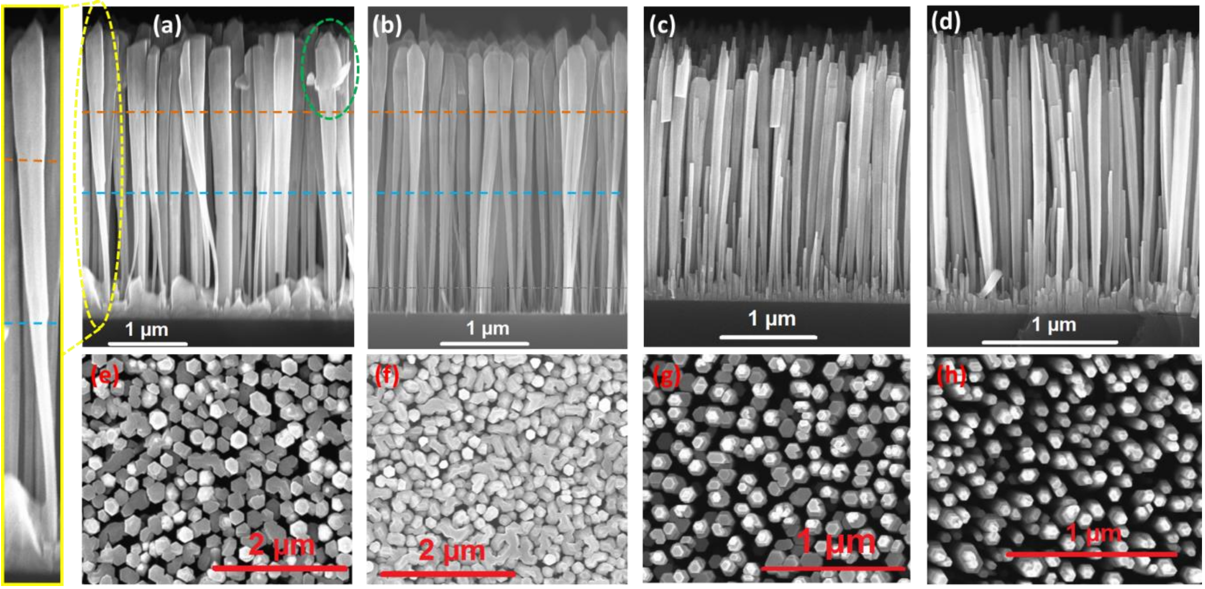

Figure 4.2.1.1: Side-view and top-view SEM images, taken in the wafer center area, of $Al_{0.35}Ga_{0.65}N$ NW pn junctions and reference grown on top of GaN NW templates in different conditions: (a) & (e) NW junction sample N2518, (b) & (f) junction sample N2520, (c) & (g) junction sample N2547, (d) & (h) NID reference sample N2540. Similar growth parameters were used for the n-part (or NID, same metallic fluxes and growth temperature corresponding to t_{des}^{Ga} = 10 s), in contrast to the p-part (see Table 4.1.1 as well): for the latter, the substrate temperature was varied over a corresponding 10-60 s t_{des}^{Ga} range ((a) & (e): 60 s, (b) & (f): 20 s, (c) & (g): 10 s). The inset framed in dashed yellow zooms over a typical NW for which transitions (NW broadening) from GaN template to n-AlGaN (blue dashed line) and from n-AlGaN to p-AlGaN (orange dashed line) are clearly visible. The NW top of image (a) framed in dashed green exhibits lateral parasitic growth resulting from too low substrate temperature.

For this $Al_{0.35}Ga_{0.65}N$ NW pn junction sample series, the temperature threshold leading to p-part significant enlargement corresponds to a Ga desorption time (measured at the wafer center) comprised between 10 and 20 s, in view of Figure 4.2.1.1 (b), (c) and Figure 4.2.1.2. The latter figure displays several SEM images taken along the wafer radius for the sample of Figure 4.2.1.1 (c) for which p-part was grown at t_{des}^{Ga} = 10 s and does not exhibit any clear broadening (sample N2547) within the wafer center area. In contrast, it can be directly seen in Figure 4.2.1.2 (c) that NW enlargement, similar to the one observed in Figure 4.2.1.1 (a) or (b) and likely resulting from enhanced Mg incorporation at lower substrate temperature, is retrieved when moving slightly out of the more homogeneous wafer center area (from 10 to 15 mm away from center).

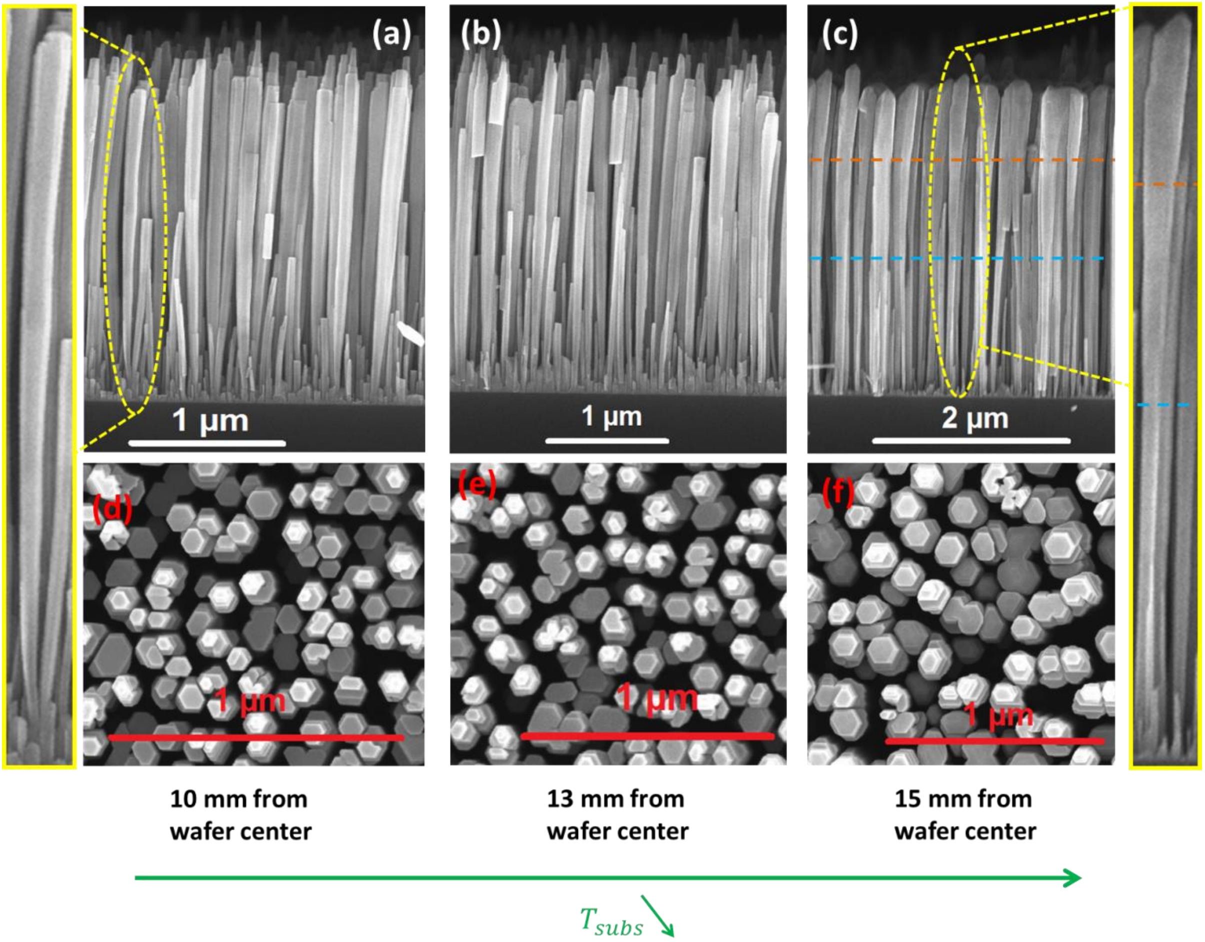

Figure 4.2.1.2: Side-view and top-view SEM images of the $Al_{0.35}Ga_{0.65}N$ NW pn junction sample displayed in Figure 4.2.1.1 (c) & (g) for which the p-part was grown at higher temperature (sample N2547, t_{des}^{Ga} = 10 s for p-part). The images were taken along the wafer radius at: (a) & (d) 10 mm from wafer center (higher substrate temperature), (b) & (e) 13 mm from wafer center, (c) & (f) 15 mm from wafer center (lower substrate temperature). The dashed yellow inset of image (a) zooms over a typical NW exhibiting no significant broadening, in contrast to the other dashed yellow inset provided in (c). Indeed, on the latter, transitions between different regions, from GaN template to n-doped AlGaN (blue dashed line) and especially from n-AlGaN to p-AlGaN (orange dashed line), are clearly visible. Similarly to samples exhibited in Figure 4.2.1.1 (a) & (b), the NW p-part broadening is likely to result from more significant Mg incorporation at low enough growth temperature.

Regarding the NW widening observed from n-GaN NW template to n-AlGaN part in Figure 4.2.1.1, it is likely to be mostly induced by non-negligible AlN radial growth rates at these substrates temperatures, rather than significant Si incorporation near NW surface. Indeed, n-doped GaN NWs grown using the same Si atomic flux did not exhibit significant enlargement with respect to NID GaN NWs [425]. It must be noted that bundling phenomena can be observed for the n-doped GaN NW bases (see for instance Figure 4.2.1.1 (a)), as previously reported [307]: when getting long enough, such templates can bend and coalesce due to electrostatic interactions between them.

Figure 4.2.1.3 (a) and (e) display typical STEM-BF and HAADF images of two dispersed $Al_{0.35}Ga_{0.65}N$ NW pn junctions grown on top of n-GaN NW bases. On all images, a chemical contrast between the Ga-richer NW core and the Al-richer shell is visible, as expected. Zoomed images provided for the first NW from Figure 4.2.1.3 (b) to Figure 4.2.1.3 (d) reveal that this shell surrounds almost the whole NW, down to the GaN NW template bottom, which may complicate electrical characterization of the AlGaN NW core in experiments such as KPFM presented further. Figure 4.2.1.3 (f) shows the transition between the n-GaN NW base and the AlGaN pn junction: the contrast difference between both parts is not marked due to the rather low Al content within the alloy. At macroscopic scale, the AlGaN junction core seems rather homogeneous given the absence of net contrast fluctuations in both Figure 4.2.1.3 (e) and (f).

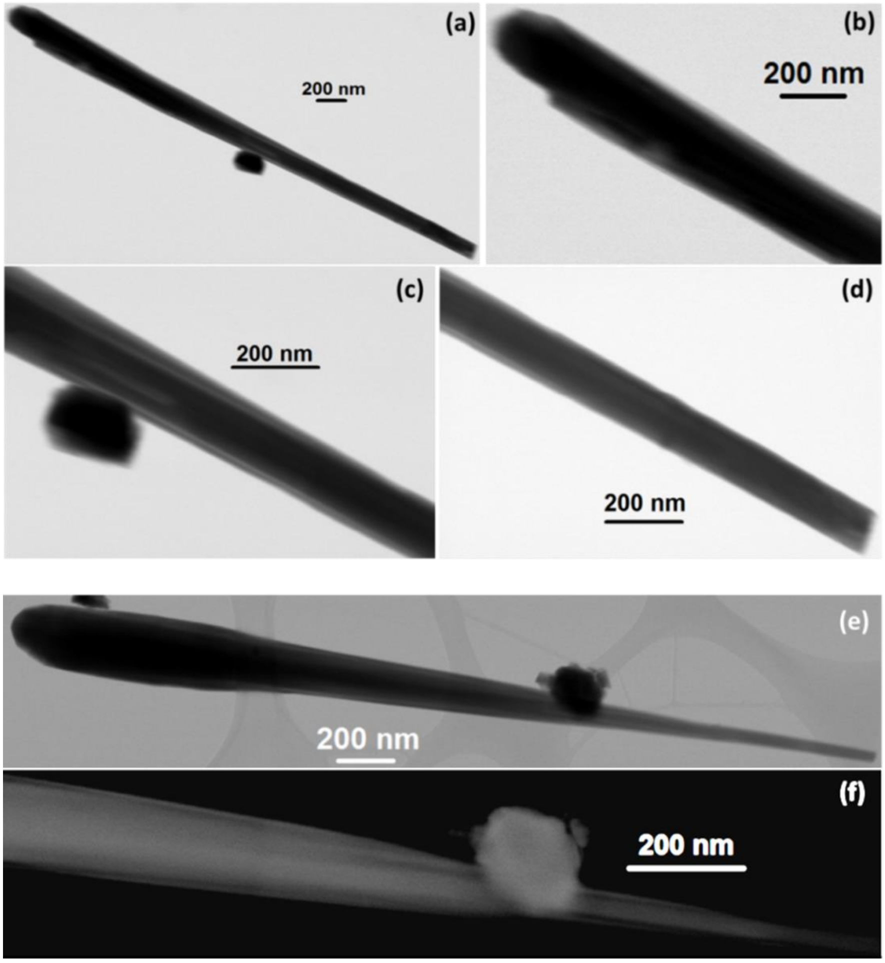

Figure 4.2.1.3: (a) STEM-BF image of an $Al_{0.35}Ga_{0.65}N$ NW pn junction grown on top of GaN NW template (from sample N2518, p-part grown at t_{des}^{Ga} = 60 s). Zoomed images were recorded along the NW, from top (b) to bottom (d). An Al-richer shell is present almost all along the NW. (e) STEM-BF image for another NW from the same sample: the different NW regions (n-GaN template, n-AlGaN, p-AlGaN on top) are clearly visible here. (f) STEM-ADF image taken around the transition from GaN template to n-AlGaN.

Quantitative EDX analysis was then carried out on AlGaN NW pn junctions grown at several AlN molar fractions. Scans along the NW growth axis and along the NW diameter were performed on a few dispersed $Al_{0.35}Ga_{0.65}N$ and $Al_{0.6}Ga_{0.4}N$ junctions, as provided respectively in Figure 4.2.1.4 and Figure 4.2.1.5. Before detailing the results, it must be mentioned that the evolution of the N/(N + metal) ratio is given for all scan profiles: the latter must remain close to 50% so that EDX quantification can be considered accurate. In addition, regarding displayed profiles of Al/(Al + Ga) ratio, i.e. Al composition, the contribution of the thin Al-richer shell wrapping the NW is not removed here so that the provided local Al compositions within the NW core are likely to be very slightly overestimated. In contrast, local compositions within the shell can be underestimated depending on the size of the electron beam with respect to the shell thickness: a slight part of the Ga-richer core may be integrated in related measurements.

First, axial and radial scans highlight respectively an Al-richer section preferentially nucleating on top of GaN NWs in the case of the Al-richer junction sample and an Al-richer shell surrounding the AlGaN core for both p- and n-parts, as expected in view of previous chapters. From the latter scans, the shell Al composition is of the order of 60% and 100% (pure AlN) for $Al_{0.35}Ga_{0.65}N$ and $Al_{0.6}Ga_{0.4}N$ NW pn junctions, respectively. As for the junction core composition, the latter is consistent with the nominal AlN molar fractions and in good agreement with average Al composition measured by XRD: 38.8% for the $Al_{0.35}Ga_{0.65}N$ NW pn junction sample (N2518) and 57.4% for the $Al_{0.6}Ga_{0.4}N$ sample (N2551) investigated here.

Furthermore, axial scans interestingly reveal 5-10% "pits" in the Al composition profiles of almost all investigated samples for which the NW p-part is significantly broadened: the Al composition decreases until the beginning of p-part growth, which seems correlated to an increase in the Al composition. The latter may decrease again when getting closer to the NW top. In the examples provided in Figure 4.2.1.4 and Figure 4.2.1.5, such "pit" is observed for axial scan positions around 1.1 µm, 2 µm, and 1.3 µm, respectively for $Al_{0.35}Ga_{0.65}N$ NW 1, $Al_{0.35}Ga_{0.65}N$ NW 2 and $Al_{0.6}Ga_{0.4}N$ NW 2, which corresponds to the transition between n-AlGaN and p-AlGaN for each case. Using EDX this time, we have just identified another feature distinguishing p-AlGaN from the n-doped AlGaN section. In the following, we tentatively suggest an explanation for the presence of such composition profile pits: along NW n-part growth axis, Ga incorporation gets progressively easier, similarly to the case of NID AlGaN NWs presented in chapter 3 or previously reported [139, 319-321, 323], leading to the decrease in Al composition in axial scan profiles. Then, when switching to the p-part growth, several assumptions, all leading to an increase in Al composition within NW pn junction tops, can be considered: first, the big Mg atoms preferentially replace Ga atoms rather than Al ones, since the Mg_{Ga} formation energy is inferior to the one of Mg_{Al} [456]. Second, such dopant incorporation may cause an increase in native defects such as cation vacancies [499, 500], particularly Ga ones: it was demonstrated that forming Ga vacancies V_{Ga} requires less energy than V_{Al} [465, 501]. Last, Mg adatoms may play a surfactant role during p-part growth, favoring Al incorporation at the expense of Ga: Mg-doping was proven to enhance axial and radial growth rate of AlN nanorods [502], whereas it was observed to reduce the growth window for GaN films [496, 503]. However, in view of the "pit" depth of the order of 5-10%, the last assumption seems more plausible, especially since the Al composition was observed to decrease after the pit, as visible for $Al_{0.35}Ga_{0.65}N$ NW 1 and $Al_{0.6}Ga_{0.4}N$ NW 2. Indeed, the latter observation is consistent with a significant accumulation of Ga adatoms which would result from both the preferential incorporation of Al ones due to Mg surfactant effect and the rather low growth temperature limiting Ga desorption, which makes Ga incorporation more probable at one point. Furthermore, the two other mentioned assumptions may contribute to the observed increase in Al composition but in a much lesser extent given the p-doping levels. It must be noted that the second possibility is the most unlikely among the three: cation vacancies and associated complexes in WZ nitrides exhibit specific and deep optical signatures [128, 134], which were not observed during optical characterization experiments presented in Subpart 4.3.

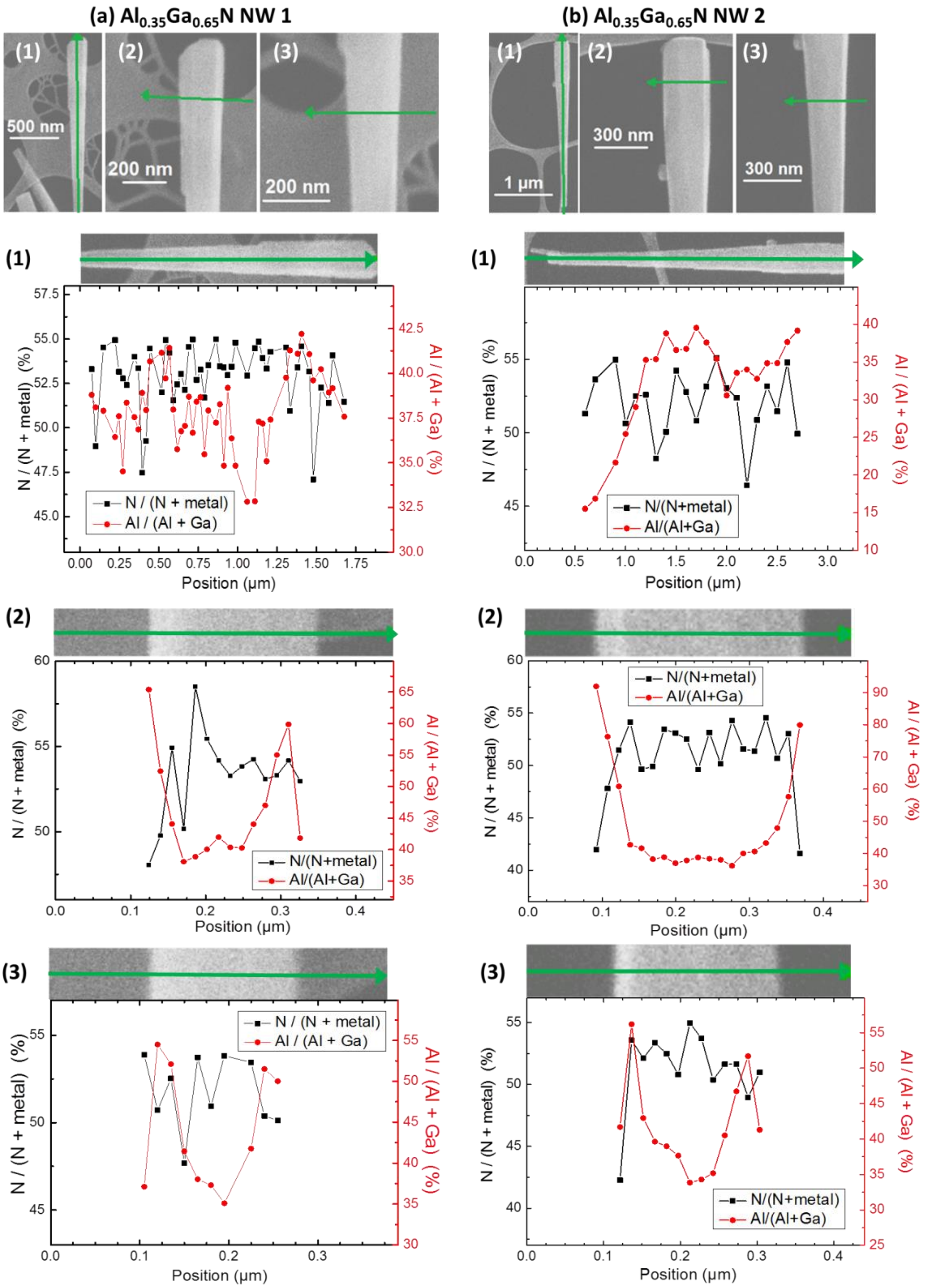

Figure 4.2.1.4: Quantified EDX analysis performed for two $Al_{0.35}Ga_{0.65}N$ NW pn junctions (a) & (b) (sample N2518, p-part grown at t_{des}^{Ga} = 60 s) along NW growth axis (1), along NW p-part diameter (2) and along NW n-part diameter (3). For each scan, experimental N/ (N + metal) and Al / (Al + Ga) ratios are displayed. The first ratio must remain around 50% in order to consider the quantification accurate, whereas the second one corresponds to the measured local Al composition (thin shell contribution not removed here). Radial scans (2) and (3) highlight the Al-richer shell and provide a rough estimation of its Al composition, whereas axial scans (1) interestingly reveal a slight “pit” in the Al composition profile, occurring at the transition between n-AlGaN and p-AlGaN region.

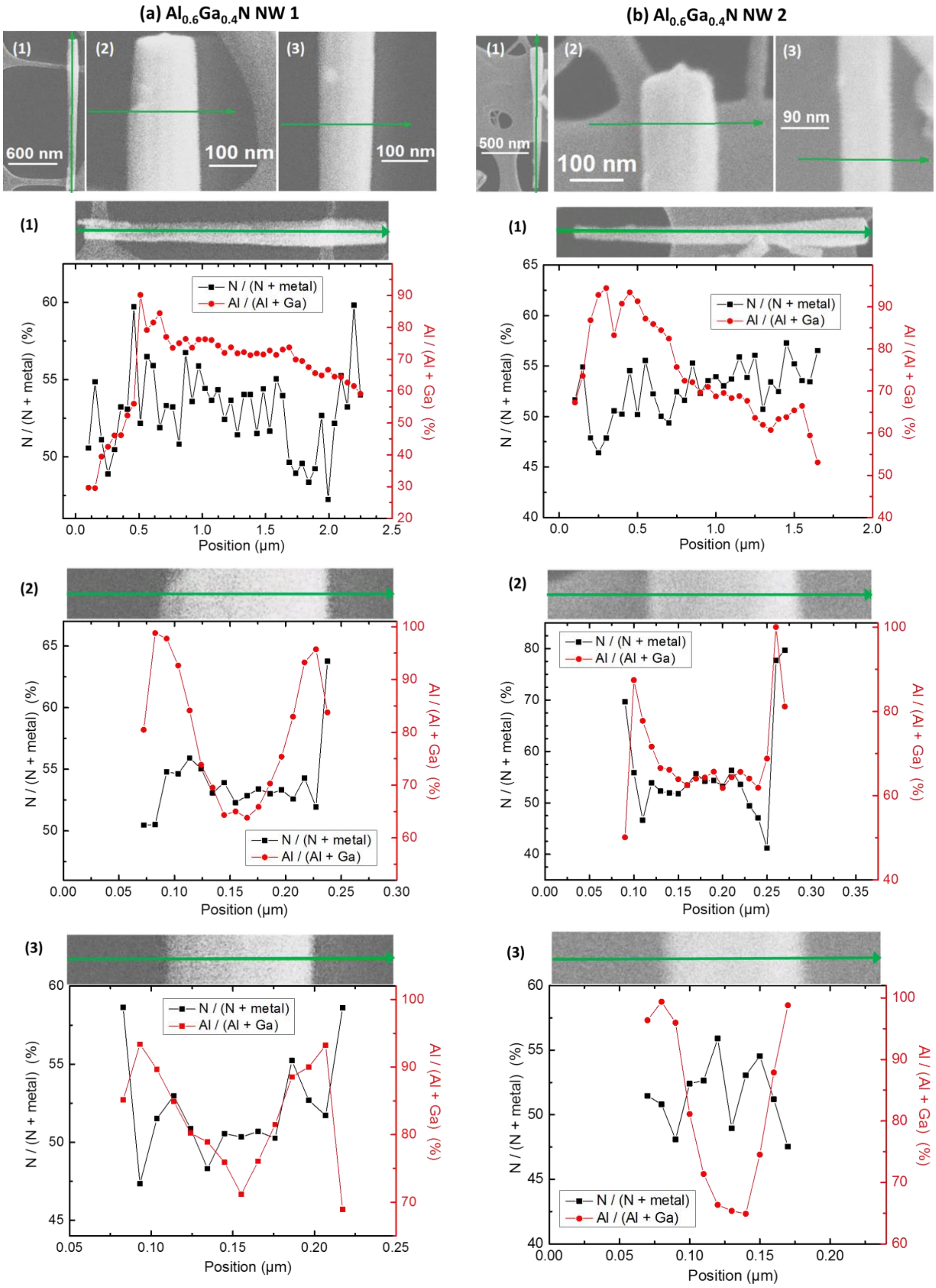

Figure 4.2.1.5: Quantified EDX analysis performed for two Al$_{0.6}$Ga$_{0.4}$N NW pn junctions (a) & (b) (sample N2551, p-part grown at t_{des}^{Ga} = 10 s) along NW growth axis (1), along NW p-part diameter (2) and along NW n-part diameter (3). For each scan, experimental N/ (N + metal) and Al / (Al + Ga) ratios are displayed. The first ratio must remain around 50% in order to consider the quantification accurate, whereas the second one corresponds to the measured local Al composition (thin shell contribution not removed here). Radial scans (2) and (3) highlight the Al-richer shell and provide a rough estimation of its Al composition, which is almost pure AlN for both NWs (a) and (b). Interestingly, axial scans (1) reveal a slight "pit" in the Al composition profile at the transition between the n-AlGaN and p-AlGaN region for NW (b), for which p-part broadening is more significant than for the other NW (a).

Using the KPFM variant of AFM structural characterization technique (see Subpart 2.2.3), we can go further than the results presented so far and electrically evidence the AlGaN NW pn junction. Such technique has been already successfully used to highlight GaN NW pn junctions [358]. When scanning along the NW axial direction from the NW top to its bottom as shown in the KPFM surface potential map of Figure 4.2.1.6 (a), a clear CPD voltage offset is visible between p-AlGaN and n-AlGaN in associated Figure 4.2.1.6 (c), highlighting for the first time an AlGaN NW pn junction through this technique. A fit with a sigmoid curve leads to an offset value of 200 meV. The evolution of height along the NW axial direction was also monitored, from the AFM topographical map provided in Figure 4.2.1.6 (b), to demarcate the AlGaN pn junction from the n-doped GaN template. Indeed, as visible in Figure 4.2.1.6 (c), the height, namely the diameter of the investigated dispersed NW, is first constant in the p-part before it progressively decreases along n-AlGaN until reaching another constant value corresponding to the GaN NW base.

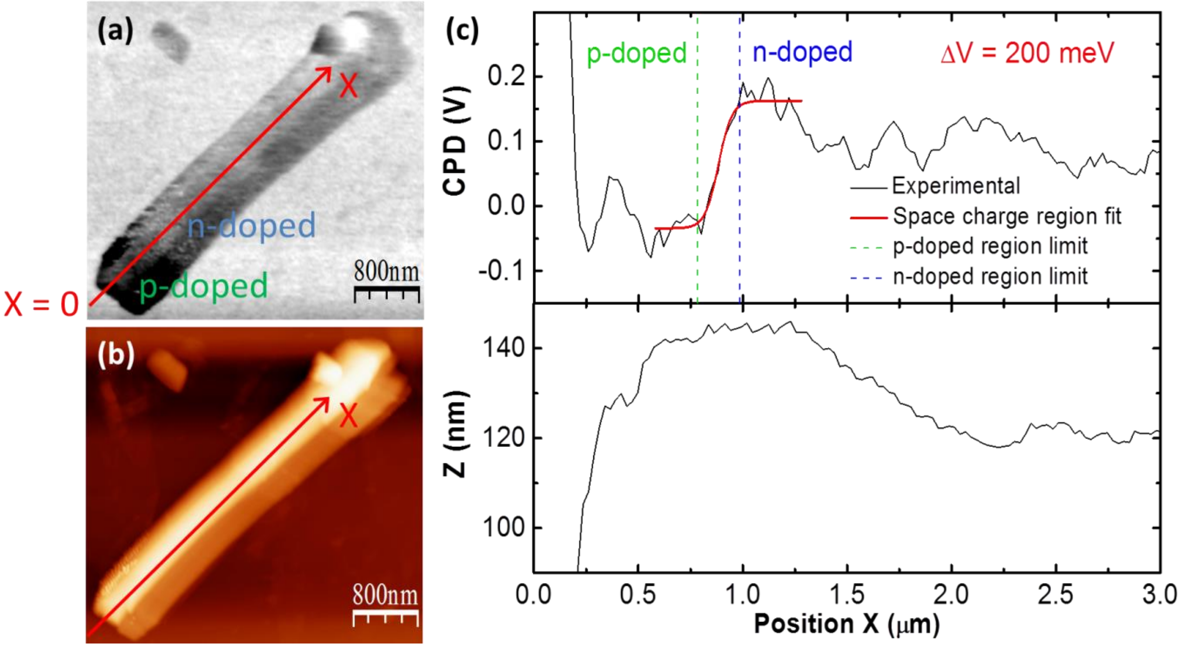

Figure 4.2.1.6: (a) Surface potential map (KPFM image) of an investigated dispersed $Al_{0.35}Ga_{0.65}N$ NW pn junction grown on top of an n-doped GaN NW template (sample N2520). The red arrow indicates the scan profile performed along the NW axial direction, from NW top to NW bottom. (b) Associated topographical AFM image. (c) Evolution of the surface potential (CPD voltage, profile from (a)) and height (Z, profile from (b)) along the NW axial direction. The CPD voltage offset (ΔV = 200 meV) indicates the presence of an AlGaN pn junction, the latter being clearly demarcated by the height variation along the NW axial direction.

Such KPFM scans were also performed for pure AlN NW pn junctions grown in various conditions but have not led so far to the observation of similar CPD voltage offset between p-AlN and n-AlN. Samples annealed post-growth in a dedicated oven under N_2 atmosphere during 15 min at several temperatures over the 750-1050°C range (using 100°C steps) were also investigated, but no improvement was noticed. Consequently, dopants, especially Mg atoms, either remained electrically inactive in spite of annealing and/or were not incorporated significantly enough during growth. In order to identify the issue, specificities of AlN NW junctions will be scrutinized in the following, starting with their structural properties in the next subpart.

4.2.2 Peculiarities of AlN nanowire pn junctions

Concomitantly to the investigation of AlGaN NW pn junctions, the structural properties of pure AlN NW pn junctions grown on top of n-doped GaN NW bases were also studied. Figure 4.2.2.1 provides typical side-view and top-view SEM images of several AlN NW pn junction samples grown with the same atomic fluxes but at various growth temperatures for the p-part. When setting low enough substrate temperatures for p-part growth, hollow cores can be observed in most NWs, as visible in Figure 4.2.2.1 (e) and its associated inset framed in yellow zooming on a typical hexagonal NW top. When increasing growth temperature, the population of hollow core NWs decreases, as visible in Figure 4.2.2.1 (f), (g), and (h). Indeed, according to values provided in Table 4.1.1, the percentage of NWs presenting such hollow cores decrease from 96% to 53% when decreasing Ga desorption time from 10 s to 2 s. In addition, Mg seems to act as a surfactant during p-part growth, similarly to previously reports [502], since increasing the Mg atomic flux, i.e. the Mg cell temperature, leads to a decrease in the hollow core NW population, as observable in Figure 4.2.2.1 (h). Indeed, in view of values of Table 4.1.1, the percentage of hollow core NWs diminishes to 33 and 5%, respectively for p-part growth at t_{des}^{Ga} = 10 s and t_{des}^{Ga} = 2 s, when increasing the Mg cell temperature by 30°C with respect to the one used for NW pn junction samples presented from Figure 4.2.2.1 (e) to (g).

At high enough substrate temperatures, with or without p-doping, NW tops are no longer hexagonal but mostly exhibit a star-like shape with 12 facets, as shown in Figure 4.2.2.1 (h), Figure 4.2.2.2 (d) and their associated yellow framed insets zooming on NW tops. This morphology indicates that the system is very far from thermodynamical equilibrium, since crystal theory applied to WZ nitrides shows that convex shapes like the hexagonal one usually observed for our NWs grown by MBE out of equilibrium are always attained for growth conditions remaining close enough to such equilibrium [301, 504] (at least up to those typically used to grow GaN NWs: substrate temperature corresponding to $t_{des}^{Ga} \approx 7$ s, and effective III/N ratio inferior or equal to stoichiometry). Here, the NW m-planes were each divided in two in order to minimize the total energy of the system, resulting in a concave shape.

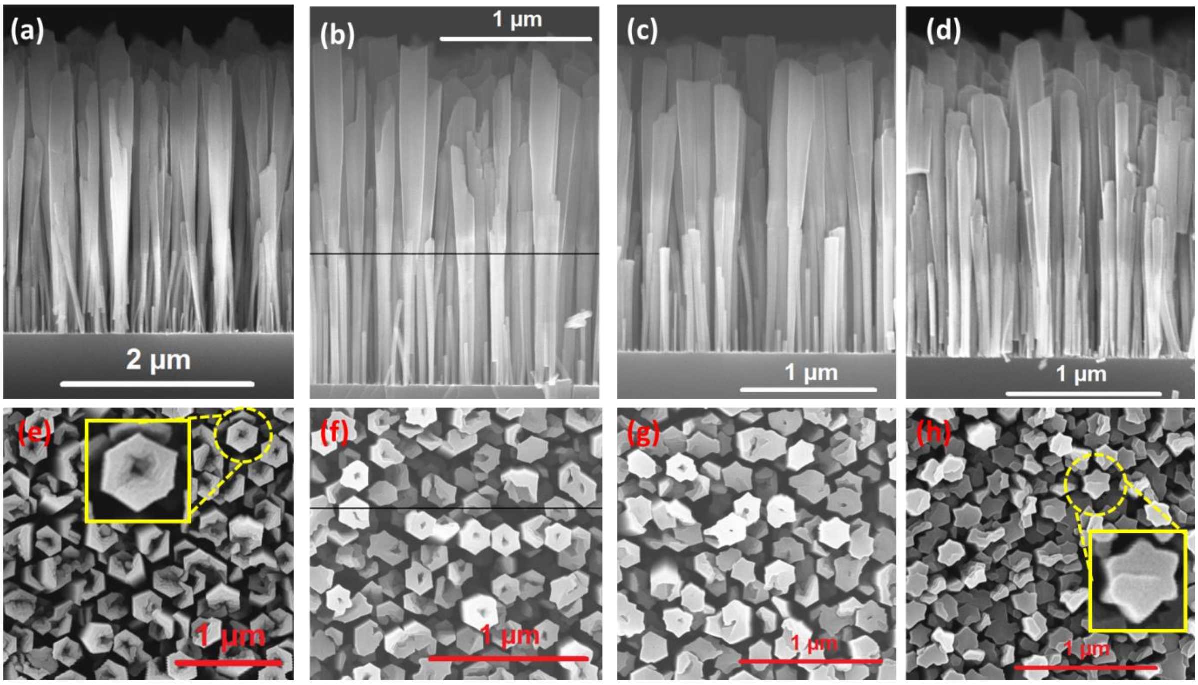

Figure 4.2.2.1: Side-view and top-view SEM images, taken within the wafer center area, of AlN NW pn junctions grown on top of GaN NW templates in various conditions: (a) & (e) NW junction sample N2524, (b) & (f) junction sample N2527, (c) & (g) junction sample N2531, (d) & (h) junction sample N2538. Similar growth parameters were used for the n-part (same atomic fluxes and growth temperatures set over a corresponding 2-3 s t_{des}^{Ga} range), in contrast to the p-part (see Table 4.1.1 as well): for the latter, the Mg cell temperature (i.e. Mg atom flux) and substrate temperature were varied over respectively a 220-250°C range and a corresponding 2-10 s t_{des}^{Ga} range, as follows: (a) & (e): 220°C, 10 s, (b) & (f): 220°C, 3 s, (c) & (g): 220°C, 2 s, (d) & (h): 250°C, 2 s. The inset of image (e) framed in dashed yellow zooms over a typical NW top exhibiting a hollow core within the hexagonal shape commonly observed over typical GaN NW growth temperature range ($t_{des}^{Ga} > 3$ s) . As for the other inset displayed in (h), the latter highlights the NW star-like shape (12 lateral facets) which prevails over the hexagonal one at high enough substrate temperatures.

Figure 4.2.2.2 provides side-view and top-view SEM images taken along the wafer radius for the NID AlN NW reference sample. The evolution of GaN NW template length along the wafer radius emphasizes the extremely high substrate temperature set in the wafer center area, in contrast to the wafer edge: the latter length is inferior to 200 nm 10 mm away from wafer center and superior to 1.5 µm 5 mm further (GaN NW template growth duration of the order of 10 h). In addition, the star-like shape, exhibited in the inset of Figure 4.2.2.2 (d), gets less and less well-defined when getting further and further away from the wafer center as expected, since we are getting closer to thermodynamical equilibrium.

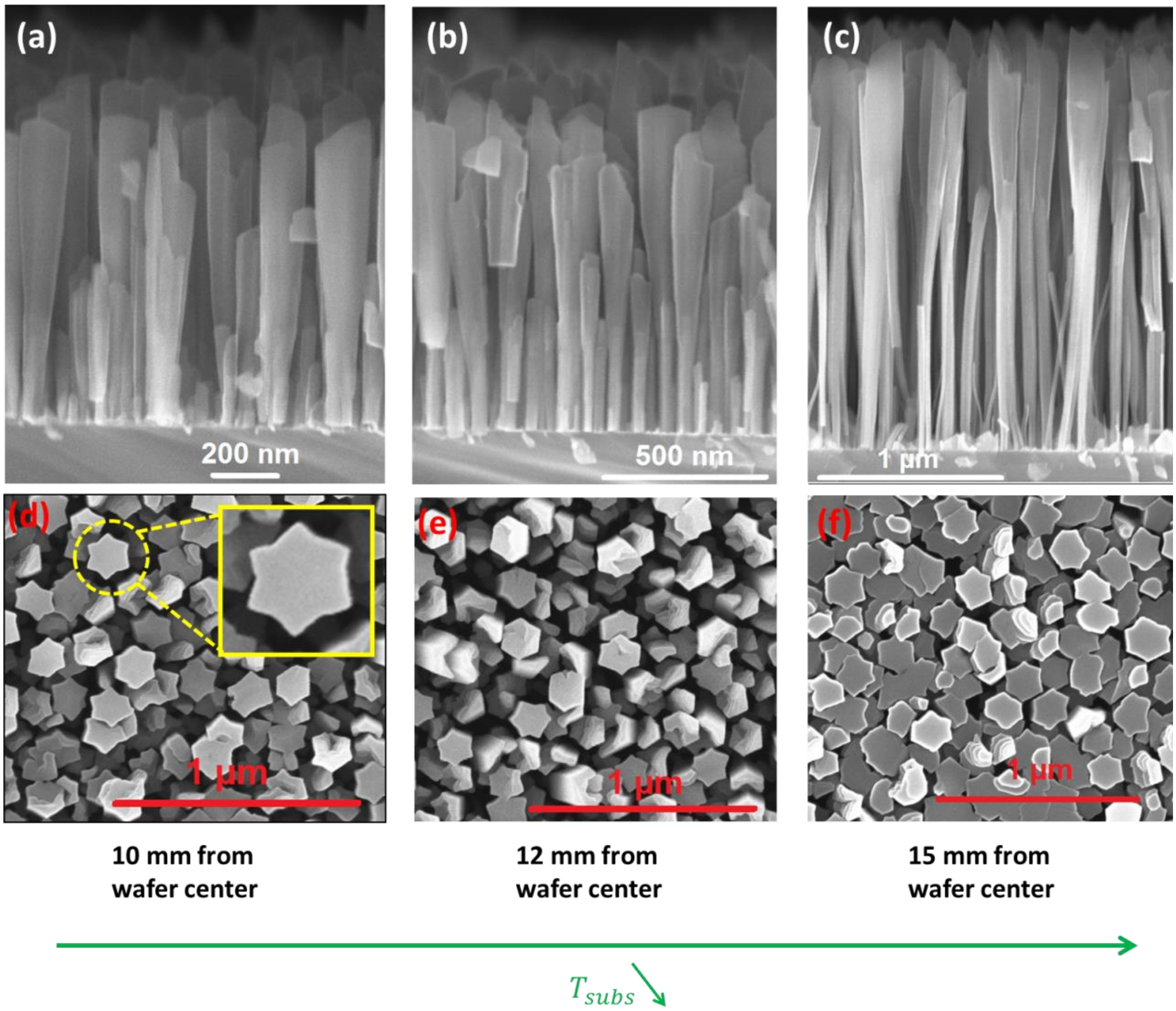

Figure 4.2.2.2: Side-view and top-view images of AlN NID NWs (from sample N2535, t_{des}^{Ga} = 2 s). The images were taken along the wafer radius at: (a) & (d) 10 mm from wafer center (higher substrate temperature), (b) & (e) 12 mm from wafer center, (c) & (f) 15 mm from wafer center (lower substrate temperature). The significant difference on GaN NW template length between (b) and (c) illustrates the abrupt change in substrate temperature occurring around 15 mm away from the wafer center. The dashed yellow inset of image (d) zooms over a typical NW top exhibiting a well-defined star-like shape, which is the dominant morphology at high enough AlN NW growth temperature.

Decreasing even more the temperature results in NWs exhibiting the usual hexagonal shape, as shown in Figure 4.2.2.3 providing SEM images for a NID AlN NW sample (N2148) grown at lower temperature than the sample edge exhibited in Figure 4.2.2.2 (c) and (f). Indeed, Figure 4.2.2.3 (b) exhibits mostly hexagonal NWs and a few star-like NWs. It must be also noted that no hollow cores are observed in NID NW tops, whatever their growth temperature, contrary to the NW pn junction tops presented in Figure 4.2.2.1, which implies that such hollow cores are induced by the mere doping.

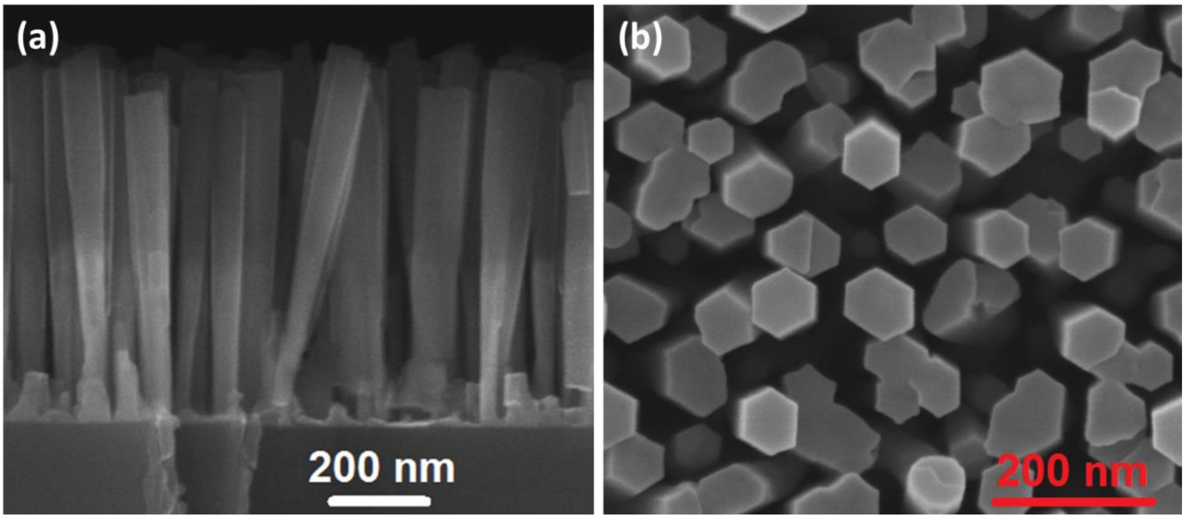

Figure 4.2.2.3: (a) Side-view SEM image of shorter NID AlN NW sections grown on top of short NID GaN NW templates (sample from a previous series: N2148, AlN growth temperature corresponding to t_{des}^{Ga} = 7 s). (b) Top-view SEM image of NID AlN NW sections. No hollow cores are observed at this growth temperature. NW tops are mostly hexagonal: the star-like shape starts appearing.

In order to estimate the depth of hollow cores in AlN NWs exhibiting them, the AFM technique (see Subpart 2.2.3 for more details) was first used. Figure 4.2.2.4 provides a typical AFM image exhibiting the sample surface topography and the results of a scan profile crossing some hollow core NWs. From several scans performed similar to the one shown in Figure 4.2.2.4 (b), a mean hollow core depth of 190 nm was found. Nevertheless, the AFM cantilever has a curving radius of 7 nm so that the setup limits regarding topography were attained. Consequently, we can only conclude at this point that the NW grooves are at least 190 nm deep in average. In other words, the mere previous result does not tell us whether the hollow cores in AlN NWs are only related to the p-part or whether the entire pn junctions are sorts of “nanotubes”.

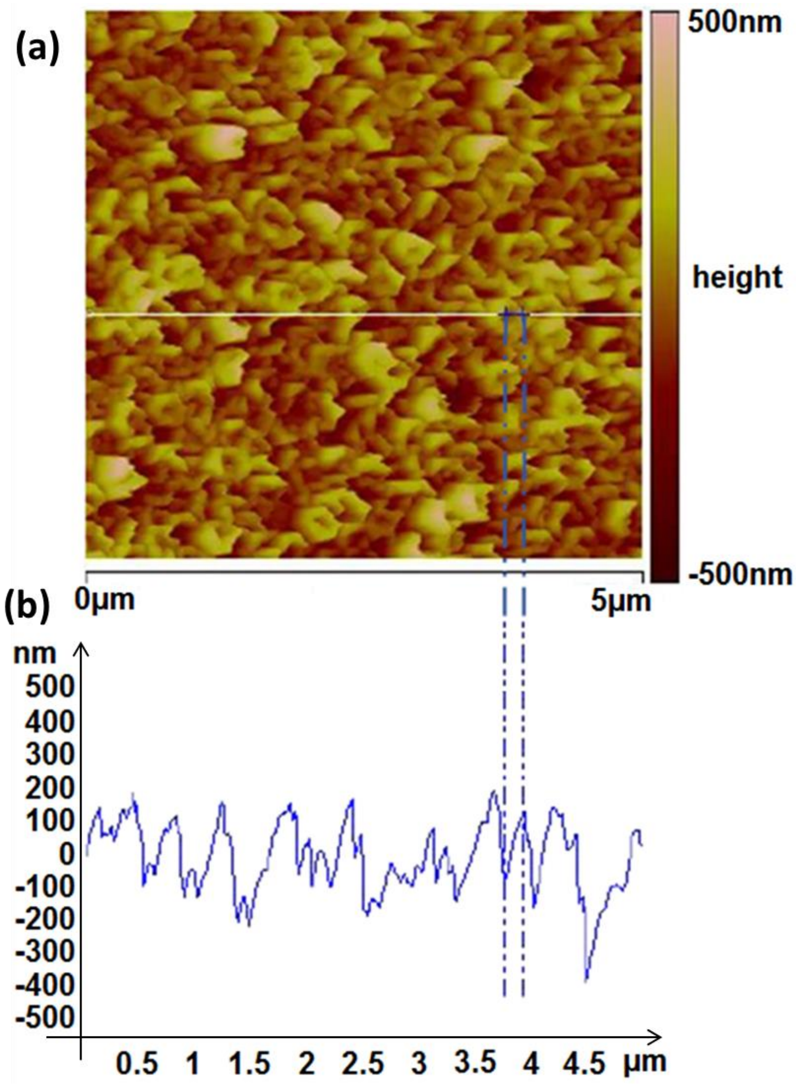

Figure 4.2.2.4: (a) Top-view topographical AFM image of AlN NW pn junctions (sample N2524, t_{des}^{Ga} = 10 s for p-part). (b) Evolution of height along the solid white line of (a): the latter notably crosses a hollow core NW (see related dashed dot blue line). From numerous AFM scans over the sample surface, a mean depth of at least 190 nm was derived for the investigated hollow cores.

To acquire more information about the hollow core depth, we can couple the result of previous AFM experiments with observations of electron microscopy images. Figure 4.2.2.5 shows STEM-HAADF images displaying typical dispersed AlN NW pn junctions grown on top on GaN NW bases and exhibiting hollow cores. Clear variations in contrast can be directly noticed within the AlN section, on all provided images. The latter variations correspond in fact to the hollow cores, so that their depth can be more accurately estimated. From the images at our disposal, hollow core depth was found to vary between 105 and 480 nm, which is in any case inferior to the length of the p-part (given our growth recipes). Therefore, we can safely conclude that these hollow cores result from Mg doping performed at low enough growth temperature.

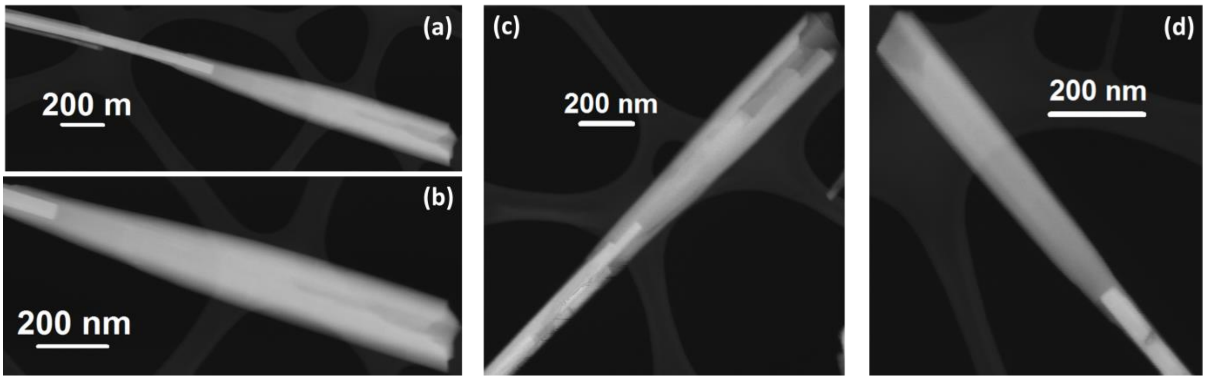

Figure 4.2.2.5: STEM-HAADF images of three AlN NW pn junctions (sample N2527, t_{des}^{Ga} = 3 s for p-part): (a), (c) and (d). The clear contrast only observable at the NW top part is consistent with hollows related to pn junctions rather than nanotubes. Their depth can be roughly estimated from such images.

4.3 Optical signature of Al$_x$Ga$_{1-x}$N nanowire pn junctions

4.3.1 Luminescence of as-grown ensembles of doped Al$_x$Ga$_{1-x}$N nanowires

As a first step, macro-optical characterization was performed on as-grown samples to assess the average optical signature of AlGaN NW pn junctions. Macro-PL experiments were first carried out using the setup detailed in Subpart 2.3.1.1 and equipped with the 244 nm CW laser, similarly to those performed in chapter 3. Figure 4.3.1.1 provides macro-PL spectra recorded at low temperature (10 K) for two Al$_{0.35}$Ga$_{0.65}$N NW pn junction samples grown in different conditions (different substrate temperatures for the p-part). For each sample, two main broad peaks can be observed: the first and dominant emission at lower energy probably results from strained GaN NW templates and deep optical transitions involving Mg-related energy levels within the AlGaN bandgap, whereas the second one at higher energy likely corresponds to the AlGaN NBE luminescence. Given the low PL intensity of the latter compared to the lower energy peak and knowing the experimental geometry, the NBE luminescence is likely to mostly originate from the n-AlGaN section. Indeed, the NW top, namely p-AlGaN here, mostly absorbs the incident laser beam before the latter reaches the n-AlGaN section below. Similarly to some PL spectra of chapter 3, the NBE presents several peaks or shoulderings, also attributed to variation in Al composition. It must be noted that the PL of sample grown at lower temperature for the p-part (sample N2518) is globally blue-shifted with respect to the other one (N2520), especially the dominant peak at lower energy. Regarding the NBE, its blue-shift is in fact lower, when comparing the peak shouldering at high energy for sample N2520 more visible in Figure 4.3.1.1 (b) with the main NBE peak observed for sample N2518. This global blue-shift can be first explained by the average AlN molar fraction found to be slightly superior for sample N2518 (0.388

versus 0.347 using XRD), despite the lower growth temperature set for a part of AlGaN NW section (p-AlGaN) and the use of identical atomic fluxes. Second, the Stokes shift may be lower in the case of sample N2518, due to enhanced alloy homogeneity induced by the lower growth temperature used for p-part.

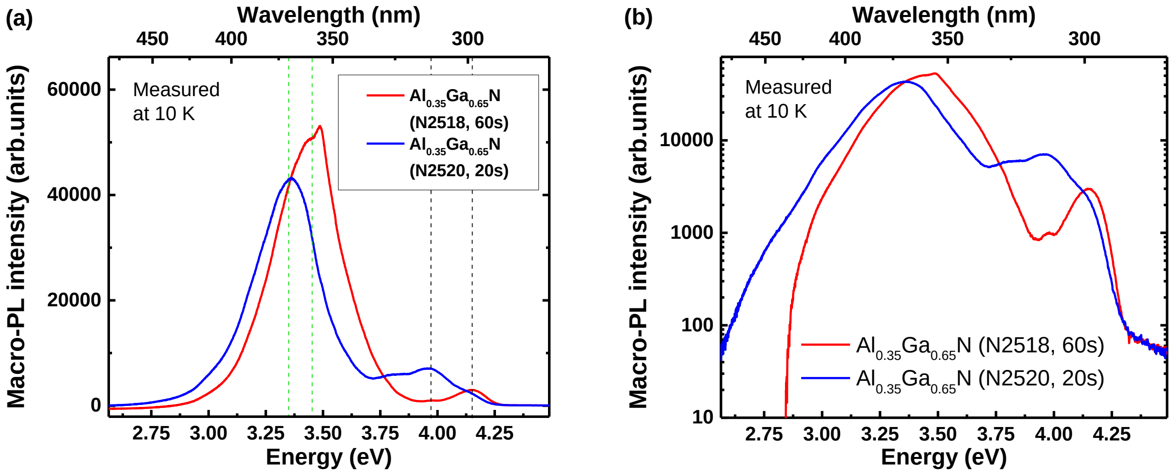

Figure 4.3.1.1: (a) Macro-PL spectra on linear scale recorded at low temperature (10 K) for two $Al_{0.35}Ga_{0.65}N$ NW pn junction samples (N2518 and N2520). The sample number and associated substrate temperature used to grow the p-part (the corresponding t_{des}^{Ga}) are given between brackets in legend. The dark dashed lines indicate the main peaks attributed to AlGaN NBE, whereas the green dashed lines point out the main lower energy peaks assigned to Mg-related energy levels. (b) Same macro-PL spectra on logarithm scale.

Figure 4.3.1.2 shows macro-PL spectra recorded at low temperature (10 K) for AlGaN NW pn junction samples grown at various nominal AlN molar fractions over the 0.35-0.75 range (experimentally, average AlN molar fractions of 0.347, 0.574 and 0.758 were determined by XRD respectively for samples N2520, N2551, and 2569). It can be seen that both peaks attributed to AlGaN NBE and Mg-related optical transitions shift with Al content. Power-dependent macro-PL data exhibit no or very slight blue-shift with excitation power for the lower energy peak, as visible in Figure 4.3.1.3 (a) and (b) for $Al_{0.35}Ga_{0.65}N$ and $Al_{0.75}Ga_{0.25}N$ NW pn junction samples (respectively N2520 and N2569). Results of temperature-dependent macro-PL experiments are also displayed for the same sample (N2569), as well as for $Al_{0.6}Ga_{0.4}N$ NWs (N2551), in Figure 4.3.1.3 (c) and (d), revealing PL intensity quenching with temperature much lower, for the peaks assigned to Mg-related transitions compared to the NBE ones. Indeed, I_{300K}/I_{10K} ratios are of the order of 20-25% for the lower energy peaks in investigated samples, whereas they are over the 1-5% range for NBE peaks recordable with our setup and are expected to be of this order for the Al-richer sample (N2569). It must be noted that the lower intensity quenching observed at lower emission energy is likely to partly result from carrier thermal escape towards lower energy levels. In view of the two previous observations, these lower energy peaks likely originate, in all investigated samples, from the same Mg-related transition, which is unlikely a DAP transition involving a deep level, since we do not observe a significant blue-shift with excitation power. The origin of this transition will be further discussed in the next subpart.

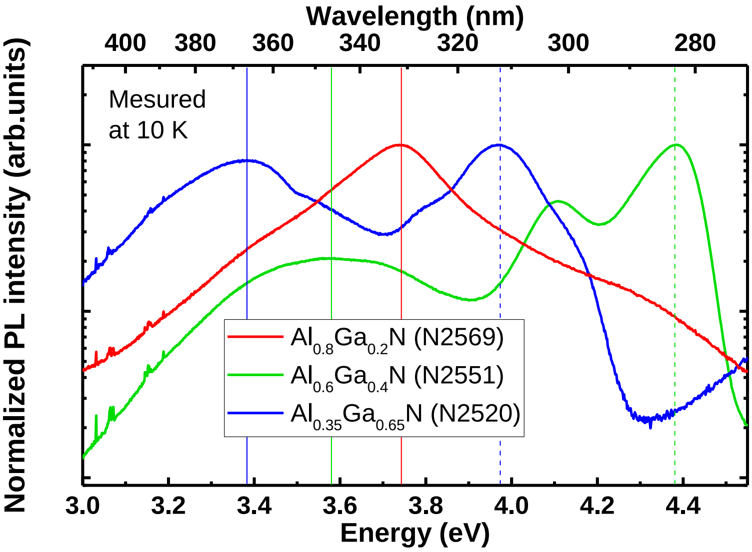

Figure 4.3.1.2: Macro-PL spectra recorded at low temperature (10 K) for three AlGaN NW pn junction samples grown at various nominal AlN molar fractions (x = 0.35, 0.6, and 0.75 respectively for samples N2520, N2551, and 2569). The solid lines point out the lower energy peaks attributed to Mg-related transitions, whereas the dashed lines indicate the main AlGaN NBE for the two lowest AlN molar fractions. For the present figure, the used excitation source was a pulsed laser emitting at 266 nm, temporarily replacing the 244 nm CW laser: the excitation power density was therefore higher than usual.

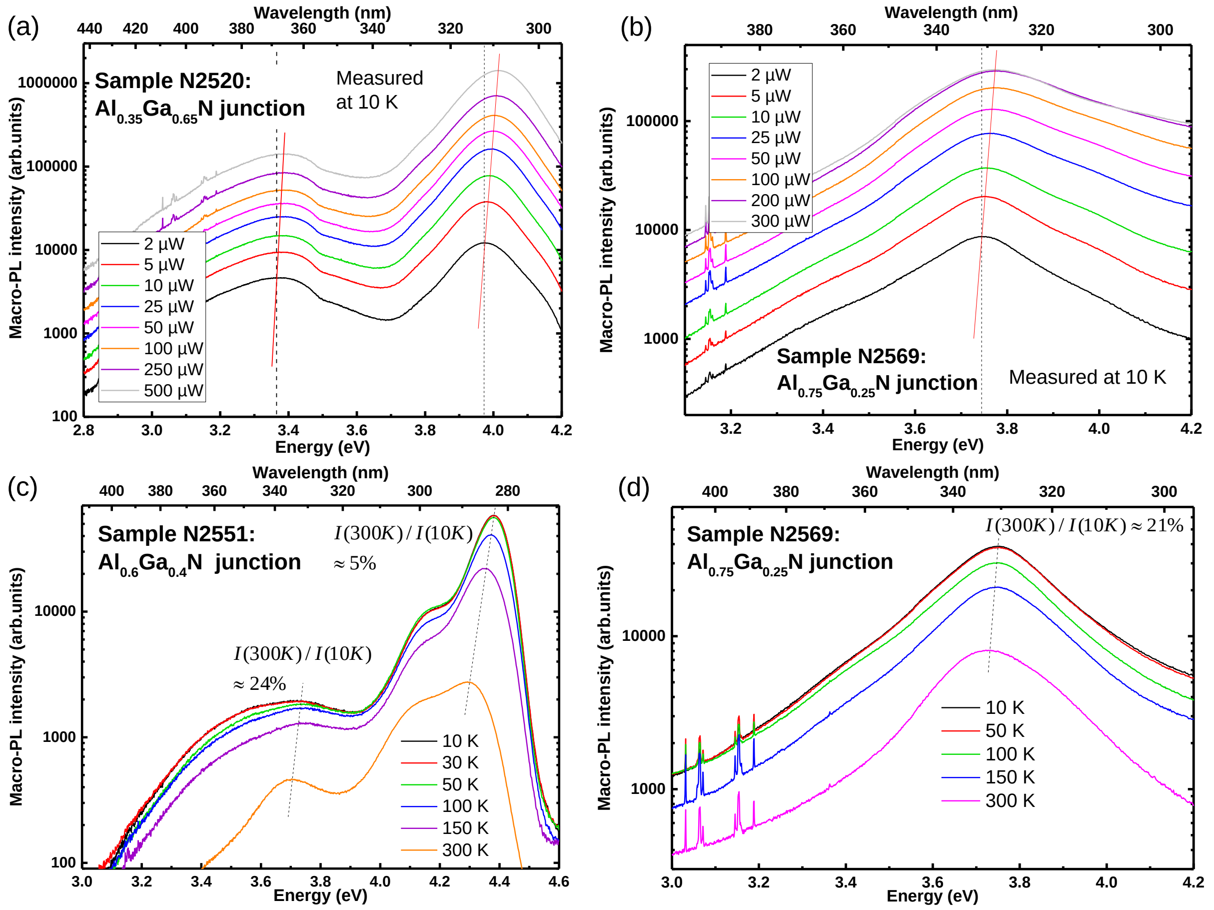

Figure 4.3.1.3: (a) & (b) Power-dependent macro-PL spectra for $Al_{0.35}Ga_{0.65}N$ (N2520) and $Al_{0.75}Ga_{0.25}N$ (N2569) NW pn junctions, respectively. Guide lines are displayed, exhibiting almost no/very slight blue-shift with power of peaks. (c) & (d) Temperature-dependent macro-PL spectra, respectively for $Al_{0.6}Ga_{0.4}N$ (N2551) and $Al_{0.75}Ga_{0.25}N$ (N2569) NW pn junctions. Dashed guide lines are displayed for the main peaks. PL intensity quenching with temperature of lower energy peaks is lower than for NBE. For the whole figure, the used excitation source was a pulsed laser emitting at 266 nm, temporarily replacing the 244 nm CW laser: the excitation power density was thus higher than usual.

Raman spectroscopy (see Subpart 2.3.3) was also performed in collaboration with Ana Cros' group (Institute of material science, University of Valencia, Spain) on as-grown NWs, first for $Al_{0.35}Ga_{0.65}N$ NW pn junction samples (N2518 and N2520). The resulting GaN-like mode peaks (E_{2h}, A_1(TO), A_1(LO)) over the 500-900 cm^{-1} frequency range are displayed in Figure 4.3.1.4 (a). The peak around 710 cm^{-1} was attributed to the silent mode B_1 activated by disorder. However, it could also correspond to the surface optical mode from GaN activated by NW geometry and its reduced dimensions. Future measurements on AlGaN pn junctions of other Al content should confirm or invalidate the latter assignment, since B_1 mode is supposed to shift with AlN molar fraction. Another peak/shouldering visible around 755 cm^{-1} was assigned to the surface optical mode SO_2. The latter contribution will not be further discussed in the following.

For the main observed GaN-like modes (A_1(TO), E_{2h}, and A_1(LO)), the related Raman shift values obtained for one of the $Al_{0.35}Ga_{0.65}N$ NW pn junction samples (N2520) were superimposed on the evolution of such shifts with AlN molar fraction for relaxed AlGaN (taken from literature [397]), from Figure 4.3.1.4 (b) to (d). The latter values are on the whole in good agreement with the 0.35 (0.347) AlN molar fraction value determined by XRD. Only the shift obtained for E_{2h} is slightly below the expected value, but a similar downshift is also observed for the GaN NW pn junction sample (N2495), as shown in Figure 4.3.1.4 (c).

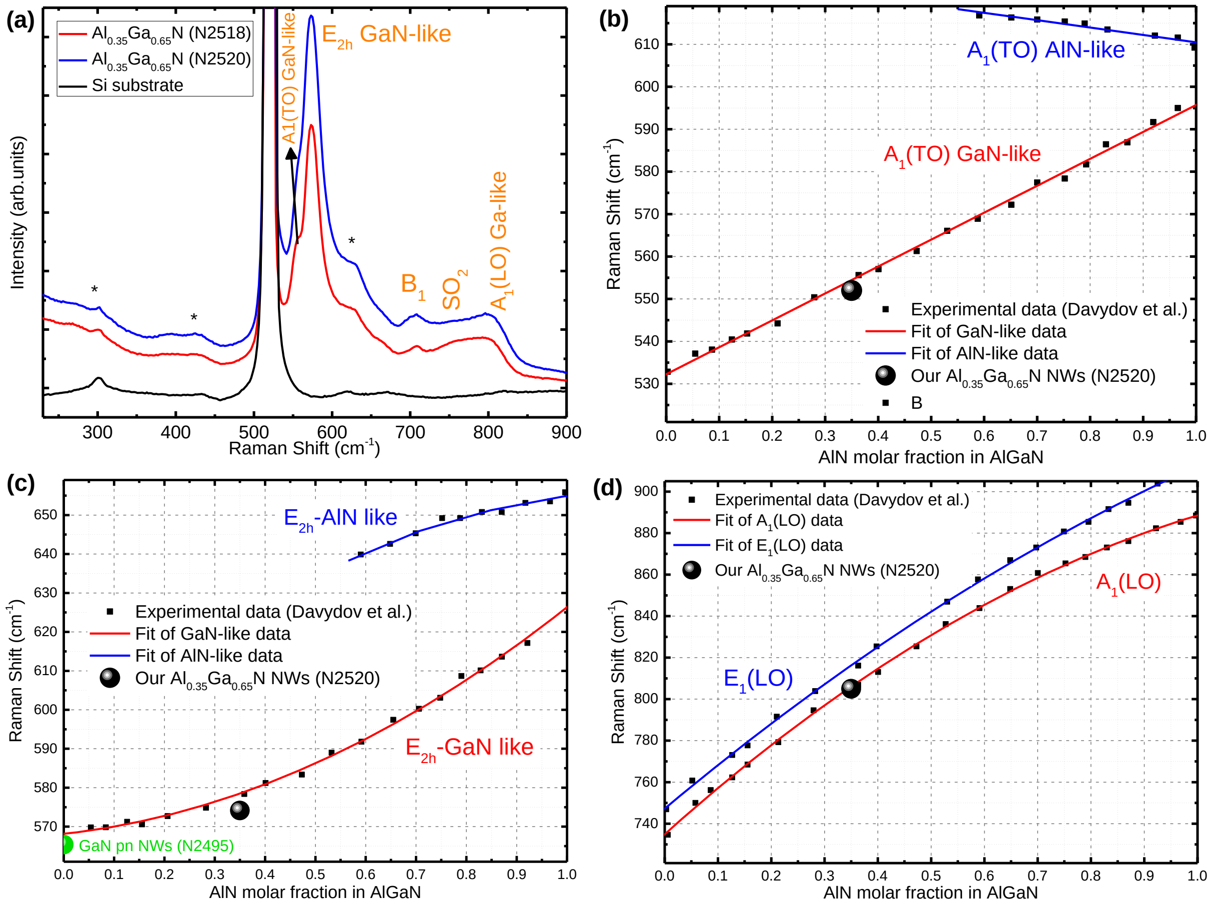

Figure 4.3.1.4: (a) Raman spectra recorded at room temperature for two $Al_{0.35}Ga_{0.65}N$ NW pn junction samples (samples N2518 and N2520). The reference spectrum for Si substrate is also provided and must be subtracted. (b) Raman shift of the A_1(TO) GaN-like mode displayed for one of the $Al_{0.35}Ga_{0.65}N$ NW pn junction samples (N2520, big dot) and superimposed on the evolution of this mode shift with AlN molar fraction recorded for relaxed $Al_xGa_{1-x}N$ 2D layers (data from [397]). (c) Raman shift of the E_{2h} GaN-like mode displayed for the same $Al_{0.35}Ga_{0.65}N$ NW pn junction sample (N2520, big dot) and for a pure GaN pn junction sample (N2495). The data is superimposed on the evolution of this mode shift with AlN molar fraction for relaxed $Al_xGa_{1-x}N$ (data from [397]). (d) Raman shift of the A_1(LO) GaN-like mode displayed for the same $Al_{0.35}Ga_{0.65}N$ NW pn junction sample (N2520, big dot) and superimposed on the evolution of this mode shift with AlN molar fraction for relaxed $Al_xGa_{1-x}N$ (data from [397]).

Figure 4.3.1.5 provides the Raman spectra for the same $Al_{0.35}Ga_{0.65}N$ NW pn junction samples (N2518-N2520) and the GaN NW pn junction sample (N2495) taken as reference here over a higher frequency range (2000-2500 cm^{-1}). For all three samples, clear Mg-H modes around 2150 cm^{-1} are observed, similarly to previous reports on GaN grown by MBE [505, 506], proving that a lot of Mg was incorporated in the samples. Indeed, given the very low residual hydrogen level within the MBE chamber in contrast to MOVPE or HVPE growth, the observation of such modes was not expected, unless Mg incorporation was significant enough. This is the first time that such modes have been reported for AlGaN grown by MBE, so that estimating doping levels from these measurements is complicated for the time being. For GaN, a similar spectrum would correspond to Mg content of the order of 5 10^{19} cm^{-3} [493]. Compared to Mg-H modes observed in GaN, those in AlGaN are slightly shifted and broader. The latter broadening is assigned to alloy intrinsic inhomogeneity. As for the slight frequency shift, the frequency of local modes depends very weakly on the binary host (GaN or AlN), but Mg-H atoms may adopt different disposition or slightly alter the material bond length, leading to such small changes in Raman shift values. In addition, Mg-H modes were not observed in the lower frequency range of Figure 4.3.1.4 for our AlGaN samples, in contrast to GaN NWs [493]. In order to dissociate these Mg-H complexes and fully activate Mg dopants, post-growth annealing was carried out in a dedicated oven under N_2 atmosphere during 15 min at several temperatures (from 750°C to 1050°C, every 100°C), but did not result in noticeable decrease in related peak intensities in Raman spectra so far.

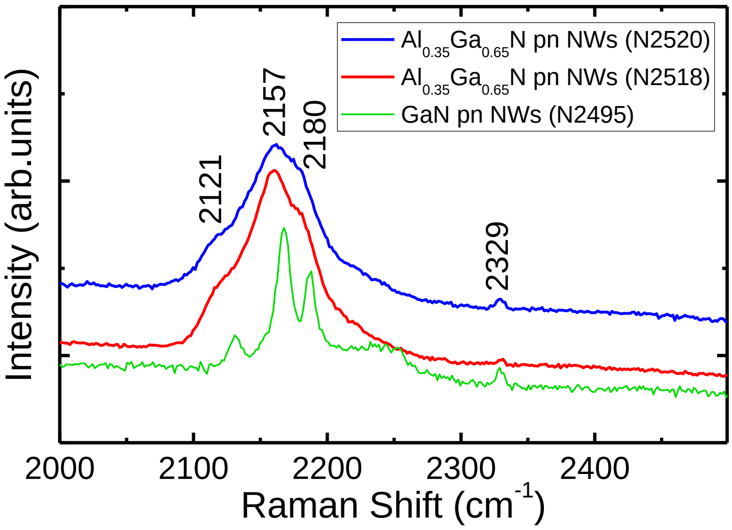

Figure 4.3.1.5: Raman spectra recorded at room temperature and displayed at high Raman shifts for two $Al_{0.35}Ga_{0.65}N$ NW pn junction samples (samples N2518 and N2520) and one GaN NW pn junction sample (N2495). Mg-H modes are clearly observable around 2150 cm^{-1} for the three samples, as well as the N_2-related (Raman experiment atmosphere) mode at 2329 cm^{-1}.

Raman spectroscopy (see Subpart 2.3.3) was also performed on as-grown AlN NW pn junction samples (N2524, N2527 and N2531 introduced in Figure 4.2.2.1). Frequency values for A_1(TO) and

E_{2h} modes are respectively 610 cm^{-1} and 655 cm^{-1}, according to Figure 4.3.1.6 (a) in good agreement with values for relaxed AlN (see Figure 4.3.1.4 and/or Table 2.3.3.1). Contrary to $Al_{0.35}Ga_{0.65}N$, no peculiar signature was observed over low frequency ranges, in view of Figure 4.3.1.6 (a), and no Mg-H modes were highlighted over higher ranges, as shown in Figure 4.3.1.6 (b), meaning that either Mg incorporation in AlN was much less significant than for $Al_{0.35}Ga_{0.65}N$ or that Mg-H complexes did not form during growth. However, C-H modes were observed in AlN samples, highlighting the presence of residual carbon and hydrogen within the MBE chamber during growth. Moreover, $Al_{0.35}Ga_{0.65}N$ and AlN samples mostly investigated in Raman were grown consecutively. Consequently, the assumption about lesser Mg incorporation in AlN is more plausible.

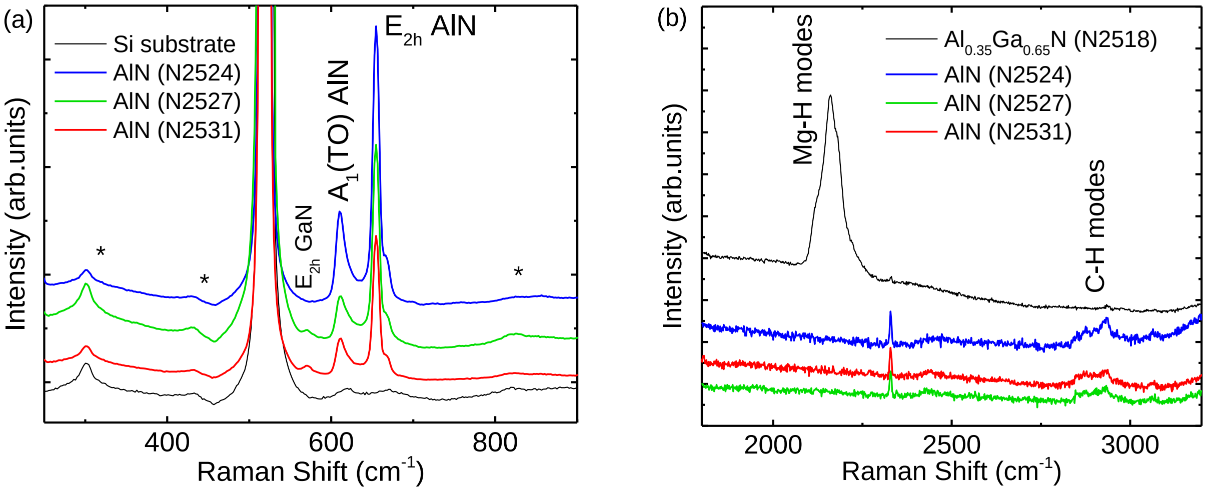

Figure 4.3.1.6: (a) Raman spectra recorded at room temperature for three AlN NW pn junction samples (samples N2524, N2527 and N2531). (b) Raman spectra displayed at higher Raman shifts for the same AlN pn junction samples and one $Al_{0.35}Ga_{0.65}N$ pn junction sample (N2518). Mg-H modes are not observable for the three AlN samples, in contrast to C-H modes.

4.3.2 Investigation at smaller scale of dispersed $Al_xGa_{1-x}N$ nanowire pn junctions

We then investigated the optical properties of smaller quantity of matter, through the characterization of bunches of or single dispersed NW pn junctions. µ-PL experiments were first performed on such objects, using the same CW laser as macro-PL (244 nm emission, setup described in Subpart 2.3.1.1). As expected in view of the results about NID AlGaN NWs presented in chapter 3, the µ-PL spectra provided for bunches of dispersed $Al_{0.35}Ga_{0.65}N$ NW pn junctions (samples N2518 and N2520) in Figure 4.3.2.1 exhibit many sharp lines, particularly at high emission energies corresponding to NBE, attributed as well to alloy compositional fluctuations. These lines are indeed much more numerous within the NBE range than over lower emission energy ranges that likely correspond to transitions involving Mg-related levels. Consequently, energy levels involved in the latter transitions, other than the acceptor levels related to the mere substitutional Mg, are unlikely to result from compositional fluctuations but would better correspond to defect-related or complex-related levels, especially since the transition is quite deep: when taking a look at macro-PL spectra of Figure 4.3.1.1, the Mg-related transition energy is below the GaN band gap whereas the NBE is around 4.1 eV. Such assumption will be discussed more in detail further.

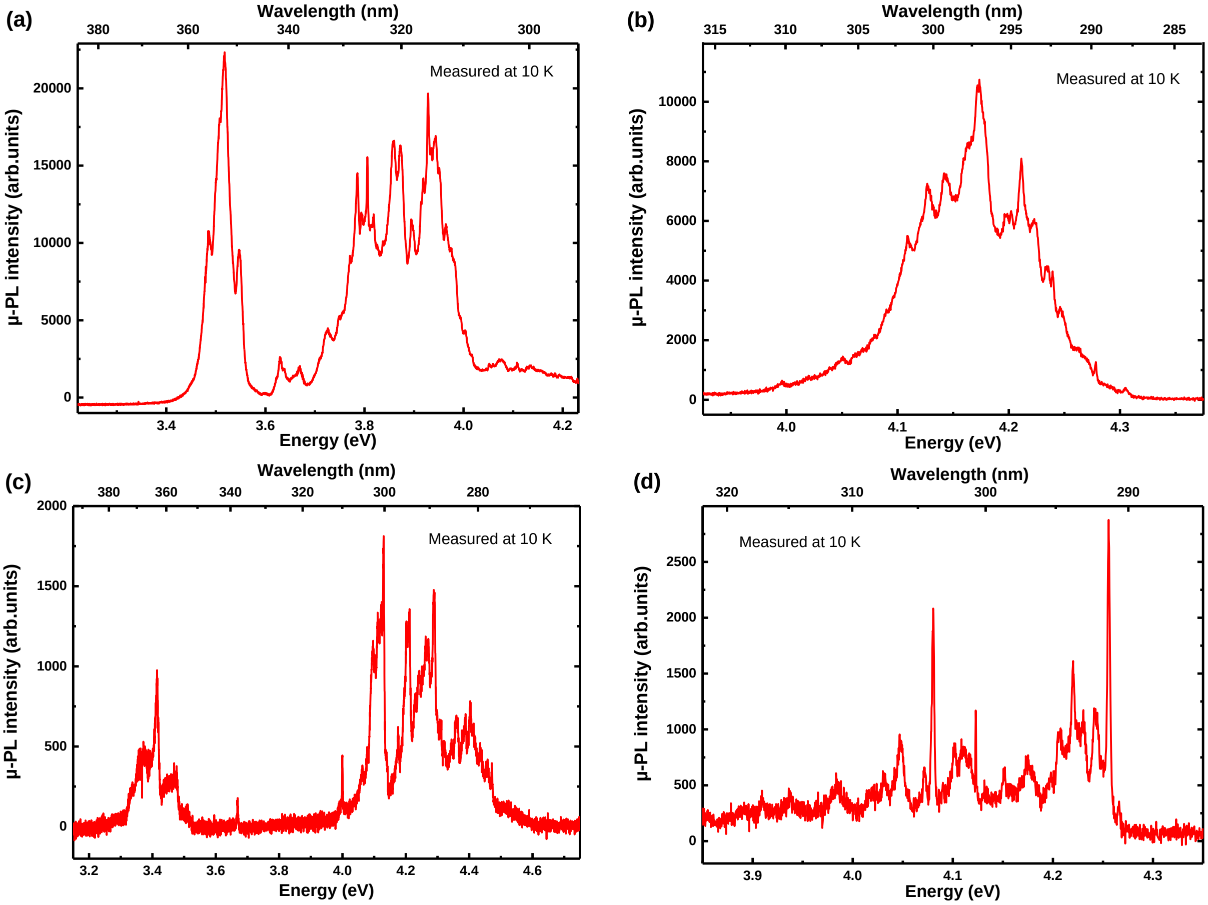

Figure 4.3.2.1: µ-PL spectra recorded at low temperature (10 K) for dispersed $Al_{0.35}Ga_{0.65}N$ NW pn junctions (samples N2518: (a) & (b), N2520: (c) & (d)) grown (at different substrate temperatures for the p-part, corresponding to t_{des}^{Ga} = 60 s and t_{des}^{Ga} = 20 s respectively for N2518 and N2520) on top of GaN NW templates. Spectra given in (a) and (c) are displayed over a wider range including the GaN NBE, in contrast to those provided in (b) and (d) focusing on the AlGaN NBE.

To confirm or invalidate our previous assumptions, nanoCL experiments were performed in collaboration with Mathieu Kociak and Luiz Tizei (from LPS, Orsay), first on bunches of dispersed AlGaN NW pn junctions. Figure 4.3.2.2 and Figure 4.3.2.3 show the results obtained for two $Al_{0.35}Ga_{0.65}N$ NW pn junction samples (respectively for samples N2518 and N2520). Luminescence from rectangular frame areas placed along the NW axis (see Figure 4.3.2.2 (a) and Figure 4.3.2.3 (a) for position of frames) confirm that the NBE mostly originates from n-AlGaN NW section, whereas the broad emission at lower energy visible in macro-PL spectra stems from both GaN NW templates and p-AlGaN NW section. As expected, the contribution of the latter is much broader than the one of templates, as supported by Figure 4.3.2.2 (d) and Figure 4.3.2.3 (d). Similarly to the assignment made for macro-PL data of Figure 4.3.1.1, the several peaks observed at various emission energies within the NBE range in Figure 4.3.2.3 (d) are also attributed to compositional inhomogeneity within the AlGaN alloy. When comparing our experimental emission energies for both the NBE peak and the Mg-related transition to those calculated from bowing-like relationship (bowing parameter b=1) and from the average emission energy values of Si-related and Mg-related transitions reported for GaN and AlN binaries, it appears that our PL and CL data are consistent with transitions involving the shallow Si donor and the AlGaN valence band for the NBE emission, and transitions between a deep level and a shallower acceptor level related to Mg for the broad emission at lower emission energy. Indeed, in the case of the NBE emission, the shallow donor transition is commonly observed around 3.471 eV for GaN and 6.016 eV for AlN (values for bulk taken from Table 1.2.1.2 and similar for NWs, as seen in Subpart 2.3.1.2), which results in 4.128 eV for $Al_{0.35}Ga_{0.65}N$ (using an average x value of 0.347 determined by XRD, for sample N2520), in very good agreement with CL data below and associated macro-PL data of Figure 4.3.1.1. As for the deeper and broader emission, a BL band related to the mentioned deep level/Mg-acceptor transition has been reported around 2.8 eV for GaN, widely for films [134, 507, 508] and more rarely for nanostructures [509-511], whereas a similar transition for AlN has been observed around 4.7 eV in both 2D layers [128, 380] and NWs [376]. It then results in 3.233 eV for $Al_{0.35}Ga_{0.65}N$ (sample N2520), consistently with CL data below and associated macro-PL data of Figure 4.3.1.1.

Performing the same calculation for other samples leads to 4.687 eV and 3.646 eV, respectively for $Al_{0.6}Ga_{0.4}N$ NBE and deeper emission (XRD average x value: 0.574, for sample N2551), and to 4.057 eV for $Al_{0.75}Ga_{0.25}N$ deep emission (XRD average x value: 0.758, for sample N2569). The latter calculated emission energy values are consistent on the whole with the experimental ones in view of macro-PL data of Figure 4.3.1.2. It can be seen that the difference between the experimental and theoretical values for the Al-richest sample (N2569) is higher than for other samples, which can be explained by the more significant Stokes shift expected at higher Al content (see Subpart 3.2.1). It must be also noted that the emission energy and width of the Mg-related deep transition for GaN and AlN binaries can vary from one report to another, increasing the calculation error bar.

The origin of this Mg-related transition is still under debate, particularly in GaN for which reports investigating the latter transition are much more numerous. Indeed, the BL band has been attributed for long to a DAP transition between a deep donor level related to V_N and a shallower acceptor level corresponding to substitutional Mg, for both GaN [134, 512] and AlN [128, 380, 467], but more recent theoretical and experimental reports on GaN tend to refute this assignment and assign the donor level of the DAP transition to an H-related complex [507, 508]. The latter assumption is supported not only by the fact that almost no reports on GaN grown by MBE exhibit the BL band but also by annealing studies, according to which this band is greatly enhanced by hydrogen plasma treatment [513]. Consequently, it is compatible with our mere Raman results exhibiting Mg-H modes but not with our entire set of data, since no significant shifts with excitation power specific to deep DAP transitions were observed in power-dependent macro-PL. Interestingly, recent calculations attribute the BL band in GaN (2.70 eV) to transition from conduction band to Mg_{Ga} and predict the equivalent transition for AlN at 4.77 eV [456], which would be consistent with our whole set of data.

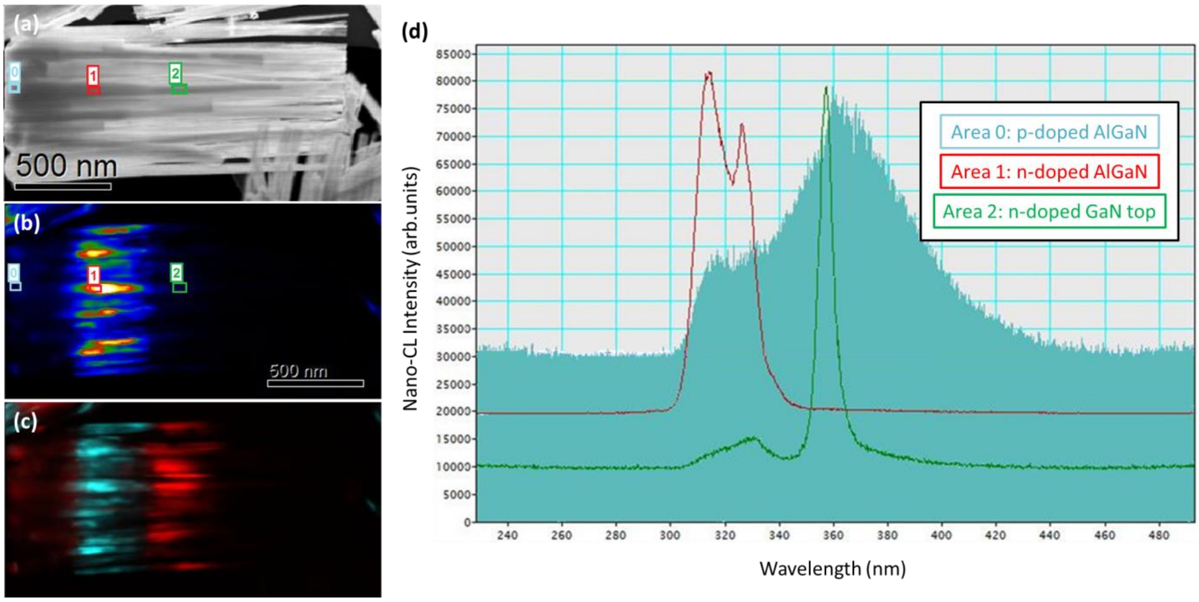

Figure 4.3.2.2: (a) STEM-HAADF image of the investigated bunch of dispersed $Al_{0.35}Ga_{0.65}N$ NW pn junctions (sample N2518). The three colored frames numbered from 0 to 2 correspond to the p-AlGaN part (light blue), the n-AlGaN region (red), and the n-doped GaN template (green), respectively. (b) Associated panchromatic map, exhibiting dominant emission over the 310-320 nm wavelength range (around red frame n°1 corresponding to the n-part). (c) Color filtered image, depending on the CL emission wavelength: the blue color corresponds to emission over the 310-320 nm range whereas the red one is associated with 352-361 nm emission. (d) CL spectra corresponding to the three frames displayed in (a) and (b).

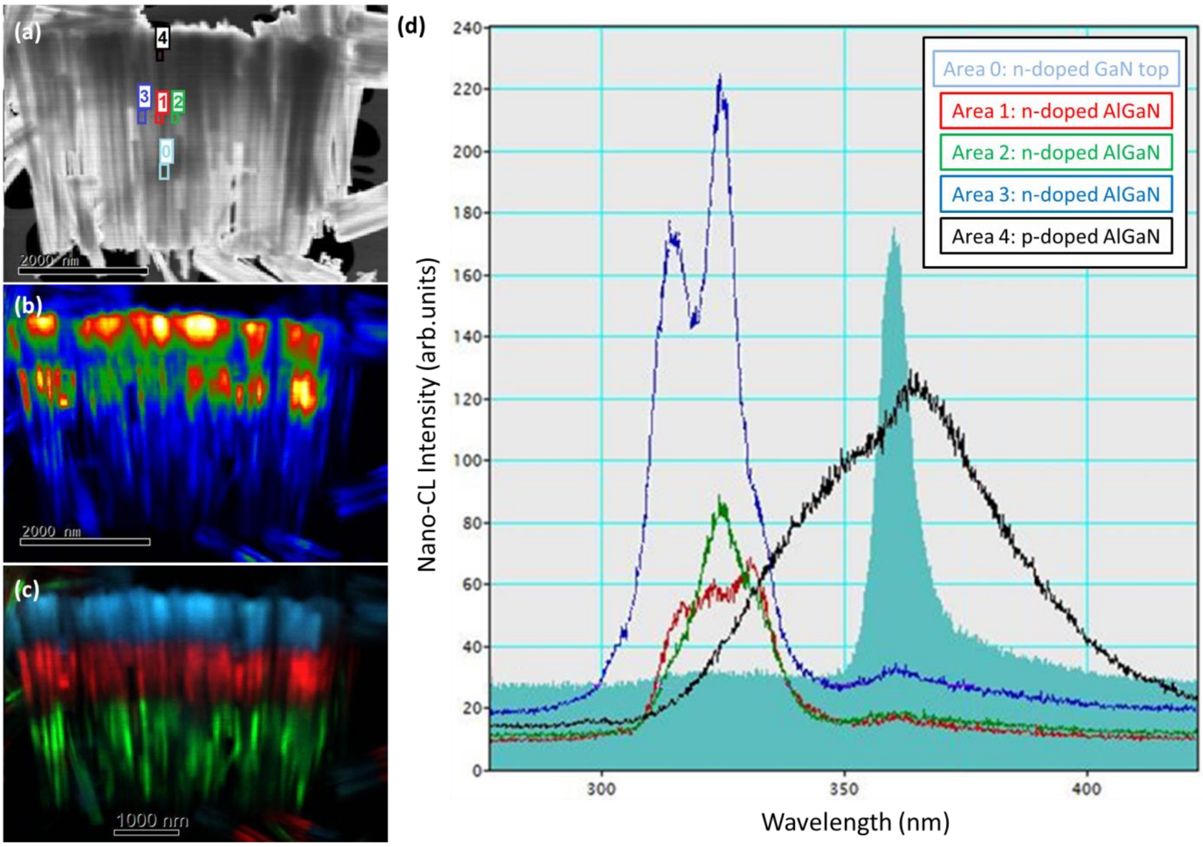

Figure 4.3.2.3: (a) STEM-HAADF image of the investigated bunch of dispersed $Al_{0.35}Ga_{0.65}N$ NW pn junctions (sample N2520). The five colored frames numbered from 0 to 4 correspond to the n-doped GaN NW template (light blue), the n-AlGaN part (red, green, blue), and the p-AlGaN region (black), respectively. (b) Associated panchromatic map, highlighting emission for the pn junctions (around frames n°1-3 and black frame n°4, respectively corresponding to the n-part and p-part). (c) Color filtered image, depending on the CL emission wavelength: the blue color corresponds to emission over the 377-389 nm range, the red one to 301-333 nm, whereas the green one is associated with 358-362 nm emission. Each color is normalized to its maximum intensity here. (d) CL spectra corresponding to the five frames displayed in (a) and (b).

NanoCL experiments were then performed on single dispersed AlGaN NW pn junctions. Figure 4.3.2.4 and Figure 4.3.2.5 show the results obtained for axial CL scans performed along two $Al_{0.35}Ga_{0.65}N$ NW pn junction samples (respectively for samples N2518 and N2520). The second figure displays an axial CL scan more spatially resolved than the one provided in the first one. Both scans highlight the transition from the GaN NW templates to the AlGaN pn junction which is quite abrupt in view of CL spectra recorded along the NW growth axis provided in Figure 4.3.2.5 (e). Similarly to previous observations, several peaks at various emission energies are obtained within the AlGaN NBE range and attributed to variation in Al composition in the alloy.

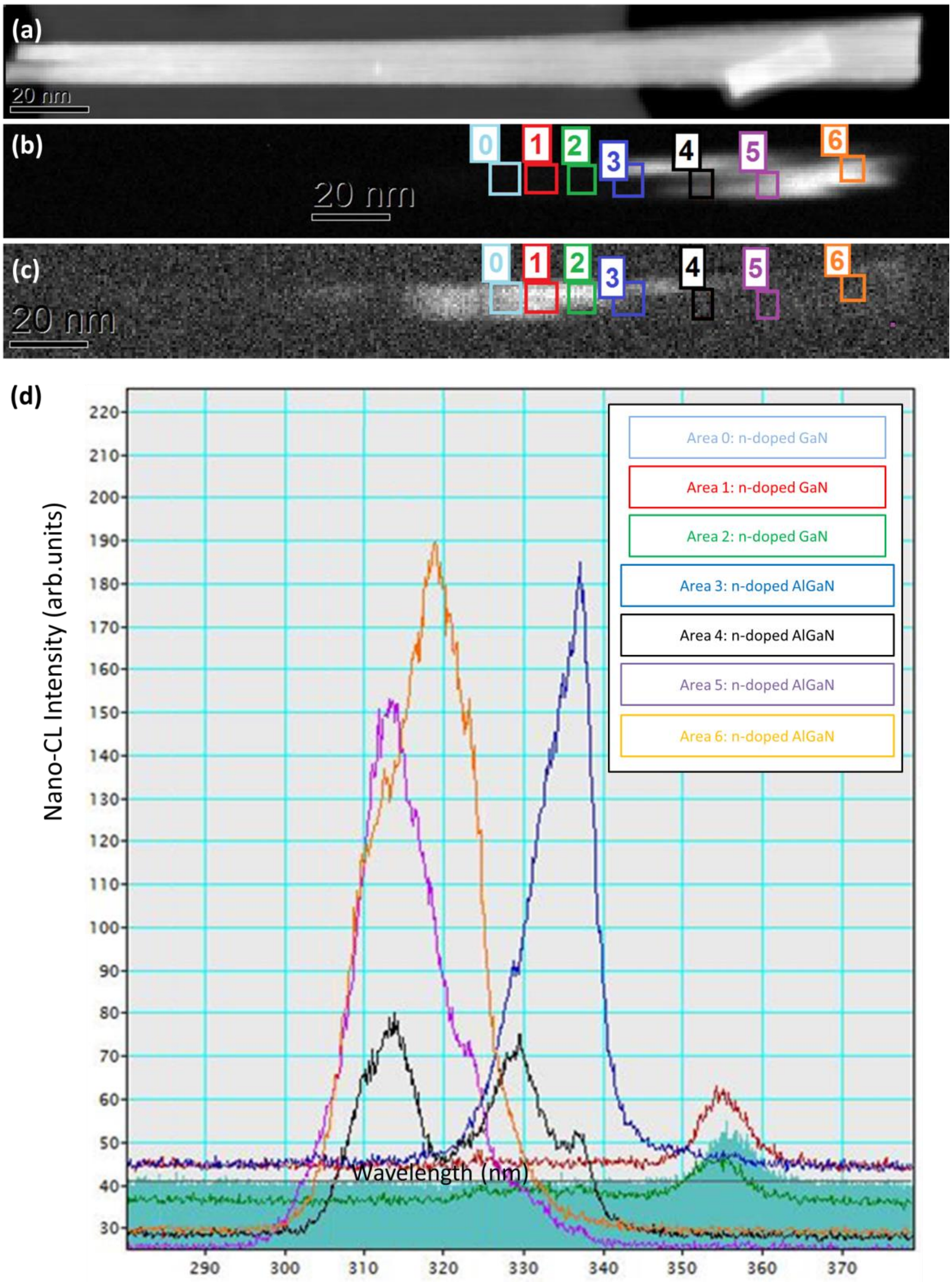

Figure 4.3.2.4: (a) STEM-HAADF image of a dispersed $Al_{0.35}Ga_{0.65}N$ NW pn junction (sample N2518). The NW top is broken. (b) Associated panchromatic map, exhibiting emission over the 306-345 nm wavelength range. The seven colored frames numbered from 0 to 6 correspond to the transition from the n-GaN template (light blue, red, green) to the n-AlGaN part (blue, black, purple, orange). (c) Associated panchromatic map, exhibiting emission over the 348-364 nm wavelength range. (d) CL spectra corresponding to the seven frames displayed in (b) and (c).

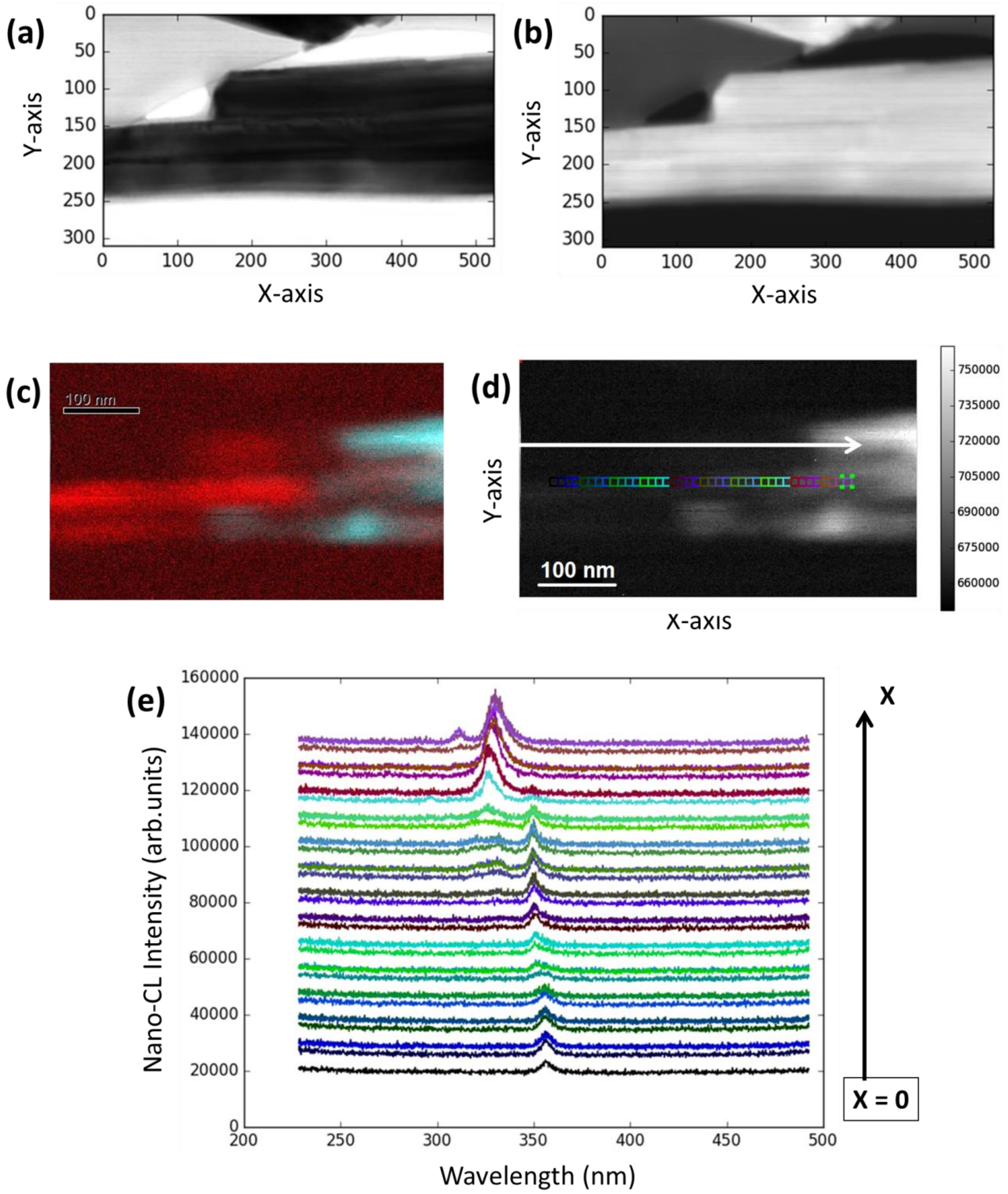

Figure 4.3.2.5: More spatially resolved analysis of the transition between n-GaN template and the Al$_{0.35}$Ga$_{0.65}$N pn junction (only n-part investigated here, sample N2520). (a) STEM-BF image of investigated NW regions. (b) Corresponding STEM-HAADF image. (c) Associated color filtered image, depending on the CL emission wavelength: the blue color corresponds to emission over the 301-339 nm range, whereas the red one is associated with 342-366 nm emission. Each color is normalized to its maximum intensity here. (d) Associated panchromatic map, exhibiting NW luminescence from n-part. The numerous colored frames follow the transition from the n-GaN template to the n-AlGaN part, as indicated by the white arrow. (e) CL spectra corresponding to the frames displayed in (c). The black arrow corresponds to the white one displayed in (c).

In addition to macro-Raman results presented in Subpart 4.3.1, µ-Raman scans were performed, still in collaboration with Ana Cros' group (Institute of material science, University of Valencia, Spain), along the NW axial direction of dispersed AlGaN NW pn junctions grown on GaN NW templates. Figure 4.3.2.6 and Figure 4.3.2.7 present each the µ-Raman data recorded every 0.5 µm for one $Al_{0.35}Ga_{0.65}N$ NW pn junction and its GaN NW base (sample N2520). The spectra labeled in green in Figure 4.3.2.6 (c) & (d) and Figure 4.3.2.7 (c) & (d) correspond to the GaN NW template, those labeled in orange to the transition zone between GaN and n-AlGaN, and those labeled in purple to the pn junction. Regarding the latter, when moving from the n-part to the p-doped region, it can be first noticed that an intense and broad A_1 (LO) GaN-like mode for AlGaN seems to arise from disorder around 800 cm^{-1} in both Figure 4.3.2.6 (c) and Figure 4.3.2.7 (c). Moreover, the mode around 710 cm^{-1} attributed to silent mode B_1 in Subpart 4.3.1 is absent in the GaN template, appears in the n-AlGaN section and gets more intense within the p-part, which supports our initial assumption. Finally, at lower frequencies, p-part globally exhibits more intense Raman signal, especially for the E_{2h} GaN-like mode for AlGaN. By combining all these clues, we are able to distinguish between n- and p-AlGaN. Consequently, we have just shown that we can evidence a Raman signature for a NW pn junction using the µ-Raman technique.

Interestingly, it must be noted that, when moving from n-part to p-part, the E_{2h} GaN-like mode for AlGaN was observed to slightly red-shift (to shift towards lower phonon frequency), whereas the A_1 (TO) GaN-like mode for AlGaN rather tends to blue-shift very slightly, as visible in Figure 4.3.2.6 (e) and Figure 4.3.2.7 (e). Such observation cannot be related to the mere evolution of strain or Al composition along the NW pn junction axial direction, and remains unexplained for the time being. In addition, the evolution along the GaN NW template axis of the frequency of the A_1(TO) GaN-like mode for AlGaN, corresponding here to the shouldering over the 540-550 cm^{-1} of the main A_1(TO) mode peak for the GaN NW template at about 532-533 cm^{-1} (see Figure 4.3.2.6 (d) & (e) and Figure 4.3.2.7 (d) & (e)), remains unclear as well but is probably related to the Al-shell partly wrapping the long GaN base. The latter base is quasi-relaxed at its bottom in view of the corresponding frequency value (see Table 2.3.3.1 giving phonon frequency values for relaxed binaries at 300 K) and progressively gets compressively strained by the shell as expected, since the main A_1(TO) mode peak for GaN blue-shifts.

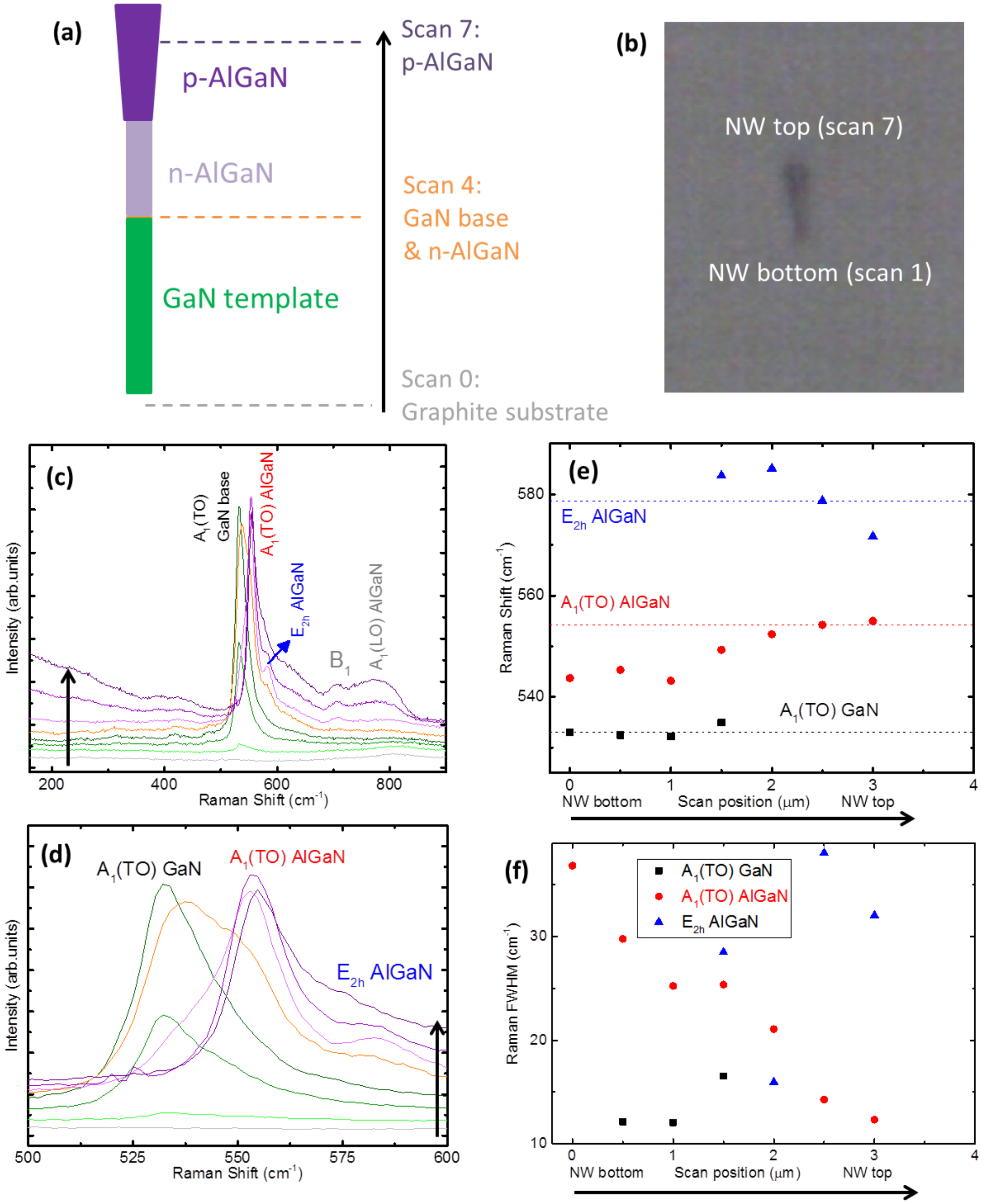

Figure 4.3.2.6: (a) Illustration of an $Al_{0.35}Ga_{0.65}N$ NW pn junction (sample N2520) and µ-Raman scans performed along the NW growth axis (one scan every 0.5 µm). (b) Image of the investigated NW recorded with the Raman setup. (c) Raman spectra taken along the NW growth axis. Grey spectrum: graphite substrate (scan 0). Green spectra: GaN NW template (scan 1 to 3). Orange spectrum: GaN template & n-AlGaN bottom part (scan 4). Purple spectra: AlGaN NW pn junction (scan 5 to 7). (d) Zoom on (c) over the 500-600 cm^{-1} range. (e) Evolution of Raman shift along the NW growth axis for several modes: A_1(TO) for GaN NW template, A_1(TO) GaN-like for AlGaN and E_{2h} GaN-like for AlGaN. (f) Evolution of related Raman linewidth for these three modes. For all figures, the black arrow corresponds to the scan profile sketched in (a).

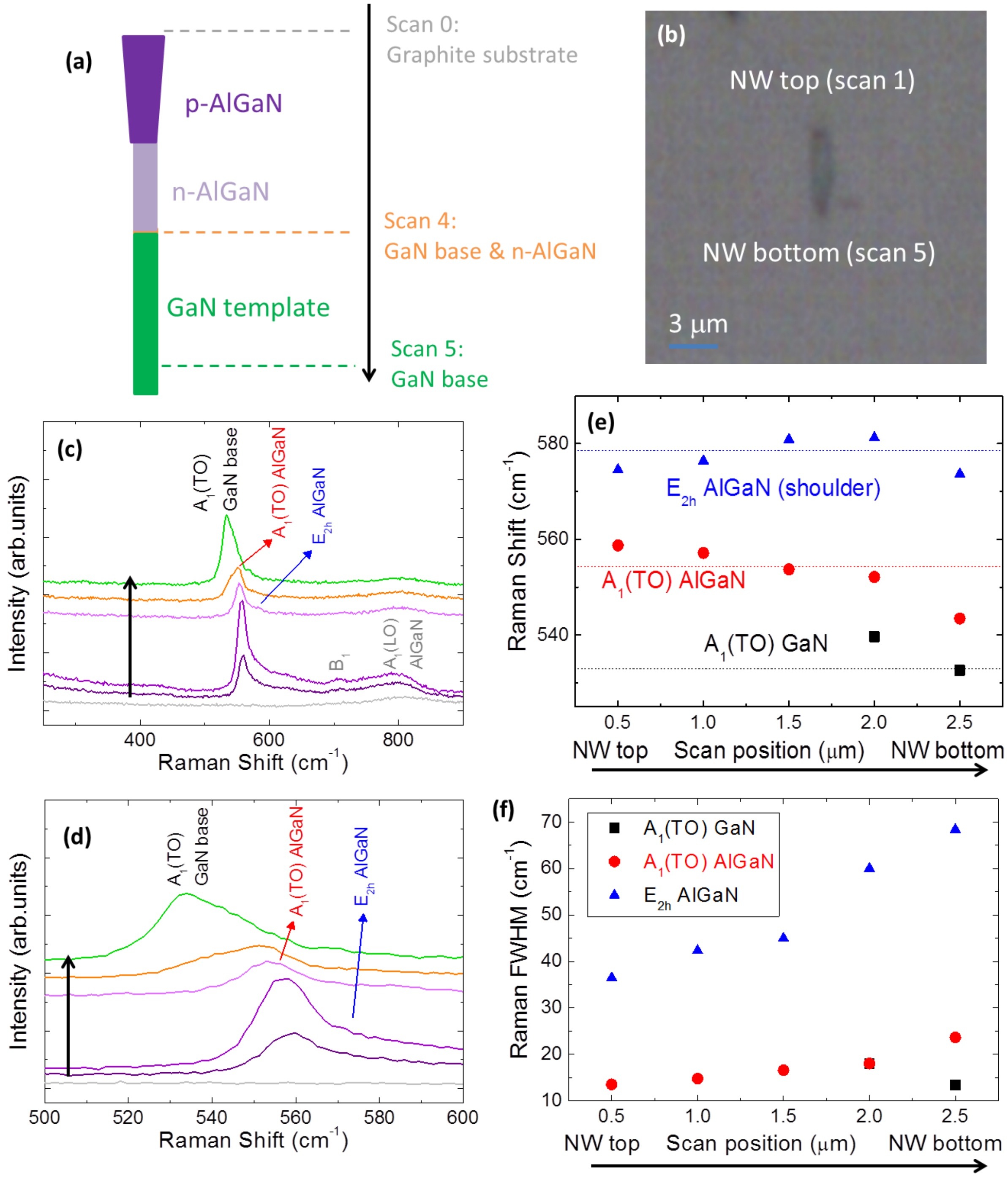

Figure 4.3.2.7: (a) Illustration of another Al$_{0.35}$Ga$_{0.65}$N NW pn junction (sample N2520) and µ-Raman scans performed along the axial direction (one scan every 0.5 µm). (b) Image of the investigated NW recorded with the Raman setup. (c) Raman spectra taken along the NW growth axis. Grey spectrum: graphite substrate (scan 0). Purple spectra: AlGaN NW pn junction (scan 1 to 3). Orange spectrum: GaN template & n-AlGaN bottom part (scan 4). Green spectrum: GaN NW template (scan 5). (d) Zoom on (c) over the 500-600 cm^{-1} range. (e) Evolution of Raman shift along the NW growth axis for several modes: A$_1$(TO) for GaN NW template, A$_1$(TO) GaN-like for AlGaN and E$_{2h}$ GaN-like for AlGaN. (f) Evolution of related Raman linewidth for these three modes. For all figures, the black arrow corresponds to the scan profile sketched in (a).

4.4 Additional discussion, conclusion and prospects of the chapter

In summary, AlGaN NW pn junctions doped using Si (n-part) and Mg (p-part) dopants, as well as references, were synthesized for various AlN molar fractions, varying from 0.35 to 0.75.

Structural characterization first highlighted specific signature of dopant incorporation within AlGaN NW sections. First, clear enlargement at low enough growth temperature of the p-doped NW tops and pits in axial composition profiles at the pn junction interface were revealed through electron microscopy techniques. Second, pn junctions were electrically evidenced using the KPFM variant of AFM structural characterization technique.

Optical characterization of doped samples also gave concluding information about dopant activation in AlGaN NW pn junctions, especially for Mg atoms. PL experiments first confirmed that the latter atoms are incorporated, since Mg-related transitions were observed at lower emission energies than the AlGaN NBE, which was further confirmed by nanoCL analysis showing specific optical signature for each part of pn junctions. The latter contrast in optical behavior between n- and p-parts was also evidenced by µ-Raman data recorded along the axial direction of investigated AlGaN NW pn junctions. Electrically, the latter are active, in view of KPFM results, but not entirely, given that macro-Raman experiments exhibited Mg-H modes indicating a passivation of some Mg dopants by hydrogen species that were residually present during growth in the MBE chamber. Post-growth annealing at several temperatures under N_2 atmosphere was then performed in order to enhance dopant activation but the first results for annealed samples were not conclusive. The whole combination of presented experiments will be performed soon on AlGaN NW pn junctions Al-richer than $Al_{0.35}Ga_{0.65}N$ in order to support our past observations, while additional annealing tries will be carried out to fully dissociate Mg-H complexes. In addition, extra optical characterization experiments must be performed in order to determine the origin of the Mg-related peak at lower energy and potentially estimate ionization energy of Mg dopants for various Al content.

Concomitantly, AlN NW pn junctions were also investigated and presented interesting features, especially in terms of morphology. Indeed, deep hollow cores were first observed in NWs and assigned to Mg doping performed at low enough growth temperature. Second, at higher substrate temperatures, the NW top morphology switched from the usual hexagonal shape to a star-like shape exhibiting 12 facets. This change from convex to concave shapes is a signature of growth carried out in conditions very far from thermodynamical equilibrium. In contrast to investigated AlGaN samples, Raman experiments did not highlight any Mg-H complexes in AlN pn junctions grown under similar conditions than their AlGaN counterparts, meaning that either Mg incorporation was significantly lower or Mg-H complexes did not form during growth. In view of residual impurity levels and C-H modes observed in Raman, the first assumption is more likely. Additional optical characterization of

AlN NW pn junctions (CL or PL with laser emitting at low enough wavelength) is firstly required to go further and will be performed in a near future. Then, depending on the observed Mg-related optical signature, the next growth run recipes will have to be adjusted accordingly.

General conclusion and prospects

The objective of the work presented in this manuscript was to investigate the fundamental properties of NID and doped AlGaN NW sections grown on top of GaN NW templates. To do so, nanostructures were elaborated by PA-MBE and analyzed using a combination of structural and optical characterization techniques, both at macro- and micro/nano-scales.

Investigation of carrier localization in $Al_xGa_{1-x}N$ nanowires

In chapter 3, the structural characterization of AlGaN NWs first evidenced a growth mechanism of AlGaN NWs governed by kinetics, supporting the growth model previously reported [139, 321, 322]. A compromise on the growth kinetic parameters fixing the average AlN molar fraction, namely the growth temperature and the metallic fluxes, had to be adopted to reduce the length of Al-richer sections preferentially nucleating on top of GaN NW templates. The full comprehension of their formation remains obscure: additional work including atomistic simulations is needed to go further.

It was then shown that NWs provide an ideal tool for studying basic optical properties of tiny amounts of III-nitride alloys free of extended defects such as grain boundaries or dislocations. In the present case, it was demonstrated, through HBT and power-dependent μ-PL experiments that the carrier localization centers highlighted in μ-PL exhibit QD-like behavior [417] and result from compositional fluctuations in AlGaN NW sections. This behavior was observed in AlGaN NWs for a wide range of values of growth temperatures and metallic fluxes. Our results are consistent with the spontaneous formation of small Ga-richer regions shown, using a combination of CW-PL and TRPL analysis, to share similar μ-optical properties over a given emission wavelength range, whatever the growth conditions explored in this study. Such regions exhibiting the single-photon emission character are present at very small scale, as signs of their existence were also evidenced in thin AlGaN QDisks embedded in AlN NWs.

More generally, this research emphasizes the potential of NWs for studying basic μ-optical properties of alloys, opening a path to its application to other III-V or II-VI alloy materials. To our knowledge, similar combination of μ-optical characterization techniques including HBT experiments has been only used so far on well-defined quantum structures, such as single InGaN QDs in NWs [514, 515], as well as self-assembled objects bigger and better-defined than the Ga-richer regions in our AlGaN NWs, as reported for AlGaAs clusters [516]. We could go even further by correlating HBT experiments with structural information in a CL setup, as successfully demonstrated for simpler objects recently [517, 518]. Another way to deepen this study would be to perform a combination of atom probe tomography (APT) experiments and simulations to derive the associated electronic structure, as reported for random AlGaAs clusters likely bigger than our self-assembled AlGaN QDs [519]. However, it has to be considered that we might be limited by the spatial resolution of the APT technique, in view of the expected size of our QD-like centers.

Study of $Al_xGa_{1-x}N$ nanowire pn junctions

In chapter 4, signatures specific to dopant incorporation, particularly Mg atoms, within AlGaN NWs were highlighted, over certain ranges of growth kinetic parameter values, through basic structural characterization. First, NWs noticeably broaden upon significant doping concentration, especially for p-doped section, which is attributed to the segregation of dopants near the NW surface. Second, the Al composition abruptly varies at the interface between n- and p-parts in AlGaN NW pn junctions, which is assigned to Mg surfactant effect favoring Al incorporation at the expense of Ga and preferential formation of substitutional Mg on Ga sites. Incorporated dopants were then demonstrated to be at least partly active through the KPFM variant of structural AFM technique. Indeed, using the latter technique, pn junctions were electrically evidenced.

Optical characterization of doped samples first confirmed that dopants, particularly Mg, are incorporated in AlGaN NW pn junctions, since Mg-related transitions were highlighted in PL at lower emission energies than the AlGaN NBE. The previous observation was further confirmed by nanoCL analysis showing specific optical signature for each part of pn junctions. An optical contrast between n- and p-parts was also evidenced by μ-Raman experiments performed along the growth axis of AlGaN NW pn junctions. Macro-Raman experiments exhibited Mg-H modes which indicate a passivation of some Mg dopants by residual hydrogen species during growth, meaning that junctions are not fully electrically active. To deal with the latter issue, post-growth annealing was performed in order to dissociate Mg-H complexes but the first results were not conclusive.

Concomitantly, AlN NW pn junctions were also examined and exhibited interesting morphological features. Indeed, deep hollow cores were observed in NWs and attributed to Mg doping performed at low growth temperature. When increasing substrate temperatures, these hollow cores disappear, while the NW top morphology was observed to switch from 6-fold hexagonal to star-like shape exhibiting 12 facets, emphasizing growth performed in conditions very far from thermodynamical equilibrium. In contrast to AlGaN samples, Raman analysis did not highlight any

Mg-H complexes in AlN pn junctions grown under similar conditions than their AlGaN counterparts. Therefore, it can be deduced that either Mg incorporation was significantly lower or Mg-H complexes did not form during growth. In view of residual impurity levels and C-H modes observed in Raman, the first assumption is more likely. Other performed optical characterization experiments have not revealed Mg-related transition so far.

More generally, this study highlights the potential of an original combination of various structural and optical characterization techniques to investigate pn junctions of very small dimensions such as those grown in self-induced NWs by PA-MBE. Such combination will be notably complemented by other methods allowing more quantitative assessment of junction electrical properties, such as direct transport and field effect transport (FET) measurements on contacted doped NWs, electron beam-induced current (EBIC) analysis on such NWs, and higher resolution EDX experiments. The use of latter techniques was successfully initiated on Si-doped GaN NWs [425, 493], Mg-doped GaN NWs [493] or GaN NW pn junctions grown by PA-MBE [493], depending on the technique, and will be extended to their $Al_xGa_{1-x}N$ counterparts.

Annexes

Annex 1: Crystallography in hexagonal systems

Annex 1.1 Miller notations for hexagonal structures

For cubic systems, the different permutations of the (hkl) Miller indices describe the whole family of symmetrically equivalent planes. Nevertheless, these indices are not convenient for hexagonal structures and a fourth index i defined as $i = -h - k$ must be introduced to fix the issue. A thorough description of the hexagonal crystal can then be made by using the Bravais-Miller four-index notation $(hkil)$. Indeed, when permuting the 3 indices h, k, and i, we describe the whole family of equivalent planes. For instance, the c-plane (0001) illustrated in Figure A.1.1.1 has no symmetric equivalent, whereas the m-plane $(1\bar{1}00)$ has five equivalents: $(10\bar{1}0)$, $(\bar{1}100)$, $(\bar{1}010)$, $(01\bar{1}0)$ and $(0\bar{1}10)$. Similarly, the a-plane $(11\bar{2}0)$ has also five equivalents.

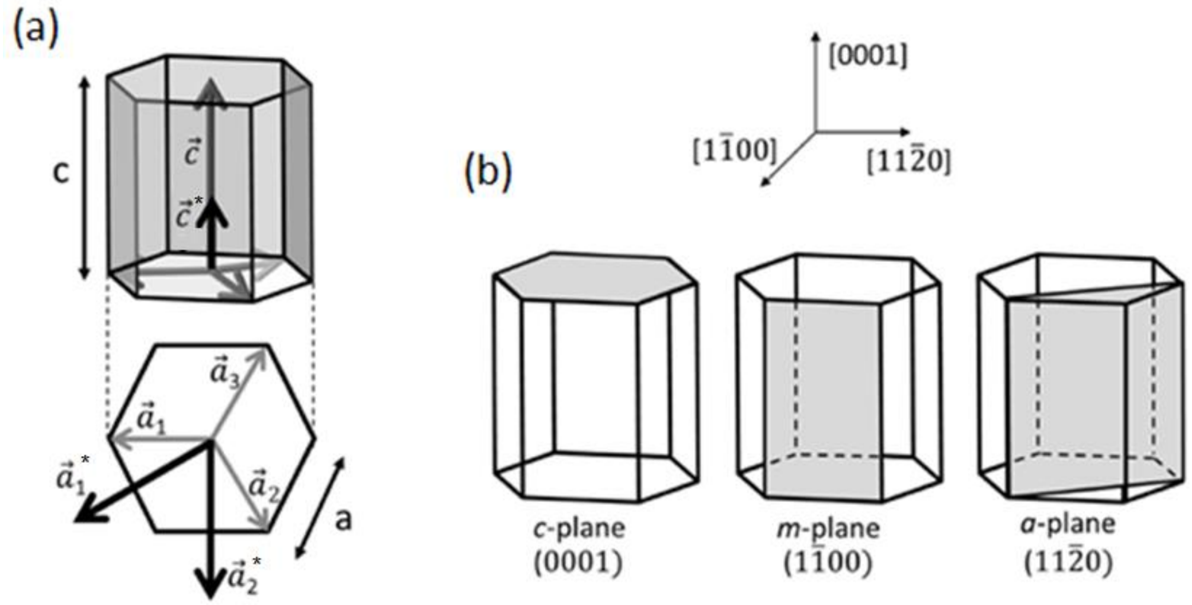

Figure A.1.1.1: (a) Direct and reciprocal space vectors for hexagonal structures. (b) Most common planes in such structures. Taken from [103].

Planes in hexagonal systems can be either expressed using the three-index or the four-index notation. The relations between the two notations are the following:

$$(hkil) \rightarrow (h,k,l) \qquad \text{(A.1.1.1)}$$
$$(xyz) \rightarrow (x,y,-x-y,z)$$

Regarding the description of directions, the four-index notation must be taken with caution. Indeed, h, k, i, and l are indeed given in the referential defined by the four basis vectors ($\vec{a}_1$, $\vec{a}_2$, $\vec{a}_3$, $\vec{c}$) shown in Figure A.1.1.1. The latter are not independent, since [520]:

$$\forall\ (i,j) \in [1,3] \times [1,3]\ \&\ i \neq j, \vec{a}_i.\vec{a}_j = \|\vec{a}_i\|\|\vec{a}_j\|\cos(\pm 120°) \neq 0 \qquad \text{(A.1.1.2)}$$
$$\vec{a}_3 = -\vec{a}_1 - \vec{a}_2$$

Consequently, the relations between the three- and the four-index notation are not as straightforward as for planes [520]:

$$[tuvw] \rightarrow [t-v, u-v, w]$$
$$[xyz] \rightarrow [\frac{2x-y}{3}, \frac{-x+2y}{3}, \frac{-x-y}{3}, z] \qquad \text{(A.1.1.3)}$$

The conversion between three-index and four-index directions can be better seen in Figure A.1.1.2.

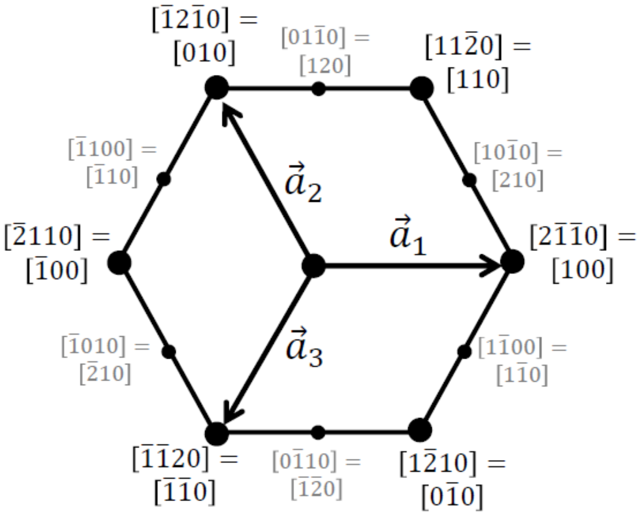

Figure A.1.1.2: Representation of the equivalence between three- and four- index notations for some directions of the hexagonal structure. Taken from [521].

The reciprocal space vectors ($\vec{a}_1^*$, $\vec{a}_2^*$, $\vec{c}^*$) are also displayed in Figure A.1.1.1. The basal reciprocal space vectors $\vec{a}_1^*$ and $\vec{a}_2^*$ are rotated of 30° compared to $\vec{a}_1$ and $\vec{a}_2$ counterclockwise and clockwise, respectively. They therefore form an angle equal to 60° and are perpendicular to $\vec{c}^*$. Norms of the reciprocal space vectors are:

$$\|\vec{a}_1^*\| = \|\vec{a}_2^*\| = \frac{2}{a\sqrt{3}} \qquad \text{(A.1.1.4)}$$

$$\|\vec{c}^*\| = \frac{1}{c}$$

By definition of Miller indices, the reciprocal space vector $\vec{Q} = h\vec{a}_1^* + k\vec{a}_2^* + l\,\vec{c}^*$ is perpendicular to the plane $(hkil)$ which intersects the real space vectors $(\vec{a}_1, \vec{a}_2, \vec{c})$ at $(1/h, 1/k, 1/l)$. However, it must be noted that in the hexagonal structure, the real space vector $\vec{R} = h\vec{a}_1 + k\vec{a}_2 + l\vec{c}$ is not perpendicular to the plane $(hkil)$, except in a few special cases but $\overrightarrow{R'} = h\vec{a}_1 + k\vec{a}_2 + \frac{3}{2}\frac{a^2}{c^2}l\vec{c}$ is.

Annex 1.2 Characteristic distances and angles in the hexagonal symmetry

In this symmetry, the expression of the interplanar distance between 2 planes of the $\{hkil\}$ family is:

$$d_{(hkl)} = \frac{1}{\sqrt{\frac{4}{3a^2}(h^2 + k^2 + hk) + \frac{l^2}{c^2}}} \qquad \text{(A.1.2.1)}$$

The angle α between two planes $(hkil)$ and $(h'k'i'l')$ is given by:

$$\cos(\alpha) = \frac{hh' + kk' + \frac{1}{2}(hk' + h'k) + \frac{3a^2}{4c^2}ll'}{\sqrt{(h^2 + k^2 + hk + \frac{3a^2}{4c^2}l^2)((h'^2 + k'^2 + h'k' + \frac{3a^2}{4c^2}l'^2)}} \qquad \text{(A.1.2.2)}$$

Table A.1.2.1 gives the values of some angles between the c-plane family and other planes frequently described in the literature about WZ nitrides and/or probed during XRD experiments.

		Family planes								
		$\{1\bar{1}00\}$ *m-plane*	$\{11\bar{2}0\}$ *a-plane*	$\{1\bar{1}02\}$ *r-plane*	$\{11\bar{2}2\}$	$\{11\bar{2}\bar{2}\}$	$\{10\bar{1}3\}$	$\{10\bar{1}4\}$	$\{10\bar{1}5\}$	$\{11\bar{2}4\}$
c-plane GaN	(0001)	90°	90°	43.2°	58.4°	121.6°	32.0°	25.1°	20.6°	39.1°
	$(000\bar{1})$	90°	90°	136.8°	121.6°	58.4°	148.0°	154.9°	159.4°	140.9°
c-plane AlN	(0001)	90°	90°	42.7°	58.0°	122.0°	31.6°	24.8°	20.3°	38.7°
	$(000\bar{1})$	90°	90°	137.3°	122.0°	58.0°	148.4°	155.2°	159.7°	141.3°

Table A.1.2.1: Angles (unit: degrees) between the c-plane family and other planes.

Annex 1.3 Hexagonal cell reduction

When performing structural characterization experiments, like resonant XRD presented in Annex 2, on samples made of several materials having different atomic arrangements (hexagonal and cubic), it can be convenient to normalize everything in the same reduced cell. For instance, in the case of our WZ nitride NWs grown on diamond Si (111) substrates, everything was expressed in the reduced Si cell to ease acquisition and processing of our anomalous XRD data.

To do so, the ZB and diamond structures can be described by a hexagonal unit cell. Figure A.1.3.1 shows how we build the hexagonal framework from the cubic one. Lattice parameters of the reduced hexagonal cell can be then expressed as $a^{hex} = a\sqrt{2}/2$ and $c^{hex} = a\sqrt{3}$. With $a_{Si} = 5.431$ Å, we obtain $a_{Si}^{hex} = 3.840$ Å and $c_{Si}^{hex} = 9.408$ Å.

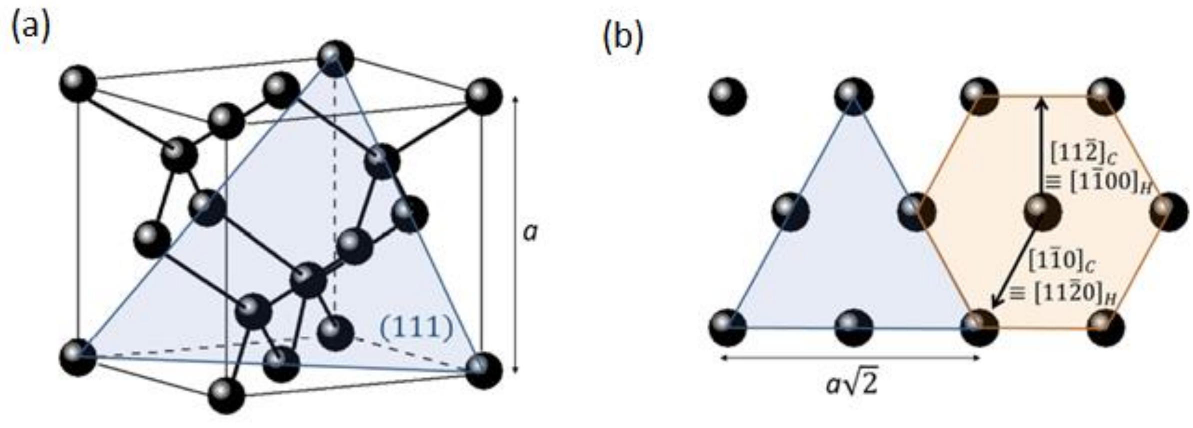

Figure A.1.3.1: (a) Diamond cell structure for Si. (b) Atomic arrangement in the (111) plane highlighted. The latter serves as a basis for the definition of the hexagonal framework.

Vectors $\vec{u}_H = (h, k, i, l)$ in the four-index notation of the hexagonal framework can be obtained from:

$$\vec{v} = (v_1, v_2, v_3) = M\vec{u}_C \qquad \text{(A.1.3.1)}$$

where:

- $\vec{u}_C$ is the vector expressed in the cubic framework
- $M = \begin{pmatrix} -\frac{1}{2} & \frac{1}{2} & 0 \\ 0 & -\frac{1}{2} & \frac{1}{2} \\ 1 & 1 & 1 \end{pmatrix}$
- Once calculated, $\vec{v}$ must be normalized to its smallest integer.

Then, $h = v_1$, $k = v_2$, $i = -v_1 - v_2$ and $l = v_3$.

Annex 2: Resonant (anomalous) X-ray diffraction

Annex 2.0: Introduction to anomalous X-ray diffraction.

Experiments were performed under the supervision of Hubert Renevier (LMGP, Grenoble) on the BM02 beam line of the European Synchrotron Radiation Facility (ESRF) of Grenoble. The synchrotron facility provides a very brilliant radiation, particularly suitable for the investigation of nanostructures. In addition, the possibility to tune the energy of the incident X-ray beam around one of the absorption edges of selected (resonant) atoms allows one to enhance the scattering from the latter atoms and to solve experimentally the crystallographic phase problem [352]. The aim of this subpart is to briefly introduce some of the advanced techniques based on resonant XRD carried out at ESRF to deepen our knowledge of AlGaN NW structural properties:

- Diffraction anomalous fine structure (DAFS).
- Multi-wavelength anomalous diffraction (MAD).

The MAD technique allows one to extract the scattering amplitudes of resonant and non-resonant atoms, and therefore to perform chemical mapping in the reciprocal space, while carrying out DAFS spectroscopy in the near-absorption edge spectral range and in the extended fine structure region can provide information about the electronic states (valence, empty orbitals, bonding information, etc.) and about the local atomic environment (neighboring species, coordinence numbers, bond length, bond disorders, etc.), respectively, of anomalous atoms selected by the diffraction condition, similarly to X-ray absorption fine structure (XAFS) spectroscopy. In contrast to the latter technique, DAFS provides not only both the advantages of XRD and absorption, but is also simultaneously a site and chemically selective probe. For instance, in the case of samples in which different local environments coexist, XAFS spectroscopy may fail to give pertinent information since, due to the lack of spatial selectivity, all the different environments are probed, whereas the DAFS technique allows the selection of individual sites and may consequently help to overcome this issue.

Knowing that XRD is a powerful tool for measuring strain fields, the combination of both MAD, adding chemical sensitivity to XRD, and DAFS, determining the local environment of atoms located in an iso-strain volume, therefore allows one to better disentangle strain and composition, similarly to previous reports [522].

In addition, the use of the mere DAFS technique can provide other information such as:

- The crystallographic polarity for WZ structure, as already shown for GaN NWs [117, 118] and ZnO NWs [523]. The determination of the latter is based on the breakdown of Friedel's law (stating $I(hkl) = I(\bar{h}\bar{k}\bar{l})$) in the case of a non-centrosymmetric crystal structure such as WZ, when tuning the incident X-ray beam energy close to an atom absorption edge. Indeed, a disparity in the diffracted intensity of Bijvoet's pairs of reflections (i.e. pairs that are symmetry-related, including the additional inversion center) can be observed at the absorption edge.

- The average composition in the case of WZ alloys, simultaneously determined with polarity.

At last, it must not be forgotten that resonant XRD is a non-destructive method that averages over many individual nanostructures and thus gives relevant statistics.

Regarding our experiments, DAFS data was recorded with a recent 2D detector (from Xpad) over a 10-11 keV range including the Ga K-edge (10.368 keV) for a whole series of as-grown AlGaN NW samples grown in various conditions, mostly in order to probe for short-range order, namely down to the scale of the next nearest neighbors of the resonant Ga atoms, within the AlGaN alloy as a function of its growth kinetic parameters (temperature and metallic fluxes setting the Al composition). The specificities of this sample series will be provided in Annex 2.4, while experimental conditions will be more detailed in the following subparts presenting experimental results.

Concomitantly, MAD was performed by recording RSMs, for a few samples of the series and a few reflections investigated through DAFS, at a dozen of different beam energies around the Ga K-edge (with the same detector as DAFS). We can then recover both the Ga and the Al+N scattering contributions corresponding to the resonant atoms and the non-resonant atoms, respectively, so that strain and composition of our AlGaN NWs can be better disentangled.

The processing of DAFS data over the extended fine structure region, namely extended DAFS (EDAFS) oscillations (visible in spectra above the edge), as well as MAD data is time-consuming and still remains to be accomplished. In the following, results extracted from DAFS data will be presented: the polarity of our AlGaN NW samples will be determined together with the average Al composition within the alloy in Annex 2.5, before preliminarily providing in Annex 2.6 normalized EDAFS data which will be quantitatively assessed in a near future. Analyzing resonant-XRD data first requires being familiar with its formalism: Annex 2.1 presents the basics, Annex 2.2 subsequently provides the formalism required for determining simultaneously the polarity of AlGaN and its average Al composition and Annex 2.3 finally presents briefly the formalism needed for the preliminary insight of the extended fine structure analysis.

Annex 2.1: Basics of resonant X-ray diffraction formalism

Let us introduce some notions required to analyze resonant diffraction experimental data quantitatively. First, the atomic scattering factor $f(\vec{Q},E)$, which is generally noted and expressed as:

$$f(\vec{Q},E) = f(Q,E) = f^0(Q) + f'(E) + if''(E) \qquad \text{(A.2.1.1)}$$

with:

- $\vec{Q} = \vec{k}' - \vec{k}$ the scattering vector, $\vec{k}$ and $\vec{k}'$ being the incident and outgoing wavevectors, respectively, and $Q = \|\vec{Q}\|$ is the norm of $\vec{Q}$.
- E the energy of the incident X-ray beam.
- $f^0(Q)$ the Thomson scattering term representing the elastic diffusion. It does not depend on the beam energy and is actually obtained by the Fourier transform of the electronic density in the atom. In addition, it constitutes the non-resonant term of the atomic scattering factor.
- $f'(E) + if''(E)$ representing the resonant scattering. More specifically, $f'(E)$ is related to dispersion and $if''(E)$ is related to absorption. The magnitude of this resonant contribution depends on the chemical nature of the scattering atom and becomes significant when the photon energy is close to one of the absorption edges of this atom.

Second, in an ideal case, the total structure factor can be expressed, by summing the scattering contributions of all atoms (number N_{all}) present in the lattice, as:

$$F(\vec{Q},E) = \sum_{site\ n}^{N_{all}} f_n(Q,E)e^{i\vec{Q}.\vec{r}_n} \qquad \text{(A.2.1.2)}$$

with:

- $f_n(Q,E)$ the scattering factor of the n^{th} atom site in the lattice.
- $\vec{r}_n$ the position vector of the m^{th} atom site in the lattice.

Size or thermal effects can be also considered through correction factors, such as the Debye-Waller factor which takes into account the diffracted intensity attenuation due to thermal effects. Its expression is of the following form, for the atom on the nth site, with M_n a constant and $\vec{Q}$ the scattering vector:

$$DWF_n(\vec{Q}) = e^{-M_n \times \|\vec{Q}\|^2} \qquad \text{(A.2.1.3)}$$

so that the total structure factor expression can be written, based on Equation (A.2.1.2):

$$F(\vec{Q},E) = \sum_{site\ n}^{N_{all}} f_n(Q,E)e^{-M_n \times Q^2} e^{i\vec{Q}.\vec{r}_n} \tag{A.2.1.4}$$

Then, the expression of measured diffracted intensity I can be derived. Indeed, it is proportional to $|F\,|^2$ and can be written:

$$I(\vec{Q},E) = S \times D(E) \times C(E) \times A(\vec{Q},E) \times L(\vec{Q},E) \times P(\vec{Q},E) \times \left|F(\vec{Q},E)\,\right|^2 \tag{A.2.1.5}$$

where:

- S is a scaling factor.
- D takes into account the detector efficiency over the investigated energy range. Its expression is usually of the form:

  $$D(E) = 1 + slope \times (E - E_{edge}) \tag{A.2.1.6}$$

  as it was for the former 1D detector used for previous DAFS experiments.
- C is a corrective term which had to be added to both better describe the new 2D detector instrumental response and take into account slight experimental drifts of the diffracted beam. Its expression is of the form:

  $$C(E,\alpha) = (E/E_{edge})^{\alpha} \tag{A.2.1.7}$$

  with α a real exponent. This term will be briefly discussed hereafter in Annex 2.5.
- A is an absorption correction term, taking into account the experimental geometry (in reflection here). Its expression is of the form:

  $$A(E) = \frac{1 - e^{-\frac{2\mu(E)t}{\sin(\theta)}}}{2\mu(E)} \tag{A.2.1.8}$$

  with θ the incident angle, t the equivalent layer thickness (or equivalent NW section length) and $\mu(E)$ the absorption coefficient for the investigated material.
- L and P are respectively the Lorentz and polarization correction terms. These terms mainly depend on the experimental configuration and can be easily determined [352]. Here, knowing that the polarization vectors of the incident and diffracted beams are perpendicular to the scattering plane, we have:

$$L(E) = (E/E_{edge})^3 \qquad \text{(A.2.1.9)}$$
$$P = 1$$

Annex 2.2: DAFS formalism specific to the assessment of AlGaN polarity and average alloy composition

Let us now develop the formalism related to the DAFS-based crystallographic polarity and AlN molar fraction determination. Using the description of the WZ nitride lattice given in Subpart 1.1.1 and Equation (A.2.1.2), we can express the average total structure factor for $Al_xGa_{1-x}N$ of average AlN molar fraction x, in terms of hkl indices ($\vec{Q}$ and E omitted in the expression hereafter to lighten notations), as:

$$\begin{gathered} F\big(\vec{Q}(hkl),E\big) = F(hkl) = \\ = x\left(f_{Al}e^{2i\pi\left(\frac{1}{3}h+\frac{2}{3}k\right)} + f_{Al}e^{2i\pi\left(\frac{2}{3}h+\frac{1}{3}k+\frac{1}{2}l\right)}\right) + \\ (1-x)\left(f_{Ga}e^{2i\pi(\frac{1}{3}h+\frac{2}{3}k)} + f_{Ga}e^{2i\pi(\frac{2}{3}h+\frac{1}{3}k+\frac{1}{2}l)}\right) + f_N e^{2i\pi(\frac{1}{3}h+\frac{2}{3}k+ul)} \\ + f_N e^{2i\pi(\frac{2}{3}h+\frac{1}{3}k+(\frac{1}{2}+u)l)} \end{gathered} \qquad \text{(A.2.2.1)}$$

with $u = \frac{3}{8}$ for a perfect WZ crystal. It must be noted that the previous expression is valid in the ideal case: terms taking size or thermal effects into account, such as the Debye-Waller factor, are not shown here in order to lighten the expressions but can be considered in software programs used to process the data. From Equation (A.2.2.1), we can then express the structural factor modulus squared $|F\,|^2$ as (lightened notations):

$$\begin{gathered} |F(hkl)\,|^2 = \\ \big[(1-x)^2\, f_{Ga}f_{Ga}^* + x^2 f_{Al}f_{Al}^* + f_N f_N^* + x(1-x)(f_{Al}f_{Ga}^* + f_{Ga}f_{Al}^*) \\ + (1-x)\big(f_{Ga}f_N^* e^{2i\pi ul} + f_N f_{Ga}^* e^{-2i\pi ul}\big) \\ + x\big(f_{Al}f_N^* e^{2i\pi ul} + f_N f_{Al}^* e^{-2i\pi ul}\big)\big] \\ \times 2\left[1 + \cos\left(2\pi\left(\frac{1}{3}(h-k) + \frac{1}{2}l\right)\right)\right] \end{gathered} \qquad \text{(A.2.2.2)}$$

so that we can write the intensity difference for a Bijvoet’s pair (notations lightened hereafter):

$$\begin{aligned} I(hkl) - I(hk\bar{l}) &\propto \left(|F(hkl)|^2 - \left|F(hk\bar{l})\right|^2\right) \\ &\propto \left[1 + \cos\left(2\pi\left(\frac{1}{3}(h-k) + \frac{1}{2}l\right)\right)\right] \\ &\times 8\Big[\big((1-x)(f_{Ga}^0 + f_{Ga}{}') + x(f_{Al}^0 + f_{Al}{}')\big) f_N'' \\ &- (f_N^0 + f_N{}')\big((1-x)f_{Ga}'' + x f_{Al}''\big)\Big] \sin(2\pi u l) \end{aligned} \quad (A.2.2.3)$$

The previous expression notably shows that this difference cancels out when $l = 4n$, n being an integer. It also gets near 0 when exciting a sample over incident X-ray beam energy ranges which exclude any atom absorption edge. Indeed, all the f' and f'' terms would be small in this case and we would then retrieve Friedel's law. In contrast, when exciting a sample at the Ga K-edge, the f' and f'' anomalous scattering factors for N and Al remain constant and small in comparison with those of Ga, as shown in Figure A.2.2.1 giving the tabulated f' and f'' factors for the three species over the investigated beam energy range [524]. Although these values of f' and f'' are tabulated, f'' can be precisely experimentally determined through fluorescence measurements and f' is then derived from f'' thanks to Kramers-Kronig relations, as shown further in Annex 2.5. The tabulated Thomson scattering factors f^0 are also given for the three species in Figure A.2.2.2 so that the intensity difference for a Bijvoet's pair can be directly calculated [524]. From Equation (A.2.2.3), the latter can be approximated, for a x not too close to 1, by (lightened notations):

$$\begin{aligned} &|F(hkl)|^2 - \left|F(hk\bar{l})\right|^2 \cong \\ &-8\left[1 + \cos\left(2\pi\left(\frac{1}{3}(h-k) + \frac{1}{2}l\right)\right)\right] f_N^0 (1-x) f_{Ga}'' \sin(2\pi u l) \end{aligned} \quad (A.2.2.4)$$

The latter expression directly shows that the intensity difference abruptly increases when going above the Ga-K absorption edge.

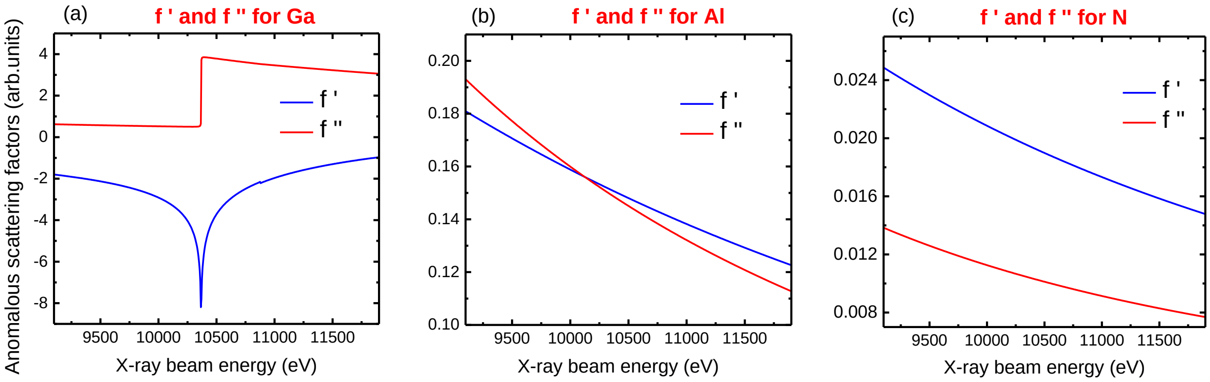

Figure A.2.2.1: Tabulated anomalous scattering factors f' and f'' over an incident X-ray beam energy range including the Ga-K edge, for: (a) Ga, (b) Al and (c) N. Adapted from [524].

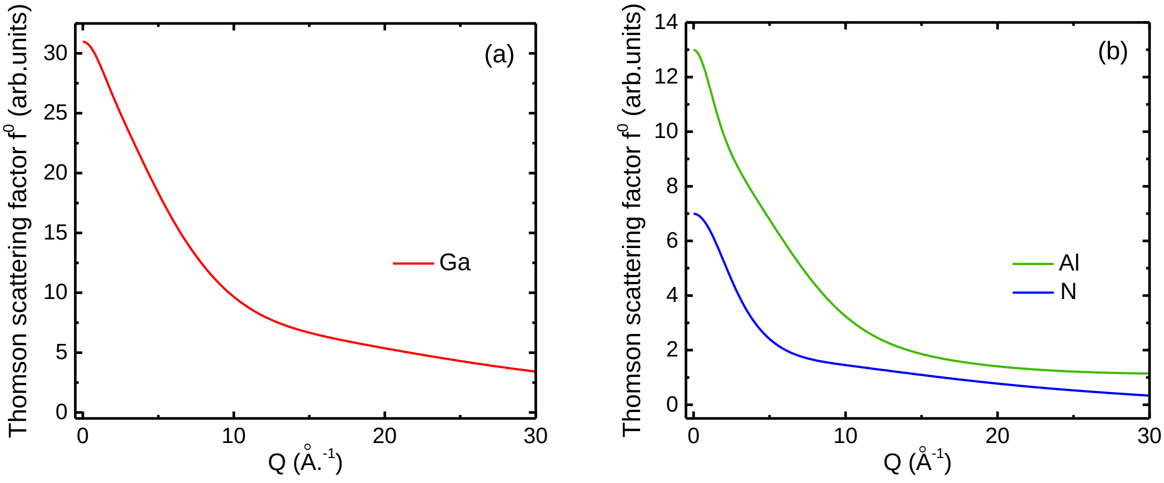

Figure A.2.2.2: Tabulated Thomson scattering factor f^0 as a function of Q for: (a) Ga, (b) Al and N. Adapted from [524].

Provided that fluorescence signal and absorption attenuation can be properly estimated, the DAFS measurement for one reflection among a well-chosen Bijvoet's pair is sufficient to not only determine the AlGaN polarity but also to estimate/check the average AlN molar fraction x in the alloy, as shown further in Annex 2.5 for all the investigated AlGaN NW samples presented in Annex 2.4.

Annex 2.3: DAFS formalism peculiar to the extended fine structure analysis

In this subpart, we will briefly introduce the formalism needed for a preliminary overview of the extended fine structure region analysis. The latter first requires a rewriting of the atomic scattering factor. Above the absorption edge, the latter for an anomalous Ga atom on the j$^{\text{th}}$ site may be split into a "smooth" and an "oscillatory" part:

$$\begin{aligned} f_{Ga,j}(Q,E) &= f^0_{Ga}(Q) + f'_{Ga,j}(E) + if''_{Ga,j}(E) \\ &= f^0_{Ga}(Q) + {f^0_{Ga}}'(E) + i{f^0_{Ga}}''(E) + \Delta {f^0_{Ga}}''(E)\left[\chi'_j(E) + i\chi''_j(E)\right] \end{aligned} \qquad \text{(A.2.3.1)}$$

where:

- $f'_{Ga,j}(E) = {f^0_{Ga}}'(E) + \Delta {f^0_{Ga}}''(E)\chi'_j(E)$ and $f''_{Ga,n}(E) = {f^0_{Ga}}''(E) + \Delta {f^0_{Ga}}''(E)\chi''_j(E)$ are respectively the "smooth" and "oscillatory" parts of the anomalous atomic scattering factors.
- f^0_{Ga} is the Thomson scattering of Ga resonant atoms. ${f^0_{Ga}}' + i{f^0_{Ga}}''$ is the anomalous scattering of bare neutral atoms. $f^0_{Ga} + {f^0_{Ga}}' + i{f^0_{Ga}}''$ is the smooth atomic scattering factor.
- $\Delta {f^0_{Ga}}''$ is the contribution of the resonant scattering to ${f^0_{Ga}}''$.

- $\chi'_j(E) + i\chi''_j(E) = \tilde{\chi}_j(E)$ is the complex EDAFS term. χ'_j and χ''_j are related by the Kramers-Kronig transforms. It must be emphasized that, although DAFS contains contributions of both the real and imaginary parts of the complex anomalous scattering factors (XAFS is only proportional to the imaginary part), EDAFS data can be analyzed like extended XAFS (EXAFS) data [522, 525]. Indeed, χ''_j is related to the equivalent EXAFS χ_j term by the following equation:

$$\chi_{EXAFS,j}(E) = Im_{\tilde{\chi}_j}(\vec{Q} = \vec{0}, E). \tag{A.2.3.2}$$

From Equation (A.2.1.2), the total structure factor can be then rewritten, with N_{Ga} the number of anomalous Ga atoms:

$$F(\vec{Q}, E) = F_0(\vec{Q}, E) + \frac{\Delta f_{Ga}^{0''}(E)}{f_{Ga}^0(Q)} \sum_j^{N_{Ga}} F_j(\vec{Q})[\chi'_j(E) + i\chi''_j(E)] \tag{A.2.3.3}$$

where:

- $F_0 = |F_0|e^{i\varphi_0}$ is the total structure factor without the contribution of extended fine structure, in other words the smooth structure factor. We note φ_0 its phase.
- F_j is the partial structure factor of an anomalous Ga atom on the jth site.

We can then derive the diffracted intensity $I(\vec{Q}, E)$ proportional to the modulus squared of the structure factor. The latter can be then approximated at the first-order by the following expression ($\vec{Q}$ and E omitted in order to lighten notations):

$$|F|^2 \cong |F_0|^2 + \frac{2|F_0||F_{Ga}|\Delta f_{Ga}^{0''}}{f_{Ga}^0}\chi_Q \tag{A.2.3.4}$$

where $F_{Ga} = |F_{Ga}|e^{i\varphi_{Ga}}$ is the partial structure factor of all resonant Ga atoms (φ_{Ga} being its phase) and χ_Q is the first-order EDAFS term. The full expression of $|F(\vec{Q}, E)|^2$ with the second-order terms, negligible in most cases, can be found in the literature [525]. Neglecting the latter terms, the first-order EDAFS $\chi_Q(k)$ for a given scattering vector $\vec{Q}$ can be literally expressed in k-space (left term below) and extracted directly out of the experimental spectrum (right term below), as follows (lightened notations):

$$\chi_Q(k) = \cos(\varphi_0 - \varphi_{Ga}) \sum_j^{N_{Ga}} w_j' \chi_j' + \sin(\varphi_0 - \varphi_{Ga}) \sum_j^{N_{Ga}} w_j'' \chi_j'' = S_D \frac{I_{exp} - I_{0,exp}}{I_{0,exp}} \tag{A.2.3.5}$$

where:

- k is the photoelectron wave number, which is equal to:

$$k = \sqrt{2m(E - E_{edge})}/\hbar \tag{A.2.3.6}$$

  where m is the effective mass, $\hbar$ is the reduced Planck constant, and E_{edge} is the absorption edge energy.
- I_{exp} is the experimental DAFS intensity corrected for the background intensity (mainly fluorescence).
- $I_{0,exp}$ is the smooth DAFS intensity (without the EDAFS oscillations).
- S_D is the DAFS normalization factor ($S_D = f_{Ga}^0 |F_0| / (2|F_{Ga}|\Delta f_{Ga}^{0''})$).
- w_j' and w_j'' are the crystallographic weights.

Experimental $\chi_Q(k)$ spectra will be provided in Annex 2.6 for examined AlGaN NW samples presented in Annex 2.4. The determination of normalization factor S_D and the phase difference $\varphi_0 - \varphi_A$ does not require any crystallographic model and can be done directly from the experimental data. As for the crystallographic weights, they can be either calculated from the crystallographic structure, provided that the latter is known, or experimentally determined if the individual $\chi_j'(\chi_j'')$ are known by fitting Equation (A.2.3.5) to the experimental χ_Q. It must be stressed that the w_j'' weights emphasize the site/spatial selectivity of the EDAFS technique, in contrast to EXAFS. Once all the required parameters are known, the χ_j' and χ_j'' terms carrying the extended fine structure information can be finally extracted for each anomalous Ga atom site by iteratively solving the linear system formed by the $\chi_Q(k)$ (see Equation (A.2.3.5)) at each wave number k and using the Kramers-Kronig transforms as an additional constraint to relate χ_j' and χ_j''.

At last, it must be noted that a peculiar formalism called the “path formalism” can be used to facilitate the extraction of short-range structural information from the extended fine structure region. This formalism is not detailed here since we do not present any quantitative analysis in Annex 2.6 but its full description can be found in previous reports [522, 525]. In a nutshell, it consists in writing the complex fine structure $\tilde{\chi}_j$ related to a given resonant Ga atom on the jth site as an expansion over the scattering paths of the photoelectron around the absorbing atom. Doing so implies then to rewrite Equation (A.2.3.5) accordingly and allows one to ease the parametrization of the linear system mentioned just above, to treat the EDAFS data as EXAFS data, as well as to avoid using the Kramers-Kronig iterative method which is demanding in terms of calculation.

Annex 2.4: Samples investigated by anomalous X-ray diffraction

For our experimental needs, six samples, consisting of NID AlGaN NW sections on top of GaN NW templates, were grown by PA-MBE using the same protocol as described in Subpart 3.1, except that typical NW dimensions were different and specifically adapted to these ESRF experiments. Indeed, the GaN NW templates were first grown shorter (length inferior to 200 nm) in order to limit their fluorescence. Consequently, given that experiments were only performed on as-grown samples, the NW density had to be even more carefully controlled to avoid as much as possible parasitic Al-rich 2D layers nucleating between GaN bases (see Subpart 2.1.4). Second, AlGaN NW sections were short as well and chosen to be about 250 nm long, which is sufficient to obtain intense DAFS signal in view of the AlGaN-related scattering factors over the investigated beam energy range [524]. It must be also stressed that NWs were grown on a thin AlN buffer synthesized on a Si (111) buffer in order to improve NW orientation, similarly to those examined in chapter 3.

From one sample to another, GaN NW templates were grown in similar conditions, whereas the nominal AlN molar fraction in the AlGaN alloy and its growth temperature were set:

- At one among three different x values for the molar fraction, either x = 0.3 or x = 0.5 or x = 0.75 (same atomic fluxes for a given composition).
- At one of two distinct T_{subs} values for the growth temperature, either T_{subs} ≈ 860°C or T_{subs} ≈ 790°C corresponding to $t_{des}^{Ga} \approx$ 10 s and $t_{des}^{Ga} \approx$ 60 s (also designated by higher temperature (HT) and lower temperature (LT) in the following), respectively.

Table A.2.4.1 provides the AlGaN growth conditions for the six investigated samples, some structural parameters required for processing the data (notably to calculate the absorption coefficient), as well as the average AlN molar fraction values derived from experimental a and c lattice parameter values determined in two different ways. The first one was to measure these parameters by using the extended Bond method [355] in a standard diffractometer (see Subpart 2.2.2 for the method and laboratory setup details), whereas the second one consisted in deriving them from Bragg peak positions corresponding to AlGaN NW sections in RSMs recorded for several reflections (at least 112 and 103) at the BM02 beam line of ESRF. In both cases, once the lattice parameters (averaged over the investigated reflections) were known, the average AlN molar fraction x in our $\mathrm{Al}_x\mathrm{Ga}_{1-x}\mathrm{N}$ NW sections could be estimated by combining Vegard's law with Equation (2.2.2.3) of Subpart 2.2.2 linking the relaxed lattice parameters (taken from literature [13]) and the strained (experimental) ones, similarly to previous reports [355]. The experimental lattice parameters determined from ESRF data are sketched further for all samples, in Figure A.2.4.3.

It must be noted that the accuracy on the lattice parameter values extracted from ESRF data is expected to be higher than for those obtained on the standard laboratory setup with the extended Bond method. Indeed, the instrumental resolution, which can be notably adjusted by varying the sample-detector distance (1.05 m for our experiments), and the signal-to-noise ratio are firstly much higher with the ERSF setup than with the standard laboratory diffractometer. Moreover, every ESRF data acquisition was performed in the reduced hexagonal cell of Si (presented in Annex 1.3) taken as reference, allowing a quasi-absolute determination of the lattice parameters.

When briefly looking at Table A.2.4.1, it can be noticed that all estimated Al composition values are of the order of targeted nominal Al contents, except for the first $Al_{0.3}Ga_{0.7}N$ NW sample (N2497 HT), which is surprisingly much Al-richer than expected, despite the use of same atomic fluxes during growth as the other $Al_{0.3}Ga_{0.7}N$ NW sample (N2499 LT).

Sample		$Al_xGa_{1-x}N$ growth parameters		Structural parameters		Average Al composition from XRD	
Reference number	Nominal x_{Al} (%)	T_{subs} (°C)	t_{des}^{Ga} (s)	Average AlGaN section length (nm)	Fill factor (%)	Standard XRD setup (%)	ESRF RSM data (%)
N2497 (HT)	30	867	10	226	38.8	53.7	50.7
N2499 (LT)	30	789	60	273	43.7	30.2	33.7
N2502 (HT)	50	847	10	262	45.8	46.8	53.8
N2504 (LT)	50	795	60	285	35.4	42.9	44.7
N2501 (HT)	75	859	10	224	41.1	75.8	78.2
N2507 (LT)	75	785	60	224	36	67	73.2

Table A.2.4.1: Summary of growth conditions and experimental average AlN molar fractions for the six AlGaN NW samples investigated on the BM02 beam line of ESRF.

Figure A.2.4.1 displays SEM images corresponding to the X-ray beam impinging area, for each investigated sample, while Figure A.2.4.2 gives typical STEM images of dispersed NWs for some samples, exhibiting Al-richer shells around AlGaN NW cores and parasitic Al-richer sections preferentially nucleating on top of GaN NW templates, as already described in Subpart 3.1. It can be seen from Figure A.2.4.2 that the length of the latter sections is zero or negligible for $Al_{0.3}Ga_{0.7}N$ and $Al_{0.5}Ga_{0.5}N$ NW samples, in contrast to $Al_{0.75}Ga_{0.25}N$ NW samples for which such sections are pure AlN and must be taken into account when estimating the equivalent NW length required for calculating the AlGaN absorption coefficient. To do so, statistics on the AlN NW section length were performed based on STEM images and the resulting average length of this section was subtracted from the AlGaN+AlN section length estimated from side-view SEM images. It must be noted that the error bar on the AlGaN absorption coefficient will be higher for the $Al_{0.75}Ga_{0.25}N$ sample grown at high temperature (N2501 HT) in view of the significant disparity on the AlGaN section length for this sample (see Figure A.2.4.2 (c)).

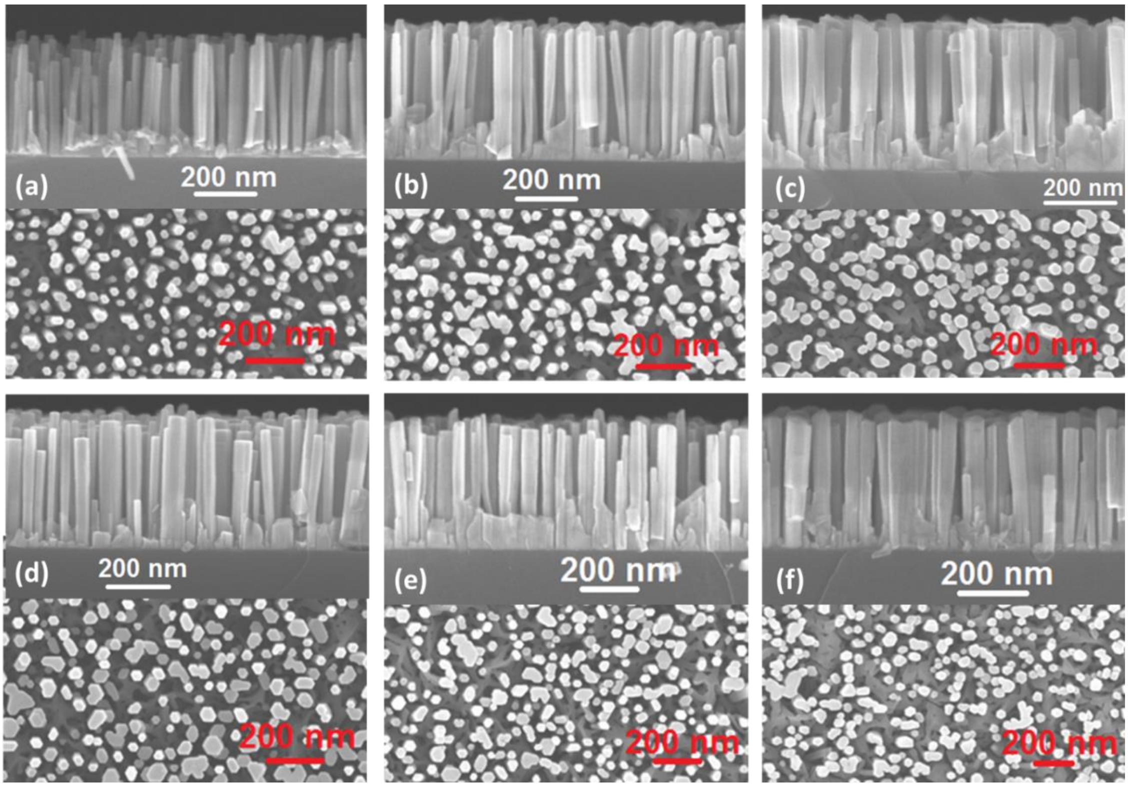

Figure A.2.4.1: Side-view and top-view SEM images taken in the area of X-ray beam impinging area for $Al_{0.3}Ga_{0.7}N$ NWs ((a): N2497, $t_{des}^{Ga} \approx$ 10 s and (d): N2499, $t_{des}^{Ga} \approx$ 60 s), $Al_{0.5}Ga_{0.5}N$ NWs ((b): N2502, $t_{des}^{Ga} \approx$ 10 s and (e): N2504, $t_{des}^{Ga} \approx$ 60 s) and $Al_{0.75}Ga_{0.25}N$ NWs ((c): N2501, $t_{des}^{Ga} \approx$ 10 s and (f): N2507, $t_{des}^{Ga} \approx$ 60 s).

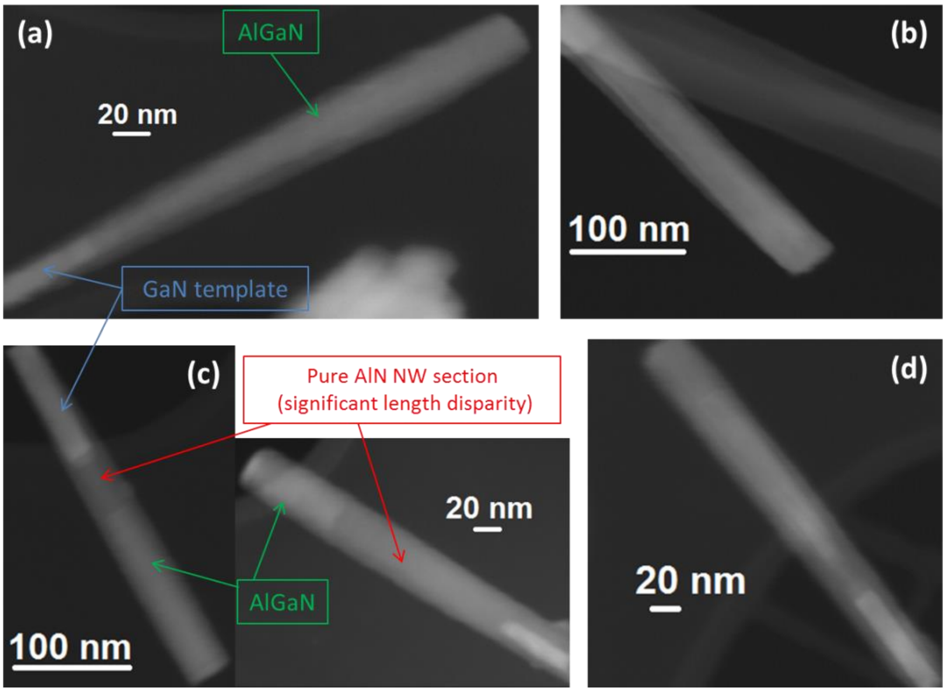

Figure A.2.4.2: STEM images of dispersed NWs for: (a) $Al_{0.5}Ga_{0.5}N$ sample grown at $t_{des}^{Ga} \approx$ 10 s (N2502 HT), (b) $Al_{0.5}Ga_{0.5}N$ sample grown at $t_{des}^{Ga} \approx$ 60 s (N2504 LT), (c) $Al_{0.75}Ga_{0.25}N$ sample grown at $t_{des}^{Ga} \approx$ 10 s (N2501 HT), and (d) $Al_{0.75}Ga_{0.25}N$ sample grown at $t_{des}^{Ga} \approx$ 60 s (N2507 LT).

Figure A.2.4.3 compares the experimental lattice parameter values for the six investigated samples with those calculated assuming relaxed AlGaN in these samples. We can directly notice that the AlGaN NW sections are not as relaxed as we could have expected knowing that strain relaxation is eased in NWs by their sidewalls. Indeed, AlGaN NW sections undergo no or slight out-of-plane compressive strain due to the thin Al-richer shells, and more significant in-plane tensile strain, induced by the growth on lattice mismatched GaN NW templates. In fact, strain is progressively relaxed along AlGaN NW growth axis, as already mentioned in Subpart 2.1.4 (strain pulling effect) and Subpart 3.1, so that it is likely to be not fully relaxed for AlGaN NW sections as short as those specifically grown for these experiments. As expected, the gap between the experimental lattice parameter values and those for relaxed AlGaN rises when increasing the Al content, which mostly results from the more significant in-plane tensile strain in this case.

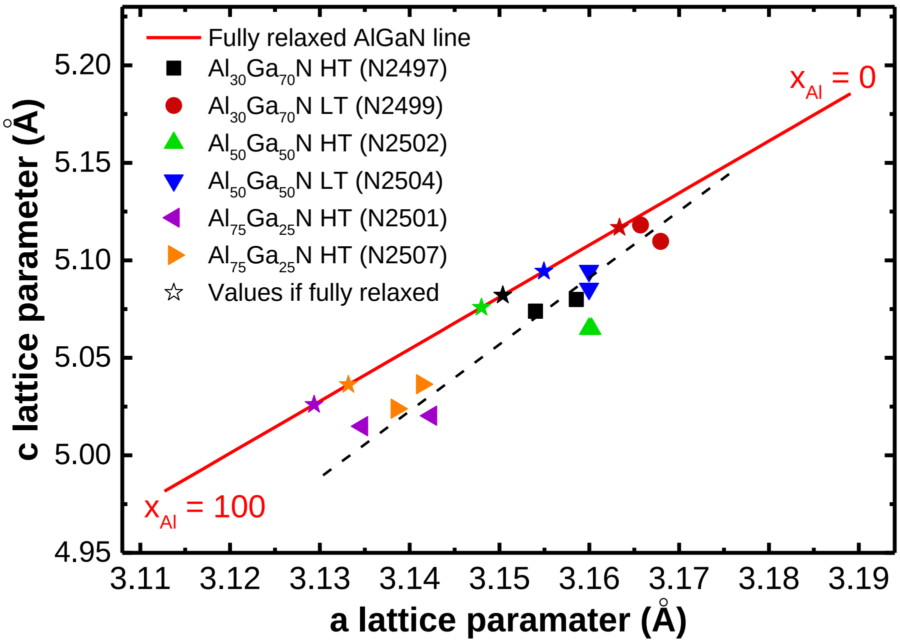

Figure A.2.4.3: Experimental lattice parameter c versus a for the six investigated samples. For each sample, two points, derived from RSMs around 103 and 112 reflections recorded at BM02 beam line at ESRF, are displayed. The solid red line corresponds to the values expected for fully relaxed AlGaN when varying the AlN molar fraction from 0 to 1, whereas the dashed black line represents the evolution of strained AlGaN lattice parameters with AlN molar fraction for our samples. The stars indicate the expected lattice parameter values calculated from average Al composition values provided in the last column of Table A.2.4.1, if the six samples were fully relaxed.

Annex 2.5: Simultaneous determination of the polarity and average Al composition of AlGaN NWs through DAFS spectroscopy

DAFS spectra were recorded at Bragg peak positions related to AlGaN, for beam energies in the 10-11 keV range (around the Ga-K edge at 10.368 keV) and at least for two reflections for each sample. The 103, 112 and 002 reflections were chosen, notably because they are among the most intense reflections for WZ nitrides. In the following, the first two reflections were mostly investigated. Concomitantly, fluorescence was also recorded by a point detector (scintillator detector) in order to obtain the experimental resonant scattering factor for Ga displayed in Figure A.2.5.1: its imaginary part f'' was directly extracted from the fluorescence data and its real part f' was obtained from f'' thanks to Kramers-Kronig relations.

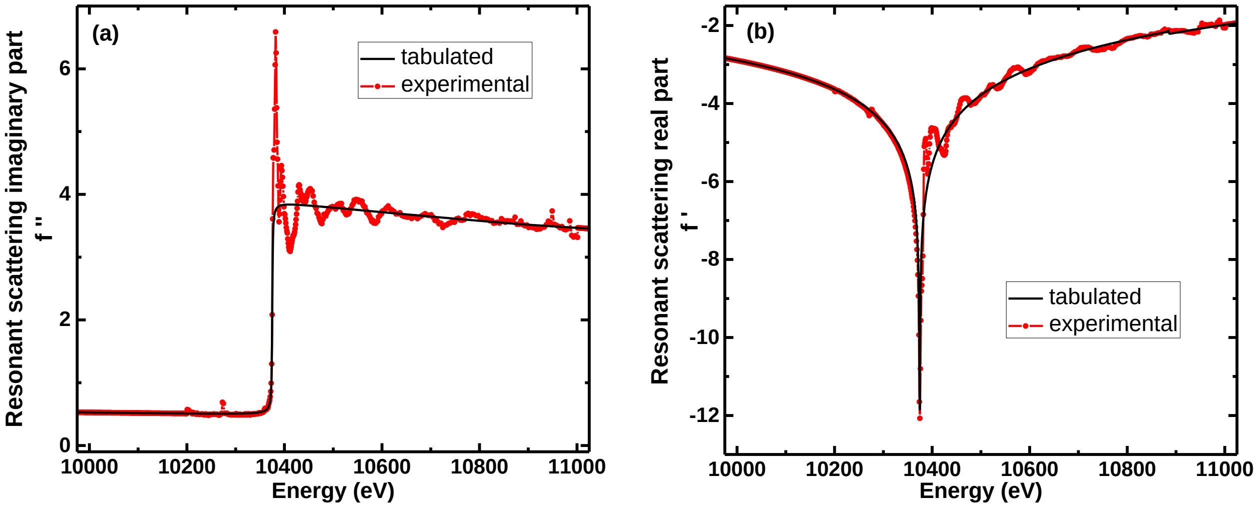

Figure A.2.5.1: Ga resonant scattering experimentally determined from the fluorescence (red line): (a) imaginary part f'' and (b) real part f' determined from f'' using Kramers-Kronig relations. The theoretical values (tabulation also displayed in Figure A.2.2.1 of Annex 2.2) are provided (black lines), as references.

Using a software program (DAFIT) based on the formalism introduced in Annexes 2.1 and 2.2 (crystallographic model), the DAFS spectra (corrected for background) were fitted to derive the NW polarity and the average AlN molar fraction at the same time. DAFS data before the Ga-K threshold mostly determine the average Al composition value and had to be perfectly fitted. As for the part of DAFS spectra above the absorption edge, several parameters, including the AlGaN equivalent thickness (corresponding to the product of the average AlGaN NW section length and the fill factor, both provided in Table A.2.4.1), the beam incident angle and the experimental Ga anomalous scattering factor, had to be entered in the program to properly calculate the AlGaN absorption correction. Moreover, an additional correction factor $C(E,\alpha)$, presented in Annex 2.1, had to be introduced both to consider the additional spectral distortion induced by the 2D detector with respect to the former 1D detector over the investigated beam energy range, especially above the edge, and to take into account the slight experimental drifts of the diffracted beam observed during experiments. The α exponent could slightly vary from one investigated sample and/or reflection to another. Figure A.2.5.2, Figure A.2.5.3, and Figure A.2.5.4 provide several examples of DAFS spectra for our investigated samples, exhibiting the fits for the three investigated reflections of an $Al_{0.5}Ga_{0.5}N$ sample (N2502 HT), those for the same reflection (103) recorded for three samples of different nominal Al content grown at the same temperature (N2499 LT, N2504 LT, N2507 LT), and those for two reflections (103 and 112) recorded for two samples of same nominal Al composition but grown at different substrate temperatures ($Al_{0.75}Ga_{0.25}N$, N2501 HT and N2507 LT), respectively.

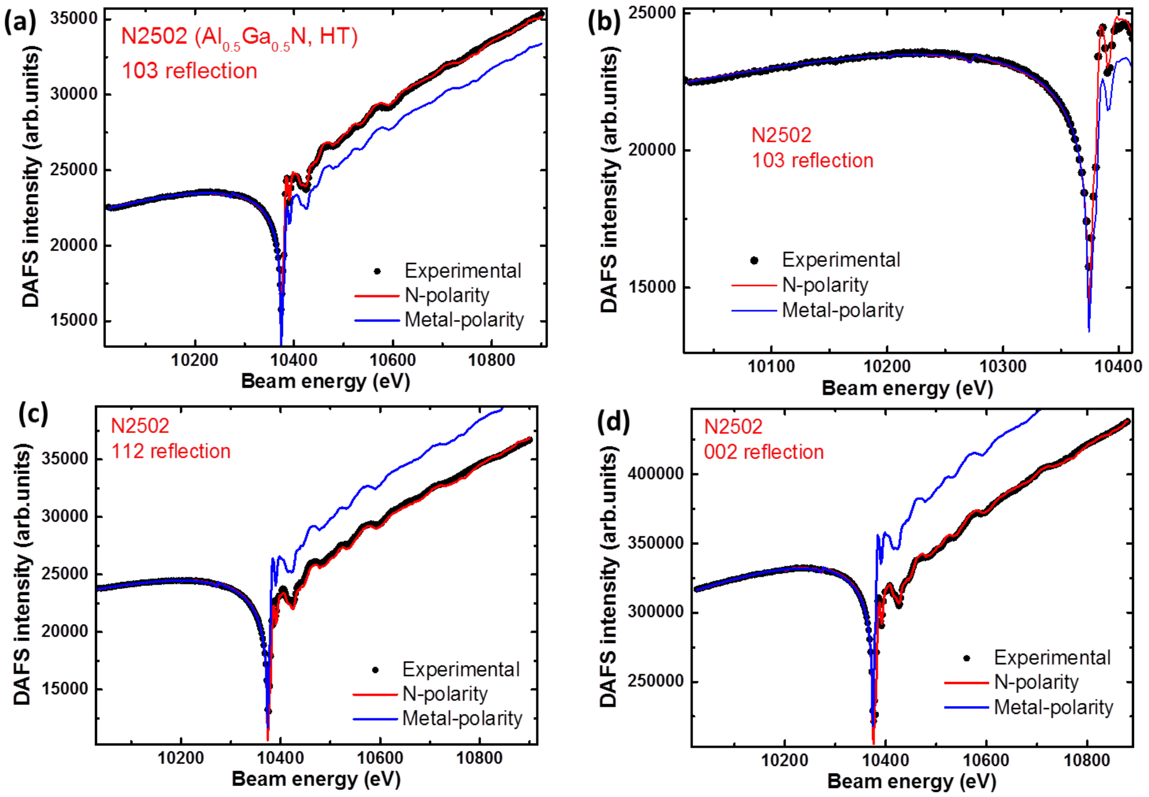

Figure A.2.5.2: DAFS spectra recorded around the Ga-K edge at the Bragg peak position related to $Al_{0.5}Ga_{0.5}N$ NW sections grown at $t_{des}^{Ga} \approx$ 10 s (N2502 HT), for the following reflections: (a) & (b) 103, (c) 112, (d) 002. Fits performed for the two reflections of Bijvoet's pair are displayed on each spectrum: the sample is clearly N-polar, in view of the DAFS intensity difference between both cases above the threshold. (b) zooms on the energy range before the Ga-K threshold: DAFS data over this range mostly sets the Al composition value and must be perfectly fitted.

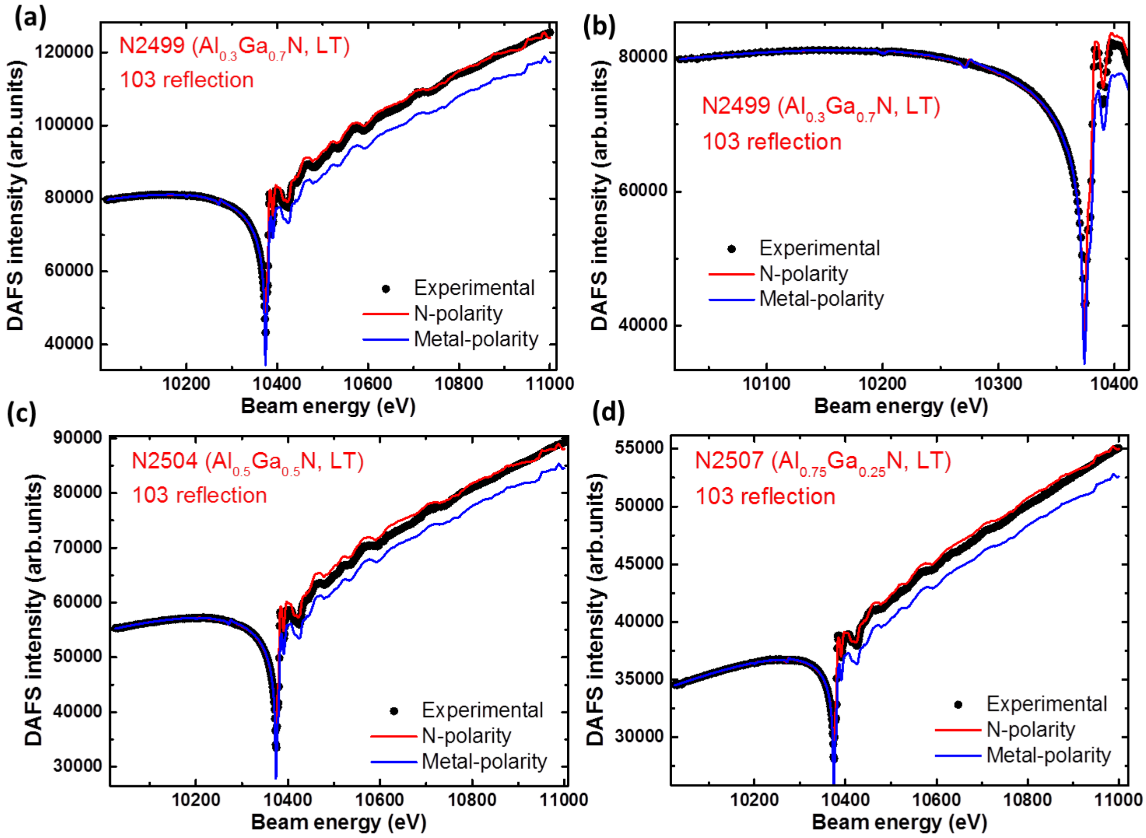

Figure A.2.5.3: DAFS spectra recorded around the Ga-K edge at the Bragg peak position related to AlGaN NW sections for the 103 reflection, provided for three samples of different nominal AlN molar fractions grown at the same temperature ($t_{des}^{Ga} \approx$ 60 s): (a) & (b) $Al_{0.3}Ga_{0.7}N$ (N2499 LT), (c) $Al_{0.5}Ga_{0.5}N$ (N2504 LT), (d) $Al_{0.75}Ga_{0.25}N$ (N2507 LT). Fits performed for the two reflections of Bijvoet's pair are displayed on each spectrum: the sample is clearly N-polar, in view of the DAFS intensity difference between both cases above the energy threshold. (b) zooms over the beam energy range before the threshold for the $Al_{0.3}Ga_{0.7}N$ sample (N2499 LT), showing an excellent fit over the latter range.

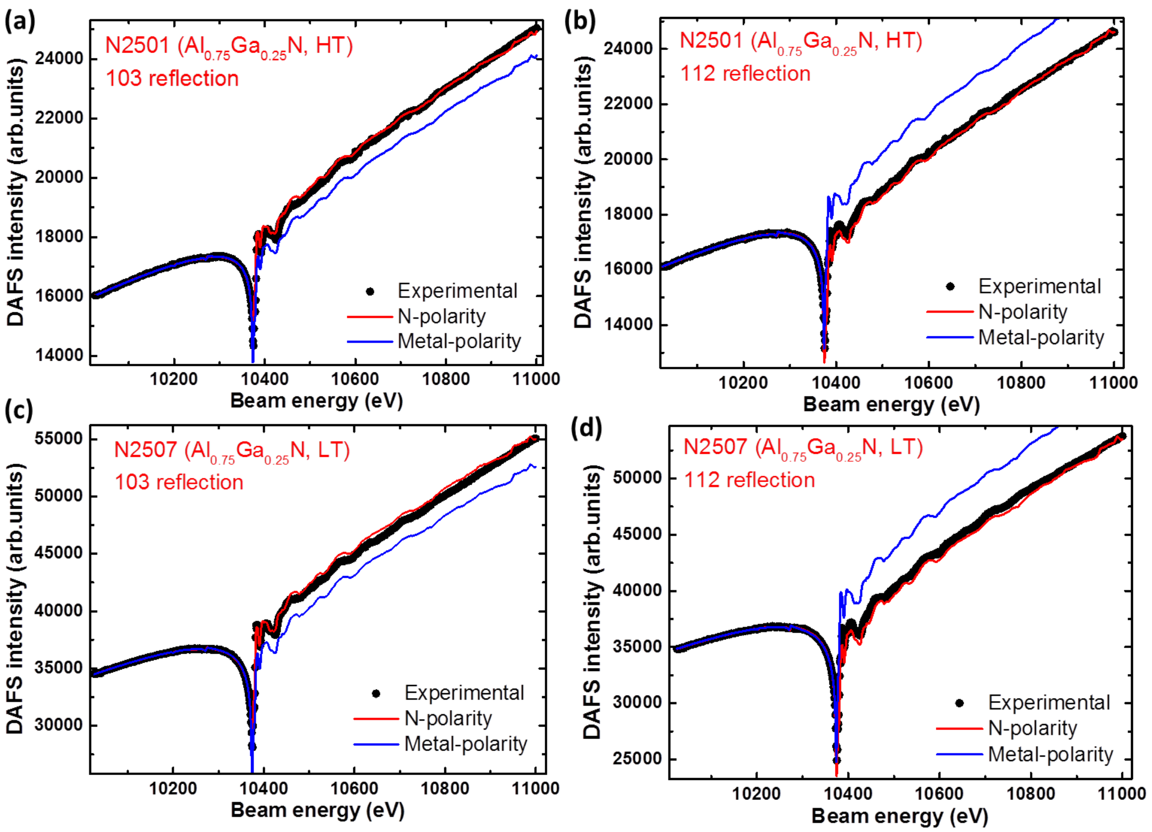

Figure A.2.5.4: DAFS spectra recorded around the Ga-K edge at the Bragg peak position related to AlGaN NW sections for the 103 and 112 reflections, provided for two samples of same nominal Al content ($Al_{0.75}Ga_{0.25}N$) but grown at different substrate temperatures: (a) & (b) 103 & 112 for N2501 HT, (c) & (d) 103 & 112 for N2507 LT. Fits performed for the two reflections of Bijvoet's pair are displayed on each spectrum: the sample is clearly N-polar, in view of the DAFS intensity difference between both cases above the energy threshold.

As expected, it can be directly seen that AlGaN NWs are N-polar, in view of the excellent fits in the latter case and the intensity difference with respect to its Bijvoet counterpart, namely the metal-polar case, above the Ga-K edge (see Equations (A.2.2.3) and (A.2.2.4) for the intensity difference literal expression). About 5-10% of NWs are expected to be metal-polar, given the previous reports for GaN NWs grown by MBE [117, 313]. Regarding the values of average AlN molar fractions obtained from the fitting procedure, Table A.2.5.1 gathers them for all samples and compares them to those estimated from lattice parameter values extracted from ESRF data and those determined with a standard diffractometer using the extended Bond method, similarly to values provided in Table A.2.4.1.

		Average Al composition deduced from XRD data (%)							
Sample		INAC	ESRF: RSM data			ESRF: fitted DAFS spectra			
Reference number	Nominal x_{Al} (%)	Standard XRD Bond method	RSM 103	RSM 112	RSM avg.	Fit 103	Fit 112	Fit 002	Fit avg.
N2497 (HT)	30	53.7	52.5	48.8	50.7	54.3	47.4	-	50.9
N2499 (LT)	30	30.2	32.5	34.8	33.7	29.6	29.3	-	29.4
N2502 (HT)	50	46.8	53.8	53.9	53.8	53.9	47.7	53.4	51.7
N2504 (LT)	50	42.9	43.0	46.3	44.7	40.6	38.9	-	39.7
N2501 (HT)	75	75.8	76.0	80.5	78.2	81.3	80.9	-	81.1
N2507 (LT)	75	67	70.4	76.0	73.2	71.5	73	-	72.2

Table A.2.5.1: Comparison of average Al compositions, for the six investigated AlGaN samples, derived from three methods: first, from lattice parameters determined by the extended Bond method performed on a standard diffractometer; second, from lattice parameters measured using RSM data recorded for several reflections at ESRF, and last, from DAFS spectra fitting.

Values resulting from the fits are on the whole very close to those derived from other methods, supporting the fact that DAFS spectroscopy is a powerful tool for getting ensemble averaged structural information such as the polarity and the average composition of AlGaN NWs, in addition to the short-range information usually extracted from this technique.

Annex 2.6: Preliminary overview of the extended fine structure region

In a next stage, DAFS spectra recorded for 103, 112 and 002 reflections over the 10-11 keV range around the Ga-K edge were normalized in the k-space specifically for the analysis of the extended fine structure region: using the right term of Equation (A.2.3.5), the experimental first-order EDAFS $\chi_Q(k)$ were derived. For each spectrum, the S_D normalization factor was extracted from fits of experimental DAFS spectra performed in Annex 2.5, while $I_{0,exp}$ was computed using the ATHENA software [524]. The experimental first-order EDAFS $\chi_Q(k)$ are exhibited for a few examples below in Figure A.2.6.1, Figure A.2.6.2 and Figure A.2.6.3.

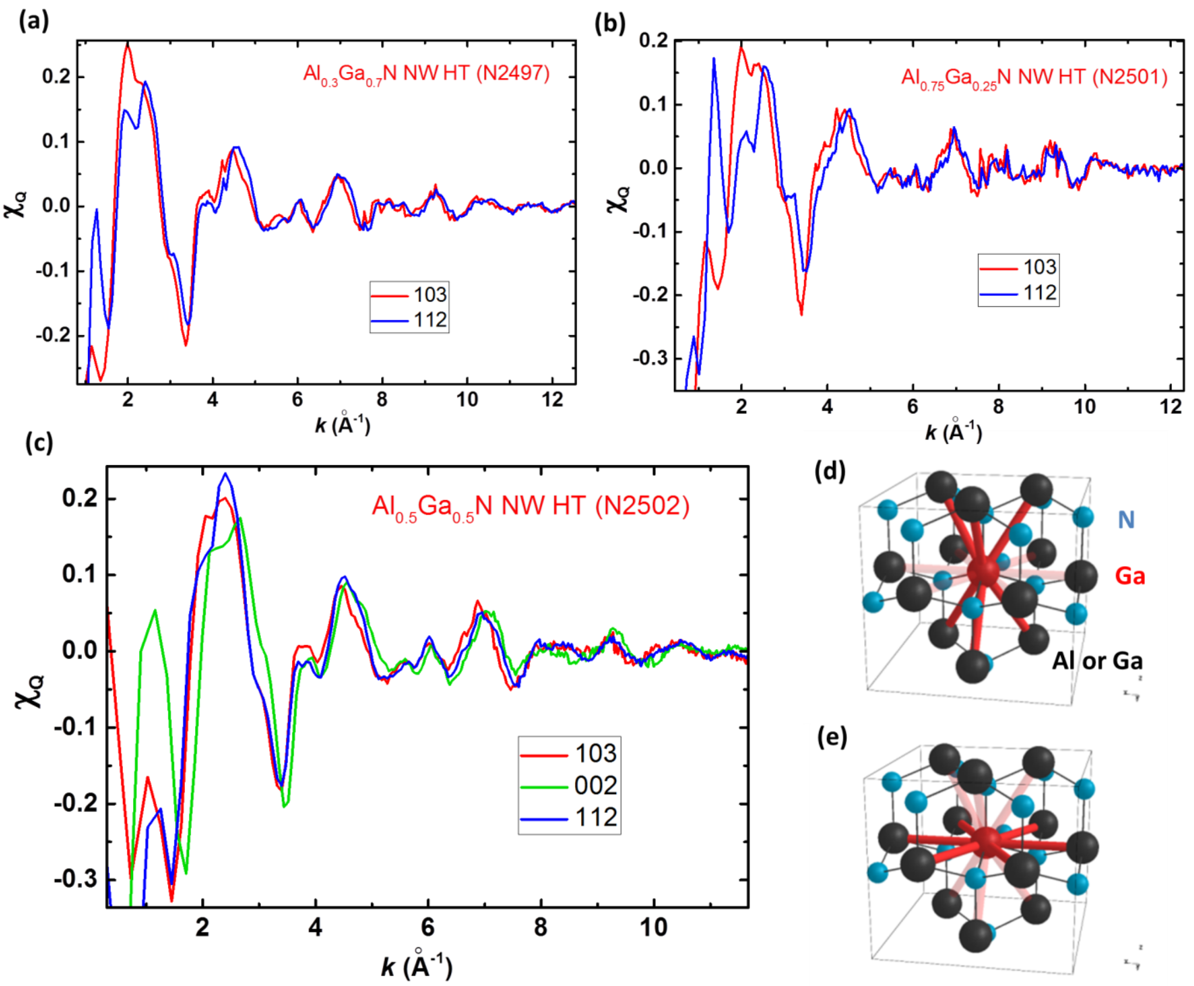

Figure A.2.6.1: Experimental first-order EDAFS $\chi_Q(k)$ compared for several reflections (103, 112 and 002) investigated for the following AlGaN NW samples, of various nominal Al content but all grown at the same high temperature: (a) $Al_{0.3}Ga_{0.7}N$ (sample N2497), (b) $Al_{0.75}Ga_{0.25}N$ (sample N2501), and (c) $Al_{0.5}Ga_{0.5}N$ (sample N2502). Scheme of the Ga nearest neighbors probed: (d) out-of-plane ([0001] direction), (e) in-plane.

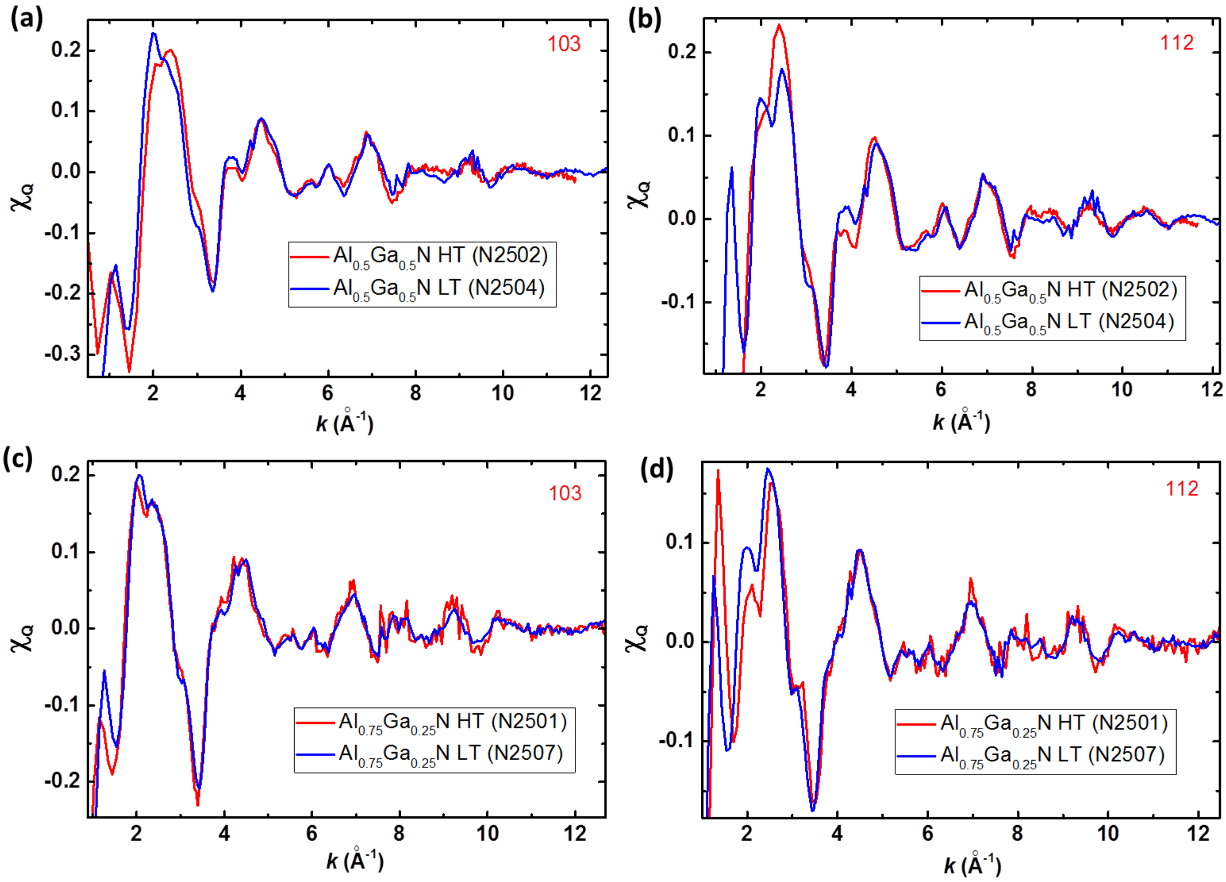

Figure A.2.6.2: Experimental first-order EDAFS $\chi_Q(k)$ compared for two AlGaN NW samples of same AlN molar fraction but grown at different temperatures, in the following cases: (a) $Al_{0.5}Ga_{0.5}N$, reflection 103, (b) $Al_{0.5}Ga_{0.5}N$, reflection 112, (c) $Al_{0.75}Ga_{0.25}N$, reflection 103, (d) $Al_{0.75}Ga_{0.25}N$, reflection 112.

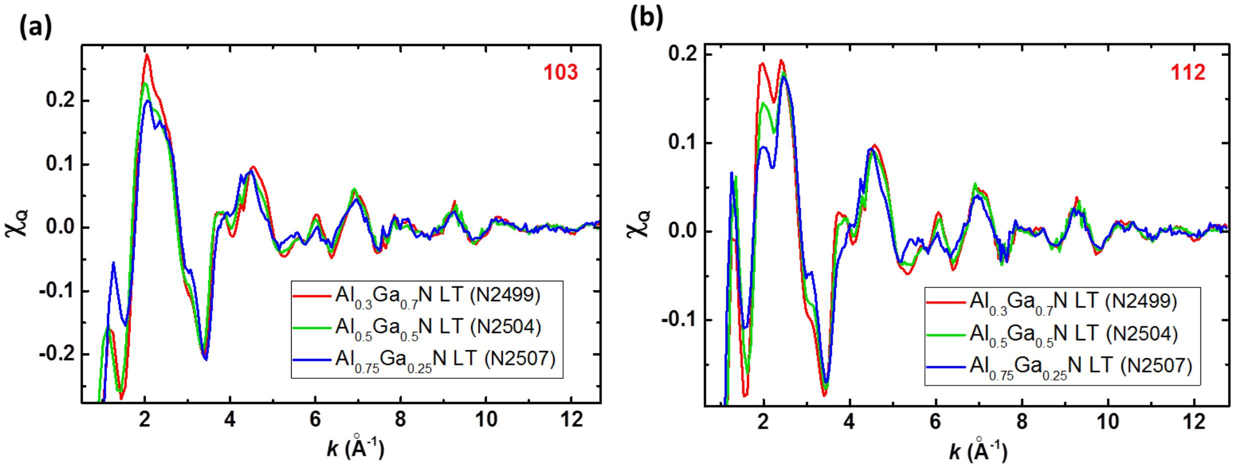

Figure A.2.6.3: Experimental first-order EDAFS $\chi_Q(k)$ compared for three AlGaN NW samples of various nominal AlN molar fractions but all grown at the same low temperature ($x = 0.3$, 0.5 and 0.75, for samples N2499, N2504 and N2507, respectively), for the following reflections: (a) 103, (b) 112.

It must be stressed that, in addition to their high intensity, the 103, 112 and 002 reflections were also chosen because they allow one to probe nitride samples for short-range structural information differently with respect to out-of-plane and in-plane directions illustrated in Figure A.2.6.1 (d) and (e), depending on the scalar product of the polarization vectors of the incident and diffracted beams with the Ga-to-nearest-neighbor vector. Therefore, comparing such reflections could lead to the observation of anisotropic short-range order, as reported for InGaN NWs [454]. In the case of our experiments, noticeable differences can be directly observed on the whole when comparing, for a given AlGaN NW sample, the EDAFS oscillations derived for all investigated reflections (103 and 112 for all samples, in addition 002 for N2502), as visible in Figure A.2.6.1. Such differences are likely not to be explained by the mere linear dichroism. In contrast, fewer differences were globally noticed, for a given reflection, when comparing the oscillations for two samples of the same nominal Al content but grown at different temperatures (except for $Al_{0.3}Ga_{0.7}N$ samples), as illustrated in Figure A.2.6.2. The latter observation is consistent with the fact that the average Al composition estimated for these two samples remains close and that similar μ-optical properties attributed to compositional fluctuations within the alloy were evidenced for AlGaN NWs of comparable Al content but grown at various temperatures. When varying the average AlN molar fraction, differences are expected, starting with the signal-to-noise ratio which logically decreases with the AlN molar fraction, as observable in Figure A.2.6.3. To go much further than our initial observations, a quantitative analysis of EDAFS oscillations based on the formalism introduced in Annex 2.3 will be performed soon.

Annex 2.7: Conclusion and prospects

After having introduced the resonant XRD formalism needed for processing the DAFS data, we have firstly successfully identified the polarity of AlGaN NWs and estimated their average Al composition simultaneously, emphasizing the large range of possibilities provided by the DAFS technique. Indeed, the latter allows one not only to extract structural information at the scale of the next nearest neighbors of resonant atoms but also to obtain ensemble averaged structural information such as the polarity of WZ materials which can be determined simultaneously with the average composition in the case of WZ alloys.

We have then given a brief overview of the EDAFS oscillations that will be quantitatively analyzed in a near future. Some differences could be directly observed on the provided graphs, especially when comparing, for a given sample, oscillations obtained for various reflections. Such differences may not only result from linear dichroism but also from compositional anisotropy, in other words anisotropic short-range order, within the alloy. The latter will be investigated when processing the oscillations, after having compared the Ga content in the next nearest neighbor (NNN) shell to the average composition and having estimated the NNN distance.

Summary in French

Introduction

Durant ces 25 dernières années, les matériaux semi-conducteurs nitrures (III-N), à savoir le GaN, l'AlN, l'InN et leurs alliages, ont suscité un intérêt croissant au sein des milieux académiques et industriels, tout particulièrement depuis la réalisation des premières diodes électroluminescentes (DELs) et diodes laser (DLs) à base de nitrures dans les années 90 [1-8]. En raison de leur gap direct et de la large plage de longueurs d'onde d'émission couverte par les différents alliages, qui s'étend du proche infrarouge (IR) à l'ultraviolet (UV) profond, les semi-conducteurs III-N ont été depuis massivement utilisés dans la fabrication de composants optoélectroniques tels que les DELs bleues/vertes/blanches et les DLs violettes/bleues/vertes, en particulier la LD émettant à 405 nm et utilisée pour la technologie Blu-Ray. En outre, les nitrures présentent une grande stabilité chimique, des mobilités électroniques élevées, de fortes tensions de claquage, et une bonne conductivité thermique, ce qui les rend adaptés pour une large gamme de dispositifs fonctionnant à haute température, haute fréquence et/ou forte puissance [10-13].

Un bref historique de la recherche sur les nitrures: de la préhistoire des matériaux III-N à l'intérêt récent porté aux nanofils.

Les premiers articles traitant des semi-conducteurs III-N datent du début du XX^{ème} siècle et décrivent la croissance d'AlN [14], GaN [15] et InN [16] polycristallins, respectivement en 1907, 1932 et 1938. Pourtant, la croissance épitaxiale de ces matériaux ne fut pas rapportée avant les années 60 et 70 [17-19]. En particulier, les couches de GaN crûes à cette époque étaient de mauvaise qualité cristalline et présentaient un fort dopage de type n, bien qu'elles n'étaient pas intentionnellement dopées. Ce n'est qu'en 1986 que la qualité structurale du GaN fut significativement améliorée, par l'utilisation d'une couche tampon d'AlN (« buffer ») [20]. Du GaN dopé p fut ensuite obtenu pour la première fois en 1989, en utilisant des dopants Mg [21]. Ces deux dernières découvertes ont jeté les bases des avancées majeures en optoélectronique mentionnées plus haut.

Etonnamment, il fut constaté, durant la campagne expérimentale menée durant les années 80 et le début des années 90 pour optimiser la croissance des couches de GaN, que ce dernier avait tendance à croître en formant des cristaux colonnaires coalescés [22]. Quelques années plus tard, il fut démontré que le GaN pouvait, sous certaines conditions de croissance par épitaxie par jets moléculaires (EJM), croître en formant de lui-même des colonnes bien séparées et de dimensions nanométriques [23, 24]. Les premiers nanofils nitrures auto-induits étaient nés, ouvrant au sein de la communauté III-N un nouveau domaine de recherche, dont l'intérêt réside principalement dans:

- L'absence de défauts cristallins étendus, tels que les dislocations ou les joints de grain communément observés pour la croissance 2D, dans ces nanostructures de type « bottom-up » (du bas vers le haut), même si ces dernières sont crûes sur des substrats en fort désaccord de maille. Cette caractéristique vient du rapport d'aspect élevé (longueur/diamètre) des nanofils, leur permettant de relaxer facilement les contraintes sur leur périphérie.
- La versatilité relative de la croissance nanofilaire, qui permet d'ajuster, dans une certaine mesure, les dimensions, la densité ou encore la structure des nanofils, et de s'affranchir des limites physiques imposées par les approches conventionnelles, dites « top-down » (du haut vers le bas), comme la lithographie [26, 27].
- La croissance plus simple d'hétérostructures le long des directions dites non-polaires, dans le but d'annuler l'effet Stark confiné quantiquement. En effet, une telle croissance reste complexe dans le cas 2D en raison de la forte anisotropie sur les propriétés des surfaces non-polaires [28-30], ce qui engendre des densités de dislocations et de fautes d'empilements plus élevées que pour une croissance 2D le long des directions polaires [31] ou que pour une croissance radiale sur les facettes latérales des nanofils [32, 33].

La croissance de nanofils par d'autres techniques plus adaptées à la production à grande échelle, comme le dépôt chimique ou l'épitaxie en phase vapeur (EPV), a été également étudiée et s'est avérée plus complexe à maîtriser que sa contrepartie EJM. Diverses approches furent considérées: l'utilisation de catalyseurs dans un premier temps [34, 35, 38, 39, 42], suivie de celle de substrats patternés [36, 37], avant d'aboutir finalement à la croissance de nanocolonnes auto-induites bien orientées [40, 41] comme pour l'EJM.

D'un point de vue applicatif, les nanofils III-N sont des alternatives prometteuses aux couches planaires conventionnelles pour améliorer le rendement des composants et/ou réduire les coûts de production. En optoélectronique, des entreprises telles qu'Aledia ou Glō [45, 46] visent à produire des DELs hautement efficaces et moins chères, à base de fils de GaN crûes sur des substrats Si peu coûteux. Le rapport d'aspect élevé des fils devrait de plus permettre de réduire le volume des dispositifs, en d'autres termes la quantité de matériau déposé, tout en préservant, voire même en améliorant, le rendement. Dans cette perspective, la croissance d'hétérostructures radiales sur les facettes latérales des nanofils a été explorée, permettant par la même occasion de s'affranchir de l'effet Stark. En particulier, différents types de composants basés sur ces hétérostructures ont été réalisés: DELs [47-49], transistors à mobilité électronique élevée [50], cellules photovoltaïques [51-53] …

En raison de leurs propriétés uniques, les nanofils III-N ont rendu accessible des domaines d'applications qui ne l'étaient pas, ou peu, pour les couches fines. Par exemple, leurs faibles dimensions font d'eux les plus petits objets diélectriques permettant le guidage d'onde [54, 55] ou la réalisation de contacts électriques [56-58]. Les nanocolonnes nitrures présentent également, en raison de leur géométrie, des propriétés optiques et électriques toutes deux fonction de leur orientation, faisant de ces objets des candidats prometteurs pour la conception de photodétecteurs sensibles à la polarisation [59]. En outre, le rapport surface sur volume élevé de ces nanostructures entraîne une plus grande interaction avec le milieu ambiant, ce qui les rend particulièrement adapté, non seulement pour des applications de type nanocapteurs biologiques [63, 64] et chimiques [60-62], mais également pour la production de molécules telles que l'hydrogène et l'oxygène à partir du craquage de l'eau [65, 66]. Enfin, en raison de leurs intéressantes propriétés piézoélectriques, les nanofils III-N présentent un fort potentiel pour la fabrication de nanocapteurs [67] et nanogénérateurs [68] piézoélectriques.

Contexte et motivations de ce travail de recherche

Mon travail de thèse est axé sur les matériaux semiconducteurs nitrures émettant dans l'UV, sur la plage 200-350 nm, à savoir l'alliage AlGaN. Ce matériau est très prometteur pour la réalisation de DELs et lasers émettant dans l'UV destinés à des applications variées dans l'UV-A (impression 3D, séchage par UV), l'UV-B (photothérapie dermatologique, croissance de plantes), et l'UV-C (purification de l'eau, stérilisation) [69, 70]. Le développement de tels composants, en tant qu'alternatives aux sources actuellement disponibles sur la gamme d'émission étudiée, présente de forts enjeux économiques, environnementaux, et sociétaux. En effet, la plupart des sources UV commerciales sont à gaz (lampes au mercure, au deutérium, lasers excimer,…), et par conséquent peu efficaces, nocives pour l'environnement et peu transportables [69, 70].

Durant cette thèse, l'Al(Ga)N a été crû sous forme de nanofils afin d'atteindre une qualité cristalline supérieure à celle des couches 2D, en l'absence de défauts structuraux étendus dans ces nanostructures [71, 72]. Pour ce qui est des applications, cette amélioration devrait permettre aux DELs UV basées sur ces nanofils d'atteindre des rendements plus élevés que leurs contreparties 2D. Jusqu'à présent, les efficacités rapportées pour les structures planaires restent faibles, particulièrement aux faibles longueurs d'onde [69, 73]. Dernièrement, des DELs à base de nanofils d'AlGaN [77-88, 93-97], et même d'AlN [78], ont été réalisées par EJM et des rendements prometteurs ont été rapportés pour certaines d’entre elles. En parallèle, des DLs [81, 82, 98-100] à base de nanofils d’AlGaN émettant dans l’UV-B et l’UV-C ont également été démontrées.

Bien qu’une partie significative de la communauté III-N concentre ses efforts sur le développement de dispositifs, comme mis en exergue par la vue d’ensemble du domaine donnée jusqu’à présent, plusieurs groupes de chercheurs, dont le nôtre, continuent de partager le même intérêt pour l’étude et la compréhension des propriétés fondamentales des semiconducteurs nitrures. Cette dernière démarche demeure de toute façon nécessaire dans l’optique de contrôler totalement toutes les étapes de fabrication de ces composants.

Dans le cas des nanofils AlGaN, la question des inhomogénéités d’alliage à l’échelle nanométrique reste à éclaircir. Afin d’y répondre, les fluctuations de composition et la localisation de porteurs associée seront examinées dans le chapitre 3, essentiellement par le biais de techniques de caractérisation optique. Pour nos expériences, des nanofils d’AlGaN seront crûs par EJM dans des conditions variées, de manière à potentiellement ajuster les compositions de fluctuations et à sonder par conséquent, si possible, des centres de localisation de taille et de composition différentes.

Le dopage des nanofils d’AlGaN, surtout celui de type p, est également loin d’être compris et maîtrisé. En particulier, le problème de l’incorporation ainsi que de l’activation optique et électrique dans les fils demeure nébuleux. Cette question sera étudiée dans le chapitre 4, notamment pour des jonctions pn nanofilaires d’AlGaN crûes par EJM.

Collaborations

Avant la fin de cette introduction, il doit être souligné que les résultats présentés dans ce manuscrit sont le fruit de plusieurs collaborations, aussi bien internes au groupe NPSC de l’INAC qu’externes au laboratoire. Les collaborateurs qui ont contribué le plus directement à cette thèse sont nommés ci-dessous.

La croissance par EJM a été effectuée sous la supervision de mon directeur de thèse Bruno Daudin (NPSC) et en collaboration avec plusieurs étudiants du groupe.

Les résultats de PL ont été pour la plupart obtenus sous la supervision de mon co-encadrant Bruno Gayral (NPSC). Une campagne expérimentale de TRPL fut également menée au laboratoire Charles Coulomb à Monpellier, en collaboration avec Pierre Valvin, Thierry Guillet, Christelle Brimont et Pierre Lefebvre.

Des expériences de nanocathodoluminescence ont été menées par Mathieu Kociak et Luiz Tizei, du laboratoire de physique des solides (LPS) à Orsay.

Des analyses Raman and KPFM ont été effectuées en collaboration avec le groupe d'Ana Cros, de l'Institut de science des matériaux, à l'université de Valence, en Espagne.

Des expériences de diffraction à rayon X anomale ont été réalisées sous la supervision d'Hubert Renevier, du LMGP à Grenoble.

Quelques observations en microscopie électronique ont été effectuées par Lynda Amichi et Catherine Bougerol (NPSC).

Organisation du manuscrit

Chapitre 1: Propriétés et croissance des matériaux semi-conducteurs III-N

Ce premier chapitre donne une vue d'ensemble des propriétés fondamentales des matériaux binaires III-V, plus particulièrement celles du GaN et de l'AlN, ainsi que celles de leurs alliages. L'objectif de ce chapitre n'est pas d'être exhaustif mais de fournir les notions les plus pertinentes pour la compréhension du manuscrit.

Premièrement, des notions basiques relatives aux propriétés structurales des nitrures [102, 105] sont introduites, telles que la structure cristalline, qui est le plus souvent wurtzite, la polarité dans la structure wurtzite, ou encore les polarisations spontanées et piézoélectriques dans cette structure.

En second lieu, les propriétés électroniques des semi-conducteurs III-N sont détaillées [152]: la structure de bande des matériaux binaires, les différents types de transitions excitoniques/ électroniques ainsi que l'effet de paramètres extérieurs telle que la température sur ces dernières sont expliqués, avant d'aborder les spécificités de la structure électronique des alliages [171, 172] puis d'expliciter l'effet de la dimensionnalité d'objets tels que les nanofils [229] ou les structures quantiques [189] sur ces même propriétés.

Enfin, la croissance épitaxiale des matériaux III-N est présentée: les techniques de croissance communément utilisées telles que l'EJM [257], utilisée durant cette thèse, et l'EPV [255] sont brièvement définies dans un premier temps puis les principaux mécanismes de croissance par EJM, comprenant entre autres les phénomènes de surface dépendant de la cinétique, les relaxation élastique et plastique des contraintes ou encore les différents modes de croissance, sont détaillés.

Chapitre 2: Méthodes expérimentales

Dans ce deuxième chapitre, les nombreuses techniques utilisées pour croître et caractériser nos échantillons sont présentées plus ou moins exhaustivement. Tout comme le chapitre 1, le but est de passer en revue les concepts et détails les plus pertinents pour l'obtention et la compréhension des résultats.

Tout d'abord, les spécificités de notre machine EJM, le protocole complet de calibration des croissances [103, 290, 303], ainsi que les conditions de croissance appropriées pour des nanofils GaN [296] et AlGaN [139] sur cette installation sont mis en évidence.

Deuxièmement, les principales méthodes de caractérisation structurale utilisées dans le cadre cette thèse, à savoir la microscopie électronique (MEB/MEBT, EDX) [344, 345], la diffraction aux rayons X (DRX) [352] et la microscopie à force atomique (AFM) [357], sont introduites plus ou moins brièvement.

En dernier lieu, les techniques de caractérisation optique utilisées telles que la photoluminescence (PL) [359], la cathodoluminescence (CL) [385] et la spectroscopie Raman [359, 394] sont également expliquées. En raison des différentes variantes de PL utilisées et leurs utilisations fréquentes au cours de la thèse, la description est plus exhaustive pour cette méthode: en plus de sa contrepartie continue, la PL résolue en temps (TRPL) ainsi que le principe de la corrélation de photons (HBT) [382] sont présentés. Enfin, des spectres de PL typiques acquis pour des nanofils de nitrures binaires GaN [224] et AlN [139, 315, 375, 376] crûs par EJM sont expliqués.

Chapitre 3: Etude la localisation des porteurs dans les nanofils d'AlGaN

Dans ce troisième chapitre, les propriétés fondamentales de sections d'AlGaN non intentionnellement dopées (NID) crûes sur des bases nanofilaires de GaN sont examinées. Les spécificités structurales des échantillons étudiés sont d'abord mises en évidence, avant l'examen de leurs propriétés optiques. En particulier, la localisation des porteurs est scrutée pour de petits volumes d'AlGaN, à savoir des sections nanofilaires uniques dispersées.

Premièrement, la caractérisation structurale des nanofils d'AlGaN met en évidence un mécanisme de croissance dominé par la cinétique, étayant le modèle de croissance développé précédemment [139, 321, 322]. Un compromis sur les paramètres cinétiques de croissance qui détermine la composition moyenne de l'alliage, à savoir la température de croissance et les flux métalliques, doit être adopté pour réduire la longueur des sections plus riches Al qui nucléent préférentiellement au sommet des bases nanofilaires de GaN. La pleine compréhension de la formation de ces sections reste obscure: un travail supplémentaire, comprenant notamment des simulations atomistiques, est nécessaire pour y voir plus clair.

En second lieu, cette étude met en exergue que les nanofils constituent un outil idéal pour examiner les propriétés optiques fondamentales de très petites quantités de matière d'AlGaN exemptes de défauts étendus tels que les joints de grain ou les dislocations. Plus particulièrement, il est prouvé, au travers d'expériences de µ-PL dépendantes de la puissance d'excitation et HBT, que les centres de localisation de porteurs observés en µ-PL se comportent comme des boîtes quantiques [417] et résultent en fait des fluctuations de composition présentes au sein de l'alliage. Ces caractéristiques sont observées pour des fils d'AlGaN crûs dans des conditions variées, les valeurs de la température de croissance et des flux métalliques ayant été modulées sur de larges plages. Il est ensuite démontré, au moyen d'une combinaison d'expériences de PL et de TRPL, que les régions plus riches Ga spontanément formées durant la synthèse des sections nanofilaires d'AlGaN partagent des propriétés µ-optiques similaires sur une plage de longueur d'onde d'émission donnée, quel que soit les conditions de croissance explorées dans le cadre de cette étude. De telles régions, émettrices de photons uniques, sont présentes à petite échelle, puisque elles ont été également mises en évidence dans des nanodisques quantiques d'AlGaN très fins entourés de barrières d'AlN.

Chapitre 4: Une autre étape vers les dispositifs: étude de jonctions pn nanofilaires d'AlGaN

Dans ce chapitre 4, le dopage dans des sections d'Al(Ga)N crûes sur des bases nanofilaires de GaN est exploré. En particulier, des jonctions pn nanofilaires d'AlGaN et d'AlN sont étudiées dans l'optique de mettre en évidence une signature structurale, optique et électrique particulière pour les sections dopées n et p.

Des signatures propres à l'incorporation des dopants, surtout pour Mg, ont tout d'abord été mises en évidence par le biais de techniques basiques de caractérisation structurale, pour des sections nanofilaires d'AlGaN crûes dans certaines conditions. Premièrement, les nanofils s'élargissent de manière significative pour des niveaux de dopage suffisamment élevés, particulièrement pour le dopage p, ce qui est attribué à la ségrégation des dopants près de la surface des fils. En second lieu, la composition en Al varie de manière abrupte à l'interface entre la partie dopée n et celle dopée p au sein des jonctions pn nanofilaires d'AlGaN, ce qui résulte probablement d'un effet surfactant des atomes Mg qui favoriserait l'incorporation des atomes Al au détriment des atomes de Ga et la substitution préférentielle de ces derniers par des atomes Mg. Il est ensuite démontré que les dopants incorporés sont au moins partiellement actifs par le biais de la variante KPFM [358] de l'AFM. En effet, des jonctions pn ont été mises en évidence électriquement à l'aide de cette technique.

La caractérisation optique des échantillons dopés a ensuite confirmé que les dopants, particulièrement Mg, sont bel et bien incorporés, étant donné que des transitions associées aux atomes Mg sont visibles en PL à des énergies d'émission bien plus basses que le bord de bande de l'AlGaN [128, 134]. Une signature optique spécifique pour chaque partie des jonctions pn a par la suite été mise en évidence, aussi bien par le biais d'analyses en nanoCL que des expériences µ-Raman. Des modes Mg-H [505, 506] ont de plus été observés, ce qui indique qu'une partie des atomes Mg incorporés a été passivée par de l'hydrogène résiduel durant la croissance et que les jonctions ne sont par conséquent pas entièrement actives électriquement. Afin de résoudre ce dernier problème, des recuits ont été effectués dans le but de dissocier les complexes Mg-H [469, 470] mais les résultats ne se sont pas avérés concluants pour le moment.

En parallèle, des jonctions pn nanofilaires d'AlN ont été étudiées et présentent une morphologie intéressante. En effet, des creux profonds sont visibles dans les nanofils et attribués au dopage Mg effectué à des températures de croissance basses. Quand on augmente la température de croissance, il a été observé que ces creux disparaissent et que la morphologie des fils change, passant d'une forme hexagonale à 6 facettes latérales à une forme étoilée présentant 12 facettes et caractéristique de croissance effectuée dans des conditions très éloignées de l'équilibre thermodynamique [301, 504]. Contrairement aux échantillons d'AlGaN, les analyses Raman n'ont révélé aucun complexe Mg-H dans des jonctions d'AlN crûes dans des conditions voisines de leurs contreparties AlGaN. Par conséquent, soit l'incorporation des atomes Mg dans l'AlN a été beaucoup moins significative, soit les complexes Mg-H ne se sont pas formés durant la croissance. Au vu des niveaux résiduels d'hydrogène dans la chambre, de la présence de modes C-H en Raman et les résultats préliminaires d'autres expériences d'optique, la première hypothèse est plus probable.

Annexes:

Annexe 1: Cristallographie dans les systèmes hexagonaux

Dans cette première annexe, des notions relatives à la structure cristallographique des nitrures, complémentaires de celles déjà introduites dans le chapitre 1 et requises pour l'analyse des données DRX (résonante ou non), sont fournies.

Annexe 2: Résultats préliminaires pour la diffraction aux rayons X résonante

Dans cette seconde annexe, la technique de DRX résonante ainsi que son intérêt dans le cadre de cette thèse sont tout d'abord brièvement présentés. Ensuite, le formalisme requis pour l'analyse des données est décrit avant la présentation des résultats associés. Il est démontré que la technique permet de déterminer simultanément la polarité des fils AlGaN, azote pour nos échantillons, et leur composition moyenne en aluminium assez précisément. Des résultats préliminaires à l'analyse quantitative de l'environnement local des atomes résonants (à l'échelle des plus proches voisins) sont également présentés.

Bibliography

[1] I. Akasaki, H. Amano, M. Kito, and K. Hiramatsu, Photoluminescence of Mg-doped p-type GaN and electroluminescence of GaN pn junction LED *Journal of luminescence*, vol. 48, pp. 666–670, 1991.

[2] I. Akasaki, H. Amano, K. Itoh, and N. Koide, GaN-based UV/blue light emitting devices in *CONFERENCE SERIES-INSTITUTE OF PHYSICS*, vol. 129, pp. 851–851, IOP PUBLISHING LTD, 1993.

[3] S. Nakamura, T. Mukai, and M. Senoh, High-power GaN pn junction blue-light-emitting diodes *Japanese Journal of Applied Physics*, vol. 30, no. 12A, p. L1998, 1991.

[4] S. Nakamura, T. Mukai, and M. Senoh, Candela-class high-brightness InGaN/AlGaN double-heterostructure blue-light-emitting diodes *Applied Physics Letters*, vol. 64, no. 13, pp. 1687–1689, 1994.

[5] S. Nakamura, M. Senoh, N. Iwasa, and S.-i. Nagahama, High-brightness InGaN blue, green and yellow light-emitting diodes with quantum well structures *Japanese Journal of Applied Physics*, vol. 34, no. 7A, p. L797, 1995.

[6] S. Nakamura, M. Senoh, N. Iwasa, S.-i. Nagahama, T. Yamada, and T. Mukai, Superbright green InGaN single-quantum-well-structure light-emitting diodes *Japanese Journal of Applied Physics*, vol. 34, no. 10B, p. L1332, 1995.

[7] S. Nakamura, M. Senoh, S.-i. Nagahama, N. Iwasa, T. Yamada, T. Matsushita, H. Kiyoku, and Y. Sugimoto, InGaN-based multi-quantum-well-structure laser diodes *Japanese Journal of Applied Physics*, vol. 35, no. 1B, p. L74, 1996.

[8] S. Nakamura, M. Senoh, S.-i. Nagahama, N. Iwasa, T. Yamada, T. Matsushita, H. Kiyoku, Y. Sugimoto, T. Kozaki, H. Umemoto, *et al.*, InGaN/GaN/AlGaN-based laser diodes with modulation-doped strained-layer superlattices grown on an epitaxially laterally overgrown GaN substrate *Applied Physics Letters*, vol. 72, no. 2, pp. 211–213, 1998.

[9] S. Nakamura, S. Pearton, and G. Fasol, *The blue laser diode: the complete story*. Springer Science & Business Media (Berlin), 2013.

[10] O. Ambacher, Growth and applications of group III-nitrides *Journal of Physics D: Applied Physics*, vol. 31, no. 20, p. 2653, 1998.

[11] S. Pearton, J. Zolper, R. Shul, and F. Ren, GaN: Processing, defects, and devices *Journal of applied physics*, vol. 86, no. 1, pp. 1–78, 1999.

[12] H. Morkoç, *Handbook of Nitride Semiconductors and Devices: GaN-based Optical and Electronic Devices*, vol. 3. Wiley (New York), 2008.

[13] H. Morkoç, *Nitride Semiconductor Devices: Fundamentals and Applications*. John Wiley & Sons (New York), 2013.

[14] F. Fichter, Über Aluminiumnitrid *Zeitschrift für anorganische Chemie*, vol. 54, no. 1, pp. 322–327, 1907.

[15] W. Johson, J. Parsons, and M. Crew, Nitrogen coumponds of Gallium-III. Gallic nitride *J. Phys. Chem*, vol. 36, p. 2651, 1932.

[16] R. Juza and H. Hahn, Über die kristallstrukturen von Cu3N, GaN und InN metallamide und metallnitride *Zeitschrift für anorganische und allgemeine Chemie*, vol. 239, no. 3, pp. 282–287, 1938.

[17] H. P. Maruska and J. Tietjen, The preparation and properties of Vapor-Deposited single-crystal-line GaN *Applied Physics Letters*, vol. 15, no. 10, pp. 327–329, 1969.

[18] H. Manasevit, F. Erdmann, and W. Simpson, The use of metalorganics in the preparation of semiconductor materials IV. The nitrides of aluminum and gallium *Journal of the Electrochemical Society*, vol. 118, no. 11, pp. 1864–1868, 1971.

[19] S. Yoshida, S. Misawa, and A. Itoh, Epitaxial growth of aluminum nitride films on sapphire by reactive evaporation *Applied Physics Letters*, vol. 26, no. 8, pp. 461–462, 1975.

[20] H. Amano, N. Sawaki, I. Akasaki, and Y. Toyoda, Metalorganic vapor phase epitaxial growth of a high quality GaN film using an AlN buffer layer *Applied Physics Letters*, vol. 48, no. 5, pp. 353–355, 1986.

[21] H. Amano, M. Kito, K. Hiramatsu, and I. Akasaki, P-type conduction in Mg-doped GaN treated with low-energy electron beam irradiation (LEEBI) *Japanese Journal of Applied Physics*, vol. 28, no. 12A, p. L2112, 1989.

[22] K. Hiramatsu, S. Itoh, H. Amano, I. Akasaki, N. Kuwano, T. Shiraishi, and K. Oki, Growth mechanism of GaN grown on sapphire with A1N buffer layer by MOVPE *Journal of Crystal Growth*, vol. 115, no. 1, pp. 628–633, 1991.

[23] M. Yoshizawa, A. Kikuchi, M. Mori, N. Fujita, and K. Kishino, Growth of self-organized GaN nanostructures on Al2O3 (0001) by RF-radical source molecular beam epitaxy *Japanese Journal of Applied Physics*, vol. 36, no. 4B, p. L459, 1997.

[24] M. Sanchez-Garcia, E. Calleja, E. Monroy, F. Sanchez, F. Calle, E. Munoz, and R. Beresford, The effect of the III/V ratio and substrate temperature on the morphology and properties of GaN-and AlN-layers grown by molecular beam epitaxy on Si (1 1 1) *Journal of crystal growth*, vol. 183, no. 1-2, pp. 23–30, 1998.

[25] M. Tchernycheva, C. Sartel, G. Cirlin, L. Travers, G. Patriarche, J. Harmand, L. S. Dang, J. Renard, B. Gayral, L. Nevou, *et al.*, Growth of GaN free-standing nanowires by plasma-assisted molecular beam epitaxy: structural and optical characterization *Nanotechnology*, vol. 18, no. 38, p. 385306, 2007.

[26] R. Agarwal and C. Lieber, Semiconductor nanowires: optics and optoelectronics *Applied Physics A*, vol. 85, no. 3, p. 209, 2006.

[27] W. Lu and C. M. Lieber, Semiconductor nanowires *Journal of Physics D: Applied Physics*, vol. 39, no. 21, p. R387, 2006.

[28] H. Wang, C. Chen, Z. Gong, J. Zhang, M. Gaevski, M. Su, J. Yang, and M. A. Khan, Anisotropic structural characteristics of (1120) GaN templates and coalesced epitaxial lateral overgrown films deposited on (1012) sapphire *Applied physics letters*, vol. 84, no. 4, pp. 499–501, 2004.

[29] L. Lymperakis and J. Neugebauer, Large anisotropic adatom kinetics on nonpolar GaN surfaces: Consequences for surface morphologies and nanowire growth *Physical Review B*, vol. 79, no. 24, p. 241308, 2009.

[30] R. Farrell, E. Young, F. Wu, S. DenBaars, and J. Speck, Materials and growth issues for high-performance nonpolar and semipolar light-emitting devices *Semiconductor Science and Technology*, vol. 27, no. 2, p. 024001, 2012.

[31] T. Paskova, V. Darakchieva, P. Paskov, J. Birch, E. Valcheva, P. Persson, B. Arnaudov, S. Tungasmitta, and B. Monemar, Properties of nonpolar a-plane GaN films grown by HVPE with AlN buffers *Journal of crystal growth*, vol. 281, no. 1, pp. 55–61, 2005.

[32] R. Koester, J.-S. Hwang, D. Salomon, X. Chen, C. Bougerol, J.-P. Barnes, D. L. S. Dang, L. Rigutti, A. de Luna Bugallo, G. Jacopin, *et al.*, M-plane core-shell InGaN/GaN multiple-quantum-wells on GaN wires for electroluminescent devices *Nano letters*, vol. 11, no. 11, pp. 4839–4845, 2011.

[33] C. Durand, C. Bougerol, J.-F. Carlin, G. Rossbach, F. Godel, J. Eymery, P.-H. Jouneau, A. Mukhtarova, R. Butté, and N. Grandjean, M-Plane GaN/InAlN multiple quantum wells in core-shell wire structure for UV emission *ACS photonics*, vol. 1, no. 1, pp. 38–46, 2013.

[34] X. Duan and C. M. Lieber, Laser-assisted catalytic growth of single crystal GaN nanowires *Journal of the American Chemical Society*, vol. 122, no. 1, pp. 188–189, 2000.

[35] C.-C. Chen, C.-C. Yeh, C.-H. Chen, M.-Y. Yu, H.-L. Liu, J.-J. Wu, K.-H. Chen, L.-C. Chen, J.-Y. Peng, and Y.-F. Chen, Catalytic growth and characterization of gallium nitride nanowires *Journal of the American Chemical Society*, vol. 123, no. 12, pp. 2791–2798, 2001.

[36] P. Deb, H. Kim, V. Rawat, M. Oliver, S. Kim, M. Marshall, E. Stach, and T. Sands, Faceted and vertically aligned GaN nanorod arrays fabricated without catalysts or lithography *Nano letters*, vol. 5, no. 9, pp. 1847–1851, 2005.

[37] S. D. Hersee, X. Sun, and X. Wang, The controlled growth of GaN nanowires *Nano letters*, vol. 6, no. 8, pp. 1808–1811, 2006.

[38] T. Kuykendall, P. Pauzauskie, S. Lee, Y. Zhang, J. Goldberger, and P. Yang, Metalorganic chemical vapor deposition route to GaN nanowires with triangular cross sections *Nano Letters*, vol. 3, no. 8, pp. 1063–1066, 2003.

[39] G. T. Wang, A. A. Talin, D. J. Werder, J. R. Creighton, E. Lai, R. J. Anderson, and I. Arslan, Highly aligned, template-free growth and characterization of vertical GaN nanowires on sapphire by metal-organic chemical vapour deposition *Nanotechnology (Print)*, vol. 17, no. 23, pp. 5773–5780, 2006.

[40] R. Koester, J. Hwang, C. Durand, D. S. Dang, and J. Eymery, Self-assembled growth of catalyst-free GaN wires by metal-organic vapour phase epitaxy. *Nanotechnology*, vol. 21, no. 1, p. 015602, 2010.

[41] X. J. Chen, G. Perillat-Merceroz, D. Sam-Giao, C. Durand, and J. Eymery, Homoepitaxial growth of catalyst-free GaN wires on N-polar substrates *Applied Physics Letters*, vol. 97, no. 15, p. 151909, 2010.

[42] G. Avit, K. Lekhal, Y. André, C. Bougerol, F. Réveret, J. Leymarie, E. Gil, G. Monier, D. Castelluci, and A. Trassoudaine, Ultralong and defect-free GaN nanowires grown by the HVPE Process *Nano letters*, vol. 14, no. 2, pp. 559–562, 2014.

[43] C. Chèze, L. Geelhaar, B. Jenichen, and H. Riechert, Different growth rates for catalyst-induced and self-induced GaN nanowires *Applied Physics Letters*, vol. 97, no. 15, p. 153105, 2010.

[44] C. Chèze, L. Geelhaar, O. Brandt, W. M. Weber, H. Riechert, S. Münch, R. Rothemund, S. Reitzenstein, A. Forchel, T. Kehagias, *et al.*, Direct comparison of catalyst-free and catalyst-induced GaN nanowires *Nano Research*, vol. 3, no. 7, pp. 528–536, 2010.

[45] “Official website of aledia: http://www.aledia.com/en/.”

[46] “Official website of glo: http://www.glo.se/.”

[47] F. Qian, S. Gradecak, Y. Li, C.-Y. Wen, and C. M. Lieber, Core/multishell nanowire heterostructures as multicolor, high-efficiency light-emitting diodes *Nano letters*, vol. 5, no. 11, pp. 2287–2291, 2005.

[48] J. R. Riley, S. Padalkar, Q. Li, P. Lu, D. D. Koleske, J. J. Wierer, G. T. Wang, and L. J. Lauhon, Three-dimensional mapping of quantum wells in a GaN/InGaN core-shell nanowire light-emitting diode array *Nano letters*, vol. 13, no. 9, pp. 4317–4325, 2013.

[49] M. Tchernycheva, P. Lavenus, H. Zhang, A. Babichev, G. Jacopin, M. Shahmohammadi, F. Julien, R. Ciechonski, G. Vescovi, and O. Kryliouk, InGaN/GaN core-shell single nanowire light emitting diodes with graphene-based p-contact *Nano letters*, vol. 14, no. 5, pp. 2456–2465, 2014.

[50] Y. Li, J. Xiang, F. Qian, S. Gradecak, Y. Wu, H. Yan, D. A. Blom, and C. M. Lieber, Dopant-free GaN/AlN/AlGaN radial nanowire heterostructures as high electron mobility transistors *Nano letters*, vol. 6, no. 7, pp. 1468–1473, 2006.

[51] Y. Dong, B. Tian, T. J. Kempa, and C. M. Lieber, Coaxial group III-nitride nanowire photovoltaics *Nano letters*, vol. 9, no. 5, pp. 2183–2187, 2009.

[52] B. Tian, T. J. Kempa, and C. M. Lieber, Single nanowire photovoltaics *Chemical Society Reviews*, vol. 38, no. 1, pp. 16–24, 2009.

[53] J. J. Wierer Jr, Q. Li, D. D. Koleske, S. R. Lee, and G. T. Wang, III-nitride core-shell nanowire arrayed solar cells *Nanotechnology*, vol. 23, no. 19, p. 194007, 2012.

[54] A. B. Greytak, C. J. Barrelet, Y. Li, and C. M. Lieber, Semiconductor nanowire laser and nanowire waveguide electro-optic modulators *Applied Physics Letters*, vol. 87, no. 15, p. 151103, 2005.

[55] D. J. Sirbuly, M. Law, H. Yan, and P. Yang, Semiconductor nanowires for subwavelength photonics integration *The Journal of Physical Chemistry B*, vol. 109, no. 32, pp. 15190–15213, 2005.

[56] Y. Huang, X. Duan, Y. Cui, and C. M. Lieber, Gallium nitride nanowire nanodevices *Nano Letters*, vol. 2, no. 2, pp. 101–104, 2002.

[57] J.-R. Kim, H. M. So, J. W. Park, J.-J. Kim, J. Kim, C. J. Lee, and S. C. Lyu, Electrical transport properties of individual gallium nitride nanowires synthesized by chemical-vapor-deposition *Applied physics letters*, vol. 80, no. 19, pp. 3548–3550, 2002.

[58] R. Calarco, M. Marso, T. Richter, A. I. Aykanat, R. Meijers, A. vd Hart, T. Stoica, and H. Lüth, Size-dependent Photoconductivity in MBE-Grown GaN-Nanowires *Nano letters*, vol. 5, no. 5, pp. 981–984, 2005.

[59] S. Han, W. Jin, D. Zhang, T. Tang, C. Li, X. Liu, Z. Liu, B. Lei, and C. Zhou, Photoconduction studies on GaN nanowire transistors under UV and polarized UV illumination *Chemical Physics Letters*, vol. 389, no. 1, pp. 176–180, 2004.

[60] V. Dobrokhotov, D. McIlroy, M. G. Norton, A. Abuzir, W. Yeh, I. Stevenson, R. Pouy, J. Bochenek, M. Cartwright, L. Wang, *et al.*, Principles and mechanisms of gas sensing by GaN nanowires functionalized with gold nanoparticles *Journal of applied physics*, vol. 99, no. 10, p. 104302, 2006.

[61] W. Lim, J. Wright, B. Gila, J. L. Johnson, A. Ural, T. Anderson, F. Ren, and S. Pearton, Room temperature hydrogen detection using Pd-coated GaN nanowires *Applied Physics Letters*, vol. 93, no. 7, p. 072109, 2008.

[62] G. S. Aluri, A. Motayed, A. V. Davydov, V. P. Oleshko, K. A. Bertness, N. A. Sanford, and M. V. Rao, Highly selective GaN-nanowire/TiO2-nanocluster hybrid sensors for detection of benzene and related environment pollutants *Nanotechnology*, vol. 22, no. 29, p. 295503, 2011.

[63] D. Guo, A. Abdulagatov, D. M. Rourke, K. A. Bertness, S. George, Y. Lee, and W. Tan, GaN nanowire functionalized with atomic layer deposition techniques for enhanced immobilization of biomolecules *Langmuir*, vol. 26, no. 23, pp. 18382–18391, 2010.

[64] C.-P. Chen, A. Ganguly, C.-Y. Lu, T.-Y. Chen, C.-C. Kuo, R.-S. Chen, W.-H. Tu, W. B. Fischer, K.-H. Chen, and L.-C. Chen, Ultrasensitive in situ label-free DNA detection using a GaN nanowire-based extended-gate field-effect-transistor sensor *Analytical chemistry*, vol. 83, no. 6, pp. 1938–1943, 2011.

[65] M. Kibria, S. Zhao, F. Chowdhury, Q. Wang, H. Nguyen, M. Trudeau, H. Guo, and Z. Mi, Tuning the surface Fermi level on p-type gallium nitride nanowires for efficient overall water splitting *Nature communications*, vol. 5, p. 3825, 2014.

[66] M. Kibria, F. Chowdhury, S. Zhao, B. AlOtaibi, M. Trudeau, H. Guo, and Z. Mi, Visible light-driven efficient overall water splitting using p-type metal-nitride nanowire arrays *Nature communications*, vol. 6, no. 6797, 2015.

[67] Y. S. Zhou, R. Hinchet, Y. Yang, G. Ardila, R. Songmuang, F. Zhang, Y. Zhang, W. Han, K. Pradel, L. Montès, *et al.*, Nano-Newton Transverse Force Sensor Using a Vertical GaN Nanowire based on the Piezotronic Effect *Advanced Materials*, vol. 25, no. 6, pp. 883–888, 2013.

[68] C.-T. Huang, J. Song, W.-F. Lee, Y. Ding, Z. Gao, Y. Hao, L.-J. Chen, and Z. L. Wang, GaN nanowire arrays for high-output nanogenerators *Journal of the American Chemical Society*, vol. 132, no. 13, pp. 4766–4771, 2010.

[69] M. Kneissl and J. Rass, *III-Nitride Ultraviolet Emitters: Technology and Applications.* Springer (Berlin), vol. 227, 2016.

[70] M. Kneissl, T. Kolbe, C. Chua, V. Kueller, N. Lobo, J. Stellmach, A. Knauer, H. Rodriguez, S. Einfeldt, Z. Yang, *et al.*, Advances in group III-nitride-based deep UV light-emitting diode technology *Semiconductor Science and Technology*, vol. 26, no. 1, p. 014036, 2010.

[71] J. Ristic, M. Sánchez-Garcá, J. Ulloa, E. Calleja, J. Sanchez-Páramo, J. Calleja, U. Jahn, A. Trampert, and K. Ploog, AlGaN nanocolumns and AlGaN/GaN/AlGaN nanostructures grown by molecular beam epitaxy *physica status solidi (b)*, vol. 234, no. 3, pp. 717–721, 2002.

[72] K. Bertness, A. Roshko, N. Sanford, J. Barker, and A. Davydov, Spontaneously grown GaN and AlGaN nanowires *Journal of Crystal Growth*, vol. 287, no. 2, pp. 522–527, 2006.

[73] H. Hirayama, N. Maeda, S. Fujikawa, S. Toyoda, and N. Kamata, Recent progress and future prospects of AlGaN-based high-efficiency deep-ultraviolet light-emitting diodes *Japanese Journal of Applied Physics*, vol. 53, no. 10, p. 100209, 2014.

[74] S. F. Chichibu, A. Uedono, T. Onuma, B. A. Haskell, A. Chakraborty, T. Koyama, P. T. Fini, S. Keller, S. P. DenBaars, J. S. Speck, *et al.*, Origin of defect-insensitive emission probability in In-containing (Al, In, Ga) N alloy semiconductors *Nature materials*, vol. 5, no. 10, pp. 810–816, 2006.

[75] H. Zhao, G. Liu, J. Zhang, J. D. Poplawsky, V. Dierolf, and N. Tansu, Approaches for high internal quantum efficiency green InGaN light-emitting diodes with large overlap quantum wells *Optics express*, vol. 19, no. 104, pp. A991–A1007, 2011.

[76] Y. Narukawa, M. Ichikawa, D. Sanga, M. Sano, and T. Mukai, White light emitting diodes with super-high luminous efficacy *Journal of physics D: Applied physics*, vol. 43, no. 35, p. 354002, 2010.

[77] Q. Wang, A. Connie, H. Nguyen, M. Kibria, S. Zhao, S. Sharif, I. Shih, and Z. Mi, Highly efficient, spectrally pure 340 nm ultraviolet emission from AlxGa1-xN nanowire based light emitting diodes *Nanotechnology*, vol. 24, no. 34, p. 345201, 2013.

[78] S. Zhao, A. Connie, M. Dastjerdi, X. Kong, Q. Wang, M. Djavid, S. Sadaf, X. Liu, I. Shih, H. Guo, *et al.*, Aluminum nitride nanowire light emitting diodes: Breaking the fundamental bottleneck of deep ultraviolet light sources *Scientific reports*, vol. 5, p. 8332, 2015.

[79] S. Zhao, M. Djavid, and Z. Mi, Surface Emitting, High Efficiency Near-Vacuum Ultraviolet Light Source with Aluminum Nitride Nanowires Monolithically Grown on Silicon *Nano letters*, vol. 15, no. 10, pp. 7006–7009, 2015.

[80] Z. Mi, S. Zhao, A. Connie, and M. H. T. Dastjerdi, High efficiency AlGaN deep ultraviolet light emitting diodes on silicon in *SPIE OPTO*, pp. 937306–937306, International Society for Optics and Photonics, 2015.

[81] Z. Mi, S. Zhao, S. Woo, M. Bugnet, M. Djavid, X. Liu, J. Kang, X. Kong, W. Ji, H. Guo, *et al.*, Molecular beam epitaxial growth and characterization of Al(Ga)N nanowire deep ultraviolet light emitting diodes and lasers *Journal of Physics D: Applied Physics*, vol. 49, no. 36, p. 364006, 2016.

[82] S. Zhao and Z. Mi, Al (Ga) N Nanowire Deep Ultraviolet Optoelectronics *Semiconductors and Semimetals*, vol. 96, pp. 167–199, 2017.

[83] T. F. Kent, S. D. Carnevale, A. Sarwar, P. J. Phillips, R. F. Klie, and R. C. Myers, Deep ultraviolet emitting polarization induced nanowire light emitting diodes with AlxGa1-xN active regions *Nanotechnology*, vol. 25, no. 45, p. 455201, 2014.

[84] A. Sarwar, B. J. May, and R. C. Myers, Effect of quantum well shape and width on deep ultraviolet emission in AlGaN nanowire LEDs *physica status solidi (a)*, vol. 213, no. 4, pp. 947-952, 2015.

[85] B. J. May, A. G. Sarwar, and R. C. Myers, Nanowire LEDs grown directly on flexible metal foil *Applied Physics Letters*, vol. 108, no. 14, p. 141103, 2016.

[86] A. Sarwar, S. D. Carnevale, F. Yang, T. F. Kent, J. J. Jamison, D. W. McComb, and R. C. Myers, Semiconductor Nanowire Light-Emitting Diodes Grown on Metal: A Direction Toward Large-Scale Fabrication of Nanowire Devices *Small*, vol. 11, no. 40, pp. 5402–5408, 2015.

[87] A. G. Sarwar, B. J. May, M. F. Chisholm, G. J. Duscher, and R. C. Myers, Ultrathin GaN quantum disk nanowire LEDs with sub-250 nm electroluminescence *Nanoscale*, vol. 8, no. 15, pp. 8024–8032, 2016.

[88] B. Janjua, H. Sun, C. Zhao, D. H. Anjum, D. Priante, A. A. Alhamoud, F. Wu, X. Li, A. M. Albadri, A. Y. Alyamani, *et al.*, Droop-free AlxGa1-xN/AlyGa1-yN quantum-disks-in-nanowires ultraviolet LED emitting at 337 nm on metal/silicon substrates *Optics Express*, vol. 25, no. 2, pp. 1381–1390, 2017.

[89] B. H. Le, S. Zhao, X. Liu, S. Y. Woo, G. A. Botton, and Z. Mi, Controlled Coalescence of AlGaN Nanowire Arrays: An Architecture for Nearly Dislocation-Free Planar Ultraviolet Photonic Device Applications *Advanced Materials*, vol. 28, no. 38, pp. 8446–8454, 2016.

[90] S. D. Carnevale, T. F. Kent, P. J. Phillips, M. J. Mills, S. Rajan, and R. C. Myers, Polarization-induced pn diodes in wide-band-gap nanowires with ultraviolet electroluminescence *Nano letters*, vol. 12, no. 2, pp. 915–920, 2012.

[91] A. G. Sarwar, S. D. Carnevale, T. F. Kent, F. Yang, D. W. McComb, and R. C. Myers, Tuning the polarization-induced free hole density in nanowires graded from GaN to AlN *Applied Physics Letters*, vol. 106, no. 3, p. 032102, 2015.

[92] S. D. Carnevale, T. F. Kent, P. J. Phillips, A. Sarwar, C. Selcu, R. F. Klie, and R. C. Myers, Mixed polarity in polarization-induced p-n junction nanowire light-emitting diodes *Nano letters*, vol. 13, no. 7, pp. 3029–3035, 2013.

[93] C. Selcu, S. C. Carnevale, T. F. Kent, F. Akyol, P. J. Phillips, M. J. Mills, S. Rajan, J. P. Pelz, and R. C. Myers, Investigation of the electronic transport in polarization-induced nanowires using conductive atomic force microscopy (AFM) in *APS Meeting Abstracts*, vol. 1, p. 22006, 2013.

[94] T. F. Kent, S. D. Carnevale, and R. C. Myers, Atomically sharp 318 nm Gd: AlGaN ultraviolet light emitting diodes on Si with low threshold voltage *Applied Physics Letters*, vol. 102, no. 20, p. 201114, 2013.

[95] A. G. Sarwar, B. J. May, J. I. Deitz, T. J. Grassman, D. W. McComb, and R. C. Myers, Tunnel junction enhanced nanowire ultraviolet light emitting diodes *Applied Physics Letters*, vol. 107, no. 10, p. 101103, 2015.

[96] S. M. Sadaf, Y.-H. Ra, T. Szkopek, and Z. Mi, Monolithically Integrated Metal/Semiconductor Tunnel Junction Nanowire Light-Emitting Diodes *Nano letters*, vol. 16, no. 2, pp. 1076–1080, 2016.

[97] S. M. Sadaf, S. Zhao, Y. Wu, Y.-H. Ra, X. Liu, S. Vanka, and Z. Mi, An AlGaN Core-Shell Tunnel Junction Nanowire Light Emitting Diode Operating in the Ultraviolet-C Band *Nano letters*, vol. 17, no. 2, pp. 1212–1218, 2017.

[98] S. Zhao, X. Liu, S. Woo, J. Kang, G. Botton, and Z. Mi, An electrically injected AlGaN nanowire laser operating in the ultraviolet-C band *Applied Physics Letters*, vol. 107, no. 4, p. 043101, 2015.

[99] K. Li, X. Liu, Q. Wang, S. Zhao, and Z. Mi, Ultralow-threshold electrically injected AlGaN nanowire ultraviolet lasers on Si operating at low temperature *Nature nanotechnology*, vol. 10, no. 2, pp. 140–144, 2015.

[100] S. Zhao, X. Liu, Y. Wu, and Z. Mi, An electrically pumped 239 nm AlGaN nanowire laser operating at room temperature *Applied Physics Letters*, vol. 109, no. 19, p. 191106, 2016.

[101] M. Djavid and Z. Mi, Enhancing the light extraction efficiency of AlGaN deep ultraviolet light emitting diodes by using nanowire structures *Applied Physics Letters*, vol. 108, no. 5, p. 051102, 2016.

[102] H. Morkoç, *Handbook of Nitride Semiconductors and Devices: Materials Properties, Physics and Growth*, vol. 1. Wiley (New York), 2008.

[103] K. Hestroffer, *Growth and Characterization of GaN Nanowires and of GaN/AlN Nanowire Heterostructures*. PhD thesis, Université de Grenoble, 2012.

[104] S. Strite and H. Morkoç, GaN, AlN, and InN: a review *Journal of Vacuum Science & Technology B*, vol. 10, no. 4, pp. 1237–1266, 1992.

[105] “web database: www.ioffe.ru/sva/nsm.”

[106] C.-Y. Yeh, Z. Lu, S. Froyen, and A. Zunger, Zinc-blende-wurtzite polytypism in semiconductors *Physical Review B*, vol. 46, no. 16, p. 10086, 1992.

[107] B. Daudin, G. Feuillet, J. Hübner, Y. Samson, F. Widmann, A. Philippe, C. Bru-Chevallier, G. Guillot, E. Bustarret, G. Bentoumi, *et al.*, How to grow cubic GaN with low hexagonal phase content on (001) SiC by molecular beam epitaxy *Journal of applied physics*, vol. 84, no. 4, pp. 2295–2300, 1998.

[108] X. Sun, Y. Wang, H. Yang, L. Zheng, D. Xu, J. Li, and Z. Wang, Strain and photoluminescence characterization of cubic (In, Ga) N films grown on GaAs (001) substrates *Journal of Applied Physics*, vol. 87, pp. 3711–3714, 2000.

[109] A. Wright, Basal-plane stacking faults and polymorphism in AlN, GaN, and InN *Journal of applied physics*, vol. 82, no. 10, pp. 5259–5261, 1997.

[110] A. I. Duff, L. Lymperakis, and J. Neugebauer, Understanding and controlling indium incorporation and surface segregation on InxGa1-xN surfaces: An ab initio approach *Physical Review B*, vol. 89, no. 8, p. 085307, 2014.

[111] P. Schuck, M. Mason, R. Grober, O. Ambacher, A. Lima, C. Miskys, R. Dimitrov, and M. Stutzmann, Spatially resolved photoluminescence of inversion domain boundaries in GaN-based lateral polarity heterostructures *Applied Physics Letters*, vol. 79, no. 7, pp. 952–954, 2001.

[112] R. Kirste, R. Collazo, G. Callsen, M. R. Wagner, T. Kure, J. S. Reparaz, S. Mita, J. Xie, A. Rice, J. Tweedie, *et al.*, Temperature dependent photoluminescence of lateral polarity junctions of metal organic chemical vapor deposition grown GaN *Journal of Applied Physics*, vol. 110, no. 9, p. 093503, 2011.

[113] P. Coulon, M. Mexis, M. Teisseire, M. Jublot, P. Vennéguès, M. Leroux, and J. Zuniga-Perez, Dual-polarity GaN micropillars grown by metalorganic vapour phase epitaxy: Cross-correlation between structural and optical properties *Journal of Applied Physics*, vol. 115, no. 15, p. 153504, 2014.

[114] T. Zywietz, J. Neugebauer, and M. Scheffler, Adatom diffusion at GaN (0001) and (0001) surfaces *Applied physics letters*, vol. 73, no. 4, pp. 487–489, 1998.

[115] J. Renard, R. Songmuang, G. Tourbot, C. Bougerol, B. Daudin, and B. Gayral, Evidence for quantum-confined Stark effect in GaN/AlN quantum dots in nanowires *Physical Review B*, vol. 80, no. 12, p. 121305, 2009.

[116] D. C. Mojica and Y.-M. Niquet, Stark effect in GaN/AlN nanowire heterostructures: Influence of strain relaxation and surface states *Physical Review B*, vol. 81, no. 19, p. 195313, 2010.

[117] K. Hestroffer, C. Leclere, C. Bougerol, H. Renevier, and B. Daudin, Polarity of GaN nanowires grown by plasma-assisted molecular beam epitaxy on Si (111) *Physical Review B*, vol. 84, no. 24, p. 245302, 2011.

[118] J. Zúñiga-Pérez, V. Consonni, L. Lymperakis, X. Kong, A. Trampert, S. Fernández-Garrido, O. Brandt, H. Renevier, S. Keller, K. Hestroffer, *et al.*, Polarity in GaN and ZnO: Theory, measurement, growth, and devices *Applied Physics Reviews*, vol. 3, no. 4, p. 041303, 2016.

[119] A. Minj, A. Cros, N. Garro, J. Colchero, T. Auzelle, and B. Daudin, Assessment of polarity in GaN self-assembled nanowires by electrical force microscopy *Nano letters*, vol. 15, no. 10, pp. 6770–6776, 2015.

[120] L. Largeau, E. Galopin, N. Gogneau, L. Travers, F. Glas, and J.-C. Harmand, N-polar GaN nanowires seeded by Al droplets on Si (111) *Crystal Growth & Design*, vol. 12, no. 6, pp. 2724–2729, 2012.

[121] O. Romanyuk, S. Fernández-Garrido, P. Jircek, I. Bartoš, L. Geelhaar, O. Brandt, and T. Paskova, Non-destructive assessment of the polarity of GaN nanowire ensembles using low-energy electron diffraction and x-ray photoelectron diffraction *Applied Physics Letters*, vol. 106, no. 2, p. 021602, 2015.

[122] X. Kong, J. Ristic, M. Sanchez-Garcia, E. Calleja, and A. Trampert, Polarity determination by electron energy-loss spectroscopy: application to ultra-small III-nitride semiconductor nanocolumns *Nanotechnology*, vol. 22, no. 41, p. 415701, 2011.

[123] O. Romanyuk, P. Jircek, T. Paskova, I. Bieloshapka, and I. Bartoš, GaN polarity determination by photoelectron diffraction *Applied Physics Letters*, vol. 103, no. 9, p. 091601, 2013.

[124] F. Bernardini, V. Fiorentini, and D. Vanderbilt, Spontaneous polarization and piezoelectric constants of III-V nitrides *Physical Review B*, vol. 56, no. 16, p. R10024, 1997.

[125] J. Lähnemann, O. Brandt, U. Jahn, C. Pfüller, C. Roder, P. Dogan, F. Grosse, A. Belabbes, F. Bechstedt, A. Trampert, *et al.*, Direct experimental determination of the spontaneous polarization of GaN *Physical Review B*, vol. 86, no. 8, p. 081302, 2012.

[126] J. F. Nye, *Physical properties of crystals: their representation by tensors and matrices*. Oxford university press, 1985.

[127] K. Shimada, First-Principles Determination of Piezoelectric Stress and Strain Constants of Wurtzite III-V Nitrides *Japanese journal of applied physics*, vol. 45, no. 4L, p. L358, 2006.

[128] T. Koppe, H. Hofsäss, and U. Vetter, Overview of band-edge and defect related luminescence in aluminum nitride *Journal of Luminescence*, vol. 178, pp. 267–281, 2016.

[129] J. Zhang, H. Zhao, and N. Tansu, Effect of crystal-field split-off hole and heavy-hole bands crossover on gain characteristics of high Al-content AlGaN quantum well lasers *Applied Physics Letters*, vol. 97, no. 11, p. 111105, 2010.

[130] B. Neuschl, J. Helbing, M. Knab, H. Lauer, M. Madel, K. Thonke, T. Meisch, K. Forghani, F. Scholz, and M. Feneberg, Composition dependent valence band order in c-oriented wurtzite AlGaN layers *Journal of Applied Physics*, vol. 116, no. 11, p. 113506, 2014.

[131] J. Wu, W. Walukiewicz, K. Yu, W. Shan, J. Ager Iii, E. Haller, H. Lu, W. J. Schaff, W. Metzger, and S. Kurtz, Superior radiation resistance of In1-xGaxN alloys: Full-solar-spectrum photovoltaic material system *Journal of Applied Physics*, vol. 94, no. 10, pp. 6477–6482, 2003.

[132] A. D'Andrea and R. D. Sole, Wannier-Mott excitons in semi-infinite crystals: Wave functions and normal-incidence reflectivity *Physical Review B*, vol. 25, pp. 3714–3730, 1982.

[133] X. He, Excitons in anisotropic solids: The model of fractional-dimensional space. *Physical review. B, Condensed matter*, vol. 43, no. 3, pp. 2063–2069, 1991.

[134] M. A. Reshchikov and H. Morkoc, Luminescence properties of defects in GaN *Journal of applied physics*, vol. 97, no. 6, p. 061301, 2005.

[135] T. Mattila and R. M. Nieminen, Point-defect complexes and broadband luminescence in GaN and AlN *Physical Review B*, vol. 55, no. 15, p. 9571, 1997.

[136] R. Liu, A. Bell, F. Ponce, C. Chen, J. Yang, and M. A. Khan, Luminescence from stacking faults in gallium nitride *Applied Physics Letters*, vol. 86, no. 2, p. 1908, 2005.

[137] J. Haynes, Experimental proof of the existence of a new electronic complex in silicon *Physical Review Letters*, vol. 4, no. 7, p. 361, 1960.

[138] J. Haynes, Experimental observation of the excitonic molecule *Physical Review Letters*, vol. 17, no. 16, p. 860, 1966.

[139] A. Pierret, *Propriétés structurales et optiques de nanostructures III-N semiconductrices à grand gap: nanofils d'AlxGa1-xN synthétisés par épitaxie par jets moléculaires et nanostructures de nitrure de bore.* PhD thesis, Université Pierre et Marie Curie-Paris VI, 2013.

[140] D. Demchenko, I. Diallo, and M. Reshchikov, Yellow luminescence of gallium nitride generated by carbon defect complexes *Physical review letters*, vol. 110, no. 8, p. 087404, 2013.

[141] M. A. Reshchikov, D. Demchenko, A. Usikov, H. Helava, and Y. Makarov, Carbon defects as sources of the green and yellow luminescence bands in undoped GaN *Physical Review B*, vol. 90, no. 23, p. 235203, 2014.

[142] F. Xu, B. Shen, L. Lu, Z. Miao, J. Song, Z. Yang, G. Zhang, X. Hao, B. Wang, X. Shen, *et al.*, Different origins of the yellow luminescence in as-grown high-resistance GaN and unintentional-doped GaN films *Journal of Applied Physics*, vol. 107, no. 2, p. 023528, 2010.

[143] A. Uedono, S. Ishibashi, S. Keller, C. Moe, P. Cantu, T. Katona, D. Kamber, Y. Wu, E. Letts, S. Newman, *et al.*, Vacancy-oxygen complexes and their optical properties in AlN epitaxial films studied by positron annihilation *Journal of Applied Physics*, vol. 105, no. 5, p. 054501, 2009.

[144] T. Sugahara, H. Sato, M. Hao, Y. Naoi, S. Kurai, S. Tottori, K. Yamashita, K. Nishino, L. T. Romano, and S. Sakai, Direct evidence that dislocations are non-radiative recombination centers in GaN *Japanese journal of applied physics*, vol. 37, no. 4A, p. L398, 1998.

[145] C. Dreyer, A. Janotti, and C. Van de Walle, Effects of strain on the electron effective mass in GaN and AlN *Applied Physics Letters*, vol. 102, no. 14, p. 142105, 2013.

[146] R. Pässler, Moderate phonon dispersion shown by the temperature dependence of fundamental band gaps of various elemental and binary semiconductors including wide-band gap materials *Journal of Applied Physics*, vol. 88, pp. 2570–2577, 2000.

[147] D. Song, M. Basavaraj, S. Nikishin, M. Holtz, V. Soukhoveev, A. Usikov, and V. Dmitriev, The influence of phonons on the optical properties of GaN *Journal of applied physics*, vol. 100, no. 11, p. 113504, 2006.

[148] S. Sohal, W. Feng, M. Pandikunta, V. Kuryatkov, S. Nikishin, and M. Holtz, Influence of phonons on the temperature dependence of the band gap of AlN and AlxGa1-xN alloys with high AlN mole fraction *Journal of Applied Physics*, vol. 113, no. 4, p. 043501, 2013.

[149] Y. P. Varshni, Temperature dependence of the energy gap in semiconductors *Physica*, vol. 34, no. 1, pp. 149–154, 1967.

[150] L. Vina, S. Logothetidis, and M. Cardona, Temperature dependence of the dielectric function of germanium *Physical Review B*, vol. 30, no. 4, p. 1979, 1984.

[151] R. Pässler, Temperature dependence of fundamental band gaps in group IV, III-V, and II-VI materials via a two-oscillator model *Journal of Applied Physics*, vol. 89, no. 11, pp. 6235–6240, 2001.

[152] H. Morkoç, *Handbook of Nitride Semiconductors and Devices: Electronic and Optical Processes in Nitrides*, vol. 2. Wiley (New York), 2008.

[153] H. Murotani, T. Kuronaka, Y. Yamada, T. Taguchi, N. Okada, and H. Amano, Temperature dependence of excitonic transitions in a-plane AlN epitaxial layers *Journal of Applied Physics*, vol. 105, no. 8, p. 083533, 2009.

[154] W. Shan, T. Schmidt, X. Yang, S. Hwang, J. Song, and B. Goldenberg, Temperature dependence of interband transitions in GaN grown by metalorganic chemical vapor deposition *Applied physics letters*, vol. 66, no. 8, pp. 985–987, 1995.

[155] X. Zhang, T. Taliercio, S. Kolliakos, and P. Lefebvre, Influence of electron-phonon interaction on the optical properties of III nitride semiconductors *Journal of Physics: Condensed Matter*, vol. 13, no. 32, p. 7053, 2001.

[156] J. Li, K. Nam, J. Lin, and H. Jiang, Optical and electrical properties of Al-rich AlGaN alloys *Applied Physics Letters*, vol. 79, no. 20, pp. 3245–3247, 2001.

[157] Z. Dridi, B. Bouhafs, and P. Ruterana, First-principles investigation of lattice constants and bowing parameters in wurtzite AlxGa1-xN, InxGa1-xN and InxAl1-xN alloys *Semiconductor science and technology*, vol. 18, no. 9, p. 850, 2003.

[158] A. Bell, S. Srinivasan, C. Plumlee, H. Omiya, F. Ponce, J. Christen, S. Tanaka, A. Fujioka, and Y. Nakagawa, Exciton freeze-out and thermally activated relaxation at local potential fluctuations in thick AlxGa1-xN layers *Journal of applied physics*, vol. 95, no. 9, pp. 4670–4674, 2004.

[159] R. Pelá, C. Caetano, M. Marques, L. Ferreira, J. Furthmüller, and L. Teles, Accurate band gaps of AlGaN, InGaN, and AlInN alloys calculations based on LDA-1/2 approach *Applied Physics Letters*, vol. 98, no. 15, p. 151907, 2011.

[160] V. Jmerik, E. Lutsenko, and S. Ivanov, Plasma-assisted molecular beam epitaxy of AlGaN heterostructures for deep-ultraviolet optically pumped lasers *physica status solidi (a)*, vol. 210, no. 3, pp. 439–450, 2013.

[161] C. Coughlan, S. Schulz, M. A. Caro, and E. P. O'Reilly, Band gap bowing and optical polarization switching in Al1-xGaxN alloys *physica status solidi (b)*, vol. 252, no. 5, pp. 879–884, 2015.

[162] V. Y. Davydov, A. Klochikhin, V. V. Emtsev, A. Sakharov, S. Ivanov, V. Vekshin, F. Bechstedt, J. Furthmüller, J. Aderhold, J. Graul, *et al.*, Bandgap of hexagonal InN and InGaN alloys in *10th International Symposium on Nanostructures: Physics and Technology*, pp. 68–71, International Society for Optics and Photonics, 2002.

[163] P. G. Moses and C. G. Van de Walle, Band bowing and band alignment in InGaN alloys *Applied Physics Letters*, vol. 96, no. 2, p. 021908, 2010.

[164] E. Sakalauskas, Ö. Tuna, A. Kraus, H. Bremers, U. Rossow, C. Giesen, M. Heuken, A. Hangleiter, G. Gobsch, and R. Goldhahn, Dielectric function and bowing parameters of InGaN alloys *physica status solidi (b)*, vol. 249, no. 3, pp. 485–488, 2012.

[165] G. Orsal, Y. El Gmili, N. Fressengeas, J. Streque, R. Djerboub, T. Moudakir, S. Sundaram, A. Ougazzaden, and J.-P. Salvestrini, Bandgap energy bowing parameter of strained and relaxed InGaN layers *Optical Materials Express*, vol. 4, no. 5, pp. 1030–1041, 2014.

[166] M. Ferhat and F. Bechstedt, First-principles calculations of gap bowing in InxGa1-xN and InxAl1-xN alloys: Relation to structural and thermodynamic properties *Physical Review B*, vol. 65, no. 7, p. 075213, 2002.

[167] R. Jones, R. Broesler, E. Haller, K. Yu, J. Ager III, W. Walukiewicz, X. Chen, and W. Schaff, Band gap bowing parameter of In1-xAlxN *Journal of Applied Physics*, vol. 104, no. 12, pp. 123501, 2008.

[168] E. Iliopoulos, A. Adikimenakis, C. Giesen, M. Heuken, and A. Georgakilas, Energy bandgap bowing of InAlN alloys studied by spectroscopic ellipsometry *Applied Physics Letters*, vol. 92, no. 19, p. 1907, 2008.

[169] S. Schulz, M. A. Caro, L.-T. Tan, P. J. Parbrook, R. W. Martin, and E. P. O'Reilly, Composition-dependent band gap and band-edge bowing in AlInN: A combined theoretical and experimental study *Applied Physics Express*, vol. 6, no. 12, p. 121001, 2013.

[170] N. Nepal, J. Li, M. Nakarmi, J. Lin, and H. Jiang, Temperature and compositional dependence of the energy band gap of AlGaN alloys *Applied Physics Letters*, vol. 87, no. 24, p. 242104, 2005.

[171] O. Goede, L. John, and D. Hennig, Compositional disorder-induced broadening for free excitons in II-VI semiconducting mixed crystals *physica status solidi (b)*, vol. 89, no. 2, pp. K183–K186, 1978.

[172] E. Schubert, E. Göbel, Y. Horikoshi, K. Ploog, and H. Queisser, Alloy broadening in photoluminescence spectra of AlxGa1-xAs *Physical Review B*, vol. 30, no. 2, p. 813, 1984.

[173] K. Nam, J. Li, M. Nakarmi, J. Lin, and H. Jiang, Unique optical properties of AlGaN alloys and related ultraviolet emitters *Applied Physics Letters*, vol. 84, no. 25, pp. 5264–5266, 2004.

[174] N. Nepal, J. Li, M. Nakarmi, and J. Lin, Exciton localization in AlGaN alloys *Applied physics letters*, vol. 88, no. 6, p. 062103, 2006.

[175] S. Zhao, S. Woo, S. Sadaf, Y. Wu, A. Pofelski, D. Laleyan, R. Rashid, Y. Wang, G. Botton, and Z. Mi, Molecular beam epitaxy growth of Al-rich AlGaN nanowires for deep ultraviolet optoelectronics *APL Materials*, vol. 4, no. 8, p. 086115, 2016.

[176] B. Meyer, G. Steude, A. Göldner, A. Hoffmann, H. Amano, and I. Akasaki, Photoluminescence Investigations of AlGaN on GaN Epitaxial Films *Physica Status Solidi B Basic Research*, vol. 216, pp. 187–192, 1999.

[177] K. Bajaj, Use of excitons in materials characterization of semiconductor system *Materials Science and Engineering: R: Reports*, vol. 34, no. 2, pp. 59–120, 2001.

[178] A. Westmeyer, S. Mahajan, K. Bajaj, J. Lin, H. Jiang, D. Koleske, and R. Senger, Determination of energy-band offsets between GaN and AlN using excitonic luminescence transition in AlGaN alloys *Journal of applied physics*, vol. 99, no. 1, p. 013705, 2006.

[179] Q. Li, S. Xu, M. Xie, and S. Tong, Origin of the S-shaped temperature dependence of luminescent peaks from semiconductors *Journal of Physics: Condensed Matter*, vol. 17, no. 30, p. 4853, 2005.

[180] Y.-H. Cho, G. Gainer, J. Lam, J. Song, W. Yang, and W. Jhe, Dynamics of anomalous optical transitions in AlxGa1-xN alloys *Physical Review B*, vol. 61, no. 11, p. 7203, 2000.

[181] S. Chung, M. S. Kumar, H. Lee, and E.-K. Suh, Investigations on alloy potential fluctuations in AlxGa1-xN epilayers using optical characterizations *Journal of applied physics*, vol. 95, pp. 3565–3568, 2004.

[182] T. Onuma, S. F. Chichibu, A. Uedono, T. Sota, P. Cantu, T. M. Katona, J. F. Keading, S. Keller, U. K. Mishra, S. Nakamura, *et al.*, Radiative and nonradiative processes in strain-free AlxGa1-xN films studied by time-resolved photoluminescence and positron annihilation techniques *Journal of applied physics*, vol. 95, no. 5, pp. 2495–2504, 2004.

[183] S. Fan, Z. Qin, C. He, M. Hou, X. Wang, B. Shen, W. Li, W. Wang, D. Mao, P. Jin, *et al.*, Optical investigation of strong exciton localization in high Al composition AlxGa1-xN alloys *Optics express*, vol. 21, no. 21, pp. 24497–24503, 2013.

[184] J. Mickevicius, G. Tamulaitis, M. Shur, M. Shatalov, J. Yang, and R. Gaska, Correlation between carrier localization and efficiency droop in AlGaN epilayers *Applied Physics Letters*, vol. 103, no. 1, p. 011906, 2013.

[185] J. Mickevicius, G. Tamulaitis, J. Jurkevicius, M. Shur, M. Shatalov, J. Yang, and R. Gaska, Efficiency droop and carrier transport in AlGaN epilayers and heterostructures *physica status solidi (b)*, vol. 252, no. 5, pp. 961–964, 2015.

[186] T. Lin, J. Fan, and Y. Chen, Effects of alloy potential fluctuations in InGaN epitaxial films *Semiconductor science and technology*, vol. 14, no. 5, p. 406, 1999.

[187] S. Hammersley, D. Watson-Parris, P. Dawson, M. Godfrey, T. Badcock, M. Kappers, C. McAleese, R. Oliver, and C. Humphreys, The consequences of high injected carrier densities on carrier localization and efficiency droop in InGaN/GaN quantum well structures *Journal of Applied Physics*, vol. 111, no. 8, p. 083512, 2012.

[188] J. Kamimura, K. Kishino, and A. Kikuchi, Low-temperature photoluminescence studies of In-rich InAlN nanocolumns *physica status solidi (RRL)-Rapid Research Letters*, vol. 6, no. 3, pp. 123–125, 2012.

[189] P. Harrison and A. Valavanis, *Quantum wells, wires and dots: theoretical and computational physics of semiconductor nanostructures*. John Wiley & Sons (New York), 2016.

[190] J. Renard, *Optical properties of GaN quantum dots and nanowires*. PhD thesis, Université Joseph-Fourier-Grenoble I, 2009.

[191] C. Adelmann, E. Sarigiannidou, D. Jalabert, Y. Hori, J.-L. Rouviere, B. Daudin, S. Fanget, C. Bru-Chevallier, T. Shibata, and M. Tanaka, Growth and optical properties of GaN/AlN quantum wells *Applied physics letters*, vol. 82, no. 23, pp. 4154–4156, 2003.

[192] G. Bastard, E. Mendez, L. Chang, and L. Esaki, Exciton binding energy in quantum wells *Physical Review B*, vol. 26, no. 4, p. 1974, 1982.

[193] H. Mathieu, P. Lefebvre, and P. Christol, Simple analytical method for calculating exciton binding energies in semiconductor quantum wells *Physical Review B*, vol. 46, no. 7, p. 4092, 1992.

[194] L. Bányai, I. Galbraith, C. Ell, and H. Haug, Excitons and biexcitons in semiconductor quantum wires *Physical Review B*, vol. 36, no. 11, p. 6099, 1987.

[195] R. Rinaldi, R. Cingolani, M. Lepore, M. Ferrara, I. Catalano, F. Rossi, L. Rota, E. Molinari, P. Lugli, U. Marti, *et al.*, Exciton binding energy in GaAs V-shaped quantum wires *Physical review letters*, vol. 73, no. 21, p. 2899, 1994.

[196] T. Takagahara, Excitonic optical nonlinearity and exciton dynamics in semiconductor quantum dots *Physical Review B*, vol. 36, no. 17, p. 9293, 1987.

[197] T. Takagahara, Effects of dielectric confinement and electron-hole exchange interaction on excitonic states in semiconductor quantum dots *Physical Review B*, vol. 47, no. 8, p. 4569, 1993.

[198] L. C. Andreani, F. Tassone, and F. Bassani, Radiative lifetime of free excitons in quantum wells *Solid state communications*, vol. 77, no. 9, pp. 641–645, 1991.

[199] D. Citrin, Radiative lifetimes of excitons in quantum wells: Localization and phase-coherence effects *Physical Review B*, vol. 47, no. 7, p. 3832, 1993.

[200] D. Citrin, Long intrinsic radiative lifetimes of excitons in quantum wires *Physical review letters*, vol. 69, no. 23, p. 3393, 1992.

[201] D. Gershoni, M. Katz, W. Wegscheider, L. Pfeiffer, R. Logan, and K. West, Radiative lifetimes of excitons in quantum wires *Physical Review B*, vol. 50, no. 12, p. 8930, 1994.

[202] J. Feldmann, G. Peter, E. Göbel, P. Dawson, K. Moore, C. Foxon, and R. Elliott, Linewidth dependence of radiative exciton lifetimes in quantum wells *Physical review letters*, vol. 59, no. 20, p. 2337, 1987.

[203] U. Bockelmann, Exciton relaxation and radiative recombination in semiconductor quantum dots *Physical Review B*, vol. 48, no. 23, p. 17637, 1993.

[204] N. Grandjean, B. Damilano, S. Dalmasso, M. Leroux, M. Laügt, and J. Massies, Built-in electric-field effects in wurtzite AlGaN/GaN quantum wells *Journal of applied physics*, vol. 86, no. 7, pp. 3714–3720, 1999.

[205] P. Bigenwald, P. Lefebvre, T. Bretagnon, and B. Gil, Confined Excitons in GaN-AlGaN Quantum Wells *physica status solidi (b)*, vol. 216, no. 1, pp. 371–374, 1999.

[206] P. Ramvall, S. Tanaka, S. Nomura, P. Riblet, and Y. Aoyagi, Observation of confinement-dependent exciton binding energy of GaN quantum dots *Applied physics letters*, vol. 73, no. 8, pp. 1104–1106, 1998.

[207] J.-j. Shi and Z.-z. Gan, Effects of piezoelectricity and spontaneous polarization on localized excitons in self-formed InGaN quantum dots *Journal of applied physics*, vol. 94, no. 1, pp. 407–415, 2003.

[208] O. Ambacher, B. Foutz, J. Smart, J. Shealy, N. Weimann, K. Chu, M. Murphy, A. Sierakowski, W. Schaff, L. Eastman, *et al.*, Two dimensional electron gases induced by spontaneous and piezoelectric polarization in undoped and doped AlGaN/GaN heterostructures *Journal of applied physics*, vol. 87, no. 1, pp. 334–344, 2000.

[209] J. Simon, N. Pelekanos, C. Adelmann, E. Martnez-Guerrero, R. André, B. Daudin, L. S. Dang, and H. Mariette, Direct comparison of recombination dynamics in cubic and hexagonal GaN/AlN quantum dots *Physical Review B*, vol. 68, no. 3, p. 035312, 2003.

[210] T. Bretagnon, P. Lefebvre, P. Valvin, R. Bardoux, T. Guillet, T. Taliercio, B. Gil, N. Grandjean, F. Semond, B. Damilano, *et al.*, Radiative lifetime of a single electron-hole pair in GaN/ AlN quantum dots *Physical Review B*, vol. 73, no. 11, p. 113304, 2006.

[211] R. Cingolani, A. Botchkarev, H. Tang, H. Morkoç, G. Traetta, G. Coli, M. Lomascolo, A. Di Carlo, F. Della Sala, and P. Lugli, Spontaneous polarization and piezoelectric field in GaN/Al0.15Ga0.85N quantum wells: Impact on the optical spectra *Physical Review B*, vol. 61, no. 4, p. 2711, 2000.

[212] A. D. Andreev and E. P. O'Reilly, Optical transitions and radiative lifetime in GaN/AlN self-organized quantum dots *Applied Physics Letters*, vol. 79, no. 4, pp. 521–523, 2001.

[213] T. Takeuchi, S. Sota, M. Katsuragawa, M. Komori, H. Takeuchi, H. Amano, and I. Akasaki, Quantum-confined Stark effect due to piezoelectric fields in GaInN strained quantum wells *Japanese Journal of Applied Physics*, vol. 36, no. 4A, p. L382, 1997.

[214] P. Lefebvre, A. Morel, M. Gallart, T. Taliercio, J. Allègre, B. Gil, H. Mathieu, B. Damilano, N. Grandjean, and J. Massies, High internal electric field in a graded-width InGaN/GaN quantum well: Accurate determination by time-resolved photoluminescence spectroscopy *Applied Physics Letters*, vol. 78, no. 9, pp. 1252–1254, 2001.

[215] J. W. Robinson, J. H. Rice, K. H. Lee, J. H. Na, R. A. Taylor, D. G. Hasko, R. A. Oliver, M. J. Kappers, C. J. Humphreys, and G. A. D. Briggs, Quantum-confined Stark effect in a single InGaN quantum dot under a lateral electric field *Applied Physics Letters*, vol. 86, no. 21, p. 213103, 2005.

[216] M. J. Holmes, Y. S. Park, J. H. Warner, and R. A. Taylor, Quantum confined Stark effect and corresponding lifetime reduction in a single InxGa1-xN quantum disk *Applied Physics Letters*, vol. 95, no. 18, p. 181910, 2009.

[217] Y. S. Park, M. J. Holmes, T. W. Kang, and R. A. Taylor, Quantum confined Stark effect of InGaN/GaN multi-quantum disks grown on top of GaN nanorods *Nanotechnology*, vol. 21, no. 11, p. 115401, 2010.

[218] E. Kuokstis, C. Chen, M. Gaevski, W. Sun, J. Yang, G. Simin, M. A. Khan, H. Maruska, D. Hill, M. Chou, *et al.*, Polarization effects in photoluminescence of C-and M-plane GaN/AlGaN multiple quantum wells *Applied Physics Letters*, vol. 81, no. 22, p. 4130, 2002.

[219] M. Craven, P. Waltereit, J. Speck, and S. DenBaars, Well-width dependence of photoluminescence emission from a-plane GaN/AlGaN multiple quantum wells *Applied physics letters*, vol. 84, no. 4, pp. 496–498, 2004.

[220] N. Garro, A. Cros, J. Budagosky, A. Cantarero, A. Vinattieri, M. Gurioli, S. Founta, H. Mariette, and B. Daudin, Reduction of the internal electric field in wurtzite a-plane GaN self-assembled quantum dots *Applied Physics Letters*, vol. 87, no. 1, p. 011101, 2005.

[221] T. Onuma, H. Amaike, M. Kubota, K. Okamoto, H. Ohta, J. Ichihara, H. Takasu, and S. Chichibu, Quantum-confined Stark effects in the m-plane In0. 15Ga0. 85N/ GaN multiple quantum well blue light-emitting diode fabricated on low defect density freestanding GaN substrate *Applied Physics Letters*, vol. 91, no. 18, p. 181903, 2007.

[222] H. Ng, Molecular-beam epitaxy of GaN/AlxGa1-xN multiple quantum wells on R-plane (1012) sapphire substrates *Applied physics letters*, vol. 80, no. 23, pp. 4369–4371, 2002.

[223] M. Kappers, J. Hollander, C. McAleese, C. Johnston, R. Broom, J. Barnard, M. Vickers, and C. Humphreys, Growth and characterisation of semi-polar InGaN/GaN MQW structures *Journal of crystal growth*, vol. 300, no. 1, pp. 155–159, 2007.

[224] D. Sam-Giao, *Optical study of GaN nanowires and GaN/AlN microcavities*. PhD thesis, PhD Thesis, Joseph Fourier University, Grenoble, France, 2012.

[225] T. Auzelle, *GaN/AlN nanowires: nucleation, polarity and quantum heterostructures*. PhD thesis, Université Grenoble Alpes, 2015.

[226] J. K. Zettler, P. Corfdir, C. Hauswald, E. Luna, U. Jahn, T. Flissikowski, E. Schmidt, C. Ronning, A. Trampert, L. Geelhaar, *et al.*, Observation of dielectrically confined excitons in ultrathin GaN nanowires up to room temperature *Nano letters*, vol. 16, no. 2, pp. 973–980, 2016.

[227] S. Fernández-Garrido, G. Koblmüller, E. Calleja, and J. S. Speck, In situ GaN decomposition analysis by quadrupole mass spectrometry and reflection high-energy electron diffraction *Journal of applied physics*, vol. 104, no. 3, p. 033541, 2008.

[228] C. Pfüller, O. Brandt, F. Grosse, T. Flissikowski, C. Chèze, V. Consonni, L. Geelhaar, H. T. Grahn, and H. Riechert, Unpinning the Fermi level of GaN nanowires by ultraviolet radiation *Physical Review B*, vol. 82, no. 4, p. 045320, 2010.

[229] R. Calarco, T. Stoica, O. Brandt, and L. Geelhaar, Surface-induced effects in GaN nanowires *Journal of materials research*, vol. 26, no. 17, pp. 2157–2168, 2011.

[230] O. Demichel, M. Heiss, J. Bleuse, H. Mariette, and A. F. i Morral, Impact of surfaces on the optical properties of GaAs nanowires *Applied Physics Letters*, vol. 97, no. 20, p. 201907, 2010.

[231] Q. Li and G. T. Wang, Spatial distribution of defect luminescence in GaN nanowires *Nano letters*, vol. 10, no. 5, pp. 1554–1558, 2010.

[232] A. Armstrong, Q. Li, Y. Lin, A. Talin, and G. Wang, GaN nanowire surface state observed using deep level optical spectroscopy *Applied Physics Letters*, vol. 96, no. 16, p. 163106, 2010.

[233] P. Huang, H. Zong, J.-j. Shi, M. Zhang, X.-h. Jiang, H.-x. Zhong, Y.-m. Ding, Y.-p. He, J. Lu, and X.-d. Hu, Origin of 3.45 ev emission line and yellow luminescence band in GaN nanowires: Surface microwire and defect *ACS nano*, vol. 9, no. 9, pp. 9276–9283, 2015.

[234] O. Brandt, C. Pfüller, C. Chèze, L. Geelhaar, and H. Riechert, Sub-meV linewidth of excitonic luminescence in single GaN nanowires: Direct evidence for surface excitons *Physical Review B*, vol. 81, no. 4, p. 045302, 2010.

[235] T. Hanrath and B. A. Korgel, Chemical surface passivation of Ge nanowires *Journal of the American Chemical Society*, vol. 126, no. 47, pp. 15466–15472, 2004.

[236] Y. Dan, K. Seo, K. Takei, J. H. Meza, A. Javey, and K. B. Crozier, Dramatic reduction of surface recombination by in situ surface passivation of silicon nanowires *Nano letters*, vol. 11, no. 6, pp. 2527–2532, 2011.

[237] A. Hangleiter, J. S. Im, H. Kollmer, S. Heppel, J. Off, and F. Scholz, The role of piezoelectric fields in GaN-based quantum wells *MRS Internet Journal of Nitride Semiconductor Research*, vol. 3, p. e15, 1998.

[238] V. Ranjan, G. Allan, C. Priester, and C. Delerue, Self-consistent calculations of the optical properties of GaN quantum dots *Physical Review B*, vol. 68, no. 11, p. 115305, 2003.

[239] S. Kalliakos, T. Bretagnon, P. Lefebvre, T. Taliercio, B. Gil, N. Grandjean, B. Damilano, A. Dussaigne, and J. Massies, Photoluminescence energy and linewidth in GaN/AlN stackings of quantum dot planes *Journal of applied physics*, vol. 96, no. 1, pp. 180–185, 2004.

[240] D. Williams, A. Andreev, D. Faux, and E. O'Reilly, Surface integral determination of built-in electric fields and analysis of exciton binding energies in nitride-based quantum dots *Physica E: Low-dimensional Systems and Nanostructures*, vol. 21, no. 2, pp. 358–362, 2004.

[241] R. Miller, D. Kleinman, A. Gossard, and O. Munteanu, Biexcitons in GaAs quantum wells *Physical Review B*, vol. 25, no. 10, p. 6545, 1982.

[242] D. Kleinman, Binding energy of biexcitons and bound excitons in quantum wells *Physical Review B*, vol. 28, no. 2, p. 871, 1983.

[243] Y. Hu, S. W. Koch, M. Lindberg, N. Peyghambarian, E. Pollock, and F. F. Abraham, Biexcitons in semiconductor quantum dots *Physical review letters*, vol. 64, no. 15, p. 1805, 1990.

[244] Y. Hu, M. Lindberg, and S. W. Koch, Theory of optically excited intrinsic semiconductor quantum dots *Physical Review B*, vol. 42, no. 3, p. 1713, 1990.

[245] S. Kako, K. Hoshino, S. Iwamoto, S. Ishida, and Y. Arakawa, Exciton and biexciton luminescence from single hexagonal GaN/ AlN self-assembled quantum dots *Applied physics letters*, vol. 85, no. 1, pp. 64–66, 2004.

[246] D. Simeonov, A. Dussaigne, R. Butté, and N. Grandjean, Complex behavior of biexcitons in GaN quantum dots due to a giant built-in polarization field *Physical Review B*, vol. 77, no. 7, p. 075306, 2008.

[247] S. Amloy, K. Yu, K. Karlsson, R. Farivar, T. Andersson, and P.-O. Holtz, Size dependent biexciton binding energies in GaN quantum dots *Applied Physics Letters*, vol. 99, no. 25, p. 251903, 2011.

[248] R. Seguin, S. Rodt, A. Strittmatter, L. Reißmann, T. Bartel, A. Hoffmann, D. Bimberg, E. Hahn, and D. Gerthsen, Multi-excitonic complexes in single InGaN quantum dots *Applied physics letters*, vol. 84, no. 20, pp. 4023–4025, 2004.

[249] A. F. Jarjour, R. A. Oliver, A. Tahraoui, M. J. Kappers, C. J. Humphreys, and R. A. Taylor, Control of the oscillator strength of the exciton in a single InGaN-GaN quantum dot *Physical review letters*, vol. 99, no. 19, p. 197403, 2007.

[250] S. Amloy, E. Moskalenko, M. Eriksson, K. F. Karlsson, Y. Chen, K. Chen, H. Hsu, C. Hsiao, L. Chen, and P.-O. Holtz, Dynamic characteristics of the exciton and the biexciton in a single InGaN quantum dot *Applied Physics Letters*, vol. 101, no. 6, p. 061910, 2012.

[251] K. Choi, S. Kako, M. J. Holmes, M. Arita, and Y. Arakawa, Strong exciton confinement in site-controlled GaN quantum dots embedded in nanowires *Applied Physics Letters*, vol. 103, no. 17, p. 171907, 2013.

[252] R. Zimmermann, A. Euteneuer, J. Möbius, D. Weber, M. Hofmann, W. Rühle, E. Göbel, B. Meyer, H. Amano, and I. Akasaki, Transient four-wave-mixing spectroscopy on gallium nitride: Energy splittings of intrinsic excitonic resonances *Physical Review B*, vol. 56, no. 20, p. R12722, 1997.

[253] R. Bardoux, A. Kaneta, M. Funato, Y. Kawakami, A. Kikuchi, and K. Kishino, Positive binding energy of a biexciton confined in a localization center formed in a single InxGa1-xN/GaN quantum disk *Physical Review B*, vol. 79, no. 15, p. 155307, 2009.

[254] J. Renard, R. Songmuang, C. Bougerol, B. Daudin, and B. Gayral, Exciton and biexciton luminescence from single GaN/AlN quantum dots in nanowires *Nano letters*, vol. 8, no. 7, pp. 2092–2096, 2008.

[255] G. B. Stringfellow, *Organometallic vapor-phase epitaxy: theory and practice*. Academic Press (Cambridge), 1999.

[256] D. J. Miller, J. S. Harris, M. McGehee, and G. Solomon, *Gallium nitride epitaxy by a novel hybrid VPE technique*. Stanford University, 2011.

[257] M. A. Herman and H. Sitter, *Molecular beam epitaxy: fundamentals and current status*, vol. 7. Springer Science & Business Media (Berlin), 2012.

[258] A. Madhukar, Far from equilibrium vapour phase growth of lattice matched III-V compound semiconductor interfaces: Some basic concepts and monte-carlo computer simulations *Surface Science*, vol. 132, no. 1-3, pp. 344–374, 1983.

[259] K. Kim, W. R. Lambrecht, and B. Segall, Elastic constants and related properties of tetrahedrally bonded BN, AlN, GaN, and InN *Physical Review B*, vol. 53, no. 24, p. 16310, 1996.

[260] A. Wright, Elastic properties of zinc-blende and wurtzite AlN, GaN, and InN *Journal of Applied Physics*, vol. 82, no. 6, pp. 2833–2839, 1997.

[261] A. Polian, M. Grimsditch, and I. Grzegory, Elastic constants of gallium nitride *Journal of Applied Physics*, vol. 79, no. 6, pp. 3343–3344, 1996.

[262] R. Schwarz, K. Khachaturyan, and E. Weber, Elastic moduli of gallium nitride *Applied physics letters*, vol. 70, no. 9, pp. 1122–1124, 1997.

[263] M. Yamaguchi, T. Yagi, T. Azuhata, T. Sota, K. Suzuki, S. Chichibu, and S. Nakamura, Brillouin scattering study of gallium nitride: elastic stiffness constants *Journal of Physics: Condensed Matter*, vol. 9, no. 1, p. 241, 1997.

[264] M. Kazan, E. Moussaed, R. Nader, and P. Masri, Elastic constants of aluminum nitride *physica status solidi (c)*, vol. 4, no. 1, pp. 204–207, 2007.

[265] J. Serrano, A. Bosak, M. Krisch, F. J. Manjón, A. H. Romero, N. Garro, X. Wang, A. Yoshikawa, and M. Kuball, InN Thin Film Lattice Dynamics by Grazing Incidence Inelastic X-Ray Scattering *Phys. Rev. Lett.*, vol. 106, p. 205501, May 2011.

[266] R. Jiménez-Riobóo, R. Cuscó, N. Domènech-Amador, C. Prieto, T. Yamaguchi, Y. Nanishi, and L. Artús, Surface acoustic waves and elastic constants of InN epilayers determined by Brillouin scattering *physica status solidi (RRL)- Rapid Research Letters*, vol. 6, no. 6, pp. 256–258, 2012.

[267] S. Lester, F. Ponce, M. Craford, and D. Steigerwald, High dislocation densities in high efficiency GaN-based light-emitting diodes *Applied Physics Letters*, vol. 66, no. 10, pp. 1249–1251, 1995.

[268] V. Consonni, M. Knelangen, L. Geelhaar, A. Trampert, and H. Riechert, Nucleation mechanisms of epitaxial GaN nanowires: Origin of their self-induced formation and initial radius *Physical Review B*, vol. 81, no. 8, p. 085310, 2010.

[269] K. Hestroffer, R. Mata, D. Camacho, C. Leclere, G. Tourbot, Y. Niquet, A. Cros, C. Bougerol, H. Renevier, and B. Daudin, The structural properties of GaN/AlN core-shell nanocolumn heterostructures *Nanotechnology*, vol. 21, no. 41, p. 415702, 2010.

[270] G. Tourbot, C. Bougerol, A. Grenier, M. Den Hertog, D. Sam-Giao, D. Cooper, P. Gilet, B. Gayral, and B. Daudin, Structural and optical properties of InGaN/GaN nanowire heterostructures grown by PA-MBE *Nanotechnology*, vol. 22, no. 7, p. 075601, 2011.

[271] B. Daudin and F. Widmann, Layer-by-layer growth of AlN and GaN by molecular beam epitaxy *Journal of crystal growth*, vol. 182, no. 1, pp. 1–5, 1997.

[272] A. Rajamani, B. W. Sheldon, E. Chason, and A. F. Bower, Intrinsic tensile stress and grain boundary formation during Volmer-Weber film growth *Applied physics letters*, vol. 81, no. 7, pp. 1204–1206, 2002.

[273] B. W. Sheldon, A. Rajamani, A. Bhandari, E. Chason, S. Hong, and R. Beresford, Competition between tensile and compressive stress mechanisms during Volmer-Weber growth of aluminum nitride films *Journal of applied physics*, vol. 98, no. 4, p. 043509, 2005.

[274] F. Widmann, B. Daudin, G. Feuillet, Y. Samson, J. Rouviere, and N. Pelekanos, Growth kinetics and optical properties of self-organized GaN quantum dots *Journal of applied physics*, vol. 83, no. 12, pp. 7618–7624, 1998.

[275] C. Adelmann, J. Simon, G. Feuillet, N. Pelekanos, B. Daudin, and G. Fishman, Self-assembled InGaN quantum dots grown by molecular-beam epitaxy *Applied Physics Letters*, vol. 76, no. 12, pp. 1570–1572, 2000.

[276] C. Adelmann, J. Brault, D. Jalabert, P. Gentile, H. Mariette, G. Mula, and B. Daudin, Dynamically stable gallium surface coverages during plasma-assisted molecular-beam epitaxy of (0001) GaN *Journal of applied physics*, vol. 91, no. 12, pp. 9638–9645, 2002.

[277] C. Adelmann, J. Brault, G. Mula, B. Daudin, L. Lymperakis, and J. Neugebauer, Gallium adsorption on (0001) GaN surfaces *Physical Review B*, vol. 67, no. 16, p. 165419, 2003.

[278] F. Glas and B. Daudin, Stress-driven island growth on top of nanowires *Physical Review B*, vol. 86, no. 17, p. 174112, 2012.

[279] J. M. Cowley, *Electron diffraction techniques*, vol. 1. Oxford University Press, 1992.

[280] J. E. Mahan, K. M. Geib, G. Robinson, and R. G. Long, A review of the geometrical fundamentals of reflection high-energy electron diffraction with application to silicon surfaces *Journal of Vacuum Science & Technology A*, vol. 8, no. 5, pp. 3692–3700, 1990.

[281] L. Daweritz and K. Ploog, Contribution of reflection high-energy electron diffraction to nanometre tailoring of surfaces and interfaces by molecular beam epitaxy *Semiconductor science and technology*, vol. 9, no. 2, p. 123, 1994.

[282] R. Nötzel, L. Däweritz, and K. Ploog, Topography of high-and low-index GaAs surfaces *Physical Review B*, vol. 46, no. 8, p. 4736, 1992.

[283] P. Dobson, B. Joyce, J. Neave, and J. Zhang, Current understanding and applications of the RHEED intensity oscillation technique *Journal of Crystal Growth*, vol. 81, no. 1, pp. 1–8, 1987.

[284] S. Ino, An investigation of the Si (111) 7× 7 surface structure by RHEED *Japanese Journal of Applied Physics*, vol. 19, no. 7, p. 1277, 1980.

[285] P. Bennett and M. Webb, The Si (111) 7× 7 to 1× 1 transition *Surface Science*, vol. 104, no. 1, pp. 74–104, 1981.

[286] G. Binnig, H. Rohrer, C. Gerber, and E. Weibel, 7× 7 reconstruction on Si (111) resolved in real space *Physical review letters*, vol. 50, no. 2, p. 120, 1983.

[287] W. Telieps and E. Bauer, The (7× 7) (1× 1) phase transition on Si (111) *Surface Science*, vol. 162, no. 1-3, pp. 163–168, 1985.

[288] J. Golovchenko, The tunneling microscope: a new look at the atomic world *Science*, vol. 232, no. 4746, pp. 48–53, 1986.

[289] C.-W. Hu, H. Hibino, T. Ogino, and I. Tsong, Hysteresis in the (1× 1)-(7× 7) first-order phase transition on the Si (111) surface *Surface science*, vol. 487, no. 1, pp. 191–200, 2001.

[290] O. Landré, R. Songmuang, J. Renard, E. Bellet-Amalric, H. Renevier, and B. Daudin, Plasma-assisted molecular beam epitaxy growth of GaN nanowires using indium-enhanced diffusion *Applied Physics Letters*, vol. 93, no. 18, p. 183109, 2008.

[291] O. Landré, *Study of nucleation and growth of GaN and AlN nanowires like structures*. PhD thesis, Université de Grenoble, 2010.

[292] G. Tourbot, *Croissance par épitaxie par jets moléculaires de nanofils InGaN/GaN*. PhD thesis, Université de Grenoble, 2012.

[293] B. Joyce, P. Dobson, J. Neave, K. Woodbridge, J. Zhang, P. Larsen, and B. Bolger, RHEED studies of heterojunction and quantum well formation during MBE growth-from multiple scattering to band offsets *Surface Science*, vol. 168, no. 1-3, pp. 423–438, 1986.

[294] C. Foxon, S. Novikov, J. Hall, R. Campion, D. Cherns, I. Griffiths, and S. Khongphetsak, A complementary geometric model for the growth of GaN nanocolumns prepared by plasma-assisted molecular beam epitaxy *Journal of Crystal Growth*, vol. 311, no. 13, pp. 3423–3427, 2009.

[295] K. Hestroffer and B. Daudin, A geometrical model for the description of the AlN shell morphology in GaN-AlN core-shell nanowires *Journal of Applied Physics*, vol. 114, no. 24, p. 244305, 2013.

[296] S. Fernández-Garrido, J. Grandal, E. Calleja, M. Sánchez-Garcá, and D. López-Romero, A growth diagram for plasma-assisted molecular beam epitaxy of GaN nanocolumns on Si (111) *Journal of Applied Physics*, vol. 106, no. 12, p. 126102, 2009.

[297] J. K. Zettler, P. Corfdir, L. Geelhaar, H. Riechert, O. Brandt, and S. Fernádez-Garrido, Improved control over spontaneously formed GaN nanowires in molecular beam epitaxy using a two-step growth process *Nanotechnology*, vol. 26, no. 44, p. 445604, 2015.

[298] R. Mata, K. Hestroffer, J. Budagosky, A. Cros, C. Bougerol, H. Renevier, and B. Daudin, Nucleation of GaN nanowires grown by plasma-assisted molecular beam epitaxy: The effect of temperature *Journal of Crystal Growth*, vol. 334, no. 1, pp. 177–180, 2011.

[299] J. K. Zettler, C. Hauswald, P. Corfdir, M. Musolino, L. Geelhaar, H. Riechert, O. Brandt, and S. Fernández-Garrido, High-temperature growth of GaN nanowires by molecular beam epitaxy: toward the material quality of bulk GaN *Crystal Growth & Design*, vol. 15, no. 8, pp. 4104–4109, 2015.

[300] S. Fernández-Garrido, J. K. Zettler, L. Geelhaar, and O. Brandt, Monitoring the formation of nanowires by line-of-sight quadrupole mass spectrometry: a comprehensive description of the temporal evolution of GaN nanowire ensembles *Nano letters*, vol. 15, no. 3, pp. 1930–1937, 2015.

[301] H. Li, L. Geelhaar, H. Riechert, and C. Draxl, Computing equilibrium shapes of wurtzite crystals: The example of GaN *Physical review letters*, vol. 115, no. 8, p. 085503, 2015.

[302] E. Galopin, L. Largeau, G. Patriarche, L. Travers, F. Glas, and J. Harmand, Morphology of self-catalyzed GaN nanowires and chronology of their formation by molecular beam epitaxy *Nanotechnology*, vol. 22, no. 24, p. 245606, 2011.

[303] R. Songmuang, T. Ben, B. Daudin, D. González, and E. Monroy, Identification of III-N nanowire growth kinetics via a marker technique *Nanotechnology*, vol. 21, no. 29, p. 295605, 2010.

[304] V. Consonni, V. Dubrovskii, A. Trampert, L. Geelhaar, and H. Riechert, Quantitative description for the growth rate of self-induced GaN nanowires *Physical Review B*, vol. 85, no. 15, p. 155313, 2012.

[305] S. Fernández-Garrido, V. M. Kaganer, K. K. Sabelfeld, T. Gotschke, J. Grandal, E. Calleja, L. Geelhaar, and O. Brandt, Self-regulated radius of spontaneously formed GaN nanowires in molecular beam epitaxy *Nano letters*, vol. 13, no. 7, pp. 3274–3280, 2013.

[306] R. Calarco, R. J. Meijers, R. K. Debnath, T. Stoica, E. Sutter, and H. Lüth, Nucleation and growth of GaN nanowires on Si (111) performed by molecular beam epitaxy *Nano letters*, vol. 7, no. 8, pp. 2248–2251, 2007.

[307] V. M. Kaganer, S. Fernandez-Garrido, P. Dogan, K. K. Sabelfeld, and O. Brandt, Nucleation, growth and bundling of GaN nanowires in molecular beam epitaxy: Disentangling the origin of nanowire coalescence *Nano letters*, vol. 16, no. 6, pp. 3717–3725, 2016.

[308] H. Sekiguchi, T. Nakazato, A. Kikuchi, and K. Kishino, Structural and optical properties of GaN nanocolumns grown on (0001) sapphire substrates by rf-plasma-assisted molecular-beam epitaxy *Journal of crystal growth*, vol. 300, no. 1, pp. 259–262, 2007.

[309] L. Largeau, D. Dheeraj, M. Tchernycheva, G. Cirlin, and J. Harmand, Facet and in-plane crystallographic orientations of GaN nanowires grown on Si (111) *Nanotechnology*, vol. 19, no. 15, p. 155704, 2008.

[310] O. Landré, C. Bougerol, H. Renevier, and B. Daudin, Nucleation mechanism of GaN nanowires grown on (111) Si by molecular beam epitaxy *Nanotechnology*, vol. 20, no. 41, p. 415602, 2009.

[311] T. Stoica, E. Sutter, R. J. Meijers, R. K. Debnath, R. Calarco, H. Lüth, and D. Grützmacher, Interface and Wetting Layer Effect on the Catalyst-Free Nucleation and Growth of GaN Nanowires *Small*, vol. 4, no. 6, pp. 751–754, 2008.

[312] K. Hestroffer, C. Leclere, V. Cantelli, C. Bougerol, H. Renevier, and B. Daudin, In situ study of self-assembled GaN nanowires nucleation on Si (111) by plasma-assisted molecular beam epitaxy *Applied Physics Letters*, vol. 100, no. 21, p. 212107, 2012.

[313] T. Auzelle, B. Haas, A. Minj, C. Bougerol, J.-L. Rouvière, A. Cros, J. Colchero, and B. Daudin, The influence of AlN buffer over the polarity and the nucleation of self-organized GaN nanowires *Journal of Applied Physics*, vol. 117, no. 24, p. 245303, 2015.

[314] M. Musolino, A. Tahraoui, S. Fernández-Garrido, O. Brandt, A. Trampert, L. Geelhaar, and H. Riechert, Compatibility of the selective area growth of GaN nanowires on AlN-buffered Si substrates with the operation of light emitting diodes *Nanotechnology*, vol. 26, no. 8, p. 085605, 2015.

[315] O. Landré, V. Fellmann, P. Jaffrennou, C. Bougerol, B. Daudin, H. Renevier, and A. Cros, Molecular beam epitaxy growth and optical properties of AlN nanowires *Applied Physics Letters*, vol. 96, no. 6, 2010.

[316] E. Iliopoulos and T. Moustakas, Growth kinetics of AlGaN films by plasma-assisted molecular-beam epitaxy *Applied physics letters*, vol. 81, no. 2, pp. 295–297, 2002.

[317] V. Jindal, J. Grandusky, N. Tripathi, M. Tungare, and F. Shahedipour-Sandvik, Density functional calculations of the binding energies and adatom diffusion on strained AlN (0001) and GaN (0001) surfaces in *MRS Proceedings*, vol. 1040, pp. 1040–Q06, Cambridge Univ Press, 2007.

[318] W. A. Harrison, *Electronic Structure and the Properties of Solids: The Physics of the Chemical Bond*. Courier Corporation (North Chelmsford), 1989.

[319] R. F. Allah, T. Ben, R. Songmuang, *et al.*, Imaging and analysis by transmission electron microscopy of the spontaneous formation of Al-rich shell structure in AlxGa1-xN/GaN nanowires *Applied Physics Express*, vol. 5, no. 4, p. 045002, 2012.

[320] A. Pierret, C. Bougerol, B. Gayral, M. Kociak, and B. Daudin, Probing alloy composition gradient and nanometer-scale carrier localization in single AlGaN nanowires by nanocathodoluminescence *Nanotechnology*, vol. 24, no. 30, p. 305703, 2013.

[321] A. Pierret, C. Bougerol, M. d. Hertog, B. Gayral, M. Kociak, H. Renevier, and B. Daudin, Structural and optical properties of AlxGa1-xN nanowires *physica status solidi (RRL)-Rapid Research Letters*, vol. 7, no. 10, pp. 868–873, 2013.

[322] A. Pierret, C. Bougerol, S. Murcia-Mascaros, A. Cros, H. Renevier, B. Gayral, and B. Daudin, Growth, structural and optical properties of AlGaN nanowires in the whole composition range *Nanotechnology*, vol. 24, no. 11, p. 115704, 2013.

[323] R. F. Allah, T. Ben, and D. González, Structural and Chemical Evolution of the Spontaneous Core-Shell Structures of AlxGa1-xN/GaN Nanowires *Microscopy and Microanalysis*, vol. 20, no. 4, p. 1254, 2014.

[324] C. Himwas, M. den Hertog, L. S. Dang, E. Monroy, R. Songmuang, *et al.*, Alloy inhomogeneity and carrier localization in AlGaN sections and AlGaN/AlN nanodisks in nanowires with 240-350 nm emission *Applied Physics Letters*, vol. 105, no. 24, p. 241908, 2014.

[325] S. Zhao, S. Woo, M. Bugnet, X. Liu, J. Kang, G. A. Botton, and Z. Mi, Three-dimensional quantum confinement of charge carriers in self-organized AlGaN nanowires: A viable route to electrically injected deep ultraviolet lasers *Nano letters*, vol. 15, no. 12, pp. 7801–7807, 2015.

[326] L. Rigutti, J. Teubert, G. Jacopin, F. Fortuna, M. Tchernycheva, A. D. L. Bugallo, F. Julien, F. Furtmayr, M. Stutzmann, and M. Eickhoff, Origin of energy dispersion in AlxGa1-xN/GaN nanowire quantum discs with low Al content *Physical Review B*, vol. 82, no. 23, p. 235308, 2010.

[327] Q. Wang, H. Nguyen, K. Cui, and Z. Mi, High efficiency ultraviolet emission from AlxGa1-xN core-shell nanowire heterostructures grown on Si (111) by molecular beam epitaxy *Applied Physics Letters*, vol. 101, no. 4, p. 043115, 2012.

[328] P. J. Phillips, S. D. Carnevale, R. Kumar, R. C. Myers, and R. F. Klie, Full-Scale Characterization of UVLED AlxGa1-xN Nanowires via Advanced Electron Microscopy *ACS nano*, vol. 7, no. 6, pp. 5045–5051, 2013.

[329] S. Y. Woo, L. Tizei, M. Bugnet, S. Zhao, Z. Mi, M. Kociak, and G. A. Botton, Carrier Localization at Atomic-Scale Compositional Fluctuations in Single AlGaN Nanowires with Nano-Cathodoluminescence in *European Microscopy Congress 2016: Proceedings*, Wiley Online Library, 2016.

[330] J. Ristic, M. Sánchez-Garcá, E. Calleja, J. Sanchez-Páramo, J. Calleja, U. Jahn, and K. Ploog, AlGaN nanocolumns grown by molecular beam epitaxy: optical and structural characterization *physica status solidi (a)*, vol. 192, no. 1, pp. 60–66, 2002.

[331] J. Ristic, E. Calleja, M. Sanchez-Garcia, J. Ulloa, J. Sanchez-Paramo, J. Calleja, U. Jahn, A. Trampert, and K. Ploog, Characterization of GaN quantum discs embedded in AlxGa1-xN nanocolumns grown by molecular beam epitaxy *Physical Review B*, vol. 68, no. 12, p. 125305, 2003.

[332] K. Bertness, N. Sanford, J. Barker, J. Schlager, A. Roshko, A. Davydov, and I. Levin, Catalyst-free growth of GaN nanowires *Journal of electronic materials*, vol. 35, no. 4, pp. 576–580, 2006.

[333] E. Calleja, J. Ristic, S. Fernández-Garrido, L. Cerutti, M. Sánchez-Garcá, J. Grandal, A. Trampert, U. Jahn, G. Sánchez, A. Griol, *et al.*, Growth, morphology, and structural properties of group-III-nitride nanocolumns and nanodisks *physica status solidi (b)*, vol. 244, no. 8, pp. 2816–2837, 2007.

[334] N. Katcho, M. Richard, O. Landré, G. Tourbot, M. Proietti, H. Renevier, V. Favre-Nicolin, B. Daudin, G. Chen, J. Zhang, *et al.*, Structural properties of Ge/Si (001) nano-islands and AlGaN nanowires by Diffraction Anomalous Fine Structure and Multiwavelength Anomalous Diffraction in *Journal of Physics: Conference Series*, vol. 190, p. 012129, IOP Publishing, 2009.

[335] G. Tourbot, C. Bougerol, F. Glas, L. F. Zagonel, Z. Mahfoud, S. Meuret, P. Gilet, M. Kociak, B. Gayral, and B. Daudin, Growth mechanism and properties of InGaN insertions in GaN nanowires *Nanotechnology*, vol. 23, no. 13, p. 135703, 2012.

[336] H. Lin, Y. Chen, T. Lin, C. Shih, K. Liu, and N. Chen, Direct evidence of compositional pulling effect in AlxGa1-xN epilayers *Journal of crystal growth*, vol. 290, no. 1, pp. 225–228, 2006.

[337] A. Mizerov, V. Jmerik, M. Yagovkina, S. Troshkov, P. Kop'ev, and S. Ivanov, Role of strain in growth kinetics of AlGaN layers during plasma-assisted molecular beam epitaxy *Journal of Crystal Growth*, vol. 323, no. 1, pp. 68–71, 2011.

[338] V. Fellmann, P. Jaffrennou, D. Sam-Giao, B. Gayral, K. Lorenz, E. Alves, and B. Daudin, Ternary AlGaN Alloys with High Al Content and Enhanced Compositional Homogeneity Grown by Plasma-Assisted Molecular Beam Epitaxy *Japanese Journal of Applied Physics*, vol. 50, no. 3R, p. 031001, 2011.

[339] V. Fellmann, *Croissance et caractérisations structurales et optiques d'hétérostructures de nitrures d'éléments III émettant dans l'UV*. PhD thesis, Grenoble, 2012.

[340] S. Ivanov, D. Nechaev, A. Sitnikova, V. Ratnikov, M. Yagovkina, N. Rzheutskii, E. Lutsenko, and V. Jmerik, Plasma-assisted molecular beam epitaxy of Al(Ga)N layers and quantum well structures for optically pumped mid-UV lasers on c-Al2O3 *Semiconductor Science and Technology*, vol. 29, no. 8, p. 084008, 2014.

[341] E. Shevchenko, D. Nechaev, V. Jmerik, V. K. Kaibyshev, S. Ivanov, and A. Toropov, Enhanced photoluminescence efficiency in AlGaN quantum wells with gradient-composition AlGaN barriers in *Journal of Physics: Conference Series*, vol. 741, p. 012118, IOP Publishing, 2016.

[342] T. D. Moustakas, Ultraviolet optoelectronic devices based on AlGaN alloys grown by molecular beam epitaxy *MRS Communications*, vol. 6, no. 3, pp. 247–269, 2016.

[343] E. Monroy, B. Daudin, E. Bellet-Amalric, N. Gogneau, D. Jalabert, F. Enjalbert, J. Brault, J. Barjon, and L. S. Dang, Surfactant effect of In for AlGaN growth by plasma-assisted molecular beam epitaxy *Journal of applied physics*, vol. 93, no. 3, pp. 1550–1556, 2003.

[344] J. Goldstein, D. E. Newbury, P. Echlin, D. C. Joy, A. D. Romig Jr, C. E. Lyman, C. Fiori, and E. Lifshin, *Scanning electron microscopy and X-ray microanalysis: a text for biologists, materials scientists, and geologists*. Springer Science & Business Media (Berlin), 2012.

[345] L. Reimer, *Transmission electron microscopy: physics of image formation and microanalysis*, vol. 36. Springer (Berlin), 2013.

[346] R. Egerton, P. Li, and M. Malac, Radiation damage in the TEM and SEM *Micron*, vol. 35, pp. 399–409, 2004.

[347] "web site: zeiss.com."

[348] "web database: physics.nist.gov, x-ray transition energies."

[349] G. Cliff and G. Lorimer, The quantitative analysis of thin specimens *Journal of Microscopy*, vol. 103, no. 2, pp. 203–207, 1975.

[350] M. Watanabe and D. Williams, The quantitative analysis of thin specimens: a review of progress from the Cliff-Lorimer to the new ζ-factor methods *Journal of microscopy*, vol. 221, no. 2, pp. 89–109, 2006.

[351] B. Bonef, M. Lopez-Haro, L. Amichi, M. Beeler, A. Grenier, E. Robin, P.-H. Jouneau, N. Mollard, I. Mouton, E. Monroy, *et al.*, Composition Analysis of III-Nitrides at the Nanometer Scale: Comparison of Energy Dispersive X-ray Spectroscopy and Atom Probe Tomography *Nanoscale Research Letters*, vol. 11, no. 1, p. 461, 2016.

[352] J. Als-Nielsen and D. McMorrow, *Elements of modern X-ray physics*. John Wiley & Sons (New York), 2011.

[353] W. L. Bond, Precision lattice constant determination *Acta Crystallographica*, vol. 13, no. 10, pp. 814–818, 1960.

[354] S. Grosswig, K.-H. Jäckel, R. Kittner, B. Dietrich, and U. Schellenberger, Determination of the complanar geometric lattice parameters of monocrystals with high precision *Crystal Research and Technology*, vol. 20, no. 8, pp. 1093–1100, 1985.

[355] N. Herres, L. Kirste, H. Obloh, K. Köhler, J. Wagner, and P. Koidl, X-ray determination of the composition of partially strained group-III nitride layers using the Extended Bond Method *Materials Science and Engineering: B*, vol. 91, pp. 425–432, 2002.

[356] M. Moram and M. Vickers, X-ray diffraction of III-nitrides *Rep. Prog. Phys*, vol. 72, no. 036502, p. 036502, 2009.

[357] P. Eaton and P. West, *Atomic force microscopy*. Oxford University Press, 2010.

[358] A. Minj, A. Cros, T. Auzelle, J. Pernot, and B. Daudin, Direct assessment of p-n junctions in single GaN nanowires by Kelvin probe force microscopy *Nanotechnology*, vol. 27, no. 38, p. 385202, 2016.

[359] S. Perkowitz, *Optical characterization of semiconductors: infrared, Raman, and photoluminescence spectroscopy*. Elsevier (Amsterdam), 2012.

[360] A. Wysmolek, K. Korona, R. Stepniewski, J. Baranowski, J. Boniarz, M. Potemski, R. Jones, D. C. Look, J. Kuhl, S. Park, *et al.*, Recombination of excitons bound to oxygen and silicon donors in freestanding GaN *Physical Review B*, vol. 66, no. 24, p. 245317, 2002.

[361] W. Rieger, T. Metzger, H. Angerer, R. Dimitrov, O. Ambacher, and M. Stutzmann, Influence of substrate-induced biaxial compressive stress on the optical properties of thin GaN films *Applied physics letters*, vol. 68, no. 7, pp. 970–972, 1996.

[362] J. Lähnemann, U. Jahn, O. Brandt, T. Flissikowski, P. Dogan, and H. T. Grahn, Luminescence associated with stacking faults in GaN *Journal of Physics D: Applied Physics*, vol. 47, no. 42, p. 423001, 2014.

[363] P. Corfdir, C. Hauswald, J. Zettler, T. Flissikowski, J. Lähnemann, S. Fernández-Garrido, L. Geelhaar, H. Grahn, and O. Brandt, Stacking faults as quantum wells in nanowires: Density of states, oscillator strength, and radiative efficiency *Physical Review B*, vol. 90, no. 19, p. 195309, 2014.

[364] F. Furtmayr, M. Vielemeyer, M. Stutzmann, J. Arbiol, S. Estradé, F. Peirò, J. R. Morante, and M. Eickhoff, Nucleation and growth of GaN nanorods on Si (111) surfaces by plasma-assisted molecular beam epitaxy-The influence of Si-and Mg-doping *Journal of Applied Physics*, vol. 104, no. 3, p. 034309, 2008.

[365] P. Corfdir, P. Lefebvre, J. Ristic, P. Valvin, E. Calleja, A. Trampert, J.-D. Ganière, and B. Deveaud-Plédran, Time-resolved spectroscopy on GaN nanocolumns grown by plasma assisted molecular beam epitaxy on Si substrates *Journal of Applied Physics*, vol. 105, no. 1, p. 013113, 2009.

[366] P. Lefebvre, S. Fernández-Garrido, J. Grandal, J. Ristic, M.-A. Sánchez-Garcá, and E. Calleja, Radiative defects in GaN nanocolumns: Correlation with growth conditions and sample morphology *Applied Physics Letters*, vol. 98, no. 8, p. 083104, 2011.

[367] D. Sam-Giao, R. Mata, G. Tourbot, J. Renard, A. Wysmolek, B. Daudin, and B. Gayral, Fine optical spectroscopy of the 3.45 eV emission line in GaN nanowires *Journal of Applied Physics*, vol. 113, no. 4, p. 043102, 2013.

[368] T. Auzelle, B. Haas, M. Den Hertog, J.-L. Rouvière, B. Daudin, and B. Gayral, Attribution of the 3.45 eV GaN nanowires luminescence to inversion domain boundaries *Applied Physics Letters*, vol. 107, no. 5, p. 051904, 2015.

[369] C. Pfüller, P. Corfdir, C. Hauswald, T. Flissikowski, X. Kong, J. K. Zettler, S. Fernández-Garrido, P. Dogăn, H. T. Grahn, A. Trampert, *et al.*, Nature of excitons bound to inversion domain boundaries: Origin of the 3.45-eV luminescence lines in spontaneously formed GaN nanowires on Si (111) *Physical Review B*, vol. 94, no. 15, p. 155308, 2016.

[370] A. Fiorek, J. Baranowski, A. Wysmoek, K. Pakua, M. Wojdak, I. Grzegory, and S. Porowski, Two-electron transition in homoepitaxial GaN layers *Acta Physica Polonica A*, vol. 4, no. 92, pp. 742–744, 1997.

[371] C. Kirchner, V. Schwegler, F. Eberhard, M. Kamp, K. Ebeling, K. Kornitzer, T. Ebner, K. Thonke, R. Sauer, P. Prystawko, *et al.*, Homoepitaxial growth of GaN by metalorganic vapor phase epitaxy: A benchmark for GaN technology *Applied physics letters*, vol. 75, no. 8, pp. 1098–1100, 1999.

[372] K. Kornitzer, T. Ebner, K. Thonke, R. Sauer, C. Kirchner, V. Schwegler, M. Kamp, M. Leszczynski, I. Grzegory, and S. Porowski, Photoluminescence and reflectance spectroscopy of excitonic transitions in high-quality homoepitaxial GaN films *Physical Review B*, vol. 60, no. 3, p. 1471, 1999.

[373] L. H. Robins, K. A. Bertness, J. M. Barker, N. A. Sanford, and J. B. Schlager, Optical and structural study of GaN nanowires grown by catalyst-free molecular beam epitaxy. I. Near-band-edge luminescence and strain effects *Journal of applied physics*, vol. 101, no. 11, p. 113505, 2007.

[374] P. Corfdir and P. Lefebvre, Role of the dielectric mismatch on the properties of donors in semiconductor nanostructures bounded by air *Journal of Applied Physics*, vol. 112, no. 10, p. 106104, 2012.

[375] Q. Wang, S. Zhao, A. Connie, I. Shih, Z. Mi, T. Gonzalez, M. Andrews, X. Du, J. Lin, and H. Jiang, Optical properties of strain-free AlN nanowires grown by molecular beam epitaxy on Si substrates *Applied Physics Letters*, vol. 104, no. 22, p. 223107, 2014.

[376] A. T. Connie, S. Zhao, S. M. Sadaf, I. Shih, Z. Mi, X. Du, J. Lin, and H. Jiang, Optical and electrical properties of Mg-doped AlN nanowires grown by molecular beam epitaxy *Applied Physics Letters*, vol. 106, no. 21, p. 213105, 2015.

[377] A. Sedhain, N. Nepal, M. Nakarmi, J. Lin, H. Jiang, Z. Gu, J. H. Edgar, *et al.*, Photoluminescence properties of AlN homoepilayers with different orientations *Applied Physics Letters*, vol. 93, no. 4, p. 1905, 2008.

[378] B. Neuschl, K. Thonke, M. Feneberg, S. Mita, J. Xie, R. Dalmau, R. Collazo, and Z. Sitar, Optical identification of silicon as a shallow donor in MOVPE grown homoepitaxial AlN *physica status solidi (b)*, vol. 249, no. 3, pp. 511–515, 2012.

[379] K. Nam, M. Nakarmi, J. Li, J. Lin, and H. Jiang, Mg acceptor level in AlN probed by deep ultraviolet photoluminescence *Applied physics letters*, vol. 83, no. 5, pp. 878–880, 2003.

[380] M. Nakarmi, N. Nepal, C. Ugolini, T. Altahtamouni, J. Lin, and H. Jiang, Correlation between optical and electrical properties of Mg-doped AlN epilayers *Applied physics letters*, vol. 89, no. 15, p. 152120, 2006.

[381] K.-T. Tsen, D. Ferry, A. Botchkarev, B. Sverdlov, A. Salvador, and H. Morkoc, Time-resolved Raman studies of the decay of the longitudinal optical phonons in wurtzite GaN *Applied physics letters*, vol. 72, no. 17, pp. 2132–2134, 1998.

[382] R. H. Brown and R. Q. Twiss, Correlation between photons in two coherent beams of light *Nature*, vol. 177, no. 4497, pp. 27–29, 1956.

[383] R. Loudon, *The quantum theory of light*. OUP Oxford, 2000.

[384] M. Fox, *Quantum optics: an introduction*, vol. 15. OUP Oxford, 2006.

[385] B. G. Yacobi and D. B. Holt, *Cathodoluminescence microscopy of inorganic solids*. Springer Science & Business Media (Berlin), 2013.

[386] C. A. Klein, Bandgap dependence and related features of radiation ionization energies in semiconductors *Journal of Applied Physics*, vol. 39, no. 4, pp. 2029–2038, 1968.

[387] A. M. Goodman, A method for the measurement of short minority carrier diffusion lengths in semiconductors *Journal of Applied Physics*, vol. 32, no. 12, pp. 2550–2552, 1961.

[388] A. Gustafsson, J. Bolinsson, N. Sköld, and L. Samuelson, Determination of diffusion lengths in nanowires using cathodoluminescence *Applied Physics Letters*, vol. 97, no. 7, p. 072114, 2010.

[389] G. Nogues, T. Auzelle, M. Den Hertog, B. Gayral, and B. Daudin, Cathodoluminescence of stacking fault bound excitons for local probing of the exciton diffusion length in single GaN nanowires *Applied Physics Letters*, vol. 104, no. 10, p. 102102, 2014.

[390] N. Pauc, M. Phillips, V. Aimez, and D. Drouin, Carrier recombination near threading dislocations in GaN epilayers by low voltage cathodoluminescence *Applied physics letters*, vol. 89, no. 16, p. 161905, 2006.

[391] L. F. Zagonel, S. Mazzucco, M. Tencé, K. March, R. Bernard, B. Laslier, G. Jacopin, M. Tchernycheva, L. Rigutti, F. H. Julien, *et al.*, Nanometer scale spectral imaging of quantum emitters in nanowires and its correlation to their atomically resolved structure *Nano letters*, vol. 11, no. 2, pp. 568–573, 2010.

[392] L. Tizei, S. Meuret, K. March, K. Hestroffer, T. Auzelle, B. Daudin, and M. Kociak, A polarity-driven nanometric luminescence asymmetry in AlN/GaN heterostructures *Applied Physics Letters*, vol. 105, no. 14, p. 143106, 2014.

[393] L. Zagonel, L. Tizei, G. Vitiello, G. Jacopin, L. Rigutti, M. Tchernycheva, F. Julien, R. Songmuang, T. Ostasevicius, F. de la Peña, *et al.*, Nanometer-scale monitoring of quantum-confined Stark effect and emission efficiency droop in multiple GaN/AlN quantum disks in nanowires *Physical Review B*, vol. 93, no. 20, p. 205410, 2016.

[394] I. R. Lewis and H. Edwards, *Handbook of Raman spectroscopy: from the research laboratory to the process line*. CRC Press (Boca Raton), 2001.

[395] H. Harima, Properties of GaN and related compounds studied by means of Raman scattering *Journal of Physics: Condensed Matter*, vol. 14, no. 38, p. R967, 2002.

[396] A. Cros, H. Angerer, O. Ambacher, M. Stutzmann, R. Höpler, and T. Metzger, Raman study of the optical phonons in AlxGa1-xN alloys *Solid state communications*, vol. 104, no. 1, pp. 35–39, 1997.

[397] V. Y. Davydov, I. Goncharuk, A. Smirnov, A. Nikolaev, W. Lundin, A. Usikov, A. Klochikhin, J. Aderhold, J. Graul, O. Semchinova, *et al.*, Composition dependence of optical phonon energies and Raman line broadening in hexagonal AlxGa1-xN alloys *Physical Review B*, vol. 65, no. 12, p. 125203, 2002.

[398] M. Wölz, J. Lähnemann, O. Brandt, V. M. Kaganer, M. Ramsteiner, C. Pfüller, C. Hauswald, C. N. Huang, L. Geelhaar, and H. Riechert, Correlation between In content and emission wavelength of InxGa1-xN/GaN nanowire heterostructures *Nanotechnology*, vol. 23, no. 45, p. 455203, 2012.

[399] M. Gómez-Gómez, N. Garro, J. Segura-Ruiz, G. Martinez-Criado, A. Cantarero, H. Mengistu, A. Garcá-Cristóbal, S. Murcia-Mascarós, C. Denker, J. Malindretos, *et al.*, Spontaneous core-shell elemental distribution in In-rich InxGa1-xN nanowires grown by molecular beam epitaxy *Nanotechnology*, vol. 25, no. 7, p. 075705, 2014.

[400] J. Segura-Ruiz, G. Martnez-Criado, C. Denker, J. Malindretos, and A. Rizzi, Phase Separation in Single InxGa1-xN Nanowires Revealed through a Hard X-ray Synchrotron Nanoprobe *Nano letters*, vol. 14, no. 3, pp. 1300–1305, 2014.

[401] M. Ebaid, J.-H. Kang, Y.-S. Yoo, S.-H. Lim, Y.-H. Cho, and S.-W. Ryu, Vertically aligned InGaN nanowires with engineered axial In composition for highly efficient visible light emission *Scientific reports*, vol. 5, p. 17003, 2015.

[402] T. Stankevic, E. Hilner, F. Seiboth, R. Ciechonski, G. Vescovi, O. Kryliouk, U. Johansson, L. Samuelson, G. Wellenreuther, G. Falkenberg, *et al.*, Fast Strain Mapping of Nanowire Light-Emitting Diodes Using Nanofocused X-ray Beams. *ACS nano*, vol. 9, no. 7, p. 6978, 2015.

[403] Ž. Gacevic, N. Vukmirovic, N. Garcá-Lepetit, A. Torres-Pardo, M. Müller, S. Metzner, S. Albert, A. Bengoechea-Encabo, F. Bertram, P. Veit, *et al.*, Influence of composition, strain, and electric field anisotropy on different emission colors and recombination dynamics from InGaN nanodisks in pencil-like GaN nanowires *Physical Review B*, vol. 93, no. 12, p. 125436, 2016.

[404] E. A. Serban, P. O. Å. Persson, I. Poenaru, M. Junaid, L. Hultman, J. Birch, and C.-L. Hsiao, Structural and compositional evolutions of InxAl1-xN core-shell nanorods grown on Si (111) substrates by reactive magnetron sputter epitaxy *Nanotechnology*, vol. 26, no. 21, p. 215602, 2015.

[405] Q. S. Paduano, D. W. Weyburne, L. O. Bouthillette, S.-Q. Wang, and M. N. Alexander, The Energy Band Gap of AlxGa1-xN *Japanese Journal of Applied Physics*, vol. 41, p. 1936, 2002.

[406] M. Albrecht, L. Lymperakis, J. Neugebauer, J. Northrup, L. Kirste, M. Leroux, I. Grzegory, S. Porowski, and H. Strunk, Chemically ordered AlxGa1-xN alloys: Spontaneous formation of natural quantum wells *Physical Review. B, Condensed Matter and Materials Physics*, vol. 71, no. 3, pp. 035314–035314, 2005.

[407] C. Collins, A. Sampath, G. Garrett, W. Sarney, H. Shen, M. Wraback, A. Y. Nikiforov, G. Cargill III, and V. Dierolf, Enhanced room-temperature luminescence efficiency through carrier localization in AlxGa1-xN alloys *Applied Physics Letters*, vol. 86, no. 3, p. 031916, 2005.

[408] H. Kim, R. Mair, J. Li, J. Lin, and H. Jiang, Time-resolved photoluminescence studies of AlxGa1-xN alloys *Applied Physics Letters*, vol. 76, no. 10, pp. 1252–1254, 2000.

[409] J. Mickevicius, R. Aleksiejunas, A. Kadys, J. Jurkevicius, G. Tamulaitis, M. Shur, M. Shatalov, J. Yang, R. Gaska, *et al.*, Nonradiative Recombination, Carrier Localization, and Emission Efficiency of AlGaN Epilayers with Different Al Content *Journal of Electronic Materials*, vol. 44, no. 12, p. 4706, 2015.

[410] J. Mickevicius, G. Tamulaitis, M. Shur, M. Shatalov, J. Yang, and R. Gaska, Internal quantum efficiency in AlGaN with strong carrier localization *Applied Physics Letters*, vol. 101, no. 21, p. 211902, 2012.

[411] N. Grandjean, J. Massies, P. Vennegues, M. Leroux, F. Demangeot, M. Renucci, and J. Frandon, Molecular-beam epitaxy of gallium nitride on (0001) sapphire substrates using ammonia *Journal of applied physics*, vol. 83, no. 3, pp. 1379–1383, 1998.

[412] G. Parish, S. Keller, S. Denbaars, and U. Mishra, SIMS investigations into the effect of growth conditions on residual impurity and silicon incorporation in GaN and AlxGa1-xN *Journal of Electronic Materials*, vol. 29, no. 1, pp. 15–20, 2000.

[413] J. M. Hollas, *Modern spectroscopy*. John Wiley & Sons (Berlin), 2004.

[414] D. Gammon, E. Snow, B. Shanabrook, D. Katzer, and D. Park, Homogeneous linewidths in the optical spectrum of a single gallium arsenide quantum dot *Science*, vol. 273, no. 5271, p. 87, 1996.

[415] R. Bardoux, T. Guillet, P. Lefebvre, T. Taliercio, T. Bretagnon, S. Rousset, B. Gil, and F. Semond, Photoluminescence of single GaN/AlN hexagonal quantum dots on Si (111): Spectral diffusion effects *Physical Review B*, vol. 74, no. 19, p. 195319, 2006.

[416] F. Rol, S. Founta, H. Mariette, B. Daudin, L. S. Dang, J. Bleuse, D. Peyrade, J.-M. Gérard, and B. Gayral, Probing exciton localization in nonpolar GaN/AlN quantum dots by single-dot optical spectroscopy *Physical Review B*, vol. 75, no. 12, p. 125306, 2007.

[417] M. Belloeil, B. Gayral, and B. Daudin, Quantum dot-like behavior of compositional fluctuations in AlGaN nanowires *Nano letters*, vol. 16, no. 2, pp. 960–966, 2016.

[418] S. Kako, C. Santori, K. Hoshino, S. Götzinger, Y. Yamamoto, and Y. Arakawa, A gallium nitride single-photon source operating at 200 K *Nature materials*, vol. 5, no. 11, pp. 887–892, 2006.

[419] N. Akopian, G. Patriarche, L. Liu, J.-C. Harmand, and V. Zwiller, Crystal phase quantum dots *Nano letters*, vol. 10, no. 4, pp. 1198–1201, 2010.

[420] S. Yang, K. Ding, X. Dou, X. Wu, Y. Yu, H. Ni, Z. Niu, D. Jiang, S.-S. Li, J.-W. Luo, *et al.*, Zinc-blende and wurtzite GaAs quantum dots in nanowires studied using hydrostatic pressure *Physical Review B*, vol. 92, no. 16, p. 165315, 2015.

[421] M. Ikezawa, Y. Sakuma, L. Zhang, Y. Sone, T. Mori, T. Hamano, M. Watanabe, K. Sakoda, and Y. Masumoto, Single-photon generation from a nitrogen impurity center in GaAs *Applied physics letters*, vol. 100, no. 4, p. 042106, 2012.

[422] M. Jo, T. Mano, T. Kuroda, Y. Sakuma, and K. Sakoda, Visible single-photon emission from a nitrogen impurity center in AlAs *Applied Physics Letters*, vol. 102, no. 6, p. 062107, 2013.

[423] S. Minari, L. Cavigli, F. Sarti, M. Abbarchi, N. Accanto, G. M. Matutano, S. Bietti, S. Sanguinetti, A. Vinattieri, and M. Gurioli, Single photon emission from impurity centers in AlGaAs epilayers on Ge and Si substrates *Applied physics letters*, vol. 101, no. 17, p. 172105, 2012.

[424] G. Popovici, W. Kim, A. Botchkarev, H. Tang, H. Morkoc, and J. Solomon, Impurity contamination of GaN epitaxial films from the sapphire, SiC and ZnO substrates *Applied physics letters*, vol. 71, no. 23, pp. 3385–3387, 1997.

[425] Z. Fang, E. Robin, E. Rozas-Jiménez, A. Cros, F. Donatini, N. Mollard, J. Pernot, and B. Daudin, Si donor incorporation in GaN nanowires *Nano letters*, vol. 15, no. 10, pp. 6794–6801, 2015.

[426] K. Chen, Y. Xi, F. Mont, J. Kim, E. Schubert, W. Liu, X. Li, and J. Smart, Recombination dynamics in ultraviolet light-emitting diodes with Si-doped AlxGa1-xN/ AlyGa1-yN multiple quantum well active regions *Journal of applied physics*, vol. 101, no. 11, p. 113102, 2007.

[427] T. Schulz, M. Albrecht, K. Irmscher, C. Hartmann, J. Wollweber, and R. Fornari, Ultraviolet luminescence in AlN *physica status solidi (b)*, vol. 248, no. 6, pp. 1513–1518, 2011.

[428] R. Kittaka, H. Muto, H. Murotani, Y. Yamada, H. Miyake, and K. Hiramatsu, Huge binding energy of localized biexcitons in Al-rich AlxGa1-xN ternary alloys *Applied Physics Letters*, vol. 98, no. 8, p. 1907, 2011.

[429] Y. Yamada, K. Choi, S. Shin, H. Murotani, T. Taguchi, N. Okada, and H. Amano, Photoluminescence from highly excited AlN epitaxial layers *Applied Physics Letters*, vol. 92, no. 13, 2008.

[430] Y. Hayakawa, T. Fukuno, K. Nakamura, H. Miyake, K. Hiramatsu, and Y. Yamada, Binding energy of localized biexcitons in AlGaN-based quantum wells *Applied Physics Express*, vol. 7, no. 12, p. 122101, 2014.

[431] D. Hirano, T. Tayagaki, Y. Yamada, and Y. Kanemitsu, Dynamics of biexciton localization in AlxGa1-xN mixed crystals under exciton resonant excitation *Physical Review B*, vol. 77, no. 19, p. 193203, 2008.

[432] D. Hirano, T. Tayagaki, Y. Yamada, and Y. Kanemitsu, Composition dependent dynamics of biexciton localization in AlxGa1-xN mixed crystals *Physical Review B*, vol. 80, no. 7, p. 075205, 2009.

[433] Y. Shen, G. Mueller, S. Watanabe, N. Gardner, A. Munkholm, and M. Krames, Auger recombination in InGaN measured by photoluminescence *Applied Physics Letters*, vol. 91, no. 14, p. 141101, 2007.

[434] Q. Dai, M. F. Schubert, M.-H. Kim, J. K. Kim, E. Schubert, D. D. Koleske, M. H. Crawford, S. R. Lee, A. J. Fischer, G. Thaler, *et al.*, Internal quantum efficiency and nonradiative recombination coefficient of GaInN/GaN multiple quantum wells with different dislocation densities *Applied Physics Letters*, vol. 94, no. 11, p. 111109, 2009.

[435] H. Zhao, G. Liu, J. Zhang, J. D. Poplawsky, V. Dierolf, and N. Tansu, Approaches for high internal quantum efficiency green InGaN light-emitting diodes with large overlap quantum wells *Optics express*, vol. 19, no. 104, pp. A991–A1007, 2011.

[436] H. Zhao, G. Liu, J. Zhang, R. A. Arif, and N. Tansu, Analysis of internal quantum efficiency and current injection efficiency in III-nitride light-emitting diodes *Journal of Display Technology*, vol. 9, no. 4, pp. 212–225, 2013.

[437] M. Gurioli, A. Vinattieri, M. Colocci, C. Deparis, J. Massies, G. Neu, A. Bosacchi, and S. Franchi, Temperature dependence of the radiative and nonradiative recombination time in GaAs/AlxGa1-xAs quantum-well structures *Physical Review B*, vol. 44, no. 7, p. 3115, 1991.

[438] B. Amstatt, J. Renard, C. Bougerol, E. Bellet-Amalric, B. Gayral, and B. Daudin, Growth of m-plane GaN quantum wires and quantum dots on m-plane 6H-SiC *Journal of Applied Physics*, vol. 102, no. 7, p. 4913, 2007.

[439] E. Rashba and G. Gurgenishvili, Edge absorption theory in semiconductors *Soviet Physics-Solid State*, vol. 4, no. 4, pp. 759–760, 1962.

[440] C. Henry and K. Nassau, Lifetimes of bound excitons in CdS *Physical Review B*, vol. 1, no. 4, p. 1628, 1970.

[441] M. G. Bawendi, M. L. Steigerwald, and L. E. Brus, The quantum mechanics of larger semiconductor clusters ("quantum dots") *Annual Review of Physical Chemistry*, vol. 41, no. 1, pp. 477–496, 1990.

[442] R. C. Hilborn, Einstein coefficients, cross sections, f values, dipole moments, and all that *American Journal of Physics*, vol. 50, no. 11, pp. 982–986, 1982.

[443] L. C. Andreani, G. Panzarini, and J.-M. Gérard, Strong-coupling regime for quantum boxes in pillar microcavities: Theory *Physical Review B*, vol. 60, no. 19, p. 13276, 1999.

[444] J. Hours, P. Senellart, E. Peter, A. Cavanna, and J. Bloch, Exciton radiative lifetime controlled by the lateral confinement energy in a single quantum dot *Physical Review B*, vol. 71, no. 16, p. 161306, 2005.

[445] E. O. Kane, Band structure of indium antimonide *Journal of Physics and Chemistry of Solids*, vol. 1, no. 4, pp. 249–261, 1957.

[446] S. Chuang and C. Chang, kâ‹… p method for strained wurtzite semiconductors *Physical Review B*, vol. 54, no. 4, p. 2491, 1996.

[447] J. Im, A. Moritz, F. Steuber, V. Härle, F. Scholz, and A. Hangleiter, Radiative carrier lifetime, momentum matrix element, and hole effective mass in GaN *Applied physics letters*, vol. 70, no. 5, pp. 631–633, 1997.

[448] A.-L. Henneghien, G. Tourbot, B. Daudin, O. Lartigue, Y. Desieres, and J.-M. Gérard, Optical anisotropy and light extraction efficiency of MBE grown GaN nanowires epilayers *Optics Express*, vol. 19, no. 2, pp. 527–539, 2011.

[449] S. Keller and S. P. DenBaars, Metalorganic chemical vapor deposition of group III nitrides-a discussion of critical issues *Journal of crystal growth*, vol. 248, pp. 479–486, 2003.

[450] X. Wang, D. Zhao, D. Jiang, H. Yang, J. Liang, U. Jahn, and K. Ploog, Al compositional inhomogeneity of AlGaN epilayer with a high Al composition grown by metal-organic chemical vapour deposition *Journal of Physics: Condensed Matter*, vol. 19, no. 17, p. 176005, 2007.

[451] A. Pinos, V. Liuolia, S. Marcinkevicius, J. Yang, R. Gaska, and M. Shur, Localization potentials in AlGaN epitaxial films studied by scanning near-field optical spectroscopy *Journal of Applied Physics*, vol. 109, no. 11, p. 113516, 2011.

[452] A. Pinos, S. Marcinkevicius, V. Liuolia, J. Yang, R. Gaska, and M. S. Shur, Scanning near-field optical spectroscopy of AlGaN epitaxial layers *physica status solidi (c)*, vol. 9, no. 7, pp. 1617–1620, 2012.

[453] Q. Li and G. T. Wang, Strain influenced indium composition distribution in GaN/InGaN core-shell nanowires *Applied Physics Letters*, vol. 97, no. 18, p. 181107, 2010.

[454] C. Leclere, N. Katcho, G. Tourbot, B. Daudin, M. Proietti, and H. Renevier, Anisotropic In distribution in InGaN core-shell nanowires *Journal of Applied Physics*, vol. 116, no. 1, p. 013517, 2014.

[455] M. Kumar, T. N. Bhat, B. Roul, M. K. Rajpalke, A. Kalghatgi, and S. Krupanidhi, Carrier concentration dependence of donor activation energy in n-type GaN epilayers grown on Si (111) by plasma-assisted MBE *Materials Research Bulletin*, vol. 47, no. 6, pp. 1306–1309, 2012.

[456] J. L. Lyons, A. Janotti, and C. G. Van de Walle, Shallow versus deep nature of Mg acceptors in nitride semiconductors *Physical review letters*, vol. 108, no. 15, p. 156403, 2012.

[457] S. Brochen, J. Brault, S. Chenot, A. Dussaigne, M. Leroux, and B. Damilano, Dependence of the Mg-related acceptor ionization energy with the acceptor concentration in p-type GaN layers grown by molecular beam epitaxy *Applied Physics Letters*, vol. 103, no. 3, p. 032102, 2013.

[458] Y. Taniyasu, M. Kasu, and T. Makimoto, Electrical conduction properties of n-type Si-doped AIN with high electron mobility (> 100 cm2 V-1 s-1) *Applied physics letters*, vol. 85, no. 20, pp. 4672–4674, 2004.

[459] Y. Taniyasu, M. Kasu, and T. Makimoto, An aluminium nitride light-emitting diode with a wavelength of 210 nanometres *Nature*, vol. 441, no. 7091, pp. 325–328, 2006.

[460] B. Neuschl, K. Thonke, M. Feneberg, R. Goldhahn, T. Wunderer, Z. Yang, N. Johnson, J. Xie, S. Mita, A. Rice, *et al.*, Direct determination of the silicon donor ionization energy in homoepitaxial AlN from photoluminescence two-electron transitions *Applied Physics Letters*, vol. 103, no. 12, p. 122105, 2013.

[461] A. Polyakov, N. Smirnov, A. Govorkov, M. Mil'Vidskii, J. Redwing, M. Shin, M. Skowronski, D. Greve, and R. Wilson, Properties of Si donors and persistent photoconductivity in AlGaN *Solid-State Electronics*, vol. 42, no. 4, pp. 627–635, 1998.

[462] C. Stampfl and C. G. Van de Walle, Doping of AlxGa1-xN *Applied Physics Letters*, vol. 72, no. 4, pp. 459–461, 1998.

[463] Y. Taniyasu, M. Kasu, and N. Kobayashi, Intentional control of n-type conduction for Si-doped AlN and AlxGa1-xN (0.42<=x<1) *Applied physics letters*, vol. 81, pp. 1255–1257, 2002.

[464] M. Nakarmi, K. Kim, K. Zhu, J. Lin, and H. Jianga, Transport properties of highly conductive n-type Al-rich AlxGa1-xN (x>=0.7) *Applied physics letters*, vol. 85, no. 17, 2004.

[465] C. G. Van de Walle and J. Neugebauer, First-principles calculations for defects and impurities: Applications to III-nitrides *Journal of Applied Physics*, vol. 95, no. 8, pp. 3851–3879, 2004.

[466] J. Li, T. Oder, M. Nakarmi, J. Lin, and H. Jiang, Optical and electrical properties of Mg-doped p-type AlxGa1-xN *Applied physics letters*, vol. 80, no. 7, pp. 1210–1212, 2002.

[467] M. Nakarmi, N. Nepal, J. Lin, and H. Jiang, Photoluminescence studies of impurity transitions in Mg-doped AlGaN alloys *Applied Physics Letters*, vol. 94, no. 9, p. 91903, 2009.

[468] S. Nakamura, N. Iwasa, M. Senoh, and T. Mukai, Hole compensation mechanism of p-type GaN films *Japanese Journal of Applied Physics*, vol. 31, no. 5R, p. 1258, 1992.

[469] S. Nakamura, T. Mukai, M. Senoh, and N. Iwasa, Thermal annealing effects on p-type Mg-doped GaN films *Japanese Journal of Applied Physics*, vol. 31, no. 2B, p. L139, 1992.

[470] W. Götz, N. Johnson, J. Walker, D. Bour, and R. Street, Activation of acceptors in Mg-doped GaN grown by metalorganic chemical vapor deposition *Applied Physics Letters*, vol. 68, no. 5, pp. 667–669, 1996.

[471] C. Wang and R. F. Davis, Deposition of highly resistive, undoped, and p-type, magnesium-doped gallium nitride films by modified gas source molecular beam epitaxy *Applied physics letters*, vol. 63, no. 7, pp. 990–992, 1993.

[472] W. Kim, A. Salvador, A. Botchkarev, O. Aktas, S. N. Mohammad, and H. Morcoc, Mg-doped p-type GaN grown by reactive molecular beam epitaxy *Applied physics letters*, vol. 69, no. 4, pp. 559–561, 1996.

[473] S. Bradley, S. Goss, L. Brillson, J. Hwang, and W. Schaff, Deep level defects and doping in high Al mole fraction AlGaN *Journal of Vacuum Science & Technology B*, vol. 21, no. 6, pp. 2558–2563, 2003.

[474] K. Nam, M. Nakarmi, J. Lin, and H. Jiang, Deep impurity transitions involving cation vacancies and complexes in AlGaN alloys *Applied Physics Letters*, vol. 86, no. 22, pp. 222108–222108, 2005.

[475] N. Nepal, M. Nakarmi, J. Lin, and H. Jiang, Photoluminescence studies of impurity transitions in AlGaN alloys *Applied physics letters*, vol. 89, no. 9, p. 092107, 2006.

[476] R. Collazo, S. Mita, J. Xie, A. Rice, J. Tweedie, R. Dalmau, and Z. Sitar, Progress on n-type doping of AlGaN alloys on AlN single crystal substrates for UV optoelectronic applications *physica status solidi (c)*, vol. 8, no. 7-8, pp. 2031–2033, 2011.

[477] S. Hautakangas, J. Oila, M. Alatalo, K. Saarinen, L. Liszkay, D. Seghier, and H. Gislason, Vacancy defects as compensating centers in Mg-doped GaN *Physical review letters*, vol. 90, no. 13, p. 137402, 2003.

[478] J. Kim, E. Waldron, Y.-L. Li, T. Gessmann, E. Schubert, H. Jang, and J.-L. Lee, P-type conductivity in bulk AlxGa1-xN and AlxGa1-xN/AlyGa1-yN superlattices with average Al mole fraction> 20% *Applied Physics Letters*, vol. 84, no. 17, pp. 3310–3312, 2004.

[479] M. Nakarmi, K. Kim, J. Li, J. Lin, and H. Jiang, Enhanced p-type conduction in GaN and AlGaN by Mg-δ-doping *Applied physics letters*, vol. 82, no. 18, pp. 3041–3043, 2003.

[480] J. Simon, V. Protasenko, C. Lian, H. Xing, and D. Jena, Polarization-induced hole doping in wide-band-gap uniaxial semiconductor heterostructures *Science*, vol. 327, no. 5961, pp. 60–64, 2010.

[481] S. Li, M. Ware, J. Wu, P. Minor, Z. Wang, Z. Wu, Y. Jiang, and G. J. Salamo, Polarization induced pn-junction without dopant in graded AlGaN coherently strained on GaN *Applied Physics Letters*, vol. 101, no. 12, p. 122103, 2012.

[482] S. Li, T. Zhang, J. Wu, Y. Yang, Z. Wang, Z. Wu, Z. Chen, and Y. Jiang, Polarization induced hole doping in graded AlxGa1-xN (x= 0.7-1) layer grown by molecular beam epitaxy *Applied Physics Letters*, vol. 102, no. 6, p. 062108, 2013.

[483] Z. Bryan, I. Bryan, B. E. Gaddy, P. Reddy, L. Hussey, M. Bobea, W. Guo, M. Hoffmann, R. Kirste, J. Tweedie, *et al.*, Fermi level control of compensating point defects during metalorganic chemical vapor deposition growth of Si-doped AlGaN *Applied Physics Letters*, vol. 105, no. 22, p. 222101, 2014.

[484] T. Kinoshita, T. Obata, H. Yanagi, and S.-i. Inoue, High p-type conduction in high-Al content Mg-doped AlGaN *Applied Physics Letters*, vol. 102, no. 1, p. 012105, 2013.

[485] S. Zhao, S. Fathololoumi, K. Bevan, D. Liu, M. Kibria, Q. Li, G. Wang, H. Guo, and Z. Mi, Tuning the surface charge properties of epitaxial InN nanowires *Nano letters*, vol. 12, no. 6, pp. 2877–2882, 2012.

[486] S. Zhao, B. Le, D. Liu, X. Liu, M. Kibria, T. Szkopek, H. Guo, and Z. Mi, p-Type InN nanowires *Nano letters*, vol. 13, no. 11, pp. 5509–5513, 2013.

[487] Z. Chine, A. Rebey, H. Touati, E. Goovaerts, M. Oueslati, B. E. Jani, and S. Laugt, Stress and density of defects in Si-doped GaN *physica status solidi (a)*, vol. 203, no. 8, pp. 1954–1961, 2006.

[488] K. Forghani, L. Schade, U. T. Schwarz, F. Lipski, O. Klein, U. Kaiser, and F. Scholz, Strain and defects in Si-doped (Al)GaN epitaxial layers *Journal of Applied Physics*, vol. 112, no. 9, p. 093102, 2012.

[489] J. Sánchez-Páramo, J. Calleja, M. Sánchez-Garcá, and E. Calleja, Optical investigation of strain in Si-doped GaN films *Applied Physics Letters*, vol. 78, p. 4124, 2001.

[490] P. Vennegues, M. Benaissa, B. Beaumont, E. Feltin, P. De Mierry, S. Dalmasso, M. Leroux, and P. Gibart, Pyramidal defects in metalorganic vapor phase epitaxial Mg doped GaN *Applied Physics Letters*, vol. 77, no. 6, pp. 880–882, 2000.

[491] A. Bell, R. Liu, F. Ponce, H. Amano, I. Akasaki, and D. Cherns, Light emission and microstructure of Mg-doped AlGaN grown on patterned sapphire *Applied physics letters*, vol. 82, no. 3, pp. 349–351, 2003.

[492] F. Schuster, A. Winnerl, S. Weiszer, M. Hetzl, J. A. Garrido, and M. Stutzmann, Doped GaN nanowires on diamond: Structural properties and charge carrier distribution *Journal of Applied Physics*, vol. 117, no. 4, pp. 044307–044307, 2015.

[493] Z. Fang, *GaN nanowires: from growth to electrical properties*. PhD thesis, Université Grenoble Alpes, 2017.

[494] J. Neugebauer, Surfactants and antisurfactants on group-III-nitride surfaces *physica status solidi (c)*, no. 6, pp. 1651–1667, 2003.

[495] T. Cheng, S. Novikov, C. Foxon, and J. Orton, Mechanisms of magnesium incorporation into GaN layers grown by molecular beam epitaxy *Solid state communications*, vol. 109, no. 7, pp. 439–443, 1999.

[496] E. Monroy, T. Andreev, P. Holliger, E. Bellet-Amalric, T. Shibata, M. Tanaka, and B. Daudin, Modification of GaN (0001) growth kinetics by Mg doping *Applied physics letters*, vol. 84, no. 14, pp. 2554–2556, 2004.

[497] M. Tchernycheva, V. Neplokh, H. Zhang, P. Lavenus, L. Rigutti, F. Bayle, F. Julien, A. Babichev, G. Jacopin, L. Largeau, *et al.*, Core-shell InGaN/GaN nanowire light emitting diodes analyzed by electron beam induced current microscopy and cathodoluminescence mapping *Nanoscale*, vol. 7, no. 27, pp. 11692–11701, 2015.

[498] L. Rigutti, Semiconductor Nanowires *Wiley Encyclopedia of Electrical and Electronics Engineering* (New York), 2014.

[499] K. Saarinen, J. Nissilä, P. Hautojärvi, J. Likonen, T. Suski, I. Grzegory, B. Lucznik, and S. Porowski, The influence of Mg doping on the formation of Ga vacancies and negative ions in GaN bulk crystals *Applied physics letters*, vol. 75, no. 16, pp. 2441–2443, 1999.

[500] A. Uedono, K. Tenjinbayashi, T. Tsutsui, Y. Shimahara, H. Miyake, K. Hiramatsu, N. Oshima, R. Suzuki, and S. Ishibashi, Native cation vacancies in Si-doped AlGaN studied by monoenergetic positron beams *Journal of Applied Physics*, vol. 111, no. 1, p. 013512, 2012.

[501] C. Stampfl and C. Van de Walle, Theoretical investigation of native defects, impurities, and complexes in aluminum nitride *Physical Review B*, vol. 65, no. 15, p. 155212, 2002.

[502] H. Hu, Z. Wu, W. Zhang, H. Li, R. Zhuo, D. Yan, J. Wang, and P. Yan, Effect of Mg doping on growth and photoluminescence of AlN hexagonal nanorods *Journal of Alloys and Compounds*, vol. 624, pp. 241–246, 2015.

[503] Q. Sun, A. Selloni, T. Myers, and W. A. Doolittle, Energetics of Mg incorporation at GaN (0001) and GaN (0001) surfaces *Physical Review B*, vol. 73, no. 15, p. 155337, 2006.

[504] V. Jindal and F. Shahedipour-Sandvik, Theoretical prediction of GaN nanostructure equilibrium and nonequilibrium shapes *Journal of Applied Physics*, vol. 106, no. 8, p. 083115, 2009.

[505] M. Brandt, J. Ager III, W. Götz, N. Johnson, J. Harris Jr, R. Molnar, and T. Moustakas, Local vibrational modes in Mg-doped gallium nitride *Physical Review B*, vol. 49, no. 20, p. 14758, 1994.

[506] A. Kaschner, H. Siegle, G. Kaczmarczyk, M. Strassburg, A. Hoffmann, C. Thomsen, U. Birkle, S. Einfeldt, and D. Hommel, Local vibrational modes in Mg-doped GaN grown by molecular beam epitaxy *Applied physics letters*, vol. 74, no. 22, pp. 3281–3283, 1999.

[507] B. Monemar, P. Paskov, G. Pozina, C. Hemmingsson, J. Bergman, S. Khromov, V. Izyumskaya, V. Avrutin, X. Li, H. Morkoç, *et al.*, Properties of the main Mg-related acceptors in GaN from optical and structural studies *Journal of Applied Physics*, vol. 115, no. 5, p. 053507, 2014.

[508] M. A. Reshchikov, D. Demchenko, J. McNamara, S. Fernández-Garrido, and R. Calarco, Green luminescence in Mg-doped GaN *Physical Review B*, vol. 90, no. 3, p. 035207, 2014.

[509] M. Reshchikov, F. Shahedipour-Sandvik, B. Messer, V. Jindal, N. Tripathi, and M. Tungare, Defect-related photoluminescence in Mg-doped GaN nanostructures *Physica B: Condensed Matter*, vol. 404, no. 23, pp. 4903–4906, 2009.

[510] P. Huang, C. Chen, J. Chen, G. Chi, C. Pan, C. Kuo, L. Chen, C. Hsu, K. Chen, S. Hung, *et al.*, Optical and structural properties of Mg-ion implanted GaN nanowires *Vacuum*, vol. 83, no. 5, pp. 797–800, 2009.

[511] S. N. Das, S. Patra, J. P. Kar, M.-J. Lee, S. H. Hwang, T. I. Lee, and J.-M. Myoung, Growth and characterization of Mg-doped GaN nanowire synthesized by the thermal evaporation method *Materials Letters*, no. 106, pp. 352–355, 2013.

[512] Y.-H. Kwon, S. Shee, G. Gainer, G. Park, S. Hwang, and J. Song, Time-resolved study of yellow and blue luminescence in Si-and Mg-doped GaN *Applied Physics Letters*, vol. 76, no. 7, pp. 840–842, 2000.

[513] Y. Kamiura, M. Kaneshiro, J. Tamura, T. Ishiyama, Y. Yamashita, T. Mitani, and T. Mukai, Enhancement of blue emission from mg-doped GaN using remote plasma containing atomic hydrogen *Japanese journal of applied physics*, vol. 44, no. 7L, p. L926, 2005.

[514] S. Deshpande, J. Heo, A. Das, and P. Bhattacharya, Electrically driven polarized single-photon emission from an InGaN quantum dot in a GaN nanowire *Nature communications*, vol. 4, p. 1675, 2013.

[515] S. Deshpande, A. Das, and P. Bhattacharya, Blue single photon emission up to 200 K from an InGaN quantum dot in AlGaN nanowire *Applied Physics Letters*, vol. 102, no. 16, p. 161114, 2013.

[516] M. Heiss, Y. Fontana, A. Gustafsson, G. Wüst, C. Magen, D. O'regan, J. Luo, B. Ketterer, S. Conesa-Boj, A. Kuhlmann, *et al.*, Self-assembled quantum dots in a nanowire system for quantum photonics *Nature materials*, vol. 12, no. 5, pp. 439–444, 2013.

[517] L. Tizei and M. Kociak, Spatially resolved quantum nano-optics of single photons using an electron microscope *Physical review letters*, vol. 110, no. 15, p. 153604, 2013.

[518] S. Meuret, L. Tizei, T. Cazimajou, R. Bourrellier, H. Chang, F. Treussart, and M. Kociak, Photon bunching in cathodoluminescence *Physical review letters*, vol. 114, no. 19, p. 197401, 2015.

[519] N. Jeon, B. Loitsch, S. Morkoetter, G. Abstreiter, J. Finley, H. J. Krenner, G. Koblmueller, and L. J. Lauhon, Alloy fluctuations act as quantum dot-like emitters in GaAs-AlGaAs core-shell nanowires *ACS nano*, vol. 9, no. 8, pp. 8335–8343, 2015.

[520] F. Frank, On Miller-Bravais indices and four-dimensional vectors *Acta Crystallographica*, vol. 18, no. 5, pp. 862–866, 1965.

[521] H. C. Adelmann, *Growth and strain relaxation mechanisms of group III nitride heterostructures*. PhD thesis, Université Joseph Fourier (Grenoble), 2002.

[522] V. Favre-Nicolin, M. Proietti, C. Leclere, N. Katcho, M.-I. Richard, and H. Renevier, Multiwavelength anomalous diffraction and diffraction anomalous fine structure to study composition and strain of semiconductor nanostructures *The European Physical Journal Special Topics*, vol. 208, no. 1, pp. 189–216, 2012.

[523] S. Guillemin, R. Parize, J. Carabetta, V. Cantelli, D. Albertini, B. Gautier, G. Brémond, D. D.Fong, H. Renevier, and V. Consonni, Quantitative and simultaneous analysis of the polarity of polycrystalline ZnO seed layers and related nanowires grown by wet chemical deposition *Nanotechnology*, vol. 28, no. 9, p. 095704, 2017.

[524] B. Ravel and M. Newville, ATHENA, ARTEMIS, HEPHAESTUS: data analysis for X-ray absorption spectroscopy using IFEFFIT *Journal of synchrotron radiation*, vol. 12, no. 4, pp. 537–541, 2005.

[525] M. Proietti, H. Renevier, J. Hodeau, J. Garcia, J. Bérar, and P. Wolfers, Diffraction-anomalous-fine-structure spectroscopy applied to the study of III-V strained semiconductors *Physical Review B*, vol. 59, no. 8, p. 5479, 1999.

Abstract

Using specific conditions, AlGaN nanowire (NW) sections can be grown in epitaxy on top of self-induced GaN NW templates. Such NW growth, performed by plasma-assisted molecular beam epitaxy in the present case, allows the subsequent characterization of very small volume of material free of extended defects commonly observed in planar structures. This absence of defects makes these NWs very promising for optoelectronic devices operating in the ultraviolet. However, achieving such devices requires a better understanding of the NW fundamental properties.

The issue of alloy inhomogeneity at nanoscale has notably remained obscure so far. In order to make it clearer, the latter has been first investigated in the present work, especially through optical characterization at the single nanowire level. For our experiments, non-intentionally doped (NID) AlGaN NWs have been grown in various conditions in order to potentially tune the compositional fluctuations within the AlGaN alloy and therefore possibly probe for carrier localization centers of different size and Al composition. It has been firstly observed through structural characterization that the length of Al-rich sections preferentially nucleating on top of GaN NWs can be tuned by varying the growth kinetical parameters, emphasizing a growth mechanism governed by kinetics. Optical studies have then evidenced that compositional fluctuations induce carrier localization and exhibit a quantum dot-like behavior. The latter has been observed whatever the growth conditions explored in this work. Our results are consistent with the spontaneous formation during growth of tiny Ga-richer regions shown to share similar micro-optical features over a given emission wavelength range for all investigated growth conditions. Such regions exhibiting the single-photon emission character are present at very small scale, as signs of their existence have been also evidenced in thin NID AlGaN quantum disks.

In addition, doping in Al(Ga)N NW, especially p-type, is far from being fully understood. In particular, the issue of dopant incorporation as well as optical and electrical activation in such NWs remains unclear. The latter has been examined in Al(Ga)N NW pn junctions doped with Mg and Si atoms. First, signatures specific to dopant incorporation in NWs have been highlighted through structural characterization, before evidencing AlGaN pn junctions electrically. Moreover, optical analysis have revealed particular signature for both dopant types. Nonetheless, Mg dopants are but partially active electrically due to passivation by hydrogen emphasized by the observation of Mg-H complexes. To cope with the latter issue, post-growth annealing experiments have been attempted. Concomitantly, AlN NW pn junctions have been also preliminarily investigated and present interesting morphological features. Indeed, deep hollow cores have been observed in NWs and associated with Mg doping carried out at low growth temperature. The NW morphology can be tuned by varying growth kinetical parameters and by using the surfactant effect of Mg atoms. When increasing growth temperature, these hollow cores disappear, while the NW top shape has been observed to switch from hexagonal to star-like, emphasizing growth conditions very far from thermodynamical equilibrium. Electrical activation of dopants has not been evidenced so far in AlN NW pn junctions.

Keywords: AlGaN nanowires, MBE growth, optical characterization, UV emission, compositional fluctuations, doping

Résumé

Dans des conditions spécifiques, des sections nanofilaires d'AlGaN peuvent croître en épitaxie sur des bases nanofilaires de GaN auto-induites. De telles croissances, effectuées par épitaxie par jets moléculaires dans le cas présent, permettent la caractérisation ultérieure de petits volumes d'AlGaN exempt de défauts étendus communément observés dans les couches planaires. Cette absence de défauts rend ces fils prometteurs pour les dispositifs optoélectroniques émettant dans l'ultraviolet. Cependant, la réalisation de tels composants nécessite de mieux comprendre les propriétés fondamentales des fils.

La question des inhomogénéités d'alliage à l'échelle nanométrique reste notamment à éclaircir. Afin d'y voir plus clair, ces dernières ont été dans un premier temps étudiées dans cette thèse, particulièrement par des techniques de caractérisation optique à l'échelle du nanofil unique. Pour nos expériences, des nanofils d'AlGaN non-intentionnellement dopés (NID) ont été crûs dans des conditions variées afin d'ajuster potentiellement les fluctuations de composition de l'alliage et ainsi sonder éventuellement des centres de localisation de porteurs de taille et composition différentes. Il a premièrement été observé au moyen de méthodes de caractérisation structurale que la longueur des sections plus riches Al qui nucléent préférentiellement au sommet des fils de GaN peut être ajustée en variant les paramètres cinétiques de croissance, mettant en lumière un mécanisme de croissance gouverné par la cinétique. Des études optiques ont ensuite démontré que les fluctuations de composition induisent de la localisation et présentent un comportement de type boîte quantique. Ce dernier a été observé quel que soit les conditions de croissance explorées dans ce travail. Il est ensuite démontré que les régions plus riches Ga spontanément formés durant la synthèse de l'AlGaN partagent des propriétés µ-optiques similaires sur une plage de longueur d'onde d'émission donnée, pour toutes les conditions de croissance utilisées dans cette étude. De telles régions, émettrices de photons uniques, sont présentes à très petite échelle, puisque elles ont été également mises en évidence dans des nanodisques quantiques d'AlGaN très fins.

En outre, le dopage des nanofils d'AlGaN, surtout de type p, est loin d'être totalement compris. En particulier, En particulier, le problème de l'incorporation ainsi que de l'activation optique et électrique dans les fils demeure nébuleux. Cette question a été étudiée pour des jonctions pn nanofilaires d'AlGaN dopées avec des atomes Mg et Si. Premièrement, des signatures propres à l'incorporation des dopants dans les nanofils ont été mises en exergue au travers de techniques de caractérisation structurale, avant que des jonctions pn AlGaN soient mises en évidence électriquement. De plus, des analyses optiques ont mis en lumière une signature spécifique pour chaque type de dopants. Néanmoins, les dopants Mg ne sont que partiellement actifs électriquement en raison de la passivation par l'hydrogène mise en évidence par l'observation de complexes Mg-H. Pour résoudre ce problème, des recuits post-croissance ont été effectués. En parallèle, des jonctions pn nanofilaires d'AlN ont été préliminairement examinées et présentent des caractéristiques morphologiques intéressantes. En effet, des creux profonds ont été observés dans les fils et associés au dopage Mg effectué à basse température de croissance. La morphologie des fils peut être ajustée en jouant sur les paramètres cinétiques de croissance et sur l'effet surfactant des atomes Mg. En augmentant la température, les creux disparaissent tandis que la forme du sommet des fils, usuellement hexagonale, change pour devenir « étoilée », mettant en exergue des conditions de croissance très éloignées de l'équilibre thermodynamique. L'activation électrique des dopants n'a pas été observée jusqu'à présent dans ces jonctions pn d'AlN.

Mots clés: nanofils AlGaN, croissance EJM, caractérisation optique, émission UV, fluctuations de composition, dopage